Advances in Intelligent Systems and Computing 317

Jan Awrejcewicz
Roman Szewczyk
Maciej Trojnacki
Małgorzata Kaliczyńska *Editors*

Mechatronics: Ideas for Industrial Applications

Springer

Advances in Intelligent Systems and Computing

Volume 317

Series editor

Janusz Kacprzyk, Polish Academy of Sciences, Warsaw, Poland
e-mail: kacprzyk@ibspan.waw.pl

About this Series

The series "Advances in Intelligent Systems and Computing" contains publications on theory, applications, and design methods of Intelligent Systems and Intelligent Computing. Virtually all disciplines such as engineering, natural sciences, computer and information science, ICT, economics, business, e-commerce, environment, healthcare, life science are covered. The list of topics spans all the areas of modern intelligent systems and computing.

The publications within "Advances in Intelligent Systems and Computing" are primarily textbooks and proceedings of important conferences, symposia and congresses. They cover significant recent developments in the field, both of a foundational and applicable character. An important characteristic feature of the series is the short publication time and world-wide distribution. This permits a rapid and broad dissemination of research results.

Advisory Board

More information about this series at http://www.springer.com/series/11156

Jan Awrejcewicz · Roman Szewczyk
Maciej Trojnacki · Małgorzata Kaliczyńska
Editors

Mechatronics: Ideas for Industrial Applications

Springer

Editors
Jan Awrejcewicz
Lodz University of Technology
Lodz
Poland

Roman Szewczyk
Industrial Research Institute for Automation and Measurements PIAP
Warsaw
Poland

Maciej Trojnacki
Industrial Research Institute for Automation and Measurements PIAP
Warsaw
Poland

Małgorzata Kaliczyńska
Industrial Research Institute for Automation and Measurements PIAP
Warsaw
Poland

ISSN 2194-5357 ISSN 2194-5365 (electronic)
ISBN 978-3-319-10989-3 ISBN 978-3-319-10990-9 (eBook)
DOI 10.1007/978-3-319-10990-9

Library of Congress Control Number: 2014948177

Springer Cham Heidelberg New York Dordrecht London

Printed on acid-free paper

Springer is part of Springer Science+Business Media (www.springer.com)

Foreword

Broadly perceived control, automation, robotics and measuring techniques belong to the most relevant fields of science and technology, both from the point of view of theoretical challenges and practical importance. In spite of being separate areas of research, knowledge and expertise, they are strongly related, both in terms of paradigms and tools and techniques employed, as well as in terms of their industrial scope of applications. Therefore, an industrial, practice oriented perspective is an important aspect of those areas. Moreover, automation, robotics and measuring techniques have a significant innovative potential as the current industrial practice calls for a further integration of all kinds of production systems, more ecological and energy efficient solutions as well as cost and time effective production and manufacturing processes.

Among many important problems and challenges faced by automation and control, most of which have been reflected in the scope of the papers included in this volume, one can mention, for instance, discrete systems, actuators, diagnostics, and modern tools exemplified by fuzzy logic, evolutionary computation, neural networks, probabilistic approaches, etc.

In robotics, in particular in its part related to the development of mobile robots, one can quote as crucial problems and challenges various problem solving tasks related to the control of walking robots, control of manipulators, motors and drivers, mechatronic systems, and tracking control.

Measuring techniques and systems have to overcome, first of all, barriers implied by environmental conditions and limitations. They call for the development of novel sensors (also utilizing novel materials such as graphene), advanced signal processing and a more foundational development focused on the theory of metrology.

This book presents the recent advances and developments in control, automation, robotics, and measuring techniques that are trying to meet those challenges and to fulfil those technological, economic and social needs. It presents contributions of top experts in the fields, focused on both theory and industrial practice. The particular chapters present a deep analysis of a specific technical problem which is in general followed by a numerical analysis and simulation, and results of an implementation for the solution of a real world problem.

We strongly believe that the presented theoretical results, practical solutions and guidelines will be useful for both researchers working in the area of engineering sciences and for practitioners solving industrial problems.

Warsaw
July 2014

Jan Awrejcewicz
Roman Szewczyk
Maciej Trojnacki
Małgorzata Kaliczyńska

Contents

Part I: Control and Automation

Part II: Robotics

Part III: Measuring Techniques and Systems

Part IV: Mechatronics

About the Editors

Professor Jan Awrejcewicz has been graduated from the Lodz University of Technology (LUT) in 1977 (Mechanics) and from the University of Lodz in 1978 (Philosophy). He obtained PhD in 1981, DSc in 1990, and he became the full professor in 1997. Now he is a chair person of Department of Automation, Biomechanics and Mechatronics, head of a 4-years Doctoral School on Mechanics, and a head of the Mechatronics Study at LUT. His research area includes: nonlinear mechanics (analytical, numerical and experimental methods), continuous systems (plates, shells, beams, and structures), thermo-elasticity, mathematical methods in mechanics, asymptotic methods, dynamics of lumped mechanical systems, bifurcation and chaos, numerical methods as well as non-smooth and discontinuous systems. Prof. Awrejcewicz is an editor of 12 books and Guest-Editor of 18 journal special issues. He is the Editor of the Journal of Modeling, Simulation, Identification, and Control, Columbia International Publishing, USA. He supervised 20 PhD theses.

Professor Roman Szewczyk received both his PhD and DSc in the field of mechatronics. He is specializing in the modelling of properties of magnetic materials as well as in sensors and sensor interfacing, in particular magnetic sensors for security applications. He is the leading the development of a sensing unit for a mobile robot developed for the Polish Police Central Forensic Laboratory and of methods of non-destructive testing based on the magnetoelastic effect. Professor Szewczyk was involved in over 10 European Union funded research projects within the FP6 and FP7 as well as projects financed by the European Defence Organization. Moreover, he was leading two regional and national scale technological foresight projects and was active in the organization and implementation of technological transfer between companies and research institutes. Roman Szewczyk is Secretary for Scientific Affairs in the Industrial Research Institute for Automation and Measurements (PIAP). He is also Associate Professor at the Faculty of Mechatronics, Warsaw University of Technology and a Vice-chairman of the Academy of Young Researchers of the Polish Academy of Sciences.

Dr. Maciej Trojnacki received his MSc Eng. degree in aeronautic control systems in 1999 and his PhD degree in machine construction and use in 2003, both from the Faculty of Mechanical Engineering and Aeronautics, Rzeszow University of Technology, Rzeszow, Poland. Currently he is an Assistant Professor in the Industrial Research Insti-

tute for Automation and Measurements (PIAP), and the Warsaw University of Technology, both in Warsaw, Poland. He is an Associate Editor of the "Journal of Automation, Mobile Robotics and Intelligent Systems" (JAMRIS). His research interests include mechanics, control and robotics. In particular, he is a specialist in ground mobile robots (wheeled, legged, tracked and hybrid ones) in terms of construction, modeling and simulation as well as motion stabilization and control.

Dr. Małgorzata Kaliczyńska received her MSc Eng. degree in cybernetics from the Faculty of Electronics, Wroclaw University of Technology, and her PhD degree in the field of fluid mechanics from the Faculty of Mechanical and Power Engineering in this same university. Now she is Assistant Professor in the Industrial Research Institute for Automation and Measurement (PIAP) and Editor of the scientific and technological magazine "Measurements, Automation, Robotics". Her areas of research interest include distributed control systems, information retrieval and webometrics.

Part I
Control and Automation

Rational Use of Primary Energy in Single-Family Residential Houses

Dominik Ambroziak, Łukasz Skarbek, Piotr M. Tojza, Jacek Jaworski, Dawid Gradolewski, and Grzegorz Redlarski

Gdansk University of Technology, Gdansk, Poland
{dambroziak,lskarbek,ptojza,jjaworski,gradolewski,
g.redlarski}@eia.pg.gda.pl

Abstract. This work presents results of the primary energy use for heating residential single-family house. Analysis includes domestic hot water system (DHW) and heating, ventilation and air condition system (HVAC). During researches the conventional and alternative energy sources (natural gas, biomass, fuel oil, bituminous coal, lignite, or electric energy obtained from electric power system – EPS) were used in DHW and HVAC systems. Furthermore in the article, the analysis of sulfur dioxide emission to the atmosphere during energetic combustion of energy source was performed.

Keywords: primary energy, energy politick, sulfur dioxide emission, single-family residential house.

1 Introduction

Dynamic industrial development of European Union Countries makes the issues of effective utilization of fuels as essential task in the immediate future [4, 6, 7]. Example of this initiative is the ruling of Kioto Protocol [21] (implemented in 2005) determining the international agreement concerning limitations of pollutants emission to the atmosphere through the increase in renewable energy utilization.

The consequence of these decisions are numerous regulations in terms of effective energy utilization, introduced both by the European Parliament [2, 15–17] and by the all member states of the European Union – including Poland [10–14].

Constantly growing energy demand [20] causes a great number of problems concerning environmental pollutions and creates difficulties related to the energy balancing. Depending on the source type of generated power (electrical, thermal, nuclear, etc.), further appear inconveniences associated with the optimal delivery of energy raw material for energy production.

Analyzing the usage of primary energy sources in Poland, the dominant role of coal as a primary resource can be noticed. This is due to substantial deposits of this material in Poland, located mainly in the southern part of the country. This arrangement results in the location of the power plants majority almost exclusively in the areas of energy resource deposits occurrence (Fig. 1). Such situation creates another issue related to the necessity of electricity transmission to other parts of the country.

J. Awrejcewicz et al. (eds.), *Mechatronics: Ideas for Industrial Applications*,
Advances in Intelligent Systems and Computing 317, DOI: 10.1007/978-3-319-10990-9_1

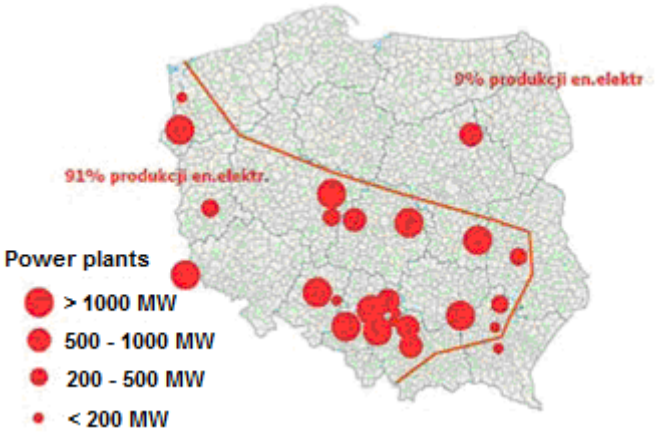

Fig. 1. Distribution of system power plants in Poland (source: [9])

It should be noted that in the 50 % Polish area the 91 % of total energy from system plants is generated. Existing imbalance prompts the obvious loss of energy resulting from the transport over long distances (Table 1).

Table 1. Values of electric energy consumption and losses in Poland over the last decade [5, 20]

Value [GWh]	2005	2007	2008	2009	2010	2011
Domestic consumption:	131,186	139,584	143,700	136,996	144,453	147,668
Household consumption:	26,565	27,713	28,425	28,684	29,774	29,383
Energy losses:	14,563	14,416	11,255	12,533	11,851	10,638

The analysis of data presented in Table. 1 shows that approx. 7.2 % of domestic electric energy consumption accounts for the losses associated with the generation, transmission, control and storage. Hence, they are so essential that could satisfy approx. 36.2 % of the total electric energy consumption of all the households in Poland. Such a significant share of losses, on a global scale, means that the issue of energy effectiveness is currently of particular importance. Instances are inter alia: new regulations placed on residential building including single family houses. These requirements are of particular concern to the need of reducing the consumption of non-renewable energy, used for the purpose of exploitation.

Currently, most of household energy consumption (from 60 % to 90 %) is associated with the operation of systems: domestic hot water system and heating, ventilation and air condition system. Therefore, the analyses of those systems are performed further in the article.

2 Analysis of Annual Energy Demands and Sulfur Dioxide Emissions to the Atmosphere in a Single-Family Residential Building

2.1 The Assumptions and Analysis Range

Fig. 2 presents the scheme of single-family residential building used as a base for the simulations and further analysis. In this research, to supply the domestic hot water system (DHW) and heating ventilation and air condition system (HVAC), were used traditional energy sources such as: bituminous coal, lignite, natural gas, fuel oil, electric energy as well as environmentally friendly biomass.

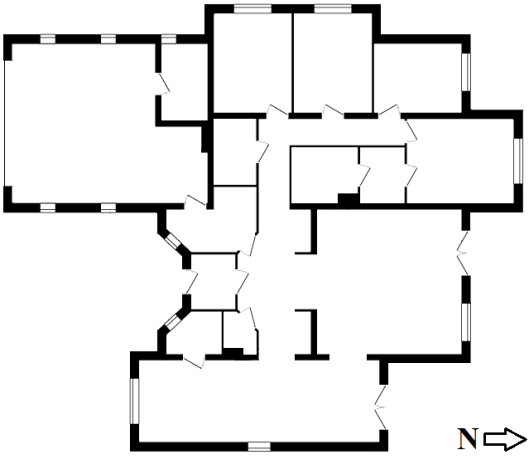

Fig. 2. Scheme of single-family residential building used in the research

Table 2. Summary of the building parameters used in the analysis

Surface:	216.2 m^2
Cubature:	535.1 m^3
Place	Gdansk (1st climatic zone)
Type of cooling system:	non
Type of ventilation system:	gravitational
Citizens:	5

Moreover, it was assumed that the object of the research is located in the first climatic zone in Gdansk and is inhabited by five citizens (very important information due to calculations of annual energy consumption). Table 2 presents the statement of the building parameters used in the analysis, as: cubature, type of cooling and ventilation systems, or number of inhabitants.

2.2 The Calculation of Annual Sulfur Dioxide Emissions and Building Demands for Primary Energy

The calculation methodology results from the adoption of normative value of losses on building heating and ventilation – according to requirements of EN 13790:2008 [3, 18, 19] standard. In the next step the primary energy was obtained, in accordance to current methodology pertain to determining the energy efficiency of buildings. The value of this energy depends mainly on the total surface of the building (Af), as well as total energy consumption for each subsystem ($Q_{P,W}$ for HVAC system and $Q_{P,H}$ for DHW system).

$$EP = \frac{Q_{P,W} + Q_{P,H}}{A_f} \tag{1}$$

The amount of annual emission of sulfur dioxide mainly depends on fuel ratio (B_w, B_K), emissions of sulfur dioxide ratio ($SO_{2,W}$, $SO_{2,H}$) and normalization coefficient (m_W, m_K) [18].

$$SO_2 = B_W \cdot SO_{2,W} \cdot m_W + B_K \cdot SO_{2,K} \cdot m_K \tag{2}$$

This method allows to estimate the total primary energy consumption in residential buildings and the total annual sulfur dioxide emission to atmosphere. This approach also enables to determine the benefits of utilize the non-conventional energy sources.

3 Results of the Analysis

Table 3 presents results of the above mentioned analysis, taking into account: annual energy demand for HVAC system ($Q_{K,H}$), annual energy demand for DHW system ($Q_{K,W}$), total annual emissions of sulfur dioxide to the atmosphere from selected energy source (SO_2) and total annual demand for primary energy of the object (EP).

Table 3. Summary of the analysis results

Energy source	$Q_{K,H}$ [kWh·a^{-1}]	$Q_{K,W}$ [kWh·a^{-1}]	SO_2	EP
Biomass	24,154.94	3501.56	4.46	25.58
Bituminous coal	18,558.06	3501.56	55.01	112.23
Lignite	18,558.06	3501.56	522.88	112.23
Fuel oil	17,098.44	3501.06	17.47	104.81
Natural gas	17,098.44	3501.06	0.00	104.81
Electric energy	12,171.58	2433.03	132.90	202.65

Due to the similar nature of HVAC and DHW systems the analyses results of final energy demand for bituminous coal and lignite energy sources are the same (for natural gas and fuel oil the approach is analogical).

In order to better present the annual primary energy demand and total annual sulfur dioxide emission, depending on use of different energy source, Fig. 3 and Fig. 4 illustrate summary those analysis results.

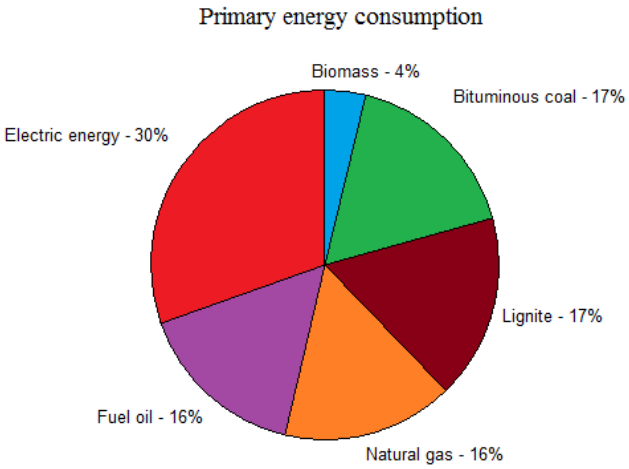

Fig. 3. Summary of primary energy consumption for the referential object

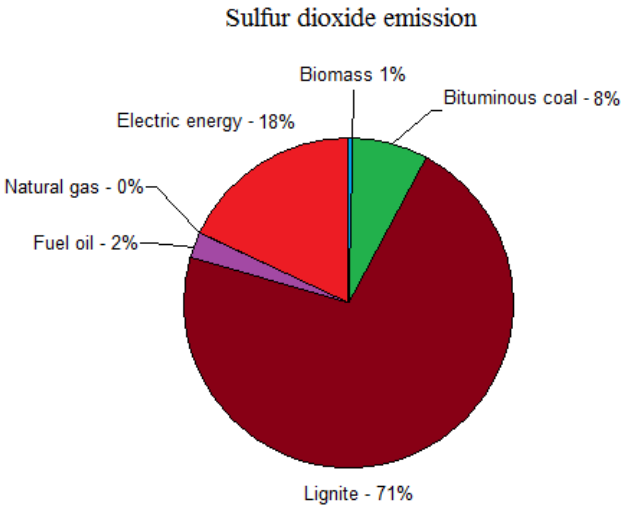

Fig. 4. Summary of sulfur dioxide emission to the atmosphere for the referential object

The results clearly show that primary energy consumption is greatest when HVAC system and DHW system utilize electric energy obtained from the EPS as an energy source. Simultaneously, the results show on biomass as the lowest primary energy consumption source of energy.

This information is very important on the grounds of planning energy development strategy, because it shows how to limit the consumption of raw materials. Evidence to support that thesis is possibility to utilize biomass as an energy source to reduce primary energy demands by up to 87 %, compared to the worst scenario (electric energy obtained from electrical power system). Taking into account this fact, the utilize of non-conventional energy sources is particularly important, especially for areas distant from the power plants, or/and heating plants. Due to utilize biomass as energy source, energy losses associated with its transmission can be sharply reduced. Also it should be noted that in Poland the bituminous coal is the main energy raw material which during the energetic combustion emits great amounts of carbon and sulfur dioxide to the atmosphere.

Definitely the greatest sulfur dioxide emission to the atmosphere was in the case of lignite used as a source of energy. Furthermore biomass and natural gas were characterized by the lowest sulfur dioxide emission to the atmosphere.

The analysis clearly shows superiority pro ecological solutions over conventional solutions (bituminous coal, lignite, fuel oil, or electricity) in view of environmental impact. The worst results was gained for lignite and electrical energy obtained from EPS.

4 Conclusions

The mentioned above issues, in the light of current topics of primary energy ergonomic use, take on special meaning especially when referring to the current European Union guidelines and to the problems related to environmental protection. Thus it is particularly valuable to conduct diverse forms of support for any thermomodernization projects, especially for those which seek to use renewable energy sources. An example of government policy in this area is undoubtedly the law act of supporting thermomodernisation projects that, following an energy audit, allow for applying for a 20% refund of the contracted for this purpose investment loan amount.

It should be noted also that although the presented results refer to a specific type of residential building, they can be considered as representative of the majority of residential buildings. The differences in primary energy consumption for other buildings, will result most of all from the application of other than the assumed in the analysis technological solutions – including the efficiency of certain devices.

References

1. Bartnik, R.: Elektrownie i elektrociepłownie gazowo parowe. Efektywność energetyczna i ekonomiczna. Wydawnictwa Naukowo-Techniczne (2009)
2. The European Parliament and the Council of the European Union. Directive 2002/91/EC of the European Parliament and of the Council of 16 December 2002 on the energy performance of buildings. Official Journal of the European Union 46, 65–71 (2002)
3. EN 13790:2008. Energy performance of buildings – Calculation of energy use for space heating and cooling (ISO 13790:2008). European Committee for Standardization (2008)

4. Kamrat, W.: Perspektywy rozwoju energetyki w Polsce. Wokół Energetyki 2 (2007)
5. Central Standard Office: Concise Statistical Yearbook of Poland 2010. Warsaw (2010)
6. Marecki, J.: Perspektywy rozwoju elektroenergetyki w Polsce do 2020 roku. Komitet Problemów Energetyki przy Prezydium PAN. Gdańsk (2001)
7. Marecki, J., Kamrat, W., Augusiak, A.: Perspektywy rozwoju energetyki w świetle polityki energetycznej do 2020 roku i w dalszej perspektywie. Cenference FSNT-NOT, Warszawa (2000)
8. Ministry of Economy and Labour. Zespół do spraw polityki energetycznej. Polityka Energetyczna Polski do 2025 roku. Council of Ministers (2005)
9. Niernsee, M.: Kryteria doboru lokalizacji nowych elektrowni węglowych – praktyczne podejście w warunkach polskich. Energetyka 2(668), 83–87 (2010)
10. Polish ministry of infrastructure: w sprawie metodologii obliczania charakterystyki energetycznej budynku i lokalu mieszkalnego lub części budynku stanowiącej samodzielną całość techniczno-użytkową oraz sposobu sporządzania i wzorów świadectw ich charakterystyki energetycznej (2008)
11. Polish ministry of infrastructure: w sprawie zmiany rozporządzenia zmieniającego rozporządzenie w sprawie szczegółowego zakresu i formy projektu budowlanego. Warszawa (2008)
12. Polish ministry of infrastructure: w sprawie szczegółowego zakresu i form audytu energetycznego oraz części audytu remontowego, wzorów kart audytów, a także algorytmu oceny opłacalności przedsięwzięcia termo modernizacyjnego, Warszawa (2009)
13. Polish ministry of infrastructure: zmieniające rozporządzenie w sprawie szczegółowego zakresu i formy projektu budowlanego, Warszawa (2008)
14. Polish ministry of infrastructure: zmieniające rozporządzenie w sprawie warunków technicznych, jakim powinny odpowiadać budynki i ich usytuowanie, Warszawa (2009)
15. The European Parliament and the Council of the European Union. Directive 2009/28/EC of the European Parliament and of the Council of 23 April 2009 on the promotion of the use of energy from renewable sources and amending and subsequently repealing directives 2001/77/EC and 2003/30/EC. Official journal of the European union 52, 16–62 (2009)
16. The European Parliament and the Council of the European Union. Directive 2009/29/EC of the European Parliament and of the Council of 23 April 2009 amending directive 2003/87/EC so as to improve and extend the greenhouse gas emission allowance trading scheme of the community. Official Journal of the European Union 52, 63–87 (2009)
17. The European Parliament and the Council of the European Union. Directive 2009/31/EC of the European Parliament and of the Council of 23 April 2009 on the geological storage of carbon dioxide and amending council directive 85/ 337/EEC. European parliament and council directives 2000/60/EC, 2001/80/EC, 2004/35/EC, 2006/12/EC, 2008/1/EC and regulation (EC) No. 1013/2006. Official Journal of the European Union 52, 114–135 (2009)
18. Redlarski, G., Piechocki, J., Kupczyk, J., Ambroziak, D.: The analysis of conventional energy carriers with biomass for heating purposes. Part 1. Description of the issue and the research method. Agricultural Engineering 143, 279–287 (2013)
19. Piechocki, J., Ambroziak, D., Palkowski, A., Redlarski, G.: Use of Modified Cuckoo Search algorithm in the design process of integrated power systems for modern and energy self-sufficient farms. Applied Energy 114, 901–908 (2014)
20. Central Standard Office: Concise Statistical Yearbook of Poland 2013, Warszawa (2010)
21. The president of Poland: Protokół z Kioto do Ramowej konwencji Narodów Zjednoczonych w sprawie zmian klimatu (1997) (in Polish)

Determination of Jiles-Atherton Model Parameters Using Differential Evolution

Rafał Biedrzycki[1], Roman Szewczyk[2], Peter Švec Sr.[3], and Wojciech Winiarski[4]

[1] Faculty of Electronics and Information Technology,
Warsaw University of Technology,
Nowowiejska 15/19 str., 00-665 Warsaw, Poland
rbiedrzy@elka.pw.edu.pl
[2] Institute of Metrology and Biomedical Engineering, Warsaw University of Technology,
św. A. Boboli 8 str., Warsaw, Poland
szewczyk@mchtr.pw.edu.pl
[3] Institute of Physics, Slovak Academy of Sciences,
Dúbravská cesta 9, 845 11 Bratislava, Slovak Repulic
peter.svec@savba.sk
[4] Industrial Research Institute for Automation and Measurements PIAP,
Al. Jerozolimskie 202, 02-486 Warsaw, Poland
wwiniarski@piap.pl

Abstract. Effective and robust method of determination of Jiles-Atherton model's parameters is one of the most significant problem connected with magnetic hysteresis loop modelling. Parameters of this model are determined during the optimisation process targeting experimental results of hysteresis loop measurements. However, due to appearance of local minima, the cognitive methods have to be applied. One of the most common method are evolutionary strategies. On the other hand, typical evolutionary strategies, such as $\mu+\lambda$ are expensive from the point of view of calculation time. To overcome this problem, differential evolution was applied. As a result, the calculation time for determination of Jiles-Atherton model's parameters was significantly reduced.

Keywords: magnetic hysteresis model, differential evolution.

1 Introduction

In spite of the fact, that Jiles-Atherton model of magnetization process [1, 2] was presented the first time in 1984, it is still very popular and utilized for crystalline and amorphous alloys [3–9]. Recent developments of Jiles-Atherton model are mainly focused on physical aspects [10–13] and engineering [14] applications.

However, all these works require robust, reliable and cost-effective methods of determination of Jiles-Atherton model's parameters. Since the beginning, for this task optimisation methods were used [15]. However, efficiency of gradient optimisation methods is significantly limited due to the fact, that typical target function exhibit local minima [16]. For this reason, cognitive method of global optimisation were

J. Awrejcewicz et al. (eds.), *Mechatronics: Ideas for Industrial Applications*,
Advances in Intelligent Systems and Computing 317, DOI: 10.1007/978-3-319-10990-9_2

used, such as genetic algorithms [17] or evolutionary strategies [18]. Among used solutions, the (μ+λ) strategy, together with simulating annealing and local gradient optimisation [19] is popular. However, such solution is extremely expensive from the point of view of calculation time.

This paper presents new approach to determination of Jiles-Atherton model parameters oriented on differential evolution algorithm. As a result the computation time was significantly limited without reduction of efficiency and robustness of determination of Jiles-Atherton model's parameters given for specific experimental results.

2 Principles of Jiles-Atherton Model of Magnetic Hysteresis

Modelling the magnetic hysteresis with Jiles-Atherton model covers two steps [2]: determination of anhysteretic magnetization M_{ah} and modelling the hysteresis by differential equation considering the sign of changes of magnetizing field H. This approach is recently criticized [10], however good agreement with experimental data can be achieved.

In Jiles-Atherton model anhysteretic magnetization for isotropic magnetic materials M_{ah_iso} is given by the Langevin equation [2]:

$$M_{ah\_iso} = M_s \left[\coth\left(\frac{H_e}{a}\right) - \left(\frac{a}{H_e}\right) \right] \tag{1}$$

where a is determined by the domain walls density in the magnetic material [2], whereas effective magnetizing field H_e is given as [1]:

$$H_e = H + \alpha \cdot M \tag{2}$$

where α determines interdomain coupling.

According to corrected Ramesh extension of Jiles-Atherton model for anisotropic, ferromagnetic materials, anhysteretic magnetization in anisotropic magnetic materials M_{ah_aniso} [20, 21] is given as:

$$M_{ah\_aniso} = M_s \left[\frac{\int_0^{\pi} e^{0.5(E(1)+E(2))} \sin\theta \cdot \cos\theta \cdot d\theta}{\int_0^{\pi} e^{0.5(E(1)+E(2))} \sin\theta \cdot d\theta} \right] \tag{3}$$

where

$$E(1) = \frac{H_e}{a}\cos\theta - \frac{K_{an}}{M_s \cdot \mu_0 \cdot a}\sin^2(\psi - \theta) \tag{4}$$

$$E(2) = \frac{H_e}{a}\cos\theta - \frac{K_{an}}{M_s \cdot \mu_0 \cdot a}\sin^2(\psi + \theta) \tag{5}$$

Presented equations are valid for uniaxial anisotropy, where K_{an} is the average energy density and ψ is the angle between direction of magnetizing field and the easy axis of magnetization due to the anisotropy. Other types of anisotropy were also considered [22], however, any form of anisotropic anhysteretic magnetization equation can be solved using antiderivatives. As a result, it have to be solved using numerical integration.

In Jiles-Atherton model, the hysteresis loop is determined by the irreversible magnetization M_{irr} [1]:

$$\frac{dM_{irr}}{dH} = \delta_M \frac{M_{ah} - M_{irr}}{\delta \cdot k} \tag{6}$$

where the parameter k quantifies average energy required to break pining site. In this equation parameter $\delta = +1$ for $\frac{dH}{dt} \geq 0$ and $\delta = -1$ for $\frac{dH}{dt} < 0$. Additional parameter $\delta_M = 0$ when $\frac{dH}{dt} < 0$ and $M_{an} - M > 0$ as well as when $\frac{dH}{dt} \geq 0$ and $M_{ah} - M < 0$. In other cases $\delta_M = 1$. Parameter δ_M guarantees that incremental susceptibility is always positive, what is physically judged [4, 17].

In the original Jiles-Atherton model, parameter k is constant [1, 2]. However, even Jiles and Atherton indicated, that this assumption is not judged from the physical point of view. Changes of parameter k are caused by changes of the average energy required to break pining site [23]. For this reason, J-A-S model's parameter k can be connected with the magnetic state of the material (described by magnetization M) by the following equation [24]:

$$k = k_0 + \frac{e^{k_2 \cdot (1 - |M| / Ms)} - 1}{e^{k_2} - 1} \cdot (k_1 - k_0) \tag{7}$$

where M_s is saturation magnetization, whereas k_0, k_1 and k_2 describe the function determining k. In given equation, parameter k_0 determines the minimal value of k, parameter k_1 determines the maximal value of k, and k_2 is shape parameter. For positive values of k_2 the $k(|M|/M_s)$ function is concave, and for negative value of k_2 this function is convex [25].

In the Jiles-Atherton model, the reversible magnetization M_{rev} is given by the equation [2]:

$$M_{rev} = c \cdot (M_{an} - M_{irr}) \tag{8}$$

where c is parameter describing magnetization reversibility. Finally, total magnetization M may be calculated from following ordinary differential equation (ODE) [4, 17]:

$$\frac{dM}{dH} = \frac{\delta_M}{1+c} \frac{M_{ah} - M}{\delta \cdot k - \alpha(M_{ah} - M)} + \frac{c}{1+c} \frac{dM_{ah}}{dH} \tag{9}$$

considering the initial state of demagnetizated material, where $H = 0$ and $M = 0$.

It should be highlighted, that accurate solving of Jiles-Atherton model's equation is not trivial. Anhysteretic magnetization should be calculated using Gauss-Kronrod approximation for cyclic functions [26], whereas for solving the differential equation (9), the 4th order Runge-Kutta [27] method is recommended.

3 Determination of Jiles-Atherton Model's Parameters Using Differential Evolution

To use optimization methods for determination of the Jiles-Atherton model's parameters, the target function has to be proposed. In presented investigation, the target function was given by the following equation:

$$F = \sum_{i=1}^{n} (B_{JA}(H_i) - B_{meas}(H_i))^2 \tag{10}$$

where B_{JA} were the results of the modelling for magnetizing field H_i and B_{meas} were the results of the experimental measurements respectively. It should be indicated that during the optimization process, target function F was calculated simultaneously for 3 hysteresis loops measured for different magnetizing fields. This enabled optimization focused on achieving the model's parameters suitable for wider range of the magnetizing field.

The differential evolution algorithm [28] is stochastic derivative-free method, designed for difficult non-linear non-convex optimization problems in continuous domain. As most of the other members of evolutionary algorithms family, differential evolution process group of solutions (called population of individuals). The algorithm is iterative – at each iteration t each solution from $t - 1$ is modified by mutation and crossover. The thing that is specific to differential evolution algorithm is a mutation operator. In the canonical version of the algorithm, a mutant v_i is generated by adding difference between two randomly selected solutions to the third randomly selected solution, i.e.:

$$v_i = x_{r0} + F \cdot (x_{r1} - x_{r2}) \tag{11}$$

where

$F \in (0, 1)$ is scale factor and it is a parameter of the algorithm.

There are several variants of this canonical schema. We used variant called differential evolution/local-to-best/1/bin, where the *i*-th mutant is a result of the sum of *i*-th solution, difference of two randomly selected solutions and difference of the best solution in current population and *i*-th solution, i.e.:

$$v_i = x_i + F \cdot (x_{best} - x_i) + F \cdot (x_{r1} - x_{r2}) \tag{12}$$

The model and search algorithm were implemented in R language [29]. We used differential evolution version implemented by Ardia et al. [30]. We accepted parameters of algorithm proposed by the implementation, i.e. 200 generations, 60 individuals, $F = 0.8$, $CF = 0.5$ (crossover probability).

4 Results of Modelling

During the experiment, the parameters of $B(H)$ magnetic hysteresis loops of Finemet $Fe_{73.5}Si_{13.5}Nb_3Cu_1B_9$ nanocrystalline alloy were determined using differential evolution algorithm. Since algorithm is stochastic, 25 independent runs were performed. Summary of the results is presented in Table 1, whereas Table 2 presents values of Jiles-Atherton parameters determined by the best solution found. These parameters were used to calculate theoretical magnetic hysteresis loop. The result if its comparison to measurements is depicted in Fig. 1. It can be seen, that acceptable agreement between experimental data and results of modelling was achieved.

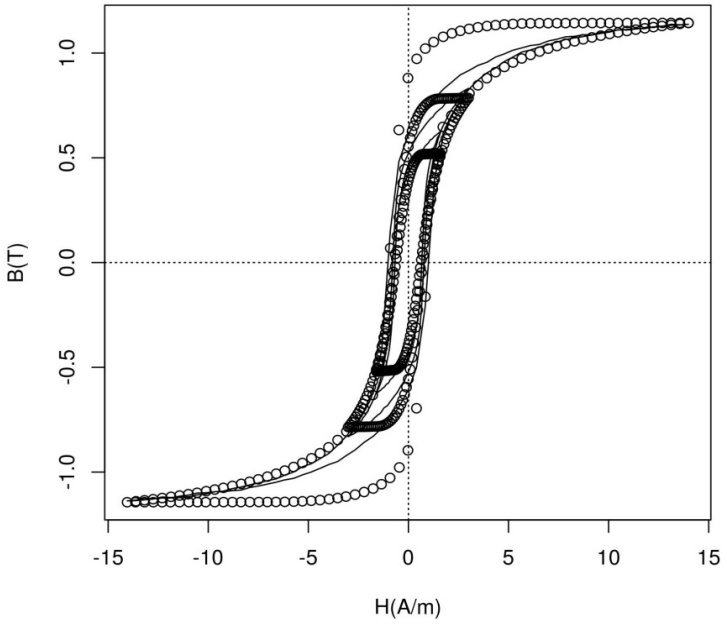

Fig. 1. Magnetic hysteresis loop of Finemet $Fe_{73.5}Si_{13.5}Nb_3Cu_1B_9$ nanocrystalline alloy: experimental results (lines) and results of modeling (circles)

Table 1 presents the values of Jiles-Atherton parameters determined during the experiment, whereas Table 2 presents the parameters describing efficiency differential evolution algorithm.

Table 1. Values of Jiles-Atherton parameters determined by differential evolution algorithm

Parameter		Value
A	A/m	1.464
k_0	A/m	330.5
k_1	A/m	0.556
k_2		–18.50
c		0.3906
M_s	A/m	$1.045\ 10^6$
α		$9.837\ 10^{-7}$
K_{an}	J/m^3	2791

Table 2. Summary of the results of 25 independent runs of differential evolution algorithm. An average, best and standard deviation of objective function value (equation 10) is reported together with an average time of one algorithm run

average	best	standard deviation of objective function value	time of calculations (h)
4.33	3.66	0.41	21

5 Conclusion

Presented results confirm, that differential evolution algorithm is interesting alternative for (μ+λ) evolutionary strategy algorithm used previously [5]. Time of calculation required for differential evolution algorithm is about 10 times lower than for (μ+λ) evolutionary strategy. On the other hand, both algorithms determine global minima of target function with accuracy sufficient for most of technical applications.

The support of the bilateral project APVV-Sk-PL-0043-12 is acknowledged from Slovak side. Polish side (Institute of Metrology and Biomedical Engineering) was supported by statutory founds within Polish-Slovak bilateral cooperation.

Calculations for the modelling were made in the Interdisciplinary Centre for Mathematical and Computational Modelling of Warsaw University, within grant G36-10.

References

1. Jiles, D.C., Atherton, D.: Theory of ferromagnetic hysteresis. Journal of Applied Physics, Vol. 55 (1984) 2115
2. Jiles, D.C., Atherton, D.: Theory of ferromagnetic hysteresis. Journal of Magnetism and Magnetic Materials, Vol. 61 (1986) 48

3. Pop, N., Caltun, O.: Jiles-Atherton model used in the magnetization process study for the composite magnetoelectric materials based on cobalt ferrite and barium titanate. Canadian Journal of Physics, Vol. 89 (2011) 787
4. Chwastek, K., Szczyglowski, J.: Estimation methods for the Jiles-Atherton model parameters – a review. Electrical Review (Przegląd Elektrotechniczny), Vol. 84 (2008) 145
5. Szewczyk, R.: Modelling of the magnetic and magnetostrictive properties of high permeability Mn-Zn ferrites. PRAMANA-Journal of Physics, Vol. 67, 1165–1171 (2006)
6. Xiong, E., Wang, S., Miao, X.: Research on magnetomechanical coupling effect of Q235 steel member specimens. Journal of Shanghai Jiaotong University (Science), Vol. 17 (2012) 605
7. Jia, Z., Liu, H., Wang, F., Ge, C.: Research on a novel force sensor based on giant magnetostrictive material and its model. Mathematics and Computers in Simulation, Vol. 80 (2010) 1045
8. Zheng, J., Cao, S., Wang, H.: Modeling of magnetomechanical effect behaviors in a giant magnetostrictive device under compressive stress. Sensors & Actuators: A. Physical, Vol. 143 (2008) 204
9. Zhang, D., Kim, H., Li, W., Koh, C.: Analysis of magnetizing process of a new anisotropic bonded NdFeB permanent magnet using FEM combined with Jiles-Atherton hysteresis model. IEEE Transactions on Magnetics, Vol. 49 (2013) 2221
10. Zirka, S.E., Moroz, Y., Harrison, R., Chwastek, K.: On physical aspects of the Jiles-Atherton hysteresis models. Journal of Applied Physics, Vol. 112 (2012) 043916
11. Messal, O., Sixdenier, F., Morel, L., Burais, N.: Temperature dependent extension of the Jiles-Atherton model: Study of the variation of microstructural hysteresis parameters. IEEE Transactions on Magnetics, Vol. 48 (2012) 2567
12. Xu, M., Xu, M., Li, J., Ma, S.: Discuss on using Jiles-Atherton theory for charactering magnetic memory effect. Journal of Applied Physics, Vol. 112 (2012) 093902
13. Li, J., Xu, M.: Modified Jiles-Atherton-Sablik model for asymmetry in magnetomechanical effect under tensile and compressive stress. Journal of Applied Physics, Vol. 110 (2011) 063918
14. Huang, S., Chen, H., Wu, C., Guan, C.: Distinguishing Internal Winding Faults From Inrush Currents in Power Transformers Using Jiles-Atherton Model Parameters Based on Correlation Coefficient. IEEE Transactions on Power Delivery, Vol. 27 (2012) 548
15. Jiles, D.C., Thoelke, J.B.: Theory of ferromagnetic hysteresis: determination of model parameters from experimental hysteresis loops. IEEE Trans. Magn. Vol. 25 (1989) 3928
16. Pop, N.C., Caltun, O.F.: Jiles-Atherton Magnetic Hysteresis Parameters Identification. Acta Physica Polonica A, Vol. 120 (2011) 491
17. Chwastek, K., Szczygłowski, J.: Identification of a hysteresis model parameters with genetic algorithms. Mathematics and Computers in Simulation, Vol. 71 (2006) 206
18. Szewczyk, R., Frydrych, P.: Extension of the Jiles-Atherton Model for Modelling the Frequency Dependence of Magnetic Characteristics of Amorphous Alloy Cores for Inductive Components of Electronic Devices. Acta Physica Polonica A, Vol. 118 (2010) 782
19. Jackiewicz, D., Szewczyk, R., Salach, J.: Modelling the magnetic characteristics of construction steels. Pomiary Automatyka Robotyka, Vol. 16, No. 2, 552–555 (2012) (in Polish)
20. Ramesh, A., Jiles, D.C., Bi, Y.: Generalization of hysteresis modeling to anisotropic materials. Journal of Applied Physics, Vol. 81 (1997) 5585
21. Ramesh, A., Jiles, D., Roderik, J.: A model of anisotropic anhysteretic magnetization. IEEE Transactions on Magnetics, Vol. 32 (1996) 4234

22. Baghel, A., Kulkarni, S.: Hysteresis modeling of the grain-oriented laminations with inclusion of crystalline and textured structure in a modified Jiles-Atherton model. Journal of Applied Physics, Vol. 113 (2013) 043908
23. Scholz, W., Forster, H., Suess, D., Schrefl, T., Fidler, J.: Micromagnetic simulation of domain wall pinning and domain wall motion. Computational Materials Science, Vol. 25 (2002) 540
24. Szewczyk, R.: Extension for the model of the magnetic characteristics of anisotropic metallic glasses. Journal of Physics D – Applied Physics, Vol. 40 (2007) 4109
25. Szewczyk, R.: Modeling the magnetic properties of amorphous soft magnetic materials for sensor applications. Journal of Optoelectronics and Advanced Materials, Vol. 6 (2007) 1723
26. Shampine, L.F.: Vectorized Adaptive Quadrature in MATLAB. Journal of Computational and Applied Mathematics, Vol. 211 (2008) 131
27. Daomin, M., Shengtao, L.: A comparison of numerical methods for charge transport simulation in insulating materials. IEEE Transactions on Dielectrics and Electrical Insulation, Vol. 20 (2013) 955
28. Storn, R.: Differential evolution research trends and open questions. in U. Chakraborty (Ed.), Advances in Differential Evolution, Vol. 143 of Studies in Computational Intelligence, Springer Berlin Heidelberg, 1–31 (2008)
29. R Core Team. R: A Language and Environment for Statistical Computing. R Foundation for Statistical Computing, Vienna, Austria (2013). [www.R-project.org]
30. Ardia, D., Mullen, K.M., Peterson, B.G., Ulrich, J.: DEoptim: Differential Evolution in R. Version 2.2.2

The Application of Microcontrollers Diagnostic System for Evaluation of Stirling Engine

Bohdan Borowik[1,2,*], Barbara Borowik[3], and Igor P. Kurytnik[1]

[1] University of Bielsko-Biala, Poland
[2] Geocarbon Ltd., Katowice, Poland
bborowik@ath.bielsko.pl
[3] Cracow University of Technology, Poland
cnborowi@cyf-kr.edu.pl

Abstract. The article presents the microcontroller system for diagnostic and evaluation of the Stirling engine performance. For this purpose the model for the prototype engine analysis has been developed, to present the engine's improved benchmarking results. The most relevant objective in this respect was to achieve a uniform heat transfer across each tube of the hot gas heat exchanger. The functioning of this engine has been analyzed with the aim to find and optimize the main working parameters. To obtain this goal the Stirling engine has been equipped with different kinds of electronic sensors. A microcontroller testing circuit has been designed, which uses the acquisition of data from the data module. One of the important tasks of testing a Stirling engine is to present a model, which is able to represent the dynamics involved in all essential processes of the engine.

Keywords: Stirling engine, heat transfer, regenerator, performance.

1 Introduction

A Stirling engine is an external combustion engine based on the Stirling Cycle. Developed first in 1816 by Robert Stirling, this engine produces power from differences in temperature. The working fluid inside the engine, typically air, hydrogen or helium, is heated on one end and cooled on the other, consequently causing the gas to expand and compress, respectively. In addition, the expansion and compression of the working fluid moves two pistons within the engine cylinder, which in turn are depending on the configuration, coupled in some manner with a drive mechanism to produce a net power output [16]. The Stirling engine requires a sufficient temperature difference ($T_{max} - T_{min}$) to operate. The low temperature Stirling engine operating on small temperature differences was studied in 1991 by Senft [5]. This machine runs with a temperature difference of only 0.4 ºC. In this construction was used a glass cylinder and a graphite piston, and it is not easy to manufacture such a system locally. A PTFE (PolytetraFluoroEthylene) cup was developed using 0.2 mm thick pure PTFE sheet.

* Corresponding author.

J. Awrejcewicz et al. (eds.), *Mechatronics: Ideas for Industrial Applications*,
Advances in Intelligent Systems and Computing 317, DOI: 10.1007/978-3-319-10990-9_3

The manufacturing method was complex and this engine performance was not as good as reported but the Stirling machine run continuously for several months and has started and run only from the heat of a human hand.

The maximum temperature difference is limited by the heat sink temperature, usually atmospheric and by the temperature limit of the hot end material. The heat source can be chemical, solar, nuclear or some other one, typical for thermal storage. By the use of heat pipe technology the heat source does not have to act directly on the hot end of the heat exchanger (Hargreaves, 1991) [6]. This can allow a more conventional heat exchanger design and much higher rates of heat transfer.

As stated by the Second Law of Thermodynamics, heat must be dissipated from the Stirling engine. Considerable heat is discharged from an internal combustion engine by the exhaust directly to the atmosphere. For example, in a Diesel engine about 30 % of the heat supplied by combustion is dissipated by the exhaust and almost 35 % by the radiator. With the Stirling engine heat rejected by the exhaust has not gone through the engine cycle and is wasted. To maintain a high efficiency of an engine, more heat must be dissipated by the radiator. This puts about twice the thermal load on the radiator than in a comparable Diesel engine (Walker) [7]. This is less of a concern with marine engines but can add considerable expense and bulk when the heat is dissipated to the atmosphere via radiator. Stirling engines lack a throttling method inherently built into other engines. One method of changing power output is to change the diameter of the choke point of the engine, which is the point at which the hot air flows from the heat transfer to the engine cylinder. Choke points are often specifically designed to work optimally at one setting. A choke point that can be varied is advantageous, because power output can be altered on the fly. The goal of this project is to develop a simple variable choke point for use in a small Stirling engine. Originally, types of Stirling engines were classified into three groups, according to the Kirkley-Walker classification system: Alpha, Beta, and Gamma [9], depicted on Fig. 1.

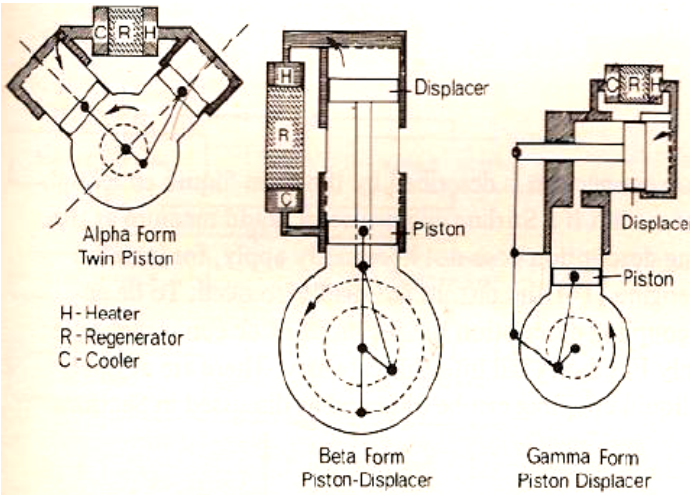

Fig. 1. Stirling engine types: Alpha, Beta, and Gamma [8]

Now these terms only describe the cylinder couplings of a Stirling engine. Cylinder coupling identifies the way, in which the displacer piston and the power piston are connected, with respect to the connection of the *variable volume working spaces*. These are the spaces inside the engine cylinder, where the working fluid is heated and cooled, respectively (Sandfort, 1962) [8]. Within the scope of R&D project presented, a new heating system for Stirling engine has been developed and optimized. The advantage of a Stirling engine is that the heat is transferred from the outside to the engine via tubing of a heater. The Stirling heater is designed for high flue gas temperature and is directly connected to the furnace. The surface temperature of the heater in Stirling engine is typically in range of 600 °C – 700 °C.

The Stirling engine is a multi energy-sourced engine, as it may use solar energy, combustion energy and heat from old coal reuse heaps. They make considerably less pollution than the traditional engines. The absence of explosive nature in converting heat energy into mechanical one, conveys to silent and cleaner operation. The power output is produced by the separate motions of the individual pistons. Piston coupling is very important in Stirling engines. There are three basic forms with many further subdivisions. A rigidly coupled Stirling engine uses a solid mechanical linkage that connects the reciprocating elements to each other and the power take-off mechanism. Typical types of rigid coupling include: slider-crank, rhombic drive, swash plate, Scotch Yoke, crank-rocker, and Ross rocker.

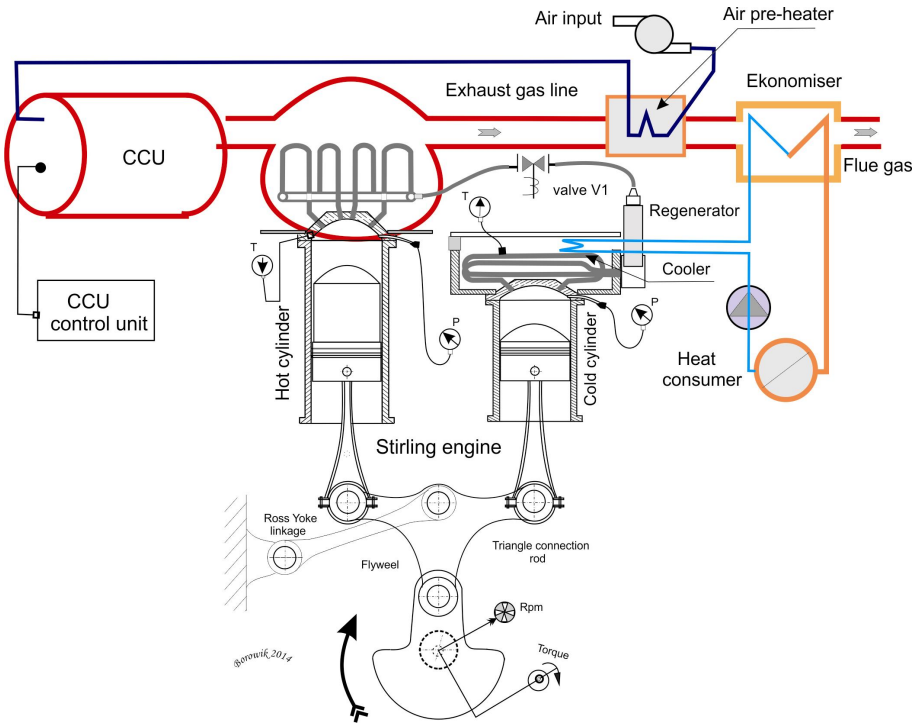

Fig. 2. The Stirling engine plant facilities

Drive mechanism poses some problems for the Alfa type Stirling engine, since discontinuous motion is required to achieve the volumetric changes that result in a net power output. For this reason, in this engine for transferring dual piston motion into rotational motion – the Ross yoke mechanism has been implemented.

On Fig. 2 the schematic of a small scale plant based on a Stirling engine is shown. To achieve a high efficiency a continuous combustion unit (CCU) has been applied as a biomass furnace. It must operate at a high temperature, but peak temperature should be impeded, in order to keep the risk of ash slogging and fouling low. The objective of the research was to study the Alfa type Stirling engine, which has been developed in order to perform modernization and to make a benchmark of it efficiency. The Alfa engine shown in Fig. 1 consists of two separate cylinders, and each one has its own piston.

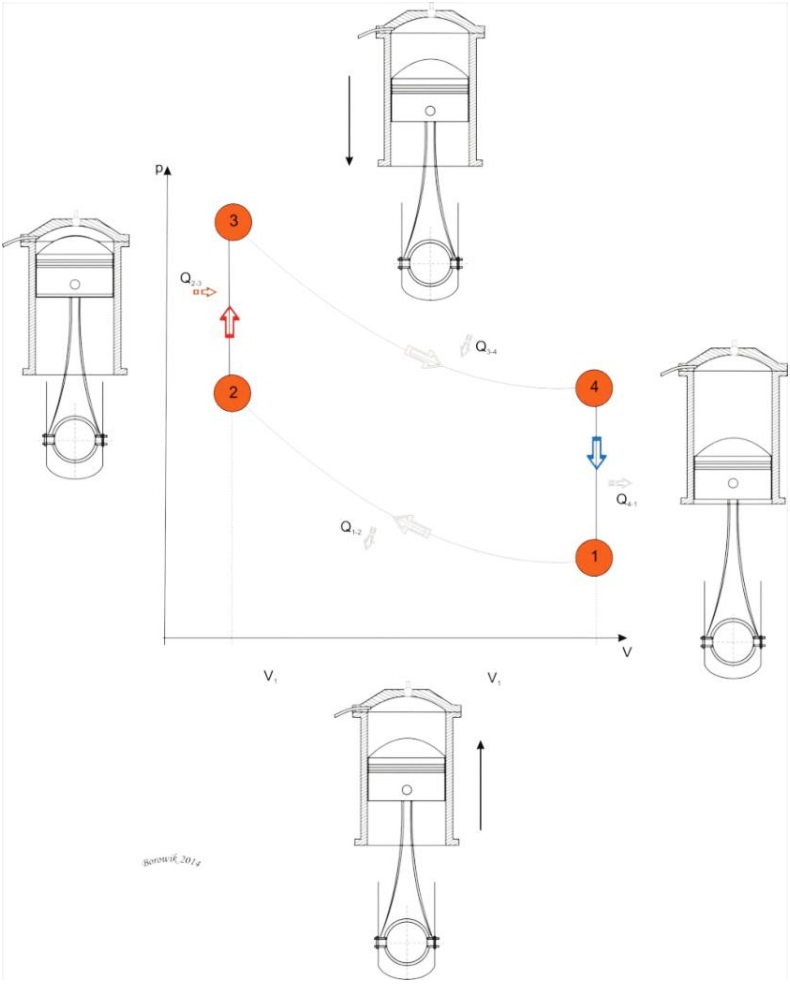

Fig. 3. Thermodynamic cycle of the Stirling engine

The Ross Yoke mechanism does not produce sinusoidal volume variations and has the advantage over the traditional system by minimizing lateral forces acting on the pistons, and leading to a more efficient and compact design. The expansion volume is maintained at high temperature, and the compression volume is maintained at low temperature. The theoretical efficiency is equivalent to the Carnot cycle. The Stirling engine works in a closed cycle, as shown in Fig. 3.

As the working gas here is helium, trapped in the machine undergoes the following transformations: from point 1 → 2 isothermal compression, from point 2 → 3 isochoric heating, from point 3 → 4 isothermal expansion, from point 4 → 1 isochoric cooling. In this cycle a constant mass of helium is alternately: relaxed, cooled, compressed and warmed. The processes of heating and cooling are improved by using a regenerator. The regenerator is generally a metal cylinder, constituted by an annular unit. Matrix for the regenerator is based on 0.14 mm steel wire. It works as a thermal sponge, which alternatively absorbs and releases heat.

2 The Stirling Engine Testing Facilities

The objectives of the test bench are mainly to characterize the performance of Stirling engines and to evaluate different control strategies for engines, which operate with variable heat sources. With respect to the thermal metrology conditions, the engine is equipped with eight thermocouples, four pressure transducers and volume transducers. Voltage delivered by this transducer is proportional to the volume of gas shunt in the Stirling engine, as shown in Fig. 4.

In order to monitor the Stirling engine performance some temperature sensors have been mounted. Measuring the temperature in the Stirling engine is not a simple matter because of the small volumes involved in the exchangers and the fast changes of the temperature of the working gas during the thermodynamic cycle. So, only the average temperature can be measured during a single cycle. The engine has been equipped with 5 temperature sensors inside the regenerator, one inside a tube from the hot side of the heat exchanger, one inside the one from the cold side, and two inside the compression chamber. Other temperature sensors were mounted in the water circuit, in the carter and in the exhaust gas circuit. The compression chamber pressure has been also monitored, together with the rotational speed of the crankshaft and the output electric power generator. To reach those objectives the system has been equipped with sensors, actuators and software arrangement that allow a flexible operation. The microcontroller based system measures Torque and Rpm on the main shaft. Using this data volume a transducer will determine the total air volume trapped in the 2 rooms, as well as in the regenerator. It delivers the signal of continuous tension. Its maximum corresponds to $V_{max} = 230\ cm^3$ and the minimum corresponds to $V_{min} = 120\ cm^3$.

The Fig. 5 shows the pressure and the temperature distributions in the various engine compartments. The heater and the cooler walls are maintained isothermally at temperatures: T_{wh} and T_{wc} respectively.

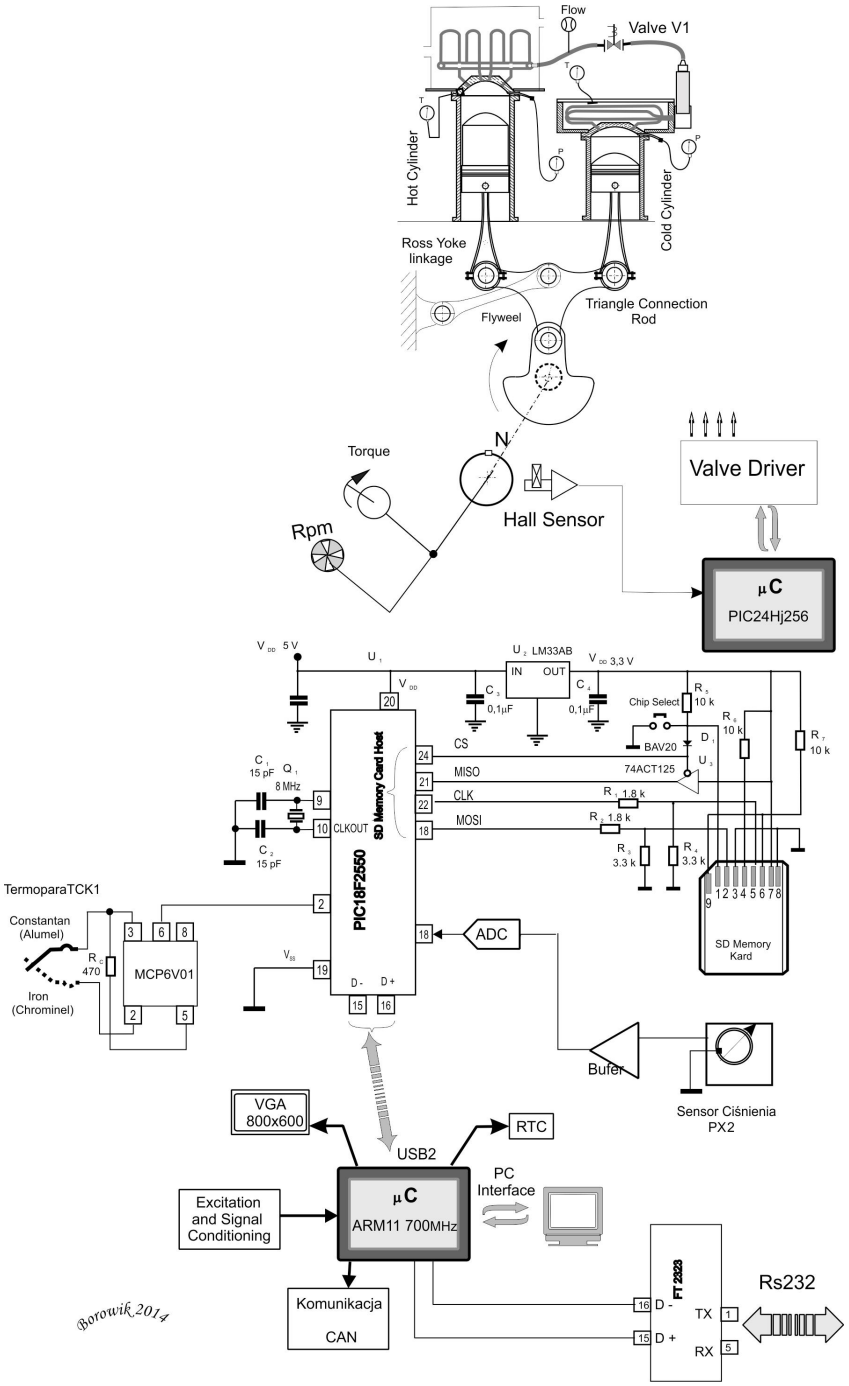

Fig. 4. Stirling engine testing facilities

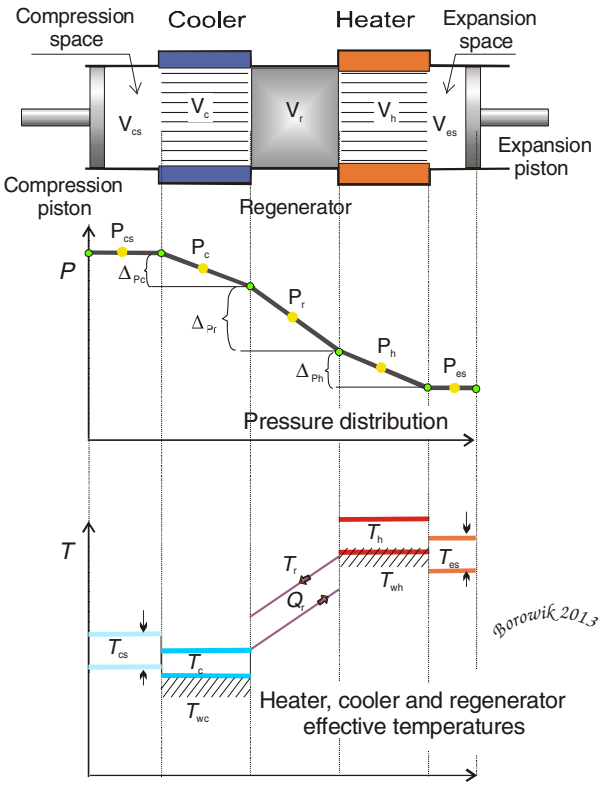

Fig. 5. Heater and cooler effective temperatures

A letter *V* denotes Volume, a letter *P* denotes Pressure, a letter *T* – Temperature, a letter *Q* – Heat, a letter R – gas constant, m – mass of gas in different compartments and some of these letters have the following subscripts: *cs* – denoting a compression space, *c* – a cooler, *r* – a regenerator, *h* – a heater, *es* – an expansion space, and *w* – wall, so for example T_{wc} denotes a temperature of a cooler's wall. The temperature of the gas in the various compartments can be calculated from the perfect gas law:

$$\begin{aligned} T_{cs} &= P_{cs} \cdot V_{cs} / R \cdot m_{cs} \\ T_c &= P_c \cdot V_c / R \cdot m_c \\ T_h &= P_h \cdot V_h / R \cdot m_h \\ T_{es} &= P_{es} \cdot V_{es} / R \cdot m_{es}. \end{aligned} \tag{1}$$

3 The Thermocouple Circuit for Temperature Monitoring

The test platform is composed of different subsystems: heating and cooling subsystem, electric subsystem, management and control subsystem. The platform allows

testing the Stirling engine under different filling pressures, shaft speeds and hot temperatures of the heat exchanger. Related to the last one, a temperature control loop implemented in the hot air generator controller (independent of the engine operating conditions) allows the hot temperature of the heat exchanger, fixing, whichever engine control system has been employed. The management software permits running semi automatic tests at different operating conditions, and with its manual version, testing new strategies for start and stop procedures. The temperature of the engine is subject to the thermal regime conditions. In the conducted testing as thermoelectric sensor Fe-CuNi/J/ class 1 we used transducers (thermocouple type TTJ/KE-361), what is shown in the schematic diagram in Fig. 6.

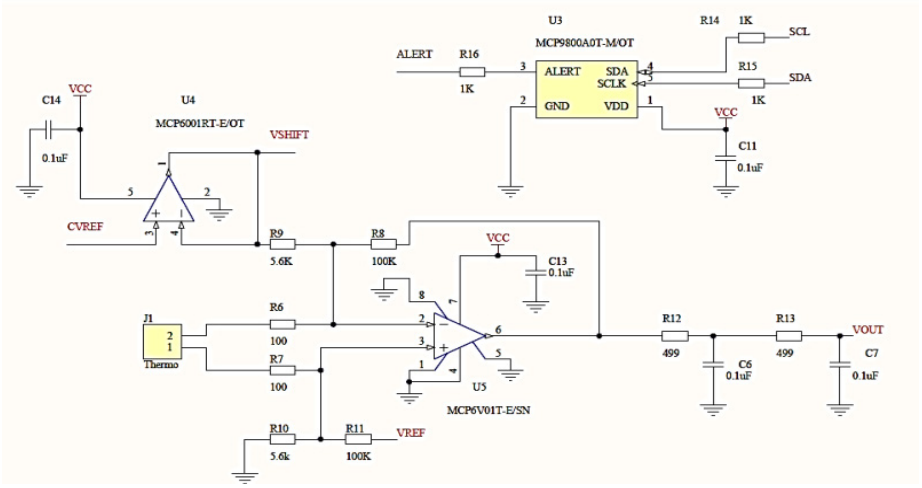

Fig. 6. The thermocouple circuit for temperature monitoring in the Stirling engine

The thermocouple matches the characteristic of type J (Iron-Constantan) and is trimmed for type K (Chromel-Alumel) inputs. Thermocouple amplifiers shown in Fig. 4 represent calibration accuracies ±1 °C, working with cold Junction Compensation and High Impedance Differential Input. It combines an ice point reference with a prefabricated amplifier to produce a high level (equal to 10 mV/°C) output directory from a thermocouple signal.

It can be used to amplify its compensation voltages directly, thereby converting it to a stand alone Celsius transducer, with a low impedance voltage output. It includes Reference temperature U_3 MCP9800A0T digital temperature sensor. The register setting allows for user selectable 12-bit temperature resolution measurements. The sensor works in industry standard I^2C. To reduce the amount of circuitry the application monitors only four signal channels, but any number of channels supported by the PIC18F2550 microcontroller could be monitored. Working gas temperature and pressure are measured at the three points, which are: the compression space, the expansion space, and the buffer space. Wall temperature of the cold side heat exchanger is measured at the top and the bottom side.

4 Engine Adjustment

For the purpose of testing and adjustment the Alpha Stirling engine was build with Ross Yoke linkage. As a Hypothesis was taken the problem of finding the choke point in small Alfa Stirling engine, allowing to increase this engine efficiency. And the goal of this project is to develop a point for opening the valve V1 to increase the power output of the Stirling engine.

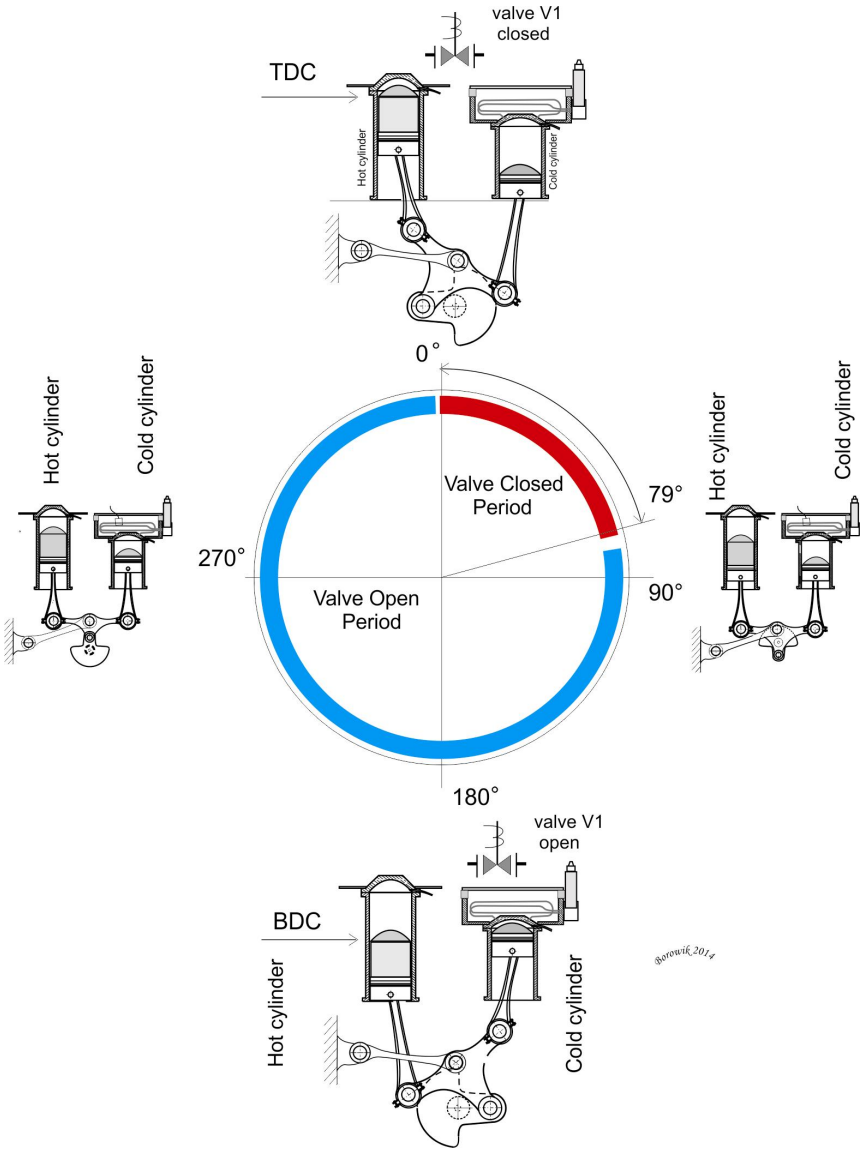

Fig. 7. The ranges of valve's open and closed periods

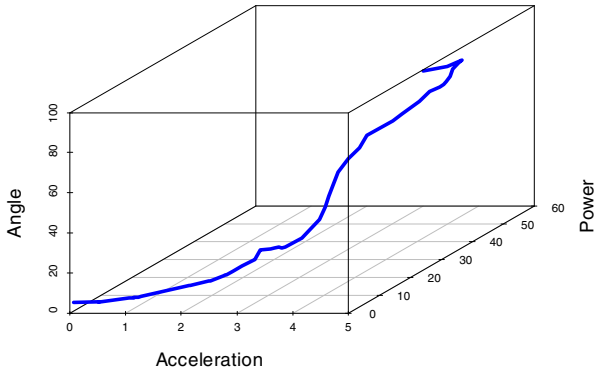

Fig. 8. Dependency of the average power output from angle and acceleration values

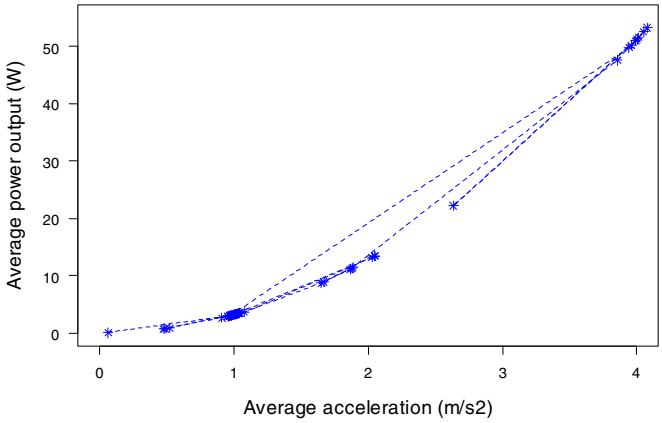

Fig. 9. Dependency of the average power output from the average acceleration value

An assumption in this investigation is that the simplified Stirling engine used in the development of the variable valve timing point models the larger, more complex ones accurately. With this assumption the valve timing point can be easily scaled up, in order to work with larger, more powerful and more usable engines. The variable timing point can be varying on programmed circuit, utilizing PIC18F4550 microcontroller. Threshold for the start – counts the time developed on a Hall sensor and driver for valve is controlled not only by time period but also by phase.

5 Conclusions

Through our test bench we have carried out experimental analysis of the α Stirling engine, which have allowed us to investigate the importance of applying the correct buffer volume pressure in order to obtain advantages in term of the power on the shaft. The resulting energy dissipation has lead to severe limitations on the maximum

attainable thermal efficiency, and non-dimensional power output *P*. These limitations were independent of the regenerator conductance. It became obvious that the power generated by the engine would be rather limited, what would make it still not very useful, but the purpose of our research was to investigate the designed Stirling engine, not just to generate a lot of power. While testing a variable valve timing point has not been yet finished, the results of this project indicate that continuing research in this area is needed and might be valuable.

Acknowledgments. This contribution was prepared in the framework of the research project No. UDA – POIG.01.04.00-24-023/10-00. Katowice.

References

1. Borowik, B., Karpinskyy, M., Lahno, V., Petrov, O.: Theory of Digital Automata. Science and Engineering. Springer (2013)
2. Borowik, B., Kurytnik, I.P.: Mikrokontrolery PIC w zastosowaniach. Wydawnictwo PAK, Warszawa (2009)
3. Organ, A.J.: The air engine: Stirling cycle power for a sustainable future. Woodhead Publishing Limited, Abington Hall (2007)
4. Graham, W.: Stirling Engines. Oxford University Press, Walton street (2000)
5. Senft, J.R.: An Ultra Low Temperature Differential Stirling Engine. In: Proc. of 5th Int. Stirling Engine Conf., Yugoslavia (1991)
6. Hargreaves, C.M.: The Philips Stirling Engine. Elsevier (1991)
7. Walkert, G., Scot, M.J.: Ross-Stirling Boat Engine. In: Proc. of 5th Int. Stirling Engine Conf., Yugoslavia (1991)
8. Sandfort, J.F.: Heat Engines. Anchor Books Doubleday & Company, INC, Anchor Books (1962)
9. Meijer, J.R.: Stirling Engines. Access Science, (September 22, 2010), http://www.accessscience.com (accessed January 15, 2014)
10. Hooper, C., Reader, G.T.: Stirling engines. University Press, Cambridge (1983)
11. Martini, W.R.: Stirling engine design manual (accessed: January 21, 2014), http://ntrs.nasa.gov
12. Kongtragool, S.W.: Thermodynamic analysis of a Stirling engine including dead volumes of hot space, cold space and regenerator. Elsevier Ltd. (2005)
13. Wiliam, R.: Stirling Engine Design Manual. Martini Engineering (1983)
14. Stine, W.B.: Stirling engines. In: The, C.R.C. (ed.) Handbook of Mechanical Engineers, pp. 67–76. CRC Press (1998)
15. Wiliam, R.: Stirling Engine Design Manual. Martini Engineering (1983)
16. Noel, P.: Nightingale Automotive Stirling Engine. Mod II Design Report. NASA CR-175106. Mechanical Technology Inc., New York (1986)
17. William, E.D., Richard, S.K.: Automotive Stirling Engine Development Project (February 1997), http://ntrs.nasa.gov (accessed: January 21, 2014)
18. Blumbergs I., Ushakov V., Sidenko N., Jeļisejevs, D.: One-way Flow Beta-type Stirling Engine, LV Patent: LV Nr.14483, (April 20, 2012)
19. Blumbergs, I., Ushakov, V.: Specifics of Stirling Engine with Recuperation Heat Exchanger. Machines, Technologies, Materials 6, 17–19 (2012)

20. Ushakov, V., Blumbergs, I.: The Computer Analysis of the Heat Exchanger of Drive Stirling with the Nonsteady Pulsing Stream of the Heat Transfer Medium. In: The 20th Int. Scientific and Technical Conf. on Transport, Road-Building, Agricultural, Hosting & Hauling and Military Technics and Technologies, Varna, Bulgaria, June 27–29, pp. 27–29 (2013)
21. Thimsen, D.: Stirling Engine Assessment. EPRI, Palo Alto (2002)
22. Energy Conversion. Encyclopedia Britannica (2010), http://www.britannica.com

Simulation Model of PEM Fuel Cell Operating at Hydrogen and Oxygen

Jerzy Garus and Adam Polak

Polish Naval Academy, Gdynia, Poland
{j.garus,a.polak}@amw.gdynia.pl

Abstract. Effective control of a fuel cell requires a proper mathematical model. Plenty of completely described models of PEM fuel cells operating on hydrogen and air are to be found in the literature. However, there is a lack of the models for the PEM fuel cells operating on pure hydrogen and oxygen. The paper proposes a static model of such an energy source. Parameters of the model are determined by the Genetic Algorithms using experimental data gathered during operation of the real hydrogen/oxygen PEM fuel cells stack.

Keywords: PEM fuel cell, polarization curve, model identification, genetic algorithms.

1 Introduction

For decades, fuel cell technology has been developed by many research facilities to bring it to the technological state that would allow to widespread its implementation and make the fuel cells a competitive alternative for other currently available energy sources. An intense development of fuel cells is caused by necessity of limiting greenhouse gases emission and, on the other hand, by possibility to achieve higher efficiency of energy conversion and higher energy density in comparison with other energy sources.

Fuel cells are electrochemical devices that convert energy, released during a chemical reaction of fuel and oxidant, into electric one in a single step process without necessity of converting energy into heat. There exist several types of fuel cells, each using a different electrolyte to separate the fuel cells electrodes. The one having the widest possible applicability is proton exchange membrane fuel cell (PEM FC), also known as the polymer exchange membrane fuel cell. It has a lot of advantages in comparison with other fuel cell types. The most important are: operation in relatively low temperatures, which assures fast start up, the highest efficiency and zero pollution emission [1–3]. The fuel cell needs to be continuously supplied with the fuel and oxidant, which in case of the PEM FC are hydrogen and oxygen, and generates electric energy, heat, and water as a product of reaction.

Effective control of the fuel cell requires having a fully defined mathematical model, i.e. dependencies describing its behavior. Many models of the specific PEM fuel cells operating on hydrogen and oxygen from air can be found in the literature [4–6].

J. Awrejcewicz et al. (eds.), *Mechatronics: Ideas for Industrial Applications*,
Advances in Intelligent Systems and Computing 317, DOI: 10.1007/978-3-319-10990-9_4

Unfortunately, they cannot be used directly as they are if the reactant composition changes. Moreover, the literature does not present models with defined parameters for the PEM FCs operating on pure hydrogen and oxygen, which is the major requirement in underwater applications [3, 7, 8]. The paper proposes a mathematical model of the hydrogen/oxygen PEM FC, convenient for a control process, and a procedure of determination of its parameters by the Genetic Algorithms.

2 Mathematical Model of PEM Fuel Cell

Reactions taking place on the electrodes of the PEM FC are described by a hydrogen oxidation reaction (1) on the anode and an oxygen reduction reaction (2) on the cathode [9]:

$$2H_2 \rightarrow 4H^+ + 4e^- \tag{1}$$

$$O_2 + 4e^- + 4H^+ \rightarrow 2H_2O \tag{2}$$

An overall reaction is expressed by the equation:

$$2H_2 + O_2 \rightarrow 2H_2O \tag{3}$$

2.1 Reversible Open Circuit Voltage

Electric energy generated by the fuel cell comes from a change of the Gibbs free energy of formation during the reaction (3). That change is equal to the difference between the Gibbs free energy of formation of the product (water) and the Gibbs free energy of formation of the reactants (oxygen and hydrogen) [1]:

$$\Delta G = G_{product} - G_{reac\tan ts} \tag{4}$$

For further considerations, it is convenient to analyze it in the molar notation, hence the formulae (4) takes a form:

$$\Delta g = g_{product} - g_{reac\tan ts} \tag{5}$$

During the reaction in the PEM FC one mole of molecular hydrogen and a half-mole of molecular oxygen are consumed by the cell per one mole of the produced water. Therefore (5) for PEM FC can be expressed as follows:

$$\Delta g = g_{H_2O} - g_{H_2} - \frac{1}{2} g_{O_2} \tag{6}$$

For each mole of reacting hydrogen, $2N$ of electrons flow through an external electric circuit (N – the Avogadro constant) and a charge transferred between the electrodes is equal to:

$$-2Ne = -2F \tag{7}$$

where: e – the charge of a single electron, F – the Faraday constant.

An electric work W_{el} done by the fuel cell is equal to:

$$W_{el} = -2FE \tag{8}$$

where E is the electromotive force of the fuel cell.

Assuming that there are no losses, the electric work would be equal to the change of the Gibbs free energy of formation:

$$W_{el} = \Delta g \tag{9}$$

Hence, the electromotive force E, of the hydrogen fuel cell operating in standard pressure, can be expressed by the following equation:

$$E = \frac{-\Delta g}{2F} \tag{10}$$

However, the Gibbs free energy also depends on the pressure of the reactants and products of the chemical reaction in the cell. For PEM FC, it is taken into account in the Nernst equation and expressed as [1, 2]:

$$E = E^0 + \frac{RT}{2F} \ln\left(\frac{P_{H_2} \cdot P_{O_2}^{\frac{1}{2}}}{P_{H_2O}} \right) \tag{11}$$

where E^0 is the electromotive force of the fuel cell at standard pressure and P_{H_2}, P_{O_2}, P_{H_2O} are the partial pressure of hydrogen, oxygen and produced water, respectively.

2.2 Voltage Losses

Modeling of the PEM FC behavior requires to consider voltage losses which occur during operation. The losses are distinguished according to their causes, but generally, in the literature they are regarded as: activation losses, concentration losses and ohmic losses [2, 4].

Activation Losses. The activation losses are caused by the limited speed of reactions that take place on the electrodes. A part of the generated electric energy is used to maintain the speed of the reaction which is determined by the load current. These losses are described by the empirical equation introduced by Tafel [9]:

$$\Delta V_{act} = A \ln\left(\frac{i}{i_0} \right) \tag{12}$$

where: i_0 – exchange current density, A – coefficient which depends on the catalyst material and the reactants composition.

In the hydrogen fuel cell, the activation losses existing on the cathode are much greater than losses appearing on the anode, thus in practical applications the last ones are neglected. Also losses associated with the fuel crossover, because of their insignificant effect on the operating voltage, are omitted [1].

Ohmic Losses. The ohmic losses are proportional to the current and the internal resistance of the fuel cell according to the following formulae [1]:

$$V_{ohmic} = IR \tag{13}$$

The resistance R can be treated as a sum of the resistance of the path through which the electrons flow (i.e. electrodes and bipolar plates), and the ionic resistance of the proton exchange membrane. The equation (13) can be written in current density terms as follows:

$$\Delta V_{ohmic} = ir \tag{14}$$

where: i is the current density in mA/cm^2, and r is the area-specific resistance given in kΩcm^2.

Concentration Losses. The mass transport losses, also named the concentration losses, are caused by reactants pressure gradient appearing in gases supply manifolds, flow channels and gas diffusion layers once a current is being drawn from the cell. A decreased partial pressure of the reactants at the catalyst site leads to the reduction of the fuel cell voltage. There are many theoretical approaches presenting models of the transport losses, but the following one is lately regarded to be of the most value [1, 9]:

$$\Delta V_{trans} = m \exp(ni) \tag{15}$$

The constants m and n in (15) depend not only on a construction of the gas flow channels and diffusion layers but also a composition of the reactants.

2.3 Operating Voltage Equation

Taking into account all the voltage losses, the operating voltage of the fuel cell at given current density can be calculated as follows [1, 2]:

$$V = E - \Delta V_{ohmic} - \Delta V_{act} - \Delta V_{trans} \tag{16}$$

Substitution (12), (14) and (15) into (16) gives the expression:

$$V = E - ir - A \ln\left(\frac{i}{i_0}\right) - m \exp(ni) \tag{17}$$

Excluding the constant i_0 from the activation losses (12) and including it into the constant value of the real open circuit voltage E_{oc}:

$$E_{oc} = E + A\ln(i_0) \tag{18}$$

leads (17) to the dependency:

$$V = E_{oc} - ir - A\ln(i) - m\exp(ni) \tag{19}$$

The above theoretical form of the polarization curve is quite simple and easy to implement into a control system of the PEM FC.

An operating voltage of a whole fuel cell stack V_{st} can be calculated from the following expression:

$$V_{st} = N_{cell} \cdot V \tag{20}$$

where N_{cell} is the number of cells in the stack.

3 Measurement of Polarization Curve

The measurements were conducted in a real fuel cell system, built in the Polish Naval Academy as an emergency power supply system for an underwater mobile platform. The heart of the system is the Nedstack 5 kW stack, composed of 68-PEM fuel cells, operating on hydrogen and air. The fuel cell system was adapted to work on pure oxygen as an air independent system in order to be prepared for exploitation inside submerged objects.

The worked out laboratory stand allows to steer and collect operating parameters of the PEM FC system, such as a temperature of the stack, reactants pressure and consumption rate, load current of the stack and voltage of the each cell. Stabilizing the temperature and reactants pressure the static polarization curves can be measured. Fig. 1 shows a graph of the polarization curve for the following operating conditions:

- T = 331 [K],
- p_{anode} = 1.23 [bar(a)],
- $p_{cathode}$ = 1 [bar(a)].

A representative polarization characteristic for all cells of the stack was calculated from dependency:

$$\mathrm{V_{cell}} = \frac{1}{N_{cell}} \sum_{\mathrm{k=1}}^{N_{cell}} \mathrm{V_k} \tag{21}$$

The current density of the cell was obtained from equation:

$$i = \frac{I}{A_{cell}} \tag{22}$$

where I is the load current and A_{cell} the active area of the cell.

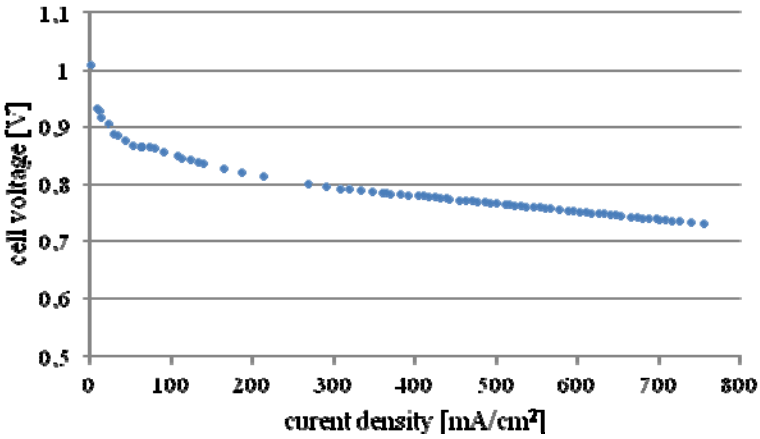

Fig. 1. Measured polarization curve of the PEM fuel cell

4 Estimation of Parameters of Polarisation Curve

The unknown parameters of (19), i.e. r, A, m and n, were determined using the Genetic Algorithms (GA), which are based on Darwin's principle of reproduction and survival of the fittest [10, 11]. In general, the GA techniques manipulate sets of individuals (solutions) by using the genetic operators (selection, reproduction, crossover and mutation) in order to propose better ones. Chromosomes represent the individuals in the population. A structure of the chromosome used in the estimation procedure illustrates Fig. 2. The chromosome consists of four values, corresponding to the searched parameters of the equation describing the polarization curve, and their tuning range has been defined as follows: $0.01 \le A \le 0.4$, $0.00001 \le r \le 0.002$, $0.00001 \le m \le 0.002$, $0.001 \le n \le 0.02$.

A	r	m	n

Fig. 2. Chromosome definition

Table 1 shows estimated parameters of the (19) achieved for the following configuration of the GA:

- population – 20,
- crossover – 0.8,
- mutation – 0.05,
- generation – 100,

and the cost function J in form:

$$J = \min_{i_k} \sum \left[V_m(i_k) - V_s(i_k) \right]^2 \tag{23}$$

where V_m and V_s are a measured voltage and a calculated one, respectively.

Table 1. Estimated parameters of the polarization curve

A	0.0347
r	0.000047
m	0.0002
n	0.0049

The polarization curves, measured and computed from (19) with the estimated coefficients A, r, m, n are shown in Fig. 3. There is clearly seen that the real polarization curve is very well approximated by the dependency (19) with parameters obtained by the GA.

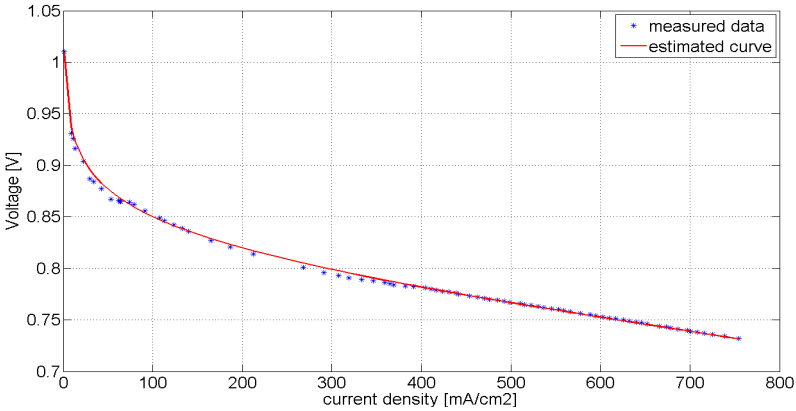

Fig. 3. Measured and calculated polarization curve

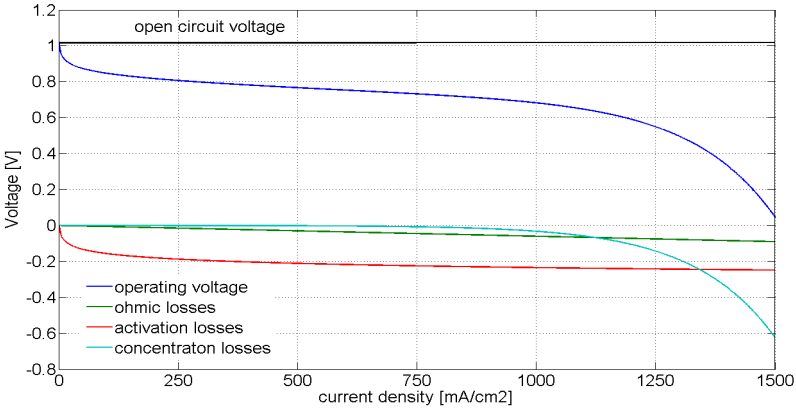

Fig. 4. Polarization curve and voltage losses for the extended current densities

It should be remembered that each voltage losses, described in Section 2.2, has different impact on a total voltage drop depending on an actual current density. For low current densities activation voltage losses strongly influence the operating voltage of

the cell, since the concentration and ohmic losses are almost negligible. However, the situation changes when the current density increases strongly. Then, the concentration losses start to play much more significant role in the total voltage drop.

Characteristics of the voltage losses, i.e. activation (12), ohmic (14) and the concentration losses (15) versus the cell current density are presented in Fig. 4. To illustrate an influence of each type of them, the polarization curve and the voltage losses characteristics were extrapolated for the current density exceeding the values from the experiment.

To estimate more correctly the parameters *m* and *n*, important for the concentration voltage losses, the polarization curve should be measured for greater current densities. It is planned in the nearest future after adapting the FC system for dissipation of larger amounts of heat.

5 Summary

The paper presents the static model of the fuel cell operating on hydrogen and oxygen in a form of the equation describing the polarization curve. The voltage losses, i.e. activation, concentration and ohmic ones, were taken into account in a process of formulation of the mathematical description of the model.

Parameters of the model were determined by the Genetic Algorithms basis on values of the polarization curve gathered in a laboratory stand with the PEM FC stack. Achieved results confirm that the proposed approach provides good estimation of the unknown parameters and the obtained model properly reflects behaviour of the real fuel cell.

A main advantage of possession of the mathematical model of the PEM FC is ability to calculate the voltage values in function of demanded current density for different operating conditions. Ability to compare the theoretical and measured voltages will be very useful during developing procedures both, control of the fuel cell system and diagnosis its proper operation.

Further research works will focus at examining whether and how pure oxygen used to supply the fuel cell influences the overall performance of the PEM FC system initially designed to operate on air.

Acknowledgement. This work was partially supported under a research grant (2011–2013) by the Polish National Centre for Research and Development.

References

1. Larminie, J., Dicks, A.: Fuel Cell Systems Explained. John Willey & Sons Ltd., Chichester (2003)
2. Barbir, F.: PEM Fuel Cells: Theory and Practice. Elsevier, California (2005)
3. Grzeczka, G., Polak, A.: The Analysis of Applicability of Fuel Cells for Autonomous Underwater Platforms. Logistyka 3, 805–814 (2011) (in Polish)

4. Pukrushpan, J., Stefanopoulou, A., Peng, H.: Control of Fuel Cell Power Systems. Advances in Industrial Control. Springer (2004)
5. Haraldsson, K., Wipke, K.: Evaluating PEM Fuel Cell System Models. Journal of Power Sources 126, 88–97 (2004)
6. Rowe, A., Li, X.: Mathematical Modeling of Proton Exchange Membrane Fuel Cells. Journal of Power Sources 102, 82–96 (2001)
7. Garus, J.: Modeling of Fuel Cell Energy System for Use in AUV. International Journal of Arts & Sciences 6(3), 15–22 (2013)
8. Żak, B., Hożyń, S.: Fuzzy Control of Reactant Supply System in PEM Fuel Cell. Solid State Phenomena 180, 11–19 (2012)
9. Al-Dabbagh, A.W., Lu, L., Mazza, A.: Modelling, Simulation and Control of a Proton Exchange Membrane Fuel Cell Power System. International Journal of Hydro-gen Energy 35, 5061–5069 (2010)
10. Goldberg, D.: Genetic Algorithms in Search, Optimisation, and Machine Learning. Adison-Wesley (1989)
11. Michalewicz, Z.: Genetic Algorithms + Data Structures = Evolution Programs. Springer (1994)

Development of Wireless Passive Sensing Platform – Communication Issues

Przemysław Gonek, Mateusz Lisowski, and Tadeusz Uhl

AGH University of Science and Technology, Krakow, Poland
mateusz.lisowski@agh.edu.pl

Abstract. This paper presents a concept and investigations on wireless sensing platform utilizing Radio Frequency Identification (RFID) technology. The platform should serve as a completely passive wireless communication interface between any connected sensor (strain gauge, accelerometer, pressure sensor) and standard RFID reader. Entire energy needed for powering is delivered via magnetic coupling between the reader and a planar coil antenna, which is one of the platform parts. The same electromagnetic signal serves for communication and data acquisition based on backscattering technique. Designed platform could be used in many applications, especially in structural health monitoring (SHM) and for advanced diagnostic purposes. Scope of the parts of investigations presented in this work was acceleration of data rate between the platform and the reader. Efficient data transfer is the primary problem in many potential applications. By improvement of communication and data storage algorithms, as well as testing of different types of RFID readers, we achieve effective data rate on the level of 18 Kbit/s. By meaning of the effective data rate, it is defined data stored from sensor on EEPROM memory, not only UID, that is transferred in typical RFID systems.

Keywords: wireless sensing platform, passive RFID, data rate.

1 Introduction

Development of sensors based on RFID technology is an easily noticeable trend in recent years. Using of specific properties related to wireless, passive communication technology allows to design sensor systems powered wirelessly without any battery. Generally there are two approaches to development of such sensor system. The first one could use transponder and its physical properties as a sensing element, the second method assumes the use of RFID transponder as a type of platform, to which one could connect a specified, low-energy sensor. Both approaches with given examples are well described in [1]. From the point of view of this paper, the most interesting reports are related to the investigation on different sensing platforms based on RFID technology with especially scope on the problem of wireless data transfer between the platform and the reader. The most advanced sensing platform is called WISP. It is widely described in many papers. One of the most accurate, related to design and performance is [2]. Any research institute could contribute to the development and

J. Awrejcewicz et al. (eds.), *Mechatronics: Ideas for Industrial Applications*,
Advances in Intelligent Systems and Computing 317, DOI: 10.1007/978-3-319-10990-9_5

thanks to this open form of the project, many papers reporting this specific application were released. One of the most interesting, related to using of WISP for the state monitoring of carbon fiber composites structure, was reported in [3]. Another sensing platform, called wireless sensor interface, in the form of specifically developed integral circuit was presented in [4]. Solution similar to that presented in this paper was reported in [5], however despite of using the same frequency band, which is the high frequency HF with the range of 13.56 MHz, reported read range is much smaller than in our solution. Other papers describing problem of data transfer are presented below. Summarizing, there are different reports concerning development of passive sensing platforms, but some of their properties cause that there is still need to search for solution better matched to defined requirements. In the case of the first platform, the problem is related to a complicated way of data transfer within ID number of the tag. In the case of the second one, the platform has not been implemented in wider application and is not available for testing. In the third one, the problem lies in a small read range.

The most important problem, from the point of view of this paper is the issue of data rate between sensing platform and typical RFID reader. Data rate in RFID systems is the complex problem concerning the versatility of RFID standard. The main reason are anti-collision algorithms which are used by any standard reader and give possibility to read as many RFID tags as it is possible in the shortest moment of time. Basic norms related only to HF and UHF range, which is in our concern, are ISO15693 and ISO18000-3 for HF and ISO18000-6 for UHF systems. Values of data rate given in norms are in the range from 6.62 Kbit/s [6] to 105.9375 Kbit/s [7] for HF systems and 40 Kbit/s for UHF [8]. The important thing is that the data rate is on sufficient level for typical RFID application, which is identification of many transponders with short UID, which states no load for communication algorithms. The problem starts, when one wants to use the RFID system for the purpose of large data transfers, for instance from the connected sensor. In this case, provided values of data rate do not correspond with reality. Unfortunately referenced papers give no straight information related to data rate of described systems and these information could be only deduced on the basis of another fact given in reports. In the case of [2, 3], the WISP was used only in the tasks with weak requirements related to data rate issues, in application such a quasi-static deformation analysis, temperature measurements or passive data logging. High values of data rate are rather impossible in this case, due to the setting of measured value into UID, which causes necessity of repeating of reader inventory round for every new portion of data, what strongly elongates data transfer. This feature could be improved by using custom commands similar to these presented in the next report. In the case of [4], the developed CMOS system send 2 bytes of sensing data in one read activity (with two additional 4 bytes related to the calibration data and source information), which value is low in comparison to 128 bytes of sensing data reported in this paper. In the paper [5], there is no any information that could be related to the estimation of the data rate achieved by authors.

To accelerate the data transfer one could develop his own communication algorithm, as it was reported in [9]. Other papers report development of completely new link layer for backscatter communication with many improvements comparing to

standard EPC code (For systems working in UHF) [10, 11]. There are also attempts to improve standard anti-collision algorithms by slightly modifying them [12]. In the case of the platform described in this paper, a method that lays between these presented above was chosen. After preliminary investigations, it was obvious, that data transfer should be accelerated, although there was not necessity to develop a new communication layer. Authors have decided to use standard, accessible communication libraries, but with simultaneous development of new software layer of standard RFID reader, as well as using specific data management algorithms on the platforms hardware. The chosen methods allow to achieve data rate sufficient for assumed requirements connected with using designed platform for SHM purposes, especially in tasks, related to structure vibration and strain monitoring with the help of strain gauges and accelerometers.

2 Concept of Sensing Platform

This paper presents a completely new concept of wireless, passive sensing platform. The entire design is based on two main devices. First one is a low-powered microcontroller STM32F051, which is responsible for data acquisition and digitalization. It also controls transfer of data via I2C protocol to the dual-interface EEPROM memory and to the AT45DB ash memory, which states the buffer for large amount of data. The second main element is the dual-interface EEPROM, that possesses communication possibilities via I^2C protocol and via wireless protocol, compliant to standard ISO15693, with typical RFID readers. This element is M24LR64-R chip from ST Microelectronics, which is intended to work in HF band and has memory size of 64 Kbit. For evaluation and investigation purposes, the first design presented on the Fig. 1, has a form of a board with many important signal probes and various powering options and communication interfaces. This allows easy monitoring of signal flow during platform activity and choosing the most efficient components for the final design.

The platform consists of four main parts, which are power supply, analog, communication and supervision circuits. The power supply contains a planar coil antenna tuned to the HF frequency to achieve the best energy transfer between the reader and the sensing platform. Antenna signal is rectified and then conditioned by different elements, operational amplifiers, diodes and inductors. The analog parts consist of an operational amplifier, that amplifies the differential signal from the strain gauge or any other sensor. Next, the signal goes to the analog-digital converter, which is the integral part of the microcontroller. This element, together with the dual-interface EEPROM, is the main part of the communication and supervision sections of the platform. Amplified analog signal from the sensor is converted to digital form and sent to the ash memory. These two processes are capable of executing simultaneously, thanks to the usage of two memory buffers created in RAM memory of the microcontroller. Data from the sensor is gathered in one buffer, while at the same time, the part of data from the second buffer is sent to the ash memory. After overloading of the first

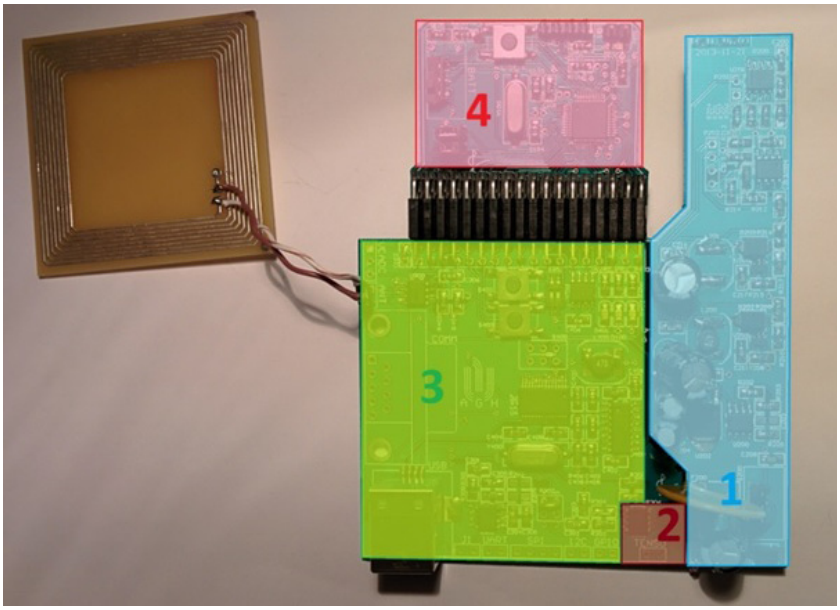

Fig. 1. Evaluation prototype board of wireless sensing platform with four main parts: power supply (1), analog (2), communication (3) and supervision (4) with additional communication planar coil antenna

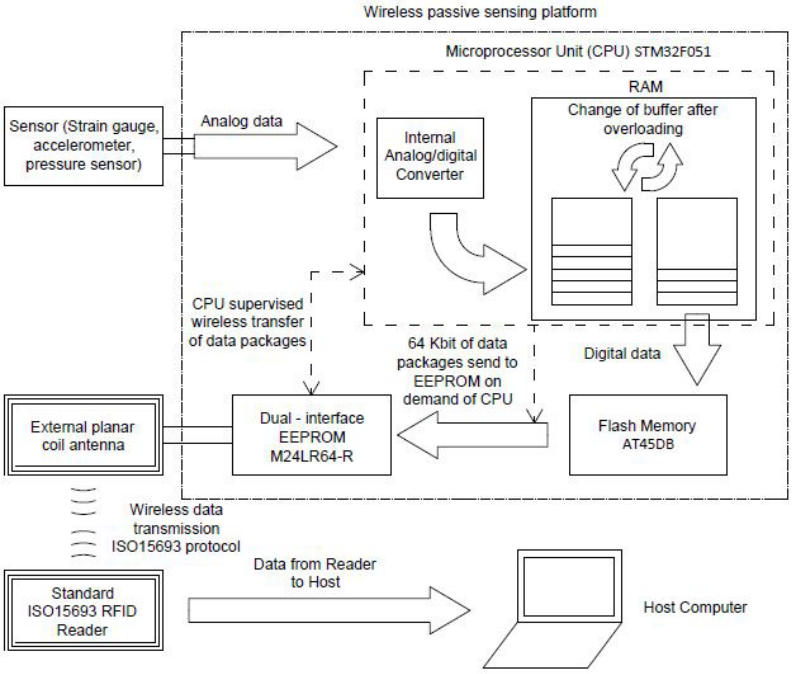

Fig. 2. Data Management process

buffer, their roles turn. This approach allows storing data on the ash memory quasi-directly, where only limitation states capacity of the ash, which in our case is 4 Mbit. Wireless data transfer is also supervised by the microcontroller. Data stored on the ash is divided into 64 Kbit packages and sent to the EEPROM by command of the processor unit. On request of the reader, packages of data are sent wirelessly to the host computer and after completion of this task, a proper signal is sent to the microprocessor from the EEPROM. Whole loop is repeated until all data stored on the ash is sent to the host computer. Entire process of data management is illustrated on the Fig. 2. The communication part also consists of FT232RL and MAX3232CSE, responsible for communication via USB and RS-232 interfaces for the testing purposes. These parts will be excluded in final design.

3 Communication Principles

Problem of communication plays an important role in many wireless data transfer systems. RFID is a technology, where this issue could be considered at different levels. First of all, one could distinguish different layers of communication system, which typically are divided into physical and software layer. This paper brings only fundamental information related to communication issues in RFID passive systems, especially the part that is important for understanding of performed investigations and their reasons. They could be treated only as the tip of the iceberg. For those, who are interested in more complex information, detailed formulas and physical principles of described phenomenon, authors recommend to reference to given sources [13, 14].

The problems related to improvement of communication performance at the physical layer needs wide knowledge and experience in antenna and microwave technology, as well as good basis in theoretical electromagnetic problems. The communication between the reader and the transponder is based on the readers electromagnetic signal reflection by the transponder and the data transfer via impedance modification, according to adopted modulation and coding method. Physical layer is strongly different from the systems based on various frequency ranges. In case of systems operating in LF and HF frequency the antennas of reader and transponder take the form of a planar coil and the contact between them is based on the mutual coupling phenomenon. In this case, important role is played by tuning the planar coil inductance in order to achieve defined frequency resonance and thus maximize the read range. This feature is considered as the most important in different wireless identification systems. In the case of inductive coupled systems, beyond the tuning of antenna, a very important attribute of the antenna is its dimension. Because the read range depends not only on the antenna tuning, but also on the number of magnetic flux lines flowing through the planar coil and on the constant maximal power of the reader antenna that is limited by particular standards, it could be maximized by increasing the transponder antenna size. This is the reason that the engineer, who designs RFID system based on HF frequency range, should always look for trade off between miniaturization and the designed read range, he wants to achieve. Accepted standard is the dimension of the planar coil antenna that corresponds to a typical dimension of a credit card. In case of

UHF systems the communication takes place between the reader and the transponder antenna via the electromagnetic waves reflection. In this case, an important issue is a proper impedance matching between the transponder circuit and the antenna. Generally UHF systems are characterized by a larger read distance, ranging up to 10 meters, but the amount of an energy delivered by the reader is much smaller, than in the case of magnetic coupling. Therefore it is more complicated to base the sensing system on the UHF range (less energy for sensing, data managing and sending of large amount of stored data purposes), although as it was shown in [2, 4], it is not impossible.

The software layer could be considered generally as a readers software section, although a part of this layer is located on the side of transponder chip. It usually is programmed by manufacturer without any possibility to implement changes. The only exception is the system reported in [2], where the standard RFID chip was not used and the role of it is played by a low-powered microcontroller, however this solution is designed for the communication with one particular type of the reader. On the side of the reader, the user could have different access to the software layer depends on the manufacturer. Typically it is ready to use software environment, designed to communicate with transponders and data storing. For users that want to create their own software, there are available libraries with typical commands compatible with particular standard, for instance ISO 15693. These commands, however are the high level instructions. For those, who want to make changes in the core level of the communication, e.g. anti-collision algorithms and management of many transponders reading, they should program the reader on the lower, hardware level, which is not always available for standard users. It should be noted, that standard RFID system is designed for the communication with as many transponders as it is possible in the shortest moment of time and these communication algorithms are not well-suited for the purpose of large amount of data transfer from lesser number of transponders and often, the changes should be introduced on this lower level. The programming part of works reported in this paper was a compromise between difficulty of the access to defined software level and the possibility to achieving better performance.

4 Investigation

The main purpose of investigations reported in this paper was achieving the best data rate, on the way of software improvements and data management optimization. By the way, the authors also estimated the maximal read range of the entire system. Investigations were performed on the evaluation board described in the Section 2. The data rate and the read range was assessed for three different setups. In the first case, the RFID reader equipped with internal antenna, compatible with the ISO 14443 standard with additional emulation that allows communication according to standard ISO 15693. In the second arrangement FEIG OBID ID ISC.MR101-A/USB reader was connected to external antenna, compatible with ISO 15693, supported by the standard software supplied by the manufacturer. In the third case, the same reader was used, but with the software developed by authors, whose nature is described in this section. The role of an exemplary data for sending instead of sensor data, was played

by a simulated curve from the signal generator. In each case, the bit rate was checked for the maximal amount of data, that is 64 Kbit, possible to be stored on EEPROM. In case of different readers, the maximal read range was also measured, by connecting the planar coil antenna with the typical credit card dimension, to the sensing platform.

The changes, that improve data rate was introduced, beside the data management algorithm described in Section 2, at the software level of reader. In the standard software, provided by manufacturer, by using multiblock read command, 8 blocks are transferred during one transmission step. It is possible to read 32 blocks at once, provided that they are in the same sector and this change was introduced. This modification is fitted to particular purpose, which is transfer of large amounts of data from one transponder in the range of reader. Additionally, the entire procedure of data transfer is placed in separate thread, what prevents blockade of software operations during reading the data from platform. In the host computer, data is stored in the form of unit16 numbers, what allows for easy export to typical computing environment, for instance MATLAB.

5 Results and Discussion

Achieved results from performed investigations, related to the data rate and the read range are presented in the Tab. 1. They are briefly discussed in this section. In the case of reader compatible with ISO 14443 standard, the short read range is caused by small dimension of the reader antenna and the fact, that it is intended for Mifare standard. The low data rate is the result of incomplete compatibility of reader with the ISO 15693 standard. It supports this standard, by predefined reader commands, which introduce abstraction level, that makes reader more versatile, but at the same time, slower for this specific use. In two next cases, the usage of external reader antenna with larger surface area, allowed to achieve a read range on the level of 30 cm. It makes the sensing platform suitable for assumed applications. The usage of self developed software allows to achieve the best data rate (two times better, than by using standard supplied software), with the value of about 18 Kbit/s. Only that value could correspond with the maximal data rate reported by manufacturer, which is 26 Kbit/s. Making assumption, that this given value corresponds only to the transfer of small amount of data, i.e. UID from transponder, experimentally achieved value seems to be reasonable. It should be noted that the achieved value of data rate corresponds to the entire read range, namely the data rate is independent from the distance between the reader and the platform. It is typical feature of standard RFID systems.

Table 1. Read range and data rate results

Setup	Mifare reader with ISO 15693 emulation	FEIG OBID ID ISC.MR101-A/USB, standard software	FEIG OBID ID ISC.MR101-A/USB, software developed by authors
Read Range	3 cm	30 cm	30 cm
Data Rate	3.5 Kbit/s	9 Kbit/s	18 Kbit/s

6 Conclusions and Future Works

The concept and prototype of wireless passive sensing platform based on RFID technology reported in this paper fits well to many diagnostic and monitoring purposes. Its features place it at the forefront of similar solutions reported in the referenced papers. Preliminary investigations described in this paper concern data transfer purposes. A data management algorithm and the method of wireless data transfer that allow to achieve a bit rate on the level of 18 Kbit/s were presented. Although typical data rate of standard RFID systems could be higher, this is the value related to the transfer of small amounts of data in the form of UID. Information connected with high-volume data transfer are not typically given by the manufacturer. Using RFID chip with EEPROM onboard memory in connection with ash memory that serves as a buffer, allows for easy wireless high-volume data transfer supervised by low-power microcontroller. Achieved read range of 30 cm is also a great advantage compared to different solutions based on HF RFID standard. Performed investigations show, that presented sensing platform could be used in applications related to structural health monitoring of flying objects, especially diagnostic of helicopter rotor blades, as well as in other advanced diagnostic purposes, with the scope on application connected with placing the sensing nodes on moving objects. It needs further investigations related to energy management systems, software optimization and above all application tests performed first in the laboratory and then, on typical exploited objects.

References

1. Lisowski, M., Uhl, T.: RFID based sensing for structural health monitoring. Key Engineering Materials 569-570, 1178–1185 (2013), doi:10.4028/www.scientific.net/KEM.569-570.1178
2. Sample, A., Yeager, D., Powledge, P., Mamishev, A., Smith, J.: Design of an RFID-based battery-free programmable sensing platform. IEEE Transactions on Instrumentation and Measurement 57(11) (November 2008), doi:10.1109/TIM.2008.925019; 2608 RFID based sensing for structural health monitoring 2615
3. Gasco, F., Feraboli, P., Braun, J., Smith, J., Stickler, P., DeOto, L.: Wireless strain measurement for structural testing and health monitoring of carbon fiber composites. Composites. Part A: Applied Science and Manufacturing 42(9), 1263–1274 (2011), doi:10.1016/j.compositesa.2011.05.008
4. Ussmueller, T., Brenk, D., Essel, J., Heidrich, J., Fischer, G., Weigel, R.: A multistandard hf/uhf-rfid-tag with integrated sensor interface and localization capability. In: 2012 IEEE International Conference on RFID, pp. 66–73 (2012), doi:10.1109/RFID.2012.6193058
5. Ikemoto, Y., Suzuki, S., Okamoto, H., Murakami, H., Lin, X., Itoh, H., Asama, H.: Force sensor system for structural health monitoring using passive rfid tags for structural health monitoring. Sensor Review 29(2), 127–136 (2009), doi:10.1108/02602280910936237
6. ISO/IEC 15693 Identification cards – Contactless integrated circuit(s) cards – Vicinity cards
7. ISO/IEC 18000-3:2010 Information technology – Radio frequency identification for item management – Part 3: Parameters for air interface communications at 13,56 MHz

8. ISO/IEC 18000-6:2013 Information technology – Radio frequency identification for item management – Part 6: Parameters for air interface communications at 860 MHz to 960 MHz General
9. Cika, D., Draganic, M., Sipus, Z.: Active wireless sensor with radio frequency identification chip. In: Proceedings of the 35th International Convention MIPRO, pp. 727–732 (2012)
10. Gummeson, J., Zhang, P., Ganesan, D.: Flit: a bulk transmission protocol for RFID-scale sensors. In: Proceedings of the 10th International Conference on Mobile Systems, Applications, and Services, MobiSys 2012 (2012), doi:10.1145/2307636.2307644
11. Zhang, P., Gummeson, J., Ganesan, D.: Blink: A high throughput link layer for backscatter communication. In: Proceedings of the 10th International Conference on Mobile Systems, Applications, and Services, MobiSys 2012, pp. 99–112 (2012), doi:10.1145/2307636.2307646
12. Alma'aitah, A., Hassanein, H., Ibnkahla, M.: Modulation silencing: Novel RFID anti-collision resolution for passive tags. In: 2012 IEEE International Conference on RFID (2012), doi:10.1109/RFID.2012.6193060
13. Finkenzeller, K.: RFID Handbook: Fundamentals and Applications in Contactless Smart Cards and Identification, 2nd edn. Wiley (2003), doi:10.1002/9780470665121
14. Lehpamer, H.: RFID Design Principles, 2nd edn. Artech House Publishers (2012)

Value of the Internet of Things for the Industry – An Overview

Małgorzata Kaliczyńska and Przemysław Dąbek

Industrial Research Institute for Automation and Measurements PIAP, Warsaw, Poland
{mkaliczynska,pdabek}@piap.pl

Abstract. The Internet of Things (IoT) is a concept according to which uniquely identifiable things can indirectly or directly collect, process or exchange data via Wide Area Network – the Internet. Recently this concept has become a hot topic in science and resulted in multiple new technology developments. There is however also a lot of ambiguity surrounding the topic, which leads to questions if the IoT is a fad or a profound phenomenon. This article aims at answering the question about the value of the IoT idea for the industry. Academic definition of the concept is presented, global standardization initiatives reviewed, and a short survey of key technologies made. Then several existing and prospective applications involving the Internet of Things technologies are analyzed to determine values of this phenomenon from the point of view of the Industry understood as production of goods and services. Business models enabled or supported by the Internet of Things are also briefly described. It is concluded that there is substance in the IoT idea and the Industry can benefit from its adoption.

Keywords: Internet of Things, industry, standards, protocols.

1 Introduction

The term *Internet of Things* (IoT) was coined by Procter & Gamble employee Kevin Ashton in 1999 in the context of supply chain management [1]. It conveys a quite simple to understand idea that *Things* (that is arbitrary objects existing in the world) become connected to *The Internet* (that is the worldwide network used by billions of people every day) and start to exchange data between each other.

Realization of this idea seems to be underway and soon we may witness proliferation of smart cities, where every street lamp, water hydrant, traffic lights, bridges and other elements of urban infrastructure will be connected to the Internet.

On the other hand the idea of connecting devices into a network is nothing new in the industrial automation domain, so is it really necessary to push the Internet-related technologies there where many solutions exist today with proprietary technologies and they function well?

Maybe the biggest winner of the *Internet of Things* will be the ICT companies that offer Internet-related solutions to the Machine-to-Machine market?

In 2010 European Telecommunications Standards Institute (ETSI) published annual report, in which it estimated that out of 50 billion machines only 50 million were

J. Awrejcewicz et al. (eds.), *Mechatronics: Ideas for Industrial Applications*,
Advances in Intelligent Systems and Computing 317, DOI: 10.1007/978-3-319-10990-9_6

connected, that is roughly 1 %, with potential 99 % market gap [2]. Major ICT market players already coined their own terms to call the concepts closely related to the *Internet of Things* like *Industrial Internet* (GE) [3], *Internet of Everything*, *Smart+Connected Manufacturing* (both Cisco) [4], *Smarter Planet* (IBM) [5].

Is there a real value for various industries in the concept of IoT, or it is more a buzzword which does not have much substance?

In the attempt to find the answer, first an academic definition of the Internet of Things concept is given, related activities of major standardization bodies are reviewed, a brief survey of available technologies is presented, and finally several industry-related existing and prospective applications are analyzed to determine value of the IoT for the industry.

2 Definition

It is possible to find in the literature many definitions associated with the term *Internet of Things* [6]. Authors of the present work decided to use the definition proposed by the IERC-European Research Cluster on the Internet of Things [7]:

"A dynamic global network infrastructure with self-configuring capabilities based on standard and interoperable communication protocols where physical and virtual *things* have identities, physical attributes, and virtual personalities and use intelligent interfaces, and are seamlessly integrated into the information network."

The above definition seems comprehensive and has been already adopted by some Authors [8].

3 Standardization Support for the Internet of Things

Development of the Internet of Things has become an important area of standardization activities undertaken by major institutions both at national and international levels (Tab. 1).

In 2012 seven of the world leading standard development organizations for information and communications technology established a new global organization – oneM2M – with aim to *create technical specifications to ensure that Machine-to-Machine communications can effectively operate on a worldwide scale* [9]. IEEE maintains a Web Portal for topics related to the Internet of Things [10], and a separate webpage where IEEE standards connected with this concept can be found [11].

Important activities are also carried out at the international level. IETF has four active working groups concerned with problems of adaptation of the protocols to the needs of low power (or constrained) devices [12]: (1) Constrained RESTful Environments, (2) IPv6 over Networks of Resource-constrained Nodes, (3) Routing Over Low power and Lossy networks and (4) Authentication and Authorization for Constrained Environments. The World Wide Web Consortium is involved in the Ubiquitous Web Applications activity, with working groups on developing standard application programming interfaces (APIs) to enable more secure device geolocation, easier use of Near-Field Communications technology or real-time communication

between web browsers [13]. The Global Standards Initiative on Internet of Things (IoT-GSI) aims to act as an umbrella for IoT standards development worldwide. Apart from that, recommendations developed under the IoT-GSI in collaboration with other standards developing organizations will enable worldwide service providers to offer the wide range of services expected by this technology [14]. Finally, there is a special working group 5 of the joint technical committee of ISO and IEC devoted to the Internet of Things which aims at consolidation of works of internal agendas and external bodies rather than at publishing standards [15, 16].

Table 1. Initiatives of major national and international standardization institutions to support development of a worldwide network of connected devices

Region	Name of the Institution	Initiative
Europe	ETSI European Telecommunications Standards Institute	oneM2M
Japan	TTC Telecommunication Technology Committee	
Japan	ARIB Association of Radio Industries and Businesses	
Korea	TTA Telecommunication Technology Association	
China	CCSA China Communications Standards Association	
USA	ATIS Alliance for Telecommunications Industry Solutions	
USA	TIA Telecommunications Industry Associations	
USA	IEEE Institute of Electrical and Electronics Engineers	IoT Web Portal
Int'l	IETF Internet Engineering Task Force	4 Working Groups
Int'l	W3C World Wide Web Consortium	Ubiquitous Web Applications Activity
Int'l	ITU International Telecommunication Union	Internet of Things Global Standards Initiative
Int'l	ISO International Organization for Standardization	ISO/IEC JTC 1/SWG 5 Internet of Things (IoT)
Int'l	IEC International Electrotechnical Commission	

4 Technology Overview

4.1 General Architecture

A general architecture of the contemporary Internet of Things (IoT) is presented in Fig. 1. A *Thing* symbolizes any object equipped with a communication module allowing it to access the Internet. Depending on the type of communication module and power capabilities of the object, connection with the Wide Area Network may be possible directly or via the IoT Gateway. The IoT Gateway differs from ordinary gateways in capability to handle different short-range communication standards (e.g. Bluetooth, ZigBee, Wi-Fi, etc.). A particular type of devices that can be connected to

the Internet are sensors, usually deployed as a wireless sensor network (WSN) including a large number of sensors characterized by the very low transmitter power and extremely low energy consumption. Data from those sensors is usually routed to final destination by the special node of greater capabilities.

The important components of the system are Service Providers that handle tasks associated with effective realization of variety of applications, e.g. provide data storage, expose sensors to top-level applications, facilitate negotiation of agreements between and users and devices owners, etc.

Some applications can be realized autonomously, but in many cases human supervision is needed or a human is the end user who receives demanded data or performs whatever actions he needs. In those cases a smartphone of the user can be the device of choice to provide the human-machine interface to the IoT application.

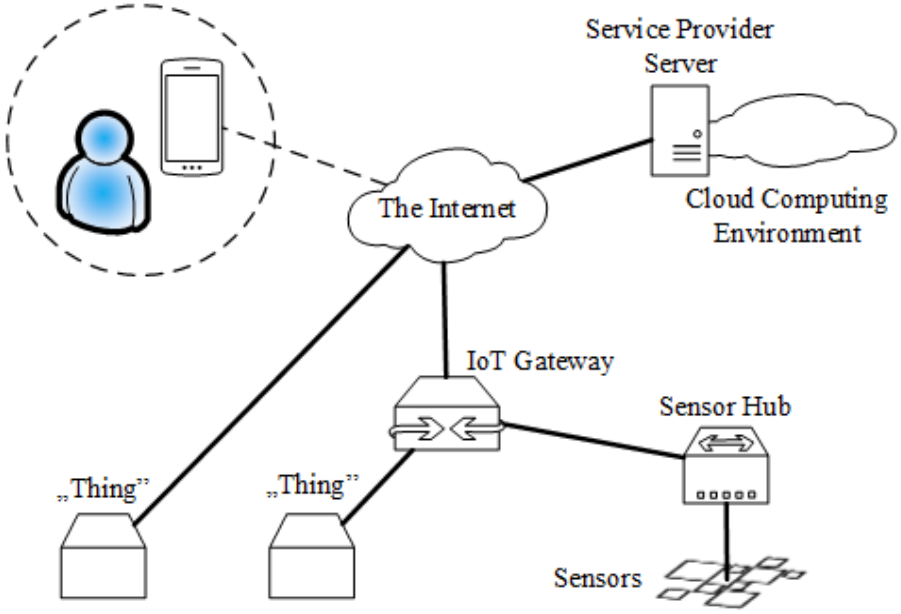

Fig. 1. The Internet of Things high-level architecture schematic

4.2 Key Technologies

Below a number of ICT technologies which enable the Internet of Things applications are briefly discussed. This review is not meant to be exhaustive, but it highlights which technologies are necessary and some available commercial solutions are also mentioned.

Hardware. The hardware layer comprises: edge devices (*Things*), optional gateways, access networks, backbone networks, equipment necessary to establish the cloud computing environment, and optional end user terminals.

Edge devices. The edge devices can be anything on condition that they have a communication module which allows direct or indirect connection to the Internet. The communication module must have appropriate size and energy consumption requirements to be easily incorporated into existing designs of *Things*. One possible solution is the Electric IMP [17] which has the size of an SD Card and provides Wi-Fi connectivity.

Gateways. Gateways are not the mandatory component, but in many scenarios they will be a part of the system as is the case with ordinary Internet solutions, because they offer enhanced protection of the local network and reduce cost and size of communication modules installed on the edge devices. Gateways for the Internet of Things should be capable of connecting devices using multiple short range communication protocols like Bluetooth Low Energy, ZigBee, Wi-Fi, etc. One of the commercial solutions is the Freescale IoT Gateway [18] which is to be introduced to the market by the end of 2014.

Access networks. Either the edge device itself or the gateway must be connected to the backbone (core) Internet via the access network with wired or wireless connection possible. Here the existing technologies used with the ordinary Internet can be used. Besides well known wired and mobile technologies (e.g. Fiber and LTE), the satellite technologies may be of greater use with the Internet of Things. They can be deployed in the areas with poor terrestial network infrastructure, which is particularly attractive for environment monitoring applications. Satellite technologies are usually viewed as expensive and having large latency. The o3b project aims at changing this stereotype, by deploying a constellation of satellites at the orbital height of about 8000 km [19] (as compared to geostationary satellites at 35 000 km orbital heights).

Backbone (*core*) *networks.* The backbone networks for the Internet of Things are likely to share the hardware technology with the ordinary Internet.

Cloud computing. Hardware technologies to provide cloud services for the Internet of Things can be the same as for the classic Internet. Bare metal servers (dedicated hardware) or virtual servers (shared hardware) completely configurable according to customer demand are offered, e.g. by SoftLayer (an IBM company) [20]. With time, growing number of connected devices and increase in amount of generated data associated with development of IoT may set new requirements for the cloud infrastructure.

End user terminals. End user terminals in many cases can be based on existing solutions, i.e. industrial panel PCs, desktop personal computers, and many kinds of mobile devices including tablets and smartphones.

Software. The software layer for the Internet of Things devices can be presented by reference to the ETSI M2M functional architecture described in [21] and discussed in [22]. This architecture is probably the most advanced proposal for the global standard for connected devices interoperability today.

The ETSI M2M functional architecture design is based on Service Capabilities that various devices connected to the network may have and conforms to the Representational State Transfer (REST) style [23]. With this architecture services offered by devices and their resources are uniquely identified by Uniform Resource Identifiers (URIs). Resources can be registered or discovered and used by applications running on devices connected to the network.

This approach allows an application to access the network resources without explicitly referring to specific protocols used by different devices.

Recently there has been a number of efforts to adapt existing protocols to the constraints of energy and computing power at small connected devices like Bluetooth Low Energy (BLE) [24], ZigBee Smart Energy Profile 2 [25]. Another important effort by IETF to bring IPv6 support in constrained devices resulted in 6LoWPAN specification [26].

For running applications on a low power connected device open source operating systems like Contiki-OS are already available. The Contiki-OS features full IP network stack and supports the recent protocols like 6LoWPAN, RPL and CoAP, and also implements mechanisms for power saving [27].

Cloud Services. There already exist providers of cloud services *specifically built for the Internet of Things* like Xively [28]. Xively offers a public cloud with searchable directory of devices, data storage for time-series archiving and API to build user applications.

As it can be seen, it is clear that from the technological point of view the Internet of Things is already possible. One of the main concerns is establishment of global standards to create good conditions for its development. International and national level initiatives towards this goal are underway and were briefly discussed in the previous section.

5 Applications

5.1 Methodology

In order to determine values for the Industry associated with the Internet of Things, the analysis of existing and possible applications was carried out.

Analyzed applications were taken from the oneM2M collection of Use Cases [9]. Out of 33 Use Cases, 9 pertaining to the Industry were selected (the Industry is understood as a business that focuses on production of goods and services).

The selected applications were classified according to their application patterns. There is a variety of applications possible across different market sectors, but it is possible to qualify those applications into several categories, according to the underlying idea of an application. This division brings clarity to the description.

Analysis of applications from the point of view of values for the Industry was conducted with the Value Reference Model [29] in mind. It is possible to group the values into those which stem from *any* connectivity of machines (things) and those which emerge only when this connectivity is realized according to the *Internet of Things* concept and with cooperation of multiple stakeholders.

Basic business models that are possible with the Internet of Things are also presented.

5.2 Application Patterns

In Table 2 selected applications from the oneM2M collection of Use Cases [9] are summarized. Names of the applications are in most cases self-explanatory and no extensive description of each application will be given here. Interested reader may find necessary details in document [9] – the symbol of the Use Case from that document is given in the column *Use Case*.

Table 2. Selected applications from oneM2M collection of Use Cases [9]

Sector	Application Name	Use Case	Application Pattern
Energy	Smart Meter Reading	5.3	SN
Transportation	Remote Maintenance Services	10.2	Data Deployment
Energy	Measurement & Control System for Advanced Transmission and Distribution Automation	5.1	SCADA
Energy	Environmental Monitoring of Remote Locations to Determine Hydropower	5.4	SCADA
Energy	Oil and Gas Pipeline Cellular/Satellite Gateway	5.5	SCADA
Transportation	Fleet Management Service using Digital Tachograph (DTG)	10.4	SCADA
Transportation	Devices, Virtual Devices and Things	8.2	Intelligent Device
Residential	Plug-in Electrical Charging Vehicles and Power Feed in Home Scenario	9.3	Intelligent Device
Residential	Semantic Device Plug and Play	9.7	Intelligent Device

Each of those specific applications can be viewed as developed around one of four application patterns: (1) Sensor Network pattern, (2) Maintenance pattern, (3) Supervisory Control and Data Acquisition pattern, and (4) Intelligent Function pattern. Definitions of those patterns, used in the present work, are given below.

Sensor Network Pattern (SN). Primary aim of application is data acquisition from a sensor or multiple sensors. Data acquired by the sensors are autonomously sent to the recipient over a network. Those data may be also analyzed in the intermediary step. The final consumer of the data is usually a human, who uses the data to make informed decisions.

Data Deployment Pattern. Primary aim of the application is data deployment to one or multiple devices. Data generated by a certain producer are autonomously sent to remote devices over a network. The producer of data is usually a human, who, for example, develops a new piece of software code and seeks an efficient way of updating firmware at target devices.

Supervisory Control And Data Acquisition Pattern (SCADA). Primary aim of this kind of application is the autonomous closed-loop control of a process involving devices with which communication is possible over single or multiple networks. With

this pattern both data acquisition from sensors and data deployment to actuators are mandatory. Also some decision center is assumed to exist, which operates autonomously with possible human intervention.

Intelligent Device Pattern. Primary aim of this type of application is to equip a thing (a device) with ability to autonomously carry out certain required actions on behalf of the owner. Unlike in the three previous patterns where the application was viewed from perspective of the whole system, here the view is shifted to the perspective of a single element of this system. The device needs network connectivity to be able to discover necessary data and make some decisions based on those data, in accordance with the rules predefined by the device owner.

5.3 Values of Connectivity of Things – A Single Operator Case

Connecting devices in a network has numerous advantages from the point of view of the Industry. Some of those advantages, which can be achieved already by efforts of only a single operator (or a small consortium of businesses of similar profile), are pointed out below.

No Necessity of Direct Contact. Big savings in business operational costs can be introduced, if it is no longer necessary for the personnel to go to remote locations. Those savings may include work hours and travel expenses.

A very good example is the introduction of smart electricity meters at consumer houses and premises, whose indications can be remotely read at any time thanks to network connectivity (Smart Meter Reading application, Table 2).

Another example is connected with remote operation of pipeline valves and equipment in the oil & gas industry (Oil and Gas Pipeline Cellular/Satellite Gateway, Table 2). Travel costs and work hours are saved, if there is no necessity to send staff to travel long distances to change valve settings for reducing or increasing flow through pipe.

Improved Quality of the Product. Improved quality of the primary function of the product contributes to gaining the competitive advantage by the producer.

In case of mechatronic devices, one of the elements which can be enhanced more frequently than others is software. The developments may include bug fixes and new functionalities which both improve end user experience. If the devices are connected to the network there is a possibility for manufacturer to deploy software updates to devices with small or no involvement of the user (Remote Maintenance Services, Table 2).

Another example may be controlling of power generation by hydroelectric power station using SCADA system (Environmental Monitoring of Remote Locations to Determine Hydropower, Table 2). Accurate information about environment state, especially about available water supply (e.g., from snow) and water levels, matters because it enables accurate predictions of power generation capabilities of the unit. This results in lower electrical energy costs. Apart from that, careful monitoring of environment allows making control adjustments to avoid natural environment damage and fines due to breaking regulations of the environmental law. As a result it may be said that product (energy) of better quality is obtained.

It should be emphasized that all of the above advantages are possible with the current state of the technology and do not require any extraordinary cooperation between business domains.

5.4 Values of Connectivity of Things – Cooperation between Operators

New possibilities to cut down on costs and improve quality of products arise when effective cooperation between resource owners or producers and consumers will become possible across business domains. This transition from the isolated model where every business develops its own solution, which requires similar infrastructure established multiple times, to the shared resources model, where necessary infrastructure and services can be rented, is viewed as the key value of the Internet of Things [30].

Below a number of opportunities introduced by the Internet of Things are discussed.

Lowering Sensor Costs. If data from a single sensor can be shared between many stakeholders instead of each stakeholder deploying proprietary sensor, cost of initial investment will be decreased. Alternatively, while retaining original level of investment costs more sensors can be installed, but in a coordinated manner, which would lead to improved quality of data.

A good example here is the Environmental Monitoring of Remote Locations to Determine Hydropower, mentioned earlier. Sensors of snow level, water level, temperature, pressure, etc. can be shared with national weather services and governmental agencies involved in crisis management activities.

Lowering Networking Costs. Similarly as in the case of sensors, network infrastructure can be shared by parallel applications. Most of the network the infrastructure for the communication between machines (devices) can be the same as the ordinary Internet infrastructure. However, there is also need for dedicated solutions to enable networking between devices of constrained energy resources (e.g. batteries) and Internet gateways. If those solutions can be standardized, then this last-mile infrastructure can be shared as well. Existence of widely accepted standards allows production of networking equipment in high volumes, which results in lower costs to the user.

Lowering Electrical Energy Costs. One of the key possibilities associated with introduction of the smart electric grid is to manage the demand for power over time so as to reduce power demand peaks [22]. Generation of additional energy to satisfy power peaks is the more expensive for the energy producer the higher is the peak. If the peaks can be made more flat, this would allow reduction of energy prices. Power peak management can be based on changing energy prices during the day, and equipment at the side of energy consumers reacting to those prices when possible (buy cheap).

An example is charging of batteries of an electric car described in the application named Plug-in Electrical Charging Vehicles and Power Feed in Home Scenario, Table 2. Vehicle can be equipped with a device that seeks the lowest energy rates from different energy suppliers based on their current tariffs updated in real time, and decides when to start and stop charging, according to rules set up by the vehicle owner.

This example is a vision of the future, but if realized then costs of electrical energy may be lower for the consumers. Similar management of electrical energy consumption may include also other devices and home appliances.

Improving Customer Satisfaction. Today it becomes more and more important for the manufacturer to deliver a product, which makes the buyer satisfied.

One of the possibilities introduced by the Internet of Things is collecting data about patterns of use of products by the customers, after they express appropriate consent. This already happens in the computer software domain, because most computers are connected to the Internet, so the information can be easily gathered. The same opportunity arises when various things become connected. If manufacturers have this data available, they can develop products which better suit the needs of a statistical buyer or even the custom made products.

An example of a product (envisioned) which improves customer experience can be the home lightning equipment: intelligent lamp and switch (Semantic Device Plug and Play, Table 2). After positioning equipment in their appropriate places in the room, the devices will autonomously communicate and register themselves in the local devices management system after power on. No configuration activity will be required from the user. This removes or reduces requirement of laying power wires in the walls for the purpose of light switching. Also the consumer can install the equipment all by themselves, because electrical skills are not necessary (if the lamp is powered through the conventional power cord with a wall plug). A graphical presentation of values described above on a blueprint of application patterns is presented in Fig. 2.

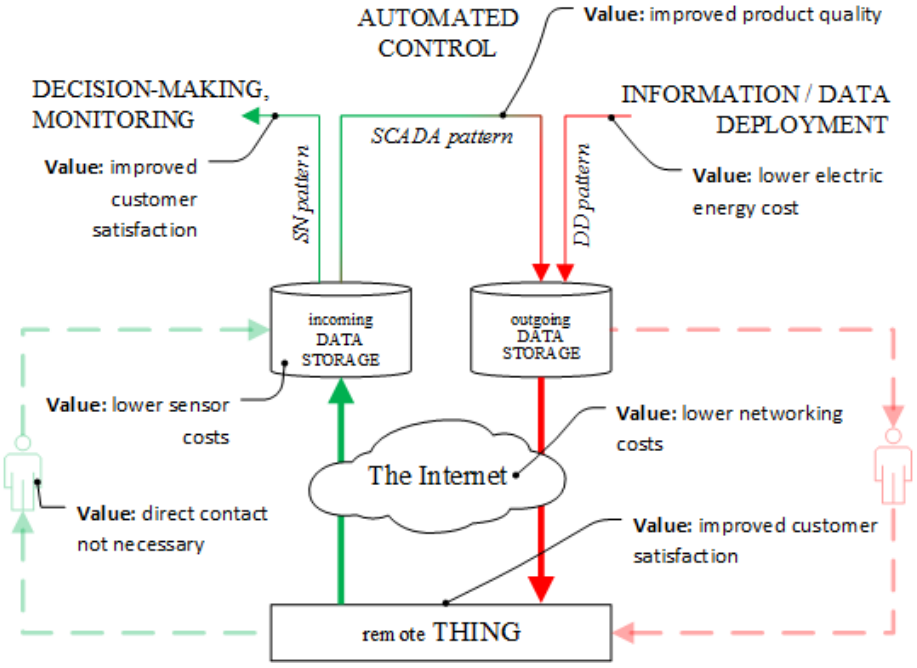

Fig. 2. Values of the Internet of Things for the Industry on a blueprint of application patterns

5.5 Business Models for Industry Enabled by the Internet of Things

The previous sections focused on the ways of improvement of a business by exploiting devices connectivity in general and their connectivity based specifically on the Internet of Things paradigm. In the present section, the basic business models, understood as methods of making profit, available with the Internet of Things are described.

Make Thing, Sell Thing. With this model, a manufacturer produces goods from raw materials and makes the profit by selling the goods to customers. When the Internet of Things is considered, this model will be used (and is already used) by manufacturers of hardware and software necessary to enable IoT functioning from the technical point of view. The market players sharing the market of the Internet hardware and software will benefit in the first place, but there may be also scope for new businesses oriented specifically to supply the IoT market, e.g. small size and low power communications modules, sensors, microcontrollers or microprocessors as well as firmware developed for those constrained embedded systems.

Selling Data from Sensors. The work [31] describes one possible model of selling data from sensors by a sensor owner to a sensor data consumer. This model assumes existence of a Sensor Publisher entity, a broker, who maintains available sensors database, provides means to find necessary sensors according to data consumer needs, and arranges contracts between the sensor owner and the data consumer. Data consumer can be, e.g. a food production company that wants to know preferences of its clients by monitoring contents of the end consumer refrigerator. In return for the data, the consumer receives either discounts on company's products or a monthly fee – the decision is made by the customer upon signing the contract.

Providing Services. The services known to be possible with the ordinary Internet, like providing access to the network, providing cloud computing services (Infrastructure-, Platform-, Software-as-a-Service), providing analytics services, etc., will probably proliferate with development of the Internet of Things. There are also opportunities for creating new services that will make the process of setting up the IoT applications easier or possible at all. One example is the Sensor Publisher service mentioned in the preceding point. Another interesting example can be management of home energy systems described in the oneM2M collection of Use Cases [9] (Use Case 9.2) for energy consumption minimization, provided by an external company on the basis of agreement with a home owner. This exemplifies a whole class of possible services, where professionals can offer their knowledge and expertise to fine tune or manage the user system.

The topic of making money from the Internet of Things is very important from the point of view of the Industry. IoT experts employed at renowned global companies (Ericsson, Nissan and Continental) share the view that the biggest challenge to overcome with the Internet of Things is monetization of the solutions [32]. The IoT solutions will likely involve agreements between multiple service providers having slightly different business models by themselves, and this will make those agreements highly complex and difficult to reach, maintain, manage and make profitable in the end.

6 Conclusion

In the article the concept and solutions associated with the Internet of Things are examined in order to get some insight in the value of this phenomenon for the Industry understood as production of goods and services. Based on the presented definition, review of global standardization initiatives, brief survey of existing and developed technologies and conducted analysis of applications from the point of view of potential value for the Industry following from introduction of the IoT, it can be concluded that the Internet of Things phenomenon is not a temporary buzz, but it is the evolution of the ordinary Internet which has capability to transform the Industry.

Availability of data from billions of connected devices containing variety of sensors may contribute to discovery of new knowledge, which will be used to improve people quality of life, to limit energy consumption and to protect natural environment. In the time span of a decade we should witness creation of *smart* environments in various domains – smart home, smart city, smart industry, etc.

Today leading automation equipment manufacturers seek their participation in the potential profits associated with the present and future Internet of Things implementations.

With rapidly increasing number of machines going on-line questions about ability of the existing and planned hardware and software to accommodate this growth should be discussed even more often to ensure harmonious development of the Internet of Things.

References

1. Ashton, K.: That 'Internet of Things' Thing. RFID Journal (2009)
2. ETSI, Annual Report (April 2010)
3. Industrial Internet|GE Intelligent Platforms, http://www.ge-ip.com/industrial-internet (accessed: June 08, 2014)
4. Internet of Everything, http://internetofeverything.cisco.com/ (accessed: June 08, 2014)
5. IBM – Smarter Planet – United States (July 03, 2014), http://www.ibm.com/smarterplanet/us/en/overview/ideas/?re=spf (accessed: June 08, 2014)
6. Internet of Things Definition, Postscapes, http://postscapes.com/internet-of-things-definition (accessed: June 07, 2014)
7. IERC-European Research Cluster on the Internet of Things, http://www.internet-of-things-research.eu/about_iot.htm (accessed: June 06, 2014]
8. Xu, L., He, W., Li, S.: Internet of Things in Industries: A Survey, IEEE Transactions on Industrial Informatics, Early Access Online (2014)
9. oneM2M|Welcome, http://www.onem2m.org/ (accessed: June 21, 2014]
10. IEEE Internet of Things, http://iot.ieee.org/ (accessed: June 05, 2014)
11. IEEE-SA – Internet of Things, http://standards.ieee.org/innovate/iot/ (accessed: June 05, 2014)
12. Active IETF Working Groups, http://datatracker.ietf.org/wg/ (accessed: June 05, 2014)

13. Ubiquitous Web Applications Activity Statement, http://www.w3.org/2007/uwa/Activity.html (accessed: June 23, 2014)
14. Internet of Things Global Standards Initiative, http://www.itu.int/en/ITU-T/gsi/iot/Pages/default.aspx (accessed: June 05, 2014)
15. Technical committees – ISO, http://www.iso.org/iso/home/standards_development/list_of_iso_technical_committees (accessed: June 05, 2014)
16. ISO/IEC JTC 1/SWG 5, Wikipedia, the free encyclopedia (June 01, 2014)
17. Electric Imp – Electric Imp, http://electricimp.com/ (accessed: June 08, 2014)
18. Video: Freescale Enables the Internet of Things...|element14, http://www.element14.com/community/videos/12405 (accessed: June 26, 2014)
19. Homepage – O3b Networks, http://www.o3bnetworks.com/ (accessed: June 08, 2014)
20. SoftLayer|Cloud Servers, Storage, Big Data, & More IAAS Solutions, http://www.softlayer.com (accessed: June 08, 2014)
21. ETSI, Machine-to-Machine communications (M2M): Functional architecture. ETSI TS 102 690
22. Hersent, O., Boswarthick, D., Elloumi, O.: The Internet of Things: Key Applications and Protocols, 2nd edn. Wiley, Chichester (2012)
23. Fielding Dissertation: Chapter 5: Representational State Transfer (REST), http://www.ics.uci.edu/~fielding/pubs/dissertation/rest_arch_style.htm (accessed: June 08, 2014)
24. Bluetooth Low Energy Technology|Bluetooth Technology Website, http://www.bluetooth.com/Pages/low-energy-tech-info.aspx (accessed: June 08, 2014)
25. ZigBee Smart Energy Profile 2, http://www.zigbee.org/Standards/ZigBeeSmartEnergy/SmartEnergyProfile2.aspx (accessed: June 08, 2014)
26. IPv6 over Low power WPAN (6lowpan) – Charter, http://datatracker.ietf.org/wg/6lowpan/charter/ (accessed: June 08, 2014)
27. Contiki: The Open Source Operating System for the Internet of Things, http://www.contiki-os.org (accessed: June 10, 2014)
28. Xively by LogMeIn – Business Solutions for the Internet of Things, https://xively.com/ (accessed: June 06, 2014)
29. Value Reference Model 3.0 – Value Chain Group, VCG Framework, Value Proposition, http://www.value-chain.org/value-reference-model (accessed: June 30, 2014)
30. Holler, J., Tsiatsis, V., Mulligan, C., Avesand, S., Karnouskos, S., Boyle, D.: From Machine-to-Machine to the Internet of Things: Introduction to a New Age of Intelligence, 1st edn. Academic Press, Amsterdam (2014)
31. Perera, C., Zaslavsky, A.: Improve the sustainability of Internet of Things through trading-based value creation. In: 2014 IEEE World Forum on Internet of Things (WF-IoT), pp. 135–140 (2014)
32. Digman, I., Luetzner, J., Lungren, M.: Free Webinar: The Internet of Things meets the Connected Car, http://vimeo.com/99903403 (accessed: July 05, 2014)

Programming and Computer Simulation of an Experimental Station for Automatic Launching of Badminton Shuttlecocks

Jerzy Karamuz, Paweł Olejnik, and Jan Awrejcewicz

Department of Automation, Biomechanics and Mechatronics,
Faculty of Mechanical Engineering of Lodz University of Technology,
1/15 Stefanowski Str., 90-924 Lodz, Poland
jerzykaramuz@gmail.com,
{pawel.olejnik,jan.awrejcewicz}@p.lodz.pl

Abstract. The aim of this work is to construct and program an experimental station for an automatic launching of badminton shuttlecocks. The station should operate as a prototype device used to help badminton players improve their training, provide recurrence and precision of various badminton shots. It extends certain knowledge in the field of programming of microcontrollers. The system of automatic launching of shuttlecocks has been designed and started by running two speed-controlled DC motors driving a spinning aluminum rings. In order to build the appropriate system a stepper motor based gripper has been applied to pull out all shuttlecocks from a tube. The control system of the designed device is based on a C program that has been implemented on a microcontroller. The speed, scope and frequency of shots are adjustable regarding to the player's requirements and abilities. In order to widen the station's applicability, the additional remote control system was incorporated into the control unit. The investigations performed with the station were focused on numerical simulations and basic experimental verification of the expected trajectory.

Keywords: badminton training station, automatic launching, programming of microcontrollers, shuttlecock dynamics, Pololu High-Power Motor Driver.

1 Introduction

Badminton is a popular game. Modern version of Badminton game was imported by the British from India to Great Britain in the middle of 19th century and spread to other parts of the world. The invention of the cheaper, more durable synthetic shuttlecock in the 1950s gave the game a wider appeal. Manufacturers tend to produce a synthetic shuttlecock that could exactly mirror the flight of the feather shuttlecock. Therefore, any playing techniques and shuttlecock dynamics investigations are still important in this context.

Paper [5] describes experiments which were devised to understand the flow regime around a shuttlecock and to accurately determine a data set of aerodynamic coefficients

J. Awrejcewicz et al. (eds.), *Mechatronics: Ideas for Industrial Applications*,
Advances in Intelligent Systems and Computing 317, DOI: 10.1007/978-3-319-10990-9_7

for selected feather and synthetic shuttlecocks. It was found between others, that the shuttlecock is a bluff body and the predominant drag mechanism is base drag.

In the study presented in [1] a motion equation for the flight of the badminton was proposed and examined. This research method was based on motion laws of aerodynamics. It applied aerodynamic theories to construct motion equation of a shuttlecock's flying trajectory under the effects of gravitational force and air resistance force. The result showed that the equation of motion of a shuttlecock's flight trajectory could be constructed by determining the terminal velocity.

At the outset it should be emphasized that the dynamic badminton shuttlecock flight is a phenomenon extremely difficult to model mathematically, mainly due to the deformability of the collar darts under the influence of air resistance forces – especially in the initial phase of flight, immediately after impact. Changes in shape cause temporary changes in such quantities as mass moments of inertia and the lift surfaces and aerodynamic resistance. Currently, badminton uses two types of shuttlecocks: synthetic and feather. A standard feather shuttlecock is generally made of sixteen overlapping feathers arranged in the shape of a cone. It is worth mentioning that not every new feather shuttlecock is perfectly symmetrical. Compared to the plastic shuttlecocks, feather ones exhibit significantly less susceptible to deformation at high speeds. Their main disadvantage a fragility, which means that after a few strikes feathers gradually become detached from the pen so that the shuttlecock completely loses its aerodynamic properties, and thus it is changed every several actions. Synthetic Shuttlecocks have similar geometric properties, such as dimensions of a cork and a collar made of nylon. To map geometry of feather shuttlecocks, synthetic ones have the collar with a non-uniform mesh density (porosity). In the case of synthetic primaries, the challenge is to accurately describe the geometry of the cone due to different density of the mesh, the mesh size, and its location and shape. Shuttlecocks of different manufacturers differ not only by appearance, but also the behavior in the air. In the case feather shuttlecocks, range of their diversity performance is much smaller.

Up to now, badminton shuttlecock has not been the subject of in-depth research and analysis. Most of the work was limited only to measurement of its speed, and the experimental designation of drag coefficient [1]. Currently, scientists allowed to take advantage of advanced simulation software, the researchers carried out a thorough research by publishing several works based on mathematical models of dynamic badminton shuttlecocks [1–6]. Programs to simulate fluid dynamics by finite element method contributed to a number of papers describing exactly the pressure distribution, the airflow around and inside the modeled shuttlecocks of any shape [3]. With the knowledge of fluid mechanics problems all the aerodynamic parameters of shuttlecock can be numerically determined. This paper focuses on the presentation of badminton shuttlecock flight as a matter of mechanics. To this end, some of the properties and phenomena will be simplified, which should greatly accelerate the calculations, without introducing significant error in the results. Accordingly, the shuttle will be treated as a rigid body in three-dimensional space described by known equations and laws.

2 Mechanical Design of the Station

The mechanism of lunching consists of two brush DC motors Nisca NC5475E that are installed on an aluminum profile-based polycarbonate plate. Parameters of the motors are as follows: supply voltage 24 V, nominal current 0.3 A (without loading) and 1.9 A (at maximum efficiency), power 32 W, maximum torque 0.46 Nm, rotational velocity 5731 rev/min (without loading) and 4948 rev/min (at maximum efficiency). Pivotal joints of the plate leave it only one degree of freedom allowing to a manual setting of the angle of lunching.

Fig. 1. CAD model of the station in Creo Parametric 2.0

Aluminum discs of 100 mm diameter and 15 mm thickness are mounted on the engines' shafts. They rotate in the same plane but in opposite direction. There exists a 27 mm gap between the rotating discs to caught the shuttlecock's base. If a PU leather covered cork base is placed between the rotating shafts, then the shuttlecock is thrown by a friction force. Initial velocity of the throw is proportional to the rotational velocity of rings. A micro-rubber belts have been placed on side surfaces of both rings to increase the coefficient of frictional contact with the shuttlecock's base.

The feeding mechanism consists of a bipolar stepper motor, gripper and a plastic tube acting as a reservoir. Stepper motor WObit 39BYGH405B is powered by 12 V and 0.5 A current. The gripper mounted to the motor shaft retrieves shuttlecocks from the tray. The purpose of the feeding mechanism is to take each time exactly one shuttlecock with a user-defined frequency.

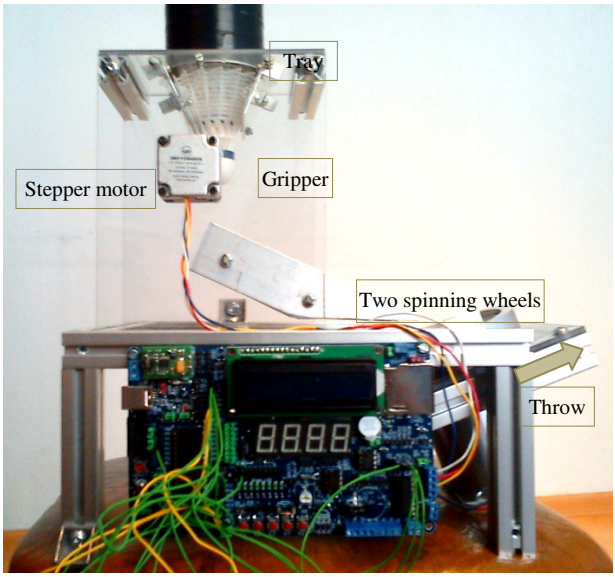

Fig. 2. A prototype of the station (side view)

Shuttlecock are arranged one above the other in the tray as shown in Fig. 2. They are maintained by two plates having the ability to swing. When the gripper gets a shuttlecock, movement of plates facilitate the work of the gripper and then, due to the cooperation with springs it is back to its original position and prevent further shuttlecocks.

3 Electronics

Electronics of station is based on a ATB kit (Atnel Test Board) equipped with ATMEGA644PA microcontroller and electronic components such as a Darlington driver ULN2803, infrared receiver type TFMSA 36 kHz, and more. Microcontroller controls the program written in C.

The program performs the following tasks:

- smooth speed control of DC motors by pulse width modulation (PWM),
- automatic or manual mode of gripper's work,
- completely remote control of station,
- communication with the user via the LCD display,
- in manual mode, the user can decide on the time of launch, while in automatic shots occur,
- automatically, the user only has the ability to adjust the frequency of these shots.

List of mechatronic components used in the project along with their technical parameters is as follows:

1. ATMEGA644P microcontroller:

- programmed in C,
- Flash memory – 64 MB,
- EEPROM (external) – 2048 B,
- SRAM – 4 KB,
- 3 hardware counter/timer's,
- 6 PWM channels,
- real time clock 32 kHz RTC (Real Time Clock),
- 32 pin configurable input/output,
- the external crystal oscillator with a frequency of 11.0952 MHz,
- IR receiver type TFMSA 36 kHz,
- RC5 remote control as an infrared transmitter (Manchester encoding standard).

2. Additional components:

- 2 × 16 LCD alphanumeric display with blue backlight,
- L293D motor controller to control the stepper motor,
- number of channels: 2,
- maximum supply voltage motors –36 V,
- average current per channel: 0.6 A,
- peak current per channel: 1.2 A,
- built-in protection diodes,
- Pololu High-Power Motor Driver 18V15 to control DC motors,
- numerous channels: 1,
- supply voltage motors : from 5.5 V to 30 V,
- the maximum continuous current output per channel: 15 A,
- the maximum PWM frequency: 40 kHz,
- the maximum voltage the logic: 5.5 V,
- SMPS 24 V 1.65 A,
- SMPS 12 V 1.6 A.

The Two High-Speed DC Motors

The experimental station is equipped with two DC brush motors running at the same speed and reverse direction of rotation. The rotational speed of these motors is proportional to the average value of their supply voltage. The most common and proven method of smooth power control of electrical devices is a pulse width modulation (PWM). Microcontroller ATMEGA644P contains three counters which can operate as a PWM signal generators. To this end, at the experimental station 8-bit Counter/Timer0 is used. Counter/Timer0 counts pulses from 0 to 255, and when compared with the set point OCR0A or OCR0B, it generates square wave signal respectively to OC0A or OC0B outputs. The PWM signal goes to the appropriate control pin located on the controller's board Pololu High-Power Motor Driver 18V15. It should be noted that the frequency of the PWM signal cannot exceed 40 kHz, since this is the maximum operating frequency of the Pololu controller.

The Stepper Motor
Drive gripper is a bipolar stepper motor company WObit combined with con-equator L293D stepper motors and DC.
Stepper motor Specification:

- model: 39BYGH405B,
- bipolar with four terminals,
- step 1.8° ±5 %,
- rated voltage of 12 V,
- rated current of 0.4 A,
- holding torque 0.21 Nm.

L293D channel is a power controller on the system board enabling the ATB to control the two DC motors and one bipolar stepper motor, as is the case with the position of the launcher.

4 The Shuttlecock during Flight

Local conditions such as temperature, humidity and the amount of the density of air at a given location on Earth, which in turn affects the resistance it puts aileron air. Depending on the conditions mentioned above, proper type of shuttlecock has to be chosen for the right type of badminton game. The shuttlecock while hitting a rocket reaches very high values of the initial speed of up to 300 km/h. This speed rapidly decreases due to the small mass of the shuttlecock and its shape. The actual trajectory was registered by camera with low resolution and the possibility of recording of only 30 frames per second. This did not prevent the receipt of clear results.

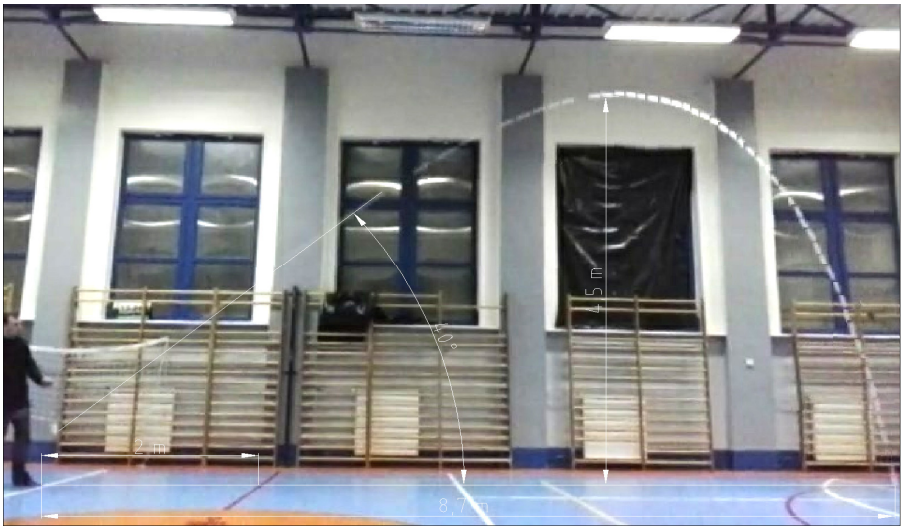

Fig. 3. Real trajectory of motion

Fig. 3 shows the trajectory of the shuttlecock obtained by applying 60 movie frames per second. Based on the Fig. 3 and distances between the court lines, maximum height attained and the initial angle of the trajectory given by the racquet strike was estimated.

To perform an experimental stroke a nylon shuttlecock (business model Yonex Mavis 500 marked in blue) was used.

4.1 The Parameters of the Ailerons

- mass: 5 grams,
- diameter basket (skirt): 68 mm,
- the diameter of the cork: 26 mm,
- time turning the ailerons: 0.020 s, a value reached during the test impacts at speeds of about 300 km/h, the time is longer than the one achieved by the ailerons leaf only 0.005 s.

Shuttlecock was struck with Carlton ISOBLADE TI racquet with the parameters:

- mass: 85 grams,
- balance: lightly on the head,
- length: 670 mm,
- tensile strength: approximately 12 kg,
- tension: Yonex BG 55.

4.2 Initial Conditions

The initial height is 0.6 m dart after hitting followed a straight path at an angle of 40° to the surface of the court, the value was read from Fig. 3. Initial shuttlecock speed was calculated by measuring the time it takes to overcome the distance from white to red court line. Additionally, initial velocity for half of that distance was measured. Two measurements were performed in order to determine a difference in speed even at such a short distance. The distance between the white and the red line is 2 m, the shuttle took off at an angle of 40 degrees, so that the total distance reached by the shuttlecock follows $d = 2/\cos(40°) = 2.61$ m, and a half of the distance equals 1.31 m. On that basis and subsequent analysis of the film frames, the following initial velocities are considered: $v_{01} = 2.61/0.133 = 19.62$ m/s and $v_{02} = 1.31/0.067 = 19.55$ m/s. The initial velocity is assumed at 19.5 m/s.

5 Numerical Simulation of the Trajectory of Motion

The trajectory of motion of the shuttlecock after hitting is an interesting and very complex phenomenon. Due to this fact, the analytical calculations assumed some simplifications involving, among others, the omission of physical deformations, especially at the moment of contact with the racquet. The dynamic equations of motion or

Newton's second law written in the differential form allow to determine the trajectory of the shuttlecock on the basis of the forces acting on it. The equation of motion dynamics according to the second Newton law for darts contained in the motion is as follows:

$$m\vec{a} = \vec{D} + \vec{L} + \vec{B} + m\vec{g} \tag{1}$$

where: m – mass of a dart, $\vec{a}$ – acceleration, $\vec{g}$ – acceleration of gravity, $\vec{D}$ – the drag force (a resistance force vector directed opposite to the vector of velocity), $\vec{L}$ – air lift, $\vec{B}$ – buoyancy force.

5.1 Drag Force

Drag force is a component of the aerodynamic force vector and its direction is consistent with the direction of movement of the body relative to the fluid, and its return is opposite to the movement of the body. There is discovered in [3] that the Reynolds number plays a key role in determination of the degree of (linear or quadratic) equation describing the force of drag. The experiment carried out in [4] allowed to determine that with respect to v the quadratic equation sufficiently describes the aerodynamic drag [6]

$$\vec{D} = 0.5 C_D \times \rho \times S_D \times \vec{v}^2, \tag{2}$$

where: $\vec{v}$ – vector of velocity, ρ – density of dry air at sea level at 20 degrees (1205 kg/m^3), C_D – a dimensionless aerodynamic drag coefficient determined experimentally (0.4–0.73 [1]), S_D – area of projection of the body onto a plane perpendicular to the vector of velocity (in our case, $S_D = \pi r^2 = \pi \times (0.034\ \text{m})^2 = 3.63 \times 10^{-3}\text{m}^2$).

The coefficient C_D of the drag force acting on shuttlecocks was measured by managing experimental methods described in [3]. In order to experimentally measure the aerodynamic properties of shuttlecocks an industrial experimental wind tunnel was used. Rod supporting the shuttlecock during the experiment was attached to the 6-axis force sensor (type JR-3). Station and software allowed for the measurement of the three forces of resistance, carrier and side and the corresponding moments too.

5.2 Terminal Velocity

In the final stage of flight the shuttle drops down almost vertically resulting in an increase of the speed and force of air resistance. The acceleration becomes zero when the force of air resistance eventually balances the force of gravity. At this point, the shuttle reaches the terminal velocity v_t and then moves uniformly. The limit for vertical drop could be determined by transforming Eq. (1) and (2), but assuming the acceleration $\vec{a} = dv/dt = 0$ and omitting the lift force that is perpendicular to the direction of motion. Assuming the drag coefficient $C_D = 0.6$, the terminal velocity is obtained

$$v_t = \sqrt{\frac{2mg}{\rho S C_D}} = \sqrt{\frac{2 \times 0.005kg \times 9.807\frac{m}{s^2}}{1.205\frac{kg}{m^3} \times 0.00363m^2 \times 0.6}} = 6.11\frac{m}{s}. \quad (3)$$

According to the research presented in [1, 2] the speed limit v_t ranges from 6.51 m/s to 6.87 m/s. Experimentally determined value of the velocity limit can be used to determine C_D of the selected shuttlecock.

5.3 Lift Force

The lift force is the second (next to the aerodynamic drag force) vector component of the aerodynamic force perpendicular to the direction of movement of the body in the fluid. The problem of lift technique is most commonly discussed in terms of its impact on airplane wings, propellers, helicopter blades, and the turbine and compressor blades. Also affects the heavy body with high speed flying in the air like missiles or rockets [7]. The value of the lift force is proportional to the square of the speed of the body, so it has a significant effect on the trajectory of the light shuttlecocks moving at speeds up to 300 km/h.

An aerodynamic lift as a vector of resistance force directed opposite to the vector of velocity $\vec{v}$ is proposed in the form

$$\vec{L} = 0.5 C_L \times \rho \times S_L \times \vec{v}^2, \quad (4)$$

where: C_L – the dimensionless lift coefficient determined empirically, depending on the shape and angle of attack of the body (for shuttlecocks it ranges from 1 to 1.2), S_L – lift area.

5.4 Buoyancy Force

It is the force acting on the shuttlecock during movement and its value is equal to the weight of the air displaced by the shuttlecock. Actually, the buoyancy force acting on the typical shuttlecock with a volume of in the air with a density of 1205 kg/m^3 is equal to $B = V\rho g = 19 \times 10^{-6}$ m^3 × 1.205 kg/m^3 × 9.807 m/s^2 = 2.237×10^{-4} N, so the gravity force mg = 0.005 kg × 9.807 m/s^2 = 0.049 N. Referring to the gravity, the buoyancy force $\frac{B}{mg} \times 100\,\% = \frac{10^{-4}\,\mathrm{N}}{0.049\,\mathrm{N}} \times 100\,\% = 0.46\,\%$. As it is seen, neglecting its impact on the trajectory of shuttlecock will have no significance on the results of calculations.

5.5 Equations of Motion

Vectors of various forces presented in Eq. (1) are projected onto x and y, the horizontal and vertical coordinates. This procedure is intended to facilitate the designation of the theoretical trajectory depending on the position of the shuttlecock in (x, y)

coordinates, i.e. a function $y = f(x)$ exists. Projecting vectors of Eq. (1) on the two axes, omitting the buoyancy force as well as taking into account Eq. (2) and (4), we get

$$m\frac{d^2x}{dt^2} = -\frac{1}{2}C_D\rho S\left(\frac{dx}{dt}\right)^2\cos\theta - \frac{1}{2}C_L\rho S\left(\frac{dx}{dt}\right)^2\sin\theta, \tag{5}$$

$$m\frac{d^2y}{dt^2} = -\frac{1}{2}C_D\rho S\left(\frac{dy}{dt}\right)^2\cos\theta - \frac{1}{2}C_L\rho S\left(\frac{dy}{dt}\right)^2\cos\theta - mg, \tag{6}$$

where $\theta = \arctan\dfrac{dy}{dx}$ is the trajectory angle with respect to the x axis.

5.6 Numerical Solution in Simulink

Basic Dynamical Modeling

A simulation diagram of the analyzed dynamical model is shown in Fig. 4. The calculations have been defined in a few subsystems to improve the readability of the diagram. Pulled out the blocks that store the coefficients C_L and C_D facilitate their rapid modification, which is essential for theoretical approximation to the actual trajectory recorded by the camera.

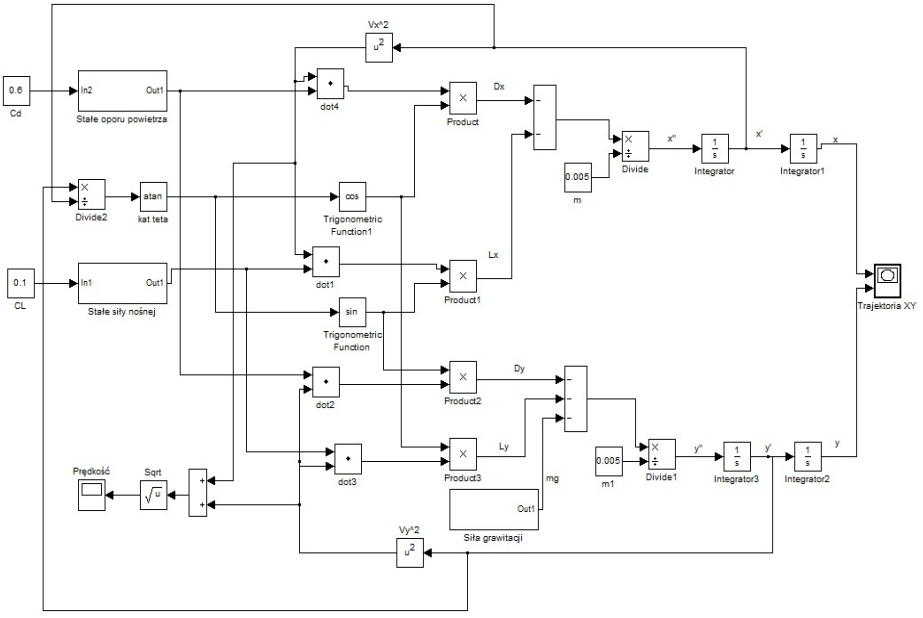

Fig. 4. Simulation diagram of the analyzed basic dynamical model

The time history in Fig. 5 shows some theoretical trajectory of the shuttlecock based on equations (5)–(6) for the following initial conditions: angle of 40°, velocity |v| = 19.5 m/s and height y_0 = 0.6 m. These conditions can be rewritten for the differential equations at $t = 0$: $\dot{x}_0 = 19.5\cos(40°) = 14.94$, $\dot{y}_0 = 19.5\sin(40°) = 12.53$.

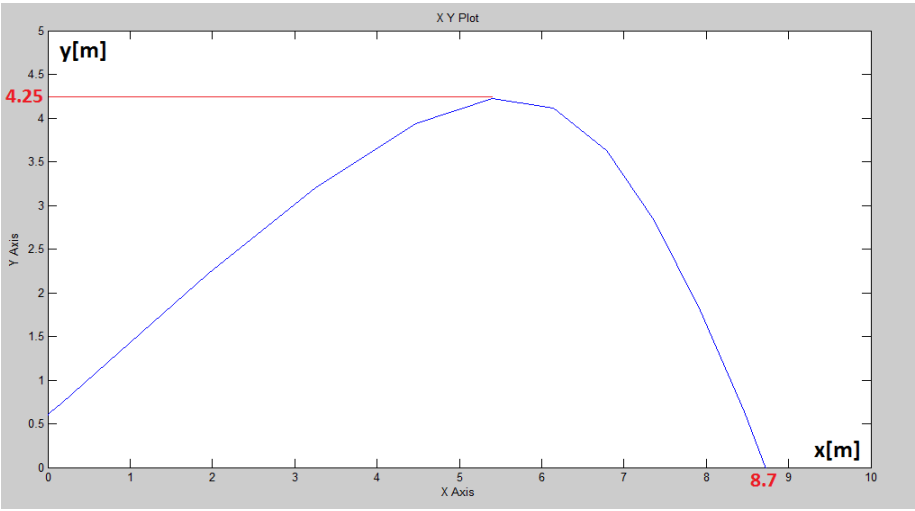

Fig. 5. Numerical solution of basic dynamics of the shuttlecock's model during planar flight

The numerically estimated trajectory shown in Fig. 5 is very similar to the real trajectory due to proper selection of the aerodynamic force coefficients, i.e. C_D = 0.5 and C_L = 0.1. Also the values obtained analytically, means the distance at 4.25 m and the height of 8.7 m are comparable to those obtained experimentally. Additionally, flight durations are similar in values 1.83 s and 1.97 s, if the theoretical and experimental flights are compared. These times were measured by an analysis of recorded movie frames and by reading in Simulink the exact value from the time course of $y(t)$. The results are visibly comparable to the average time of flight while playing badminton lasting about 2 seconds. In the initial stage of the flight the speed of the shuttlecock is high, it follows a similar path to the arc by slightly raising the lift influence which is present only at the beginning of the movement. This is due to the fact that the force is proportional to the speed of the ailerons, which decreases rapidly causing the disappearance of the lift and drag force in a later phase of flight.

Velocity course $v(t)$ from Fig. 6 allows to accurately analyze and explain the specific behavior of the shuttlecock in the air. In the initial phase of motion, when the shuttlecock increases its altitude, its speed continuously decreases and reaches a minimum of about 3.8 m/s, and after 1 second of the flight. The minimum velocity corresponds to the speed reached by the shuttlecock at the highest point of its trajectory. Then, the shuttle sharply changes the direction of its movement. It is the only time when acceleration is positive. The last phase of flight is close to the vertical drop. Velocity of the shuttlecock begins to stabilize around constant value, but acceleration is equal to zero, and the shuttle continues to move with a constant speed that is equal to the terminal velocity.

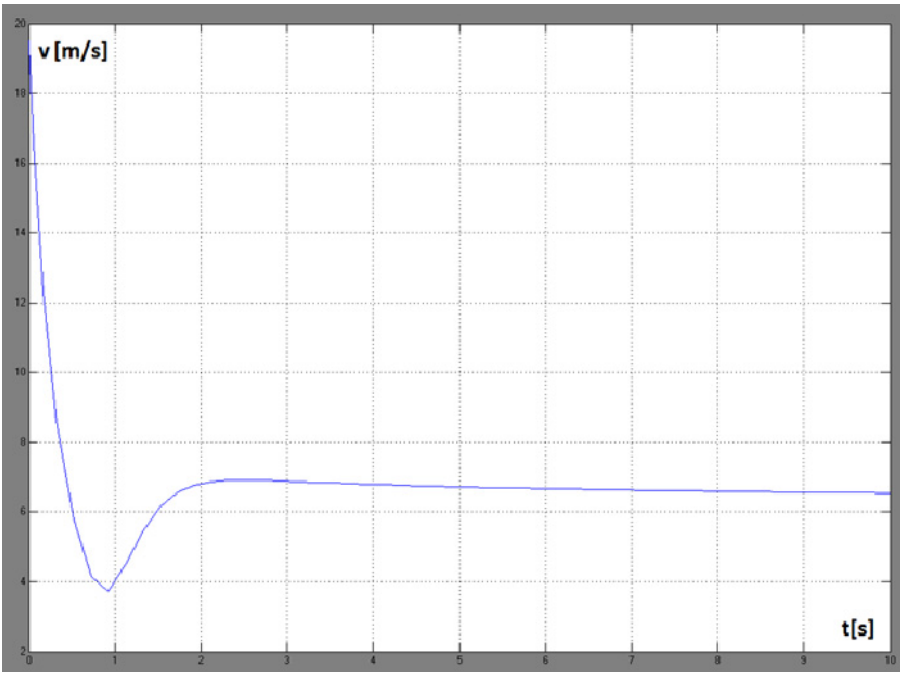

Fig. 6. Time history of velocity of the shuttlecock's in the basic model of dynamics

Extended Dynamical Modeling

Statements of the model

- Shuttlecock is treated as a rigid body with six degrees of freedom;
- Shuttlecock is an axially symmetric solid;
- Right-handed coordinate system is assumed;
- Origin of the local coordinate system of shuttlecock is adopted at its center of gravity;
- The global coordinate system is attached to the Earth;
- Shuttlecock reaches relatively short distances so the simplification assumes that the Earth is flat;
- The speed of the Earth is assumed to be constant and equal to zero.

Equations of motion

The basic dynamic model presented in previous chapter is accurate but it has a lot of simplifications and it neglects important effects. This is the reason why the extended model is being developed. This section shows an extended dynamic model of a badminton shuttlecock that is treated as a rigid body moving in the 3-dimensional space.

Equations (7)–(9) describe forces acting in the translational motion of the body. The next three provide the relation between angular momentums. Equations (13)–(14) are the relations between inertial and reference frames developed by using Euler angles.

$$m\dot{u} = -D\cos\alpha + L\sin\alpha - mg\left(-\sin\theta\right) - m\left(qw - rv\right) \tag{7}$$

$$m\dot{v} = -mg\sin\phi\cos\theta - m\left(ru - pw\right) \tag{8}$$

$$m\dot{w} = -D\sin\alpha - L\cos\alpha - mg\cos\phi\cos\theta - m\left(pv - qu\right) \tag{9}$$

$$I_{xx}\dot{p} = L - \left(I_{zz} - I_{yy}\right)qr \tag{10}$$

$$I_{yy}\dot{q} = M - \left(I_{xx} - I_{zz}\right)pr \tag{11}$$

$$I_{zz}\dot{r} = N - \left(I_{yy} - I_{xx}\right)pq \tag{12}$$

where, according to Euler angles:

$$\begin{bmatrix} u \\ v \\ w \end{bmatrix} = \frac{d}{dt}\begin{bmatrix} x_b \\ y_b \\ z_b \end{bmatrix}, \tag{13}$$

$$\begin{bmatrix} p \\ q \\ q \end{bmatrix} = \begin{bmatrix} \dot{\varphi} \\ \dot{\theta} \\ \dot{\psi} \end{bmatrix}\begin{bmatrix} 1 & 0 & -\sin\theta \\ 0 & \cos\phi & \sin\phi\cos\theta \\ 0 & -\sin\phi & \cos\phi\cos\theta \end{bmatrix}, \tag{14}$$

$$\begin{bmatrix} x_b \\ y_b \\ z_b \end{bmatrix} = \begin{bmatrix} X \\ Y \\ Z \end{bmatrix}\begin{bmatrix} \cos\theta\cos\psi & \cos\theta\sin\psi & -\sin\theta \\ \sin\phi\sin\theta\cos\psi - \cos\theta\sin\psi & \sin\phi\sin\theta\sin\psi + \cos\theta\cos\psi & \sin\phi\cos\theta \\ \cos\phi\sin\theta\cos\psi + \sin\theta\sin\psi & \cos\phi\sin\theta\sin\psi - \sin\theta\cos\psi & \cos\phi\cos\theta \end{bmatrix} \tag{15}$$

Model in Simulink

Simulation diagram of the extended dynamical system has been presented in Fig. 7. It is based on the universal dynamic block, which is placed in middle part of the diagram. The "Rigid Body 6DOF" block considers the rotation of a body-fixed coordinate frame (X_b, Y_b, Z_b) about a flat Earth reference frame (X_e, Y_e, Z_e). The origin of the body-fixed coordinate frame is the center of gravity of the body, and the body is assumed to be rigid. It eliminates the need of consideration of the forces acting between individual mass elements. The flat Earth reference frame is considered as an inertial one, an excellent approximation that allows the forces due to the Earth's motion to be neglected. Inputs F_{xyz} and M_{xyz} allow to add external forces and moments acting on a rigid body during simulated motion. Most of the formulas have been segregated in blocks in order to increase the readability of the scheme, as well as simplifying further modifications and work with the model.

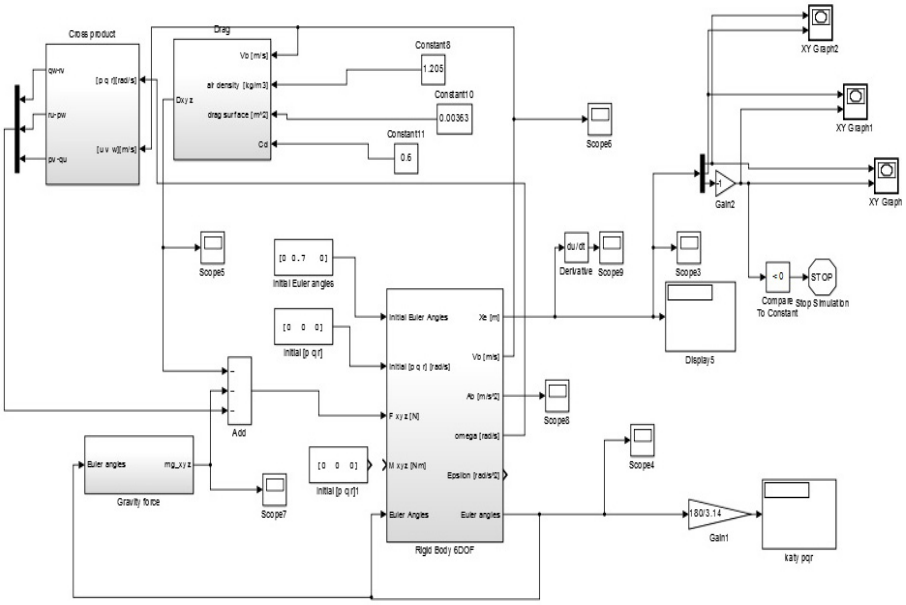

Fig. 7. Simulation diagram of the extended dynamical system

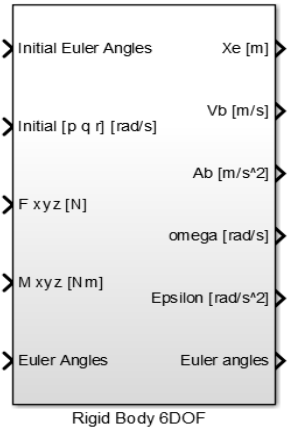

Fig. 8. Universal dynamic block in the extended modeling of the shuttlecock's motion

Additionally, during our work on advanced modeling of the shuttlecock's flight phenomenon we succeed to create an universal block visible in Fig. 8, which can be used to describe and simulate dynamics of other rigid bodies moving in the air. Solution of the extended dynamical system is shown in Fig. 9.

The shuttlecock trajectory presented in Fig. 9 is in good agreement with the typical flight paths estimated in [1].

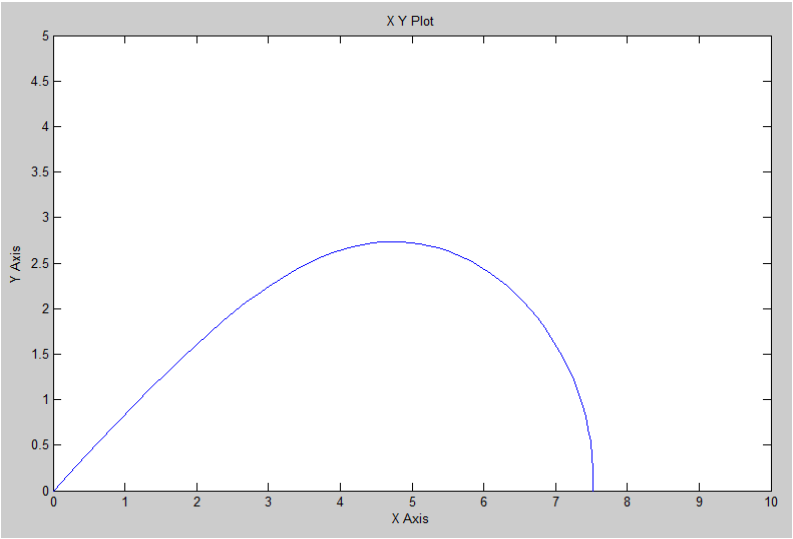

Fig. 9. Solution of the extended dynamical system given by Eq. (7)–(12)

6 Conclusions

The constructed station of the automatic launch for badminton shuttlecocks is the result of several months of work. During this time, the concept of design was changing, which was dictated by new ideas. The mechanical part was constructed by the choice of the simplest possible ideas and inexpensive solutions to follow the functions of expensive and commercial launchers available on the market. Launching mechanism between two rotating discs is the best, proven solution that provides high value of initial velocity of shuttlecocks. It is used in each device encountered in the market in this category.

As a result of the simulation performed in the Simulink, the theoretical trajectory of the badminton shuttlecock was determined. In order to compare the actual path with the theoretical one, experimental stroke was recorded by the camera, and then, the results were compared. With the estimation of the aerodynamic coefficients, the two trajectories have similar characteristics. Approximation caused in both cases the same distance 8.7 m, 0.25 m height difference and 0.138 s in the difference of flight duration.

According to [5], even at the maximum value of the Reynolds number the drag force does not exceed 2.5 N. This confirms the reliability of the result obtained during the simulation in Simulink, where the force reached a very low value of drag force D_{MAX} = 0.25 N. It was caused by low value of the initial speed equal to 19.5 m/s. Moreover, after 2 seconds of motion the value of resistance forces of the air stabilizes at 0.05 N, which is almost equal to the force of gravity force, i.e. 0.049 N accordingly to the formula from Section 4.5. Due to the balance of these forces, the shuttlecock moves with the terminal velocity which was described in Section 5.2.

Acknowledgements. The authors have been supported by the National Center of Science under the grant MAESTRO 2, No. 2012/04/A/ ST8/00738 for years 2012–2015 (Poland).

References

1. Chen, L.-M., Pan, Y.-H., Chen, Y.-J.: A study of shuttlecock's trajectory in badminton. Journal of Sports Science and Medicine 8, 657–662 (2009)
2. Subramaniyan, R.: Effect of local conditions on the flight trajectory of an indoor badminton shuttlecock, Bangalore, India (2008)
3. Alam, F., Chowdhury, H., Theppadungporn, C., Subic, A., Masud, M., Khan, K.: Aerodynamic properties of badminton shuttlecock. International Journal of Mechanical and Materials Engineering 4(3), 266–272 (2009)
4. Peastrel, M., Lynch, R., Armenti Jr., A.: Terminal velocity of a shuttlecock in vertical fall. American Journal of Physics 48, 511 (1980)
5. Cooke, A.J.: Shuttlecock aerodynamics. Sports Engineering 2, 85–96 (1999)
6. Cooke, A.J.: The aerodynamics of shuttlecocks. In: Tenth Australian Fluid Mechanics Conference, December 11-15, pp. 10.27–10.30. University of Melbourne (1989)
7. Green, S.I. (ed.): Fluid Vortices. Fluid Mechanics and Its Applications, vol. 30. Springer (1995)

Experimental Investigations of Stability in a Hybrid Stepper Motor

Radosław Kępiński[1], Jan Awrejcewicz[2], Donat Lewandowski[2], and Jakub Gajek[1]

[1] Faculty of Mechanical Engineering,
Lodz University of Technology, Poland
[2] Department of Automation, Biomechanics and Mechatronics,
Faculty of Mechanical Engineering,
Lodz University of Technology, Poland
radoslaw.kepinski@dokt.p.lodz.pl

Abstract. In our investigations we analyze the dynamics of a two-phase hybrid stepper motor. Its behavior is governed by a system of four non-linear ordinary differential equations. We focus on the instability phenomena occurring during the operation of the device at different frequency intervals. Such instabilities can lead to a loss of synchronism and consequently to motor's failure. The dynamics of a realistic system driven by a stepper motor is analyzed experimentally using a phase current sensing method in order to understand the dynamical processes governing the instability phenomena. The applied measuring system allowed to acquire a number of phase plots showing the behavior of the system at different angular velocities. Results indicate that qualitative change is phase plots is correlated with the loss of motor stability.

Keywords: stepper motor, stability, step-out.

1 Introduction

1.1 Scope of the Research

This paper deals with the analysis of dynamics of a system consisting of a hybrid stepper motor loaded with a rotating cylindrical mass. Such synchronous electrical motors are commonly used in a number of industrial and household mechatronic devices such as positioning systems, scanners, printers, digital cameras, optical drives, etc.

This type of motor possesses an important advantage over other types of drives: they can be used to design very compact and simple positioning systems using the open-loop approach, i.e. position feedback is not necessary. However, this comes with a drawback of having to incorporate an appropriate control system, that is relatively more sophisticated than, for instance, in the case of DC motors. Additionally, a number of methods increasing the system performance are widely used, such as voltage chopping and micro-stepping.

Several authors gathered the "know-how" regarding stepper motors, including the operation principles, design problems, control methods and mathematical modelling. In particular works by Kenjo [1] and Aclarney [2] should be mentioned. The former

J. Awrejcewicz et al. (eds.), *Mechatronics: Ideas for Industrial Applications*,
Advances in Intelligent Systems and Computing 317, DOI: 10.1007/978-3-319-10990-9_8

shared his knowledge gained during his long-term collaboration with Sanyo Electric Co. Ltd. who were one of the precursors of the stepper motor technology. The latter wrote a practical guide to the application of the stepper motors in engineering.

It can be observed that for high speeds this type of motor can behave unpredictably – for example rotor stalling can occur which can lead to a failure of the whole positioning system. It appears however, that those instabilities are occurring only in certain excitation frequency intervals.

Those instability phenomena attracted the attention of several researchers, such as Balakrishnan et al. [3] and Cao et al. [4]. The former carried out an experimental investigation, similar to the one described in this work and the latter analyzed the dynamic of the system of ODEs concerning stepper motors. In our research we are aimed at experimentally analyzing dynamics of a system actuated by a bipolar hybrid stepper motor on a basis of phase current measurement. A mathematical model regarding such system has been also proposed. This allows us to use a numerical simulation to confirm the phenomena observed in the experiment in the future research.

1.2 Physical System

The object of the investigations is an electro-mechanical system consisting of the following elements:

- hybrid, two phase, bipolar stepper motor,
- stepper motor controller,
- programmable logic controller (PLC),
- 36 VDC power supply unit,
- incremental rotary encoder.

The overview of the system is presented in Fig. 1. It can be seen that the velocity and position control is done by the PLC through a pulse signal passed to the motor's controller. This device is responsible for applying appropriate voltages to the motor's windings using the electrical power from the dedicated power supply. The power supply operates at 36 V DC and is not stabilized, because the controller uses a voltage chopper.

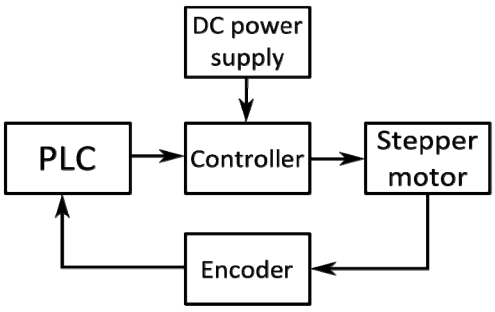

Fig. 1. Diagram showing the considered electro-mechanical system

As can be clearly seen in Table 1, the nominal voltage of the hybrid stepper motor is only 5 V. Voltage chopper circuit, however, allows to increase the performance of the motor, because larger supply voltage means that the first time derivatives of the phase currents are of a higher value (as shown in Section 2). Consequently, the windings can be energized much more rapidly, producing (on average) more torque.

Additionally, micro-stepping approach is used, which reduces the noise and vibration of the system, in addition to increasing the resolution of the positioning system.

In this system a position feedback using a rotary encoder has been introduced to allow for measuring the system response. Although we did not track accurately the position response of the system in the described experiment, this feedback signal allowed to detect the moments when a loss of synchronism occurs.

Mechanical part of device can be seen in the photo presented in Fig. 2. It consists of a shaft and cylindrical mass supported on a ball bearing coupled with the motor using Oldham's coupler.

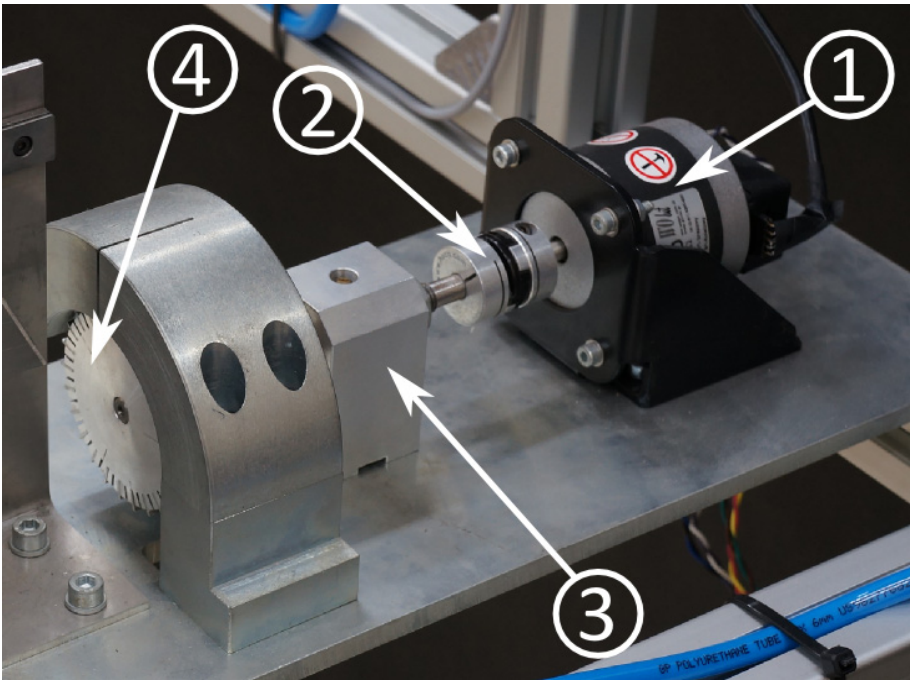

Fig. 2. Electro-mechanical system actuated by a stepper motor: stepper motor (1), Oldham's coupler (2), ball bearing support (3), rotating mass (4)

2 Mathematical Model

A hybrid stepper motor consists of a rotor made of alternately placed permanent magnet poles with equally spaced grooves placed around its circumference and a stator consisting of windings. In the case of a two phase motor we have two windings:

A and B, which have equal inductance L and resistance R. Fig. 3 shows a simplified model of a two phase bipolar hybrid stepper motor, which is the basis for further investigations.

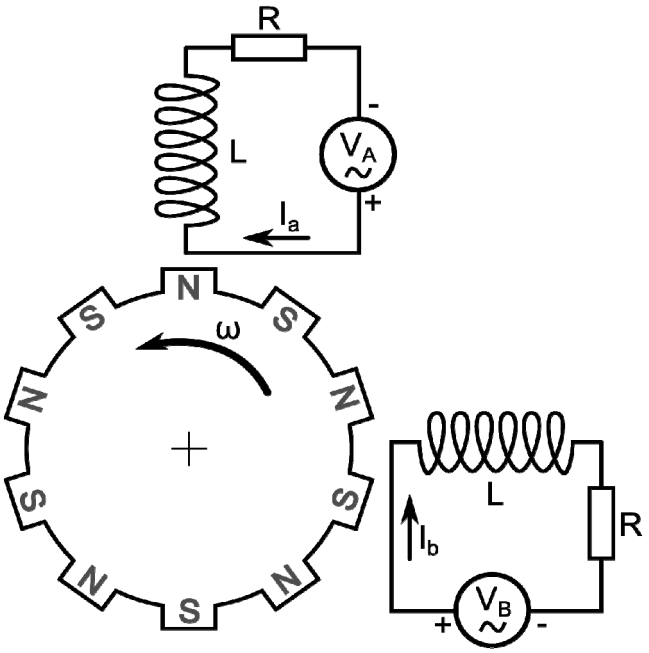

Fig. 3. Physical model of the hybrid stepper motor

The differential equations governing the dynamics of a hybrid stepper motor system have been already presented in numerous works including [1–2, 5–7]. Owing to the two main laws affecting the system (Kirchhoff's 2nd Law and Newton's 2nd Law of Motion) we can establish the following system of non-linear differential equations:

$$\begin{aligned}
&L\frac{dI_A}{dt} + RI_A = V_A + K_m\omega\sin\left(N_\gamma\varphi\right)\\
&L\frac{dI_B}{dt} + RI_B = V_B + K_m\omega\cos\left(N_\gamma\varphi\right)\\
&J\frac{d\omega}{dt} + c\omega + T_l = -K_m I_A\sin\left(N_\gamma\varphi\right) + K_m I_B\cos\left(N_\gamma\varphi\right)\\
&\frac{d\varphi}{dt} = \omega
\end{aligned} \tag{1}$$

where: I_A, I_B are currents in both phases; V_A and V_B are voltages applied to the windings; R, L are winding's resistance and inductance, respectively; K_m is the motor torque constant, c is viscous friction coefficient, N_r is the number of rotor teeth, J is rotor's moment of inertia, T_l is the load torque, ω is the rotor speed and φ is its angular position.

Table 1. Parameters of the system

R	5 Ω
L	$8.6 \cdot 10^{-3}$ H
$I_{A0} = I_{B0}$	1 A
$V_{A0} = V_{B0}$	5 V
c	$8 \cdot 10^{-4}$ N· m·s / rad
K_m	0.55 · N·m / A
J	$11 \cdot 10^{-6}$ kg· m^2
N_r	50

3 Experimental Set-Up

The phase currents, especially for high rotor velocities are changing with high speed. Because of that, a measuring system is required that can gather a sufficient number of samples per second. In this case, a digital oscilloscope has been used, which offers sampling rates of 1 Gs/s.

To measure high frequency currents an amplifying circuit is also necessary. We use a shunt resistor current sensing method, introducing two very small value resistor in series with the phase circuits. Voltage drop occurring on these resistors, owing to Ohm's Law is proportional to the current flowing through the phase. This voltage signal is then amplified using two (one for each phase) bi-directional shunt current sensors with the amplification ratio of 50. The resulting signal is passed to the two channels of the oscilloscope, allowing to draw XY plots of both phase currents, in such a way that I_A value determines the X coordinate and I_B determines the Y coordinate.

The circuit has been designed using a PCB board, with two connectors allowing to connect the device between the motor and its controller. A photo of the board can be seen in Fig. 4.

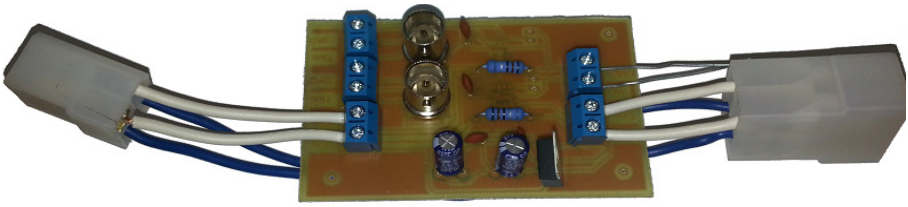

Fig. 4. Two phase bi-directional shunt current sensor

4 Methodology and Results

Following methodology has been applied for the experiment:

1. the amplifying circuit has been connected between the motor and the controller,
2. the controller has been set to 1:16 micro-stepping,

3. digital oscilloscope has been connected to the amplifier (one channel for each phase),
4. system has been excited with gradually increasing frequency (from 30 Hz up to 20 kHz),
5. for each of the frequencies an image of the XY plot has been saved,
6. frequencies at which loss of synchronism occurred have been marked as "unstable".

The results of those steps have been gathered and shown in Table 2.

Table 2. Phase current plots obtained during the experiment

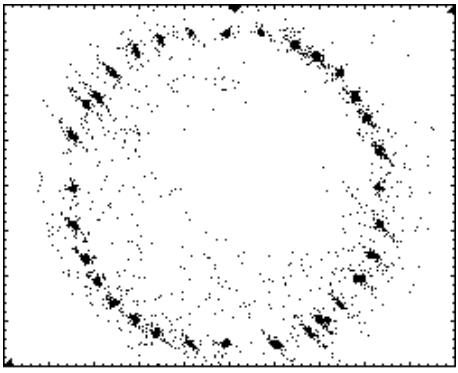

30 Hz

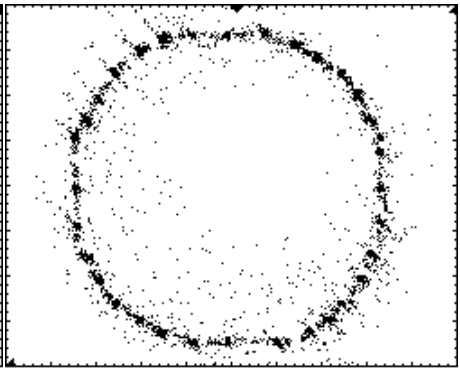

500 Hz

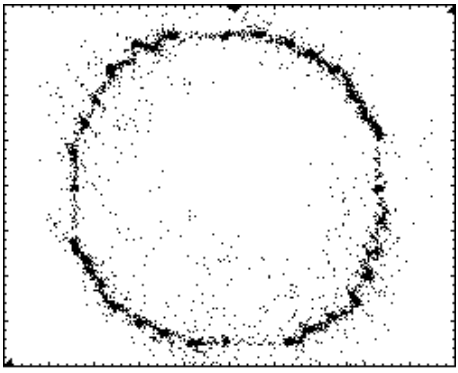

2.5 kHz

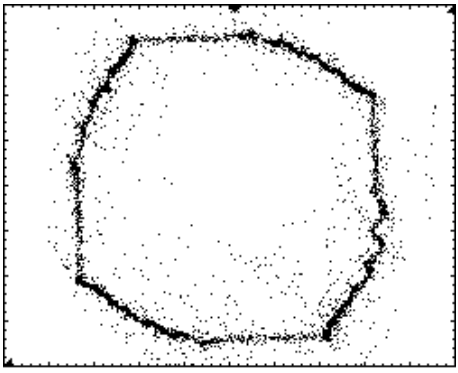

3.5 kHz

Table 2. (*continued*)

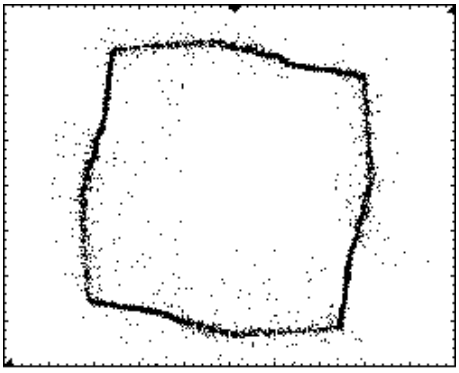

5.5 kHz

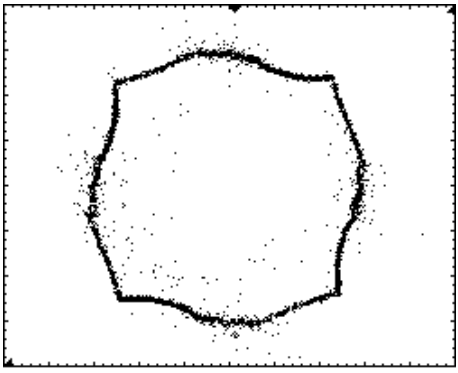

6.5 kHz

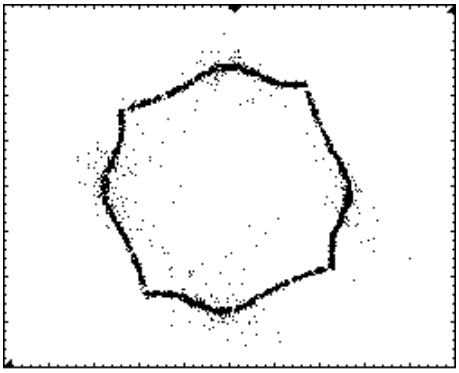

7.5 kHz

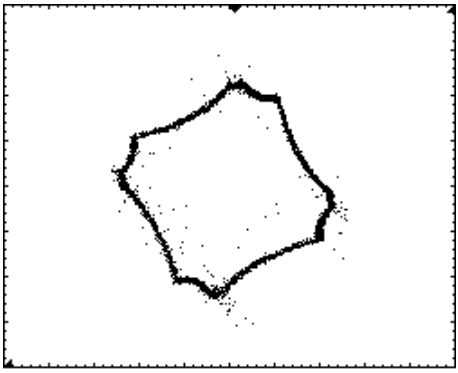

9 kHz

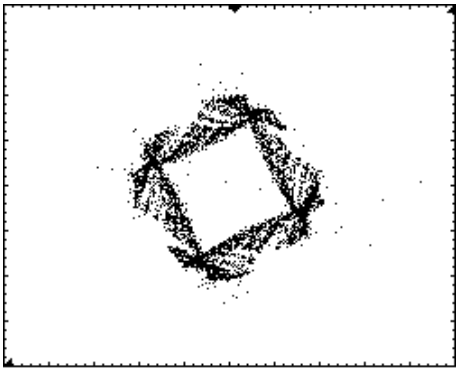

11 kHz (unstable)

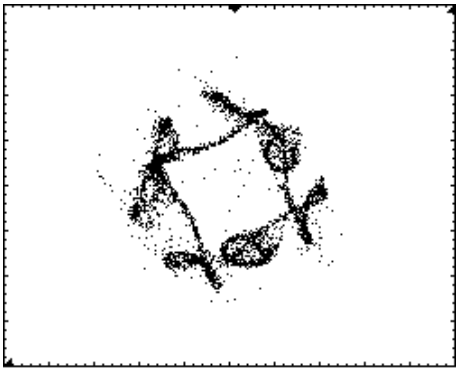

11.15 kHz (unstable)

Table 2. (*continued*)

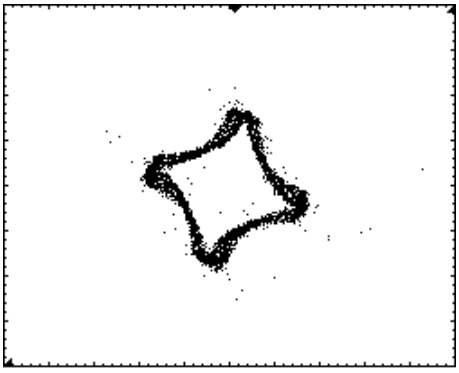

11.5 kHz

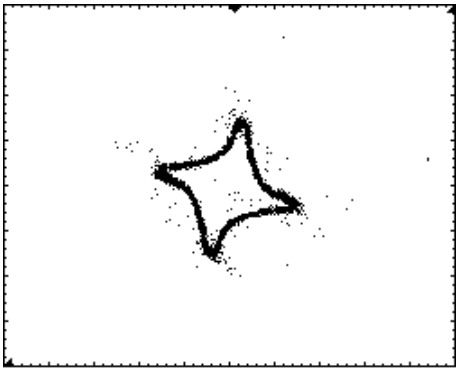

12.5 kHz

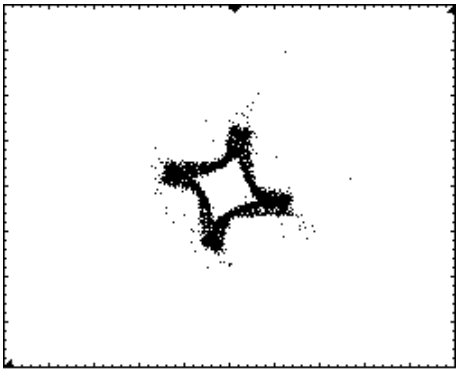

13.6 kHz

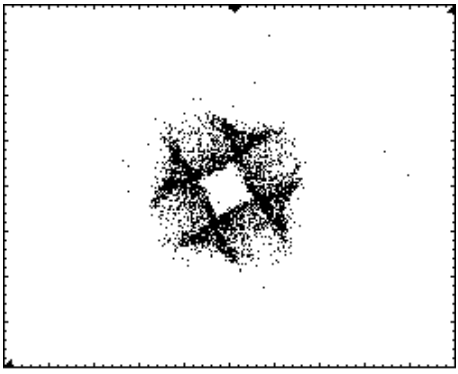

14.5 (unstable)

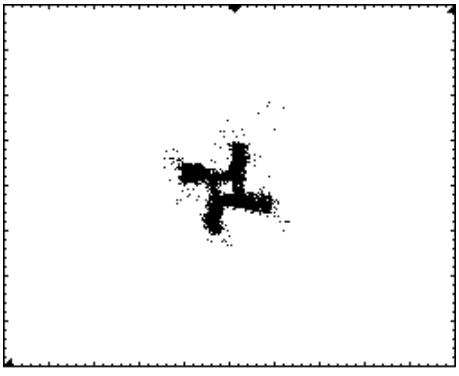

16 kHz

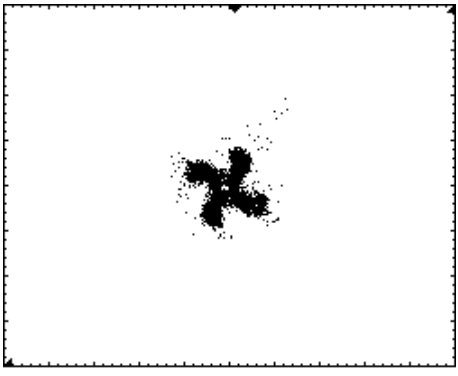

17 kHz

Table 2. (*continued*)

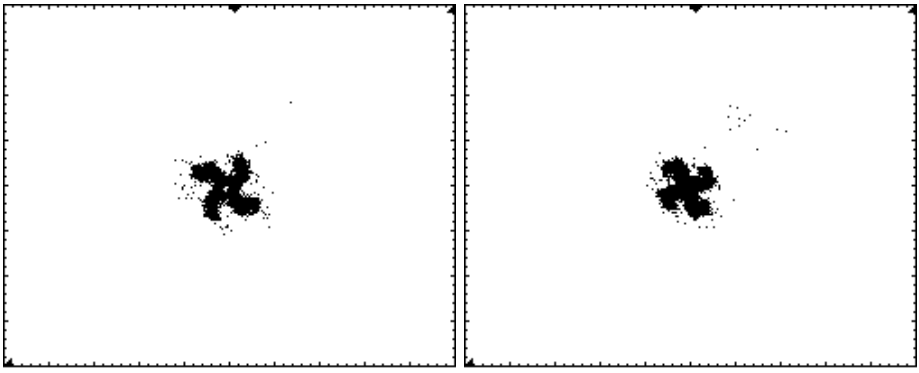

18 kHz 19.9 kHz

Plots shown in the above table allow to observe change of the trajectory on $I_A - I_B$ plane, associated with the increase of the excitation frequency. For the low frequencies (below 2.5 kHz) separate points are clearly visible, because the motion of the rotor is not smooth, as it becomes stationary between each step. In this frequency region the captured curve takes a circular shape. However, increasing the stepping speed yields gradual change of shape of the curve. At 5.5 kHz point the trajectory resembles a slightly distorted square. For excitation frequencies above 6 kHz the inner area limited by the trajectory curve starts to shrink. It means that the voltages on the windings are changing too fast to fully energize motor's coils. For the frequency interval starting at 6 kHz to around 11 kHz we observe further decrease of the inner area, as well as a progressive distortion of shape of the curve. Reaching 11 kHz results in a sudden change of the trajectory shape. This is shortly followed by a rotor stalling. We can observe that the trajectory curve starts to intersect itself in several points. The instability phenomena takes place in the region of excitation frequencies from 11 kHz up to 11.5 kHz. For 11.5 kHz up to 13.8 kHz the system behaves in a stable manner. Between 13.8 kHz and 16.5 kHz, however we deal with another wide instability section, and sudden change of shape occurs once again. Above this region, for the frequencies up to 19 kHz we observe stable operation of the motor. The inner area limited by the trajectory shrinks even further, as we increase the stepping speed. At this point the motor pull-out torque is significantly reduced, and even a small peak of the load torque can lead to the loss of synchronism. For the frequencies reaching 20 kHz the system generally behaved in an unstable manner. Frequencies past the 20 kHz point were not tested.

The experiment yields results similar to [3], but they are quantitatively inconsistent owing to the difference in stepper motor type and size. We can make an observation that when the plotted trajectory on the $I_A - I_B$ plane starts to intersect with itself we probably deal with the instability region.

5 Concluding Remarks

The proposed measurement system allowed capturing the phase current plots of the investigated system with a sufficient speed and accuracy.

Experimental results shown in the previous section allow us to conclude that in the case of the tested hybrid stepper motor we deal with several instability regions associated with different frequency intervals. The first and second observed instability region clearly exhibited a sudden qualitative change in the phase trajectory, when the plotted curve started to intersect with itself in several points.

As was expected the area limited by the trajectory decreases with the increase of the excitation frequency, after we move past the point where the windings can no longer be fully energized.

At high speeds we deal with several smaller instability regions, but the exact shape of the trajectory becomes increasingly hard to capture, because of the limited accuracy.

In further research we are planning to introduce a numerical simulation based on the system of ODEs discussed in Section 2, and to compare it to the experimental results. Additional tests, using other control methods (for instance different step divisions) will also be made.

References

1. Kenjo, T., Sugawara, A.: Stepping motors and their microprocessor control. Oxford University Press Inc., New York (1995)
2. Acarnley, P.: Stepping motors: a guide to theory and practice. The Institution of Electrical Engineers, London (2002)
3. Balakrishnan, K., Umamaheswari, B., Latha, K.: Identification of resonance in hybrid stepper motor through measured current dynamics in online for accurate position estimation and control. IEEE Trans. Ind. Inf. 9, 1056–1063 (2013)
4. Cao, L., Schwartz, H.M.: Oscillation, Instability and Control of Stepper Motors. Nonlinear Dynamics 18, 383–404 (1999)
5. Bodson, M., Chiasson, J., Novotnak, R., Rekowski, R.: High performance nonlinear feedback control of a permanent magnet stepper motor. In: Proceedings of 1st IEEE Conference on Control Systems Technology, vol. 1, pp. 510–515 (1992), doi:10.1109/CCA.1992.269821
6. Kuo, B., Tal, J.: Incremental motion control: step motors and control systems. SRL Publishing Company, Champaign (1979)
7. Lyshevski, S.E.: Electromechanical systems, electric machines and applied mechatronics. CRC Press, Boca Raton (2000)

Influence of the Controller Settings on the Behaviour of the Hydraulic Servo Drive

Klaudiusz Klarecki, Dominik Rabsztyn, and Mariusz Piotr Hetmańczyk

The Silesian University of Technology, Faculty of Mechanical Engineering,
Institute of Engineering Processes Automation and Integrated Manufacturing Systems,
44-100 Gliwice, Konarskiego 18A Street, Poland
{klaudiusz.klarecki,dominik.rabsztyn,
mariusz.hetmanczyk}@polsl.pl

Abstract. The article presents the influence of the position loop gain setting on the position error values of the hydraulic servo drive. Results of the experimental tests have also been compared with the analytically determined gain values. For the tests, servo cylinder has been loaded with the active force of 2500 N, pointed in the direction opposite to the direction of piston rod extension. The result of the experimental tests was the discovery that the accuracy and stability of the servo drive positioning depends not only on the value of K_v factor, but is also influenced by the direction of the active force loading the servo cylinder. In the tested hydraulic servo drive (hydraulic axis controller), the Compax3F controller by Parker Hannifin was used.

Keywords: hydraulic servo drives, controller settings, hydraulic proportional valves.

1 Introduction

Electrohydraulic servo drives have been in use for many years and are characterized by many beneficial features, such as high stiffness and the possibility to take high values of the velocity enhancement factor [1, 2, 4]. In spite of these advantages, the users are not particularly enthusiastic about hydraulic servo drives. One of the reasons mighty be their slightly different, when compared to typical electric servo drives. In a typical electrohydraulic servo drive, analog control signal is sent either to the modular regulator (mostly PID) or directly to the servo amplifier card with embedded PID regulator. The first solution is used in case of the systems featuring proportional control valves, where the output of the modular regulator is the control signal for the proportional amplifier. The limitations of the presented systems are as follows: no scalability and difficulties in developing/modifying machine drive systems, no possibility of digital control and hindered parameterization of servo drives [5].

The solution to these problems is modern, integrated drive systems that use both electric and hydraulic drives in a similar way. As an example, we could mention IndraMotion systems by Bosch Rexroth or Compax3 by Parker Hannifin [6].

J. Awrejcewicz et al. (eds.), *Mechatronics: Ideas for Industrial Applications*,
Advances in Intelligent Systems and Computing 317, DOI: 10.1007/978-3-319-10990-9_9

2 Impact of the Dynamics of Servo Valves on the Adjustment of the Electrohydraulic Servo Drives

Fig. 1 presents the flow chart for the electric servo drive. Due to the specificity of the hydraulic drive systems, it is usually assumed that the movable masses actuated by the cylinders or hydraulic motors are large. It may result in low natural frequencies of the cylinder – actuated inert mass assembly (hydraulic motor – actuated element with the mass moment of inertia). It is commonly assumed that for the hydraulic drives, natural frequencies of movable masses reach a few Hz. If this condition is fulfilled, the dynamics of the electrohydraulic servo drives is not limited by the velocity of the remaining elements of the system.

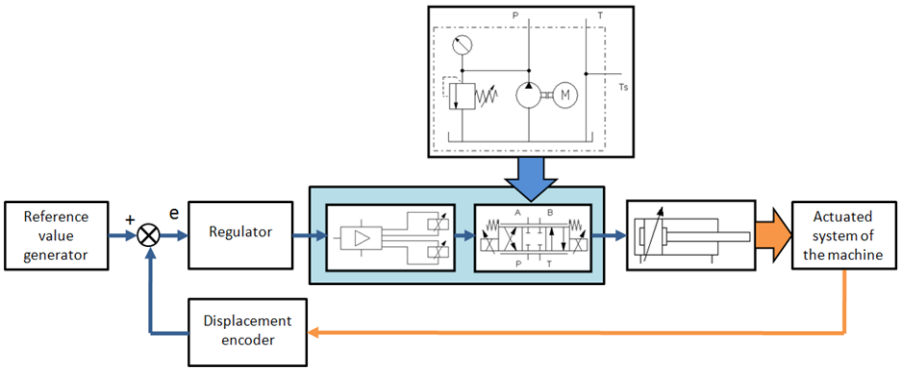

Fig. 1. Flow chart of the electrohydraulic servo drive

This paper presents the procedure of analytical selection of the adjustments for the proportional regulators [3]. First, it is necessary to determine the minimum natural pulsation of the cylinder ω_0, i.e. actuated mass system (hydraulic motor – actuated rotational mass):

$$\omega_0 = \sqrt{\frac{C_{cyl}}{m_r}} \tag{1}$$

where: C_{cyl} – hydraulic stiffness of the cylinder, m_r – movable mass reduced on the piston rod of the cylinder.

In order to do this, we must set the basic parameters of the hydraulic system fragment from the servo valve (proportional valve) to the receiver and inert mass reduced on the piston rod of the cylinder (mass moment of inertia reduced on the hydraulic motor shaft), as shown in Fig. 2.

Due to the fact that for the cylinders we can observe similar throttling on the power supply and outflow, for small oscillations of the piston we sum the hydraulic stiffness of both chambers of the cylinder.

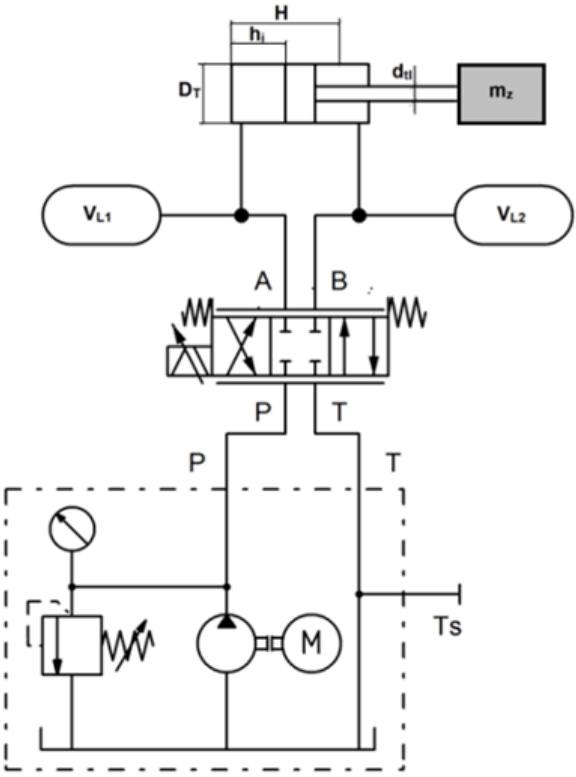

Fig. 2. Hydraulic system diagram used to determine natural pulsation of the actuated element

Hydraulic stiffness C_{cyl} of the liquid locked in the chambers of the receiver is the result of its compressibility:

$$C_{cyl} = C_1 + C_2 = \frac{A_T^2 \cdot B}{A_T \cdot h_i + V_{L1}} + \frac{A_{tl}^2 \cdot B}{A_{tl} \cdot (H - h_i) + V_{L2}} \tag{2}$$

where: H – piston stroke [m], h_i – piston position with minimum stiffness [m], A_T – piston area on the piston side [m^2], A_{tl} – piston area on the piston rod side [m^2], V_{L1} – volume of wires on the piston side [m^3], V_{L2} – volume of wires on the piston rod side [m^3], B – bulk modulus of hydraulic liquid [Pa].

The Equation 2 proves that the hydraulic stiffness depends on the position of the piston. In order to adjust the servo drive we should take the minimum value of stiffness, equivalent of the lowest value of the natural pulsation of the drive system. It will present for the piston position h_k described by the Equation 3.

Having determined the minimum value of natural pulsation of hydraulic drive ω_0, it should be compared with the pulsation of the servo valve ω_V. Pulsation of the servo valve is determined (Equation 3) taking account of the producer's cut-off frequency of a valve f_{res} and a small amplitude control signal.

$$h_k = \frac{A_{Tl} \cdot H \Big/ \sqrt{A_{Tl}^{\,3}} + V_{L1} \Big/ \sqrt{A_{Tl}^{\,3}} + V_{L2} \Big/ \sqrt{A_T^{\,3}}}{1 \Big/ \sqrt{A_{Tl}} + 1 \Big/ \sqrt{A_T}} \tag{3}$$

Usually, amplitudes of values 5–10 % of the maximum amplitude control signal for a given servo drive are taken:

$$\omega_V = 2\pi \cdot f_{res} \tag{4}$$

Producers provide f_{res} values for the servo valves and proportional control valves (directly or as frequency characteristics of valves). In case of regular proportional valves, not intended to be used in electrohydraulic servo drives, producers provide only step response T_{res}. Here, pulsation of the valve may indicatively be defined as:

$$\omega_V = \frac{\pi}{T_{res}} \tag{5}$$

If we compare natural pulsation of the drive ω_0 with the pulsation of the servo valve ω_V we distinguish [3] two types of electrohydraulic servo drives: $\omega_0 > 3\omega_V$ or $\omega_0 < 3\ \omega_V$.

In the first case, it is not required to take account of the servo drive dynamics to adjust the servo drive regulator. If the regulator is a P type regulator, we should make sure that when we select its amplifier, the value of the velocity enhancement factor K_v for the electrohydraulic servo drive complies with the following equation:

$$K_v = \frac{\omega_0}{3} \tag{6}$$

In the second case, it is necessary to take account of the servo valve dynamics. The value of the velocity enhancement factor K_v for the electrohydraulic servo drive is determined based on the equivalent pulsation ω_{eq}:

$$K_v = \frac{\omega_{eq}}{3} \tag{7}$$

Equivalent pulsation ω_{eq} of the hydraulic system with drive natural pulsation ω_0 and servo valve pulsation ω_V equals half of the harmonic mean of these two values:

$$\omega_{eq} = \frac{\omega_0 \cdot \omega_V}{\omega_0 + \omega_V} \tag{8}$$

It should be mentioned that equivalent pulsation ω_{eq} is smaller than the smallest constituent pulsation. This leads to the conclusion that if we did not take account of the valve dynamics (in the second case), the adopted value of the velocity enhancement factor for the servo drive would be too high. It could result in the instability of the servo drive.

Another conclusion is the fact that we should always make sure that the condition from the first case is met when we select servo valves. Then, the properties of a servo drive will only be limited by the pulsation of the drive (it can be improved by increasing the hydraulic stiffness).

Pairing the hydraulic drive with proportional valve of low dynamics will force the necessity of lowering the value of the velocity enhancement factor of such electrohydraulic servo drive, which in turn will result in much smaller accuracy of the servo drive positioning Δx. Servo drive positioning accuracy can be determined using the following equation [3]:

$$\Delta x = \frac{0.05 \cdot v_{\max}}{K_v} \tag{9}$$

where: v_{max} – drive speed with the servo valve fully opened.

3 Structure of the Lab Workstation

The essential element of the lab workstation is the advanced Compax3 FD2F12 I12 T11 M00 controller. The electronic part also features the position sensor type BTL7-E100-M0305-B-S32 embedded in the servo drive double-acting cylinder with unilateral piston rod CHMIXRPF24M-M1100 (piston diameter 40 mm, piston rod diameter 28 mm, piston stroke 300 mm) connected by the piston rods with the identical cylinder without positioning the piston. Both cylinders have been placed over a rigid foundation. Thanks to this, it is possible to simulate the impact of a variable load on the servo drive behaviour. Servo drive cylinder has been powered from the proportional valve with enhanced dynamics D1FPE01FC9NB00 by Parker Hannifin. Schematic diagram of the lab workstation hydraulic system is presented in Fig. 3.

The remaining elements of the hydraulic system are as follows: power supply with a fixed displacement pump with the possibility of setting the pump shaft rotational speed (power supply nominal parameters: pressure up to 10 MPa, flow rate up to 12 dm^3/min), reduction valve VM064A06VG15 to power both chambers of the cylinder loading the servo drive, necessary pressure inverters, flexible double braided hoses with dry break quick coupling and other essential hydraulic components.

For the described station, the following data essential in order to determine the natural pulsation of the mass actuated by the cylinder and the equivalent pulsation of the servo drive have been adopted: moving mass m = 10 kg, additional volumes $V_{L1} = V_{L2}$ = 86 cm^3 (cables between the proportional valve and cylinder), cut-off frequency f_{gr} = 350 Hz for the valve D1FPE01FC9NB00.

Having used the Equation 3 in order to determine the position of the piston for the minimum hydraulic stiffness (h_k = 287 mm), Equation 2 has been applied in order to determine the pulsation ω_0 of the drive (ω_0 = 1028 1/s). Pulsation of the proportional valve D1FPE01FC9NB00 has also been determined (ω_V = 2199 1/s). Having compared pulsation ω_0 and ω_V we know that we need to determine the value of the equivalent pulsation of the hydraulic system and then use it to estimate the permissible value of the velocity enhancement factor of the servo drive.

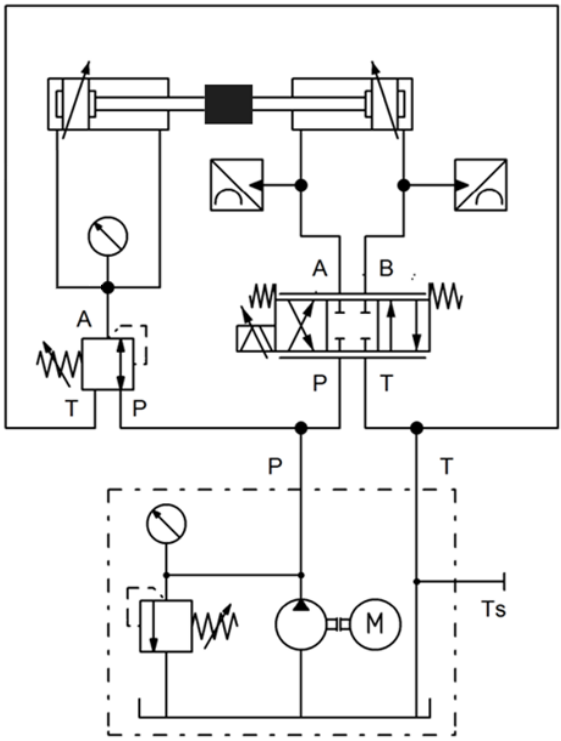

Fig. 3. Schematic diagram of the position for testing the hydraulic servo drive

After substituting the values into the Equation 8 we have received the value of the equivalent pulsation ω_{eq} = 700.7 1/s. This means that the optimum value of the velocity enhancement factor is K_v = 233.5 1/s.

Knowing the value of the suggested velocity enhancement factor of the servo drive, it is possible to determine the settings of the proportional controller (type P) using the following formula [3, 5]:

$$K_v = \frac{K_P \cdot V_q \cdot K_X}{A}$$
$$K_{P+} = \frac{K_v \cdot A_T}{V_q \cdot K_X} \tag{10}$$
$$K_{P-} = \frac{K_v \cdot A_{tl}}{V_q \cdot K_X}$$

where: K_P – proportional gain, K_{P+} – optimum proportional gain while extending the piston rod, K_{P-} – optimum proportional gain while retracting the piston rod, V_q – servo valve gain [cm^3/s/%], K_X – measuring transducer gain [%/cm], A – surface area of the piston [cm^2].

For the valve D1FPE01FC9NB00, V_q = 1.07 [cm^3/s/%] was taken with the assumed pressure drop on the control edge Δp = 1 MPa. Surface areas of the piston are relatively: A_T = 12.57 cm^2, A_{tl} = 6.16 cm^2. BTL7-E100-M0305-B-S32 position sensor amplifier gain is K_X = 3.33 [%/cm], the measuring range is 300 mm.

After substituting the values into the Equation 10 we have received the following values of the P controller settings while: extending the piston rod (K_{P+} = 824), retracting the piston rod (K_{P-} = 404).

4 Results of the Experimental Tests

The default settings of the Compax3F controller were modified prior to the tests. Feed-forward blocks were assigned zero gain for the speed and acceleration in the position regulation track. The integral action of the controller has also been switched off.

Compax3F controller is also capable of compensating the positive overlap of the servo valve. For this reason, the valve D1FPE01FC9NB00 has been previously tested at the separate measuring station in order to determine the values of the valve overlap corrections on the tracks P → A and P → B. The test revealed that the received values (17 % and 16 % relatively) differ significantly from the default values (while parameterizing the controller, the C3 ServoManager2 system has taken the default value of 23 %). Also modified were the default gain values correcting different gains of the cylinder with unilateral piston rod depending on the powered chamber. Additional gains were adopted, all equal to 1.

Variations for the selected values of the P-term parameter settings of the Compax3F controller relating to the K_v of the servo drive were presented in Fig. 4, Fig. 5 and Fig. 6.

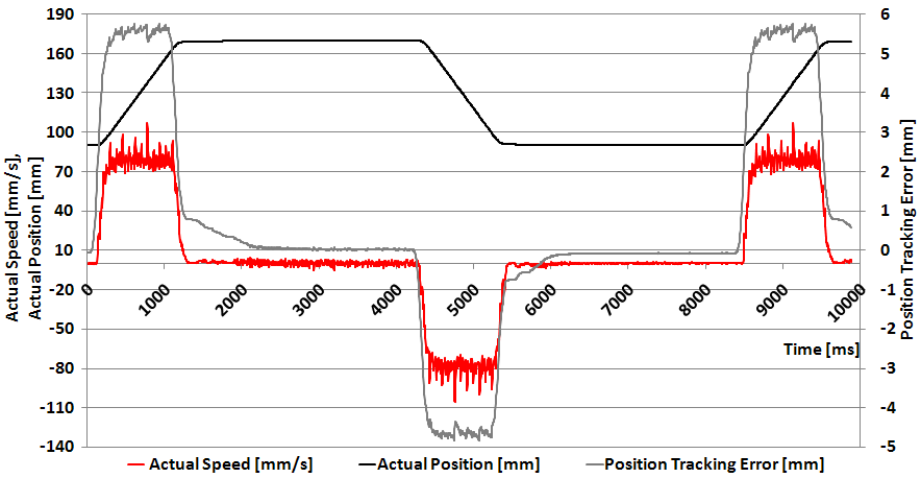

Fig. 4. Variations for the position loop gain setting P-term = 10

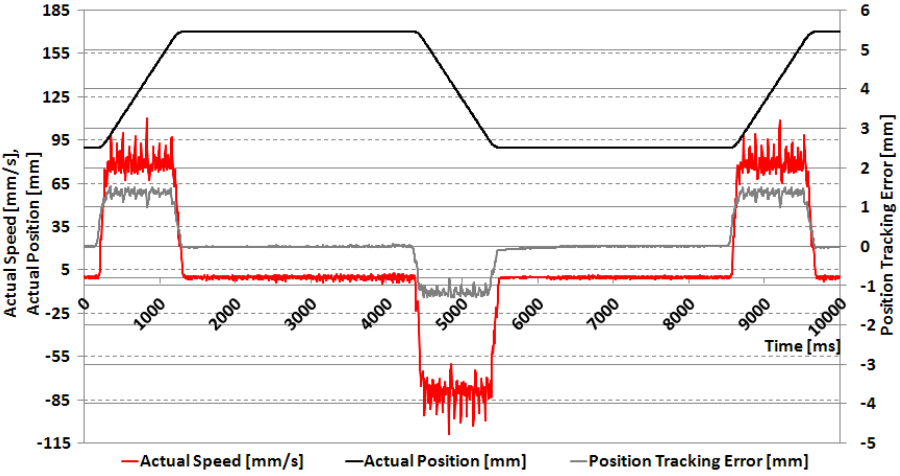

Fig. 5. Variations for the position loop gain setting P-term = 40

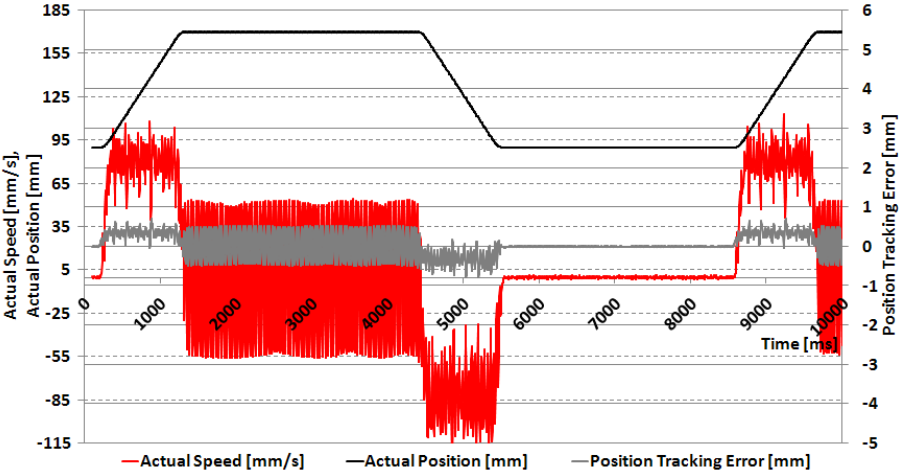

Fig. 6. Variations for the position loop gain setting P-term = 160

For the variations received as a result of the experimental tests, obtained for the subsequent adjustments of the position controller proportional gain in the Compax3F controller with the preset speed of 80 mm/s, the following values have been determined for the extension and retraction of the piston rod (average speed rate and average position offset, position loop gain, effective regulation error and shape factor).

The selected results of the conducted tests have been presented in Tables 1 and 2. The results presented in Table 1 reveal that the analytically determined value of the optimum velocity enhancement for the tested servo drive is slightly inflated. In case of the results (row No. 9) we can observe unstable operation of the servo drive, even though the adjustment of the K_v factor did not exceed the analytically determined value.

Table 1. Results of the experimental tests regarding the piston movement

Average regulation error [mm]	Average speed [mm/s]	Gain K_v [1/s]	Direction of motion	Position loop gain P-term [%/unit]	Notes
5.538	79.875	14.424	extension	10	–
–4.608	–79.901	17.339	retraction	10	–
2.603	79.967	30.727	extension	20	–
–2.253	–79.695	35.376	retraction	20	–
1.345	79.674	59.239	extension	40	–
–1.153	–79.940	69.315	retraction	40	–
0.678	79.516	117.217	extension	80	–
–0.593	–79.553	134.064	retraction	80	–
0.356	79.300	223.009	extension	160	Loss of stability
–0.337	–79.776	236.502	retraction	160	–

Table 2. Analysis of the regulation errors in the preset servo drive position for the selected controller settings

Average regulation error [mm]	Effective regulation error [mm]	Direction of motion	Position loop gain P-term [%/unit]	Shape factor	Notes
0.020	0.025	extension	10	1.180	–
–0.077	0.077	retraction	10	1.001	–
–0.003	0.011	extension	20	4.187	–
–0.035	0.038	retraction	20	1.090	–
–0.001	0.011	extension	40	12.649	–
0.007	0.009	retraction	40	1.209	–
0.001	0.014	extension	80	13.359	–
0.005	0.007	retraction	80	1.355	–
0.013	0.358	extension	160	28.361	Loss of stability
0.006	0.008	retraction	160	1.368	–

Also the comparison of K_v factor in pairs: while extracting and retracting, can be seen as surprising. Gains of the electronic part of the servo drive were constant and independent of the direction of movement. The only difference was in the cylinder gain, which was the result of different surface areas of the piston while extending and retracting the piston rod. Theoretically, we should obtain twice as high values of the K_v factor while retracting the piston rod. Also the ratio of K_v while retracting to K_v while extending the piston rod should be constant. Tests confirmed neither of those two expectations. In order to explain these discrepancies, additional tests should be performed.

The overall results of examining the positioning accuracy of the servo drive were presented in Table 2. Due to the possibility of oscillation occurring in the set position, not only the average value of the regulation error, but also the effective regulation error was determined. In order to measure the oscillation we adopted the form factor,

defined as the absolute value of the effective error to average regulation error ratio. The obtained results are to some extent consistent with the theoretical expectations. Initially, along with increasing the controller gain, both average and effective regulation error were decreasing. It has been observed that starting with the setting P-term = 40 for the position reached with the extended piston rod, the RMS value of control deviation increases, whereas the average position error decreases. The increasing tendency of the servo drive to oscillate in the steady state is evidenced by the significant increase of the shape factor value (from 4.188 for P-term = 20 to 12.649 for P-term = 40). For the setting P-term = 160, it may be assumed that there has been a loss of stability of the tested hydraulic servo drive. The positioning accuracy was by an order of magnitude worse (from 0.0114 mm for P-term= 40, to 0.3581 for P-term = 160). It is worth mentioning that the direction of the external load was contrary to the direction of the servo cylinder's movement.

5 Summary

The analysis of the obtained results of the experimental tests suggests that even for simple systems we may observe significant discrepancies between the theoretically predicted values of the servo drive controller's settings and the values of settings for which the actual servo drive works properly. Using the information received, we are able to state that theoretical settings are a good reference point to optimize the controller settings by means of the experiment carried out with the actual operating conditions of the machine.

References

1. Pizon, A.: Electro hydraulic analog and digital automation systems. WNT Publishing House, Warsaw (1995) (in Polish)
2. Milecki, A.: Linear electrohydraulic servo drives. Poznan University of Technology, Poznan (2003) (in Polish)
3. Joint publication: The Hydraulic Traineer. Proportional and Servo Valve technology, vol. 2. Mannesmann Rexroth AG, Lohr a. Main (1998) (in German)
4. Tomasiak, E., Klarecki, K., Barbachowski, E.: Servo drives in machine construction. Hydraulics and Pneumatics 1, 16–20 (2009) (in Polish)
5. Barbachowski, E., Klarecki, K.: Methods for correcting the characteristics of proportional valves. Selected Engineering Problems 2, 29–34 (2011) (in Polish)
6. Materials developed by Parker Hannifin: Operating instructions Compax3 Fluid I12T11: Control via digital I/Os & COM port. Hydraulics controller, http://divapps.parker.com/divapps/eme/EME/Literature_List/DOKUMENTATIONEN/CFI12T11%20eng.pdf

Intelligent Monitoring and Optimization of Micro- and Nano-Machining Processes

Dariusz Lipiński and Maciej Majewski

Koszalin University of Technology, Department of Mechanical Engineering
Racławicka 15-17 str., 75-620 Koszalin, Poland
{dariusz.lipinski,maciej.majewski}@tu.koszalin.pl
http://kmp.wm.tu.koszalin.pl

Abstract. The article describes an innovative concept of intelligent systems for monitoring and optimization of micro- and nano-machining processes, which are equipped with a speech interface and artificial intelligence. The developed concept proposes an architecture of the systems equipped with a data analysis layer, process supervision layer, decision layer, communication subsystem by speech and natural language, and visual communication subsystem using voice descriptions. The implemented computational intelligence methods allow for real-time data analysis of monitored processes, configuration of the system, process supervision and optimization based on the process features and quality models. The modern concept allows for the development of universal and intelligent systems which are independent of a type of manufacturing process, machining parameters and conditions.

Keywords: process monitoring, process optimization, micro- and nano-machining, intelligent system, modern machining process.

1 Introduction

In the industry processes of micro- and nano-machining can be performed using a hybrid system for monitoring, optimization and forecasting of the machining process quality, equipped with artificial intelligence methods and a layer of remote voice and visual communication between the system and human operators. This system is presented in exemplary application in the precision grinding processes. It features the possibility for many other applications, future development and experiments. Its main tasks include: modeling of the manufacturing process, assessment of inaccuracy effects, identification of inaccuracy causes, optimization of the process conditions and parameters.

The scientific aim of the research is to develop fundamentals of building interactive systems (Fig. 1) for monitoring and optimization of micro- and nano-machining processes. The design and implementation of these systems is an important field of research. This concept proposes a novel approach to these systems, with particular emphasis on their ability to be truly flexible, adaptive, human error-tolerant, and supportive both of human operators and intelligent agents in distributed systems

J. Awrejcewicz et al. (eds.), *Mechatronics: Ideas for Industrial Applications*,
Advances in Intelligent Systems and Computing 317, DOI: 10.1007/978-3-319-10990-9_10

architectures. The interactive hybrid system allows for higher organization level of manufacturing processes, which is significant for their efficiency and humanization. Decision and optimization systems can be remote elements of manufacturing processes. The design of the proposed system can be considered as an attempt to create a standard interactive system for monitoring and optimization of machining processes. It is very significant for the development of new effective and flexible manufacturing methods.

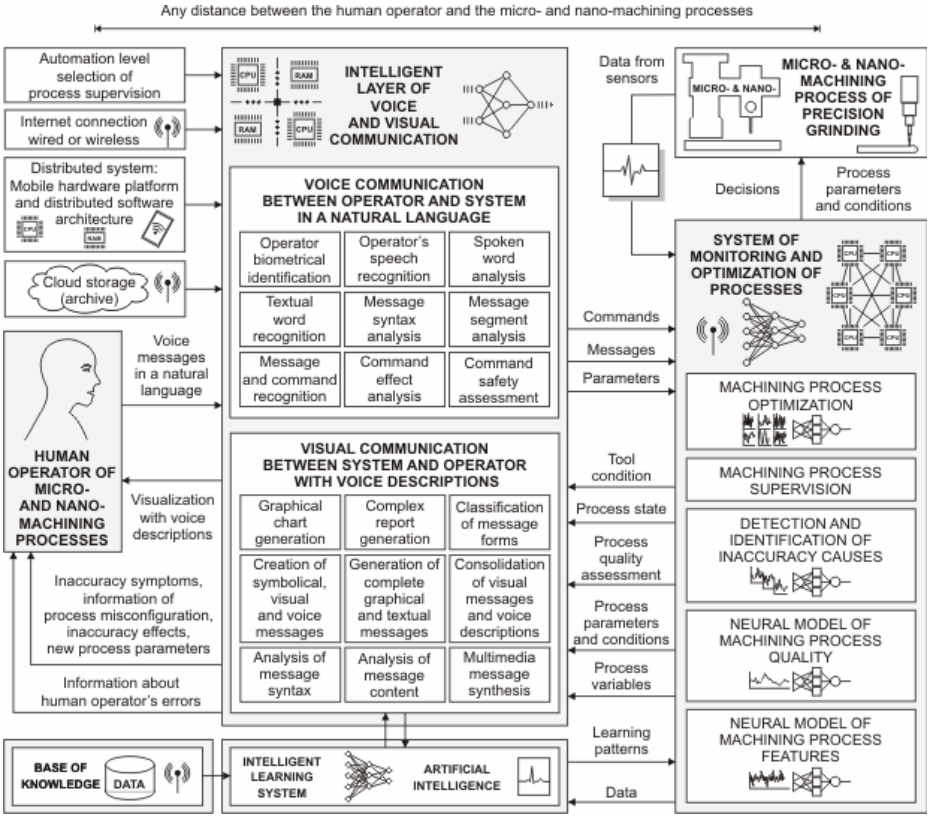

Fig. 1. Concept of interactive systems for monitoring and optimization of micro- and nano-machining processes

2 The State of the Art

There is a need for remote systems of monitoring and optimization of machining processes in reconfigurable manufacturing systems to reduce bottlenecks that occur in associated tasks to be performed by these systems using technological devices. The tasks include [1–4, 16]: modeling of process features and quality, assessment of inaccuracy effects, identification of inaccuracy causes, optimization of process conditions

and parameters. These bottlenecks can occur as a result of the mass production of custom products.

This article offers an approach by using the developed concept of the interactive hybrid system of monitoring and optimization of the processes of micro- and nano-machining to deal with the above problems. Selected article [4] presents innovative solutions in supervision of precise grinding processes and development of a system for monitoring, optimization and forecasting of machining process quality. Articles [5–15] describe the developed solutions in intelligent voice communication between human operators and technical devices.

3 Description of the System

The developed concept proposes an architecture of the interactive hybrid system for monitoring and optimization, which is equipped with a data analysis layer, process supervision layer, decision layer, communication subsystem by speech and natural language, and visual communication subsystem using voice descriptions. The structure of the system is presented in abbreviated form on Fig. 2. The numbers in the cycle represent the successive phases of information processing. The developed concept also includes the system for mobile technologies (Fig. 3). The novelty of the system consists of inclusion of adaptive intelligent layers for data analysis, supervision and decision. The system is also capable of analysis of the supervised machining process, configuration of the supervision system, neural modeling of process features, neural modeling of process quality, detection of the inaccuracies, estimation of the inaccuracy results, compensation of the inaccuracy results, and selection of the machining parameters and conditions. The core of the system consists of the following process models: the neural model of the optimal process parameters for determination of optimal values of the process features, and the neural model for assessment of influence of the measured process features on the process quality parameters.

The system contain probabilistic neural networks (Fig. 4) for forecasting the state of the abrasive tool and prediction of the surface quality. The inputs of the networks include parameters of abrasive tools, workpiece parameters, geometric and kinematic parameters, process variables. The system also consists of mechanisms (Fig. 5) for meaning analysis of operator's messages and commands given by voice in a natural language, and various visual communication forms with the operator using voice descriptions.

The interaction between the operator and the system by speech and natural language contains intelligent mechanisms for operator biometric identification, speech recognition, word recognition, recognition of messages and commands, syntax analysis of messages, and safety assessment of commands. The interaction between the system and the operator using visual messages with voice descriptions includes intelligent mechanisms for generation of graphical and textual reports, classification of message forms, generation of messages in the graphical and textual forms, consolidation and analysis of message contents, synthesis of multimedia messages.

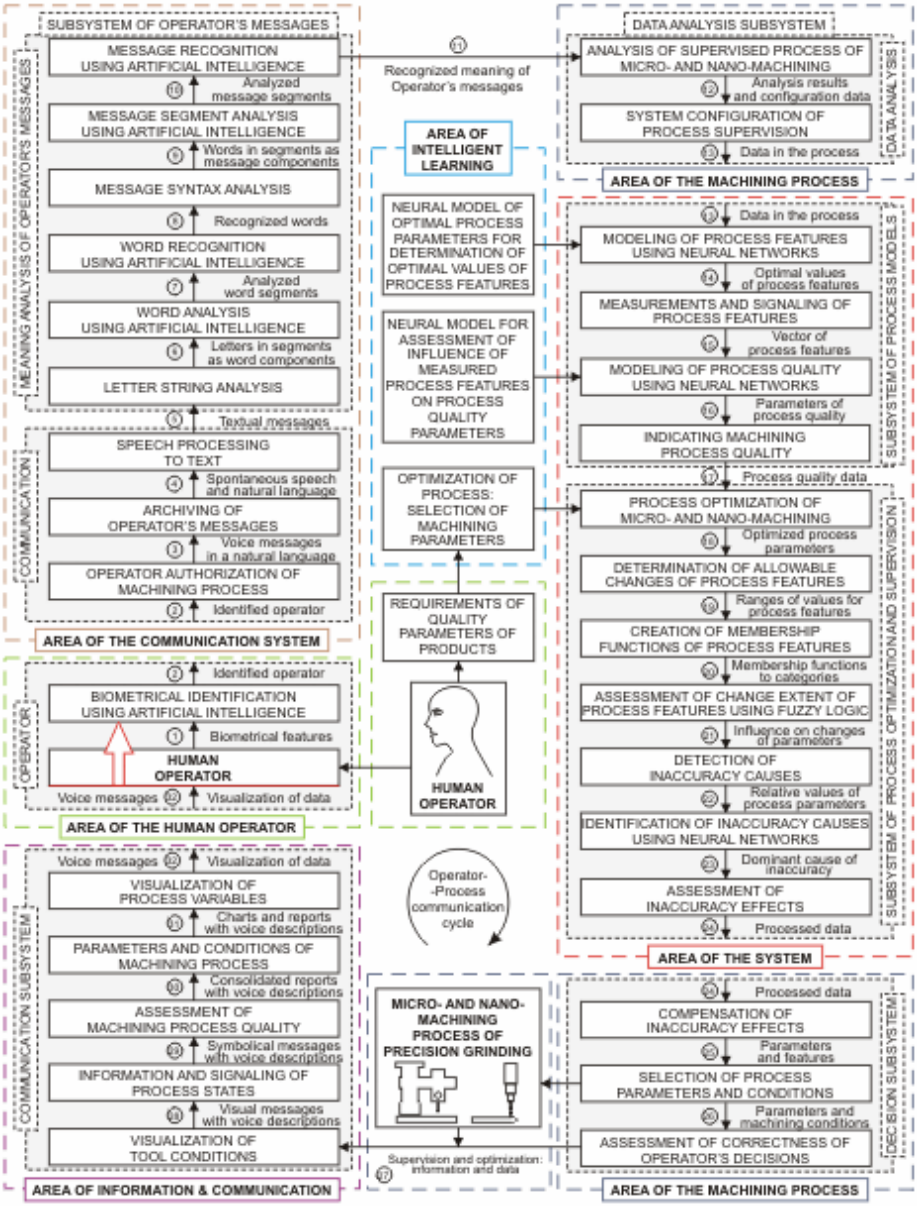

Fig. 2. Implementation structure of hybrid systems for monitoring and optimization of micro- and nano-machining processes using voice and visual communication

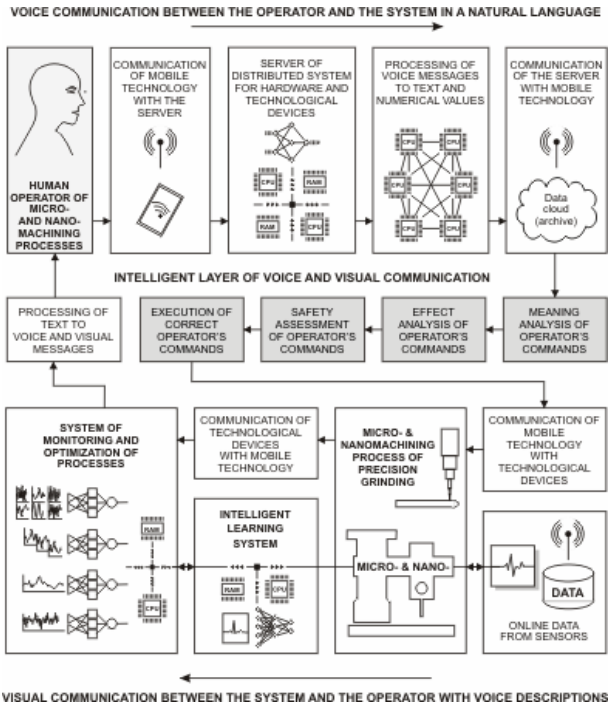

Fig. 3. Interactive system for monitoring and optimization using mobile technologies

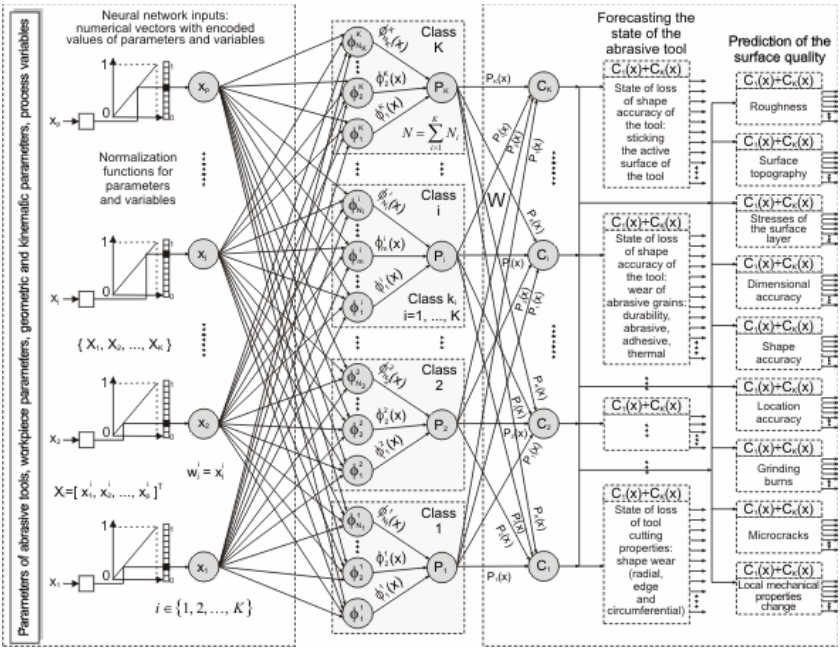

Fig. 4. Probabilistic neural networks for monitoring and optimization of processes

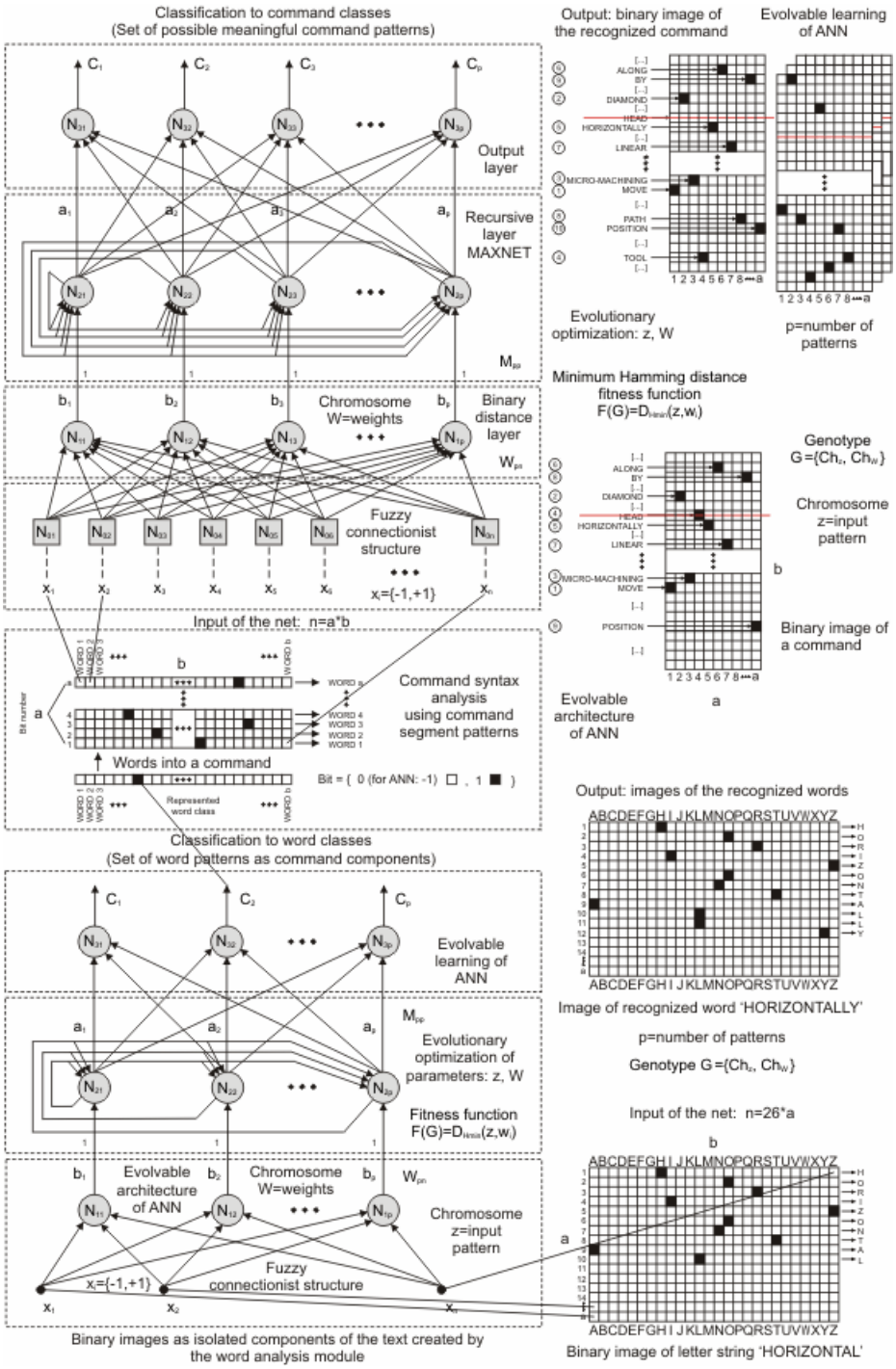

Fig. 5. Evolvable fuzzy neural networks for word and command recognition

4 Experimental Results

On the basis of experiments and extensive analysis of their results, specific requirements have been set in terms of system components and their functions. The results obtained experimentally, supported by analysis, allowed for the development of a detailed system architecture.

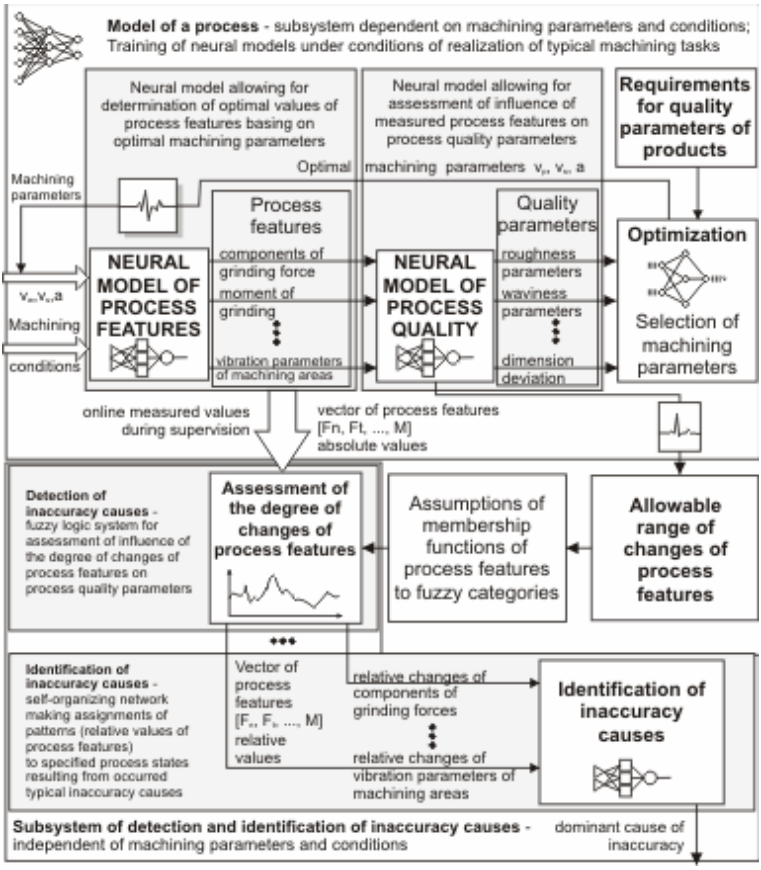

Fig. 6. System for detection of inaccuracies and optimization of machining parameters

Basing on the research, the neural models of the process features and quality have been developed for a subsystem (Fig. 6) for detection of inaccuracies and optimization of machining parameters.

The research allowed to develop the architecture of the following system presented in Fig. 7. The system preferably should contain adaptive intelligent layers for data analysis, supervision and decision. The system should be capable of analysis of the supervised machining process, configuration of the supervision system, neural modeling of process features, neural modeling of process quality, detection of the inaccuracies, estimation of the inaccuracy results, compensation of the inaccuracy results, and

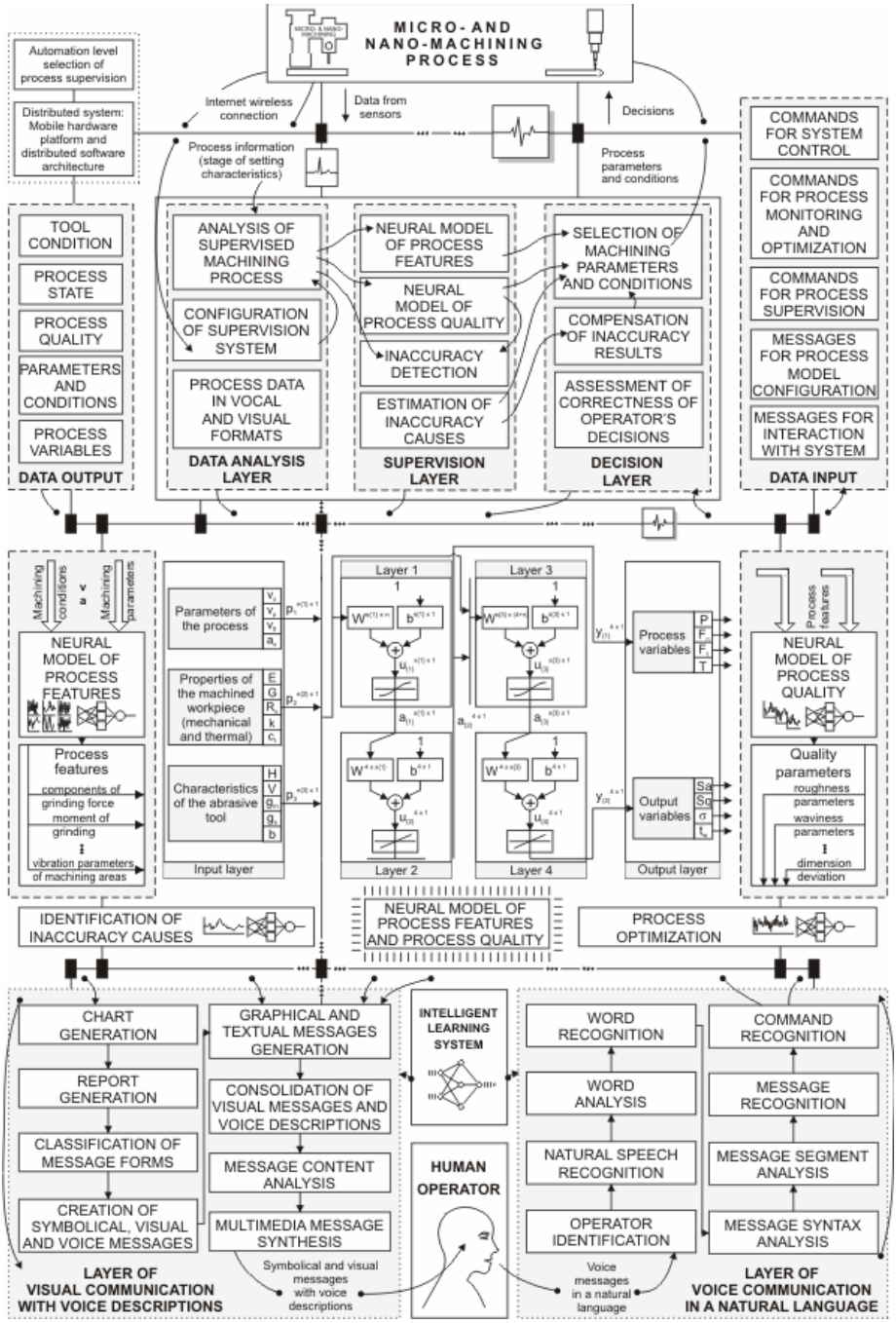

Fig. 7. The developed architecture of interactive hybrid systems for monitoring and optimization of micro- and nano-machining processes with the core of neural models of the process features and quality

selection of the machining parameters and conditions. The core of the system consists of the following process models: the neural model of the optimal process parameters for determination of optimal values of the process features, and the neural model for assessment of influence of the measured process features on the process quality parameters.

5 Conclusions and Perspectives

The proposed concept of the interactive hybrid systems for monitoring and optimization of machining processes, equipped with a speech interface and artificial intelligence, allows for the development of universal and intelligent systems which are independent of a type of manufacturing process, machining parameters and conditions. The condition of effectiveness of the system is to equip it with intelligent mechanisms for modeling of the process features and quality, assessment of inaccuracy effects, identification of inaccuracy causes, optimization of the process conditions and parameters. The experimental results of the proposed system show its promising performance. The concept can be used for further development and experiments. The system is both effective and flexible which makes its applications possible. It features the universality of application of the developed artificial intelligence algorithms. The hybrid system allows for more robustness to human's errors. The proposed complex solution also eliminates scarcities of the typical co-operation between human operators and technological devices.

Acknowledgements. The authors would like to thank The National Science Center in Poland (NCN) who provided financial support for this work.

References

1. Abellan-Nebot, J.V., Subiron, R.F.: A Review of Machining Monitoring Systems Based on Artificial Intelligence Process Models. International Journal of Advanced Manufacturing Technology 47, 237–257 (2010)
2. Brown, J.A.: Modern Manufacturing Processes. Industrial Press, New York (2011)
3. Groover, M.P.: Fundamentals of Modern Manufacturing. Wiley & Sons, Inc. (2007)
4. Lipiński, D., Kacalak, W.: Assessment of the Accuracy of the Process of Ceramics Grinding with the Use of Fuzzy Interference. In: Beliczynski, B., Dzielinski, A., Iwanowski, M., Ribeiro, B. (eds.) ICANNGA 2007. LNCS, vol. 4431, pp. 596–603. Springer, Heidelberg (2007)
5. Kacalak, W., Majewski, M.: New Intelligent Interactive Automated Systems for Design of Machine Elements and Assemblies. In: Huang, T., Zeng, Z., Li, C., Leung, C.S. (eds.) ICONIP 2012, Part IV. LNCS, vol. 7666, pp. 115–122. Springer, Heidelberg (2012)
6. Kacalak, W., Majewski, M.: Effective Handwriting Recognition System Using Geometrical Character Analysis Algorithms. In: Huang, T., Zeng, Z., Li, C., Leung, C.S. (eds.) ICONIP 2012, Part IV. LNCS, vol. 7666, pp. 248–255. Springer, Heidelberg (2012)

7. Kacalak, W., Majewski, M., Zurada, J.M.: Intelligent E-learning Systems for Evaluation of User's Knowledge and Skills with Efficient Information Processing. In: Rutkowski, L., Scherer, R., Tadeusiewicz, R., Zadeh, L.A., Zurada, J.M. (eds.) ICAISC 2010, Part II. LNCS, vol. 6114, pp. 508–515. Springer, Heidelberg (2010)
8. Kacalak, W., Majewski, M.: Natural Language Human-Robot Interface Using Evolvable Fuzzy Neural Networks for Mobile Technology. In: Huang, D.-S., Jo, K.-H., Lee, H.-H., Kang, H.-J., Bevilacqua, V. (eds.) ICIC 2009. LNCS, vol. 5754, pp. 480–489. Springer, Heidelberg (2009)
9. Kacalak, W., Majewski, M.: E-learning Systems with Artificial Intelligence in Engineering. In: Huang, D.-S., Jo, K.-H., Lee, H.-H., Kang, H.-J., Bevilacqua, V. (eds.) ICIC 2009. LNCS, vol. 5754, pp. 918–927. Springer, Heidelberg (2009)
10. Majewski, M., Zurada, J.M.: Sentence Recognition Using Artificial Neural Networks. Knowledge-Based Systems 21(7), 629–635 (2008), doi:10.1016/j.knosys.2008.03.053
11. Majewski, M., Kacalak, W.: Intelligent System for Natural Language Processing. In: Huang, D.-S., Li, K., Irwin, G.W. (eds.) ICIC 2006. LNCS (LNAI), vol. 4114, pp. 742–747. Springer, Heidelberg (2006)
12. Stuart, K.D., Majewski, M., Trelis, A.B.: Intelligent Semantic-Based System for Corpus Analysis through Hybrid Probabilistic Neural Networks. In: Liu, D., Zhang, H., Polycarpou, M., Alippi, C., He, H. (eds.) ISNN 2011, Part I. LNCS, vol. 6675, pp. 83–92. Springer, Heidelberg (2011)
13. Stuart, K., Majewski, M., Botella-Trelis, A.: Selected Problems of Intelligent Corpus Analysis through Probabilistic Neural Networks. In: Zhang, L., Lu, B.-L., Kwok, J. (eds.) ISNN 2010, Part II. LNCS, vol. 6064, pp. 268–275. Springer, Heidelberg (2010)
14. Stuart, K.D., Majewski, M.: Artificial Creativity in Linguistics using Evolvable Fuzzy Neural Networks. In: Hornby, G.S., Sekanina, L., Haddow, P.C. (eds.) ICES 2008. LNCS, vol. 5216, pp. 437–442. Springer, Heidelberg (2008)
15. Stuart, K.D., Majewski, M.: Evolvable Neuro-fuzzy System for Artificial Creativity in Linguistics. In: Huang, D.-S., Wunsch II, D.C., Levine, D.S., Jo, K.-H. (eds.) ICIC 2008. LNCS (LNAI), vol. 5227, pp. 46–53. Springer, Heidelberg (2008)
16. Teti, R., Jemielniak, K., ODonnell, G., Dornfeld, D.: Advanced Monitoring of Machining Operations. CIRP Annals – Manufacturing Technology 59, 717–739 (2010)

Analog Electronic Test Board for an Estimation of Time Characteristics of the Basic Elements of Automatic Control Systems

Paweł Olejnik, Damian Kociak, and Jan Awrejcewicz

Department of Automation, Biomechanics and Mechatronics
Faculty of Mechanical Engineering of Lodz University of Technology
1/15 Stefanowski Str., 90-924 Łódź, Poland
{pawel.olejnik,jan.awrejcewicz}@p.lodz.pl,
dkociak@gmail.com

Abstract. This work presents the design and implementation of an analog electronic test board (AETB) for determining the time characteristics of basic elements of automatic control systems. Test signals are formed to study time responses of open and closed-loop basic control systems. In the practical part, a laboratory test board was designed and manufactured. Electronic components have been installed on a PCB prototype and the whole system has been enclosed in a polycarbonate box containing BNC junctions to connect it with an external oscilloscope. The device has been divided into functional blocks such as power supply, signal generator and a system containing basic elements of automation. Moreover, parameters of both the generator and the basic elements are tunable. By using the AETB test board, it is possible to analyze properties of the PID controllers as well as the first and second-order basic elements. In the preliminary stage of the design, numerical simulations allowed to choose proper values of most electronic components. Finally, a few waveforms were examined on the oscilloscope to make a comparison with the simulation results.

Keywords: basic elements, analog electronic test board, test signals, practical PID controller, LM7812 regulator, ICL8038 generator, LF353N op-amp.

1 Introduction

Before a control system is designed and implemented, it is imperative to understand the characteristics and behavior of the processes to be controlled. In practice, the input signal to a control system is not known ahead of time but is rather random in nature, and the instantaneous input cannot be expressed analytically [1]. Only in some cases the signal input is known in advance and expressible analytically or by curves, such as in the case of the automatic control. In analyzing and designing control systems, we must have a basis of comparison of performance of various control systems. It may be settled by specifying a particular input test signals and then by comparing with them any responses of basic electronic subsystems. With respect to the above or even to many design criteria, such as stability of control systems the presented analog

J. Awrejcewicz et al. (eds.), *Mechatronics: Ideas for Industrial Applications*,
Advances in Intelligent Systems and Computing 317, DOI: 10.1007/978-3-319-10990-9_11

electronic test board (AETB) which is useful for testing basic elements of automatic control systems has been designed as a prototype and constructed.

2 Subsystems of the Analog Electronic Test Board

2.1 Power Supply

In mains-supplied electronic systems the AC input voltage must be converted into a DC voltage with the right value and degree of stabilization [7]. The design of stabilized supplies has been simplified dramatically by the introduction of voltage regulator ICs such as the L7812 and L7912, a three-terminal series regulators providing a very stable output, and additionally, including some current limiters and thermal protection functions. Fig. 1 shows how this circuit is used on the AETB test board.

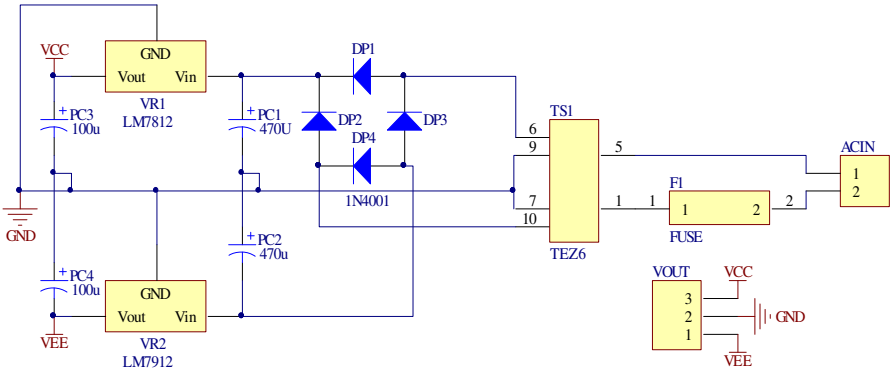

Fig. 1. Complete ±12V/1A split supply regulator circuit

An appropriate isolation strategy is defined and rigidly applied throughout the design. Creepage and clearance spacing separate all hazardous voltages from user accessible points. There is a very clear channel between primary and secondary circuits. It has been checked, that hazardous voltage levels are not present on any secondary circuits where a low voltage output is generated from a low PWM duty-cycle, high peak voltage and PWM power pulse. The AETB test board has a protective earth provided by a conductive grounded enclosure.

2.2 Generator of Test Signals

The commonly used test input signals are functions of the following kinds: step, ramp, acceleration, impulse and sinusoidal [2]. Using these test signals, some mathematical and experimental analyses of control systems can be carried out since the signals are precisely repeated and stable in time. The two basic requirements were applied and met after the design and practical implementation on the AETB. A diagram of the Generator's electronic circuit is shown in Fig. 2. Frequency, $PWM_{\%}$ duty cycle and distortion of the three output signals, i.e. sawtooth (PILA), square (PROST)

and sinusoidal (SIN) of the Generator are tuned by potentiometers P_{R215}, P_{R213} and P_{R214}, respectively. Potentiometer P_{R216} sets amplitude U_{in} of the test signals which are selectable by a 3-way switch. On the subsequent diagrams, notation GEN marks one of the test signals generated by the system shown in Fig. 2. Time histories of the test signals produced by the Regulated Signal Generator (RSG) are shown in Fig. 3.

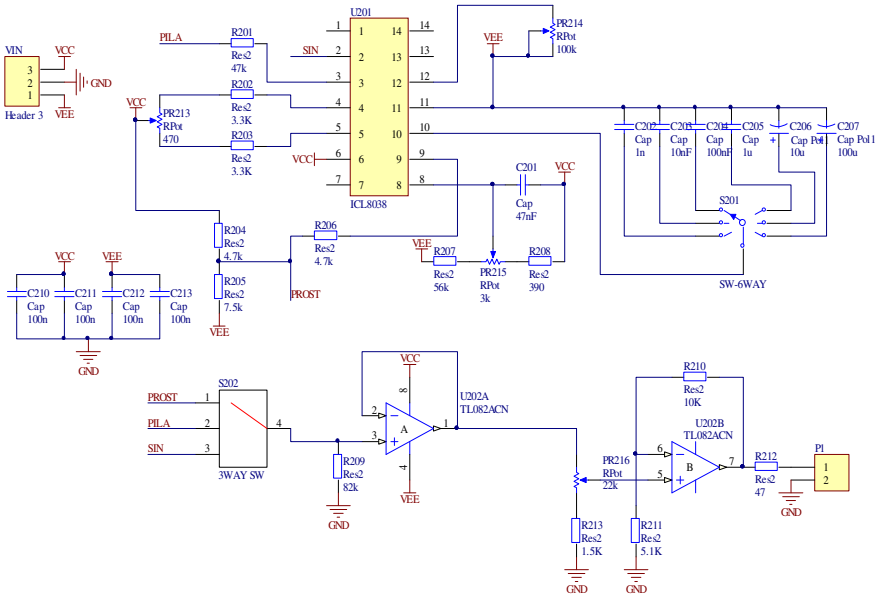

Fig. 2. A circuit diagram of the Regulated Signal Generator (RSG)

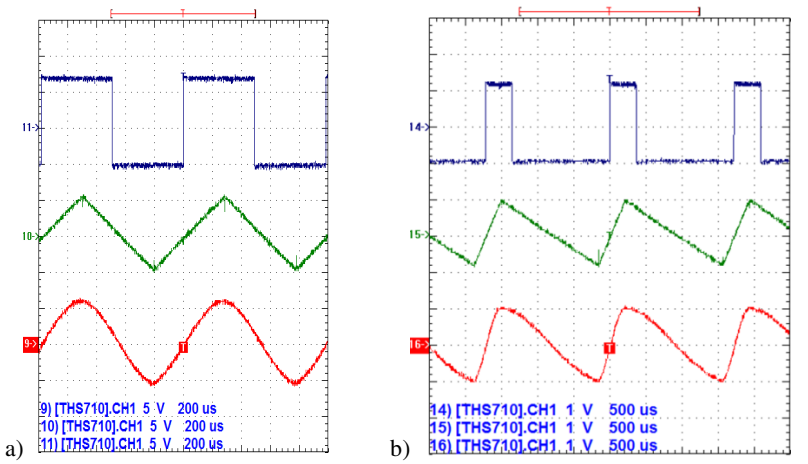

a) b)

Fig. 3. The three types of test signals measured on the RSG's output: a) U_{out} = 12 V, f_{out} = 1 kHz, $\text{PWM}_{\%}$ = 50, b) U_{out} = 2 V, f_{out} = 500 kHz, $\text{PWM}_{\%}$ = 20

The system used in the device of signal generation is capable of generating waveforms of three shapes: square, sine and sawtooth. On the main panel there are placed some switches and knobs used to adjust the parameters of the RSG. A selection between the test signals is possible by means of a rotary switch S_{202} of the signal waveform which is measured in the output. The second switch S_{201} is responsible for the selection of the frequency f_{out} of the generated signal. One can smoothly adjust the frequency using the additional potentiometer P_{R215}. The next two knobs are for the change in the amplitude of the output signal and for changing the $PWM_{\%}$ duty cycle.

The ICL8038 waveform generator is the basic IC used as the signal source on the AETB test board. It is a monolithic integrated circuit capable of producing high accuracy sine, square, triangular, sawtooth and pulse waveforms with a minimum of external components. The repetition rate (frequency) can be selected externally from 0.001 Hz to more than 300 kHz using either resistors or capacitors, frequency modulation and sweeping can be accomplished with an external voltage.

2.3 Proportional, Integral and Differentiation Components

Proportional Component is the simplest and most commonly encountered of all continuous control systems. In this action, the controller produces an output signal which is proportional to the error of regulation. Hence, the greater the magnitude of the error, the larger is the corrective action applied. Practical implementation of the Proportional Component realizing the P-action on the AETB test board is shown in Fig. 4a.

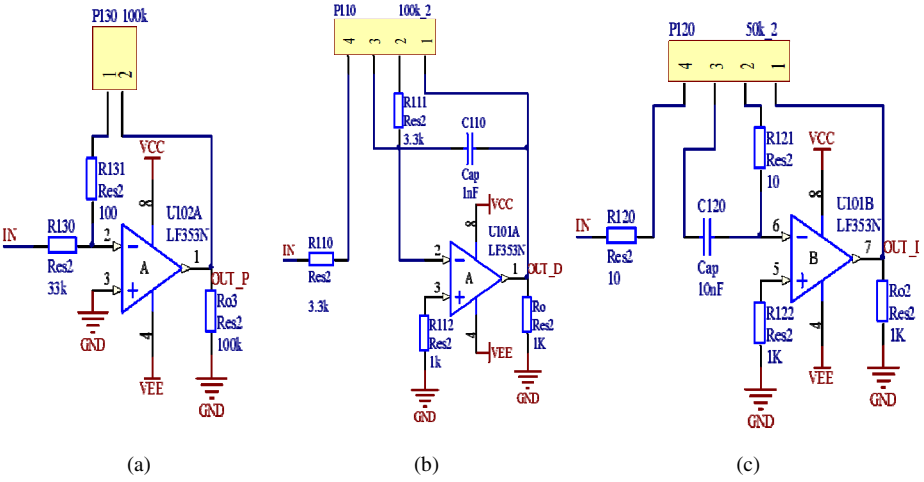

Fig. 4. Circuit diagrams of the Proportional (a), Integral (b) and Differentiation (c) components

The Integral Component sums the error of regulation over time. The result is that even a small error term will cause the Integral Component to increase slowly. The integral response will continually increase over time unless the error is zero, so the effect is to drive the steady-state error to zero. Steady-state error is the final difference between the process variable and a set point. The phenomenon called integral windup

results when I-action saturates a controller without the controller driving the error signal toward zero. Practical implementation of the Integral Component realized on the AETB test board is shown in Fig. 4b.

The Differentiation Component produces amplification of the high-frequency signals. High-frequency signals often come from the measurement noise within the system. Moreover, the D-action has no effect on steady (constant) signals. In the low-frequency range one finds that the D-action has very small gain values. It is the near-zero gain which attenuates low-frequency signals. The consequence of the possibility of measurement noise being present within the system is that we do not, in practical applications, apply the Differentiation Component directly to the measured output of the process. Instead, we introduce a Low Pass Filter. A LPF has the effect of attenuating high-frequency signals. Practical implementation of the Differentiation Component realized on the AETB test board is shown in Fig. 4c.

The three basic elements shown in Fig. 4 are built on the LF353 dual operational amplifier, which is an analog/linear JFET input operational amplifier with an internally compensated input offset voltage. The JFET input device provides wide bandwidth, low input bias currents and offset currents. Features of the electronics follow: internally trimmed offset voltage: 10 mV, low input bias current: 50 pA, wide gain bandwidth: 4 MHz, high slew rate: 13 V/μs, high input impedance: 1012 Ω.

2.4 First and Second-Order Basic Elements

The figure 5 shows a capacitor *C* in series with a resistor R forming a RC charging circuit. A resistor in series with the capacitor forms a RC circuit and the capacitor charges up gradually through the resistor until the voltage across the capacitor reaches that of the supply voltage (the difference in electric potential between an input IN and the ground GND) [6]. The time called the transient response, required for this to occur is equivalent to about 5 time constants or 5*T*. Circuit diagram of first-order basic element is shown in Fig. 5a. Connecting two *RC* charging circuits in a series we get a second-order basic element shown in Fig. 5b. A simple passive RC and a second-order LPFs have been made respectively. A LPF circuit consisting of a resistor of $R = 160\ \Omega$ in series with a capacitor of $C = 10\text{nF}$ is connected across a square-input of amplitude $U_{in} = 12\ \text{V}$ (supply voltage). The output voltage U_{out} at a frequency $f = 5\ \text{kHz}$ and reactance X_c is set in the system nearly to the input voltage U_{in} as below

$$U_{out} = \frac{U_{in}}{2\pi fC\sqrt{R^2 + X_C{}^2}} = 11.985V$$

Second-order filters are important and widely used in filter designs because when combined with first-order filters any higher-order filters can be designed using them. As it is shown, a third-order LPF is formed by connecting in series or cascading together a first- and a second-order LPF. But there is a downside too cascading together RC filter stages. Although there is no limit to the order of the filter that can be formed, as the order increases, the gain and accuracy of the higher-order filter declines.

The primary use for an inductor is found in filtering circuits, resonance or current limiting circuits, see Fig. 5c. It can be used to tune various types of oscillators [1, 6].

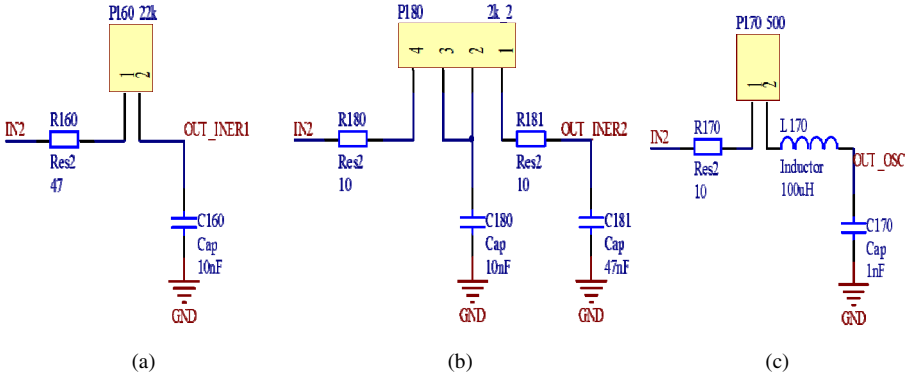

(a) (b) (c)

Fig. 5. Circuit diagrams of the first-order (a), second-order (b) and oscillatory (c) component

Series RLC circuit behavior is described well by oscillating system theory which describes the charge on the capacitor as a second-order differential equation [4]. A scope of experiments performed by means of the test board taken into the design in this work is also to observe and measure the transient responses. In particular, a transient response of an oscillatory component visible in Fig. 5c to an external voltage of some frequency has been observed and shown in Section 3. The time-varying voltage across the capacitor in a RLC loop is measured when an external voltage is applied.

2.5 Summing Amplifiers, Negative Feedback Loop and Signal Routing

The Summing Amplifier is an electronic circuit based upon the standard Inverting Operational Amplifier's configuration [5]. In the Inverting Amplifier, if we add another input resistor equal in value to the original input resistor, R_{140}, R_{141} and R_{142} we end up with another operational amplifier circuit called a Summing Amplifier (Summing Inverter or sometimes a Voltage Adder) circuit as shown in Figs. 6 and 7.

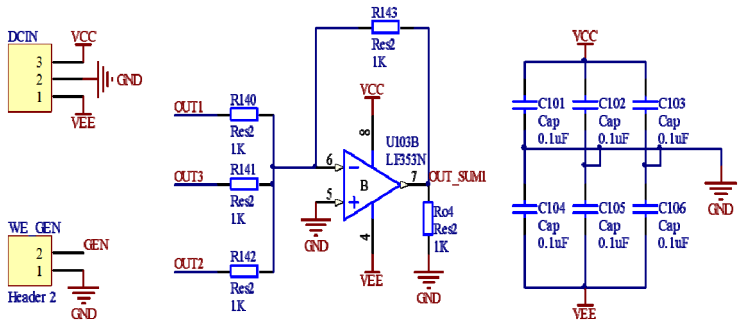

Fig. 6. Summing circuit of the P, I and D components based on the first Summing Amplifier

The output voltage U_{out} as a voltage drop on the R_{04} resistor load becomes proportional to the sum of the input voltages, U_{IN1}, U_{IN2} and U_{IN3}. A Scaling Summing Amplifier can be made if the individual input resistors are not equal. Summing up the input signals of P, I and D actions a PID controller's output is finally detectable at the output node OUT_SUM1, see Fig. 6.

A controller plays an essential role in control systems [2, 8]. Of the four basic functions of a control system like measurement, comparison, computation, and correction, the second and the third functions are solely achieved by the controller. The correction is materialized by the final control element, but this is done according to the controller's calculation.

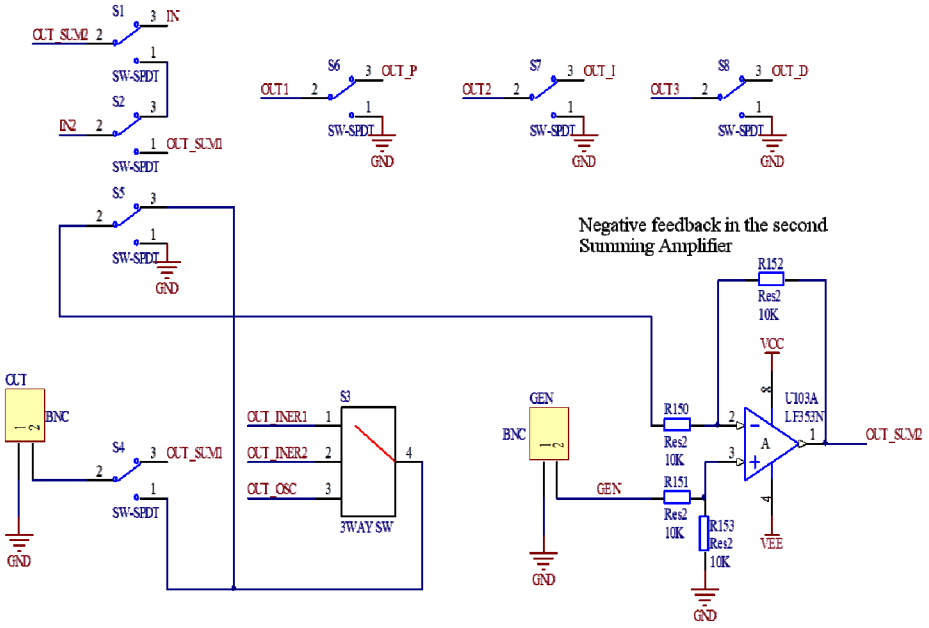

Fig. 7. A negative feedback to the second Summing Amplifier

Fig. 7 presents a negative feedback loop with the S_5 switch allowing to turn it on or off as well as to redirect the PID controller's output OUT_SUM1 to the switch S_3. At this point we are able to input the control signal to the plant which is created by the first-order (OUT_INER1), second-order (OT_INER2) or even an oscillatory component (OUT_OSC). Outputs from switches S_6–S_8 can be used to configure either P, PI, PD or PID actions visible in Fig. 4, and supplemented with Summing Amplifier from Fig. 6.

The control mechanism is the controller considered as consisting of the comparator and the controller itself. The purpose of the first is to compare the measured and the desired values of the controlled variable and then compute the difference between them as the regulation error. If there is no such error, i.e. the controlled variable is at the set point, then no action is taken [3].

If an error is detected, the second section of the controller operates to alter the setting of the final control element in such a way as to minimize the error in the least possible time with the minimum disturbance to the system. To achieve this objective, different actions could be taken by the controller, and hence, different signals are sent to the final control element.

3 Numerical Estimation of RLC Components

The numerical simulation of the investigated basic elements of automation is performed to check correctness of the electronic circuits, as well as to chose proper values of resistance R, capacitance C and inductance L of almost each real component applied on the AETB test board. This section presents the results of numerical simulations of electronic circuits representing basic elements of automation. The results are given in a form of the time characteristics of voltage changes as a response of the Proportional (Fig. 8), Integral (Fig. 9) and the second-order oscillatory component (Fig. 10) to the square-input test signal of frequency $f = 5$ kHz and amplitude $U = 5$ V.

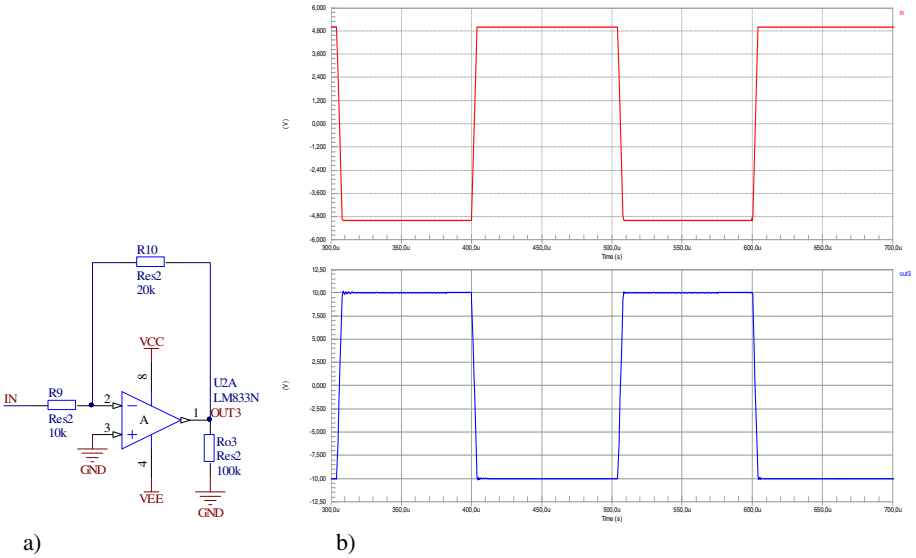

Fig. 8. Proportional action in a numerical simulation: a) the Proportional component, b) a time response of the component (blue line) in a reaction to the test square-input (red line)

In Fig. 8, the input and output signals are marked respectively with red and blue colors. As we can read from the course, the amplitude of the output signal increases two times up to 10 V. As used in the configuration of the Inverting Amplifier, the output receives a signal inverted in phase.

Simulations were performed in Altium Designer. It is a software package which allows electronic circuit designers to design, draw and simulate electronic circuit boards.

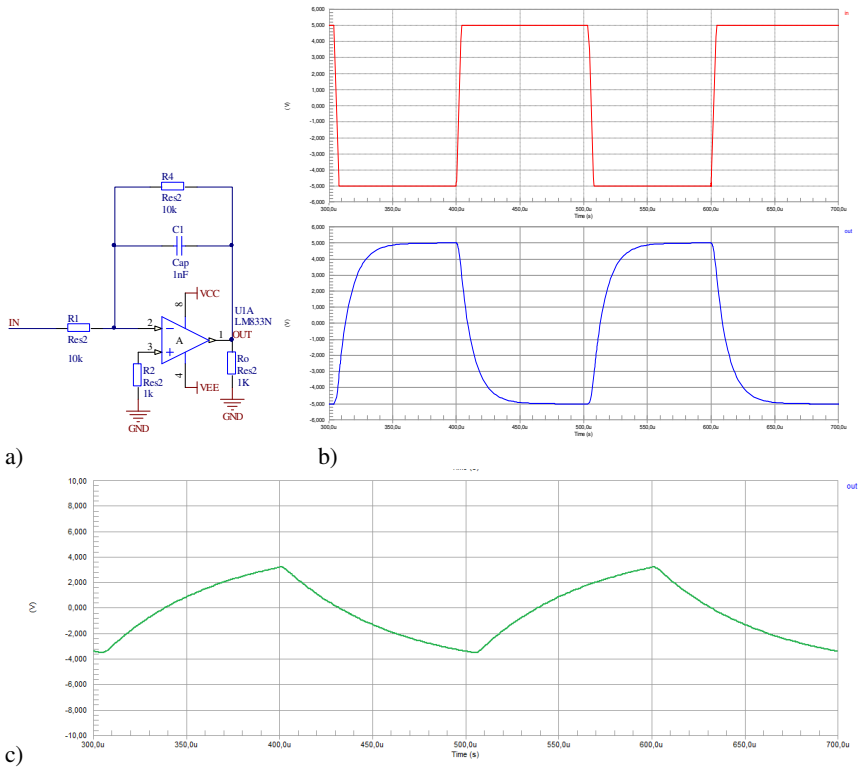

Fig. 9. Integral action in a numerical simulation: a) the Integral component, a time response of the component with b) a small time constant, c) a large time constant

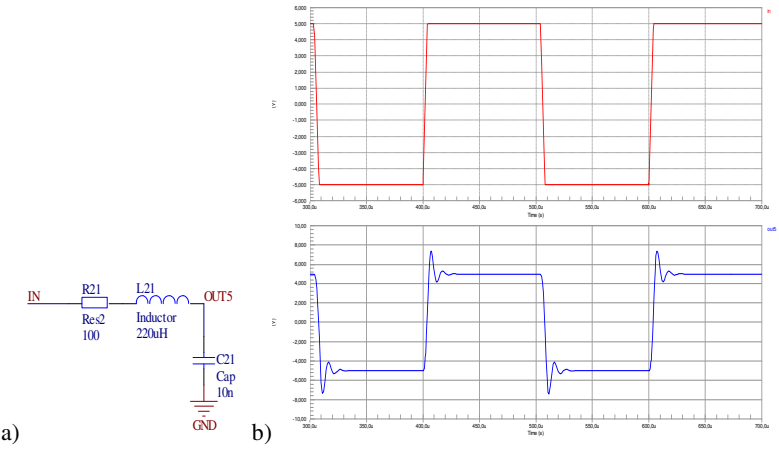

Fig. 10. Numerical simulation of a second-order element: a) RLC circuit of the oscillatory component, b) a time characteristics of the voltage calculated at point OUT5

For any large time constants, the output voltage oscillates about the constant component, while a small time constant reflects in a slightly integrated output signal. The larger the time constant compared to the waveform period ($\tau >> T$), the slower the system responds to changes in the constant component of input voltage. This reduces the amplitude of the output voltage.

4 The Experimental Station

4.1 Final View of the Electronic Board

On the left of the front panel visible in Fig. 11 a block marked by GEN is placed. It is the block of the input function generator RSG. It contains all the potentiometers regulating the signal's amplitude, frequency and duty cycle. There are also rotary switches to select the signal's shape and its frequency range. Next, the Summing Block (adder) is arranged. In the upper part of the panel along the PID block a second adder has been placed. In the lower part several potentiometers are collected to adjust the parameters of the oscillatory and inertial basic elements (IN1, IN2, OSC).

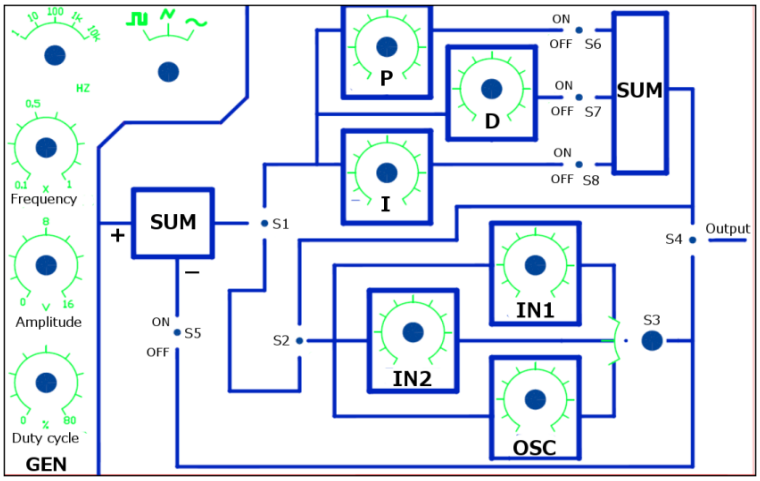

Fig. 11. Front panel markings on the AETB's housing

For the housing of the electronic system an universal box with polycarbonate transparent cover was used. The front panel of the device was prepared in a graphical program to describe all switches, potentiometers as well as routes of signals. All potentiometers and switches are grouped according to their belonging to the respective subsystems. Therefore, the operation of the AETB test board will be convenient and intuitive. The outline of the front panel is shown in Figs. 11 and 12. In the front panel of the housing a banana and BNC connectors are placed to give a possibility of connections of any external sinks of data acquisition to visualize all outputs of the RSG and outputs of the particular part of the entire system, see Fig. 12.

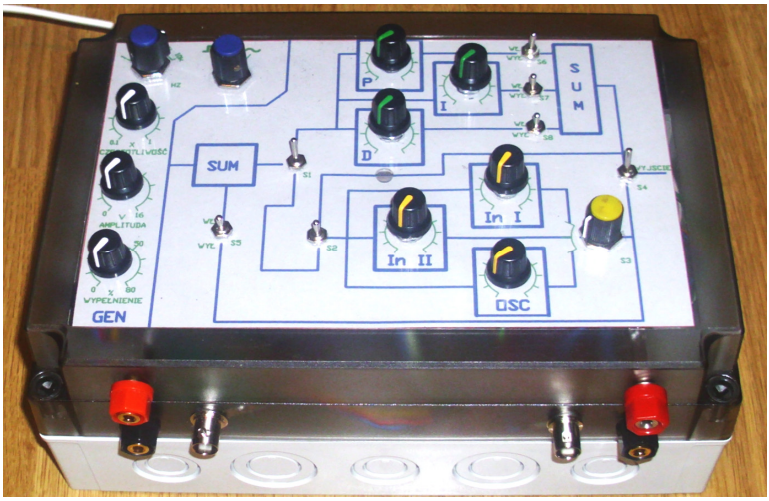

Fig. 12. Final view of the analog electronic test board (AETB) for testing selected basic elements of automation

In the module shown in Fig. 12, because of the greater number of components, and a large number of connections between the components it was necessary to make the bilayer PCB plate. Paths are routed on the underside of the plate (bottom layer) and the component side (top layer). The electronic components as far as possible have been positioned on the plate within the range of the functional blocks described in previous sections. The elements of each member are arranged close to each other. In this part of the device there is a large number of switches and potentiometers which are mounted on the housing. There are placed on the PCB connectors, which by means of wires are connected to the switches being placed at the edges of the PCB plate, so one could easily distribute cables.

At each chip, close to the powered legs some decoupling capacitors have been placed with a value of 100 nF. On this plate capacitors C_{101}–C_{106} fulfill this role. Power paths are wider than the signal paths to reduce their resistance, and hence, reduce the voltage drop.

4.2 Measurements

On the AETB test board, one can get miscellaneous waveforms depending on the settings of switches directing the signals and the corresponding potentiometers governing parameters of the electronic components. This section presents exemplary waveforms of signals measured at the outputs of almost all basic components and their configurations realized on the test board.

In Fig. 13a, there is shown a P-action's output. A gain of the corresponding system can be calculated: $U_{out}/U_{in} = R_{P130}/R_{130} = 100\ k\Omega/33\ k\Omega \approx 3$. After setting the potentiometer P_{130} at maximum position one gets three times the maximum input gain. Proportional basic element works properly. Gain can be adjusted continuously

by changing the setting of the potentiometer P_{130}, which, together with a resistor divider R_{130} appropriately shapes the component's gain. The measurement results coincide with the results of the simulation carried out in Section 3, see Fig. 8.

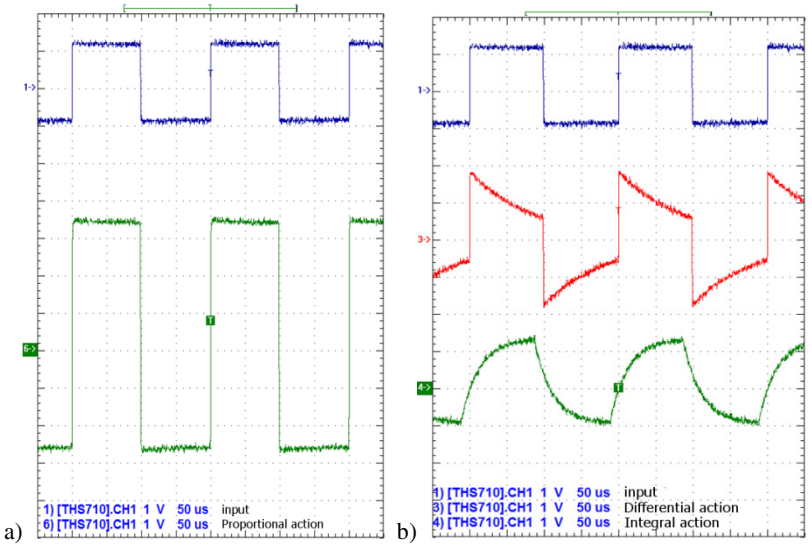

Fig. 13. An oscilloscope screenshot of the step responses: a) Proportional, b) Differential and Integral for $V_{in} = 2$ V and $f = 5$ kHz

First-order LPF (I-action) is realized on an operational amplifier as described in previous sections, where: $U_{we}(s) = RI$, $U_{wy} = I/(Cs)$. Therefore, the transfer function $G_I(s) = 1/(RCs)$. According to that, the electronic component realizes an Integral action gained by $k = 1/RC$. The time constant T for such real system reaches half of the scale of the P_{110} potentiometer: $T = RC = 50\ \text{k}\Omega \times 1\ \text{nF} = 50{\cdot}10^{-6}$ sec.

Differentiation (D-action) is realized on an operational amplifier as described in previous sections, where: $U_{we}(s) = I/Cs$, $U_{wy}(s) = RI$. Therefore, the transfer function $G_D(s) = RCs$. According to that, the electronic component realizes a Differentiation gained by $k = RC$. The time constant T for such real system reaches half of the scale of the P_{120} potentiometer: $T = RC = 25\ \text{k}\Omega \times 10\ \text{nF} = 250{\cdot}10^{-6}$ sec.

On the basis of two oscilloscope screenshots from Fig. 13b, one may note that both the Differentiation and Integral basic elements work properly. For instance, the real waveform's shape of I-action coincide with the simulation result for higher input voltage presented in Fig. 9b.

Transfer function of a first-order component is given by: $G_1(s) = 1/(1+Ts)$, where $T = RC$ is the time constant. For the real resistance (half of the P_{160} potentiometer's scale) and capacitance constants: $T = 11\ \text{k}\Omega{\cdot}10\ \text{nF} = 110{\cdot}10^{-6}$ sec. Therefore, the transfer function: $G_1(s) = 1/(1+110{\cdot}10^{-6}s)$.

Transfer function of a second-order component is given by: $G_2(s) = 1/((T_1s+1)(T_2s+1))$, where: $T_1 = R_1C_1$, $T_2 = R_2C_2$ are the time constants. For the selected real resistance and capacitance values: $T_1 = 1\ \text{k}\Omega \times 10\ \text{nF} = 10 \cdot 10^{-6}$ sec., $T_2 = 1\ \text{k}\Omega \times 47\ \text{nF} = 47 \cdot 10^{-6}$ sec. Step responses of the first- and second-order components are presented in Fig. 14.

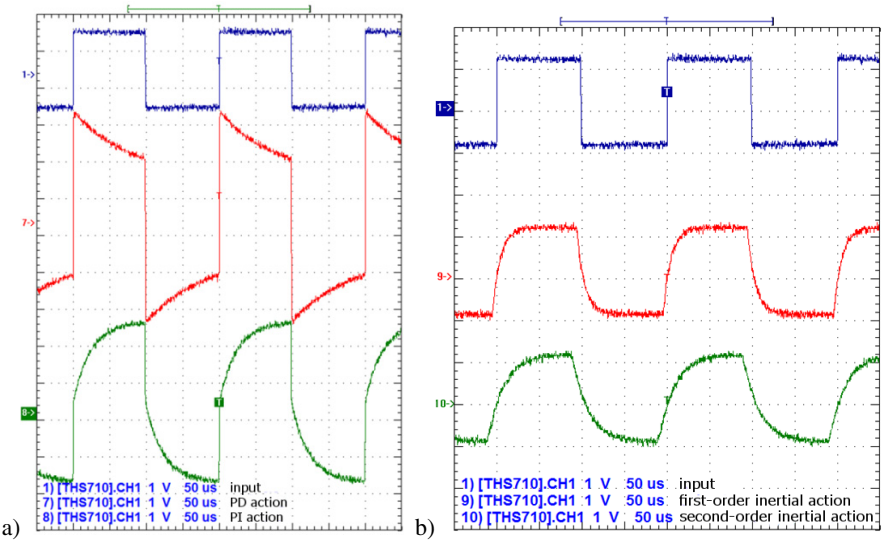

Fig. 14. An oscilloscope screenshot of the step responses: a) PD- and PI-action, b) first- and second-order components

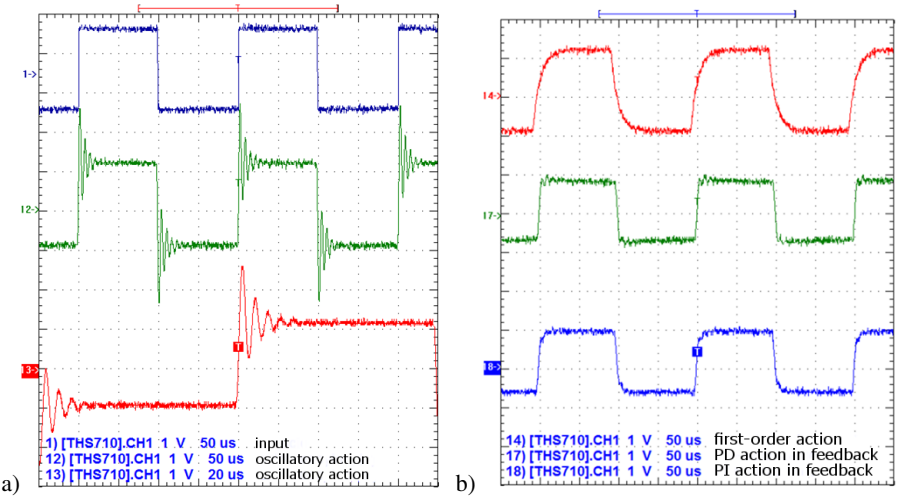

Fig. 15. An oscilloscope screenshot of the step responses: a) second-order oscillatory action, b) a first-order component as the plant subject to the PD- and PI-action in a closed-loop control system with negative feedback

On the oscilloscope screenshots we noticed some noise. It may be formed in the operational amplifiers and in other elements of the system. Offset voltage at the input of the operational amplifier and temperature drift cause greater noise at low output voltages. Also some variations of parameters of particular resistors and capacitors may cause some interference on the measurement outputs.

5 Conclusions

Test signals have been formed to study time responses of simple open- and closed-loop control systems. In the practical part, the analog electronic test board (AETB) for testing basic elements of automation was designed and successfully manufactured. The device has been divided into functional blocks such as power supply, signal generator and a system containing basic elements of automation. Parameters of both the generator and the basic elements are tunable. One could expect, that using other electronic components of better quality the observed time responses could reach higher accuracy, smaller noise and better stability too. Numerical simulations allowed to choose proper values of the electronic components included in the electronic system. Based on a comparison of output signals, the analog electronic test board could be useful in an assessment of parameters of various time characteristics acquired by electronic devices or even some transient behavior in various electronic circuits. From an educational point of view, the AETB test board may support students in learning of basics of automation.

Acknowledgements. The authors have been supported by the National Center of Science under the grant MAESTRO 2, No. 2012/04/A/ ST8/00738 for years 2012-2015 (Poland).

References

1. Veloni, A., Palamides, A.: Control System Problems. Formulas, Solutions, and Simulation Tools. Taylor & Francis Group, London (2012)
2. Chong, G., Li, Y.: PID control system analysis, design, and technology. IEEE Transactions on Control System Technology, 559–576 (2005)
3. Franklin, G.F., Powell, J.D., Emami-Naeini, A.: Feedback Control of Dynamic Systems, 3rd edn. Addison-Wesley Longman Publishing, Boston (1994)
4. Goodwin, G.C., Greabe, S.F., Salgado, M.E.: Control System Design. Prentice Hall (2001)
5. Gayakwad Ramakant, A.: Op-amps and Linear Integrated Circuits. Prentice Hall, Upper Saddle River (2000)
6. Grob, B., Schultz, M.E.: Basic Electronics. Glencoe/McGraw-Hill (2003)
7. Paynter, R.: Introductory Electronic Devices and Circuits. Prentice Hall, Upper Saddle River (2003)
8. Bischoff, H., Hofmann, D., Terzi, E.V.: Process Control System, Control of temperature, flow and filling level. Festo Didactic (1997)

Improved Control System of PM Machine with Extended Field Control Capability for EV Drive

Piotr Paplicki and Rafał Piotuch

West Pomeranian University of Technology, Szczecin, Poland
Department of Power Engineering and Electrical Drives
{paplicki,rpiotuch}@zut.edu.pl

Abstract. The paper presents novel concept of prototyping, analysis and optimization of an Electric Controlled Permanent Magnet Excited Synchronous Machine (ECPMSM) drive with a field weakening capability for electric vehicle (EV). Operation modes, features, characteristics, FEA and analytical results, improved control system of the machine, and schematic diagram of EV central drive system with ECPMSM machine were also presented.

Keywords: electric vehicles, PM machines, hybrid excitation, field weakening, control system, prototyping, optimization.

1 Introduction

Environmental as well as economic issues provide an impetus to develop clean, efficient, low-emission hybrid (HEV) and zero-emission electric vehicles (EV). Nowadays, the development of EV propulsion systems equipped with electric motor, transmission device and wheels, has been caused by rapid growth in power electronics, digital signal processors, control algorithms, and advances in material technologies [1].

Major requirements for EV motor as one of the most important element of EV drive system, can be summarized as follows: high power density, high torque at low speeds, very wide speed range including constant-torque and constant-power regions and high efficiency over wide speed and torque ranges. Moreover, important characteristics of electrical machines include flexible drive control, fault tolerant, and low acoustic noise. Additionally, motor drive must be capable of handling voltage fluctuations from the source and comply with the other requirements as: ruggedness, high torque-to-inertia ratio*;* peak torque capability of about 300 % of continuous torque rating, low electromagnetic interference and low cost.

The majority of EVs developed so far are based on DC machines, permanent magnet (PM) machines and induction machines (IM). In order to minimize their size and weight they are designed for high-speed operation for a given power rating. At present, IM machines are widely accepted and most commonly used for EV propulsion system because they are highly reliable and free from maintenance but they have relatively low power density [2, 3]. Therefore, the PM machines with excellent performance become more popular and suitable for EV drives among other machine types.

J. Awrejcewicz et al. (eds.), *Mechatronics: Ideas for Industrial Applications*,
Advances in Intelligent Systems and Computing 317, DOI: 10.1007/978-3-319-10990-9_12

There are many studies regarding PM brushless machines usage for EV drive including PM hybrid excited motors, where the air-gap magnetic field is developed by the combination of PM and additional winding [1, 2, 4–6].

There are many ways to achieve excellent efficiency of the energy conversion in the lower speed range of the PM machines [7]. One of these is oversizing PMs that they excite an increased no-load flux density and required torque values are achieved by smaller stator currents values. This advantage is inherently connected with challenges in the high speed regions, where due to the limited battery voltage values a force creating current cannot be driven into the machine windings [8].

In order to obtain required wide speed range, an optimal PM machine design for EV should offer a field weakening capability of at least 1:4. A common technique for the field weakening is based on a shift in the stator currents in such a way, that a part of current-caused field counteracts (weakens) the PM-excitation field. This requires an unfavorable oversizing of the machine and current converter [3, 4]. The technique is also commonly used in PM machines with embedded magnets [8].

This paper focuses on an Electric Controlled Permanent Magnet Excited Synchronous Machine (ECPMSM) as hybrid topology which has already been analyzed in details by the authors [2, 9–12] and others in [1, 5, 13] with Field Oriented Control (FOC) for EV applications.

2 Operation Modes of the ECPMSM Machine

The electric motor for EV drive is designed to operate at high speeds to minimize the size of the machine. Hence, gearbox is used to match high speed of the electric motor with lower speed of the wheels. Moreover, motors with extended constant power region and wide-operating speed range minimize the gearbox size, eliminate multiple gear ratios and clutch in EVs. This way, a single gear transmission in the range of 10 to 15:1 is sufficient to provide required driveshaft torque value.

Conventional electric motors have three major segments in its torque-speed characteristic: constant torque region (1), constant power region (2), and natural mode region (3) shown in Fig. 1a.

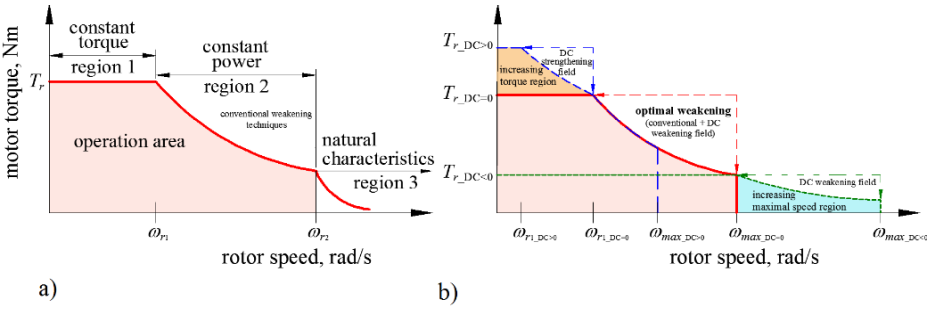

Fig. 1. Electric motor torque-speed curve: conventional motor (a), ECPMSM machine (b)

The motor delivers rated torque T_r up to the base speed ω_{r1} or up to the rated speed ω_{r2} of the motor when it reaches its power supply voltage limits. The motor operates in a constant power mode above the rated speed, where torque falls steadily at a rate that is inversely proportional to speed. Electric motors can operate at speeds higher than rated speed using field weakening techniques. There is a third natural mode region for high motor speeds, where the torque falls rapidly, being inversely proportional to the square of the speed. The natural characteristic region is an important part of the overall torque-speed curve of certain motors used in EVs. Moreover, extended constant power range capability is also extremely important to eliminate the use of multiple gear ratios and to reduce the power supply volt-ampere rating.

Hence, in order to extend the operating range of the motor and control its torque-speed characteristic the hybrid PM machines with field weakening and strengthening capability are used.

Fig. 1b shows extended torque $T_{r\_DC>0}$ and speed region of ECPMSM machine which can be operated in the field-weakening mode, similar to the DC motor, to extend the constant power range and achieve higher speeds $\omega_{max\_DC<0}$.

In order to realize field excitation control to increase or decrease the magnetization level of the ECPMSM machine an auxiliary direct current (DC) control coil is mounted in the stator of the machine. Fig. 2 (left) shows unique machine with a 12-pole double inner rotor topology and two sheeted stator cores. The machine offers broader speed range and higher overall efficiency but more complex construction and lower power density.

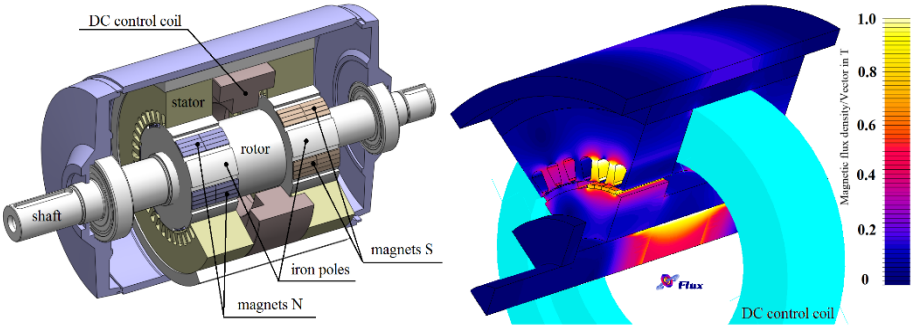

Fig. 2. The **ECPMSM** cross section with DC control coil (left); 3-D FE analysis model (right)

The ECPMSM machine design takes into account not only mechanical aspects of the machine but mainly electromagnetic considerations. The size of the motor depends on the maximum torque required on the machine shaft. During this study the maximum torque up to 100 Nm and rated speed of the motor equal to 5000 rpm have been assumed. Equation torque (1) for the ECPMSM machine shows that if a d-axis stator current i_d is constant ($i_d = 0$), generated torque is proportional to the q-axis current i_q and magnetic flux linkage Φ_d which is not constant compared to conventional PM machines. Torque and magnetic fluxes of the ECPMSM machine can be described by the following equations:

$$T = \frac{3}{2} p\left(\Phi_d i_q - \Phi_q i_d\right) \tag{1}$$

$$\Phi_d = \left(\Phi_{PM} + \Phi_{IP}\right)/2 \tag{2}$$

$$\Phi_q = L_{q,q} I_q \tag{3}$$

$$\Phi_{PM} = \Phi_{PM,PM} + \Phi_{PM,I} \tag{4}$$

$$\Phi_{IP} = \Phi_{IP,PM} + \Phi_{IP,I} \tag{5}$$

$$\Phi_{PM,I} = L_{PM,d} I_d + L_{PM,q} I_q + M_{PM,DC} I_{DC} \tag{6}$$

$$\Phi_{IP,I} = L_{IP,d} I_d + L_{IP,q} I_q + M_{IP,DC} I_{DC} \tag{7}$$

where: T – torque, p – number of pole pairs, $i_{d,q}$ – d, q-axis currents, Φ_z – z linked magnetic flux, $\Phi_{x,I}$ – x linked magnetic flux caused by current, $L_{X,Y}$ – X flux Y-current inductance, $M_{x,\mathrm{DC}}$ – x flux DC current inductance, and: z = d, q, PM or IP; $x = IP$ or PM; $X = IP$, PM, d or q; $Y = d$, q or DC.

Due to the complex electromagnetic behavior of the machine, calculation of the flux linkage characteristics is very difficult. Therefore, the linkage flux versus stator currents characteristic should be obtained by simulation or test results. In this study, the machine design have been supported by finite element analysis (FEA) and various computer-aided design tools as Flux-3D, GOT-It optimization tool, and MATLAB, making the design process highly efficient.

Calculation of the magnetic field distribution within the ECPMSM machine has been performed using the 3D-calculation code via FLUX-3D (Finite Element Electromagnetism module), and it has been shown in Fig. 2 (right).

Fig. 3 shows torque versus excitation field current I_{DC} characteristics (left) and linked flux waveform versus rotor position for different I_{DC} current values (right).

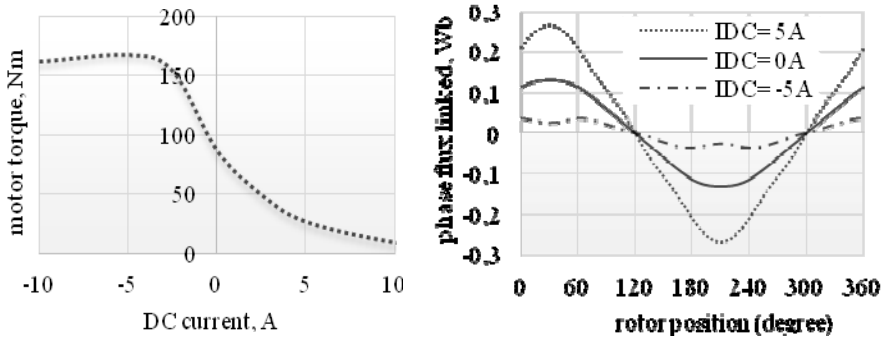

Fig. 3. 3-D FEA results of the ECPMSM machine torque versus excitation field current I_{DC} (left); FEA results of linked flux waveform versus rotor position for different excitation field current I_{DC} (right)

The equations and FEA results have been utilized to develop a prototyping and optimization system for EV drive design with ECPMSM machine. Figure 4 shows a Finite Element Modeling (FE-modeling), solving and post processing FEA block coupled with analytical block to calculate set of efficiency maps (Fig. 5), and maximum efficiency paths (Fig. 6) of the machine and EV performance evaluator. This designing procedure allows to determine optimal I_{DC} values for different torque T set and angular speed ω values to efficiently control the ECPMSM machine according to selected drive mode.

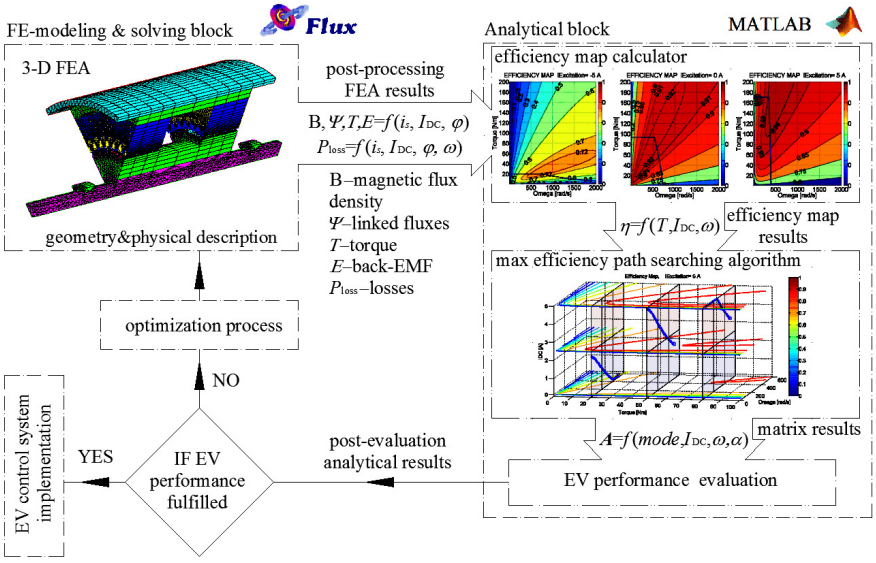

Fig. 4. Prototyping and optimizing EV drive design with **ECPMSM** machine

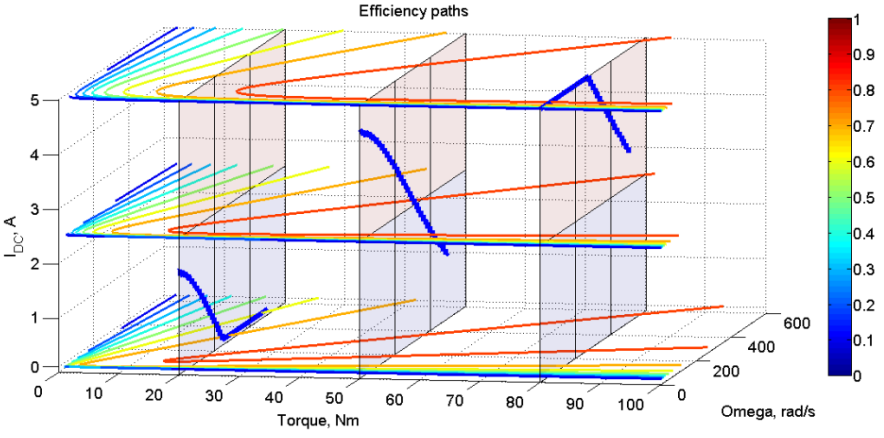

Fig. 5. Optimal maximal efficiency paths (blue lines) for three different sets torque values

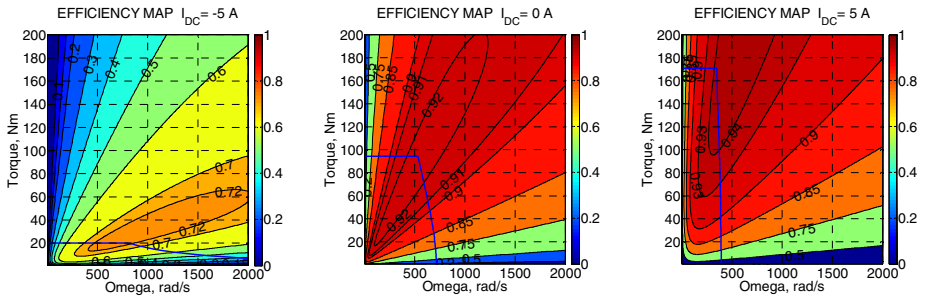

Fig. 6. Selected efficiency maps used in control algorithm regarding torque envelope

3 Vector-Controlled ECPMSM Drive

ECPMSM drive is a modern and powerful technology among various brushless motor drives. In order to achieve improved dynamic and static performance of ECPMSM drive for EV propulsion, vector control is preferred. Considering sensorless control methods problems, high precision position information of the rotor machine is also needed.

Fig. 7 shows the concept of vector control of the ECPMSM machine for EV drive. Proposed control scheme is able to control motor torque and field component current in such a way that total losses are minimized at any loading conditions.

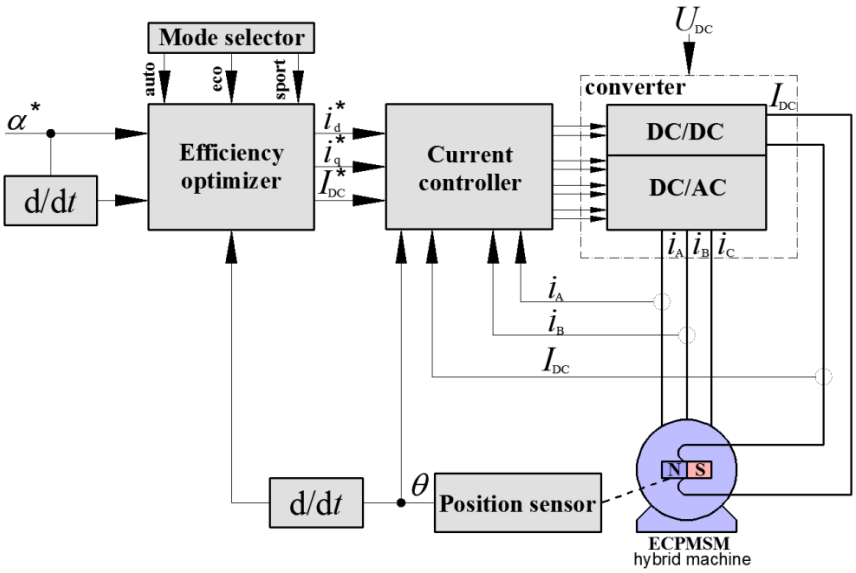

Fig. 7. Vector control of the ECPMSM machine for EV drive system

Although, FOC may offer wide speed range up to 4 times of base speed, but efficiency at high-speed range drops significantly. In order to increase the speed range

and improve the efficiency of the ECPMSM machine, i_d and i_q and I_{DC} currents can be controlled in the proper manner to improve torque-speed curve and maximize drive efficiency.

4 EV Drive Components with ECPMSM Machine

The essential components of the concept of EV drive system with the ECPMSM machine are also controller, power source, and transmission. The idea of the EV drive system are shown in Fig. 8.

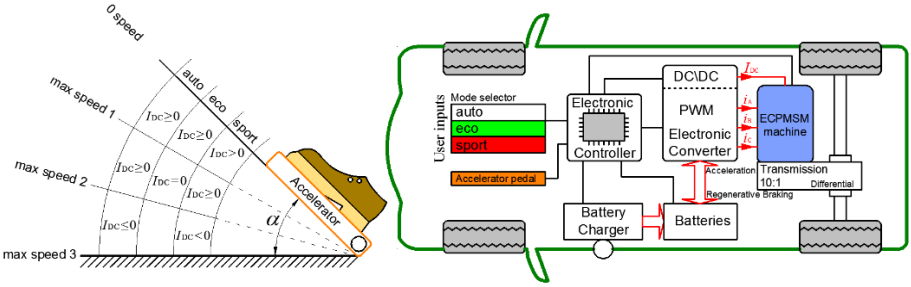

Fig. 8. The idea of the EV central drive system with ECPMSM machine with extended field control capability

It should be noted that the control algorithm considers the accelerator position α and its dynamics. The control drive system should be user-friendly to provide required EV performance, therefore authors proposed three drive modes – auto, eco and sport. Eco mode allows long-distance performance because control systems selects $I_{DC} \geq 0$ value to provide maximum efficiency and field-weakening method is never used. Sport mode is preferred to provide maximum torque without speed limitations – this mode uses field-weakening $I_{DC} < 0$ control method to extend EV speed. The Auto mode automatically switches between previous two, according to accelerator position handling dynamics.

5 Summary

The paper presents the concept for the application of ECPMSM machine in EV drive system regarding extended control algorithm aspects. It is possible to follow a maximum efficiency paths for selected torque values in different drive modes. Total EV may be evaluated considering only proper simulation models applied in FLUX and MATLAB computing tools. The proposed control algorithm for unique PMSM with hybrid excitation provides high efficiency thanks to reduced losses and extended high-speed features, thanks to field weakening. Such solution gives possible highest EV range and also increases acceleration capabilities for low speeds regions and, at the same time, increases highway-cycle characteristics.

References

1. Aydin, M., Surong, H., Lipo, T.A.: Design, Analysis, and Control of a Hybrid Field-Controlled Axial-Flux Permanent-Magnet Motor. IEEE Trans. Ind. Electron. 57(1), 78–87 (2010), doi:10.1109/TIE.2009.2028294
2. Paplicki, P.: The new generation of electrical machines applied in hybrid drive car. Electrical Review 86(6), 101–103 (2010)
3. Wang, J., Yuan, X., Atallah, K.: Design Optimization of a Surface-Mounted Permanent-Magnet Motor With Concentrated Windings for Electric Vehicle Applications. IEEE Transactions on Vehicular Technology 62(3), 1053–1064 (2013), doi:10.1109/TVT.2012.2227867
4. Ki-Chan, K.: A Novel Magnetic Flux Weakening Method of Permanent Magnet Synchronous Motor for Electric Vehicles. IEEE Trans. Magn. 48(11), 4042–4045 (2012), doi:10.1109/TMAG.2012.2198444
5. Kosaka, T., Sridharbabu, M., et al.: Design studies on hybrid excitation motor for main spindle drive in machine tools. IEEE Trans. Ind. Electron. 57(11), 3807–3813 (2010), doi:10.1109/ICELMACH.2008.4800144
6. Chaithongsuk, S., Nahid-Mobarakeh, B., Caron, J., Takorabet, N., Meibody-Tabar, F.: Optimal Design of Permanent Magnet Motors to Improve Field-Weakening Performances in Variable Speed Drives. IEEE Trans. Ind. Electron. 59(6), 2484–2494 (2012), doi:10.1109/TIE.2011.2164770
7. May, H., Palka, R., Paplicki, P., Szkolny, S., Wardach, M.: Comparative research of different structures of a permanent-magnet excited synchronous machine for electric vehicles. Electrical Review 88(12a), 53–55 (2012)
8. Duan, S., Zhou, L., Wang, J.: Flux Weakening Mechanism of Interior Permanent Magnet Synchronous Machines With Segmented Permanent Magnets. IEEE Transactions on Applied Super-conductivity 24(3) (2014), doi:10.1109/TASC.2013.2280847
9. Di Barba, P., Mognaschi, M.E., Palka, R., Paplicki, P., Szkolny, S.: Design optimization of a permanent-magnet excited synchronous machine for electrical automobiles. JAEM 39(1-4), 889–895 (2012), doi:10.3233/JAE-2012-1556
10. Putek, P., Paplicki, P., Slodička, M., Pałka, R.: Minimization of cogging torque in permanent magnet machines using the topological gradient and adjoint sensitivity in multi-objective design. JAEM 39(1-4), 933–940 (2012), doi:10.3233/JAE-2012-1562
11. Putek, P., Paplicki, P., Palka, R.: Low cogging torque design of Permanent Magnet machine using modified multi-level set method with total variation regularization. IEEE Trans. Magn. 50(2), 657–660 (2014), doi:10.1109/TMAG.2013.2286297
12. Putek, P., Paplicki, P., Slodička, M., et al.: Application of topological gradient and continuum sensitivity analysis to the multi-objective design optimization of a permanent-magnet excited synchronous machine. Electrical Review 88(7a), 256–260 (2012)
13. Hemmati, S., Lipo, T.A.: Field weakening of a surface mounted permanent magnet motor by winding switching. In: 2012 International Symposium on Power Electronics, Electrical Drives, Automation and Motion (SPEEDAM), June 20–22, pp. 736–740 (2012), doi:10.1109/SPEEDAM.2012.6264472

The Positioning of Systems Powered by McKibben Type Muscles

Wiktor Parandyk, Michał Ludwicki, Bartłomiej Zagrodny, and Jan Awrejcewicz

Lodz University of Technology, Lodz, Poland
Department of Automation, Biomechanics and Mechatronics
parandyk.wiktor@gmail.com

Abstract. In this paper a continuous control of the mechanical system positioning, powered by a pneumatic actuators (McKibben type muscles) is presented. The control system consists of appropriate sensors which allows to monitor the values of the characteristic parameters, i.e. displacement and pressure. Moreover, throttle valve controlled by stepper motor is used as regulated elements. Measured signals (displacement of the actuator and the load, calculated indirectly) provide feedback loop to the control system which operate the throttle valves. Proposed system, build of one valve (actuated by stepper motor), McKibben muscle, air compressor and electronic compartments allows for continuous control of the air flow, variable speed of shortening or stretching of artificial muscle and its smooth stop at the desired (set) position. Data acquisition system, used for measuring the characteristic parameters and for valve operation support is realized by an universal measurement and control multimodule in addition to the LabVIEW software package.

Keywords: muscle McKibben type, positioning, continuous control.

1 Introduction

Presented experimental set-up is dedicated to test the possibility of positioning pneumatic McKibben type actuators using throttle valves and position feedback. In this case we propose indirect control of the muscle position which is a resultant value of the valve opening level. In the other words the control is conducted on the compressed air flow ratio at the actuator inlet.

The FPA (flexible pneumatic actuators [1, 2]) group was developed to face the biocompatibility problem. First of all a flexible structure of each actuator located in the FPA group allows for a various form of application. In contrast to the classic linear, pneumatic cylinder in rigid housing there are no limitations due to the mounting space. Focusing on the McKibben type artificial muscle, it is convenient for it to work in horizontal/vertical orientation or to work bent even 90 degrees. The universal configuration character and flexibility cause that described actuators are finding increasing use as an alternative drive solution for robotics (see [3, 4]), automatic control systems and industry.

J. Awrejcewicz et al. (eds.), *Mechatronics: Ideas for Industrial Applications*,
Advances in Intelligent Systems and Computing 317, DOI: 10.1007/978-3-319-10990-9_13

The operating principle of the pneumatic McKibben type drive, presented in the Fig. 1, is based on the fusion of elastic properties of the inner rubber-type core with the longitudinal stiffness of the polyester cross-braid outermost layer. The increasing air pressure causes stretching of the rubber core, as a result braid fibers move relatively to each other allowing the radial displacement and muscle shortening.

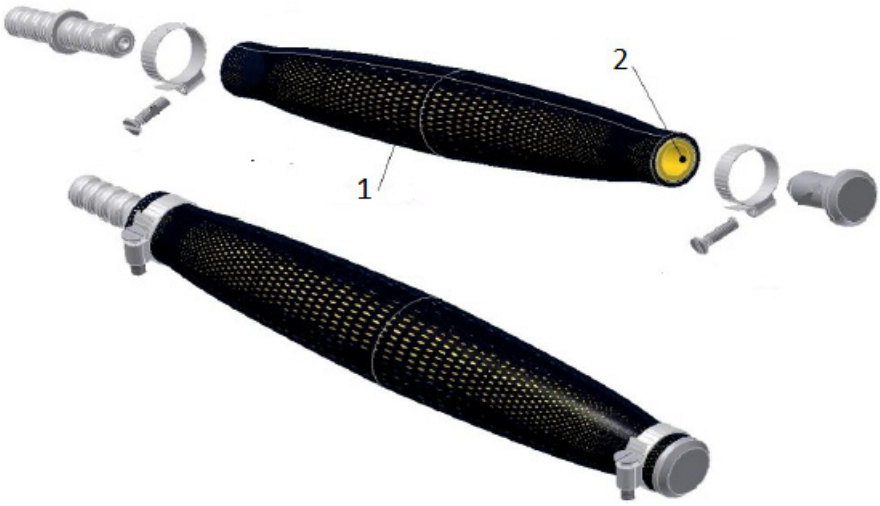

Fig. 1. Pneumatic McKibben type actuator: 1 – polyester cross-braid, 2 – rubber-type core

Because of a strong nonlinear character of artificial muscles (see for example [5]) connected with a rubber-type material properties and the friction occurrence between both the core and the braid, the displacement function of the actuator is dependent on two variables – the pressure and the load. Due to mentioned difficulties and necessity of using various types of sensors, the most convenient way of the control is a proportional regulator (see the work [6] and [7]) with the displacement feedback usage (the control system scheme is presented on the Fig. 2).

2 Experimental Set-Up

The experimental set-up (Fig. 2 and Fig. 3) consists of the McKibben type actuator connected to the linear bearing guided, load handle, mounted on the rigid frame. The control hardware is dedicated to cooperate with National Instruments DAQ module with a LabVIEW software. The indirect control of the actuator position is carried by the air flow ratio driven by a throttle valve coupled with a stepper motor (Fig. 4). Namely, the control is conducted on the compressed air flow ratio at the actuator inlet. The position feedback signal is measured by a linear displacement sensor connected to an analog input of the DAQ module. The regulator structure was developed as a part of the LabVIEW control program.

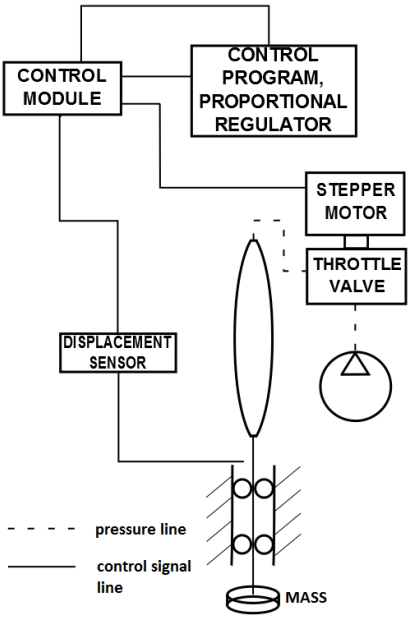

Fig. 2. The control system schematic structure

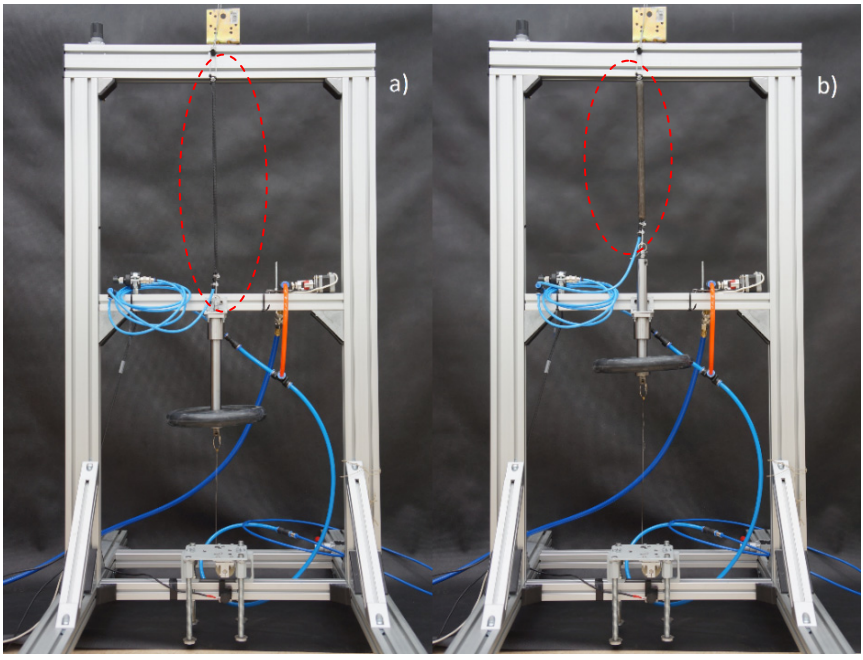

Fig. 3. The experimental set-up structure: a) unpowered actuator, b) fully contracted, loaded actuator

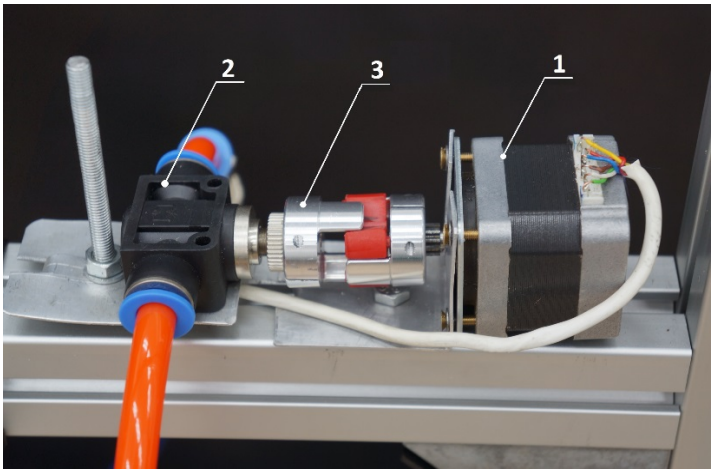

Fig. 4. Air flow control components: 1 – stepper motor, 2 – throttle valve, 3 – sliding clutch

3 Measurement and Control Software

In this project, the measurement of actual pneumatic actuator length and control of the valves' stepper motor are performed by *National Instruments USB-6009 multifunction IO module*, with all necessary AD and DA converters and digital port connected to a dedicated stepper motor controller (Fig. 5). The control algorithm as well as the communication with the IO module are developed in *National Instruments LabVIEW 2012 Developement System*. It is a good, easy to use and complete solution for this type of experiments.

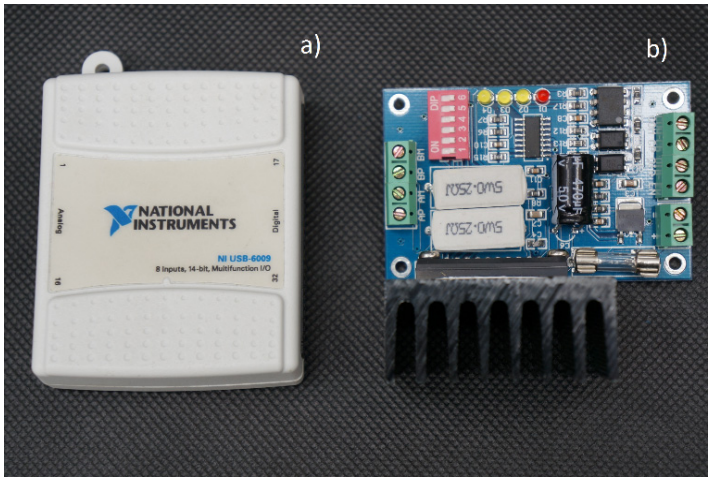

Fig. 5. The experimental set-up components: a) USB-6009 multifunction IO module, b) stepper motor controller

In the Fig. 6, complete LabVIEW control algorithm is showed. Length sensor of the actuator gives proportional, linear but noisy voltage signal (big blue analog input block on the left). This is a typical problem in AD signal acquisition. That is why standard Butterworth filter was used, to smoothen measured position value. It was necessary to make it valuable for the PID control algorithm. PID block calculates the error between real actuators length and the set one. Obtained correction value is re-scaled to the stepper motor position, expressed in number of steps. The condition block on the right, sets proper direction of the motor, depending of the error sign and starts the motor if PID-calculated number of steps are far (with some tolerance) from the actual ones. As mentioned before, in this work, only proportional P control was used.

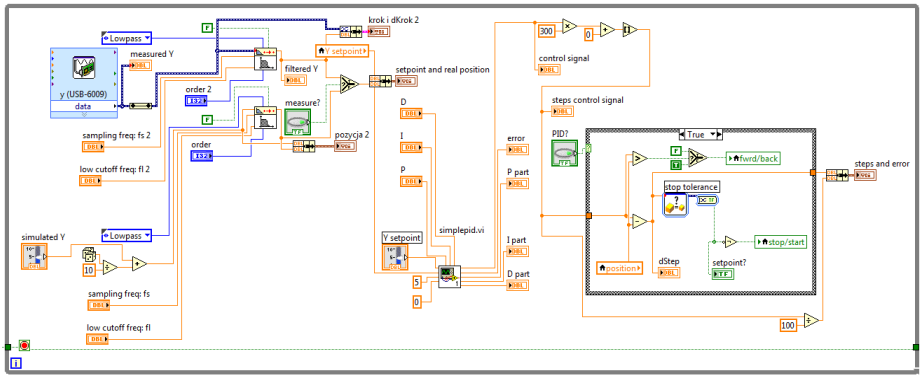

Fig. 6. Main measurement and control algorithm in LabVIEW

The stepper motor, which rotates the valve, is also controlled by the IO module and proper LabVIEW loop. Fig. 7 depicts stepper motor control loop, with ½ step division feature. Consecutive combinations of motor coils voltage supply are sent to the IO module throw the digital byte output.

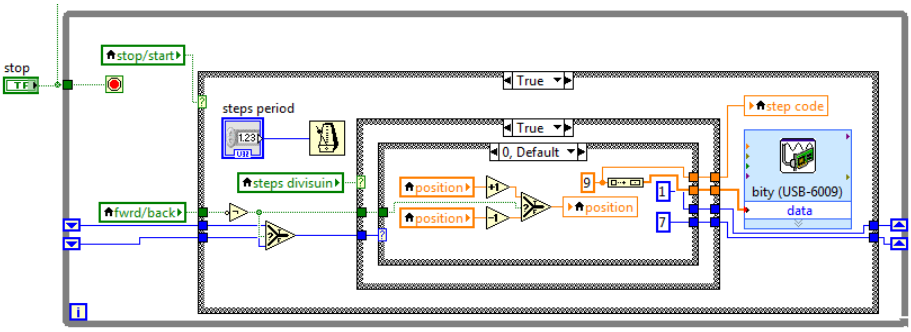

Fig. 7. Stepper motor control algorithm

In Fig. 8, graphical user interface (GUI) of developed software is showed. User can chose the value of constant speed of the motor, change each PID parameters and set desired actuators length set point. The plot presents actual actuators length, set point position and motor steps number, all vs. time. Among others, the control value of each PID parts is showed, the error, actual actuators length etc. The clock in bottom-left corner of the window shows actual motor angle of rotation, expressed in motor steps, proportional to the level of the valve opening.

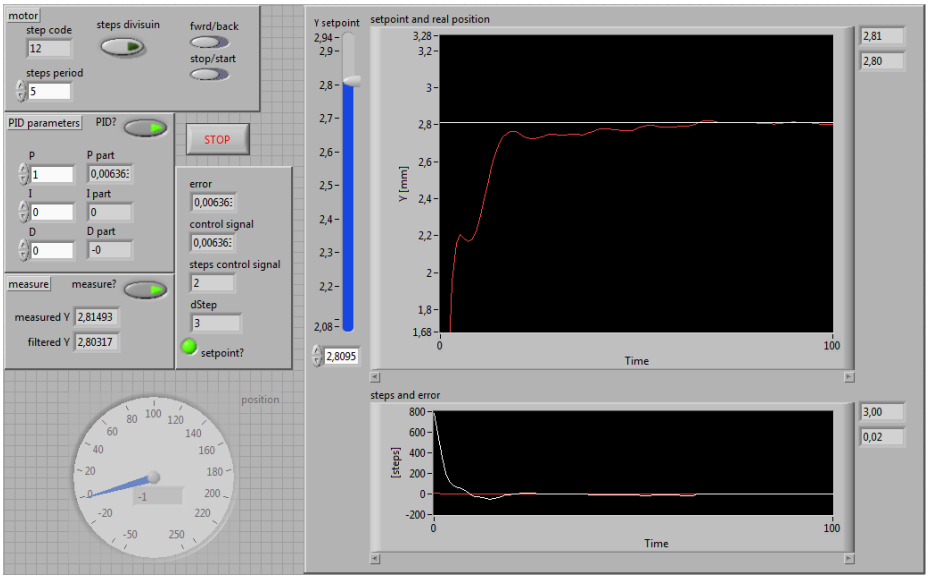

Fig. 8. LabVIEW measurement and control interface

4 Experimental Results

Each test of the experiment consisted of closing the throttle valve, homing the actuator (by lowering the pressure inside), setting the set point to half length of the actuator and starting control program. After reaching final set point with an error of minimum 0.0001 values, measurement data were saved. This procedure was repeated for different PID proportional parameter (0.5, 1.0 and 1.5) and different load (no added load, 2.5 kg, and 5.0 kg) attached to the actuators length, 5 times each.

Performed experiments showed good repeatability of the positioning sequence. Below in Figures 9–11, position control Y and its error vs. time is showed. Position of the muscle is normalized, for easier comparison.

Fig. 9 shows, that if there is no load, reaching set position (marked with black circle) is fastest for the high P value (more than 1.0) while P equals 0.5 and 1.0 gives similar times but longer than for lower P.

In Fig. 10, it can be noticed that increasing the load mass slows the position reaching. It also appears, that the best proportional coefficient is for P equals one, while other settings makes the positioning slower.

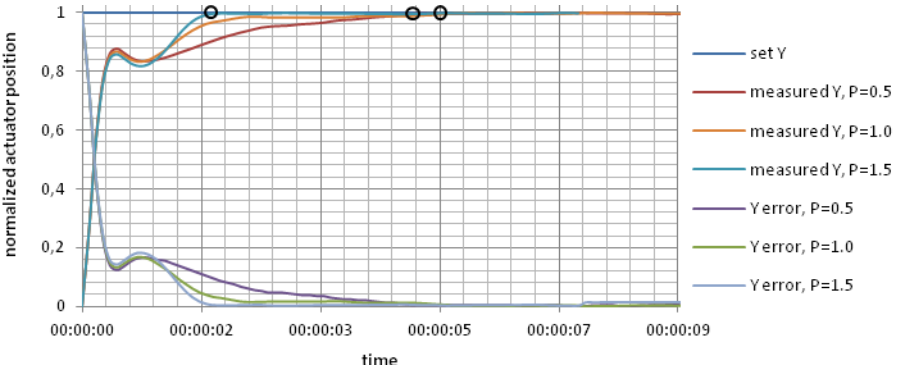

Fig. 9. Controlled position and control error vs. time for actuator with no added load

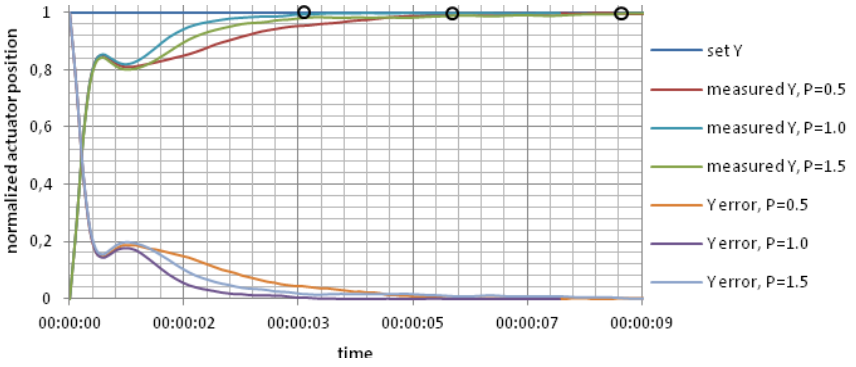

Fig. 10. Controlled position and control error vs. time for actuator with 2.5 kg load

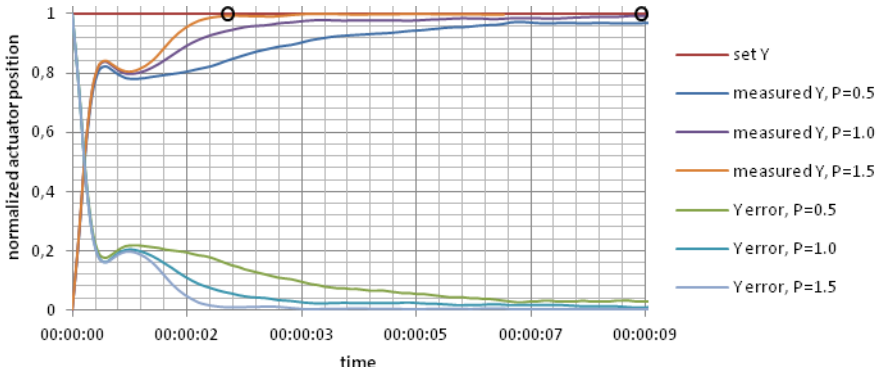

Fig. 11. Controlled position and control error vs. time for actuator with 5.0 kg load

Adding next 2.5 kg to the load makes the setting time longer but only for P value lower than 1.5. Bigger P (equals 1.5) makes the positioning much faster than for lower loads.

5 Summary

In this project, attempt of PID control algorithm of pneumatic McKibben type actuators contraction was developed. It is an extension of some earlier work [8], where the manual on-off control was used. As proved in previous sections, it is possible to automatically manipulate the air valve opening level, only measuring the actual length of the actuator as the feedback signal. This solution is probably not optimal one but valuable, especially for slow muscle movements, in one direction only, with no position overshooting.

As for the future, it is important to determine proper, optimized PID parameters, probably in function of load value. There is also necessity to add second throttle valve, to lower the air pressure after overshooting desired position. That would make a possibility of moving the pneumatic actuator in both directions and increase the positioning quality.

Acknowledgements. Project was supported by the participation of the students' scientific mechatronics group of Departure of Mechanical Engineering, Lodz University of Technology. Great gratitude for the assistance during the experimental set-up construction.

References

1. Dindorf, R.: The modeling of the pneumatic, artificial muscle systems, Department of Mechatronics, pp. 147–156. Kielce University of Technology, Kielce (2005) (in Polish, Modelowanie sztucznych układów mięśniowych aktuatorami pneumatycznymi)
2. Daerden, F., Lefeber, D.: Pneumatic Artificial Muscles: actuators for robotics and automation, Vrije Universiteit Brussel, Department of Mechanical Engineering, Brussels
3. Kawashima, K., Sasaki, T., Ohkubo, A., Miyata, T., Kagawa, T.: Application of Robot Arm Using Fiber Knitted Type Pneumatic Artificial Rubber Muscles, pp. 4937–4942. Tokyo Institute of Technology, Yokohama (2004), doi:10.1109/ROBOT.2004.1302500
4. Tondu, B., Ippolito, S., Guiochet, J.: A Seven-degrees-of-freedom Robot-arm Driven by Pneumatic Artificial Muscles for Humanoid Robots, pp. 257–274. Institut National de Sciences Appliquées, Touluse (2005), doi:10.1177/0278364905052437
5. Chou, C.-P., Hannaford, B.: Static and Dynamic Characteristics of McKibben Pneumatic Artificial Muscles, Department of Electrical Engineering, pp. 281–284. University of Washington, Seattle (1994), doi:10.1109/ROBOT.1994.350977
6. Li, Y., Heong Ang, K., Chong, G.C.Y.: PID control system analysis and design. IEEE Control Systems 26(1), 32–41 (2006), doi:10.1109/MCS.2006.1580152
7. Ko, B.-S., Edgar, T.F.: PID control performance assessment: The single loop case. AIChE Journal 50(6), 1211–1218 (2004)
8. Parandyk, W., Zagrodny, B., Awrejcewicz, J.: Selected problems of biocompatibility of the pneumatically controlled arm. Pomiary Automatyka Robotyka 17(1), 71–75 (2013)

Solenoid Actuator for a Camless Control System of the Piston Engine Valve

Eliza Tkacz, Zbigniew Kozanecki, and Jakub Łagodziński

Institute of Turbomachinery, Lodz University of Technology
90-924 Lodz, 219/223 Wolczanska St., Poland
{eliza.tkacz,zkozan,jakub.lagodzinski}@p.lodz.pl

Abstract. Simulation and experimental results of a camless valve control system for the piston engine are presented. The valve is designed to be used as a bleed valve for an additional energy recuperation system. The use of electromagnetic and not mechanical actuator follows from the need to close and open the valve on demand. The electromagnetic valve control allows for valve opening and closing independently of the engine cycle.

Keywords: camless, piston engine, engine valve, recuperation system.

1 Introduction

The paper presents results of numerical and experimental studies of a camless valve dedicated to the piston engine. It consists of an electromagnetic actuator, which can be used both to open and close the valve, without any spring or additional pneumatic system. The camless valve system was designed to improve the reliability of energy recuperation system in a car by ensuring the appropriate response speed (2 ms), the precise valve closing/opening time and the noise reduction. The final mock-up design is the result of numerical simulations. The results are summarized in this paper and consist of:

- Design, calculations and numerical simulations,
- Assembly of the mockup,
- Design and construction of the control and regulation system with its software,
- Tests to determine technical parameters of the actual mockup.

First, the preliminary shape of the ferromagnetic core was determined. Second, a feasibility study was made in order to examine if it is possible to integrate the actuator with the engine cylinder head and the valve stem. Once the mockup assembled, tests were carried out to verify the performance of the actuator by measuring parameters of current, as well as the dynamic displacement and static forces.

It has to be mentioned that the assembled mockup was not pressurized, even if pressures and loads were taken into account in the numerical simulations and the design. The behavior of the actuator under working conditions may be a subject of further studies.

J. Awrejcewicz et al. (eds.), *Mechatronics: Ideas for Industrial Applications*,
Advances in Intelligent Systems and Computing 317, DOI: 10.1007/978-3-319-10990-9_14

2 Mockup Design and Actuator Control

In the chosen design, the actuator consists of two electromagnets and a neodymium permanent magnet Fig. 1. Two electromagnets share their cylindrical axis, coincident with the valve axis, and they produce an electromagnetic field. The created electromagnetic force pushes the permanent magnet integrated with the valve stem, causing its opening and closing.

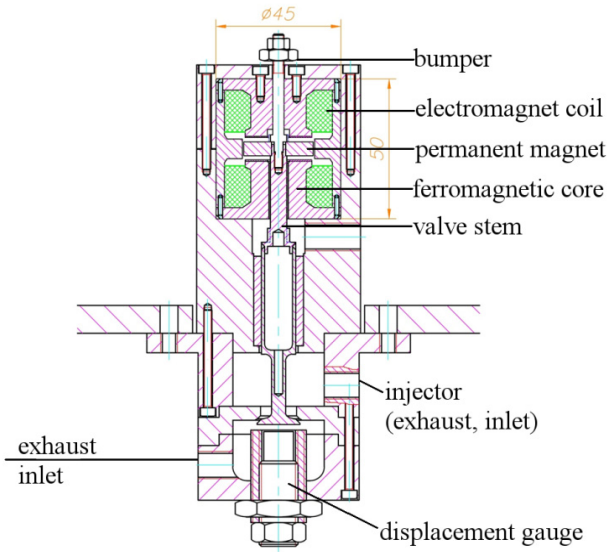

Fig. 1. Technical drawing of the mockup – a feasibility study

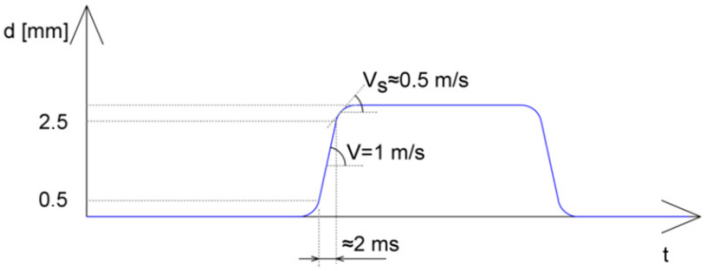

Fig. 2. Valve stroke versus time. Principle of the valve settlement in its seat under the decelerating force effect.

The principle of braking, the so-called “settlement” of the valve in its seat is shown in Fig. 2. The speed control will lengthen the lifetime of the mechanism and reduce the operating noise. General characteristics of the mockup are as follows:

- Moving mass: 44.6 g,
- Valve stroke: 3 mm,
- Voltage supply of the actuator: max. 12 V,
- Valve speed varies with the valve position according to Fig. 2,
- measured parameters: valve position (displacement), opening/closing speed (calculated as the first derivative of displacement), current.

2.1 Actuator Power and Control Design

The power supply and the control of the actuator are carried out with the Pulse Width Modulation (PWM). Its principle is to apply series of discrete voltage impulses of the well-chosen time duration. According to the chosen concept, one of the electromagnets pushes the valve and the second one slows it down (Fig. 3). Energized coil 1 opens the valve, while coil 2 closes it. The braking or the valve landing is achieved by powering the opposite coil which creates a force against the movement of the valve. For example, if coil 1 opens the valve, coil 2 is powered by the end of the valve stroke in order to slow the movement down.

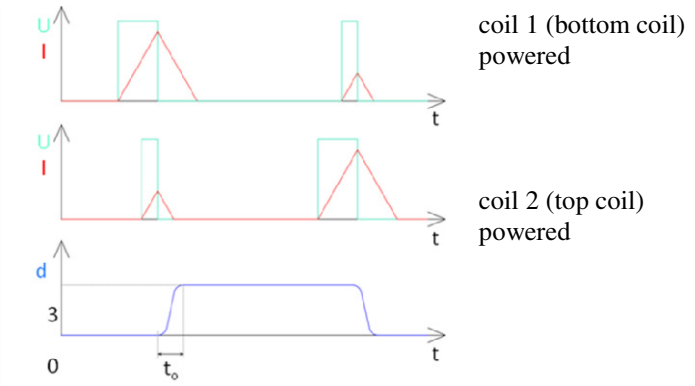

Fig. 3. Opening and closing of the valve with a deceleration effect

2.2 Actuator Numerical Simulations

The axisymmetric model of the actuator is the best schematic representation of the magnet assembly on the valve stem. In the chosen design, the diameter of the wire is 1.6 mm with 42 turns per electromagnet. The shape of the neodymium permanent magnet needs to provide the best schematic representation of the magnet assembly on the valve stem and the non-structural mesh has to be fine enough to obtain a good calculation accuracy. According to Fig. 4, the shape of the ferromagnetic core allows the correct distribution of magnetic field lines. Even if a large concentration of magnetic field could not be avoided, the inductance values vary from 0.2 mH – 0.3 mH, which will provide a good movement dynamics. The forces attracting the electromagnet are calculated from volume integration of Maxwell's weighted stress tensor. Net forces are shown in Table 1. Each of the electromagnets consumes 110 W of electric power or 55 A current and a 2 V voltage drop.

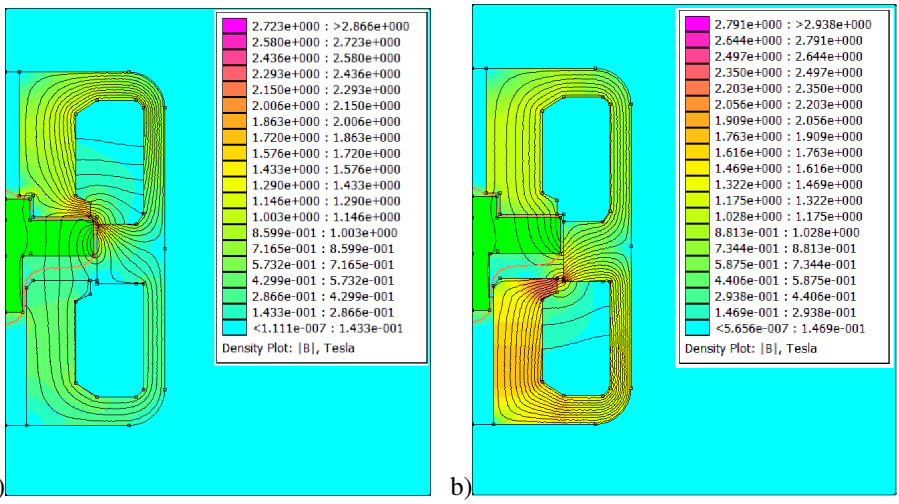

Fig. 4. Magnetic field lines and the flux density distribution in the mockup: a) the coils are not powered; the magnet is attracted to the upper core; b) the bottom coil is powered and the magnet starts moving downwards

Table 1. Comparison of electromagnetic forces for different valve positions, movement upwards and downwards

Position [mm]	Resultant force [N] when the magnet is attracted upward	Resultant force [N] when the magnet is attracted downward
3	143.4	–134.0
2	107.6	–129.8
1	109.8	–120.0
0	137.6	–141.6

3 Power and Automatic Control

In order to perform the tests it is necessary to be able to generate PWM pulses and to change their pulse width. In Fig. 5a, two coils (B1, B2) are powered by a battery of 12 V via the half-bridge transistor-diode system (TDS). A microcontroller (μC), controlled by a computer, generates PWM pulses of the width defined by an operator. In this system, two separate PWM signals are generated in order to control two TDS modules – one module for each coil. According to Fig. 5b, a PWM signal triggers the control system of power transistors (CSPT). The current flows now through the coil. If the transistors are no longer electrically controlled, the energy accumulated in the coil is returned to the power system via the diode circuit.

In order to adjust the pulse width to trigger or to brake the valve motion, software has been specially programmed. Its interface allows one to determine the precision of settings, i.e. a number of decimal places in time constants and different widths of

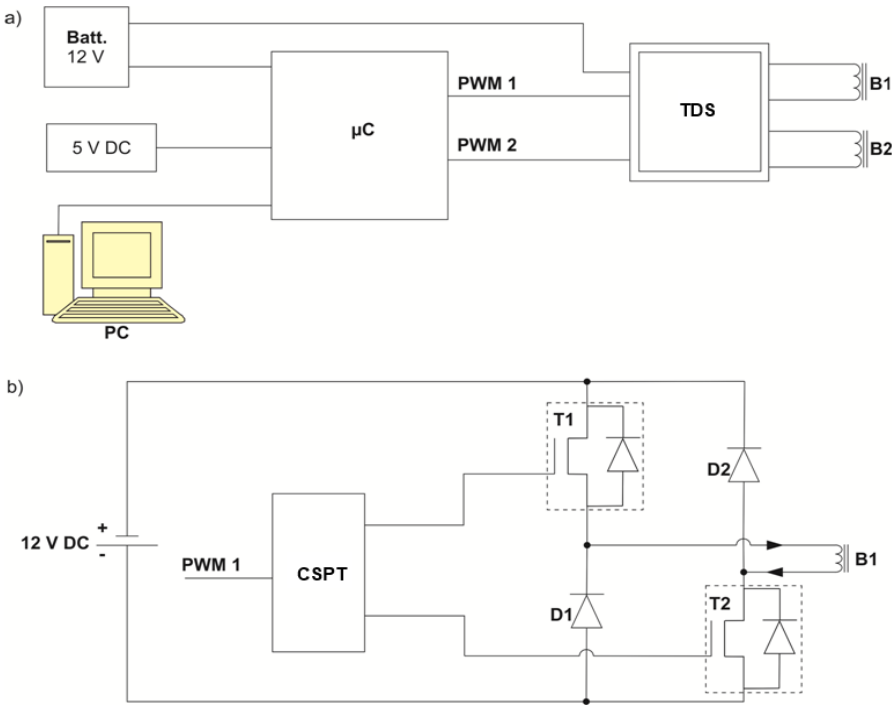

Fig. 5. Diagram of the supply and control system of actuator coils: a) connection diagram; b) circuit of the energy transfer system for one coil (B1, B2 – coils. TDS – transistor-diode system, PWM 1, PWM 2 – Pulse Width Modulations, µC – microcontroller, T1, T2 – transistors, D1, D2 – diodes, CSPT – control system of the power transistors)

PWM signals. Two decimal places are needed. Interface buttons allow one to trigger the upward or downward motion only or to start and to stop the continuous work. Settings can easily be exported to a file and loaded to the program later.

4 Valve Deceleration – Test Results

According to the first attempts for PWM of 4 ms, without valve settling, its opening and closing time was of 2.7 ms each and for PWM of 6 ms – 2.5 ms. However, the deceleration force is needed to make the valve settling in its seat. This will slightly increase the opening/closing time.

The settling is shown in Fig. 6. The trigger pulse (orange line) starts at 0.5 ms and lasts up to 6.5 ms (6 ms PWM). The valve begins to rise at about 3 ms. Approximately at 3.8 ms the braking pulse in the other coil is triggered (green line) and lasts up to about 6.7 ms, which is sufficient to stop the movement. The speed of the valve (blue line) varies during the motion and reaches the maximum value of about 1 m/s. The same principle is applied to the valve opening. Under atmospheric conditions, the braking test for PWM of 6 ms is the most relevant, since the braking coincides with the end of the trigger pulse. It will be necessary to put the mockup under pressure to continue testing with higher PWM.

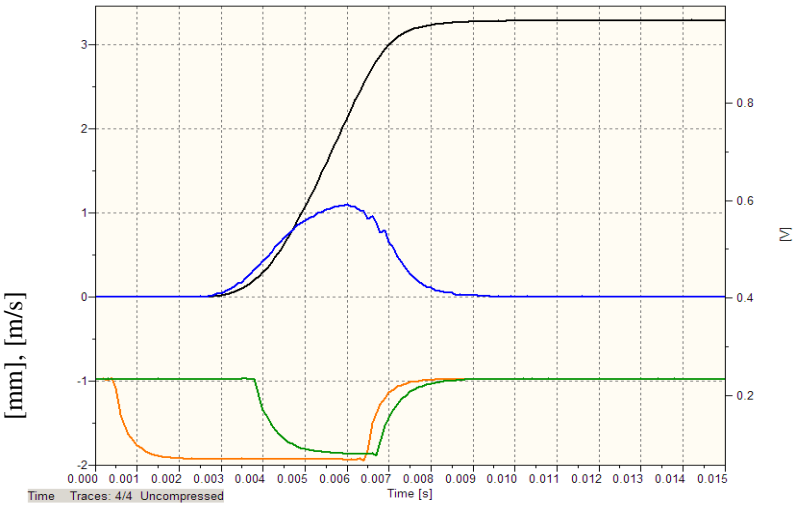

Fig. 6. Valve closing; — valve stroke, — valve speed, — motion trigger PWM of 6 ms, — motion braking PWM

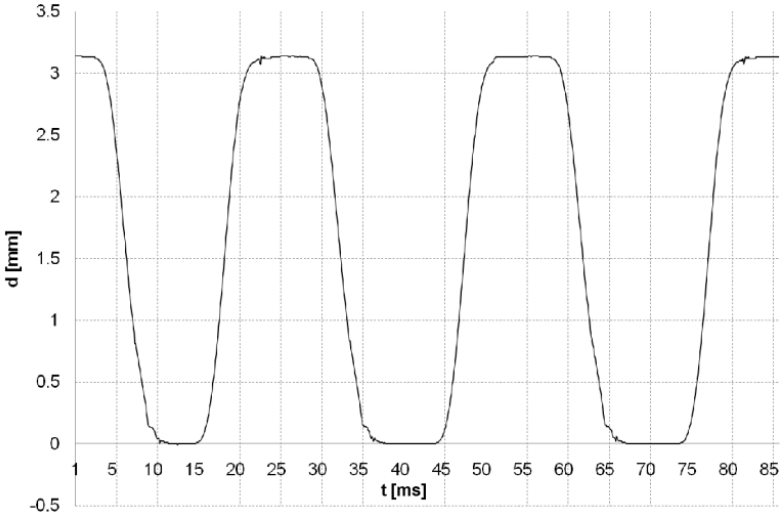

Fig. 7. Continuous work test; — valve movement in mm

From the point of view of the synchronization of the valve state with the engine work cycle, one must take into account the time between the trigger signal and the appearance of the electromagnetic force large enough to raise the valve. This time under ambient conditions is approximately 2.5 ms for the lower coil (closing motion) and 3 ms for the upper coil (opening motion) and, if necessary, it can be determined more precisely.

In Fig. 7a valve stroke in continuous motion is observed. After testing (10,000 cycles), the disassembly of the model revealed no wear of magnets or other elements made of mild steel.

5 Static Force and Current – Test Results

The tests showed that the smooth settlement of the valve is possible; subsequently the measurement of the resultant force of the actuator was made. In Fig. 8 forces and currents for different pulse widths are presented. The greater width of PWM, the greater the force is. On the other hand, the current and force saturation can be seen. The force rises less when the pulse width increases and that relationship is not linear. It can be seen that the currents attain their saturation level faster than the forces. The maximum current reaches the value of 55 A and even if the force rise is noted, the current remains constant. At this point there is a difference between the maximum force value from the simulation described in Section 2.2 and from the tests. This may be caused by friction between the mobile stem and its guide, which has not been taken into account in the simulations.

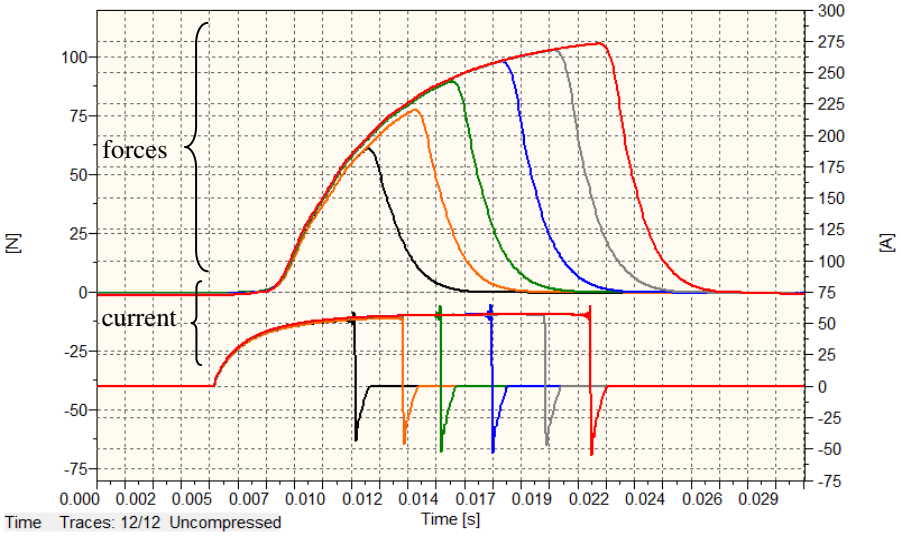

Fig. 8. Force and current evolution for different PWM; — results for PWM of 6 ms, — 8 ms, — 10 ms, — 12 ms, — 14 ms, — 16 ms

6 Conclusions

- A mockup of the electromagnetic actuator with its measurement system and its control software was made and the resulting characteristics are presented in that paper.

- It is shown that the concept of a camless valve without an additional pneumatic system or spring is possible to implement.
- The system of two coils in the described configuration provides an advantage of partial recovery of the energy stored in coils at each break of the PWM signal.
- The design of the valve settlement in its seat was examined experimentally. Its implementation is possible, which has been confirmed by characteristic curves.
- Further work, including the pressurization of the mockup and the optimization of the actuator in terms of its dimensions, needs to be conducted in order to confirm the reliability of the electromagnetic actuator under nominal working conditions. A study of ferromagnetic and permanent magnet materials should also be carried out in order to minimize the residual magnetic field that can disrupt the operational stability of the valve.

References

1. Łagodziński, J., Kozanecki, Z.: Magnetic Thrust Bearing for the ORC High – Speed Microturbine. Solid State Phenomena 198, 348–353 (2013), doi:10.4028/www.scientific.net/SSP.198.348
2. Łagodziński, J.: Modeling of Magnetic Fields with the Finite Element Method in Machine Diagnostic Systems. Solid State Phenomena 155, 147–149 (2009), doi:10.4028/www.scientific.net/SSP
3. Tomczuk, B., Schröder, G., Waindok, A.: Finite element analysis of the magnetic field and electromechanical parameters calculation for a slotted permanent magnet tubular linear motor. IEEE Trans. on Magnetics 43(7), 3229–3236 (2007)
4. Tomczuk, B., Waindok, A., Wajnert, D.: Transients in the electromagnetic actuator with the controlled supplier. Journal of Vibroengineering 14(1), 39–44 (2012)
5. Waindok, A.: Modeling and measurement of transients for a 5-phase permanent magnet tubular linear actuator including control and supply system. Solid State Phenomena 214, 121–129 (2014)

Controller Tuning Method by Shaping Its Output Step Response

Robert Ugodziński[1] and Roman Szewczyk[2]

[1] Industrial Research Institute for Automation and Measurements,
Al. Jerozolimskie 202, 02-486 Warsaw, Poland
rugodzinski@piap.pl
[2] Warsaw University of Technology, Faculty of Mechatronics,
sw. A. Boboli 8, 02-525 Warsaw, Poland

Abstract. Paper presents new method of PID controller tuning, focusing on controller output stability, in opposite to standard error minimization. Presented algorithm precisely calculate PID controller parameters by giving on its input the estimated linear model of the system, and desired time constant of the first order model step response, from the process disturbance input to the controller output. Thanks to this method stable controller output value can be achieved in a minimum amount of time. In addition, an example of the algorithm execution for identified model of a real system was shown. Unfortunately, at this moment algorithmic controller tuning work only for second order non-oscillating model of process and first order model of step response. In the future it is planned to extend this method on processes described by means of other transfer functions.

Keywords: control system, PID tuning, stable output, process control, feedback control.

1 Introduction

PID controllers there are one of the most widespread methods for process control. It is estimated that their utilization reaches approximately 90 % of all controllers. Though there are many other and better methods such as state feedback controller [1], PID controllers hold the position thanks to their simplicity and well documented tuning methods [2, 7].

However, most of them are focused on the controlled process output value [5]. But sometimes controller should establish a stable output for appearing stepping disturbance as soon as possible. Unfortunately, there is lack of tuning methods focused on controller output stability. An example of such an object is an electromagnetic weighing scale, where it is required to quickly set the stable controller output current, without the need for high-speed pan tilt compensation (i.e. the process output) under the influence of stepping disturbances (the measured mass at the input of the controlled object), so as to receive the current measurement as soon as possible [3].

J. Awrejcewicz et al. (eds.), *Mechatronics: Ideas for Industrial Applications*,
Advances in Intelligent Systems and Computing 317, DOI: 10.1007/978-3-319-10990-9_15

2 Presentation of the Problem

It is wanted to design the shape of the PID controller answer of the under the stepping disturbance influence on process input. Problem can be presented as shown on Fig. 1.

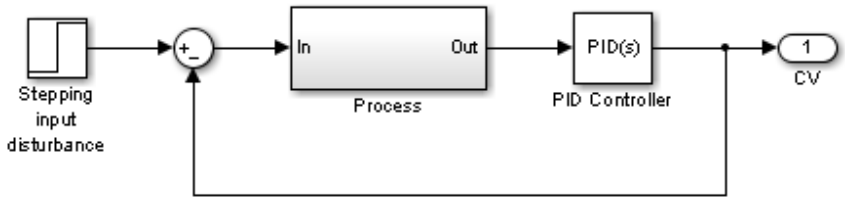

Fig. 1. Overview of a problem

Problem can be also assumed as equation:

$$\frac{CV(s)}{z(s)} = Req(s) \tag{1}$$

where *CV* is the control value, *z* is the stepping disturbance on process input and *Req* is the required response that is to be shaped.

3 Description of the New Tuning Method

Feedback loop of the control system presented on Fig. 1 can be presented as transfer function:

$$G(s) = \frac{PV(s)}{z(s)} = \frac{Process(s) \cdot PID(s)}{1 + Process(s) \cdot PID(s)} \tag{2}$$

Now, assume that it is possible to modify the *G* transfer function to shape the model characteristic.

$$G(s) = Req(s) \tag{3}$$

It is necessary to keep in mind, that the steady state proportional gain of required transfer function *Req* must be equal to 1, to sustain the feedback loop compensation of disturbance.

After joining the equation 2 and 3, equation 4 was obtained:

$$\frac{Process(s) \cdot PID(s)}{1 + Process(s) \cdot PID(s)} = Req(s) \tag{4}$$

This equation can be written as:

$$PID(s) = Process(s)^{-1} \cdot \frac{Req(s)}{1 - Req(s)} \tag{5}$$

Unfortunately, the resulting object must be able to simplify itself to the PID controller, which is a big limitation. It has been proved, however, that the equation is solvable for the second order object model and the first order expected cotroller response.

4 Calculations for the Second Order Object with the First Order Expected Regulator Response

Suppose that the controlled object has a transfer function:

$$Process(s) = \frac{k}{T_1 s^2 + T_2 s + 1} \tag{6}$$

Response of a the designed controller is:

$$Req(s) = \frac{1}{Ts + 1} \tag{7}$$

As can be seen in the design of the step response, the static boost condition $k = 1$ was kept. Substituting (6) and (7) into the controller equation (5) gives:

$$\begin{aligned} PID(s) = Process(s)^{-1} \cdot \frac{Req(s)}{1 - Req(s)} = \left(\frac{k}{T_1 s^2 + T_2 s + 1} \right)^{-1} \cdot \frac{\frac{1}{Ts+1}}{1 - \frac{1}{Ts+1}} = \\ = \frac{T_1 s^2 + T_2 s + 1}{k} \cdot \frac{\frac{1}{Ts+1}}{\frac{Ts}{Ts+1}} = \frac{T_1 s^2 + T_2 s + 1}{k} \cdot \frac{1}{Ts} = \frac{T_2}{kT} + \frac{1}{kT} \cdot \frac{1}{s} + \frac{T_1}{kT} \cdot s \end{aligned} \tag{8}$$

Hence the desired settings of the PID controller were obtained:

$$K_p = \frac{T_2}{kT}; \quad K_i = \frac{1}{kT}; \quad K_d = \frac{T_1}{kT} \tag{9}$$

As shown, the expected response time is inversely proportional to each of the settings, allowing setting the regulator response time constant by simple scalar settings multiplication.

One may also note, that the differential component does not have a filter, but experimentally it is shown that choosing suitably small filtration constant does not affect the quality of the desired response execution . Another thing worth mentioning is that

the time constants of the process must be greater than zero (negative values are not permitted due to the control system stability).

5 Stability of Described Control System

After successful identification of parameters of PID controller for second order object the stability of control system can be examined. To do this we must examine the transfer function of obtained controlled plant:

$$G(s)=\frac{Process(s)}{1+Process(s)\cdot PID(s)}=\frac{\dfrac{k}{T_1s^2+T_2s+1}}{1+\dfrac{k}{T_1s^2+T_2s+1}\cdot\left(\dfrac{T_2}{kT}+\dfrac{1}{kT}\cdot\dfrac{1}{s}+\dfrac{T_1}{kT}\cdot s\right)}= \tag{10}$$

$$=\frac{\dfrac{k}{T_1s^2+T_2s+1}}{1+\dfrac{k}{T_1s^2+T_2s+1}\cdot\dfrac{1}{kT}\left(T_2+\dfrac{1}{s}+T_1s\right)}=\frac{k}{T_1s^2+T_2s+1}\cdot\frac{Ts}{Ts+1}$$

As it can be seen, resulting transfer function is stable. First segment of transfer function is the process model, that it is known to be stable (all time constants are greater than zero). Second segment is connected with desired time constant of step response, but it is also stable as T must be greater than zero. This implies that all poles are real and smaller than zero, so the stability criterion is met [6].

6 Analysis of Control System Example

Analyses were carried out from the control of second order inertia object point of view. Such object are very common in electromagnetic actuators control systems. Analyzed system was described by the following transfer function:

$$G_{sys}(s)=\frac{1}{0.02s^2+0.6s+1} \tag{11}$$

Fig. 2 presents the step response of proposed exemplary system.

Due to the fact that proposed tuning method is parameterized by response time, many controllers can be created by solving equations (9). Parameters of these controllers are given in Table 1.

Table 1. Exemplary set of PID controller parameters

Response time parameter	K_p gain	K_i gain	K_d gain
10s	0.06	0.1	0.002
1s	0.6	1	0.02
0.1s	6	10	0.2

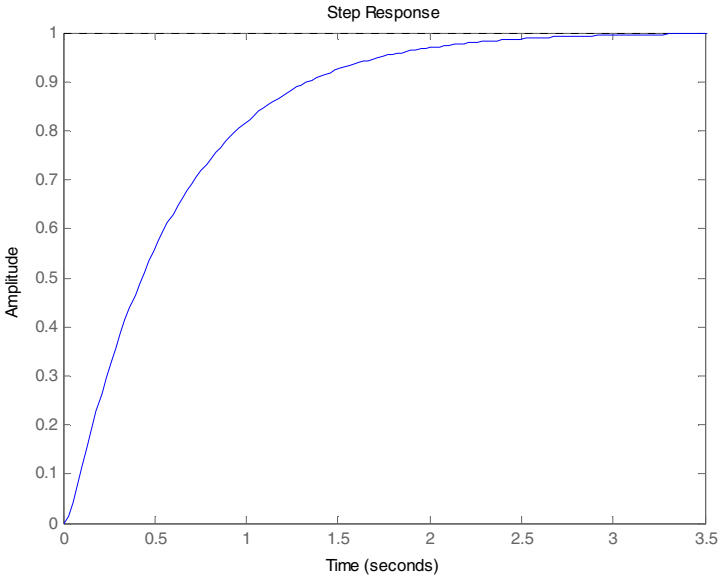

Fig. 2. Step response of proposed exemplary system

Step response times of developed systems are presented in Fig. 3 and Fig. 4.

As it can be seen, response time parameter has significant impact on controlled system output. By minimizing this parameter, PV error can be also minimized. Moreover, developed PID controller may be tuned accordingly to the technical needs.

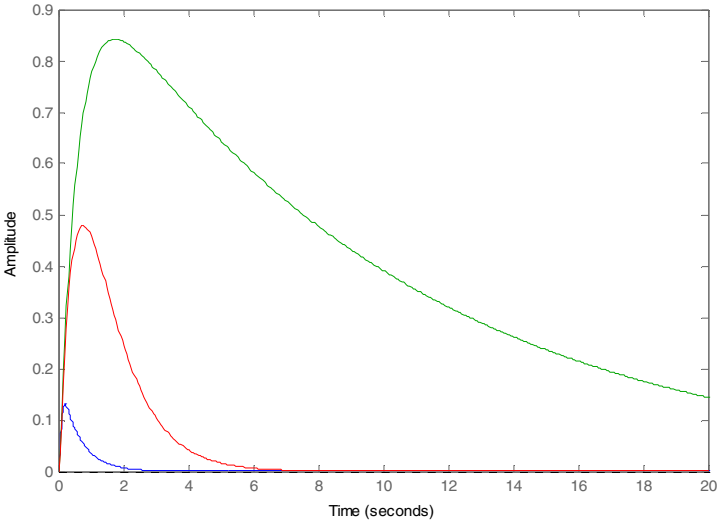

Fig. 3. Set of response characteristics for designed controllers with different expected time responses: red – 10 s, green – 1 s, blue – 0.1 s from input distortion to system output

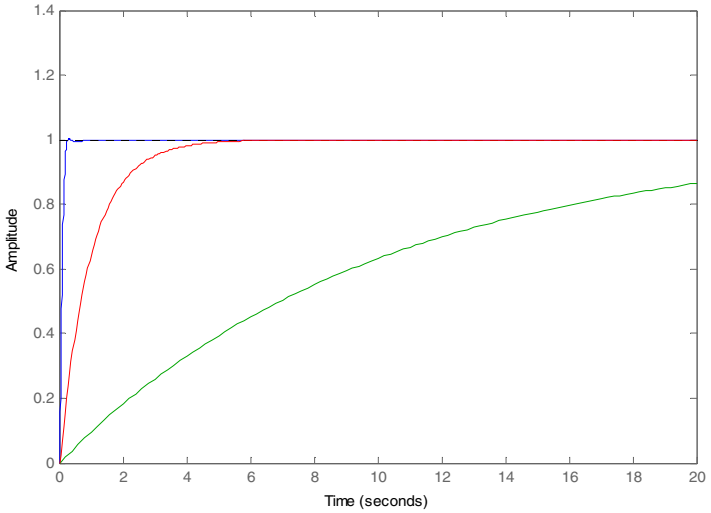

Fig. 4. Set of response characteristics for designed controllers with different expected time responses: red – 10 s, green – 1 s, blue – 0.1 s from input distortion to controller output

However, decrease of maximal acceptable PV output leads to faster response time and higher bandwidth of the controller.

7 Conclusion

Presented method of PID tuning is especially suitable for development of automatic control systems oriented on electromechanical actuators. As it was shown, the expected response time is inversely proportional to each of the settings, allowing the regulator response time constant setting by a scalar multiplication. Moreover, the differential component does not have a filter, but experimentally it is shown that choosing suitably small filtration constant does not affect the quality of the desired response execution.

It should be highlighted, that presented method is focused on control value stability, which is especially important during the tuning of regulators driving precision actuators in advanced measuring systems [4].

Acknowledgments. This work was partially supported by The National Center for Research and Development within PBS Program, grant no: PBS1/B3/8/2012.

References

1. Yue, D., Han, Q.L., Peng, C.: State feedback controller design of networked control systems. IEEE Transactions on Circuits and Systems II-Express Briefs, 640–644 (2004), doi:10.1109/CCA.2004.1387218

2. Zhong, J.: PID Controller Tuning: A Short Tutorial (2011)
3. Ugodziński, R., Szewczyk, R.: Determination of Parameters of Second Order Integration Model for Weighing Scales. Mechatronics, 161–167 (2013), doi:10.1007/978-3-319-02294-9_21
4. Ang, K.H., Chong, G.C.Y., Li, Y.: PID control system analysis, design, and technology. IEEE Transactions on Control Systems Technology 13(4), 559–576 (2005), doi:10.1109/TCST.2005.847331
5. Li, Y., Ang, K.H., Chong, G.C.Y.: PID control system analysis and design – Problems, remedies, and future directions. IEEE Control Systems Magazine 26(1), 32–41 (2006), doi:10.1109/MCS.2006.1580152
6. Goodwin, G.C., Graebe, S.F., Salgado, M.E.: Control system design, vol. 240. Prentice Hall, New Jersey (2001) ISBN-13: 9780139586538
7. O'Dwyer, A.: Handbook of PI and PID controller tuning rules, vol. 2. Imperial College Press, London (2009) ISBN-13: 9781848162426

Vector Faxing System

Marian Wrzesień and Piotr Ryszawa

Industrial Research Institute for Automation and Measurements PIAP, Warsaw, Poland
{mwrzesien,pryszawa}@piap.pl

Abstract. The vector faxing system based on USB fax modems is presented. The system was implemented and made available to users. In the adopted approach, a vector of USB modems does replace solutions based on standalone fax machines, large size of which significantly hampers the construction of a multiple line faxing system in the PSTN environment (Public Switched Telephone Network) – necessary for the effective functioning of a large company. The abstract control model ACM, adopted in the USB hosts which supports analog modem hardware (including USB fax modem devices), is analyzed. It should be emphasized that explicit discussions of the method of mapping telephone lines to – randomly activated during startup of the fax server – USB fax modems, and of the mechanism for assigning user access rights to designated fax modems, are included. Use of the described system increases immunity to threats such as spam, computer viruses, spoofing, or redirecting to fake websites (phishing). The user communicates with the faxing system by the Winprint HylaFax+ Reloaded client.

Keywords: USB Fax Modem, multiple line faxing system, CDC Class Communications Equipment, Fax Server.

1 Introduction

The aim of research work described in this article was to achieve a vector structure for the faxing system. There are in fact two problems hindering the implementation of the system in this form, which do not occur in case of the single-line, i.e., one sender – one recipient solution. The first problem is the random nature of registration of modems in a computer system after they are plugged into the USB ports. The second problem is lack of a mechanism for assigning users the rights to use particular fax modems.

The first problem was solved by software enforcement of ordering of modems by aliasing their names. The second problem was solved by the use of queue management mechanism in HylaFax+ fax server – the JobControlCmd.

In the article necessary investigations to achieve this objective as well as the complete method are described. The mentioned problems assume that there exists a fax server, the implementation of which was a separate task.

Adoption of the fax communication in large companies that have local area networks and use a large number of telephone lines provides the following advantages:

J. Awrejcewicz et al. (eds.), *Mechatronics: Ideas for Industrial Applications*,
Advances in Intelligent Systems and Computing 317, DOI: 10.1007/978-3-319-10990-9_16

increased savings and better ecology, increased order in documents, convenient service, reliability, direct connectivity and reduced cabling.

2 Implementation of the Fax System

Implementation of the system covered:

- Introduction and setting up the hardware fax server.
- Installation and configuration of the HylaFax+ software server on the hardware server.
- Development and installation of the custom control scripts for the software, for adaptation of the software to the internal requirements of the company.
- Introduction and setting up the private branch exchange to normalize the fax ringing tone.
- Assignment of fax connections to specific fax modems by creating a name table of the aliases of modems.

2.1 System Architecture

The system architecture is shown in Fig. 1. Presented here USB fax modems replace conventional fax machines of relatively large dimensions.

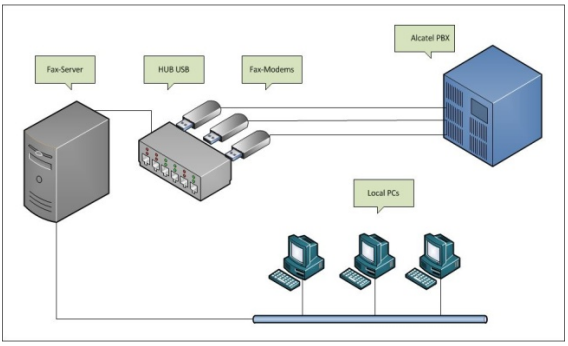

Fig. 1. Faxing system with USB fax-modems

2.2 Installing the HylaFAX+ Software Server

Configuration: Faxsetup-Server. During the implementation of the faxing system, hylaFax+ and hylaFax+ client were first installed. Installation of the hylafax+ program required prior launch of the faxsetup-server. During execution of the faxsetup, the faxmodem program was launched, whose service faxaddmodem allowed to define and configure USB fax modems with names specified by the user, that is, ttyFaxn where $n \in N$, N – the set of natural numbers. As a result of this operation, a set of

modems anticipated for use in the system was defined. Overall number of defined devices stems from the company needs and is determined by the system administrator. In PIAP 16 fax modems were prepared for use, preserving the possibility of expanding the number to 24.

As a result of execution of the faxsetup-server program, a set of files was created, that is the configuration files in the /etc/hylafax/ directory, executable files in the /usr/sbin/ directory, and utility files in the /usr/bin/ directory.

As a part of the presented work the following scripts were developed:

- 10-local.rules – which at the low level binds USB ports, where modems are attached, to dedicated telephone lines,
- ttyFaxn.conf – which initializes and maintains in standby mode the devices /dev/ttyFaxn,
- FaxDispatch – which specifies the destination address and format of incoming faxes and defines the archiving organization rules for incoming faxes (system of directories, each named after relevant date),
- FaxNotify – which specifies the destination address to be notified about events in the faxing system (activity of individual users, the status of delivery of faxes, etc.)
- StartStopModem – which starts modems and the hylafaxd program,
- makeFaxDirs – which creates directories for each device ttyFaxn,
- JobControl – which contains the mechanism for control of user permissions.

Daemons for the Faxing System. The HylaFax+ system processes are managed by daemons: hfaxd, faxq, pagesend and software modems (faxgetty with parameter ttyFaxn). The hfaxd daemon monitors the system and supports the Client-Server process; the faxq daemon supports the HylaFax+ planning system; the pagesend daemon implements the PET/TAP (Personal Entry Terminal/Telocator Alphanumeric Protocol) and UCP protocol (Universal Computer Protocol) for the HylaFax+. The faxgetty program supports the process for supervising fax receiving and fax calls (listening). It uses the ttyFaxn.conf configuration file, that ensure continuity of the /dev/ttyFaxn modem operation. Faxing system status can be read using faxstat-s program. On fax reception, the server calls the faxcrvd script.

2.3 Access to the HylaFAX System

Access to the fax functionality should be allowed based on user permissions. It should be preceded by registration of users, during which users are given IDs and passwords for subsequent identification. The program faxadduser is used for this purpose. User data is stored in the hylafax/etc/hosts.hfaxd file.

Representation of Modems in the Linux USB Host. USB (Universal Serial Bus) Implementers Forum has established a way to represent the equipment after attaching it to the USB host that complies with the CDC specifications (Communications Device Class) [1]. They also identified a way of interpreting the CDC subclasses of devices that are designed to communicate with the public telecommunications net-

work PSTN. These devices are known as a modem (MOdulator-DEModulator), because the data are modulated on the sender side and after reception are demodulated to the original state. The control model for modem devices adopted in USB hosts is the Abstract Control Model (ACM) [2], which is a subclass of CDC and supports analog hardware modems that support the ITU (International Tele-communications Union) V.250 Serial Asynchronous Automatic Dialing and Control – originally called the Hayes standard [3]. It includes a set of commands which are related to the data stream or to a separated control stream via CDC class interface. Currently host microcontrollers are equipped with an embedded system to support the exchange of data via USB. For this area, a standard way of communication is used, which is well supported by any operating system. It meets the CDC/ACM PSTN conditions for cooperation and is presented by the Linux kernel in the form of /dev/ttyACMn where $n \in N$ – supported by the acm.o kernel module.

Creation of Alias Names for Modems. Attaching each additional USB modem to the server results in creation of a /dev/ttyACMn dynamic device by the Linux system [4, 5] (Fig. 2).

```
crw-------.  1 uucp dialout 166,  0 07-04 15:47 ttyACM0
crw-------.  1 uucp dialout 166,  1 07-04 15:43 ttyACM1
crw-------.  1 uucp dialout 166,  2 07-04 15:47 ttyACM2
crw-------.  1 uucp dialout 166,  3 07-04 15:43 ttyACM3
crw-------.  1 uucp dialout 166,  4 07-04 15:43 ttyACM4
crw-rw----.  1 root dialout   4, 64 07-04 15:41 ttyS0
crw-rw----.  1 root dialout   4, 65 07-04 15:41 ttyS1
crw-rw----.  1 root dialout   4, 66 07-04 15:41 ttyS2
crw-rw----.  1 root dialout   4, 67 07-04 15:41 ttyS3
```

Fig. 2. Extract from the Linux OS folder /dev

In the described faxing system, each modem is connected to the server via 28-port USB hub. The *n*-th ttyFaxn modem is connected to the *n*-th port of the USB hub, and to the *n*-th telephone line. These connections are consistent with the record in the configuration files config.ttyFaxn. The server HylaFax+ modems are defined as ttyFaxn. These modems are represented in the host by the device: /dev/ttyACMn. After attaching fax modems to the server, to each pre-defined fax modem ttyFaxn in the system is assigned the /dev/ttyACMx device, however, in the general case the indices $n \neq x$ and this assignment is ambiguous, causing inconsistency between the device ttyFaxn, defined in config.ttyFaxn, and the phone line physically assigned by the /dev/ttyACMx device (they are related to each other in a random fashion). Persistent and unambiguous link of names of specific fax modems to telephone lines can be achieved by assigning the names of USB fax modems to appropriate USB ports. For this purpose is used the "KERNELS" parameter, which clearly defines the location of the modem in the USB hub. This was realized using the udev rules Linux functionality. Running the utility udevadm info-a-n/dev/ttyACM0 | grep KERNELS it was possible to record features of the device associated with the specific location of the

modem in the USB hub, which was attached in turn to each of the USB ports of the server. For each location of the USB modem, values of the KERNELS parameter were read. Then the file was created /etc/udev/rules.d/10-local.rules, which includes a set of relations between the pre-defined ttyFaxn modems and KERNELS parameters obtained during investigations. Presented below is an extract from the aliases file for one modem attached to port No. 1 in the USB hub, which was attached in turn to each of the 6 USB ports available on the server – the USB host.

```
SUBSYSTEMS=='usb', ATTRS{serial}=='24680246', KERNELS=='1-1.2.6', SYMLINK+='ttyFax01'
SUBSYSTEMS=='usb', ATTRS{serial}=='24680246', KERNELS=='1-2.2.6', SYMLINK+='ttyFax01'
SUBSYSTEMS=='usb', ATTRS{serial}=='24680246', KERNELS=='1-3.2.6', SYMLINK+='ttyFax01'
SUBSYSTEMS=='usb', ATTRS{serial}=='24680246', KERNELS=='1-4.2.6', SYMLINK+='ttyFax01'
SUBSYSTEMS=='usb', ATTRS{serial}=='24680246', KERNELS=='1-5.2.6', SYMLINK+='ttyFax01'
SUBSYSTEMS=='usb', ATTRS{serial}=='24680246', KERNELS=='1-6.2.6', SYMLINK+='ttyFax01'
```

Fig. 3. Extract from the 10-local.rules script

Possibility of taking into account relations contained in the above file creates situation, where each of the ttyFaxn modems is randomly tied with /dev/ttyACMx device established by the system, but at the same time is rigidly tied to a particular USB port and – thus – to the known number of telephone line (Fig. 4).

```
crw-------.      1 uucp dialout  166,     0 07-04 15:47 ttyACM0
crw-------.      1 uucp dialout  166,     1 07-04 15:43 ttyACM1
crw-------.      1 uucp dialout  166,     2 07-04 15:47 ttyACM2
crw-------.      1 uucp dialout  166,     3 07-04 15:43 ttyACM3
crw-------.      1 uucp dialout  166,     4 07-04 15:43 ttyACM4
lrwxrwxrwx. 1 root root          7 07-04 15:41 ttyFax01 -> ttyACM2
lrwxrwxrwx. 1 root root          7 07-04 15:41 ttyFax02 -> ttyACM0
lrwxrwxrwx. 1 root root          7 07-04 15:41 ttyFax03 -> ttyACM3
lrwxrwxrwx. 1 root root          7 07-04 15:41 ttyFax04 -> ttyACM1
lrwxrwxrwx. 1 root root          7 07-04 15:41 ttyFax05 -> ttyACM4
crw-rw----.      1 root dialout  4,      64 07-04 15:41 ttyS0
crw-rw----.      1 root dialout  4,      65 07-04 15:41 ttyS1
crw-rw----.      1 root dialout  4,      66 07-04 15:41 ttyS2
crw-rw----.      1 root dialout  4,      67 07-04 15:41 ttyS3
```

Fig. 4. Extract from the Linux OS folder /dev

In PIAP the principle was adopted that every dedicated telephone line is linked to a specific organizational department in which designated employees have access to the fax.

Assignment of Rights to Faxmodems. Hylafax+ server does not provide any method for assigning users who are sending faxes to individual faxmodems. In order to solve this problem the queue management mechanism – JobControlCmd – was used. JobControlCmd is a parameter of the configuration file, which specifies the script executed on fax sending event – it is shown in Fig. 5.

```
#!/bin/sh

. /var/spool/hylafax/etc/setup.cache
. /var/spool/hylafax/bin/common-functions
. /var/spool/hylafax/etc/OwnersFaxyKO
QFILE=/var/spool/hylafax/sendq/q$1
parseQfile
case "$modem" in
  ttyFax01)
      if [[ ! ${faxyFM[@]} =~ $owner ]]; then
        echo "RejectNotice: \"No rights to the modem $modem.\"";
      fi;;
  ttyFax02)
      if [[ ! ${faxyFG[@]} =~ $owner ]]; then
        echo "RejectNotice: \"No rights to the modem $modem.\"";
      fi;;
  ttyFax03)
      if [[ ! ${faxyMDS[@]} =~ $owner ]]; then
        echo "RejectNotice: \"No rights to the modem $modem.\"";
      fi;;
        *) echo "RejectNotice: "Modem is not selected"";;
esac
exit 0
```

Fig. 5. JobControlCmd script

Operation of this script ensures the fax sent by unauthorized user is rejected and a fax transmitted by the user who is located in the specified database is accepted.

2.4 System Startup and Testing

Testing Fax Modems. Confirmation of communication with each of the modems ttyFaxn was performed using minicom software. At the initial phase of testing the faxing system signals did not conform to the requirements of the certification standard [6, 7]. To solve this problem the intermediate KX-TDA100D Panasonic PBX was installed between USB modems and the main switchboard – Alcatel PBX. After this modification, control and modem communication function properly [8, 9]. This allowed for running USB fax modems and proceeding with the next step, that is, deployment of the fax system software.

Testing Communication between the PSTN Fax Modems. Connectivity and communication between the modems was tested using the sendfax program, a component of the HylaFax+ software. Fax transmission was carried out between the PIAP Alcatel PBX and PIAP Panasonic PBX. After transmission, the realization of the commands specified in the FaxDispatch was examined. On the basis of the results the correctness of the system was stated.

Testing Communication between the PSTN Fax and Fax-Modems. For this test was used fax machine connected to the telephone line. While sending fax outside the

PIAP the sendfax command was used. Then with an external fax a message was sent to the recipient's internal number in PIAP. During the transmission, the state of fax machines was monitored using faxstat command. After transmission the realization of the command specified in FaxDispatch was examined. In all cases the correct operation of the system was stated.

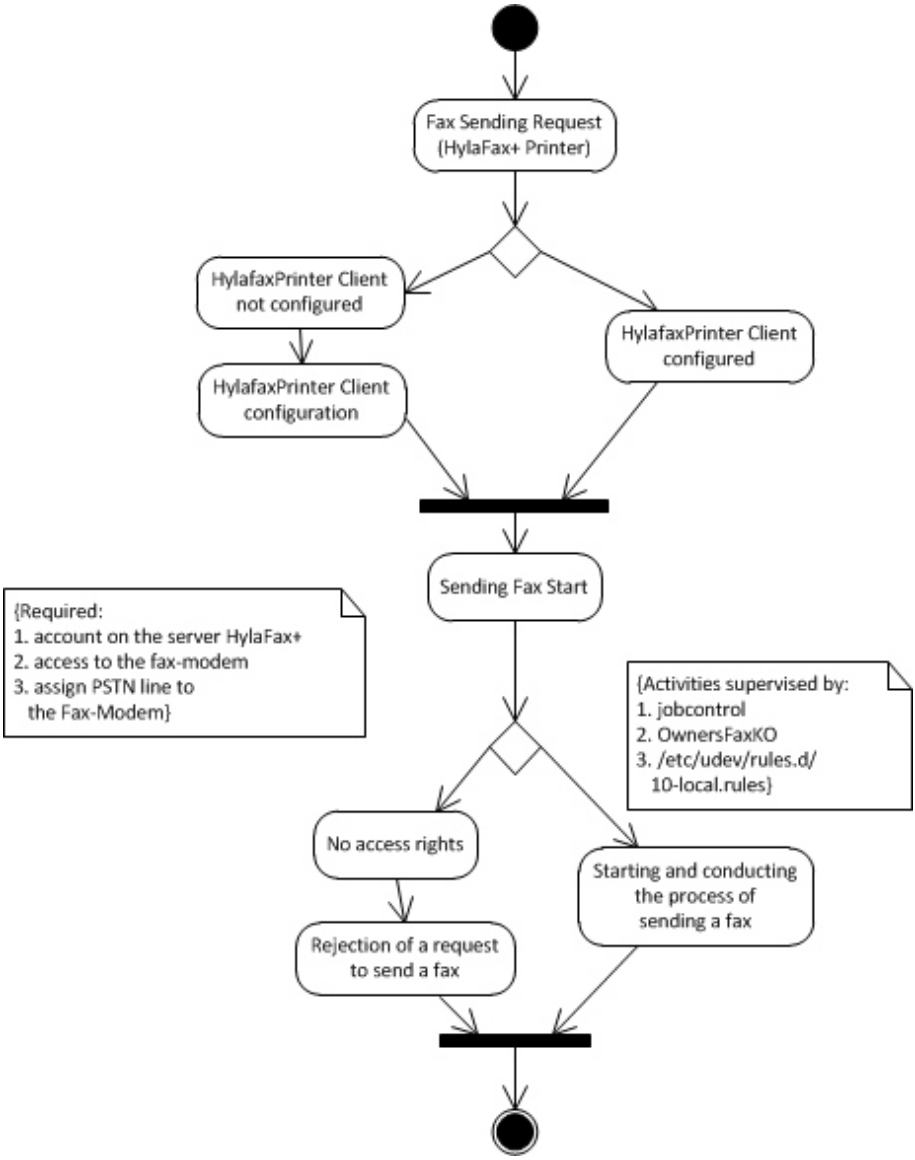

Fig. 6. Sending faxes UML algorithm diagram

2.5 Sending Faxes. Implementation of HylaFax+ Client for Windows 7

In order to allow users to send faxes you need to implement the Windows client software. For this purpose, the Open Source Software Winprint HylaFax+ Reloaded was selected of the available programs. The criteria which guided the selection of the software were: compatible with PIAP systems used in OS Windows (32 and 64 bit Windows 7, Windows 8) and intuitive user interface. Software Winprint HylaFax+ Reloaded enables you to use the integrated address book. By default, this book is stored in CSV format at the location specified by the user. There is also possibility to use the Outlook address book using MAPI (Messaging Application Program Interface) and the database which enables connecting using ODBC (Open Data Base Connectivity). Sending of faxes is illustrated in the UML algorithm diagram (Fig. 6).

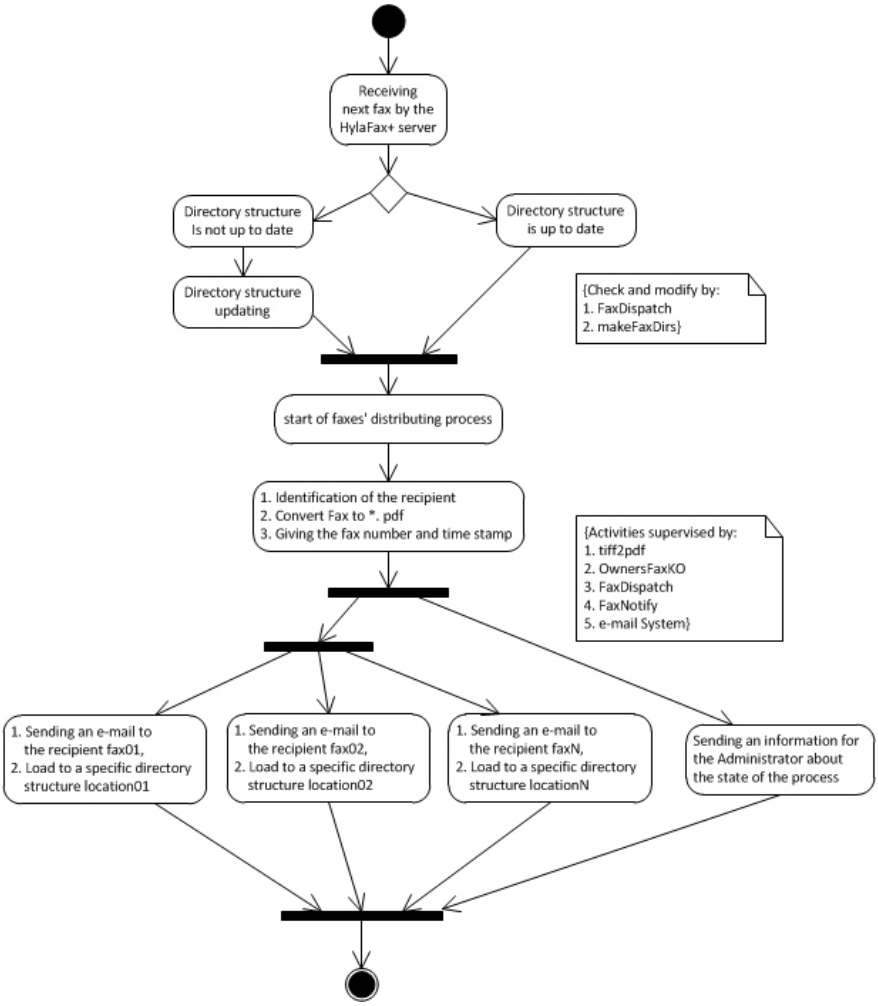

Fig. 7. Receiving faxes UML algorithm diagram

2.6 Receiving Faxes. Organization of the Distribution and Archiving of Received Faxes

Received faxes are sent by e-mail to the addressees and stored in the directories associated with each of ttyFaxn modems. The list of recipients is defined in the FaxDispatch script file. The ttyFaxn is assigned to appropriate e-mail groups of users eligible to receive faxes from the specific fax modem. These groups consist of department workers authorized to use the fax system. All recipients which are assigned to these groups are defined in the file which defines e-mail system users. Receiving faxes is illustrated in the UML algorithm diagram (Fig. 7).

```
# ! /bin/bash
#
. /var/spool/hylafax/etc/OwnersFaxyKO
FaxDirBase="/home/services/Faxy/"
ReceivedFaxesPdf="$FaxDirBase$DEVICE/$(date '+%Y')/
  $(date '+%m')/$(date '+%d')/*.pdf"
Numer=`echo $DEVICE | sed -e 's/ttyFax//;s/^0//'`
FaxyKO=(
        " "
        "faxyFM"
        "faxyFG"
        "faxyMDS"
)
LANG=pl_PL
FILETYPE=pdf
/var/spool/hylafax/bin/makeFaxDirs
/usr/bin/tiff2pdf
  $FILE -j -o $FaxDirBase$DEVICE/$(date '+%Y')/$(date '+%m')/
  $(date '+%d')/${FaxyKO[$Numer]}$(date '+%Y%m%d%H%M').pdf
chown uucp:${FaxyKO[$Numer]} $ReceivedFaxesPdf
chmod 750 $ReceivedFaxesPdf
SENDTO=${FaxyKO[$Numer]}@piap.pl
NOTIFY_FAXMASTER=errors
```

Fig. 8. FaxDispatch script for three departments

```
# ! /bin/bash
#
LANG=pl_PL
#
if [ "$WHY" != "done" ]; then
        RETURNFILETYPE=pdf;
        RETURNTECHINFO=yes;
        RETURNTRANSCRIPT=yes;
        NOTIFY_FAXMASTER=faxyNI@piap.pl
fi;
```

Fig. 9. FaxNotify script

When the FaxDispatch is executed, it runs the makeFaxDirs program contained therein that manages the creation of directories that store faxes and supervises access to these directories. Using the script ownership rights are granted to the employees belonging to the group faxyXX, where XX is the department symbol. The received faxes are included into the PIAP global system for electronic documents archiving. The method of notification of the recipients is defined in the script FaxNotify on the HylaFax+ server side.

3 Summary

As a result of the conducted work and research, the aim stated in the introduction was achieved. The problem of random representation of modems in the system was solved by means of enforced placement of modems with mechanism of modem names aliasing. The problem of establishing a methodology for assigning to the users rights to send faxes via particular fax modems was solved through the use of queue management mechanism in Hylafax fax server – JobControlCmd. The objective to equip the system with the possibility of separating the fax transmit / receive channel for an individual user, with clearly defined fax modem and telephone line corresponding to them, was achieved. A secondary objective of eliminating the bulky fax machines was also achieved thanks to miniaturized USB fax modems.

References

1. Gupta, A.: Communication Device Class (CDC) Host2009. Microchip Technology Inc. (2009), http://www.microchip.com
2. Teamwork, Universal Serial Bus Class Definitions for Communication Devices, Version Atmel Corp., AT91 USB (January 19, 1999)
3. Teamwork, Serial Asynchronous Automatic Dialing and Control, ANSI/TIA-602, http://www.eia.org
4. Teamwork, Universal Serial Bus Specification, version 1.0 and version 1, http://www.usb.org
5. Teamwork, Universal Serial Bus Common Class Specification, version 1.0, http://www.usb.org
6. Jajszczyk, A.: Wstęp do telekomutacji, WNT, Warszawa (2008) (in Polish)
7. Dziczkowska, M., Dziczkowski, L.: Obsługa i budowa modemu. Helion, Warszawa (1997) (in Polish)
8. Kula, S.: Systemy teletransmisyjne. WKL, Warszawa (2006) (in Polish)
9. Teamwork, Vademecum Teleinformatyka cz. I, IDG, Warszawa (1999) (in Polish)

Part II
Robotics

Personal Lower Limb Rehabilitation Robot for Children

Mariusz Giergiel, Aleksander Budziński, Grzegorz Piątek, and Michał Wacławski

AGH University of Science and Technology
30 Mickiewicza Av., 30-059 Krakow, Poland
{giergiel,budzin,grzegorz.piatek,mwaclaw}@agh.edu.pl
http://www.agh.edu.pl

Abstract. The article describes the process of developing a concept, design and building a working lower limb rehabilitation device with comparison to other existing systems. The described robot was designed primarily for rehabilitation of children with cerebral palsy (and other illnesses that need constant, long term rehabilitation).

Keywords: child rehabilitation, lower limb.

1 Introduction

The cerebral palsy is a set of permanent and non-progressive movement disorder and a muscle tone, as a result of the immature brain lesion. It is mostly caused by an unknown element, but to known reasons are included: development disorders, infections, intoxication or hypoxia of the fetus, as well as perinatal mechanical injuries causing brain stem strokes, or inflammation of the central nervous system [5, 11]. Physiotherapy is a health care profession concern on promotion mobility by the remediation of impairments and disabilities [2]. Application of a treatment movement cause positive changes in the locomotion system, as well as in the patient nervous, cardiovascular and the respiratory systems. It is carried by physical therapists whose responsibility is to provide individual rhythm, range and trajectory of movement. What is important from the rehabilitation point of view is the fact, that even if movement disorders intensify with time, they are not caused by deterioration of the brain damages itself, but by the impaired development caused by a muscle tone [1, 11]. In order to keep patients in a good condition and to improve they lives standard, by increasing mobility, they should be treated with rehabilitation procedures regularly and from the earliest days.

2 Existing Systems

With limited number of physical therapists and the need of having accurate treatment every day, robotic and mechanical systems have been built. Most of them are very expensive and are not available for individual customers, while the other are not capable of carrying proper treatment as described in the following subsections.

J. Awrejcewicz et al. (eds.), *Mechatronics: Ideas for Industrial Applications*,
Advances in Intelligent Systems and Computing 317, DOI: 10.1007/978-3-319-10990-9_17

2.1 Mechanical Walk Simulation

The confirmed need of providing regular and often rehabilitation procedures, was a reason of creating purely mechanical solutions like NF-Walker (Fig. 1). Because of simplicity and lack of electronics, those devices are within financial reach of most of the families, but from the other hand side, are not capable of serving more complex movement set, as is needed when treating distortion of walking "heel-finger" as observed in case of spastic patients.

Fig. 1. NF-Walker mechanical rehabilitation system [6]

2.2 Autonomous Exoskeleton

In order to increase human strength as well as because of a human aging (according to the Brian Dellon people over the age of 65 in the year 2050 will exceed 35 % of the popularity [3]), researchers works on the assistive robots. The Berkeley lower extremity exoskeleton (BLEEX) – Fig. 2 as well as the Hybrid Assistive Limb (HAL) – Fig. 3 or the ReWalk (Fig. 4) already can improve quality of live and after the control program modification can be used for a rehabilitation purposes.

2.3 Automated Stationary Orthosis

Rehabilitation requires well controlled environment especially for patients with mobility dysfunction. Because of that reason a few systems were developed like Lokomat (Fig. 5) or Rutgers Ankle (Fig. 6). Those systems even if a great rehabilitation results is

confirmed, are beyond everyday usage because of a price which for Lokomat exceed 375 000 $ [10]. That and the fact that there are number of patient waiting for rehabilitation procedure prompted Grzegorz Piątek to build AGH Rehabilitation Platform.

Fig. 2. The Berkeley lower extremity exoskeleton system [13]

Fig. 3. The Hybrid Assistive Limb [4]

Fig. 4. ReWalk Exoskeleton [8]

Fig. 5. Lokomat rehabilitation system [12]

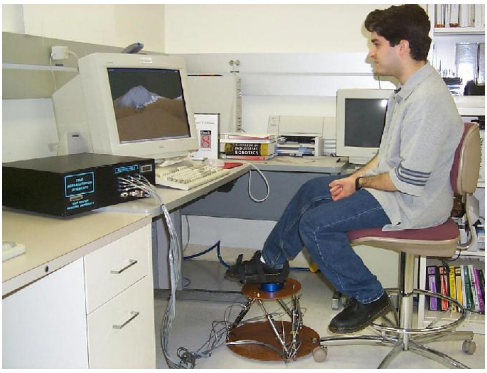

Fig. 6. Rutgers Ankle rehabilitation Robot [7]

3 Rehabilitation Platform

3.1 Design Assumptions

Device was aimed to be capable of carrying single child patient of weight below 25 kg. It was expected to allow a full control over the movement range. Especially important was to combine reciprocating legs movement with "hell-finger" walk, which was not provided by any studied device. Additional goal for our rehabilitation robot was to be capable of being integrated into the remote expert monitoring system which in near future should allow patient monitoring and tuning device for even better results. What is more important, it was expected to be save and possible cheap in order to become an everyday rehabilitation robot available for everyone who need that device.

3.2 Robot Design

After the research we found that the safest and the best performing solution is when a patient is immobilized and overhand. In such a solution the device weight is not influencing the patient, which is crucial when working with patients who suffer muscle contractors disturbing "hell-finger" walk. Moreover it gives a great mobility allowing patient to move legs independently and asynchronously makes possible exercises like squats or cycling on different radii. With all given assumptions robot design was started.

The most important was to find a solution for generating an accurate movement with low velocities. In result presented on Fig. 7 drive system was designed. The use of cyclo gear allows for application of compact servo drives which operates with 5 V only. In result drive system is compact and save for the user even in case of insulation failure. Moreover drives are small enough to be mounted directly inside robot arms improving safety even more. Final robot design is presented on Fig. 8 while on Fig. 9 the robot support is shown.

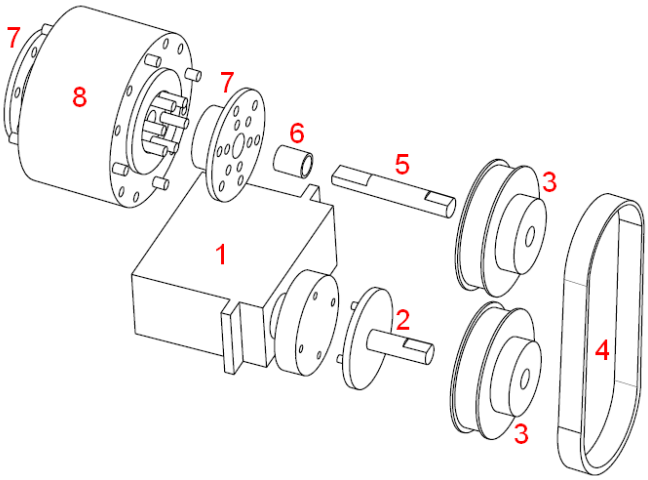

Fig. 7. The single joint drive system: 1 – servomotor HS-805BB, 2 – clutch-gear shaft, 3 – gear wheel, 4 – toothed belt, 5 – input shaft, 6 – teflon sleeve, 7 – output hub connected with a robot arm, 8 – cyclo gear

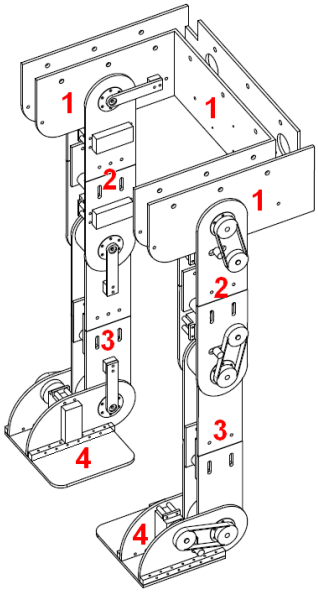

Fig. 8. Robot schematic: 1 – lap belt, 2 – limb, 3 – shank, 4 – feet

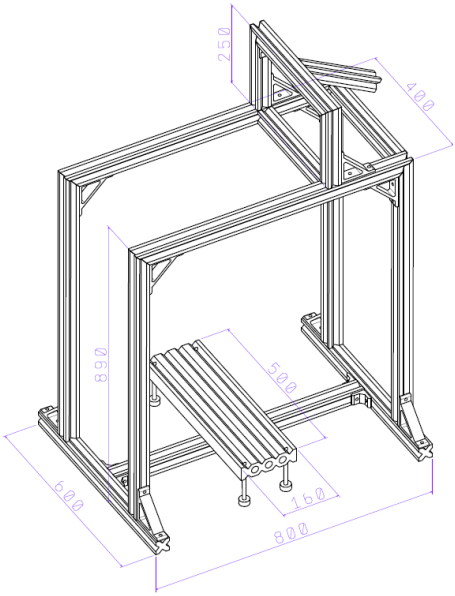

Fig. 9. Robot support schematic

3.3 Robot Tests

After the design phase the basic robot structure was build and tested together with two boys, cerebral palsy 8 years old twins. They gave an important feedback about the design details. In result the main control panel was moved behind the patient. That change highly increase a patient security and allowed a supervisor to easily access it at any time. The component length evaluation was done based on a measurements done over a year with linear growth assumption according to the data presented at the Table 1. Finally elements were equipped with easy to use length regulation which is supposed to extend operation time to more then two years having in mind the child growth.

Table 1. 7 year old patient physical changes [9]

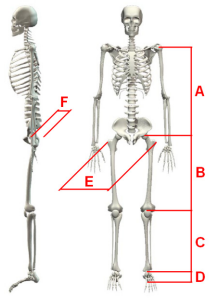	Dimension	Length at the year 2010 [mm]	Length at the year 2011 [mm]	Max. Length [mm]
	A	350	355	370
	B	260	270	320
	C	270	280	340
	D	45	50	60
	F	170	180	200
	F	90	0	100
Weight [kg]	–	18	20	24

3.4 Obtained Results

The main goal was to allow to generate a motion that is a set through the dedicated software running on the controller that is incorporated into the device. The apparatus helps to perform among others such exercises as walking with different speeds, strides with single limb, leg-cycle and squats. Without a valid and regular rehabilitation procedures abnormal muscle tone entailing secondary delays in the other areas of physical development. Our robot was already tested and confirmed its valid influence by:

- Straight line walking at different speeds program
- Feet coordination during a walk
- Counteracting reflex stepping on toes
- Preventing legs crossing

The device's elements can be adjusted to fit different age paediatric patients or to allow the device to “grow” with the patient. The adequate construction and software ensures that the patient is safe during the device's operation. The robot operations are intuitive and done using a touch-screen.

4 Summary

We create rehabilitation device other then any other available on the market. It is not only capable of forcing a valid set of limb movement, but at the same time allows ankle operation generating complex rehabilitation procedure. More importantly, presented on the Fig. 10 build by us robot, by its unique design is the only available at the market which does not force patient with its weight.

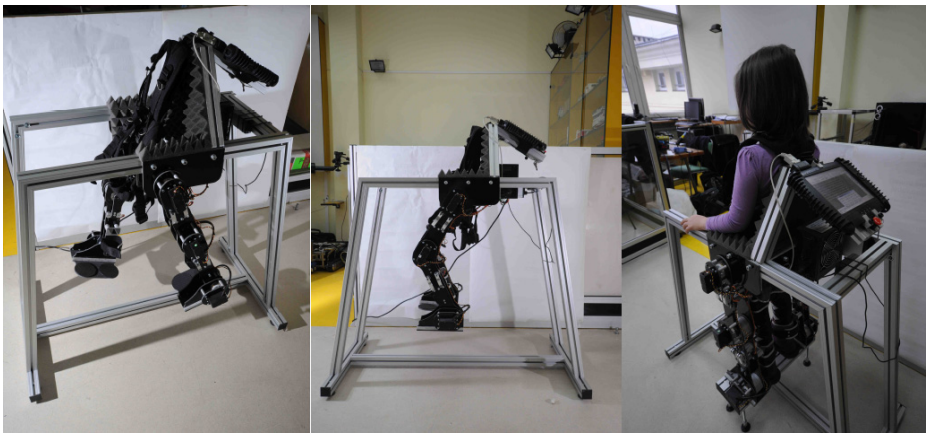

Fig. 10. Lower limb rehabilitation Robot

Our robot is used during a rehabilitation under the supervision of a physiotherapist and can be considered effective on the basis of his opinion. Moreover it was positively assed by physiotherapist and doctors. The positive reviews resulted in an award from Cracow District Medical Chamber and a positive opinion from Institute of Mother and Child. The master's thesis created during the development of the robot won the first prize during the 10th edition of the Polish nationwide competition "Open Doors" in the category of master's theses connected with rehabilitation and technological solutions benefiting the disable persons. During this anniversary competition organized by the State Fund for the Rehabilitation of the Disabled Persons the best master's and doctoral theses, whose research topics was the phenomenon of disability in the scope of work, health or society. The resulting solution is innovative and unique, real, working device, that meets safety standards and is based on anatomical limb motion and has the potential to change the effectiveness of long term rehabilitation and restore paediatric patients dexterity that will enable them function independently in a later life.

References

1. Bochenek, A., Reicher, M.: Human anatomy, vol. I. PZWL, Warszawa (2009) (in Polish)
2. Dega, W.: Orthopedics and rehabilitation. PZWL, Warszawa (1983) (in Polish)

3. Dellon, B., Matsuoka, Y.: Prosthetics, exoskeletons, and rehabilitation. IEEE Robotics & Automation Magazine (2007)
4. JIJI: Cyberdyne medical robot suit to make overseas debut in Germany (2013), http://www.japantimes.co.jp
5. Michałowicz, R.: The cerebral palsy. PZWL, Warszawa (2001) (in Polish)
6. Movement, M.F.: Nf-walker (2014), http://www.eo-funktion.pl/gfx/produkts/1/
7. Nooden, M.: Rutgers ankle robot (2009), http://njmonthly.com/articles/lifestyle/rutgers-ankle-robot.html
8. Ostrovsky, G.: Rewalk (2008), http://www.medgadget.com/2008/03/rewalk_exoskeleton.html
9. Piątek, G.: Conceptual project and construction of lower limb rehabilitation robot. Master's thesis, AGH Kraków (2012) (in Polish)
10. Reutimann, H.: Robotic technology helps patients with neurological injuries walk again. The Better World Report (2008)
11. Syczewska, M.: Rehabilitation diagnostics of children locomotion system. Standardy Medyczne 5 (2003) (in Polish)
12. University, E.: Rehabilitation robotics (2004), http://archiv.ethlife.ethz.ch/images/lokomat-l.jpg
13. Yang, S.: Berkeley lower extremity exoskeleton (2004), http://bleex.me.berkeley.edu

Some Problems of Navigation System for Criminalistic Robot

Robert Głębocki, Antoni Kopyt, and Paweł Kicman

Warsaw University of Technology, Faculty of Power and Aeronautical Engineering
akopyt@meil.pw.edu.pl

Abstract. In the paper authors presented some results of development of navigation system for criminalistic robot. Robot destination is to support police officers during forensic activities in the buildings when we have potential CBRN hazards. Robot is remotely controlled based on visual cameras observation but it has also autonomous navigation system. The robot is at the beginning of police action carry out hazard identification and, if they occur robot perform forensic activities. As part of its tasks is to make a photographic documentation of the event. This involves the registration status of the room a special 3D camera and take pictures of individual items and disclosed fingerprints. Then taken are indicated by the operator or the entire sample items. Charges are also forensic traces of biological and existing on-site chemicals substances. Robot should be able to perform most of the tasks normally performed by police forensic technicians. Big problem is when during forensic activities operator lost communications with the robot. By the existing on place CBRN hazards man can't enter the building where robot is lost. At this moment start work system of autonomy. Robot must return the same way how it arrive till the moment when operator will get communication with them again. The paper presents the autonomous control system that was created for visual navigation for police robot. The algorithm implemented on the platform already been simulated and tested in MATLAB/Simulink. The article presents the results of running the robot with the new algorithm.

Keywords: control systems, mobile robots, autonomy.

1 Introduction

The presented article is associated with construction of mobile robot for support police during forensic activity. Police in the place of the offense course leads meticulous work in collecting forensic evidence. Its results are very important in the police investigation and in very often are the basis for detection of the offender and the primary evidence in the judicial process. In the police practice, officers sometimes have the problem that at the crime place, there are hazards that make forensic activity impossible. Police cannot send technicians to collect forensic evidence. At the crime scene, very often there is a threat of presence of chemical, biological or radiological contamination. Another problem can be a presence of explosives [1]. Therefore, a need has

J. Awrejcewicz et al. (eds.), *Mechatronics: Ideas for Industrial Applications*,
Advances in Intelligent Systems and Computing 317, DOI: 10.1007/978-3-319-10990-9_18

arisen to project a robot for police forensic testing in hazardous conditions. Such forensic work usually performed in buildings [2]. There are often in basements where police have problems with access by obstacles such as stairs, household items and other objects.

The presented robot first role is detection pollution and other hazard in forensic place. If they occur robot should perform forensic activities and collect forensic evidence. A part of its tasks is to make a photographic documentation of the place. This involves the registration status of the room with a special 3D camera and take pictures of individual items and disclosed fingerprints. Then robot must takes indicated by the operator items or samples. Charges are also traces of biological and existing at the place chemicals. Robot should be able to perform most of the tasks normally performed by forensic technicians.

Robot must be easy in transport. It must be able to be transferred by two persons. With a small-size robot we are not able to put all the equipment on it at the same time. Therefore robot work is divided in different phases. Depending on the phase, its equipment is replaced. Robot decontamination must be also possible.

During police forensic action robot many times have to repeatedly commute and go to the forensic activity place, to gather and pass to secure the traces or samples. The variety of samples such as photographic recording of event traces microbiological mechanoskopic traces, traces of fingerprints, samples of the substance in the room, gathering some of the items from the scene for subsequent analysis, etc.

Work scenario provides multiple robotic missions during one inspection of the crime place. First, the platform enters the scene equipped with a set of sensors to verify the presence of CBRN hazards. If they are found , further work is also carried out through the robot.

In the first phase of his work robot is sent on a mission to recognize the existing hazards. At this phase it is equipped with sensors to detect the existence of potential hazards. It is equipped with a set of sensors to detect CBRN threats. Robot also has a navigation system that allows autonomous return along the same route when they arrived. Robot during action is controlled remotely by the operator, but due to the nature of work inside buildings and the risk of a loss of connectivity with operator it uses an additional module that allows a partially autonomous movement. Big problem is when during forensic activities operator lost communications with the robot. By the existing on place CBRN hazards man can't enter the building where robot is lost. At this moment start work the system of autonomy. Robot must return the same way how it arrive till the moment when operator will get communication with them again. Another reason is that when on the floor are a potentially important forensic traces they have not been erased by the action of the robot. Therefore, it is possible to withdrew their steps and passed through the room always on the same route during operation. This is important because the field of view of the operator is limited when operator control remotely the robot. Such a navigation module that allows partially autonomous work has been developed by a team from the Department of Automation and Aeronautical Systems of Warsaw University of Technology. Robot autonomous system is based on visual navigation, inertial and odometry [3]. Issues related to the operation of the system are subject to the considerations of this paper.

2 System Requirements

The aim of this work is to create a that supports the forensic investigations. Mobile robot that is to be used in the project has to collect data and samples from the terrain that is hard to explore by police units. In this particular use of robot, one of robots requirement is ability to return following of its own path. The mobile robot could start the return procedure in two options: when the operator wants to return without blurring of traces, or when operator-robot communication is lost. From the operational point of view the cause of the return does not impact on the autonomy system strategy. In both cases the return is realized in the same way. The operator can stop the automatic return if decides to go further by himself. In second case, of the communication is back, the automatic return is off.

In the final stage the non-GPS vision will be used to navigate the platform. Form the vision system the set of points will be registered while robot is moving. From those points the return path will be created.

3 Equipment

For the project purpose the GRYF platform (Fig. 1) is going to be applied as a mobile platform [4]. This platform is provided by PIAP (Industrial Research Institute for Automation and Measurements). The basic platform have been adopted for the project requirements. An additional handles for new optional external devices have been done. The early stage experiments have been conducted on a platform MOBOT. This platform is slightly smaller comparing to GRYF, but for the algorithm tests it did not impact on the results significantly. Both of the platforms works is the same manner. The platforms turn style resemble tank turning. Each of four wheels has its own electric motor. Both left and right pair of wheels are coupled. The control signal gives the proper voltage on teach pair of wheels. Change of direction is achieved by varying the speed between the left and right side wheels. Wheel speed range was set from –100 to 100, where the extreme values corresponds to maximum engine speeds. Due to the specific work conditions, mobile robot need to drive slowly. It is not required to move fast, so the robot does not blur the traces. Thereby, the maximum speed of wheels was limited to 50 %.

The platform is equipped with the PC-104 central unit. The whole, computing and registration system works on this computer. The control commands (start, stop, algorithm initial values, etc.) are sent to the platform from the external laptop via XStream-PKG radio modem device. The data that registered on the PC-104 were sent via WiFi to the laptop so the operator could see the actual parameters of the platform. Software sensors and main code was written in C++ environment.

For the test phase the MicroStrain IMU unit 3DM_GX3 device was used. The dynamic accuracy is close to 2 [degrees]. The key problem using such a device for positioning is the error that increase within the time. The data frame that is registered from the GX3 consists 3 linear accelerations and 3 angular speeds. It is obvious that double integrating acceleration will create a huge error. However in this particular test the accuracy of the position was not the issue [5].

Fig. 1. Mobile platform GRYF [4]

4 Control Algorithm

The control algorithm that has been developed is designed to maintain the desired course [6–8]. This course in the final stage of the project will be given from the vision navigation. In this article however, the method of selecting new waypoints is not presented. Following chapter shows the method used to keep vehicle going on the course. If this part is realized properly, and the platform follows the course good enough, adding the point from vision navigation will be proceeded.

The input values to the control law are: error between actual and desired course, K_1, K_2, M and REVERSE parameter. The parameter K_1 is a reference value for platform to chose the type of turn. The parameter K_2 is a proportional parameter amplifying the control signal. In the following trials this parameter was set to 1. The parameter M is a tolerance value that algorithm reads as an measurement error.

4.1 Platform Turning

The error value is simply the difference between the actual and desired course. The actual course is obtained from the GX-3 device. The error is calculated using a following expression:

$$E = \mathrm{K}_2 \cdot \left(\theta_{actual} - \theta_{desired}\right) \tag{1}$$

The platform by comparing difference between parameter M (initialized by the operator) and the E (eq. 2) decides if the turn should be performed. The parameter M in following tests was set to 1. If the condition (2) is true, the algorithm set the full speed to the wheels.

$$E < M \tag{2}$$

$$|E| > \mathrm{K}_1 \tag{3}$$

If the condition (2) is not true the platform starts to turn. At this point the algorithm selects the type of turn to perform. If the expression (3) is true, the platform turn aggressive. Such a type of turn is realized by giving the opposite turning sense for left and right pair of wheels. The platform though turn without forward speed. However if the condition (3) is not true, the turn is performed more gently.

5 Simulations

In the Simulink the proper model have been done (Fig. 2). The engine dynamics was estimated base on the trials previously made with the platform. The electric motor dynamics have been approximated by the first order system transfer function. The rising time (inertia of ht motor) have been derived from the previous test trials. The control algorithm that was represented as a m-file code in the Simulink model was later rewrite as a C++ code, and applied into the PC-104 console.

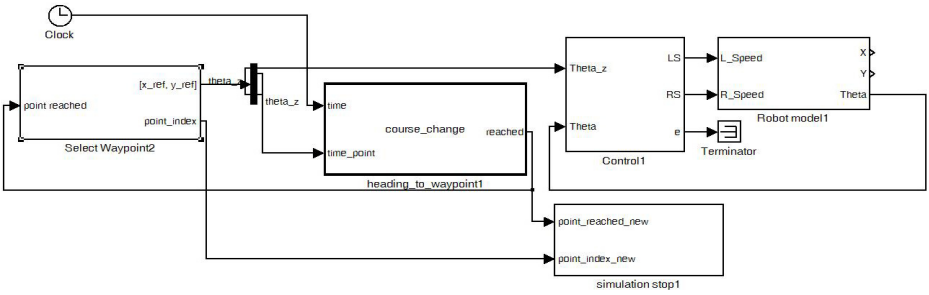

Fig. 2. Scheme of the Simulink model

The simulation allowed to adjust the control law parameters, so the robot ride, met the requirements. In the simulation, there was a possibility to simulate two types of riding: *point-to-point* and *course-time*. In first option an initial data was set of point that robot have to follow. In the second option, robot followed the desired course with the selected time duration. Both of the simulations corresponds to the real drive conditions. The driving style of mobile robot at this stage of the project corresponds to the second course-time option. With the vision navigation the driving would be changed to the *point-to-point* style.

6 Experiments

As the simulations allowed implementation on the robot computer, the test with the use of mobile platform was possible to conduct. This part was divided into two

phases. First, was to examine the algorithm on the MOBOT platform, on which the access to data and communication was easier. Secondly the similar trials were repeated on the GRYF platform at PIAP building.

6.1 MOBOT Test

This part of test were necessary to verify and validate the control laws applied to the platform. on the Fig. 3 three different trial from MOBOT tests are presented.

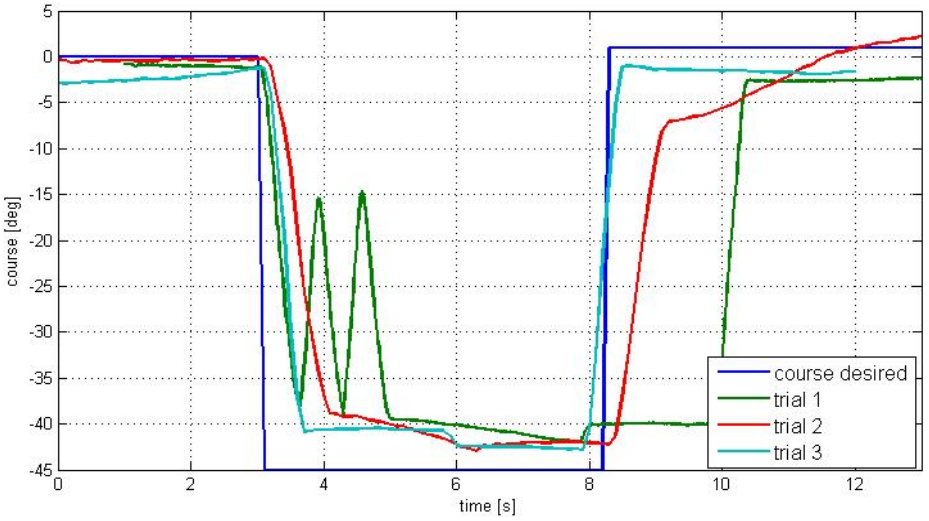

Fig. 3. Algorithm improvement

The dark blue line corresponds to the course desired, green line is the unadjusted algorithm, red line is the proper turning methods and light blue is the proper turning method with the parameters M, K_1 and K_2 properly established. On both (red and light blue) lines it is possible to notice the turn style changing moment – around 4th second. It is easier to see this occurrence on the Fig. 4, where the wheels speed is presented.

In 31th second the sudden change of the wheels turning is easy to be seen. In that particular moment the algorithm has send the information to perform an aggressive turn. Consequently, the sense of wheel rotation is different. Subsequently, when the error is not so big (expression 3 is not true) right wheels starts to catch up the left wheel speed.

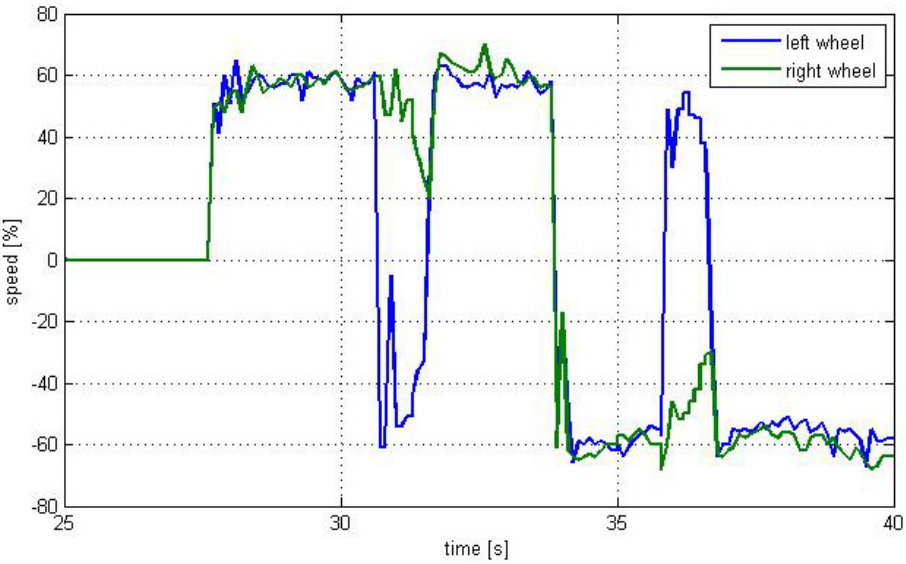

Fig. 4. Wheels speed [%]

6.2 GRYF Test

After communication, software and parameters validation on smaller platform, the appropriate test could have been conducted. First step was to create a communication between the PC-104 unit and the new platform. the pre-tests have been performed on similar platform, so there was very low risk that the platform would react completely different with algorithm prepared. Few verification tests confirmed that assumption. The results might be noticed at the Fig. 5. It is hardly possible to distinguish three different trials. Such a good results confirmed the algorithm action.

The next test that was conducted was further software development. The main action that the mobile robot has to perform is the autonomously return back. This action is realized when operator wants to back away or if the communication is lost. The action initialization is not a problem from a soft development. The first step have been accomplished (course following). The next step was to add a command that would force the platform to come back.

This feature is also possible to notice on the Fig. 5. The mobile robot had to go straight (course 0), than turn left (course 90), than turn left again (course 180), and then the special command was given (14^{th} second). From this point, platform had to come back on the same course. At the moment when robot gets the Reverse information the robot changes its sides: front is becomes back and vice versa. Such a feature is realized on the level of algorithm, where the parameter Reverse is changing sign from 1 to –1.

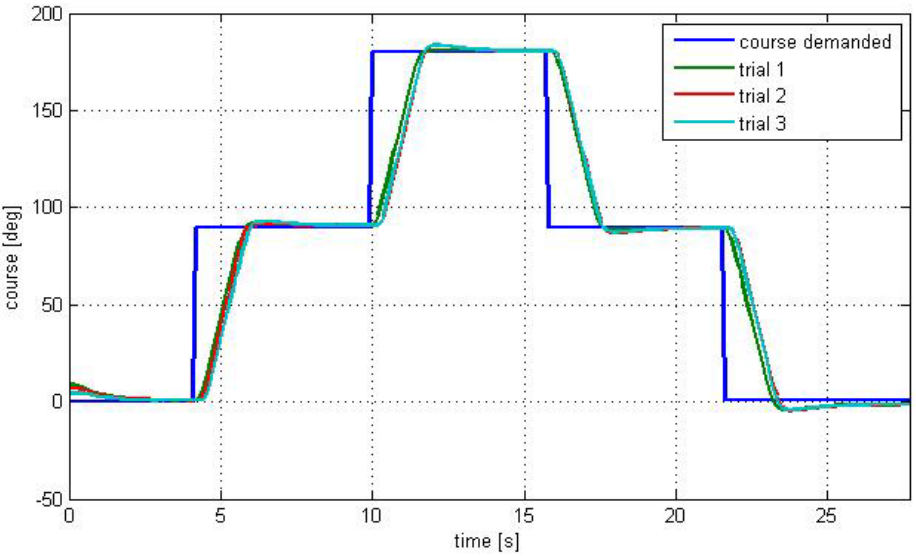

Fig. 5. Three trials – course following with GRYF platform

7 Summary

The paper presents the control algorithm for the mobile robot tested on two different platforms and in virtual environment. The results showed that the two types of turning increase robot performance and keep the ride smooth and without an oscillations. In this paper the automatic return by the same trace is presented. The presented results are basics for the vision navigation that is going to be done as a next step in the project.

Acknowledgement. The following research was done within project No. 0015/R/ID 1/2011/01, Sponsored by National Centre for Research and Development.

References

1. Port of Seattle Police Dept. Bomb Disposal Unit, SRS Presentation (January 2009)
2. Casper, J., Murphy, R.R.: Human – Robot Interaction During the Robot – Assisted Urban Search and Rescue Response at the World Trade Center. Army IEEE Transactions in System, Man, and Cybernetics – Part B: Cybernetics 33(3) (June 2003)
3. Głębocki, R., Kopyt, A., Kicman, P.: Koncepcja Platformy mobilnej do wsparcia badań kryminalistycznych. Szybkobieżne Pojazdy Gąsienicowe 1(32), 57–66 (2013)
4. http://www.antyterroryzm.com
5. Utsumo, T., Gravdahl, J.T.: Implementation and Control of Attitude Estimation Methods for Agricultural Robotics. Elsevier IFAC Publications/IFAC Proceedings series, vol. 4(1) (2013)

6. Seo, K., Lee, J.L.: Kinematic path-following control of mobile robot under bounded angular velocity error. Advanced Robotics 20(1), 1–23 (2006)
7. Nazemizadeh, M., Rahimi, H.N., Amini, K.: Trajectory planning of mobile robots using indirect solution of optimal control method in generalized point-to-point task. Frontiers of Mechanical Engineering 7(1), 23–28 (2012)
8. Klancar, G., Matko, D., Blazi, S.: Mobile Robot Control on a Reference Path. In: Mediterranean Conference on Control and Automation, Limassol, Cyprus, June 27-29 (2005)

Neural Network Control of a Four-Wheeled Mobile Robot Subject to Wheel Slip

Zenon Hendzel[1] and Maciej Trojnacki[2]

[1] Rzeszow University of Technology, Poland
zenhen@prz.edu.pl
[2] Industrial Research Institute for Automation and Measurements PIAP, Warsaw, Poland
mtrojnacki@piap.pl

Abstract. The paper presents design of a control structure that enables integration of a kinematic and a neural network controller for a four-wheeled mobile robot subject to wheels slip. The controller is proposed to make the actual velocity of the wheeled mobile robot reach the desired velocity, although the wheeled mobile robot is even with system uncertainties and disturbances. The proposed tracking control system consists of: the kinematic and proportional controller, the neural approximated term and robust term derived from the stability analysis carried out using Lyapunov stability theorem. The proposed control system works on-line, weights adaptation is realized in every discrete step of the control process, and a preliminary learning phase of neural networks weights is not required. Computer simulation was conducted to illustrate performance of the control system.

Keywords: mobile robot, tracking control, wheels' slip, Lyapunov stability, neural networks.

1 Introduction

Intelligent wheeled mobile robots are the subject of technical interest arising from possibility of practical applications in: manufacturing, civil engineering, transportation, agriculture, space exploration, deep sea penetration, help for disabled, medical surgery and in other sectors of science and technology. Application of modern methods of realization of motion of wheeled mobile robots, in which fundamental role is played by artificial intelligence methods, belongs to priority research direction in the field of modern technologies of autonomous robots. Despite significant advances in the field of autonomous robotics, still many problems remain unsolved. Most difficulties are associated with description of natural work environment of an autonomous robot. Usually, the knowledge about environment is, in general, incomplete, uncertain and approximate. To this field belong, for example, the problems concerning inclusion of the phenomena of mobile robot wheel slips into control algorithms. Recently, a lot of attention is devoted to the problems of modeling and control of wheeled mobile robots taking into account wheel slips [6, 8–10, 13–17], which follows from

J. Awrejcewicz et al. (eds.), *Mechatronics: Ideas for Industrial Applications*,
Advances in Intelligent Systems and Computing 317, DOI: 10.1007/978-3-319-10990-9_19

possibility of using those objects in practical applications, characterized, for instance, by irregular surfaces and various parameters of wheels contact with the ground.

In the present article the intelligent stable control system for position and heading of a four-wheeled mobile robot with inclusion of longitudinal and lateral slips is proposed, in which neural networks are used for compensation of nonlinearities and variable operating conditions of a mobile robot.

The structure of the article is as follows. In Section 2 basic kinematic relationships are discussed, and generalized velocities required for realization of the desired robot motion, understood as kinematic controller, are determined using the backstepping method. Dynamic equations of motion of a four-wheeled mobile robot taking into account wheel slips are given in Section 3. Section 4 concerns description of the adopted structure of neural network for compensation of robot nonlinearities. In Section 5 synthesis of tracking control of mobile robot is conducted and stability analysis of the control algorithm is carried out based on the Lyapunov theory. In Section 6 obtained results of simulations of the introduced solution are presented. Conclusions are given in Section 7.

2 Kinematic Controller for WMR

The object analyzed in the present article is a four-wheeled mobile robot. Diagram of its kinematic structure is shown in Fig. 1 [15].

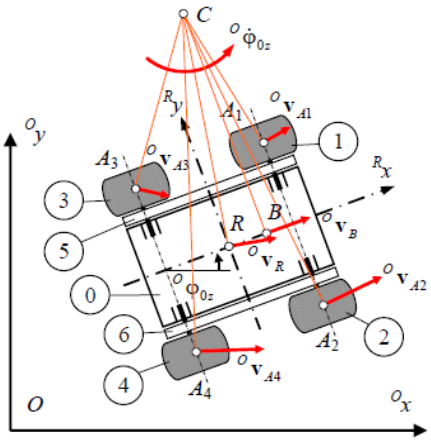

Fig. 1. Model of the analyzed robot

In the model, the following basic robot assemblies can be distinguished: 0 – mobile platform (body with additional control and measurement frame attached to it), 1–4 – wheels, 5–6 – toothed belts (caterpillars). In the analyzed robot, the front wheels are coupled with back wheels by means of the toothed belts.

The following symbols are adopted for i-th wheel: A_i – geometric centre, r_i – radius, θ_i – wheel spin angle. Mobile platform spin angle is denoted $^{o}\dot{\varphi}_{0z}$. It is assumed

that motion of the mobile robot occurs in the *Oxy* plane (as shown in Fig. 1). Position and orientation of the mobile platform are described by generalized coordinates vector:

$$ {}^{o}\mathbf{q} = \left[{}^{o}x_R,\ {}^{o}x_R,\ {}^{o}\varphi_{0z} \right]^T , \tag{1} $$

where: ${}^{o}x_R$, ${}^{o}y_R$ – coordinates of the point R of the mobile platform, $\varphi_z = {}^{o}\varphi_{0z}$ – spin angle of the mobile platform with respect to z-axis of stationary coordinate system $\{O\}$. Generalized velocities vector $\dot{\mathbf{q}}$ can be determined based on the value of velocity of motion of the point R of the robot along direction of x-axis of the $\{R\}$ system connected with the robot, that is v_R, and angular velocity of spin of the mobile platform, that is $\dot{\varphi}$, based on the kinematic equations of motion in the form:

$$ \dot{\mathbf{q}} = \begin{bmatrix} \dot{x}_R \\ \dot{y}_R \\ \dot{\varphi}_z \end{bmatrix} = \begin{bmatrix} \cos(\varphi_z) & 0 \\ \sin(\varphi_z) & 0 \\ 0 & 1 \end{bmatrix} \begin{bmatrix} v_R \\ \dot{\varphi} \end{bmatrix}. \tag{2} $$

The above equation is valid if robot moves on a horizontal ground. In the control of position and heading of the robot, one assumes that motion of the robot is realized based on the desired vector of its position and heading, which has the form:

$$ \mathbf{q}_d = \left[x_{Rd},\, x_{Rd},\, \varphi_d \right]^T , \tag{3} $$

where: x_{Rd}, y_{Rd} – desired coordinates of characteristic point R of the robot in the $\{O\}$ coordinate system in (m), $\varphi_d = {}^{o}\varphi_{0zd}$ – desired spin angle of the mobile platform with respect to z-axis of $\{O\}$ coordinate system in (rad).

In order to define the problem of tracking control, based on the relationship (2) let us define desired parameters of motion of the point R in the form of equation:

$$ \dot{\mathbf{q}}_d = \begin{bmatrix} \dot{x}_{Rd} \\ \dot{y}_{Rd} \\ \dot{\varphi}_d \end{bmatrix} = \begin{bmatrix} \cos(\varphi_d) & 0 \\ \sin(\varphi_d) & 0 \\ 0 & 1 \end{bmatrix} \begin{bmatrix} v_{Rd} \\ \omega_d \end{bmatrix}, \tag{4} $$

where: v_{Rd}, ω_d – respectively desired linear velocity of the characteristic point R of the robot in (m/s) and desired angular velocity of its mobile platform in (rad/s), in the stationary coordinate system $\{O\}$.

In the problem of tracking control one should determine vector of control of position and heading of the robot $\mathbf{u}_d = [v_s, \omega_s]^T$, such that $\mathbf{q} \to \mathbf{q}_d$ for $t \to \infty$. The errors of robot's position and heading in the coordinate system associated with the robot $\{R\}$ and in the stationary system $\{O\}$ can be determined from the relationship:

$$ \mathbf{q}_e = \begin{bmatrix} e_F \\ e_L \\ e_O \end{bmatrix} = \begin{bmatrix} \cos(\varphi_z) & \sin(\varphi_z) & 0 \\ -\sin(\varphi_z) & \cos(\varphi_z) & 0 \\ 0 & 0 & 1 \end{bmatrix} \begin{bmatrix} x_{Rd} - x_R \\ y_{Rd} - y_R \\ \varphi_{zd} - \varphi_z \end{bmatrix}, \tag{5} $$

where e_F, e_L, e_O are respectively longitudinal position error in (m), lateral position error in (m), and heading error in (rad).

Generalized velocities required for desired motion of the robot can be determined using various methods. A popular method used for this purpose is the so-called backstepping method [1, 2, 5, 12]. According to it, the vector of desired generalized velocities of motion of the robot's mobile platform expressed in the robot's coordinate system $\{R\}$ can be determined based on the following relationship [7]:

$$\mathbf{u}_d = \begin{bmatrix} v_s \\ \omega_s \end{bmatrix} = \begin{bmatrix} k_F e_F + v_{Rd}\cos(e_O) \\ \omega_d + k_L e_L v_{Rd} + k_O v_{Rd}\sin(e_O) \end{bmatrix}, \tag{6}$$

where: v_s, ω_s – desired velocities of robot motion expressed in the coordinate system $\{R\}$, that is, linear velocity of characteristic point R in (m/s) and angular velocity of the mobile platform in (rad/s), k_F (s^{-1}), k_L (rad/m^2), k_O (rad/m) – chosen positive parameters.

3 Dynamic Model of a WMR

In Fig. 2 a schematic diagram of the analyzed robot with marked reaction forces acting on the robot in the wheel-ground plane of contact is presented.

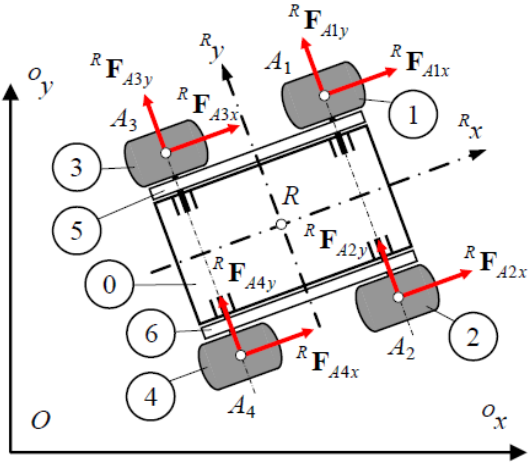

Fig. 2. Diagram of reaction forces acting on the robot in the wheel-ground contact plane

In description of motion of the four-wheeled robot it is assumed that tire-ground coefficient of adhesion changes according to the Kiencke model and values of longitudinal slip ratios λ_3, λ_4 depend respectively on angular velocities of driven wheels $\dot{\theta}_3$, $\dot{\theta}_4$ and longitudinal velocities of wheel centers $^O\mathbf{v}_{A3}$, $^O\mathbf{v}_{A4}$. Additionally, equality of driving torques for passive and active wheels is assumed, that is, $\tau_1 = \tau_3$ and $\tau_2 = \tau_4$.

After taking into account the above assumptions, dynamic equations of motion for the hybrid chassis system, i.e. with wheels and toothed belts, are written as [15]:

$$\begin{bmatrix} 2a_1 & 0 \\ 0 & 2a_1 \end{bmatrix}\begin{bmatrix} \ddot{\theta}_3 \\ \ddot{\theta}_4 \end{bmatrix}+\begin{bmatrix} 2a_2\,\mathrm{sgn}(\dot{\theta}_3)+4\lambda_p\lambda_3/(\lambda_p^2+\lambda_3^2)(a_3+a_4a_{Rx}-a_5a_{Ry})+ \\ +2(a_6+a_7a_{Rx}-a_8a_{Ry})\mathrm{sgn}(\dot{\theta}_3) \\ 2a_2\,\mathrm{sgn}(\dot{\theta}_4)+4\lambda_p\lambda_4/(\lambda_p^2+\lambda_4^2)(a_3+a_4a_{Rx}+a_5a_{Ry})+ \\ +2(a_6+a_7a_{Rx}+a_8a_{Ry})\mathrm{sgn}(\dot{\theta}_4) \end{bmatrix}=\begin{bmatrix} \tau_3 \\ \tau_4 \end{bmatrix}, \quad (7)$$

where $\lambda_p, a_{Rx}, a_{Ry}$ are respectively: a constant associated with model of wheel-ground adhesion, projections of acceleration of characteristic point R of the robot in the coordinate system associated with the robot $\{R\}$.

In turn, constants a_i that occur in equation (7) result from geometry, masses, distribution of masses of the analyzed robot and were determined in the work [15]. From kinematic relationships of the analyzed model of the mobile robot, one can determine angular velocities of driven wheels as functions of control signals that realize desired trajectory of robot's motion, according to the following relationship:

$$\begin{bmatrix} \dot{\theta}_3 \\ \dot{\theta}_4 \end{bmatrix}=\frac{1}{r}\begin{bmatrix} 1 & -W/2 \\ 1 & W/2 \end{bmatrix}\mathbf{u}_R, \quad (8)$$

where control signals' vector has the form:

$$\mathbf{u}_R=[v_R, \quad \omega]^T. \quad (9)$$

After introducing equation (8) into dynamic equations of motion of a mobile robot (7), one obtains:

$$\mathbf{M}\dot{\mathbf{u}}_R+\mathbf{F}_R(\mathbf{u}_R)+\boldsymbol{\tau}_z=\boldsymbol{\tau}, \qquad \mathbf{M}=\frac{1}{r}\begin{bmatrix} 2a_1 & -a_1W \\ 2a_1 & a_1W \end{bmatrix}, \quad (10)$$

where: $\mathbf{M}$ is a constant positive-definite inertia matrix, $\mathbf{F}_R(\mathbf{u}_R)\in\mathbf{R}^{2x1}$ is a vector describing robot nonlinearities, $\boldsymbol{\tau}_z\in\mathbf{R}^{2x1}$ denotes bounded unknown disturbances which include, for example, motion phenomena not taken into account in the description, $\boldsymbol{\tau}\in\mathbf{R}^{2x1}$ is control signals' vector identical with torques of robot driving wheels 3 and 4. Dimensionality of equation (10) results from assumption of active torques of wheels 3 and 4 and passive torques of wheels 1 and 2 being respectively equal.

4 Feed-Forward Neural Networks

Problems of control of wheeled mobile robots with inclusion of wheels' slips are complex and their solution requires application of complex methods. Because of lack of a systematic approach to analysis and synthesis of control of nonlinear systems so far, the artificial neural networks became an attractive tool used in theory of nonlinear systems. Neural networks owe their popularity to properties like: possibility of approximation of arbitrary nonlinear mappings, and ability of learning and adaptation.

Let us consider a neural network shown in Fig. 3.

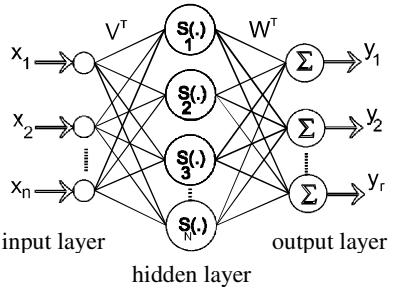

Fig. 3. Structure of a two-layer neural network

Input-output mapping for the network from Fig. 3 has the form [2, 11]:

$$y_i = \sum_{j=1}^{N} \left\{ w_{ij} S\left[\sum_{k=1}^{n} v_{jk} x_k + v_{vj} \right] + w_{wi} \right\}, \qquad i = 1,2,...,r. \tag{11}$$

After assuming the element of input vector $x_0 \equiv 1$ and the vector of threshold values $[v_{v1}, v_{v2}, ..., v_{vN}]^T$ as the first column of matrix $\mathbf{V}^T$, one obtains:

$$\mathbf{y} = \mathbf{W}^T \mathbf{S}\left(\mathbf{V}^T \mathbf{x}\right), \tag{12}$$

where $\mathbf{S} = \left[S_1(.), S_2(.),..., S_N(.)\right]^T$ is a vector of functions describing neurons, whose first element is equal to **1**, and vector $\left[w_{w1}, w_{w2},...w_{wr}\right]^T$ is the first column of matrix $\mathbf{W}^T$.

From mathematical point of view, a two-layer neural network is able to approximate any continuous nonlinear function of several variables. An arbitrary continuous function $f : D_f \subset \mathbf{R}^n \to \mathbf{R}^r$, where D_f is a compact subset of $\mathbf{R}^n$, can be approximated with arbitrary accuracy by two-layer neural network with appropriately chosen weights [11]. That is, for a given compact set D_f and a positive value of the approximation error $\boldsymbol{\varepsilon}$, there exists a two-layer neural network, such that the nonlinear function $\mathbf{f}(\mathbf{x})$ can be written as:

$$\mathbf{f}(\mathbf{x}) = \mathbf{W}^T \mathbf{S}\left(\mathbf{V}^T \mathbf{x}\right) + \boldsymbol{\varepsilon}, \tag{13}$$

for $\| \boldsymbol{\varepsilon} \| < \varepsilon_N$.

If weights of the first layer of the network $\mathbf{V}^T$ (12) are determined with certain method (e.g. randomly selected) and subsequently fixed, then weights $\mathbf{W}^T$ of the second layer of the network define its properties, and then it is a single-layer network. If one puts $\boldsymbol{\varphi}(\mathbf{x}) = \mathbf{S}\left(\mathbf{V}^T \mathbf{x}\right)$, then the relationship (12) can be written as:

$$\mathbf{y} = \mathbf{W}^T \boldsymbol{\varphi}(\mathbf{x}), \tag{14}$$

where $\mathbf{x} \in \mathbf{R}^n$, $\mathbf{y} \in \mathbf{R}^m$, $\boldsymbol{\varphi}(.): \mathbf{R}^n \to \mathbf{R}^L$ and L is a number of neurons in the hidden layer.

Network like that is linear with respect to its parameters ($\mathbf{W}^T$ weights). The form (14) will be adopted to approximate robot nonlinearities in the further analysis.

5 Control Algorithm and Stability

In the present section, the synthesis of control of position and heading of a wheeled mobile robot using the control structure of nonlinear systems will be conducted, which takes into account compensation for robot nonlinearities realized by means of the neural network linear with respect to weights described in Section 4. The task of this control will be the reduction of the actual control vector (9) to the control vector resulting from analysis of kinematics (6). To this end, let us define the velocity tracking error:

$$\mathbf{s} = \mathbf{u}_d - \mathbf{u}_R . \tag{15}$$

After differentiating relationship (15) and inserting it into (7), one obtains dynamic equations of motion written as a function of the velocity error:

$$\mathbf{M}\dot{\mathbf{s}} = \mathbf{f}(\mathbf{x}) + \boldsymbol{\tau}_z - \boldsymbol{\tau} , \tag{16}$$

where nonlinear function has the form:

$$\mathbf{f}(\mathbf{x}) = \mathbf{M}\dot{\mathbf{u}}_d + \mathbf{F}(\mathbf{u}_R) . \tag{17}$$

Vector $\mathbf{x}$ allowing determination of value of the nonlinear function can be defined as:

$$\mathbf{x} = \left[\dot{\mathbf{u}}_d{}^T, \mathbf{u}_R{}^T\right]^T \tag{18}$$

and it should be available for measurement.

The function $\mathbf{f}(\mathbf{x})$ involves all parameters of the analyzed wheeled mobile robot such as masses, mass moments of inertia, coefficients of motion resistance, description of the slip phenomenon. Quantities of this kind usually can be described only in an approximate way. Because the function $\mathbf{f}(\mathbf{x})$ is described in approximate way, if one adopts law of control with inclusion of this approximation in the form:

$$\boldsymbol{\tau} = \hat{\mathbf{f}}(\mathbf{x}) + k_p \mathbf{s} - \boldsymbol{\delta} , \tag{19}$$

where $\hat{\mathbf{f}}(\mathbf{x})$ is an output of neural network, k_p is a positive-definite diagonal matrix, and $\boldsymbol{\delta}$ is a control signal robust to non-modeled phenomena and other disturbances, then description of a closed system one may express as:

$$\mathbf{M}\dot{\mathbf{s}} = -k_p \mathbf{s} + \tilde{\mathbf{f}}(\mathbf{x}) + \boldsymbol{\tau}_z + \boldsymbol{\delta} \tag{20}$$

where velocity tracking error **s** in a significant way will depend on correct approximation of robot nonlinearities.

Approximation of the control compensating for nonlinearities **f**(**x**) is often applied in practice. For the approximation a neural network may be used. It is convenient to use neural network linear with respect to weights, described in section 4. Then, the nonlinear function approximated by the neural network one can write in the form:

$$\mathbf{f}(\mathbf{x}) = \mathbf{W}^{\mathrm{T}}\boldsymbol{\varphi}(\mathbf{x}) + \boldsymbol{\varepsilon}, \tag{21}$$

where $\boldsymbol{\varepsilon}$ is approximation error satisfying condition $\|\boldsymbol{\varepsilon}\| \le \varepsilon_N$, $\varepsilon_N = \text{const} > 0$.

The estimate of the **f**(**x**) function can be written as:

$$\hat{\mathbf{f}}(\mathbf{x}) = \hat{\mathbf{W}}^{\mathrm{T}}\boldsymbol{\varphi}(\mathbf{x}), \tag{22}$$

where $\hat{\mathbf{W}}$ is the matrix of estimated weights of an ideal neural network.

After using (22) in the control law with robot's nonlinearities compensation, the control law in the following form is obtained:

$$\boldsymbol{\tau} = \hat{\mathbf{W}}^{\mathrm{T}}\boldsymbol{\varphi}(\mathbf{x}) + k_p\mathbf{s} - \boldsymbol{\delta}. \tag{23}$$

Substitution of (21) and (22) into (20) yields:

$$\mathbf{M}\dot{\mathbf{s}} + k_p\mathbf{s} = \tilde{\mathbf{f}}(\mathbf{x}) + \boldsymbol{\tau}_z + \boldsymbol{\delta}, \tag{24}$$

where $\tilde{\mathbf{f}}(\mathbf{x})$ is an error of approximation of **f**(**x**) function, equal to:

$$\tilde{\mathbf{f}}(\mathbf{x}) = \mathbf{f}(\mathbf{x}) - \hat{\mathbf{f}}(\mathbf{x}) = \mathbf{W}^{\mathrm{T}}\boldsymbol{\varphi}(\mathbf{x}) - \hat{\mathbf{W}}^{\mathrm{T}}\boldsymbol{\varphi}(\mathbf{x}) + \boldsymbol{\varepsilon} = \tilde{\mathbf{W}}^{\mathrm{T}}\boldsymbol{\varphi}(\mathbf{x}) + \boldsymbol{\varepsilon}, \tag{25}$$

where $\tilde{\mathbf{W}} = \mathbf{W} - \hat{\mathbf{W}}$ is an error of estimation of weights of the neural network.

After using relationship (25), equation (24) is written as:

$$\mathbf{M}\dot{\mathbf{s}} + k_p\mathbf{s} = \tilde{\mathbf{W}}^{\mathrm{T}}\boldsymbol{\varphi}(\mathbf{x}) + \boldsymbol{\varepsilon} + \boldsymbol{\tau}_z + \boldsymbol{\delta}. \tag{26}$$

Structure of the system for neural network control of robot generalized velocities is shown in Fig. 4.

For derivation of an algorithm of $\hat{\mathbf{W}}$ weights learning, the theory of Lyapunov stability is used. Let us take a scalar positive-definite function:

$$V = \frac{1}{2}\mathbf{s}^{\mathrm{T}}\mathbf{M}\mathbf{s} + \frac{1}{2}\mathrm{tr}\left(\tilde{\mathbf{W}}^{\mathrm{T}}\mathbf{F}^{-1}\tilde{\mathbf{W}}\right) + k_F\left(e_F^2 + e_L^2\right) + 2k_O v_{Rd}\left(1 - \cos(e_O)\right), \tag{27}$$

where $\mathbf{F} = \mathbf{F}^{\mathrm{T}} > 0$ is a design matrix.

A derivative of *V* function with respect to time, one can write as:

$$\dot{V} = \mathbf{s}^{\mathrm{T}}\mathbf{M}\dot{\mathbf{s}} + \mathrm{tr}\left(\tilde{\mathbf{W}}^{\mathrm{T}}\mathbf{F}^{-1}\dot{\tilde{\mathbf{W}}}\right) + 2k_F\left(e_F\dot{e}_F + e_L\dot{e}_L\right) + 2k_O v_{Rd}\dot{e}_O\sin(e_O). \tag{28}$$

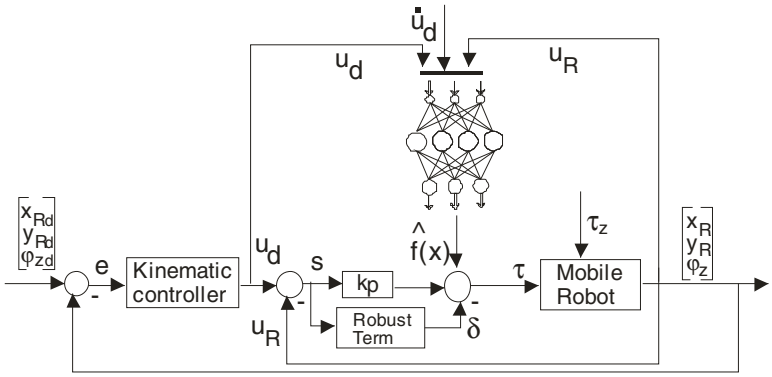

Fig. 4. Neural network control system

After inserting expression for $\mathbf{M}\dot{\mathbf{s}}$ from equation (26), one obtains:

$$\dot{V} = -\mathbf{s}^{\mathrm{T}} k_p \dot{\mathbf{s}} + \mathrm{tr}\left(\tilde{\mathbf{W}}^{\mathrm{T}} \mathbf{F}^{-1} \dot{\tilde{\mathbf{W}}} + \boldsymbol{\varphi}(\mathbf{x})\mathbf{s}^T\right) + \mathbf{s}^T\left(\boldsymbol{\varepsilon} + \boldsymbol{\tau}_z + \boldsymbol{\delta}\right) + \\ + 2k_F\left(e_F \dot{e}_F + e_L \dot{e}_L\right) + 2k_O v_{Rd} \dot{e}_O \sin(e_O). \tag{29}$$

After choosing law of adaptation of neural network weights as:

$$\dot{\tilde{\mathbf{W}}} = -\mathbf{F}\boldsymbol{\varphi}(\mathbf{x})\mathbf{s}^{\mathrm{T}} \tag{30}$$

and after introducing the robust control signal:

$$\boldsymbol{\delta} = -\left(\varepsilon_m + Z\right)\mathbf{s}/\|\mathbf{s}\| - \mathbf{s}\,, \tag{31}$$

where it was assumed that $\|\boldsymbol{\varepsilon}\| \le \varepsilon_m, \|\boldsymbol{\tau}_z\| \le Z$, relationship (29) is transformed into the form:

$$\dot{V} = -\mathbf{s}^{\mathrm{T}} k_p \dot{\mathbf{s}} + \mathrm{tr}\left(\tilde{\mathbf{W}}^{\mathrm{T}} \mathbf{F}^{-1} \dot{\tilde{\mathbf{W}}} + \boldsymbol{\varphi}(\mathbf{x})\mathbf{s}^T\right) + \mathbf{s}^T\left(\boldsymbol{\varepsilon} + \boldsymbol{\tau}_z\right) + \\ + 2k_F\left(e_F \dot{e}_F + e_L \dot{e}_L\right) + 2k_O v_{Rd} \dot{e}_O \sin(e_O) - \mathbf{s}^T\mathbf{s} - \mathbf{s}^T\left(\varepsilon_m + Z\right)\mathbf{s}/\|\mathbf{s}\| \tag{32}$$

After writing in expanded form the error of desired velocities (15) as:

$$\begin{bmatrix} s_1 \\ s_2 \end{bmatrix} = \begin{bmatrix} u_{d1} - u_{R1} \\ u_{d2} - u_{R2} \end{bmatrix} \tag{33}$$

and after determining a derivative of error (15), and putting $k_F = k_L k_O \omega_d$, one gets:

$$\dot{V} \le -k_F^2 e_F^2 - k_O^2 v_{Rd}^2 \sin^2(e_O) - k_L^2 v_{Rd}^2 e_L^2 - \left(k_F e_F - s_1\right)^2 - \left(k_O v_{Rd} \sin(e_O) - s_2\right)^2 + \\ + \|\boldsymbol{\varepsilon} + \boldsymbol{\tau}_z\|\|\mathbf{s}\| - \left(\varepsilon_m + Z\right)\|\mathbf{s}\| - k_{p\min}\|\mathbf{s}\|^2 \tag{34}$$

Because the first 5 terms of the derivative (34) are negative, eventually one obtains:

$$\dot{V} \le -k_{pmin}\left\|\mathbf{s}\right\|^2 - \left(\varepsilon_{\mathrm{m}} + Z\right)\left\|\mathbf{s}\right\| + \left\|\boldsymbol{\varepsilon} + \boldsymbol{\tau}_z\right\|\left\|\mathbf{s}\right\|, \tag{35}$$

where k_{pmin} is a minimum eigenvalue of the k_p matrix.

From relationship (35) it follows that derivative of the Lyapunov function is negative-semidefinite for $\left\|\mathbf{s}\right\| \neq 0$ and signals of control error $\mathbf{s}$ and weights of neural network $\hat{\mathbf{W}}$ are bounded. It means that the error of velocity control (15) is uniformly ultimately bounded (UUB) [12]. By increasing the minimum element of matrix k_p it is possible to decrease the tracking error $\mathbf{s}$. Such a synthesis of the adaptive neural network control permits proper operation of the control system with proportional controller, until the neural network starts adapting.

In practice, in order to guarantee that the robot stops when desired velocities are equal to zero, one can modify the control law (23) to the following form:

$$\boldsymbol{\tau} = \boldsymbol{\Theta}\left(\hat{\mathbf{W}}^{\mathrm{T}}\boldsymbol{\varphi}(\mathbf{x}) + k_p\mathbf{s} - \boldsymbol{\delta}\right), \tag{36}$$

that is, introduce matrix:

$$\boldsymbol{\Theta} = \mathrm{diag}(|\mathrm{sgn}(u_{d1})|, |\mathrm{sgn}(u_{d2})|). \tag{37}$$

Without this additional matrix, if the tracking error is different from zero, the robot still receives control signals, which results in its unintended movement continued for some time. Introduction of this matrix does not have any negative influence on stability of the proposed control system.

6 Simulation Results

For use in simulation investigations one assumes the following robot parameters:

- geometric dimensions ($A_1A_3 = A_2A_4 = L$, $A_1A_2 = A_3A_4 = W$ – see Fig. 1), $L = 0.35$ m, $W = 0.386$ m, $r_i = 0.0965$ m, $i = \{1, \ldots, 4\}$,
- masses of particular bodies: $m_0 = 15.02$ kg, $m_i = 0.66$ kg, $m_5 = m_6 = 0.17$ kg,
- rolling resistance coefficient $f_r = 0.03$,

whereas the constants a_i occurring in equation (7) were determined using methodology described in works [3, 4].

The following values of gains for the controller were assumed: $k_L = 15$, $k_F = 10$, $k_O = 5$, $k_p = \mathrm{diag}(20, 20)$.

Desired motion parameters of robot's wheels, kinematic parameters of the point R and motion path of the point R are shown in Fig. 5.

In simulation three phases of motion are assumed: acceleration, motion with constant velocity of the point R ($v_R = 0.3\,\mathrm{m/s}$) and braking. For approximation of nonlinearities and variable robot operating conditions, the neural network described in

section 4 is used with sigmoid functions describing neurons, assuming each element of the **f** vector is approximated with 6 neurons. In the simulation, parametric disturbance occurring for $t \geq 12\ s$ is assumed in the form of increase in rolling resistance coefficient by $\Delta f_r = 0.03$, when the characteristic point R of the robot moves along curvilinear path.

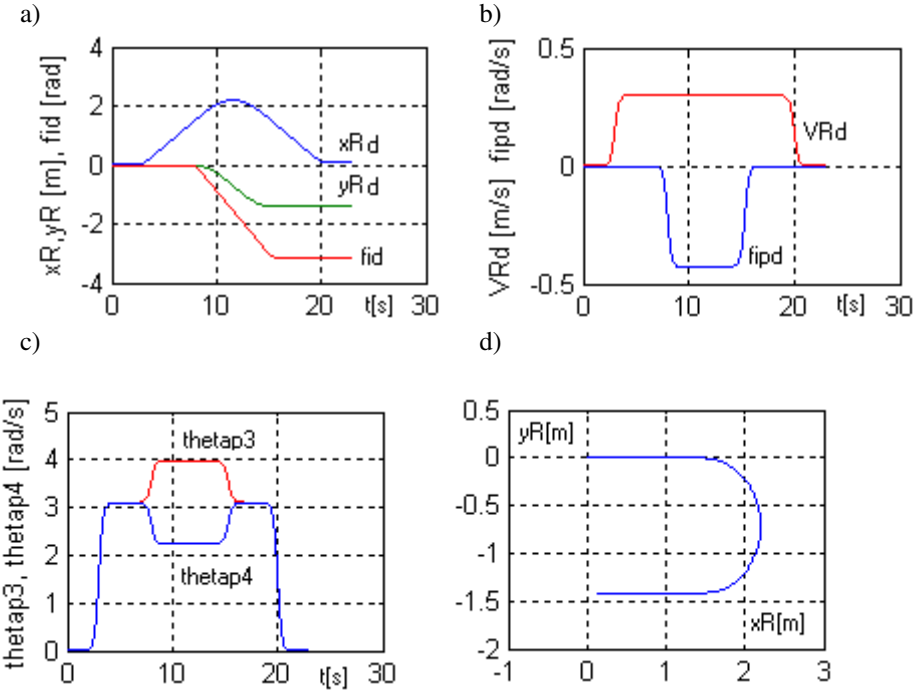

Fig. 5. Desired kinematic quantities used in simulation: a) coordinates of the point R and robot's course, b) desired velocities: linear of the point R, and angular of the robot's body, c) theoretical angular velocities of driven wheels (for non-slipping conditions), d) desired motion path of the point R

In Fig. 6 are shown obtained control signals, and in Fig. 7, errors of neural control of position and heading of the robot.

The obtained control signals τ_3, τ_4 (i.e., desired torques for driven wheels) that realize desired trajectory of motion of the point R of the mobile robot are shown in Fig. 6a. Values of torques are the largest during motion of the mobile robot along circular trajectory, their value is constant until the occurrence of a parametric disturbance. This corresponds to robot motion with constant velocity.

At the moment of occurrence of the parametric disturbance, value of the τ_3 torque increases whereas value of the τ_4 torque decreases, which results from increase of the

adopted motion resistance. For time $t \geq 12$ s values of torques decrease, which corresponds to the phase of braking and finishing motion along rectilinear path.

The discussed total control signals are generated based on control signals compensating for robot nonlinearities shown in Fig. 6b, signals generated by P-type controller (Fig. 6c), and robust control signals (Fig. 6d).

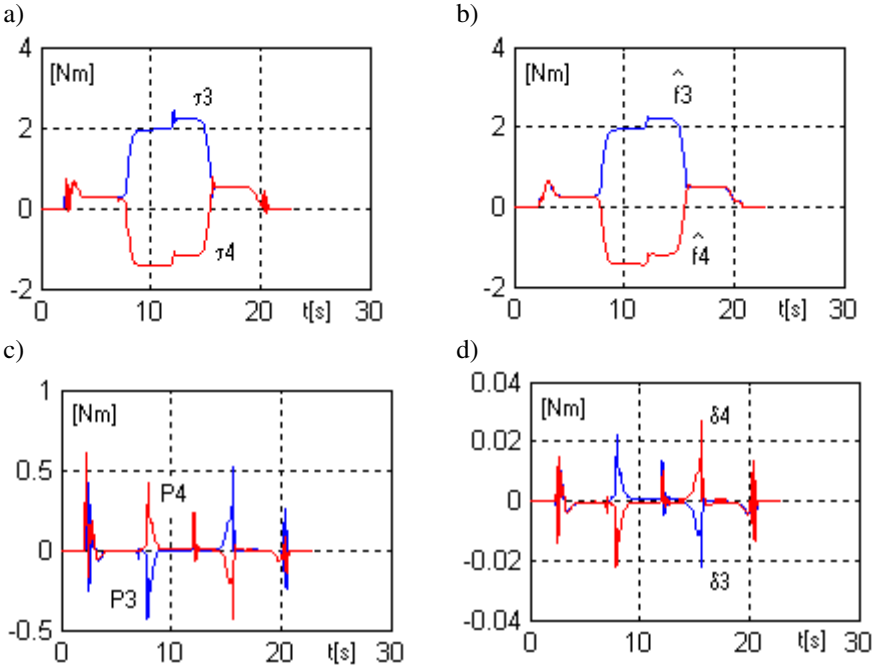

Fig. 6. Control signals: a) total control signals calculated according to relationship (23), b) control signals compensating for robot nonlinearities, c) signals generated by P-type controller, d) robust control signals

The neural compensation control has the largest influence on the total control signals, as far as level and character are concerned. In turn, the stabilizing P control and robust $\boldsymbol{\delta}$ control have the largest values during periods of occurrence of disturbances associated with wheels' slips or resulting from the character of desired velocity, desired motion path or the occurring parametric disturbances. It follows from the fact that in those motion states, the weights of neural network adapt to changing operating conditions of the robot, and only after the adaptation period the neural network generates dominant control signals. This fact of significance of influence of neural compensating control on overall quality of control is confirmed by results shown in Fig. 7a-c, in which errors of neural control of position and heading of the robot are presented.

Error values are the largest during period of motion along circular trajectory, and then as the process of adaptation of weights of the neural network progresses, they

decrease. The occurring parametric disturbance as well as changing robot operating conditions, excite the proposed control structure, which as a result generates control signals that make the control errors e_{xR}, e_{yR}, e_{φ} bounded, which confirms the theoretical considerations.

In Fig. 7d are shown the desired and actual paths realized with small errors, marked as 'trajd' and 'traj', respectively.

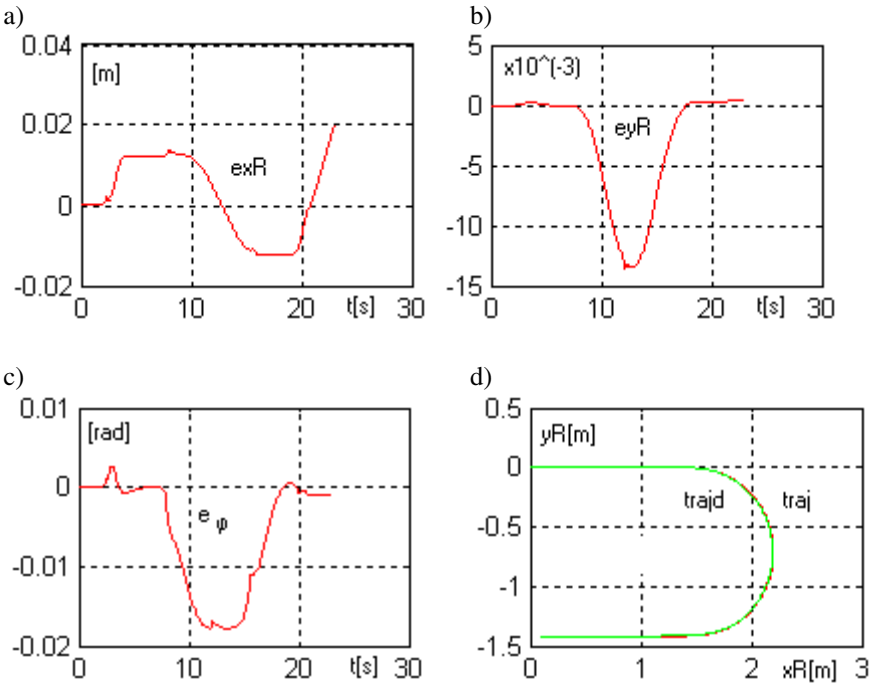

Fig. 7. Accuracy of robot motion: a-c) errors of neural control of robot's position and course, d) desired and actual motion paths

For quantitative evaluation of the generated control signals and realized tracking motion, the following quality indices are introduced:

- maximum values of the errors e_{xRmax}, e_{yRmax} in (m) and $e_{\varphi max}$ in (rad),

$$e_{(.)max} = \text{abs}(e_{(.)}(k)), \quad k = 1,2,\ldots n,$$

- the square root of the mean squared error (RMSE) of motion realization

$$e_{xR} = \sqrt{\frac{1}{n}\sum_{k=1}^{n}\left(x_{Rd}(k) - x_R(k)\right)^2} \quad \text{(m)},$$

$$e_{yR} = \sqrt{\frac{1}{n}\sum_{k=1}^{n}\left(y_{Rd}(k) - y_R(k)\right)^2} \quad \text{(m)},$$

$$e_{\varphi} = \sqrt{\frac{1}{n}\sum_{k=1}^{n}\left(\varphi_d(k)\text{-}\varphi(k)\right)^2} \text{ (rad)},$$

where k is the ordinal number of a discrete value and n = 23,000 is the total number of discrete values.

Values of all quality indices of realization of tracking motion for the neural network control system are given in Table 1, while analogous quality indexes for the control system without compensation for robot nonlinearities, that is, without neural network, are shown in Table 2.

Presented results indicate that the proposed neural network control system guarantees high accuracy of realization of tracking motion.

Table 1. Values of the introduced quality indices for neural network control system

e_{xR}	e_{yR}	e_{φ}	e_{xRmax}	e_{yRmax}	$e_{\varphi max}$
0.01009	0.005422	0.01001	0.02037	0.01355	0.01779

Table 2. Values of the introduced quality indices for control system without compensation for robot nonlinearities

e_{xR}	e_{yR}	e_{φ}	e_{xRmax}	e_{yRmax}	$e_{\varphi max}$
0.01304	0.009224	0.00200	0.02218	0.02253	0.04471

7 Conclusions

In the article a stable algorithm of control of position and heading in tracking motion of a four-wheeled mobile robot is designed. In the algorithm, the neural network linear with respect to estimated weights is used. The algorithm does not require prior knowledge of dynamic properties of the controlled object and is robust to occurring longitudinal and lateral slips of wheels as well as to parametric disturbances. Results of conducted simulation investigations lead to the conclusion that intelligent control with correctly designed kinematic controller significantly increases accuracy of realization of tracking motion. Additionally, the proposed neural control algorithm operates on-line and does not require initial learning of neural network weights.

Acknowledgements. The work has been realized as a part of the project entitled "Dynamics modeling of four-wheeled mobile robot and tracking control of its motion with limitation of wheels slip". The project is financed from the means of National Science Centre of Poland granted on the basis of decision number DEC-2011/03/B/ST7/02532.

References

1. Canudas de Wit, C., Siciliano, B., Bastin, G.: Theory of robot control. Springer (1997)
2. Fierro, R., Lewis, F.L.: Control of a nonholonomic mobile robot using neural networks. IEEE Trans. Neural Networks, 589–600 (1998)
3. Hendzel, Z., Pierlak, P.: Sterowanie robotów kołowych i manipulacyjnych (Control of wheeled and manipulating robots). Oficyna Wydawnicza Politechniki Rzeszowskiej (2011) (in Polish)
4. Hendzel, Z.: An adaptive critic neural network for motion control of a wheeled mobile robot. Nonlinear Dynamic (2007), doi:10.1007/s11071-007-9234-1
5. Jiang, Z.P., Nijmeijew, H.: Tracking control of mobile robots: a case study in backstepping. Automatica, 1393–1399 (1997)
6. Jung, S., Hsia, T.C.: Explicit lateral force control of an autonomous mobile robot with slip. In: IEEE/RSJ Int. Conf. on Intelligent Robots and Systems, IROS 2005, pp. 388–393 (2005)
7. Kanayama, Y., Kimura, Y., Miyazaki, F., Noguchi, T.: A stable tracking control method for an autonomous mobile robot. In: IEEE International Conference on Robotics and Automation, Cincinnati, OH, USA, pp. 384–389 (1990)
8. Li, L., Wang, F.Y.: Integrated longitudinal and lateral tire/road friction modeling and monitoring for vehicle motion control. IEEE Trans. on Intelligent Transportation Systems 7(1), 1–19 (2006)
9. Lin, W.-S., Chang, L.-H., Yang, P.-C.: Adaptive critic anti-slip control of wheeled autonomous robot. Control Theory & Applications, IET 1(1), 51–57 (2007)
10. Lucet, E., Grand, C., Bidaud, P.: Sliding-Mode Velocity and Yaw Control of a 4WD Skid-Steering Mobile Robot. In: Angeles, J., Boulet, B., Clark, J.J., Kövecses, J., Siddiqi, K. (eds.) Brain, Body and Machine. AISC, vol. 83, pp. 247–258. Springer, Heidelberg (2010)
11. Levis, F.L., Liu, K., Yesildirek, A.: Neural net robot controller with guaranteed tracking performance. IEEE Transaction on Neural Networks 6(3), 703–715 (1995)
12. Maalouf, E., Saad, M., Saliah, H.: A Higher Level Path Tracking Controller for a Four-Wheel Differentially Steered Mobile Robot. Robotics and Autonomous Systems 54(1), 23–33 (2006)
13. Sidek, N.: Dynamic modeling and control of nonholonomic wheeled mobile robot subjected to wheel slip. PhD thesis, Vanderbilt University, USA (2008)
14. Tian, Y., Sarkar, N.: Control of a mobile robot subject to wheel slip. Journal of Intelligent & Robotic Systems (2013), doi:10.1007/s10846-013-9871-1
15. Trojnacki, M.: Modelowanie dynamiki mobilnych robotów kołowych (Dynamics modeling of wheeled mobile robots). OW PIAP, Warszawa (2013) (in Polish)
16. Yi, J., Song, D., Zhang, J., Goodwin, Z.: Adaptive Trajectory Tracking Control of Skid-Steered Mobile Robots. IEEE International Conference on Robotics and Automation, 2605–2610 (2007)
17. Zadarnowska, K., Oleksy, A.: Motion planning of wheeled mobile robots subject to slipping. Journal of Automation Mobile Robotics and Intelligent Systems 5(3), 49–58 (2011)

Advanced Task Tracking Control Design for Robotic-Like Systems

Elżbieta Jarzębowska

Warsaw University of Technology, Institute of Aeronautics and Applied Mechanics,
00-665 Warsaw, Nowowiejska 24 st., Poland
elajarz@meil.pw.edu.pl

Abstract. The paper presents an advanced control design platform for tracking predefined tasks for a class of servicing systems referred to as robotic-like. A common feature of these ground, space or underwater systems is that they are designed to perform a variety of tasks and missions, so they all can be viewed as constrained systems. The control platform takes advantage of model-based control for constrained systems, either on a dynamics or kinematics level. The models are control-oriented what means that they account for tasks to be controlled and all other constraints put on systems or controller properties. The control platform is a fusion of an advanced modeling method for constrained systems and a new control strategy for tracking predefined tasks. It outperforms existing control methods since constraints on systems may be of an arbitrary order and type, and a constrained dynamics is in a reduced-state form, so it is ready for a controller design. A control implementation may rely upon embedded robotics which provides small and inexpensive embedded computer systems for control execution. The control design conforms then to modern mechatronics solutions that enable realizations of sophisticated control algorithms. Examples of controller designs for robotic-like systems and the control platform comparison to the traditional, Lagrange model-based method are presented.

Keywords: nonholonomic robotic-like system models, task-based constraints, quasi-coordinates, model reference tracking control strategy.

1 Introduction

Robotic-like systems perform a diversity of man servicing functions. They provide work and service, assistance and surveillance, go into hazardous environment underground and underwater, and many more. They are designed and built for industry and business goals, for research, development, and knowledge increase in variety of research areas, e.g. they mimic and reproduce some of properties biological systems generated and improved in evolution, enable getting a new insight into the Nature, take advantage of "the best" living organisms properties and use them to design systems that serve humans. We want them being more and more advanced, more reliable, and more perfect. In order to do the work they are designed to, robotic-like systems are all controlled. The demands on them make them more and more sophisticated. It makes them challenging from modeling, analysis, identification, and task-based tracking control points of view.

J. Awrejcewicz et al. (eds.), *Mechatronics: Ideas for Industrial Applications*,
Advances in Intelligent Systems and Computing 317, DOI: 10.1007/978-3-319-10990-9_20

It is critical then to have effective robotic-like system models, reliable control algorithms and their easy ways of implementations. These are then the main premises and motivations to review the modeling and control design ways for a wide class of robotic-like systems.

One more motivation for the reviewing modeling and ways of control designs for robotic-like systems is that they are constrained systems which, from the perspective of mechanics and derivation of equations of motion, may belong to the same class, e.g. be subjected to first order nonholonomic constraints. However, from the perspective of nonlinear control theory, they may differ and may not be approached by the same control strategies and algorithms. Their control properties depend upon the way they are designed and propelled, and for what task a controller is designed. Then, from the nonlinear control theory perspective a system design, way of its propulsion, control goals, other motion or work-space constraints may determine the way of their control-oriented modeling.

The paper advocates dynamics modeling and model-based control designs for robotic-like systems with the use of quasi-coordinates description. The constrained systems may be subjected to holonomic, nonholonomic or programmed constraints as well as be fully actuated or underactauted. Such systems are a large class of systems of a practical interest and they are usually approached by the Lagrange method with generalized coordinates or its modifications to obtain the motion equations. The Lagrange based dynamics are then used to generate dynamic control models for these systems. This traditional, almost routine, approach to dynamics modeling results in dynamics that lacks some properties significant from the point of view of further control design. Basically, Lagrange based dynamics can be applied to systems with constraints of first order and the number of unknowns that result from Lagrange's equations increases to include the multipliers. In order to obtain a dynamic control model, Lagrange's based dynamics require the elimination of the constraint reaction forces, i.e. Lagrange multipliers. Finally, solutions obtained from the Lagrange based models require numerical stabilization due to differentiation of constraint equations, which may complicate on-line simulations and control. Only a few works report using a quasi-coordinate approach to modeling systems, see e.g. [1, 2]. This approach proved to be effective for many constrained systems and it can be applied to control designs [3].

The use of quasi-coordinates in a development of constrained and control dynamics of robotic-like systems can be justified by a couple of properties their models possess or have to satisfy. Firstly, the constraint kinds that have to be dealt with for these systems in control setting are different than the ones considered in analytical modeling. This has led to the formulation of the unified constraint formulation and the generalized programmed motion equations [3, 4]. Secondly, a dynamics control model that is passed to a control engineer to design and apply to it an appropriate controller, may be made a control oriented, i.e. may facilitate this controller design. The two properties are not separate from each other. They both can be appropriately treated at the modeling step of a control design project using the latest modeling tools and the modeling process may serve an effective control design.

The dynamics modeling in quasi-coordinates presented herein, which is incorporated in the advanced model-based control design platform for constrained systems

eliminates many disadvantages related to Lagrange's based dynamics modeling and a subsequent control design.

In the paper we present the theoretic model-based control oriented modeling framework. It yields equations of motion for constrained systems in quasi-coordinates. It is based on the generalized Boltzmann-Hamel equations [3]. This dynamics framework yields equations of motion of a constrained system in a reduced-state form, from which the dynamic control model directly follows. The framework applies to fully actuated and underactuated systems, it is computationally efficient, and may facilitate a subsequent controller design. Based on the framework, a tracking control strategy dedicated to track predefined motions referred to as programmed may be designed. It is referred to as the model reference tracking control strategy for programmed motion and has been developed for dynamics in generalized coordinates [5]. It can be redesigned to constrained and control dynamics developed in quasi-coordinates.

The paper contribution two-folded. Firstly, it presents an advanced constrained systems modeling platform – it may serve for motion analysis, prototyping and redesigning, and fast generation of control models. Secondly, it presents an advanced control platform that is a fusion of modern control oriented modeling, control algorithms and embedded controller systems.

The paper focuses then upon two essential steps in control design. The first is an advanced constrained systems modeling framework, which may serve motion analysis, prototyping and redesigning, and fast generation of control models. The second is an advanced control platform, which is a fusion of modern control oriented modeling, control algorithms and embedded controllers.

The paper is organized as follows. Section 2 reviews constraint descriptions that can be put upon robotic-like systems. In Section 3 the modeling framework in quasi-coordinates is presented. Section 4 details an advanced control platform and Section 5 presents examples of dynamics modeling and control design for robotic-like systems. Section 6 presents some preliminary experimental tests in implementation control algorithms for a wheeled mobile platform. The paper closes with conclusions and a list of references.

2 Material and Task-Based Constraints on Robotic-Like Systems

Robotic-like systems are subjected to variety of constraints so they all can be considered constrained control systems. The constraints that usually determinate the system classification can be listed as follows [5]:

- Wheeled robotic-like vehicles and mobile manipulators – nonholonomic with the no-slip rolling condition (material constraints) and task-based constraints – robots, rehabilitation devices, toys and recreation vehicles.
- Robotic-like systems with "conservation laws" – free-floating space systems, models in a flying phase.
- Underactuated robotic-like systems – biologically inspired models, space vehicles, systems which were damaged in action and needed to finish their missions, systems designed as underactuated to reduce costs, weight or dimensions.

– Multi-constrained robotic-like systems with task-based constraints added to enable them performing work.
– According to this classification, modeling methods are developed, specialized and modified or updated as the ones dedicated to some specific group of system models. Such an approach is not flexible and often non-transferable to other groups of models.

2.1 Wheeled Robotic-Like Vehicles

Wheeled mobile robots and manipulators are the well known group of nonholonomic systems due to material constraints. The constraints are due to roll their wheels without slipping. Also, they may be subjected to task-based constraints, which we discuss in the subsequent subsection. The wheeled mobile robots are also, rehabilitation devices, toys and recreation vehicles, e.g. a roller-racer, trikke, or a snake-board. The nonholonomic constraints equations are of the form $A(q)\dot{q} = 0$. For example, for a car with a trailer model, which we consider in Section 5, the nonholonoimc constraint equations due to roll a car and a trailer wheels without slipping are

$$\begin{aligned} \dot{x}_1 \sin(\theta_1 + \Phi_1) - \dot{y}_1 \cos(\theta_1 + \Phi_1) - \dot{\theta}_1 L_0 \cos \Phi_1 = 0, \\ \dot{x}_1 \sin\theta_1 - \dot{y}_1 \cos\theta_1 = 0, \\ \dot{x}_1 \sin(\theta_2 + \Phi_2) - \dot{y}_1 \cos(\theta_2 + \Phi_2) + \dot{\theta}_2 L_1 \cos \Phi_2 = 0. \end{aligned} \tag{1}$$

Many of these wheeled mobile robots are underactuated due to their designs. It is because of less control inputs available than degrees of freedom. We address underactuated system models in subsection 2.2. Note, that all wheeled vehicles with passive wheels are nonholonomic and underactuated.

2.2 Underactuated Robotic-Like Systems

There are many underactuated system models, e.g. biologically inspired models, space vehicles, systems which were damaged in action and needed to finish its mission, or systems designed as underactuated to reduce their weight and costs. A good example is a snake-like robot presented in Fig. 1.

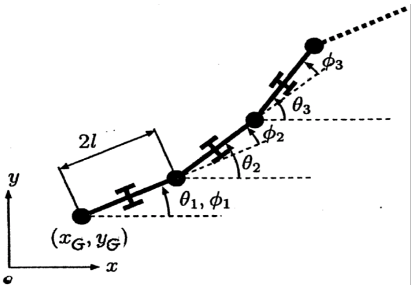

Fig. 1. A snake-like manipulator model

It is nonholonomic and underactauted. It is equipped with one pair of wheels per segment and it is not enough constraint equations to build a kinematic control model. A dynamic control model is needed [6].

Another example is a human model, e.g. model of a gymnast. It is underactuated since there is no control torque in a wrist, see Fig. 2.

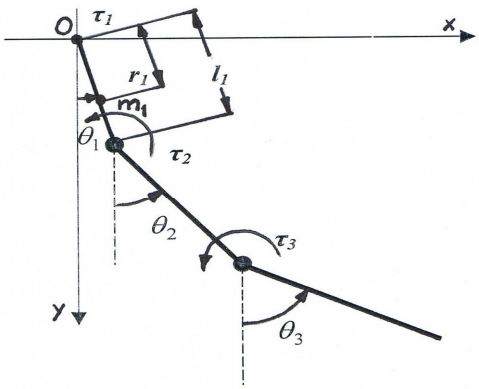

Fig. 2. A three link planar model of a gymnast

The gymnast model dynamics can be gathered by the equations

$$M\ddot{\theta} + B(\theta,\dot{\theta})\dot{\theta} + C = U, \tag{2}$$

where $U = [\tau_1 - \tau_2 \quad \tau_2 - \tau_3 \quad \tau_3]^T$ and $\tau_1 = 0$,

$$\tau_2 = k_1[\theta_{1d} - (\theta_2 - \theta_1)] - k_2(\dot{\theta}_2 - \dot{\theta}_1) + c_2 + c_3,$$

$$\tau_3 = k_3[\theta_{2d} - (\theta_3 - \theta_2)] - k_4(\dot{\theta}_3 - \dot{\theta}_2) + c_3.$$

Other examples of underactuated systems are underwater autonomous vehicle models [7]. A damaged manipulator with one of its actuators failed during task-based motion is also an example of an underactuated system.

2.3 Robotic-Like Systems with "Conservation Laws"

Robotic-like systems with extra conditions of "conservation laws", which in control setting play roles of constraint equations, are free-floating space systems, mechanical system models in a flying phase, and human models in a flying phase. Let us consider an example of a simple three degrees of freedom plane model of a diver in a flying phase presented in Fig. 3.

If the initial angular momentum of a diver is denoted by K_0, then the angular momentum conservation law takes the form

$$K_0 = [B_1(\theta_2,\theta_3) \quad B_2(\theta_2,\theta_3) \quad B_3(\theta_2,\theta_3)][\dot{\theta}_1 \quad \dot{\theta}_2 \quad \dot{\theta}_3] \tag{3}$$

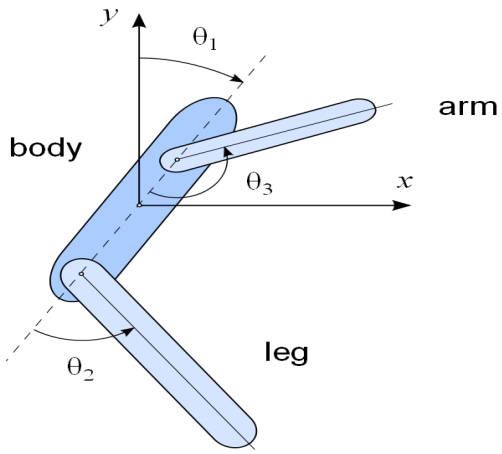

Fig. 3. Plane model of a diver in a flying

A kinematic control model for the diver model, with the selection of $u_1 = \dot{\theta}_2$, $u_2 = \dot{\theta}_3$, is

$$\begin{bmatrix} \dot{\theta}_1 \\ \dot{\theta}_2 \\ \dot{\theta}_3 \end{bmatrix} = \begin{bmatrix} \frac{K_0}{B_1} \\ 0 \\ 0 \end{bmatrix} + \begin{bmatrix} \frac{-B_2}{B_1} \\ 1 \\ 0 \end{bmatrix} u_1 + \begin{bmatrix} \frac{-B_3}{B_1} \\ 0 \\ 1 \end{bmatrix} u_2 = \tag{4}$$

$$= f(\theta_2, \theta_3) + g_1(\theta_2, \theta_3)u_1 + g_2(\theta_2, \theta_3)u_2.$$

A drift term $f(\theta_2, \theta_3)$ shows up. It is a nonlinear function of shape variables.

The same kinematic constraint equation as (3) has to be added to a free-floating space manipulator model, e.g. the one presented in Fig. 4 [8].

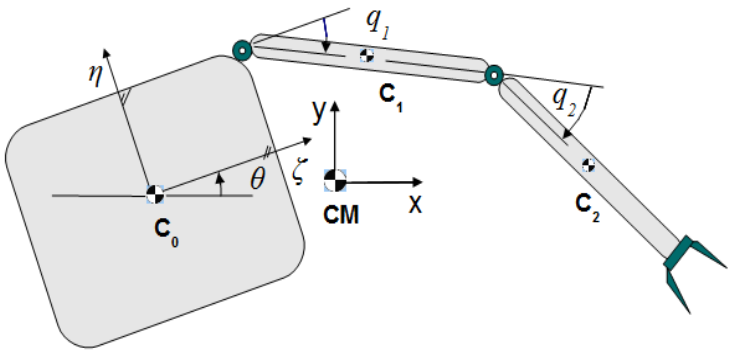

Fig. 4. Free-floating space manipulator model

The conservation law for a planar space manipulator model has the form [8]

$$K = M(x_0\dot{y}_0 - \dot{x}_0 y_0) + I_0\dot{\theta} + m_1(x_1\dot{y}_1 - \dot{x}_1 y_1) + I_1\left(\dot{\theta} + \dot{q}_1\right) + m_2(x_2\dot{y}_2 - \dot{x}_2 y_2) + I_2\left(\dot{\theta} + \dot{q}_1 + \dot{q}_2\right). \tag{5}$$

and its transformation to the *CMxy* frame yields

$$K = \sum_0^2 K_i = K_0(\theta, q_1, q_2)\dot{\theta} + K_1(\theta, q_1, q_2)\dot{q}_1 + K_2(\theta, q_1, q_2)\dot{q}_2 = 0. \tag{6}$$

The angle of a base rotation θ is not actuated in a free-floating regime.
The "conservation law" equation has the form $A(q)\dot{q} = 0$ and is treated as a nonholonomic constraint equation.

2.4 Multi-constrained Robotic-Like Systems

Any of the robotic-like systems dedicated to work and service is subjected to other constraints, usually task-based, which we refer to as programmed and control constraints. It means that constraint equations, e.g. (1) or (3) are supplemented by other constraints. They may be requirements such as motion along a pre-specified trajectory – the constraint equation is an algebraic equation, motion with a pre-specified velocity or acceleration, or their change in time – the constraint equations are differential equations then.

The routine approach is, however, not to specify the other constraints by equations but to add them at the level of a controller design. They are then induced by a control algorithm accommodated to the specific constraint. The approach presented in the paper advocates adding all constraints on a system model at the modeling level. In next section we discuss a constraint representation in details.

3 Multi-option Modeling Framework

The modeling framework is expected, as one of its options, to accommodate to various constraints on systems. It is expected then, it can serve multi-constrained systems as presented in examples of Section 2. The resulting models, either dynamic or kinematic, should be control oriented. We also would like to have modeling flexible with respect to parameters, i.e. the coordinate selection for modeling. Other desirable modeling framework options would be its easy automation for computer equations generation and adaptability to an addition of new options, e.g. for optimality. In the subsequent subsections we discuss these options as they may enter the framework.

3.1 Constraints on Robotic-Like Systems

The constraints can be specified by constraint equations or by other means, e.g. by an error function [9, 10].

Constraints specified by equations can be classified as follows:

1. Constraints given *a priori* and put through other bodies or physical systems. They are position and kinematic constraints "given" by the Nature. Material nonholonomic constraints which come from an assumption about rolling vehicle wheels without slipping are first order and they are typical for wheeled mobile vehicles, multi-finger hands working on surfaces. Their common form is as (1), i.e.

$$\varphi_\beta(t, q_1,..., q_n, \dot{q}_1,..., \dot{q}_n) = 0 \qquad \beta = 1,...,b, \quad b < n \qquad (7)$$

Functions φ_β are defined on a $(2n + 1)$-dimensional manifold and have continuous derivatives.

2. Conservation laws – they come from the angular momentum conservation for free floating space manipulators or for a sportsman in an exercise flying phase. Their equation form is the same as (1) or (3) [11]. Notice, that in mechanics they are not referred to as constraints. They show up in a control setting.

3. Tasks (programmed constraints) – they can be formulated for any physical system, e.g. a robot or a manipulator and they can specify a task, work to do or a limitation in a system motion, e.g. a limitation in velocity or acceleration. Also, it may specify a trajectory to follow but then it is a holonomic constraint. Many task formulations are reported in [12–20]. However, none of the tasks is formulated in algebraic or differential constraint equation forms at a system modeling level; such equations are formulated later at a level of a controller design and then a specific controller modification for each task is needed the most often. The earliest formulation of programmed constraints known to the author was given by Appell in [15]. He described them as constraints "that can be realized not through a direct contact". Similar ideas were introduced by Mieszczerski at the beginning of the 20th century. Beghin developed a concept of servo-constraints [16]. These new "constraint sources" motivated to specify constraints by the formulations like

$$\varphi_\beta(t, q_1,..., q_n, \dot{q}_1,..., \dot{q}_n) = 0\,, \qquad \beta = 1,...,k, \quad k < n \qquad (8)$$

The history of evolution of the programmed constraints (3) confirms both their usefulness in formulations of requirements for dynamical systems performance and leads to a formulation of a "unified constraint formulation", which is [4]

$$B_\beta(t,q,\dot{q},...,q^{(p)}) = 0, \qquad \beta = 1,...,k,\ k < n \quad (9)$$

where p is a constraint order and B_β is a k-dimensional vector. Equations (9) can be nonlinear in $q^{(p)}$. Differentiation of (9) with respect to time, until the highest derivative of a coordinate is linear, results in constraint equations linear with respect to this highest coordinate derivative. We assume that "p" stands for the highest order derivative of a coordinate which appears linearly in a constraint equation. For simplicity we assume that they are linear in all p-th order derivatives of q's and we rewrite (9) as

$$B(t,q,\dot{q},...,q^{(p-1)})q^{(p)} + s(t,q,\dot{q},...,q^{(p-1)}) = 0, \qquad (10)$$

where B is a $(k\times n)$-dimensional full rank matrix, $n>k$, and s is a $(k\times 1)$-vector. The constraint (10) is referred to as a unified constraint formulation [4]. We may conclude

then that the equations of constraints in the form (10) can specify both material and programmed constraints. Since now on the constraint form (10) is used.

4. Design or control constraints – they can be put upon manipulators and robots with underactuated degrees of freedom [17]. Then, they have the form (10) with p=2.

5. Other design, control or operation constraints on robots, manipulators and on other vehicles or robotic systems, which can be presented as (10), can be found reported in the literature but never formulated in the equation form:

- in navigation of wheeled mobile robots, to avoid the wheel slippage and mechanical shock during motion, dynamic constraints such as acceleration limits have to be imposed [12, 13],
- in path planning problems, for car-like robots, to secure motion smoothness two additional constraints are added: on a trajectory curvature and its time derivative so additional constraints of the second and third order are imposed [13],
- in manipulator trajectory tracking, jerk must be limited for reducing manipulator wear and improving tracking accuracy [21],
- in vehicle dynamics constraints are added when different maneuvers are to be performed [18],
- bounded lateral acceleration – e.g. path tracking experiments depend on the precision of the odometry. If the lateral acceleration of the vehicle is too large, the wheels can lose close contact to the ground and the odometry data is no longer meaningful.

Design or other source constraints can be specified by, e.g. an error function. It is dedicated to task-based constraints [9, 10]. The error function is predefined by a designer. The error function dynamics ensures the convergence of a system to a predefined motion. It can be formulated at a kinematic level. Then, a kinematic error function formulation is as follows: $E: Q \times R \to R$ and create a cost function on the base of a position error $E(q(t))$ with a change of an error value

$$\dot{E} = \frac{\partial E}{\partial t} + \nabla E \cdot \dot{q} \,, \tag{11a}$$

expected exponential convergence

$$\dot{E} = -kE \,, \tag{11b}$$

and higher order convergence conditions

$$\ddot{E} + d_1 \dot{E} + d_2 E = 0. \tag{11c}$$

The constraint classification in classical mechanics and a variety of requirements on system's motions reported in the literature can be summarized as follows:

- Many problems are formulated as synthesis problems and motion requirements may be viewed as non-material constraints imposed on a system before it is designed and put into operation.
- Constraints that specify motion requirements may be of orders higher than one or two.
- Non-material constraints may arise in modeling and analysis of electro and biomechanical systems.

- No unified approach to the specification of non-material constraints or any other unified constraint has been formulated in classical mechanics.

These conclusions lead to an idea of an extended constraint concept [4]. It is formulated in two definitions:

Definition 1: A programmed constraint is any requirement put on a physical system motion specified by an equation (10).

Definition 2: A programmed motion is a system motion that satisfies a programmed constraint (10).

A system can be subjected to both material and programmed constraints. Programmed constraints do not have to be satisfied during all motion of a system.

3.2 Modeling Robotic-Like Systems Dynamics in Quasi-Coordinates

The constrained dynamics which we formulate below using the quasi-coordinate description can be directly use as a control dynamics, and it serves both fully actuated and underactuated systems constrained by the constraints (10) [4].

Let us start from recalling the concepts of quasi-coordinates and quasi-velocities. They were introduced to derive the Boltzmann-Hamel equations of motion [22]. Relations between the generalized velocities and quasi-velocities were assumed linear and non-integrable, i.e.

$$\omega_r = \omega_r(t, q_\sigma, \dot{q}_\sigma), \qquad \sigma, r = 1,...,n, \quad (12)$$

With respect to the extended constraint concept (10), our first step is to let (12) be nonlinear [3]. Inverse transformations for (12) can be computed as

$$\dot{q}_\lambda = \dot{q}_\lambda(t, q_\sigma, \omega_r). \qquad \lambda = 1,...,n \quad (13)$$

Quasi-coordinates can be introduced as

$$d\pi_r = \sum_{\sigma=1}^{n} \frac{\partial \omega_r}{\partial \dot{q}_\sigma} dq_\sigma, \qquad r = 1,...,n \quad (14)$$

and (14) are non-integrable. Based on (12)–(14), q's and ω's are related as

$$dq_\lambda = \sum_{\mu=1}^{n} \frac{\partial \dot{q}_\lambda}{\partial \omega_\mu} d\pi_\mu. \qquad \lambda = 1,...,n \quad (15)$$

The principal form of the dynamics motion equation [4] has the form

$$\frac{d}{dt} \sum_{\sigma=1}^{n} p_\sigma \delta q_\sigma = \delta \Gamma + \sum_{\sigma=1}^{n} Q_\sigma \delta q_\sigma + \sum_{\sigma=1}^{n} p_\sigma \left[(\delta q_\sigma)^{\cdot} - \delta \dot{q}_\sigma \right] \delta q_\sigma \quad (16)$$

Transforming its left and right hand side terms using the relations between $\delta\pi_r$ and δq_λ we obtain

$$\frac{d}{dt} \sum_{\mu=1}^{n} \tilde{p}_\mu \delta \pi_\mu = \delta \tilde{\Gamma} + \sum_{\mu=1}^{n} \tilde{Q}_\mu \delta \pi_\mu + \sum_{r=1}^{n} \tilde{p}_r \left[(\delta \pi_r)^{\cdot} - \delta \omega_r \right] - \sum_{r=1}^{n} \tilde{p}_r \sum_{\mu=1}^{n} W_\mu^r \delta \pi_\mu \quad (17)$$

which is the principal form of the equation of motion in quasi-coordinates for nonlinear $\omega_r = \omega_r(t, q_\sigma, \dot{q}_\sigma)$. W_μ^r are generalized Boltzmann symbols of the form: $W_\mu^r = \sum_{\lambda=1}^{n} \frac{\partial \dot{q}_\lambda}{\partial \omega_\mu} \left[\frac{d}{dt} \left(\frac{\partial \omega_r}{\partial \dot{q}_\lambda} \right) - \frac{\partial \omega_r}{\partial q_\lambda} \right]$.

Quantities $\tilde{p}_\mu$, $\tilde{T}$, $\tilde{Q}_\mu$ are all written in quasi-coordinates.

The generalized form of the Boltzmann-Hamel equations can be derived based on (17) [4]. It has the form

$$\sum_{\mu=1}^{n} \left[\frac{d}{dt} \left(\frac{\partial \tilde{T}}{\partial \omega_\mu} \right) - \frac{\partial \tilde{T}}{\partial \pi_\mu} + \sum_{r=1}^{n} \frac{\partial \tilde{T}}{\partial \omega_r} W_\mu^r - \tilde{Q}_\mu \right] \delta\pi_\mu = 0. \tag{18}$$

For a holonomic system, $\delta\pi_\mu, \mu = 1,..., n$, are independent and equations of motion are

$$\frac{d}{dt} \left(\frac{\partial \tilde{T}}{\partial \omega_\mu} \right) - \frac{\partial \tilde{T}}{\partial \pi_\mu} + \sum_{r=1}^{n} \frac{\partial \tilde{T}}{\partial \omega_r} W_\mu^r = \tilde{Q}_\mu. \qquad \mu = 1,...,n \tag{19}$$

Equations (9) are the generalized Boltzmann-Hamel equations for a holonomic system with nonlinear relations between quasi and generalized velocities. For linear relations for them, (19) become Boltzmann-Hamel equations derived in, e.g. [22]. Also, it can be easily verified that when quasi-coordinates are equivalent to generalized coordinates, i.e. $\pi_r = q_r, r = 1,..., n$, and quasi-velocities are generalized velocities, i.e. $\omega_r = \dot{q}_r, r = 1,..., n$, then (18) are Lagrange's equations with $W_\mu^r = \gamma_{\sigma\mu}^r = 0$.

For a system subjected to material or programmed nonholonomic constraints in the form

$$\omega_\beta = \omega_\beta(t, q_\sigma, \dot{q}_\sigma) = 0 \qquad \beta = 1,...,b \tag{20}$$

relations

$$\delta\pi_\beta = \sum_{\sigma=1}^{n} \frac{\partial \omega_\beta}{\partial \dot{q}_\sigma} \delta q_\sigma = 0, \qquad \beta = 1,...,b \tag{21}$$

hold for all ω_β. A system has (n–b) degrees of freedom and variations $\delta\pi_{b+1},...,\delta\pi_n$ are independent. Then, (n–b) equations of motion, based on (18), have the form

$$\frac{d}{dt} \left(\frac{\partial \tilde{T}}{\partial \omega_\mu} \right) - \frac{\partial \tilde{T}}{\partial \pi_\mu} + \sum_{r=1}^{n} \frac{\partial \tilde{T}}{\partial \omega_r} W_\mu^r = \tilde{Q}_\mu \qquad \mu = b+1,...,n \tag{22}$$

to which n kinematic relations

$$\dot{q}_\lambda = \dot{q}_\lambda(t, q_\sigma, \omega_r), \qquad \sigma, \lambda = 1,..., n,\ r = b+1,..., n \tag{23}$$

have to be added.

Equations (22) are the generalized Boltzmann-Hamel equations for a nonholonomic system. Notice that b of ω'*s* are satisfied based on the constraint

equations (23). The rest of quasi-velocities are selected arbitrarily by a designer. Equations (22) and (23) can be presented as

$$\begin{aligned} M(q)\dot{\omega} + C(q,\omega) + D(q) &= \tilde{Q}, \\ B(q,\omega) &= 0. \end{aligned} \tag{24}$$

A system dynamics control model follows directly from (24) since they are free from the constraint reaction forces

$$\begin{aligned} M(q)\dot{\omega} + C(q,\omega) + D(q) &= \tilde{Q} + \tilde{\tau}, \\ B(q,\omega) &= 0. \end{aligned} \tag{25}$$

Equations (22) have to be extended to be applicable to systems subjected to nonholonomic constraints of high order given by (10). To enable this, the following lemma can be formulated [4].

Lemma: For a function $\tilde{F}$ of the form

$$\tilde{F} = \tilde{F}(t, q_\sigma, \omega_r), \qquad \sigma, r = 1,...,n \tag{26}$$

where q_σ and ω_r are related by $\omega_r = \omega_r(t, q_\sigma, \dot{q}_\sigma)$, the following identity holds

$$\frac{d}{dt}\left(\frac{\partial \tilde{F}}{\partial \omega_\sigma}\right) = \frac{1}{p}\left(\frac{\partial \tilde{F}^{(p)}}{\partial \omega_\sigma^{(p-1)}} - \frac{\partial \tilde{F}}{\partial \pi_\sigma}\right). \qquad p = 1,2,3,.. \tag{27}$$

The proof is by mathematical induction [4]. If we replace $\tilde{F}$ by $\tilde{T} = \tilde{T}(t, q_\sigma, \omega_\sigma)$ in (26) and insert it into the generalized Boltzmann-Hamel equations (18), we get

$$\frac{1}{p}\left[\frac{\partial \tilde{T}^{(p)}}{\partial \omega_\mu^{(p-1)}} - (p+1)\frac{\partial \tilde{T}}{\partial \pi_\mu}\right] + \sum_{r=1}^{n} \frac{\partial \tilde{T}}{\partial \omega_r} W_\mu^r = \tilde{Q}_\mu . \qquad \mu = 1,...,n \text{ , } p=1, 2, 3, \tag{28}$$

Equations (28) are the extended form of the Boltzmann-Hamel equations. Now, modify them for systems with nonholonomic constraints of high order

$$\tilde{G}_\beta\left(t, q_\sigma, \omega_r, \dot{\omega}_r, ..., \omega_r^{(p-1)}\right) = 0 . \quad \beta = 1,...,b , \quad \sigma, r = 1,...,n, \; b<n \tag{29}$$

Based on the generalized definition of the virtual displacement

$$\delta G_\beta = \sum_{\sigma=1}^{n} \frac{\partial G_\beta}{\partial q_\sigma^{(p)}} \delta q_\sigma = 0, \tag{30}$$

where $G_\beta = G_\beta(t, q_\sigma, \dot{q}_\sigma, ..., q_\sigma^{(p)})$ are constraints of p-*th* order specified in q's, we obtain that

$$\delta \tilde{G}_\beta = \sum_{r=1}^{n} \frac{\partial \tilde{G}_\beta}{\partial \omega_r^{(p-1)}} \delta \pi_r = 0 . \tag{31}$$

In the constraint equation (29) we may partition the vector $\omega^{(p-1)}$ as $\omega^{(p-1)} = \left(\omega_\beta^{(p-1)} \quad \omega_\mu^{(p-1)}\right)$ with

$$\omega_\beta^{(p-1)} = \Omega_\beta^{(p-1)}\left(t, q_\sigma, \omega_\sigma, \dot{\omega}_\sigma, ..., \omega_\mu^{(p-1)}\right). \tag{32}$$

By differentiating (32) with respect to time we obtain

$$\omega_\beta^{p} = \Omega_\beta^{p}\left(t, q_\sigma, \omega_\sigma, \omega_\sigma, ..., \omega_\mu^{(p-1)}, \omega_\mu^{p}\right). \tag{33}$$

Now, using the lemma result we rewrite (19) in the form

$$\begin{aligned}&\sum_{\beta=1}^{b}\left\{\frac{1}{p}\left[\frac{\partial \tilde{T}^{(p)}}{\partial \omega_\beta^{(p-1)}} - (p+1)\frac{\partial \tilde{T}}{\partial \pi_\beta}\right] + \sum_{r=1}^{n}\frac{\partial \tilde{T}}{\partial \omega_r}W_\beta^r - \tilde{Q}_\beta\right\}\delta\pi_\beta + \\ &+ \sum_{\mu=b+1}^{n}\left\{\frac{1}{p}\left[\frac{\partial \tilde{T}^{(p)}}{\partial \omega_\mu^{(p-1)}} - (p+1)\frac{\partial \tilde{T}}{\partial \pi_\mu}\right] + \sum_{r=1}^{n}\frac{\partial \tilde{T}}{\partial \omega_r}W_\mu^r - \tilde{Q}_\mu\right\}\delta\pi_\mu = 0.\end{aligned} \tag{34}$$

Based on (31) we have that

$$\delta\pi_\beta = \sum_{\mu=b+1}^{n}\frac{\partial \Omega_\beta^{(p-1)}}{\partial \omega_\mu^{(p-1)}}\delta\pi_\mu \qquad \beta = 1,...,b$$

and then (34) takes the form for $\mu = b+1,...,n$

$$\begin{aligned}&\frac{1}{p}\left[\frac{\partial \tilde{T}^{(p)}}{\partial \omega_\mu^{(p-1)}} - (p+1)\frac{\partial \tilde{T}}{\partial \pi_\mu}\right] + \sum_{r=1}^{n}\frac{\partial \tilde{T}}{\partial \omega_r}W_\mu^r - \tilde{Q}_\mu + \\ &+ \sum_{\beta=1}^{b}\left\{\frac{1}{p}\left[\frac{\partial \tilde{T}^{(p)}}{\partial \omega_\beta^{(p-1)}} - (p+1)\frac{\partial \tilde{T}}{\partial \pi_\beta}\right] + \sum_{r=1}^{n}\frac{\partial \tilde{T}}{\partial \omega_r}W_\beta^r - \tilde{Q}_\beta\right\}\frac{\partial \Omega_\beta^{(p-1)}}{\partial \omega_\mu^{(p-1)}} = 0.\end{aligned} \tag{35}$$

We refer to (35) as the generalized programmed motion equations (GPME) in quasi-coordinates. For p=1, equations (35) become (22). They may be presented in a form similar to (25)

$$\begin{aligned}&M(q)\dot{\omega} + C(q,\omega) + D(q) = \tilde{Q}, \\ &\tilde{G}_\beta\left(t, q_\sigma, \omega_r, \dot{\omega}_r, ..., \omega_r^{(p-1)}\right) = 0\end{aligned} \tag{36}$$

where M is a $(n–k)\times n$ inertia matrix, C is a $(n-k)$-dimensional velocity dependent vector, D is a $(n–k)$ – vector of gravity forces, and $\tilde{Q}$ is a $(n–k)$ – vector of external forces.

Equations (36) are in the reduced state form, which can be transformed into a dynamic control model by adding a control torques to the right hand sides of the equations. Equations (36) are referred to as a unified dynamic model for a constrained system.

3.3 Automation of the GPME for Easy Computer Equation Generation

The generalized programmed motion equations (GPME) have been transformed to enable an easy automation of derivation of dynamic motion equations for any robotic-like system. Details of the algorithm for the GPME derivation in generalized coordinates can be found in [4]. The similar algorithm for an easy way of equations derivation in quasi-coordinates can be built. It is as follows.

Algorithm:
Assume that the constraints (4) can be solved at least locally with respect to $\omega_\beta^{(p-1)}$, as in (32), i.e.

$$\omega_\beta^{(p-1)} = \Omega_\beta^{(p-1)}\left(t, q_\sigma, \omega_\sigma, \dot{\omega}_\sigma, ..., \omega_\mu^{(p-1)}\right) \qquad \beta = 1,...,k \quad \text{(A1)}$$

1. Construct a function P_p such that

$$P_p = \frac{1}{p}\left[\tilde{T}^{(p)} - (p+1)\tilde{T}_0^{(p)}\right], \qquad \tilde{T}_0^{(p)} = \sum_{\sigma=1}^{n} \frac{\partial \tilde{T}}{\partial q_\sigma}\omega_\sigma^{(p-1)} \quad \text{(A2)}$$

2. Construct a function R_p such that

$$R_p = P_p - \sum_{\sigma=1}^{n} \omega_\sigma^{(p-1)} Q_\sigma = R_p(t, q_\sigma, \omega_\sigma, ..., \omega_\mu^{(p-1)}, \omega_\beta^{(p-1)}, \omega_\sigma^{(p)}) . \quad \text{(A3)}$$

3. Construct R_p^*, in which $\omega_\beta^{(p-1)}$ from (A3) are replaced with (A1)

$$\begin{aligned} R_p^* &= R_p^*(t, q_\sigma, \omega_\sigma, ..., \omega_\mu^{(p-1)}, \Omega_\beta^{(p-1)}(t, q_\sigma, ..., \omega_\mu^{(p-1)}), \omega_\sigma^{(p)}) = \\ &= R_p^*(t, q_\sigma, \omega_\sigma, ..., \omega_\mu^{(p-1)}, \omega_\sigma^{(p)}). \end{aligned} \quad \text{(A4)}$$

4. Assuming that $\partial Q_\sigma / \partial \omega_\sigma^{(p-1)} = 0$, the desired GPME for a system with p-th order constraints have the form

$$\frac{\partial R_p^*}{\partial \omega_\mu^{(p-1)}} = \frac{\partial R_p}{\partial \omega_\mu^{(p-1)}} + \sum_{\beta=1}^{k} \frac{\partial R_p}{\partial \omega_\beta^{(p-1)}} \frac{\partial \Omega_\beta^{(p-1)}}{\partial \omega_\mu^{(p-1)}} = 0. \qquad \mu = k+1,...,n \quad \text{(A5)}$$

Equations (A5) are (n–k) second order equations of motion and together with (A1) are equivalent to the GPME (36). Equations (A5) are free of constraint reaction forces.

Possibilities of adaptation and extension of equations (36) to adding new options, e.g. optimality is presented in the example section in conjunction with a demonstration of a control strategy and its applications.

4 Advanced Control Platform Design – A Fusion of Modern Control Oriented Modeling, Control Algorithms and Embedded Controllers

Motion generated by constrained dynamics (with programmed constraints) or by error function driven dynamics is referred to as a reference motion for a constrained mechanical system. The next step is to get the reference motion executed. The control objective of programmed motion tracking is formulated as follows: given a reference motion specified either by the constrained dynamics or error function driven dynamics, design a feedback controller that can track the reference motion.

The programmed constraints (4) or the error function are the basis for the reference dynamics generation. The reference dynamics are employed to design a tracking control strategy for constrained motions.

Advanced control platform architecture is presented in Fig. 5. The strategy is referred to as a model reference tracking control strategy for programmed motion. The reference dynamics which governs a system constrained dynamics can be generated by:

a) Dynamics-based reference motion according to (36) and the dynamic control model (also generated using the GPME framework for *p=1*), which is (25), i.e.

$$\begin{aligned} M(q)\dot{\omega} + C(q,\omega) + D(q) &= \tilde{Q} + \tilde{\tau}, \\ B(q,\omega) &= 0. \end{aligned} \tag{37}$$

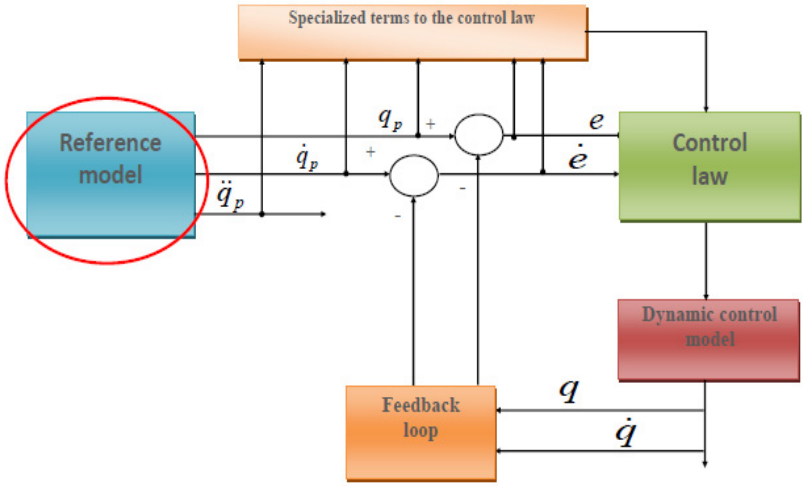

Fig. 5. Advanced control platform architecture

Note, that the control dynamics is a constrained dynamics with the material constraints on a system taken into account. Then, the control dynamics is one for a variety of reference motions plugged in through the feedback controller.

b) Error function driven dynamics reference motion can be generated using an error function predefined by a designer. The error function dynamics ensures the convergence of a system to a predefined motion. According to (11a) – (11c) the error function is specified. Then, the control dynamics gets the form

$$\ddot{q} = f(t, q, \dot{q}, u), \tag{38}$$

where u is a control input vector. An error function can be a distance from a given trajectory, i.e.

$$E(q) = (x - \alpha_x(t))^2 + (y - \alpha_y(t))^2, \tag{39}$$

where $\alpha_x(t), \alpha_y(t)$ are trajectory parameters.

Some of the advanced control platform advantages are as follows:

- The reference dynamic model (36) can include arbitrary order nonholonomic constraints. Then, any programmed motion can be planned and controlled, e.g. for underactuated systems.
- The tracking strategy extends "trajectory tracking" to "programmed motion tracking".
- The tracking strategy separates material constraints from programmed. The dynamic control model (37) is equivalent to models nonlinear control uses, i.e. models based on Lagrange's approach.
- The equivalence of (37) and models based on Lagrange's approach enables adopting existing control algorithms even these dedicated to holonomic systems.
- The equivalence of (37) and models based on Lagrange's approach enables using existing controllers (non-adaptive and adaptive) and design new ones.
- The dynamic control model (37) enables selecting states which are to be controlled.
- The tracking strategy takes advantage of one dynamic control model (37) for both holonomic and nonholonomic systems.
- The modular structure of the control platform enables adding new functional blocks, e.g. a velocity observer block.
- The strategy enables adding functionality, e.g. adding optimality options for controllers.
- The reference dynamic model can be generated off-line. A library of reference models that plan different tasks can be created. They all can be applied to one dynamic control model of a specified system.

5 Advanced Tracking Control Design – Simulation Studies

5.1 A Space Vehicle Model – A Multi-constrained System

Consider a space vehicle model presented in Fig. 4. It is a multi-constrained system with the following constraints on it:

- The constraint from conservation of the angular momentum that has the form (6), i.e.

– The constraint from underactuation (the base is not actuated), i.e.

$$\begin{aligned} M(q,\theta)\ddot{q} + C(q,\theta,\dot{q})\dot{q} = \tau, \\ \dot{\theta} = D(q,\theta)\dot{q}, \end{aligned} \tag{40}$$

with $\tau = [\tau_1, \tau_2]^T$.

– The task-based constraint, which is a desired trajectory. Two desired trajectories for the end-effector motion were selected to be

$$\mathbf{X}_d = \begin{bmatrix} x_E(t) \\ y_E(t) \end{bmatrix} = \begin{bmatrix} 1.1101 - 0.3\cos(2\pi t/15) \\ 0.0319 + 0.3\sin(2\pi t/15) \end{bmatrix} \quad \mathbf{X}_d = \begin{bmatrix} x_E(t) \\ y_E(t) \end{bmatrix} = \begin{bmatrix} 1.1101 + 0.01t\cos(0.5t) \\ 0.0319 + 0.01t\sin(0.5t) \end{bmatrix}, \tag{41}$$

where the task and joint space coordinates are related by

$$\begin{aligned} x_E = {} & \cos(\theta)(l_0 + l_1\cos(q_1) + l_2\cos(q_1+q_2) - (m_1(l_0 + b_1\cos(q_1)))/M) \\ & - \cos(\theta)((m_2(l_0 + l_1\cos(q_1) \\ & + b_2\cos(q_1+q_2)))/M) - \sin(\theta)(b_0 + l_1\sin(q_1) + l_2\sin(q_1+q_2) - \\ & (m_1(b_0 + b_1\sin(q_1)))/M) \\ & - \sin(\theta)((m_2(b_0 + l_1\sin(q_1) + b_2\sin(q_1+q_2)))/M), \end{aligned} \tag{42}$$

$$\begin{aligned} y_E = {} & \cos(\theta)(b_0 + l_1\sin(q_1) + l_2\sin(q_1+q_2) - (m_1(b_0 + b_1\sin(q_1)))/M) - \\ & \cos(\theta)((m_2(b_0 + l_1\sin(q_1) \\ & + b_2\sin(q_1+q_2)))/M) + \sin(\theta)(l_0 + l_1\cos(q_1) + l_2\cos(q_1+q_2) - \\ & (m_1(l_0 + b_1\cos(q_1)))/M) \\ & - \sin(\theta)((m_2(l_0 + l_1\cos(q_1) + b_2\cos(q_1+q_2)))/M). \end{aligned}$$

The quasi-velocities, due to a direct control of the two joints are selected to be $\omega_1 = q_1, \omega_2 = q_2, \omega_3 = \theta$.

Using the reference dynamics (36) with the constraints (6) and (41) merged into it and the control dynamics for an underactuated system (40) we can apply the control platform according to its architecture from Fig. 5.

Simulation studies are presented for two cases – for an uncontrolled motion according to two scenarios, and for controlled motions. The Scenario 1 is that the initially stretched arm may rotate due to the initial velocity $\dot{q}_2 = -0.0873$ rad/s; see Fig. 6. The Scenario 2 is that the second arm being initially folded can be stretched out due to the initial velocity $\dot{q}_2 = -0.122$ rad/s with $q_1 = -60$ deg. and $q_2 = 180$ deg. The arm could stretch after 32 seconds; see Fig. 7.

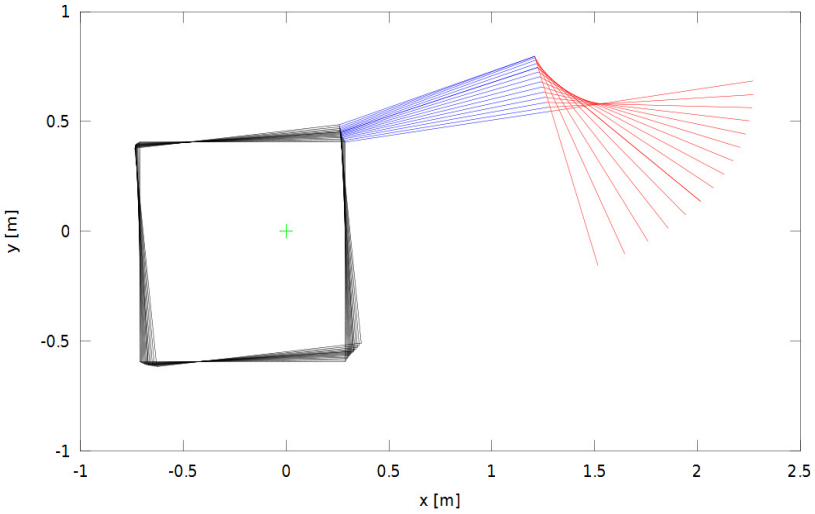

Fig. 6. Uncontrolled motion of a space manipulator according to scenario 1

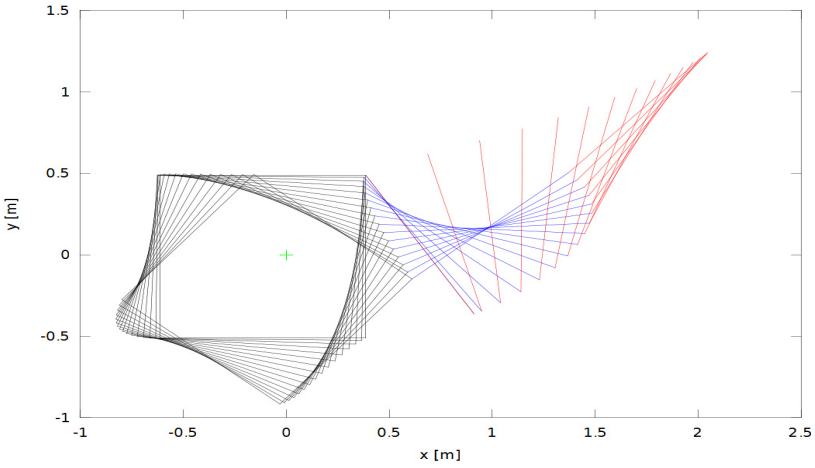

Fig. 7. Uncontrolled motion of a space manipulator according to scenario 2

For the controlled motion two controllers are applied – a computed torque and a Wen-Bayard controller. Figures 8 and 9 present tracking predefined motions.

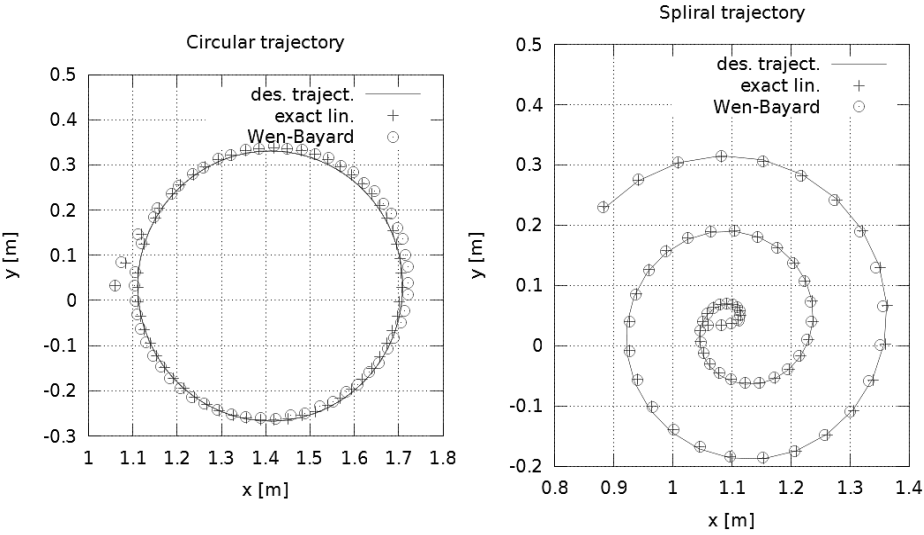

Fig. 8. Computed torque (left) and Wen-Bayard (right) controllers applied to execute programmed motion for a space manipulator end effector

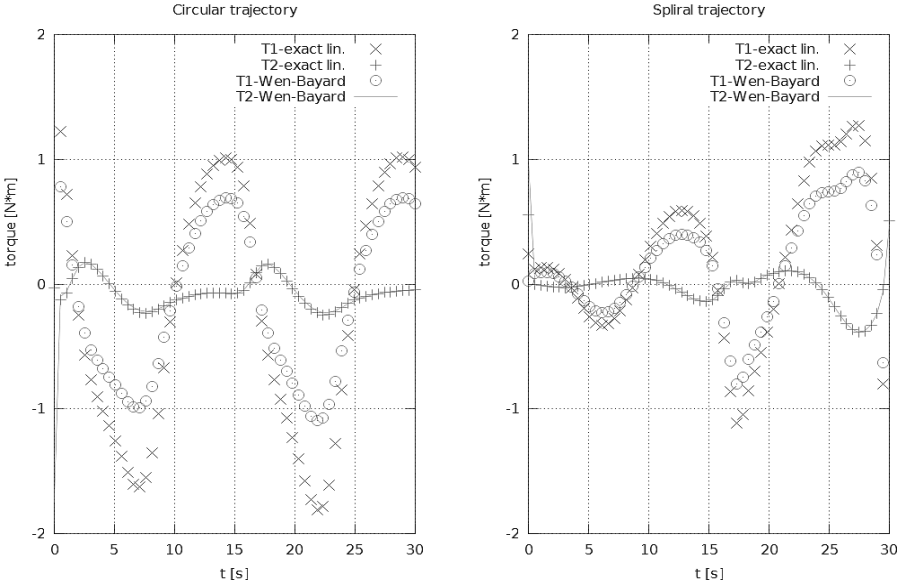

Fig. 9. Magnitudes of control torques: computed torque (left) and Wen-Bayard (right)

5.2 A Fire Track Model – Modeled in Quasi-Coordinates

Consider a fire track model presented in Fig. 10 [23]. To the best of author's knowledge, its dynamic and control has been always specified in generalized coordinates. We can show here, a quasi-coordinate description facilitates a system constrained dynamics derivation and a subsequent controller design for an execution of a desired motion.

The nonholonomic constraints for the car and a trailer system are of the form (1). The control goal is to move the car-trailer system along the circular trajectory, so the constraint (10) is a position constraint.

The system dynamics is derived using quasi-coordinates and the constrained dynamics (36). Select the quasi-coordinates as

$$\begin{aligned}
&\omega_1 = V = \dot{x}_1 \cos\theta_1 + \dot{y}_1 \sin\theta_1,\\
&\omega_2 = \dot{\phi}_1,\\
&\omega_3 = \dot{\phi}_3,\\
&\omega_4 = \dot{x}_1 \sin(\theta_1 + \Phi_1) - \dot{y}_1 \cos(\theta_1 + \Phi_1) - \dot{\theta}_1 L_0 \cos\Phi_1 = 0,\\
&\omega_5 = \dot{x}_1 \sin\theta_1 - \dot{y}_1 \cos\theta_1 = 0,\\
&\omega_6 = \dot{x}_1 \sin(\theta_2 + \Phi_2) - \dot{y}_1 \cos(\theta_2 + \Phi_2) + \dot{\theta}_2 L_1 \cos\Phi_2 = 0.
\end{aligned} \tag{43}$$

As can be seen, the three last ω's satisfy the constraint equations. The first three ones are the control inputs so they are selected for the subsequent controller design. Other quasi-velocities may be selected if suitable.

The constrained dynamics has been derived according to (36).

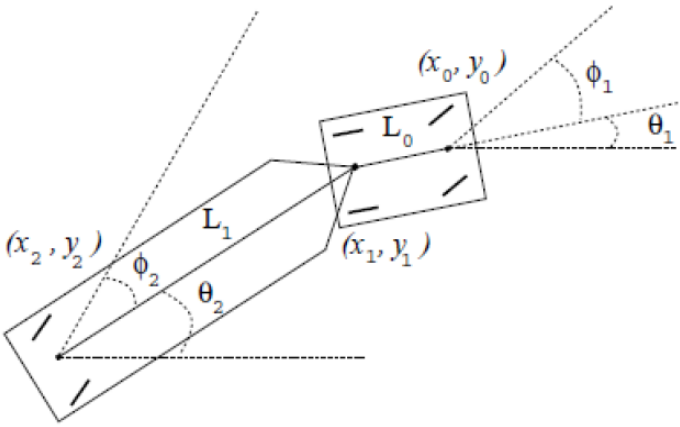

Fig. 10. A fire truck model

Results of simulation studies are presented in Fig. 11. A PD controller with a correction has been applied.

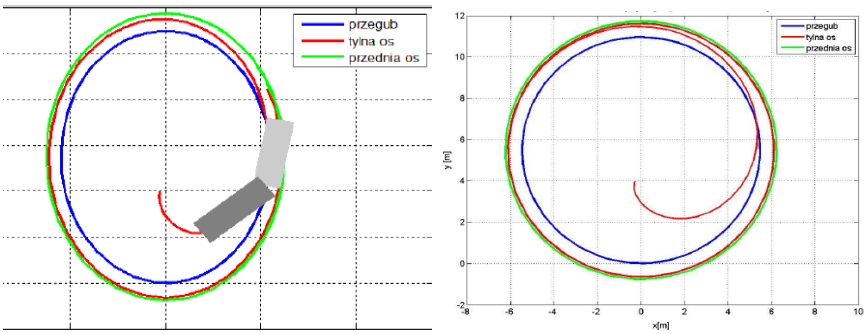

Fig. 11. Trajectory tracking for a fire truck model

5.3 A Three Link Planar Manipulator Model with a Failure of One Actuator during Tracking a Task-Based Motion

Consider a three link planar manipulator model whose end-effector is to track a predefined trajectory [24].

During motion one of actuators, the one between the second and third links, fails. A control goal is to design a controller that enables finishing the task and bring the arm to some safe position.

The manipulator fully actuated dynamic control model is holonomic so the Lagrange approach can be used. The underactuated control dynamics has the form (40) but the task-based constraint is algebraic.

The manipulator model and the preplanned trajectory for fully actuated manipulator are presented in Fig. 12.

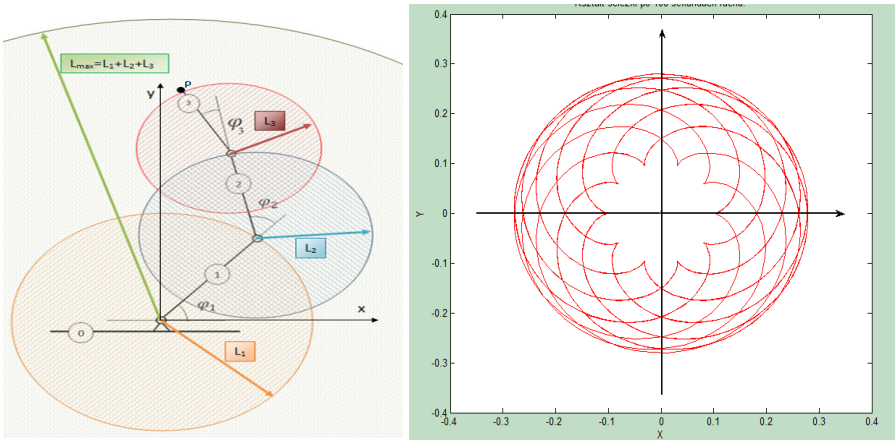

Fig. 12. Three link manipulator model (left) and trajectory followed by the end-effector (right) when the manipulator is fully actuated

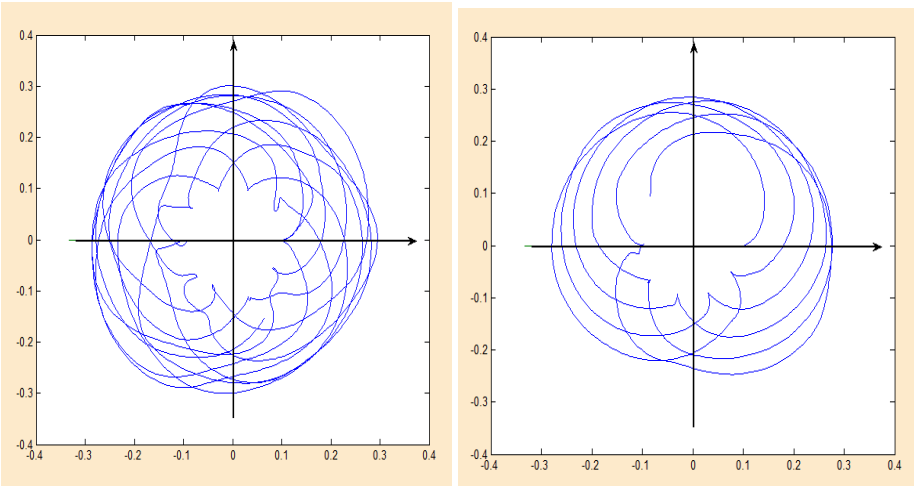

Fig. 13. Two controllers for the underactuated manipulator motion – right – controller 1, left – controller 2

After the third actuator failure, two newly designed controllers have been applied [24]. They were incorporated into the control platform. One controller is for a planar version of a manipulator – Fig. 13 and the other for a vertical version of a manipulator – Fig. 14.

The advanced control platform makes a room for applying existing controllers and designing new ones. All they are plugged into the control law module. The "specialized terms to control law" module makes room for additional data a controller may need, e.g. for an adaptive controller version.

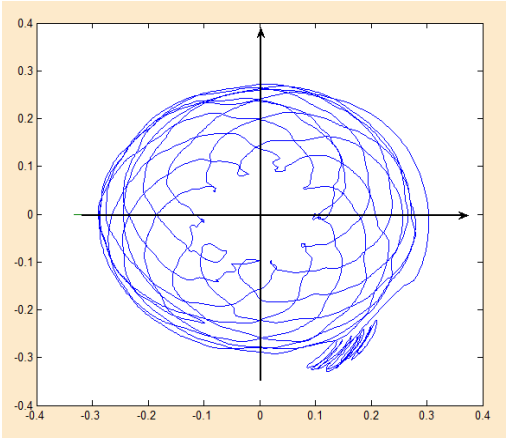

Fig. 14. Controller 2 for a vertical version of the underactuated manipulator

5.4 Error Function Driven Dynamics Reference Motion for the Unicycle and Its Tracking

To demonstrate that the strategy enables adding functionality, e.g. adding optimality options for controllers, let us consider tracing predefined option using the error function (11a) – (11c) with (39), i.e.

$$E(q) = \left(x - \alpha_x(t)\right)^2 + \left(y - \alpha_y(t)\right)^2,$$

As a system example select a a two wheeled mobile platform whose model is kinematically equivalent to a unicycle model presented in Fig. 15, so the material nonholonomic constraint equations are

$$\begin{aligned} \dot{x} - r\dot{\theta}\cos\varphi = 0, \\ \dot{y} - r\dot{\theta}\sin\varphi = 0. \end{aligned} \tag{44}$$

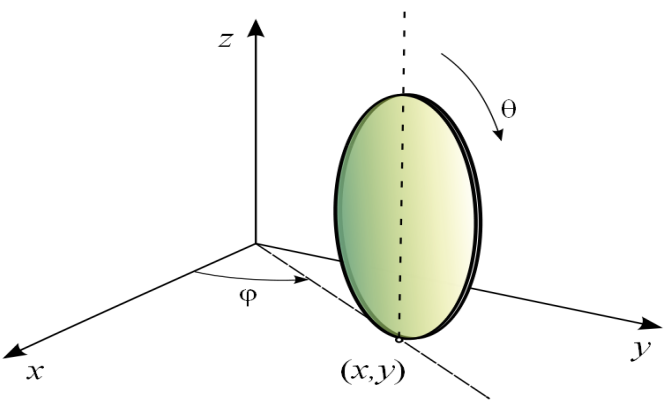

Fig. 15. A unicycle mode

The unicycle dynamics is

$$\begin{aligned} \ddot{x} &= -\frac{\left(I_\theta \dot{\varphi} r^3 \sin\varphi + I_\theta \dot{\varphi} r \sin\varphi\right)\dot{\theta} - F_\theta r\cos\varphi}{I_\theta r^2 + I_\theta} \\ \ddot{y} &= \frac{\left(I_\theta \dot{\varphi} r^3 \cos\varphi + I_\theta \dot{\varphi} r \cos\varphi\right)\dot{\theta} - F_\theta r\sin\varphi}{I_\theta r^2 + I_\theta} \\ \ddot{\varphi} &= \frac{F_\varphi}{I_\varphi} \\ \ddot{\theta} &= \frac{F_\varphi}{I_\theta r^2 + I_\theta} \end{aligned} \tag{45}$$

The performance indices are

$$J_1(q) = \int_0^T E(q) + \|u\|^2 \quad \text{and} \quad J_2(q) = \int_0^T E(q) + \left(\nabla E \cdot \dot{q} + kE\right)^2 + \|u\|^2 \tag{46}$$

Tracking according to $J_1(q)$ and $J_2(q)$ is presented in Fig. 16.

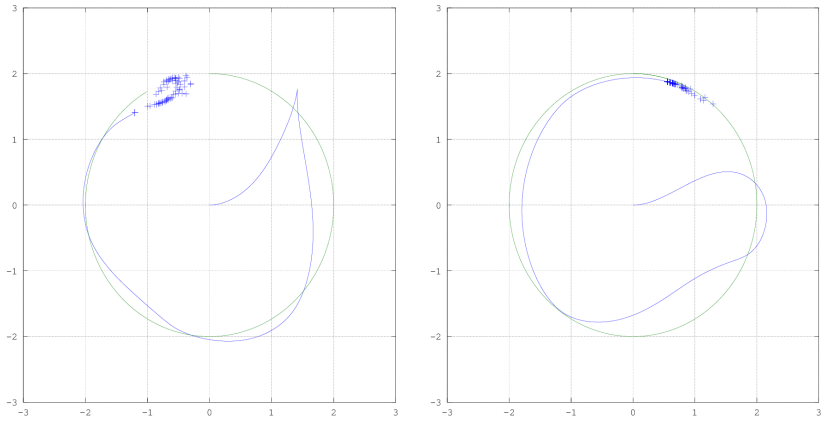

Fig. 16. Tracking predefined trajectory using the error based function approach

6 Towards Implementations

Some preliminary results of applications of nonlinear controller to robotic-like systems are presented in Figures 17–19. They were conducted at the Power and Aeronautical Engineering Department, at Warsaw University of Technology. The programmed constraints are trajectories, a circular and eight shaped ones [25]. The Pioneer software Aria and MobileSim a simulator developed by MobileRobots were used.

Fig. 17. Tracking control algorithm application for a Pioneer robot 3-DX

Tracking desired trajectories by the robot and simulated using MATLAB are presented in Fig. 18.

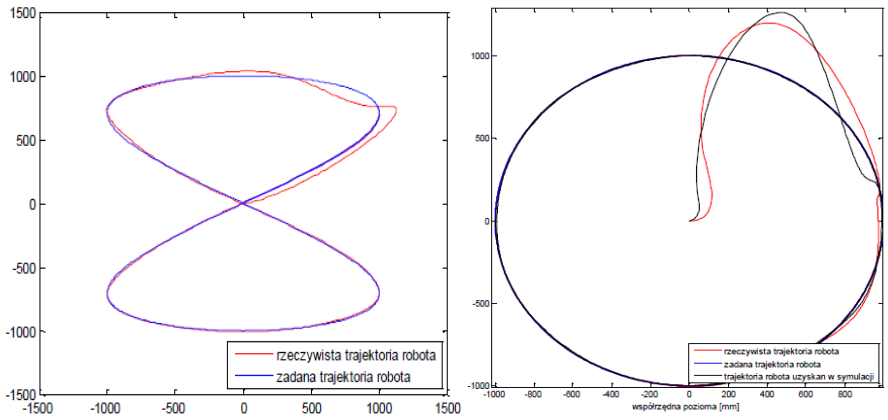

Fig. 18. Tracking desired trajectories (blue) by the robot (red)

A difference between the virtual and real worlds can be seen in Fig. 19.

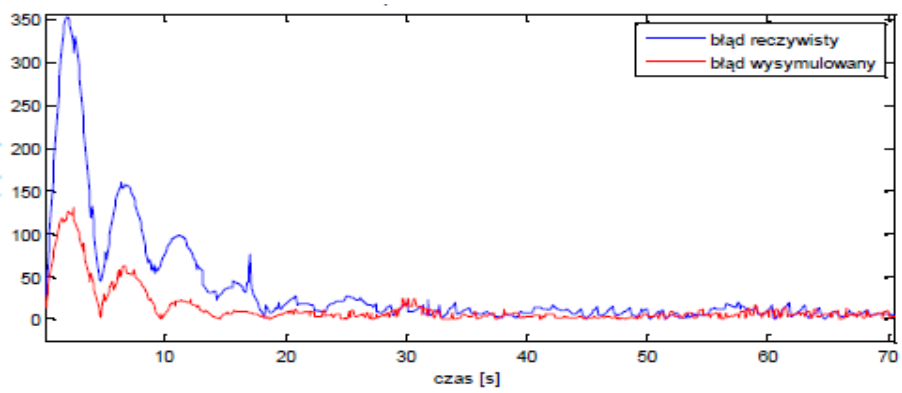

Fig. 19. Tracking errors: blue – real position error, red – simulation study error

Controller implementation is not discussed in this paper. However, embedded robotics may be a solution for implementation of effective controllers – small, inexpensive and light embedded computer systems may be used to implement real-world robot hardware to execute task-based constraints.

7 Conclusions

A multi-option modeling framework for robotic-like systems has been presented. It may be applied to robotic-like systems subjected to a variety of constraints that reflect additional requirements put upon their motion and performance. It is flexible with

respect to modeling parameters, constraints, it is easy for automated derivation of constrained or control dynamics, it can be extendable, i.e. can be applied to modeling formation of robotic-like systems, and it may be accommodated to new options, e.g. for optimality conditions added to a system dynamics. The framework is an input to the advanced control platform, which is a fusion of modern control oriented modeling, control algorithms and embedded controllers. Future research is planned in the area of design controllers using quasi-velocities description to fully exploit properties of motion equations in quasi-coordinates and quasi-velocities.

References

1. Cameron, J.M., Book, W.J.: Modeling mechanisms with nonholonomic joints using the Boltzmann-Hamel equations. Int. J. Robot. Res. 16(1), 47–59 (1997)
2. Papastavridis, J.G.: On the Boltzmann–Hamel equations of motion: a vectorial treatment. J. Appl. Mech. 61, 453–459 (1994)
3. Jarzębowska, E.: Quasi-coordinates based dynamics modeling and control design for nonholonomic systems. Nonlin. Anal. 16(16), 1741–1754 (2008)
4. Jarzębowska, E.: Model-based tracking control of nonlinear systems. CRC Press, Boca Raton (2012)
5. Jarzębowska, E.: Advanced Programmed Motion Tracking Control of Nonholonomic Mechanical Systems. IEEE Trans. Robot. 24(6), 1315–1328 (2008)
6. Prautsch, P., Mita, T.: Control and analysis of the gait of snake robots. In: Proc. IEEE Int. Conf. on Control Applications, pp. 502–507 (1999)
7. Salgado-Jimenez, T., Jouvencel, B.: Using a high order sliding modes for diving control a torpedo autonomous underwater vehicle. In: OCEANS, vol. 2, pp. 934–939 (2003)
8. Jarzębowska, E., Pietrak, K.: Constrained Mechanical Systems Modeling and Control: a Free-Floating Space Manipulator Case as a Multi-Constrained System. Robotics and Autonomous Systems (in press), doi:10.1016/j.robot.2014.04.004
9. Jarzębowska, E., Szklarz, P., Huan, S.: Kinematic Control Design for Nonholonomic Mechanical Systems Based on the Error Function. In: Awrejcewicz, J. (ed.) Modeling, Simulation and Control of Nonlinear Engineering Dynamical Systems, pp. 221–231. Springer (2009)
10. Jarzębowska, E., Szklarz San Huan, P.: Coordinate-free formulation of nonholonomic constraints for wheeled robots. In: Awrejcewicz, J. (ed.) accepted to Springer Proceedings in Mathematics and Statistics. Applied Non-Linear Dynamical Systems (2014)
11. Vafa, Z.: Space manipulator motion with no satellite attitude disturbances. In: Proc. IEEE Int. Conf. Robot. Automat., pp. 1770–1775 (1991)
12. Koh, K.C., Cho, H.S.: A smooth path tracking algorithm for wheeled mobile robots with dynamic constraints. J. Intell. Robot. Syst. 24, 367–385 (1999)
13. Scheuer, A., Laugier, C.: Planning sub-optimal and continuous-curvature paths for car-like robots. In: Proc. IEEE/RSJ Int. Conf. Intell. Robot. Syst., pp. 25–31 (1998)
14. Grioli, G.: Particular solutions in stereodynamics. Centro Intern. Matem. Estivo, Roma, 1–65 (1972) (in Italian)
15. Appell, P.: Exemple de mouvement d'un point assujeti a une liason exprimee par une relation Non lineaire entre les composantes de la vitesse. Comptes Renduss, 48–50 (1911)
16. Beghuin, H.: Course de mecanique, Paris (1947)
17. Seifried, R.: Dynamics of underactuated multibody systems: Modeling, control and optimal design (Solid mechanics and its applications). Springer, New York (2013)

18. Chee, W., Tomizuka, M., Patwardhan, S., et al.: Experimental study of lane change maneuver for AHS applications. In: Proc. Am. Control Conf., vol. 1, pp. 139–143 (1995)
19. Zotov, Y.K., Tomofeyev, A.V.: Controllability and stabilization of programmed motions of reversible mechanical and electromechanical systems. J. Appl. Math. Mech. 56(6), 873–880 (1992)
20. Zotov, Y.K.: Controllability and stabilization of programmed motions of an automobile-type transport robot. J. Appl. Maths. Mech. 67(3), 303–327 (2003)
21. Macfarlane, S., Croft, E.: Manipulator trajectory planning: design for real-time applications. IEEE Trans. Robot. Automat. 19(1), 42–51 (2003)
22. Nejmark J.I., Fufaev N.A.: Dynamics of nonholonomic systems. In: Am. Math. Soc., Providence, Rhode Island (1972)
23. Sowińska, M., Jarzębowska, E.: A fire track dynamics simulation using a quasi-coordinate description, Ms project, Warsaw University of Technology, Power and Aerospace Engineering Department, Warsaw (2014)
24. Szewczyk, A.: Motion Control of a 3-Degree of Freedom Underactuated Planar Manipulator. Ms Thesis, Warsaw University of Technology, Warsaw (2013)
25. Jamiołkowski, M.: Control of a Pioneer 3-DX Robot, Bc. Thesis, Warsaw University of Technology, Warsaw (2011)

Exploration Mobile Robot, Project and Prototype

Waldemar Mucha and Wacław Kuś

Silesian University of Technology, Institute of Computational Mechanics and Engineering, Gliwice, Poland
{waldemar.mucha,waclaw.kus}@polsl.pl

Abstract. The following paper discusses a project of a mobile robot for exploration purposes. The robot's goal is to inspect ambient conditions in places that are unavailable for a human being on account of their location, narrowness or possible danger. The robot needs to be equipped with a wireless video camera (rotated remotely in two axes to provide full visibility) in order to inspect such places. The algorithm controlling the robot includes two operation modes: manual mode, where the robot is controlled remotely by a human operator, and autonomous mode, where the robot has to reach a predefined point avoiding obstacles on the way. Autonomous mode algorithm demonstrates the robot's capability to work without any operator's supervision. The final step of the project, making a fully functional prototype, included building the robot, equipping it with a control system platform and uploading a program consistent with previously developed algorithm.

Keywords: mobile robot, exploration, inspection, control algorithm.

1 Introduction

The following paper is devoted to mobile robotics and describes a project of a mobile robot. The objective of the described project was to develop an exploration mobile robot whose role is to reach and inspect ambient conditions in places unavailable for human beings because of their location, narrowness or possible life or health threat (for example toxic gases or explosion hazard). The robot is equipped with a video camera, capable of transmitting images wirelessly in real time. To ensure a complete visibility of the robot's surroundings, the operator can remotely rotate the camera in both, horizontal and vertical, axes, in an almost 360 degrees range.

The described project has been divided into three essential stages: development of the mechanical structure and design, development of the control algorithm and building a fully functional prototype.

Development of the Mechanical Structure and Design. This stage primarily includes the concept of the main supporting structure and the choice of the robot's suspension and drivetrain. The suspension had to be optimal for driving indoors and outdoors, excluding extremely difficult conditions like sand, mud or snow. The drivetrain had to assure required power and velocity. While designing the main

J. Awrejcewicz et al. (eds.), *Mechatronics: Ideas for Industrial Applications*,
Advances in Intelligent Systems and Computing 317, DOI: 10.1007/978-3-319-10990-9_21

supporting structure, every possible loadcases had to be taken into consideration, including all components' weight and possible collisions. This stage also describes the design of the video camera supporting structure allowing the video camera to be rotated in two axes.

Development of the Control Algorithm. This stage involves creating an algorithm that supports two operation modes of the robot: manual mode and autonomous mode. In the manual mode the remote human operator controls all the movements of the robot based on the image captured from the video camera. The operator has also the ability to remotely adjust the camera's position. In the autonomous mode the robot receives target coordinates as input data and its task is to reach the target without operator's help. The route from the starting point to the target point is determined by possible obstacles – the robot has to avoid them. Obstacles' positions are intercepted by distance sensors included in the robot's equipment.

Building a Fully Functional Prototype. This final step consists of assembling the robot according to previously created technical documentation, integrating it with a programmable control system and finally uploading a program (consistent with the developed algorithm) to the control system.

2 Mechanical Structure and Design

2.1 Suspension

Two suspension variants were taken into consideration: wheeled suspension and tracked suspension [1]. As mentioned, the robot is not designed to move in difficult conditions like snow, mud or sand, so the authors of the project have decided to choose a wheeled suspension. Wheeled suspensions, compared to tracked suspensions, have many advantages like lower complexity, greater reliability, less weight and, most of all, lower friction which is very important as the motion consumes less energy. Wheeled vehicles are able to move on different types of ground – on grass, rural roads and dirt roads as well as on paved roads – and are able to overcome obstacles whose height does not exceed half the diameter of a driven wheel or 1/3 the diameter of a free wheel [1].

From different variants of wheeled suspensions, the authors have chosen tricycle suspension with two driven wheels (with differential steer) on the front and one passive caster in the back. Differential steering allows to control the moving direction by varying the rotational speed of the two driven wheels and using the third wheel, the passive caster, only to balance the robot [2]. The proposed suspension solution provides minimum weight, lower friction and ease of maneuvering while being sufficient to meet all the required conditions [1].

2.2 Main Supporting Structure

The main supporting structure is a frame (Fig. 1) with overall dimensions 590 mm × 350 mm.

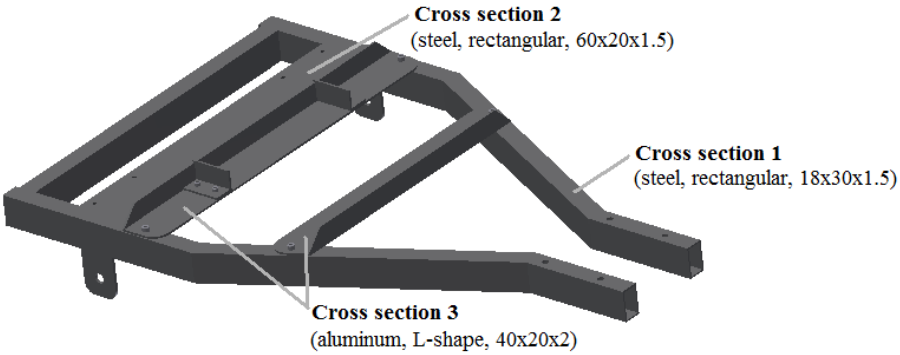

Fig. 1. CAD model of the frame

As almost all other elements of the robot (wheels, battery, drivetrain, video camera supporting structure, etc.) are connected to the frame, it had to be very durable. In order to design the main supporting structure, a series of structural strength analyses using Finite Element Method (FEM) was performed, including static structural analysis, modal analysis and four dynamic analyses assuming possible collisions with obstacles like walls or pillars (example in Fig. 2) [3]. The performed analyses ensured that the frame is durable and the design satisfying.

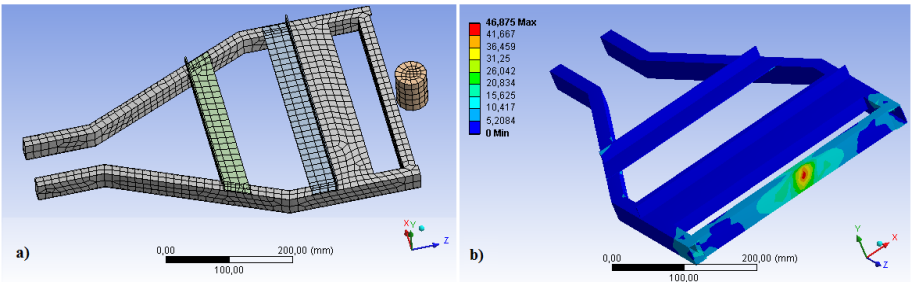

Fig. 2. Example dynamic FEM analysis of the main supporting structure (collision with a pillar): a) mesh, b) maximum (during the collision) equivalent stress (von Misses) map

2.3 Drivetrain

The drivetrain is understood as the set of components delivering power to wheels. As in the discussed robot project there are two separately driven wheels, two identical sets of components had to be used. Each set of components includes motor (*Pololu 100:1 Metal Gearmotor 37Dx57L mm*) and transmission – Fig. 3.

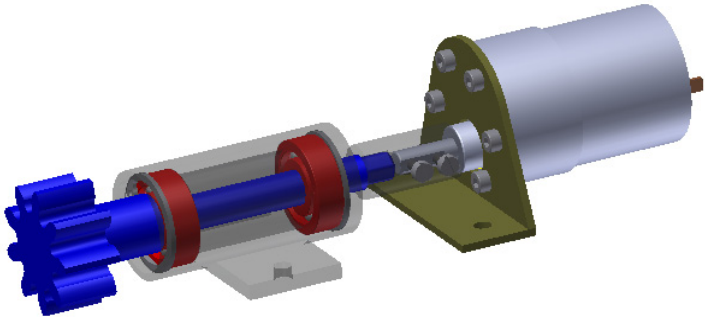

Fig. 3. CAD model of the drivetrain

The transmission consists of a clutch, bearing and gear. A hexagonal clutch transmits power from the motor shaft to the main shaft. The main shaft is supported by two ball bearings and ends with a small spur gear with 9 teeth and normal module of 3 mm. The robot wheels are directly integrated with internal gears (as shown in Fig. 4). Such solution saves space and allows to use only a single-stage gearbox that provides required torque and velocity.

Fig. 4. CAD model of the wheel (without tire)

To verify the transmission, two FEM analyses were performed – of the clutch and of the gearbox [3]. Both assumed the worst possible case – one in which the robot wheel is blocked and the motor strains the transmission with the maximum torque. However, both analyses revealed that in such case no harm will be done. Moreover, the robot has a protection that cuts power to motors whenever a wheel is blocked for more than 2 seconds, saving motors and transmission from damage. This protection is based on monitoring the currents supplying the motors and detecting when the value is exceeded.

2.4 Video Camera Supporting Structure

The video camera supporting structure is located on a pole in order to place the video camera in a good observation spot and also to allow it to be rotated in two axes: horizontal

and vertical (providing very good remote visibility of the robot environment). There are two servos which enable the rotation of the camera mounted on the top plate of the structure shown in Fig. 5.

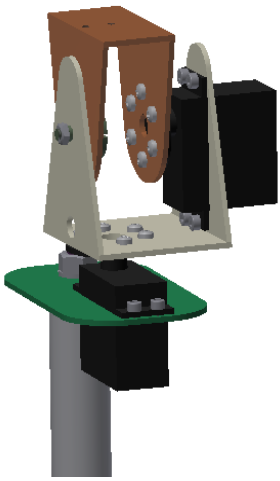

Fig. 5. CAD model of the video camera supporting structure

3 Control Algorithm

As mentioned, the control algorithm consists of two separate algorithms corresponding to two operation modes: manual and autonomous.

3.1 Manual Mode Control Algorithm

In the manual mode, a remote human operator controls all the movements of the robot, piloting its path by controlling two DC motors and adjusting the video camera position by controlling two servos.

The remote communication is performed by the *ZigBee* protocol due to its advantages: low energy consumption and ability to transmit data over long distances (about 100 meters). Low data rate (250 kbit/s) is completely sufficient for performing the aforementioned tasks. It is also possible to use *XBee* instead of *ZigBee*, as both protocols have the same physical layer, differing only in the upper layers.

In order to control the direction and velocity of a single wheel rotation, an H-bridge (based on 4 MOSFETs) has been built and connected to the programmable controller. The H-bridge is connected to PWM outputs of the controller in order to control the rotational velocity of the motor. The H-bridge allows for the use of an electric brake, where both electrical connectors of the motor are connected to the same electric potential. The electric brake turns on when the robot is not expected to move. This protection together with friction in the gear train will prevent the robot from free rolling down an incline.

3.2 Autonomous Mode Control Algorithm

In the autonomous mode the robot has to reach the target point, avoiding collisions with obstacles on the way, without any help from the human operator.

Autonomous mode control algorithm consists of path planning [4–6] and position estimation [7, 8].

Path-finding methods can be divided into global and local. Global methods assume knowledge of the whole environment's map, while local methods use only the information of the robot's immediate environment, acquired by the robot's sensors. In general, global methods can find shorter and better paths than local methods but, on the other hand, local methods have greater resistance to environment changes [3–8].

The authors of the project have developed their own local path-finding method (inspired by the Bug Method [5]) as the base of the autonomous mode algorithm. To acquire information about obstacles near the robot, six ultrasonic distance sensors are used and placed as shown in Fig. 6a.

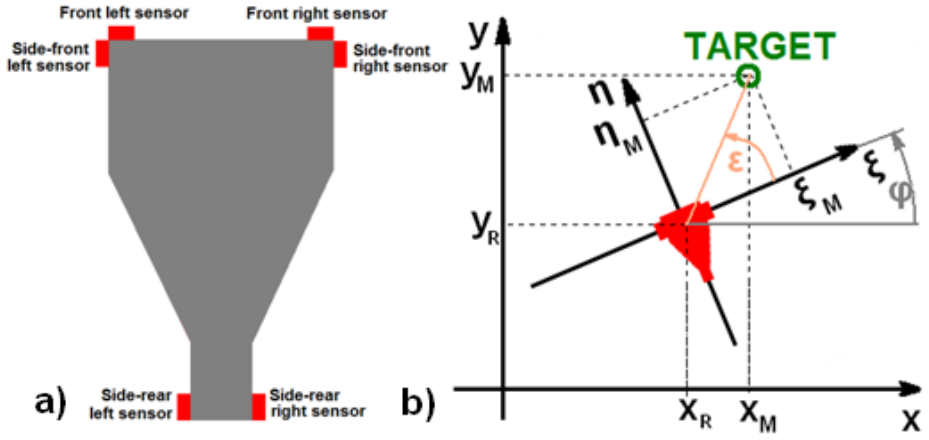

Fig. 6. Autonomous mode model: a) sensor arrangement, b) robot's workspace

The model for real-time calculations of kinematic data is shown in Fig. 6b. There are two coordinates systems: global xy and local ξη (associated with the robot's drive wheels' axle). In each iteration of the control system, robot's coordinates x_R and y_R are being calculated in order to define target's local coordinates ξ_M and η_M and robot-target angle ε. Robot's target coordinates can be calculated in each iteration from information obtained from kinematic feedback (accelerometers on robot or encoders on robot's wheels) or from signals controlling the driving motors. The second method was implemented in the prototype. However it is less accurate as there is no feedback and the positioning errors are accumulated during movement [9, 10].

In every iteration the control system determines the movement of the robot (four states are possible: going forward, turning left, turning right, stopping) based on calculated ξ_M, η_M, ε together with data from distance sensors. Details of this algorithm are presented in Fig. 7.

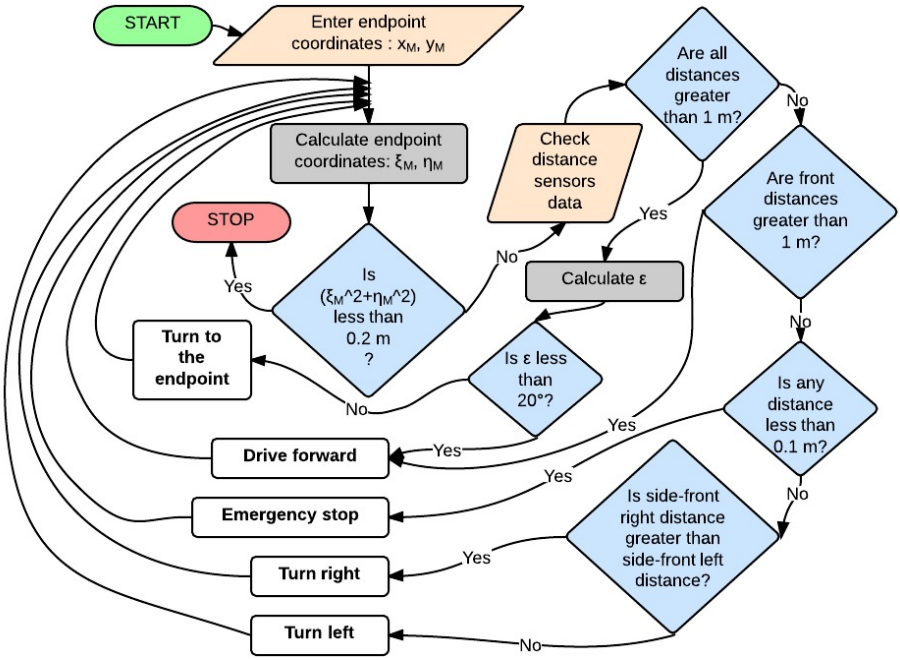

Fig. 7. Autonomous mode algorithm

4 Conclusions

A photography of the finished prototype compared to robot's CAD model is presented in Fig. 8. Both the developed mechanical design and the algorithm are satisfying. The presented solution which integrates the wheel with an internal gear allowed to simplify the construction and save space while providing required transmission ratio. The measured maximum speed of the robot was 14.35 cm/s while theoretical maximum speed is 18 cm/s. The simplest way to increase the robot's speed is to change the DC motors, however it may affect the maximum torque.

The developed autonomous algorithm has been tested. One of the tests was performed on a obstacle course where the road from the start point to the programmed finish point (determined in accordance with the developed algorithm) was about 12 meters. The test was repeated 10 times. Obstacles each time were successfully avoided, the average positioning error was 65 cm. This and other tests lead to the following conclusions: a) despite the fact that the path to the target is not always the shortest, the robot can successfully reach the target with obstacles detected and avoided, b) increasing the number of sensors with minimal software changes would provide the ability to detect smaller obstacles, c) the lack of kinematic feedback does not give good results for longer distances – on every 10 meters of the path, the positioning error is approximately from 0.5 to 1 meter. The authors decided that the robot should be equipped in accelerometers or encoders on the driven wheels in order to provide kinematic feedback and increase positioning accuracy. The authors plan to do this improvement in their future work.

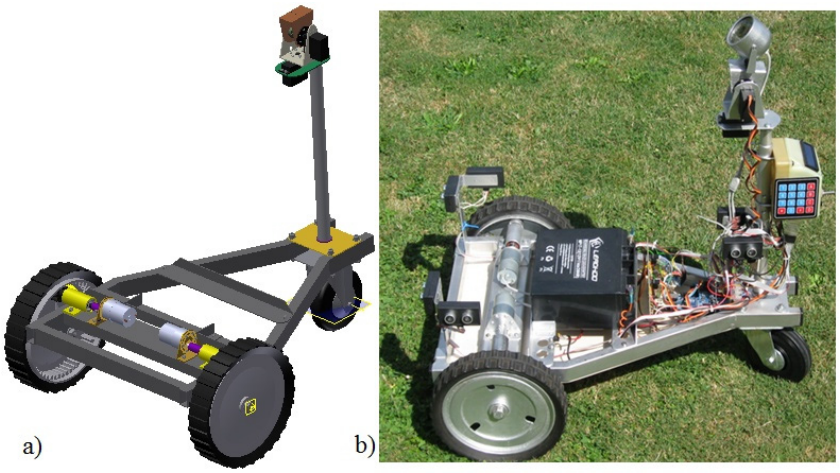

Fig. 8. Mobile robot: a) mechanical structure CAD model, b) prototype photography

References

1. Sandin, P.E.: Robot Mechanisms and Mechanical Devices Illustrated. McGraw-Hill, USA (2003)
2. Lucas, G.W.: A Tutorial and Elementary Trajectory Model for the Differential Steering System of Robot Wheel Actuators, `http://rossum.sourceforge.net/papers/DiffSteer/DiffSteer.html` (access February 28, 2014)
3. Mucha, W.: Mobile robot for exploration purposes (in Polish: Projekt i prototyp robota mobilnego do celów eksploracyjnych). Master's thesis, Institute of Computational Mechanics and Engineering, Silesian University of Technology, Gliwice (2013)
4. Giesbrecht, J.: Global Path Planning for Unmanned Ground Vehicles. Defence R&D, Canada (2004)
5. Buniyamin, N., Wan, N.W.A.J., Sariff, N., Mohamad, Z.: A Simple Local Path Planning Algorithm for Autonomous Mobile Robots. International Journal of Systems Applications, Engineering & Development 5(2) (2011)
6. Cook, G.: Mobile Robots Navigation, Control and Remote Sensing. John Wiley & Sons, Inc. (2011)
7. Hugh, L., Grantham, P.: Accelerometer for mobile robot positioning. IEEE Transactions on Industry Applications 37(3), 812–819 (2001)
8. Atanas, G., Allen, P.K.: Localization methods for a mobile robot in urban environments. IEEE Transactions on Robotic 20(5), 851–864 (2004)

Determination of Motion Parameters with Inertial Measurement Units – Part 1: Mathematical Formulation of the Algorithm

Maciej Trojnacki and Przemysław Dąbek

Industrial Research Institute for Automation and Measurements PIAP, Warsaw, Poland
{mtrojnacki,pdabek}@piap.pl

Abstract. The paper tackles the problem of determination of motion parameters of a wheeled mobile robot using the inertial measurement method. By the motion parameters one means: positions, linear velocities and accelerations of characteristic points of the robot, as well as Euler angles and angular velocity and acceleration of a robot body. Existing methods of determination of robot motion parameters, including the inertial method, the satellite navigation method and hybrid methods, are briefly discussed. The method of determination of motion parameters of a wheeled mobile robot with Inertial Measurement Units is described in details. It involves measurement of three components of acceleration of a selected point on the robot using a three-axial accelerometer and three components of angular velocity of the robot body using a three-axial gyroscope. Desired motion parameters are obtained as a result of differentiation, integration and other mathematical transformations. It was assumed that most of the analyzed motion parameters are calculated both in the coordinate system associated with the robot (moving) and in the reference coordinate system (stationary). The presented method is simple, but enables measurement of wide range of 3D motions, and as such it can be used as a benchmark for advanced algorithms of determination of motion parameters. In the Part 2 of this article, the proposed measurement method is verified in empirical experiments with a wheeled mobile robot using the Inertial Measurement Unit based on low-cost MEMS sensors.

Keywords: wheeled mobile robot, motion parameters, Inertial Measurement Unit, gyroscope, accelerometer.

1 Introduction

Analysis of solutions for chassis systems of wheeled mobile robots (WMRs) leads to recognition of two basic groups.

The first group consists of wheeled robots equipped with steered or caster wheels. For this kind of robots, it is possible to indicate the range of variability for desired motion parameters, when wheel slips are negligible. If wheel slips can be neglected, then location of the instantaneous center of rotation can be determined in an unambiguous way based on angular velocities of spin of wheels, robot geometrical parameters and laws of kinematics.

J. Awrejcewicz et al. (eds.), *Mechatronics: Ideas for Industrial Applications*,
Advances in Intelligent Systems and Computing 317, DOI: 10.1007/978-3-319-10990-9_22

An example of such design is the Azimut robot (Fig. 1a) [1].

a) b)

Fig. 1. Examples of wheeled robots representing two kinematic classes: a – Azimut robot, b – PIAP SCOUT robot [2]

The second group comprises wheeled robots with all wheels non-steered. Example of this kind of design is the PIAP SCOUT robot (Fig. 1b) [2]. In robots like that wheel slips have to be taken into account during turning, because in this case it is not possible to determine location of the instantaneous center of rotation based on angular velocities of spin of wheels and robot geometrical parameters by relying only on laws of kinematics. The occurring wheel slips depend on forces in areas of contact between wheels and the environment, that is, on robot dynamics. Robot motion is also influenced by the number of driven wheels.

For the purpose of investigations of dynamics of vehicles representing the classes described above, but especially of vehicles representing the second group, it is necessary to find means of measurement of motion parameters.

One of the most promising methods is the inertial measurement involving sensors manufactured in the micro-electro-mechanical systems (MEMS) technology.

This measurement technique can be used to carry out investigations of vehicle dynamics, but it also has the potential of application in commercial wheeled robots in order to provide input signals for advanced control systems.

The aim of the present work is presentation of the method of determination of motion parameters for a wheeled mobile robot. This method relies on signals provided by Inertial Measurement Units (IMUs).

2 Methods of Determination of Motion Parameters of Wheeled Mobile Robots

For the navigation of land vehicles, which includes the subproblem of determination of motion parameters of a mobile robot, the following main methods are used:

- odometry-based methods [3, 4],

- satellite navigation methods (e.g. GPS – *Global Positioning System*) or derived methods [5, 6],
- inertial methods (e.g. INS – *Inertial Navigation System*) [7, 8],
- methods that use sensors like laser scanners or vision systems in connection with environment maps – including the SLAM method (*Simultaneous Localization and Mapping*) [9–11],
- hybrid methods that combine several techniques, e.g. GPS and INS navigation [12, 13] or GPS navigation and exteroceptive sensors in connection with environment maps [14].

Methods based on odometry are usually appropriate in case of robots which belong to the first group mentioned in the introduction, that is, in the case when motion involves only negligible slips of wheels.

In turn, use of conventional GPS navigation does not guarantee appropriate accuracy of determination of robot position, and as a result parameters of its motion. That is why, conventional GPS receivers are increasingly replaced by GNSS receivers [15]. Receivers of the latter kind, which cooperate with reference stations, in the best conditions can guarantee accuracy of position determination at the level of centimeters. Bandwidth of changes of motion parameters that can be measured depends in this case on the frequency of data reception from visible satellites (this depends on the type of purchased license). Use of this kind of systems is limited to areas with good visibility of sky (satellites) and having necessary infrastructure (reference stations), which virtually eliminates possibility of using them inside buildings.

The inertial navigation [7], as compared to GPS, has the advantage of determination of motion parameters with better accuracy and frequency. Unfortunately, this is only true in the case of short periods of measurement, because errors of motion parameters determined by integration of accelerations (from accelerometers) and angular velocities (from gyroscopes) increase with time. Advantages of the inertial navigation based on the micro-electro-mechanical systems (MEMS) are: relatively small size of the measuring device, no dependency on infrastructure or environment properties (possibility of operation, e.g. in outer space), relatively low cost [16]. Despite the mentioned advantages, so far the Inertial Measurement Units are rarely implemented in commercial wheeled mobile robots.

Another promising approach is use of the SLAM methods recently developed for robot localization [9, 10]. Those methods can be also used for determination of motion parameters of the robot. Their limitation is associated with larger computational complexity in comparison to the previously described techniques, especially when 3D scanning is involved [11, 17].

In order to exploit advantages and mitigate drawbacks of different methods, combinations of two or more of the above methods are investigated, the most popular being GPS/INS fusion [12]. This approach is going to be investigated in further works of the authors.

3 Method of Determination of Motion Parameters of a Wheeled Mobile Robot Using Inertial Measurement Units

In this work, the inertial navigation method will be applied to determine robot motion parameters.

In one of the previous works [16], it was concluded that for measurement of motion parameters of ground vehicles low-cost MEMS accelerometers can be used, if the following conditions are satisfied:

1. Calibration of accelerometers is carried out to provide data necessary for compensation of their systematic errors.
2. Uncertainty of a time instant when measurement of acceleration takes place is reduced as far as practically possible.
3. Instruments having as high as possible signal-to-noise ratio are chosen within given economic constraints.
4. Influence of acceleration of gravity on accelerometer indications is reduced as far as practically possible.

In the present work, the scope of investigations is extended to MEMS gyroscopes, for which the Statements 1–3 are also valid. Empirical investigations of the method presented here, with particular emphasis on performance of low-cost MEMS gyroscopes, are presented in Part 2 of this article.

Robot motion parameters are determined based on measurements of acceleration $\mathbf{L}^{Ia}$ of the characteristic point I of the robot and angular velocity $\mathbf{L}^{Ig}$ of its mobile platform using the inertial sensors, and in accordance with the method discussed below. A schematic diagram of the methodology is shown in Fig. 2.

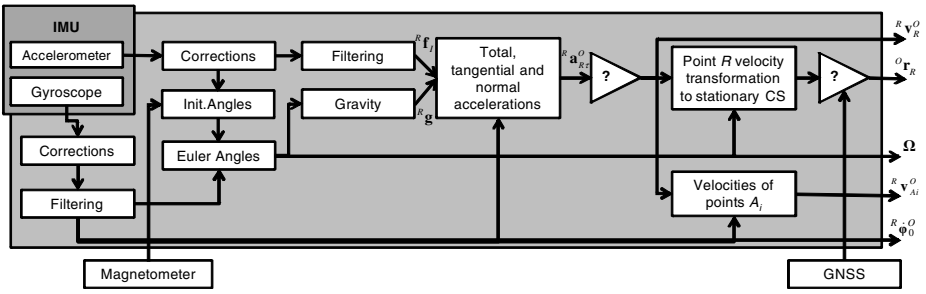

Fig. 2. Schematic diagram of the adopted methodology

3.1 Notation

Symbols used in equations describing the method refer to the kinematic structure of a four-wheeled robot with non-steered wheels shown in Fig. 3.

It is possible to distinguish the following main components of the robot: 0 – body with frame for installation of research equipment, 1–4 – wheels, 5–6 – toothed belts.

The following designations for the i^{th} wheel have been introduced in the robot model: A_i – geometrical center, r_i – radius, θ_i – rotation angle ($i = \{1, ..., 4\}$).

The dimension L denotes the wheelbase (a distance between wheel centers in longitudinal direction), and W denotes the track (a distance between wheel centers in transverse direction).

It is assumed, that the geometric center of the Inertial Measurement Unit (IMU) is located at the characteristic point I of the robot, above the point R, which lies on the intersection of diagonals passing through centers of wheels A_i.

In Fig. 3 the fixed coordinate system $\{O\} = {}^{O}x^{O}y^{O}z$ and the moving coordinate system $\{R\} = {}^{R}x^{R}y^{R}z$ associated with the robot are also introduced.

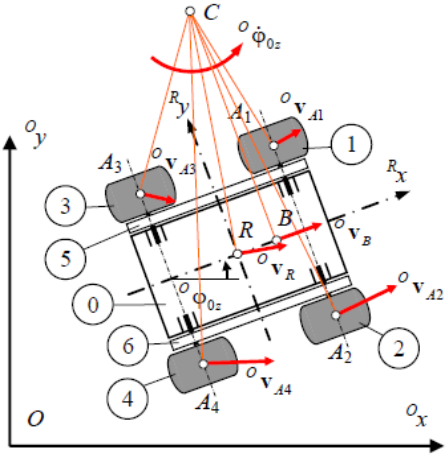

Fig. 3. The kinematic structure of a four-wheeled mobile robot ($A_1A_3 = A_2A_4 = L$, $A_1A_2 = A_3A_4 = W$) [18]

3.2 Corrections and Filtration

For tri-axial accelerometers and gyroscopes, the measurement errors for an instrument can be described in the following general form (linear models of systematic errors are assumed) [19, 20]:

$$\underbrace{\begin{bmatrix} l_x^s \\ l_y^s \\ l_z^s \end{bmatrix}}_{\mathbf{L}^s} = \underbrace{\left(\mathbf{I}_{3\times3} + \begin{bmatrix} S_{xx}^s & N_{xy}^s & N_{xz}^s \\ N_{yx}^s & S_{yy}^s & N_{yz}^s \\ N_{zx}^s & N_{zy}^s & S_{zz}^s \end{bmatrix} \right)}_{\mathbf{M}_0^s} \underbrace{\begin{bmatrix} r_x^s \\ r_y^s \\ r_z^s \end{bmatrix}}_{\mathbf{R}^s} + \underbrace{\begin{bmatrix} B_x^s \\ B_y^s \\ B_z^s \end{bmatrix}}_{\mathbf{B}^s} + \underbrace{\begin{bmatrix} \varepsilon_x^s \\ \varepsilon_y^s \\ \varepsilon_z^s \end{bmatrix}}_{\boldsymbol{\varepsilon}^s} \tag{1}$$

where $s \in \{Ia, Ig\}$ is a designation of the instrument, and if $j \in \{x, y, z\}$ is a designation of the axis, then l_j^s is indication of this instrument, r_j^s is the real value of measured quantity, B_j^s is the zero bias, $\mathbf{I}_{3x3}$ is the identity matrix, S_j^s is the scale factor error, N_{jk}^s is the non-orthogonality error for two neighboring axes (it quantifies the influence of

acceleration/angular velocity along the axis $k \in \{x, y, z\}$ on the j axis), and ε_j^s represents the random error.

Elements of the matrices $\mathbf{M}_0^s$ and $\mathbf{B}^s$ can be estimated based on data provided during calibration procedure, in which instrument indications $\mathbf{L}^s$ are obtained for different excitations $\mathbf{R}^s$. Knowing the form of matrix $\mathbf{M}_0^s$, corrected values of measured quantities are obtained from the following equation:

$$\mathbf{C}^s = (\mathbf{M}_0^s)^{-1}(\mathbf{L}^s - \mathbf{B}^s), \quad \mathbf{C}^s = [c_x^s, c_y^s, c_z^s]^T, \tag{2}$$

where c_j^s are indications of instruments after correction, further considered the measurement results, and $(\mathbf{M}_0^s)^{-1}$ is the inverse of the $\mathbf{M}_0^s$ matrix.

The random errors $\boldsymbol{\varepsilon}^s$ can be taken into account in the procedure of measurement uncertainty evaluation, similar as in the work [16].

Units of the measurement results $\mathbf{C}^{Ig}$ obtained from (2) are deg/s for gyroscopes. In case of accelerometers the result $\mathbf{C}^{Ia}$ is reported as a fraction of acceleration of gravity g, so in order to have the result in the SI units it is necessary to multiply the result by the local value of g present at the site of instrument calibration.

Finally, after correction of indications of accelerometer and gyroscope, one obtains:

$${}^R\mathbf{f}_I = \mathbf{C}^{Ia} \cdot g_{\mathrm{L}}, \quad {}^R\dot{\boldsymbol{\varphi}}_0^O = \mathbf{C}^{Ig}, \tag{3}$$

where:

g_{L} – local value of acceleration of gravity at the calibration site, in m/s^2,
${}^R\mathbf{f}_I$ – measured vector of acceleration at the characteristic point I of the robot, whose all components are in m/s^2,
${}^R\dot{\boldsymbol{\varphi}}_0^O$ – vector of angular velocity of the robot mobile platform „0", whose all components are in deg/s.

The above equations are valid on the assumption that axes of the robot coordinate system $\{R\}$ are parallel to reference axes of the sensors (i.e. coordinate axes marked on the sensor casing or printed circuit board).

According to the method diagram in Fig. 2, the next step in raw signal processing is filtering. The filtering is a topic on its own and it will be considered in further works. Authors believe that it is valuable to first demonstrate that the filtering is necessary.

3.3 Euler Angles and Angular Parameters of Robot Motion

Mobile platform orientation (which is connected with certain rotations of the $\{R\}$ coordinate system associated with the robot) with respect to the stationary coordinate system $\{O\}$, can be described using the so-called Euler angles. Use of the z-y-x Euler angles convention is assumed here (Fig. 4). This convention is used, for example, in

dynamics of aerial and automotive vehicles [21], and interpretation of the angles seems the most natural from the point of view of vehicle dynamics analysis.

Interpretation of Euler angles according to the *z-y-x* convention is as follows: Φ – roll angle, Θ – pitch angle, Ψ – yaw angle.

To carry out transformation of vectors expressed in the $\{R\}$ coordinate system, to the stationary coordinate system $\{O\}$, one may use the matrix of rotation ${}^{O}_{R}\mathbf{R}$, which (for the adopted Euler angles convention) can be written in the form:

$$ {}^{O}_{R}\mathbf{R}={}^{O}_{R}\mathbf{R}_{\Psi}\ {}^{O}_{R}\mathbf{R}_{\Theta}\ {}^{O}_{R}\mathbf{R}_{\Phi}\,. \tag{4} $$

Particular matrices are equal to [22]:

$$ {}^{O}_{R}\mathbf{R}_{\Phi}=\begin{bmatrix}1 & 0 & 0\\ 0 & c_{\Phi} & -s_{\Phi}\\ 0 & s_{\Phi} & c_{\Phi}\end{bmatrix},\ {}^{O}_{R}\mathbf{R}_{\Theta}=\begin{bmatrix}c_{\Theta} & 0 & s_{\Theta}\\ 0 & 1 & 0\\ -s_{\Theta} & 0 & c_{\Theta}\end{bmatrix},\ {}^{O}_{R}\mathbf{R}_{\Psi}=\begin{bmatrix}c_{\Psi} & -s_{\Psi} & 0\\ s_{\Psi} & c_{\Psi} & 0\\ 0 & 0 & 1\end{bmatrix}, \tag{5} $$

where: $c_{\Phi}=\cos\Phi$, $s_{\Phi}=\sin\Phi$, $c_{\Theta}=\cos\Theta$, $s_{\Theta}=\sin\Theta$, $c_{\Psi}=\cos\Psi$, $s_{\Psi}=\sin\Psi$.

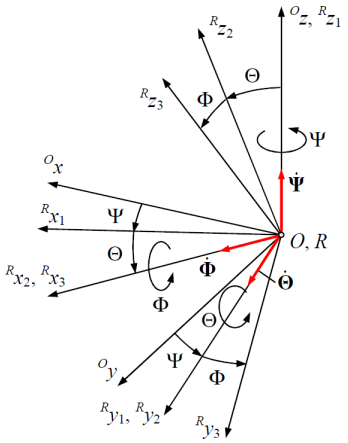

Fig. 4. Illustration of the adopted *z-y-x* Euler angles convention [18]

In the case of inverse transformation, the following relationship is valid:

$$ {}^{R}_{O}\mathbf{R}={}^{R}_{O}\mathbf{R}_{\Phi}\ {}^{R}_{O}\mathbf{R}_{\Theta}\ {}^{R}_{O}\mathbf{R}_{\Psi}\,, \tag{6} $$

where:

$$ {}^{R}_{O}\mathbf{R}_{\Phi}=\begin{bmatrix}1 & 0 & 0\\ 0 & c_{\Phi} & s_{\Phi}\\ 0 & -s_{\Phi} & c_{\Phi}\end{bmatrix},\ {}^{R}_{O}\mathbf{R}_{\Theta}=\begin{bmatrix}c_{\Theta} & 0 & -s_{\Theta}\\ 0 & 1 & 0\\ s_{\Theta} & 0 & c_{\Theta}\end{bmatrix},\ {}^{R}_{O}\mathbf{R}_{\Psi}=\begin{bmatrix}c_{\Psi} & s_{\Psi} & 0\\ -s_{\Psi} & c_{\Psi} & 0\\ 0 & 0 & 1\end{bmatrix}. \tag{7} $$

In order to determine the Euler angles $\boldsymbol{\Omega} = [\Phi, \Theta, \Psi]^T$, at first it is necessary to determine time derivatives $\dot{\boldsymbol{\Omega}}$ of those angles based on angular velocities ${}^R\dot{\boldsymbol{\varphi}}_0^O$ measured by the gyroscope, by projecting them on axes with respect to which successive rotations are made according to the *z-y-x* convention, that is, using the formula:

$$\dot{\boldsymbol{\Omega}} = {}_O^R\mathbf{E}^{-1}({}^R\dot{\boldsymbol{\varphi}}_0^O - {}^R\boldsymbol{\omega}_{I0}), \qquad {}_O^R\mathbf{E}^{-1} = \begin{bmatrix} 1 & s_\Phi s_\Theta / c_\Theta & c_\Phi s_\Theta / c_\Theta \\ 0 & c_\Phi & -s_\Phi \\ 0 & s_\Phi / c_\Theta & c_\Phi / c_\Theta \end{bmatrix}. \tag{8}$$

Determination of the Euler angles in a full range using the above formula is not possible, because of occurrence of a singularity associated with the Θ angle, which cannot take the $\pm\pi/2$ value. This problem can be eliminated by application of quaternions. However, for the purpose of analysis of dynamics of wheeled mobile robots use of quaternions is not necessary, because in normal operation the pitch angles Θ equal to $\pm\pi/2$ do not occur.

During determination of $\dot{\boldsymbol{\Omega}}$ vector, the ${}^R\boldsymbol{\omega}_{I0}$ vector should be taken into account, which contains values of angular velocities obtained from gyroscopes (with applied corrections from calibration) ${}^R\dot{\boldsymbol{\varphi}}_0^O$ averaged over the initial time interval, that is, from $t = 0$ s, to t_0, when robot stands still before the motion begins.

Based on this relationship, it is possible to calculate Euler angles using the following relationship:

$$\boldsymbol{\Omega} = \int \dot{\boldsymbol{\Omega}}\, \mathrm{d}t = \Delta\boldsymbol{\Omega} + \boldsymbol{\Omega}_0, \tag{9}$$

where: $\Delta\boldsymbol{\Omega}$ contains increments of Euler angles from the initial time instant $t = 0$ s, whereas $\boldsymbol{\Omega}_0 = [\Phi_0, \Theta_0, \Psi_0]^T$, the initial values of those angles.

The initial heading of a robot, that is Ψ_0, one may assume to be equal to 0. Alternatively, it is possible to determine the initial heading as an absolute angle with respect to the North Magnetic Pole using a magnetic field sensor.

Initial values of angles Φ and Θ can be obtained based on the knowledge of ${}^R\mathbf{f}_I$ vector at the initial time instant t_0, when the robot does not move, which is equal to:

$${}^R\mathbf{f}_{I0} = [{}^Rf_{x0},\ {}^Rf_{y0},\ {}^Rf_{z0}]^T = -{}^R\mathbf{g}_0 = -g[s_{\Theta 0}, -s_{\Phi 0}c_{\Theta 0}, -c_{\Phi 0}c_{\Theta 0}]^T, \tag{10}$$

where: $c_{\Phi 0} = \cos\Phi_0$, $s_{\Phi 0} = \sin\Phi_0$, $c_{\Theta 0} = \cos\Theta_0$, $s_{\Theta 0} = \sin\Theta_0$, and in this equation the result (14) was used.

From (10), the initial values of the Euler angles are given by:

$$\boldsymbol{\Omega}_0 = [\arctan({}^Rf_{y0}/{}^Rf_{z0}), \arctan({}^Rf_{x0}/\sqrt{({}^Rf_{y0})^2 + ({}^Rf_{z0})^2}), \Psi_0]^T. \tag{11}$$

Because accelerometer data contains noise, in practice, instead of a single value at the initial time instant t_0, mean values of components of ${}^R\mathbf{f}_I$ (eq. (3)) from the interval from $t = 0$ s to t_0, when robot stands still, may be taken into account.

Knowing the ${}^{R}\dot{\boldsymbol{\varphi}}_0^O$ vector, it is also possible to calculate by differentiation the angular acceleration of the mobile platform in the same reference coordinate system, that is ${}^{R}\ddot{\boldsymbol{\varphi}}_0^O$.

3.4 Linear Accelerations of the Robot and the Gravity Model

Accelerometer indications are affected both by the gravity force associated with the acceleration of gravity ${}^{R}\mathbf{g}$ and by the inertia force connected with robot motion with acceleration ${}^{R}\mathbf{a}_I^O$.

The inertia force following from Coriolis acceleration, associated with Earth spinning about its own axis, is not taken into account in the present work, because it is small compared to other accelerations of robot motion. However, it may be considered in the future works.

To the end of determination of the vector of acceleration associated with robot motion ${}^{R}\mathbf{a}_I^O$, at first one should subtract the vector of gravity acceleration ${}^{R}\mathbf{g}$ from the vector of acceleration measured by the instrument ${}^{R}\mathbf{f}_I$.

After assuming that the acceleration of gravity indicated by particular sensitive axis of the accelerometer is positive when this axis is pointed upwards (it is usually the case for MEMS accelerometers available on the market), one should use the formula:

$$ {}^{R}\mathbf{a}_I^O = {}^{R}\mathbf{f}_I + {}^{R}\mathbf{g}, \tag{12} $$

Then, one should transform vector of gravity to the system associated with the robot using the rotation matrix from the stationary to the moving coordinate system, for known Euler angles, using the following relationships:

$$ {}^{R}\mathbf{g} = {}_{O}^{R}\mathbf{R}\ {}^{O}\mathbf{g}, \quad {}_{O}^{R}\mathbf{R} = \begin{bmatrix} c_\Theta c_\Psi & c_\Theta s_\Psi & -s_\Theta \\ s_\Phi s_\Theta c_\Psi - c_\Phi s_\Psi & s_\Phi s_\Theta s_\Psi + c_\Phi c_\Psi & s_\Phi c_\Theta \\ c_\Phi s_\Theta c_\Psi + s_\Phi s_\Psi & c_\Phi s_\Theta s_\Psi - s_\Phi c_\Psi & c_\Phi c_\Theta \end{bmatrix}, \quad {}^{O}\mathbf{g} = [0,\ 0,\ -\mathrm{g}]^T. \tag{13} $$

Based on this one arrives at:

$$ {}^{R}\mathbf{g} = g\,[s_\Theta, -s_\Phi c_\Theta, -c_\Phi c_\Theta]^T. \tag{14} $$

The linear acceleration vector for the point R of the robot ${}^{R}\mathbf{a}_R^O$ in the coordinate system $\{R\}$ (Fig. 3) can be determined based on the known vector of acceleration of the point I of the robot ${}^{R}\mathbf{a}_I^O$ using the formula:

$$ {}^{R}\mathbf{a}_R^O = {}^{R}\mathbf{a}_I^O - {}^{R}\ddot{\boldsymbol{\varphi}}_0^O \times {}^{R}\mathbf{r}_I - {}^{R}\dot{\boldsymbol{\varphi}}_0^O \times ({}^{R}\dot{\boldsymbol{\varphi}}_0^O \times {}^{R}\mathbf{r}_I), \tag{15} $$

where ${}^{R}\mathbf{r}_I = [0,\ 0,\ {}^{R}z_I]^T$.

In general case, the vector of acceleration of the point R of the robot has both tangential and normal components, that is, the following relationships are valid:

$$ {}^{R}\mathbf{a}_{R}^{O}={}^{R}\mathbf{a}_{R\tau}^{O}+{}^{R}\mathbf{a}_{Rn}^{O}, \qquad {}^{R}\mathbf{a}_{R\tau}^{O}={}^{R}\dot{\mathbf{v}}_{R}^{O}, \qquad {}^{R}\mathbf{a}_{Rn}^{O}={}^{R}\dot{\boldsymbol{\varphi}}_{0}^{O}\times{}^{R}\mathbf{v}_{R}^{O}, \tag{16} $$

where:

$$ {}^{R}\mathbf{a}_{R\tau}^{O}=\begin{bmatrix} {}^{R}\dot{v}_{Rx}^{O} \\ {}^{R}\dot{v}_{Ry}^{O} \\ {}^{R}\dot{v}_{Rz}^{O} \end{bmatrix}, \quad {}^{R}\mathbf{a}_{Rn}^{O}=\begin{vmatrix} {}^{R}\mathbf{e}_{x} & {}^{R}\mathbf{e}_{y} & {}^{R}\mathbf{e}_{z} \\ {}^{R}\dot{\varphi}_{0x}^{O} & {}^{R}\dot{\varphi}_{0y}^{O} & {}^{R}\dot{\varphi}_{0z}^{O} \\ {}^{R}v_{Rx}^{O} & {}^{R}v_{Ry}^{O} & {}^{R}v_{Rz}^{O} \end{vmatrix}=\begin{bmatrix} {}^{R}\dot{\varphi}_{0y}^{O}\,{}^{R}v_{Rz}^{O}-{}^{R}\dot{\varphi}_{0z}^{O}\,{}^{R}v_{Ry}^{O} \\ {}^{R}\dot{\varphi}_{0z}^{O}\,{}^{R}v_{Rx}^{O}-{}^{R}\dot{\varphi}_{0x}^{O}\,{}^{R}v_{Rz}^{O} \\ {}^{R}\dot{\varphi}_{0x}^{O}\,{}^{R}v_{Ry}^{O}-{}^{R}\dot{\varphi}_{0y}^{O}\,{}^{R}v_{Rx}^{O} \end{bmatrix}, \tag{17} $$

and ${}^{R}\mathbf{e}_{j}$ are unit vectors of axes of the coordinate system associated with the robot, $j\in\{x, y, z\}$.

In a special case, when roll and pitch angles of the robot body can be assumed 0 and its motion along vertical direction can be neglected, the above relationships are reduced to the form:

$$ {}^{R}\mathbf{a}_{R}^{O}=\begin{bmatrix} {}^{R}a_{Rx}^{O} \\ {}^{R}a_{Ry}^{O} \\ 0 \end{bmatrix}, \quad {}^{R}\mathbf{a}_{R\tau}^{O}=\begin{bmatrix} {}^{R}\dot{v}_{Rx}^{O} \\ {}^{R}\dot{v}_{Ry}^{O} \\ 0 \end{bmatrix}, \quad {}^{R}\mathbf{a}_{Rn}^{O}=\begin{bmatrix} -{}^{R}\dot{\varphi}_{0z}^{O}\,{}^{R}v_{Ry}^{O} \\ {}^{R}\dot{\varphi}_{0z}^{O}\,{}^{R}v_{Rx}^{O} \\ 0 \end{bmatrix}. \tag{18} $$

Based on the knowledge of total and normal accelerations, it is possible to determine tangential acceleration of the point R using formula:

$$ {}^{R}\mathbf{a}_{R\tau}^{O}={}^{R}\mathbf{a}_{R}^{O}-{}^{R}\mathbf{a}_{Rn}^{O} \quad \Rightarrow \quad {}^{R}\dot{\mathbf{v}}_{R}^{O}={}^{R}\mathbf{a}_{R}^{O}-{}^{R}\dot{\boldsymbol{\varphi}}_{0}^{O}\times{}^{R}\mathbf{v}_{R}^{O}. \tag{19} $$

3.5 Linear Velocities of the Robot

As a result of integration of the tangential acceleration, knowing the initial velocity vector of the point R (i.e. ${}^{R}\mathbf{v}_{R0}^{O}=\mathbf{0}$), it is possible to calculate the velocity vector of this point, which can be expressed in the form:

$$ {}^{R}\mathbf{v}_{R}^{O}=\int {}^{R}\mathbf{a}_{R\tau}^{O}\mathrm{d}t={}^{R}\Delta\mathbf{v}_{R}^{O}+{}^{R}\mathbf{v}_{R0}^{O}, \tag{20} $$

where ${}^{R}\Delta\mathbf{v}_{R}^{O}$ is the increment of the velocity vector since the initial time instant.

Vectors of velocities of characteristic points A_i of the robot can be obtained using formulas:

$$ {}^{R}\mathbf{v}_{Ai}^{O}={}^{R}\mathbf{v}_{R}^{O}+{}^{R}\dot{\boldsymbol{\varphi}}_{0}^{O}\times{}^{R}\mathbf{r}_{Ai}, \tag{21} $$

where index i denotes number of wheel and for the four-wheeled robot shown in Fig. 3:

$$ {}^{R}\mathbf{r}_{Ai}=[{}^{R}x_{Ai},\ {}^{R}y_{Ai},\ {}^{R}z_{Ai}]^{T}=[\pm L/2, \pm W/2, 0]^{T}. \tag{22} $$

The '+' sign at L is valid for the front wheels, and '–' for the rear wheels, whereas the '+' sign at W is valid for the wheels of the left-hand side of the vehicle, and '–' for the right-hand side.

Based on the above relationship, one obtains:

$$ {}^{R}\mathbf{v}_{Ai}^{O} = \begin{bmatrix} {}^{R}v_{Rx}^{O} \\ {}^{R}v_{Ry}^{O} \\ {}^{R}v_{Rz}^{O} \end{bmatrix} + \begin{vmatrix} {}^{R}\mathbf{e}_{x} & {}^{R}\mathbf{e}_{y} & {}^{R}\mathbf{e}_{z} \\ {}^{R}\dot{\varphi}_{0x}^{O} & {}^{R}\dot{\varphi}_{0y}^{O} & {}^{R}\dot{\varphi}_{0z}^{O} \\ {}^{R}x_{Ai} & {}^{R}y_{Ai} & {}^{R}z_{Ai} \end{vmatrix} = \begin{bmatrix} {}^{R}v_{Rx}^{O} + {}^{R}\dot{\varphi}_{0y}^{O}\,{}^{R}z_{Ai} - {}^{R}\dot{\varphi}_{0z}^{O}\,{}^{R}y_{Ai} \\ {}^{R}v_{Ry}^{O} + {}^{R}\dot{\varphi}_{0z}^{O}\,{}^{R}x_{Ai} - {}^{R}\dot{\varphi}_{0x}^{O}\,{}^{R}z_{Ai} \\ {}^{R}v_{Rz}^{O} + {}^{R}\dot{\varphi}_{0x}^{O}\,{}^{R}y_{Ai} - {}^{R}\dot{\varphi}_{0y}^{O}\,{}^{R}x_{Ai} \end{bmatrix}. \tag{23} $$

It is also possible to calculate velocity and acceleration vectors for the analyzed points of the robot in the stationary coordinate system $\{O\}$ using the relationships:

$$ {}^{O}\mathbf{v}_{P} = {}_{R}^{O}\mathbf{R}\;{}^{R}\mathbf{v}_{P}^{O}, \qquad {}^{O}\mathbf{a}_{P} = {}_{R}^{O}\mathbf{R}\;{}^{R}\mathbf{a}_{P}^{O}, \tag{24} $$

where $P = \{R, Ai\}$, and the matrix of rotation ${}_{R}^{O}\mathbf{R}$ has the form:

$$ {}_{R}^{O}\mathbf{R} = \begin{bmatrix} c_{\Theta}c_{\Psi} & -c_{\Phi}s_{\Psi} + s_{\Phi}s_{\Theta}c_{\Psi} & s_{\Phi}s_{\Psi} + c_{\Phi}s_{\Theta}c_{\Psi} \\ c_{\Theta}s_{\Psi} & c_{\Phi}c_{\Psi} + s_{\Phi}s_{\Theta}s_{\Psi} & -s_{\Phi}c_{\Psi} + c_{\Phi}s_{\Theta}s_{\Psi} \\ -s_{\Theta} & s_{\Phi}c_{\Theta} & c_{\Phi}c_{\Theta} \end{bmatrix}. \tag{25} $$

3.6 Position Vector of the Robot

The position vector of the characteristic point R of the robot in the stationary coordinate system $\{O\}$ is calculated by means of integration of velocity of this point expressed in the stationary coordinate system, that is:

$$ {}^{O}\mathbf{r}_{R} = \int {}^{O}\mathbf{v}_{R}\,\mathrm{d}t = {}^{O}\Delta\mathbf{r}_{R} + {}^{O}\mathbf{r}_{R0}, \tag{26} $$

where ${}^{O}\Delta\mathbf{r}_{R}$ is the increment of the position vector since the initial time instant, and ${}^{O}\mathbf{r}_{R0}$ is the vector of initial position of the point R.

The initial position of the point R can be arbitrarily assumed as ${}^{O}\mathbf{r}_{R0} = [0, 0, r]^{T}$ (as mentioned before, the point R of the robot lies on the intersection of diagonals through centers of wheels A_i) or it can determined using additional measurement system, e.g. GNSS. Knowledge of position of this point in successive time instants allows determination of trajectory of its motion.

4 Conclusions and Future Works

In this work a complete mathematical formulation of a simple method of determination of parameters of robot motion using tri-axial accelerometer and tri-axial gyroscope was presented. This method enables determination of the motion parameters of a wheeled mobile robot performing a wide range of motions in space. Empirical verification of this method with low-cost MEMS sensors and the PIAP SCOUT four-wheeled mobile robot is presented in the Part 2 of this article.

Future works will focus on the following problems:

- Analysis of sensitivity of the proposed method to errors of particular measuring instruments.
- Inclusion of the Coriolis acceleration associated with Earth spin about its own axis.
- Implementation of the proposed method in the motion control system of a wheeled robot.
- Development of advanced algorithms of determination of motion parameters suitable for more demanding specialized applications.

Acknowledgements. The work has been realized as a part of the project entitled "Dynamics modeling of a four-wheeled mobile robot and tracking control of its motion with limitation of wheel slips". The project is financed from the means of National Science Centre of Poland granted on the basis of decision number DEC-2011/03/B/ST7/02532.

References

1. Lauria, M., Michaud, F., Legault, M.-A., Létourneau, D., Rétornaz, P., Nadeau, I., Lepage, P., Morin, Y., Gagnon, F., Giguère, P.: Elastic locomotion of a four steered mobile robot. In: IEEE/RSJ International Conference on Intelligent Robots and Systems, IROS 2008, pp. 2721–2722 (2008)
2. PIAP – producer of EOD equipment, EOD robots and surveillance robots, `http://www.antiterrorism.eu/en/` (accessed: April 21, 2014)
3. Palacin, J., Valgañon, I., Pernia, R.: The optical mouse for indoor mobile robot odometry measurement. Sensors and Actuators A: Physical 126(1), 141–147 (2006)
4. Papadopoulos, E., Misailidis, M.: On differential drive robot odometry with application to path planning. In: Proceedings of the European Control Conference, pp. 5492–5499 (2007)
5. Dow, J.M., Neilan, R.E., Rizos, C.: The International GNSS Service in a changing landscape of Global Navigation Satellite Systems. J. Geod. 83(3-4), 191–198 (2009)
6. Hofmann-Wellenhof, B., Lichtenegger, H., Wasle, E.: GNSS – Global Navigation Satellite Systems: GPS, GLONASS, Galileo, and more. Springer (2007)
7. Titterton, D., Weston, J.L.: Strapdown Inertial Navigation Technology, 2nd edn. IET (2004)
8. Walchko, K.J., Mason, P.A.: Inertial navigation. In: Florida Conference on Recent Advances in Robotics, pp. 1–9 (2002)
9. Perez, J.A., Castellanos, J.A., Montiel, J.M.M., Neira, J., Tardos, J.D.: Continuous mobile robot localization: vision vs. laser. In: Proceedings of 1999 IEEE International Conference on Robotics and Automation, vol. 4, pp. 2917–2923 (1999)
10. Schmidt, A., Kraft, A., Fularz, M., Domagała, Z.: On augmenting the visual slam with direct orientation measurement using the 5-point algorithm. Journal of Automation Mobile Robotics and Intelligent Systems 7(1), 5–10 (2013)
11. Siemiątkowska, B., Szklarski, J., Gnatowski, M.: Mobile robot navigation with the use of semantic map constructed from 3D laser range scans. Control and Cybernetics 40(2), 437–453 (2011)
12. Groves, P.D.: Principles of GNSS, Inertial, and Multi-Sensor Integrated Navigation Systems. Artech Print on Demand, Boston (2007)

13. Tin Leung, K., Whidborne, J.F., Purdy, D., Dunoyer, A.: A review of ground vehicle dynamic state estimations utilising GPS/INS. Vehicle System Dynamics 49(1-2), 29–58 (2011)
14. Ray, A.K., Behera, L., Jamshidi, M.: GPS and sonar based area mapping and navigation by mobile robots. In: 7th IEEE International Conference on Industrial Informatics, INDIN 2009, pp. 801–806 (2009)
15. Perski, A., Wieczyński, A., Bożek, K., Kapelko, S., Pawłowski, S.: GNSS receivers in engineering practice. Introduction to Global Navigation Satellite Systems, Pomiary Automatyka Robotyka 17(3), 103–111 (2013) (in Polish)
16. Dąbek, P.: Evaluation of low-cost MEMS accelerometers for measurements of velocity of unmanned vehicles. Pomiary Automatyka Robotyka 17(1), 102–113 (2013)
17. Bedkowski, J., Maslowski, A., Cubber, G.D.: Real time 3D localization and mapping for USAR robotic application. Industrial Robot: An International Journal 39(5), 464–474 (2012)
18. Trojnacki, M.: Modelowanie dynamiki mobilnych robotów kołowych (Dynamics modeling of wheeled mobile robots). Oficyna Wydawnicza PIAP, Warszawa (2013)
19. Hidalgo, J., Poulakis, P., Köhler, J., Del-Cerro, J., Barrientos, A.: Improving Planetary Rover Attitude Estimation via MEMS Sensor Characterization. Sensors 12(12), 2219–2235 (2012)
20. Syed, Z.F., Aggarwal, P., Goodall, C., Niu, X., El-Sheimy, N.: A new multi-position calibration method for MEMS inertial navigation systems. Measurement Science and Technology 18(7), 1897–1907 (2007)
21. Blundell, M., Harty, D.: Multibody Systems Approach to Vehicle Dynamics. Elsevier (2004)
22. Spong, M.W., Vidyasagar, M.: Robot Dynamics and Control, 1st edn. Wiley, New York (1989)

Determination of Motion Parameters with Inertial Measurement Units – Part 2: Algorithm Verification with a Four-Wheeled Mobile Robot and Low-Cost MEMS Sensors

Maciej Trojnacki and Przemysław Dąbek

Industrial Research Institute for Automation and Measurements PIAP, Warsaw, Poland
{mtrojnacki,pdabek}@piap.pl

Abstract. The paper is concerned with the problem of determination of motion parameters of a wheeled mobile robot using the inertial measurement method. The algorithm proposed in Part 1 of the article is verified in empirical experiments with a four-wheeled mobile robot PIAP SCOUT. Main design features of the robot are presented. The measurement and control system is described in details. The measurement system is based on a low-cost MEMS Inertial Measurement Unit. Selected results of empirical experiments are shown and thoroughly discussed. Performance of the algorithm with the low-cost sensors is evaluated. It is concluded that the presented simple method enables determination of unknown motion parameters, especially in applications where only short duration of experiments is required. Quality of the obtained results, however, shows scope for improvement. The weakest point of the measurement system are unreliable changes of the Euler angles obtained from the low-cost MEMS gyroscopes.

Keywords: wheeled mobile robot, motion parameters, Inertial Measurement Unit, empirical research, low-cost sensors, MEMS accelerometer, MEMS gyroscope.

1 Introduction

This is Part 2 of the paper concerned with the problem of determination of motion parameters of land vehicles by means of the inertial method of measurements. In the Part 1 the theoretical background and mathematical formulation of the algorithm necessary to determine motion parameters of an object from known acceleration and angular velocity of respectively its certain point and body are presented. In the present Part 2 of the paper, the data captured during motion of a wheeled mobile robot and processed with this algorithm are presented.

The aim of this Part 2 is assessment of performance of the simple algorithm when data are obtained from a low-cost Inertial Measurement Unit.

The Part 2 is organized as follows. In Section 2 the four-wheeled mobile robot whose motion was investigated is described. Section 3 describes the measurement and

J. Awrejcewicz et al. (eds.), *Mechatronics: Ideas for Industrial Applications*,
Advances in Intelligent Systems and Computing 317, DOI: 10.1007/978-3-319-10990-9_23

control system used during investigations. In Section 4 an overview of the performed experiments is given, and in Section 5 their results are presented and thoroughly discussed. Summary and planned works are described in Section 6.

2 The Object of Investigations

The PIAP SCOUT mobile robot [1] is used as a test bed. It was designed for quick reconnaissance of places with difficult access, i.e., vehicle chassis, places under seats in means of transportation, narrow rooms and ventilation ducts. The robot is manufactured in various versions, differing mainly in type of equipment installed on-board, which makes it suitable for specialized tasks (Fig. 1a).

The mobile platform of the robot is approximately 0.5 m by 0.5 m (length × width), and its mass is about 15 kg (only the mobile platform without manipulator and accessories).

The robot drive system is hybrid. It consists of tracks and wheels which operate simultaneously. Two rear wheels are driven independently by DC motors equipped with gear units and encoders. The drive from the rear wheels is transmitted to the front wheels via two tracks. Robot is differentially steered, that is, change of direction of motion is possible by different angular velocity of wheels at the left and right-hand side of the vehicle.

Rugged construction of small dimensions and small weight with dynamic drive system provides high maneuverability and high speed of the robot.

a) b)

Fig. 1. a – PIAP SCOUT wheeled mobile robot [1], b – the type of wheel used during investigations

In Fig. 1a the commercial version of the robot is shown. For the purpose of investigations the manipulator, camera and auxiliary front tracks were unmounted. Robot was equipped with tires of the type shown in Fig. 1b. These are non-pneumatic tires

with foam filling. Material of the outer shell is a kind of synthetic rubber called viton. Unloaded tire diameter is 193 mm.

3 Measurement and Control System

The robot has been adapted to realization of experimental research by installing additional frame to mount necessary equipment (Fig. 2). On the frame was installed the laptop computer connected to the robot CAN bus by means of the USB-CAN adapter and to the Inertial Measurement Unit directly via USB cable.

The laptop was running Windows 7 OS and dedicated software for sending control data and acquisition of measurement data. This system can be qualified as a soft-real time system, which means that occasionally the processing loop does not meet the real-time criteria leading to inferior quality of certain data points.

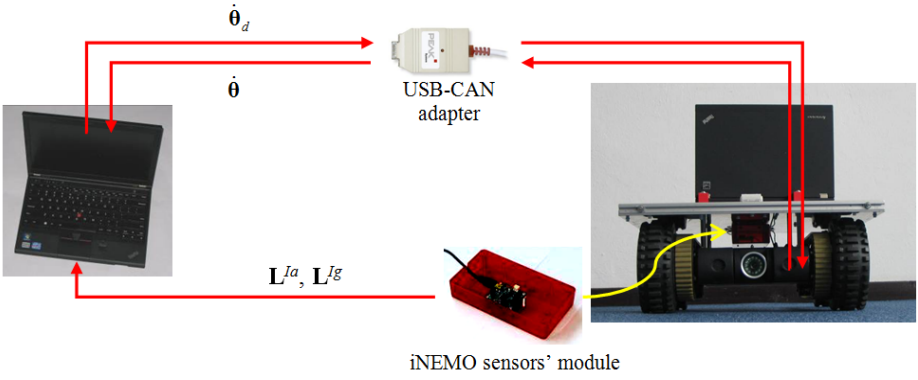

Fig. 2. Schematic diagram of a measurement and control system used in experimental research

Control variables are desired velocities of spin of wheels $\dot{\boldsymbol{\theta}}_d = [\dot{\theta}_{3d}, \dot{\theta}_{4d}]^T$. Those velocities are sent directly to drive velocity controllers for the left and right-hand side of the robot. It should be emphasized that in this version of the control system the control occurs at the level of individual drives, and not at the level of the mobile platform. As a result, even if drives realize the desired velocities perfectly there is no guarantee that the mobile platform moves as desired by the researcher in terms of its translational and rotational velocity. This effect is connected mainly with occurrence of wheel slips in areas of wheel contacts with the ground. In order to reduce this effect it is necessary to introduce the additional higher level controller, which is not done in this work, but is a topic of works [2, 3].

Measured quantities include: actual velocities of spin of wheels $\dot{\boldsymbol{\theta}} = [\dot{\theta}_3, \dot{\theta}_4]^T$, linear acceleration of the characteristic point *I* of the robot $\mathbf{L}^{Ia}$, and angular velocity $\mathbf{L}^{Ig}$ of the robot body 0, both in the moving coordinate system.

Measurements of acceleration and angular velocity are provided by a low-cost Inertial Measurement Unit, the iNEMO sensor module from STMicroelectronics. The iNEMO sensor module contains a tri-axial accelerometer and tri-axial gyroscope, whose

selected technical specifications are given in Table 1. Technical data in the table are taken from datasheets of the individual sensors.

The iNEMO IMU can be qualified into the group of the worst quality sensors, called commercial application grade sensors according to [4]. The ADIS 16488 is a tactical grade IMU (next level of quality according to [4]) whose specification is given for comparison.

In case of gyroscopes one of the most important properties is bias stability, which quantifies how the gyroscope bias changes during measurement. In the ideal situation the bias should remain the same as at the beginning of the measurement for the whole measurement period, but unfortunately it does change in a random manner. The better the gyroscope is, the lower is the value of this parameter. Unfortunately, the value of this property is not stated in datasheets of gyroscopes contained in the iNEMO sensor module. However, after [4] one can expect the value of the order of 1 deg/s.

Table 1. Excerpt from technical specification of the Inertial Measurement Unit used in experiments. Higher grade IMU shown for comparison

	iNEMO v2 [5]	ADIS 16488 [6]
Release date	2010	2014
Price (EUR)	250	1500
Accelerometer		
Range (g)	±2	±18
ND[1)] ($mg/\sqrt{Hz}$)	0.22	0.06
In-Run Bias Stability (mg)	no data	0.1
Gyroscope		
Range (°/s)	±300	±480
ND ($deg/s/\sqrt{Hz}$)	0.018	0.006
In-Run Bias Stability (deg/hr)	no data	6.25

[1)] ND – noise density, 1 σ value

4 Experiment Design

Empirical data were obtained from experiments with the wheeled mobile robot and equipment described in Section 3.

Experiments were carried out in three variants, whose nominal parameters are summarized in Table 2. Variants differed by type of maneuver and shape of the ground. The type of maneuver refers to the desired trajectory of motion for the robot. As it was mentioned in the previous section, the control variables were desired velocities of spin of wheels, which were calculated based on the desired maneuvers prior to the experiment on the assumption of lack of wheel slips (i.e. from the kinematic relationship). For two variants, the shape of the ground was assumed a horizontal plane,

and for one variant – a horizontal plane in the first phase of motion and an inclined plane in the second phase of motion. The angle of inclination was 12.4 deg and the inclination was in the ${}^{O}x^{O}z$ plane of the reference coordinate system.

Table 2. Characteristics of variants of the performed experiment

		maneuver		ground	
#	symbol	path shape	turn angle (deg)	inclination (deg)	type of surface
1	w0185	right turn	90	0	carpet flooring
2	w0183	straight line	0	12.4	carpet flooring / furniture finish
3	w0184	straight line	0	0	carpet flooring

All variants of the experiment were repeated several times. At each repetition special attention was paid to ensure repeatable starting position and orientation of the robot, however no specialized equipment was used to aid those efforts.

Raw measurement data obtained in experiments were post-processed using the algorithm presented in the Part 1 of the paper, which was implemented in MATLAB.

Values of elements of the matrices $\mathbf{M}_0^s$ and $\mathbf{B}^s$ from equation (1) (see Part 1 of the paper) were obtained during calibration procedure for the iNEMO sensor module carried out in a separate series of experiments, independent of the present investigations.

5 Results

Graphs of particular motion parameters obtained during empirical investigations and as a result of application of the described algorithm are shown in Figs. 3–5.

In Fig. 3 are shown results for the desired 90-degree right turn of the robot (experiment variant #1, Table 2). On example of those results a step by step discussion of mathematical transformations involved in the algorithm presented in the Part 1 of the paper is carried out. Numbers of cited equations refer to the numbering introduced in the Part 1.

Similarly, in Fig. 4 are presented results for desired straight-line motion of the robot, but the motion takes place partly on a horizontal ground and partly on an inclined plane (variant #2). This time only the most important quantities are discussed.

Plots in Fig. 5 present the results for robot motion along a straight line on a horizontal ground (variant #3). This is the simplest case of motion, with least impact of various influencing factors on the final result, and as such it is a good starting point to discussion of repeatability of the results obtained from the presented method.

It should be noted that in all experiments the laboratory floor covered with carpet flooring was used as a horizontal ground surface. This laboratory ground is not perfectly flat, but has minor unevenness distributed randomly all over the floor.

5.1 Experiment Variant 1 – 90-Degree Right Turn

In Fig. 3, the subfigure a) shows angular velocities of the mobile platform recorded by the gyroscope – those velocities are not the raw measurements, but the corrected measurements with corrections determined in the calibration process applied according to the formulas (2) and (3). (The corrections applied in this step are meant to mitigate static scale factor, non-orthogonality and zero bias errors of the instruments. It is not possible to correct dynamic changes of those parameters (errors) which may occur, e.g. during experiment, with this procedure.)

In subfigure a) apart from change of the angular velocity associated with robot rotation about its vertical axis ${}^{R}z$, which occurs in the time interval corresponding to turning, there are also visible changes of the remaining angular velocities. Changes of those velocities (about robot longitudinal axis ${}^{R}x$ and lateral axis ${}^{R}y$) have small amplitude during whole duration of the experiment. Those changes are associated with minor unevennesses of the laboratory floor. There are is also visible the change of a larger amplitude in the time interval corresponding to turning (black line, about 1.5 s). This change in velocity reflects changes of orientation of the robot body caused by the centrifugal force acting on the robot mass centre during turning.

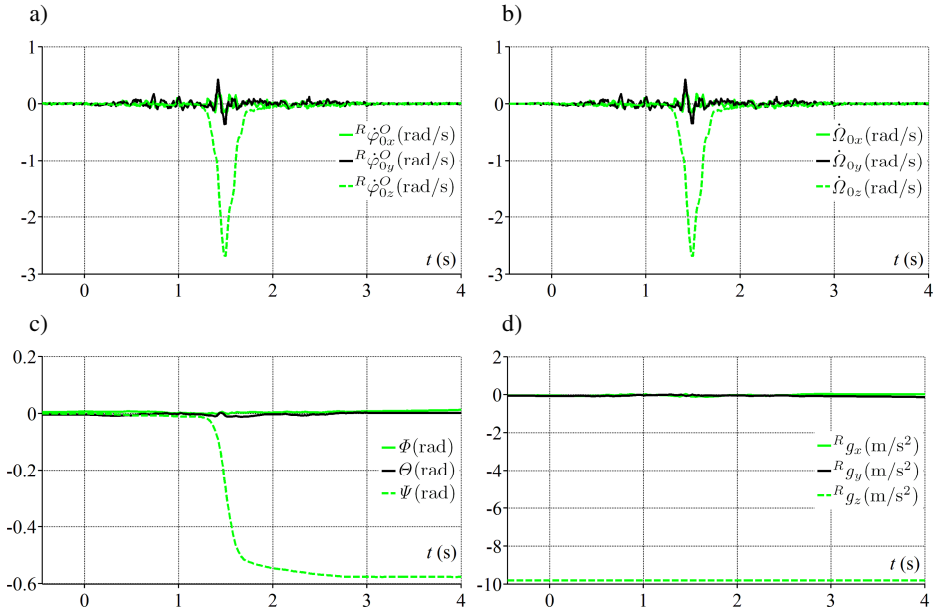

Fig. 3. Robot motion parameters obtained as a result of the experiment in variant no. 1 (right turn): a – angular velocities of the mobile platform measured by gyroscope, b – time derivatives of Euler angles, c – Euler angles for the mobile platform, d – components of gravity acceleration in the robot coordinate system, e – measured linear accelerations of the point I of the mobile platform, f – measured linear accelerations corrected for influence of gravity acceleration, g – components of tangential acceleration of the point R, h – components of normal acceleration of the point R, i – components of linear velocity of the point R and reference velocities from wheel encoders, j – components of linear velocity of the point R in the stationary coordinate system, k – components of linear velocity of the front left wheel center, l – actual and desired paths of the point R

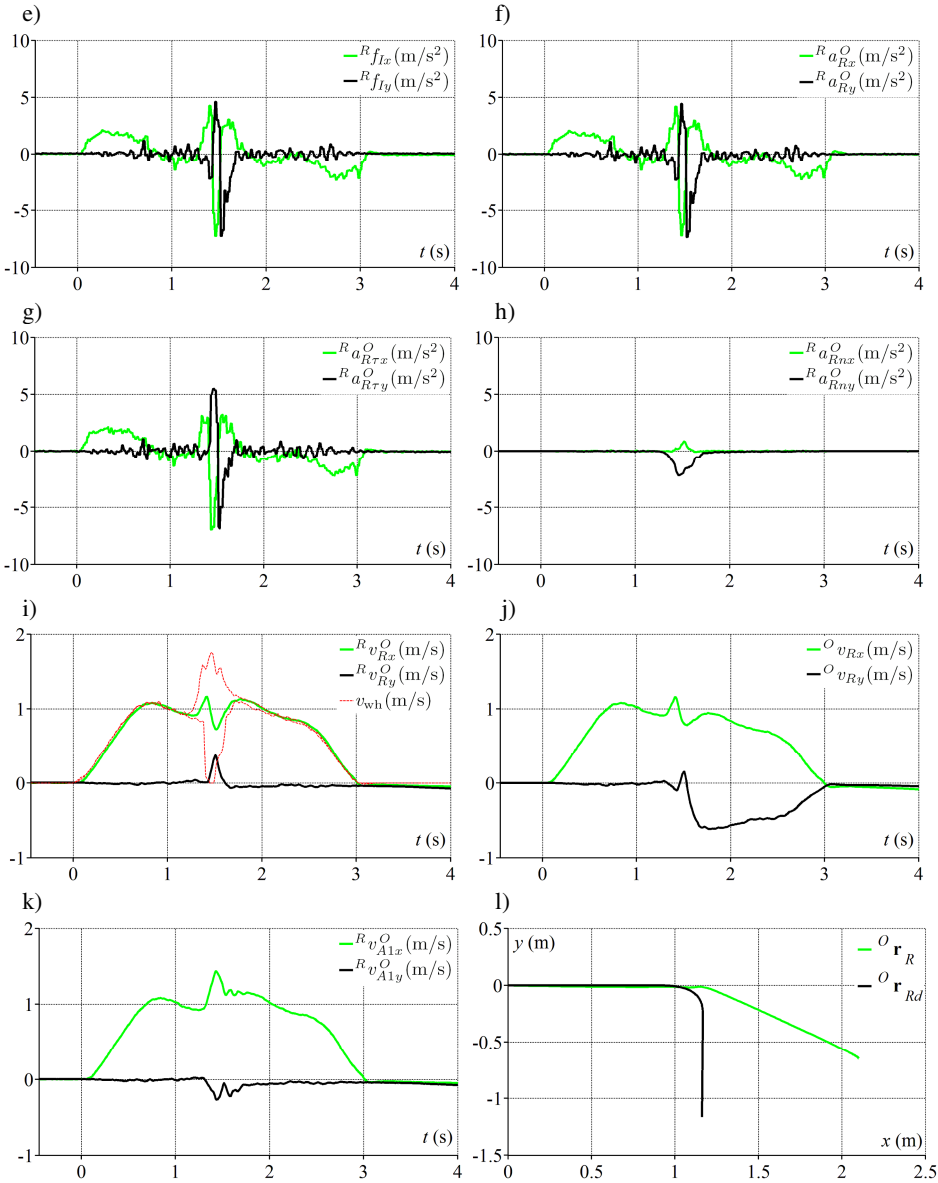

Fig. 3. (*continued*)

The subfigure b) shows time derivatives of Euler angles obtained from equation (8). The differences of time-plots shown in subfigures a) and b) are negligible for the presented experiment variant.

In the subfigure c) three Euler angles calculated by integration (eq. (9)) from their time derivatives (subfig. b)) are shown. In turn, in the subfigure d) are visible components of gravity acceleration in the moving coordinate system $\{R\}$, calculated based

on formula (13). Values of roll Ψ and pitch Θ angles have direct influence on those values.

In Fig. 3e two components of acceleration of the point I (which is the point of mounting of the accelerometer, just above the characteristic point R of the mobile platform) are shown. Similarly as in the case of angular velocities, those are the corrected indications of the measuring instruments (acceleration sensors) ${}^{R}\mathbf{f}_{I}$.

From measurements of acceleration ${}^{R}\mathbf{f}_{I}$, the components of the gravity acceleration ${}^{R}\mathbf{g}$ (subfig. d)) are subtracted according to equation (12), and the result is shown in the subfigure f). The difference between subfigures e) and f) is very small, but it can be noticed, for example, up from the 3 s of motion.

The components of tangential acceleration shown in subfigure g) are obtained by subtracting components of normal acceleration ${}^{R}a_{Rn}^{O}$ (subfig. h)) from the corresponding components of acceleration ${}^{R}a_{R}^{O}$ – subfigure f) – according to equation (19). This must be done, because the normal acceleration is sensed by accelerometers, and otherwise it would appear as apparent lateral velocity of sliding.

Velocities in subfigure i) are obtained from formula (20), that is after integration of components of tangential acceleration shown in the subfigure g). In the subfigure i) linear velocities of points at the circumferences of wheels (based on indications of wheel encoders) are also presented for reference. It should be emphasized that in a general case, velocities of those points at the circumference of wheels are not necessarily the same as the velocity of the mobile platform, because of the wheel slip phenomenon. However, in the presented motion one expects that linear velocity of the mobile platform is very close to the velocity associated with spinning of wheels during straight-line motion phases (i.e. 0–1.20 s and 1.80–3.00 s), because the linear accelerations of the desired motion are deliberately made small to prevent large wheel slips. For the presented set of results this expectation is confirmed in reality. During period of motion from 1.30 s to 1.75 s, there is a fluctuation of ${}^{R}v_{Rx}^{O}$ velocity, which first increases, then decreases and increases again. This effect is associated with turning realized on the basis of the differential-steering principle, and it can be also observed in investigations of mathematical model of this mobile platform in the simulations [3]. Also the character of the plot of lateral velocity ${}^{R}v_{Ry}^{O}$, and in particular the occurrence of a rapid change to the value of about 0.4 m/s, is generally according to expectations, because simulation of the presented maneuver predicts occurrence of the lateral sliding velocity during turning [3].

Fig. 3j shows transformation of the point R velocity from the robot $\{R\}$ to the absolute $\{O\}$ coordinate system, according to relationship (24).

Subfigure k) presents velocity of the point A_1, that is, of the wheel center of the front left wheel (denoted 1 in Fig. 3, Part 1 of the article). It can be noticed here, that during robot turning, increase of velocity component along axis ${}^{R}x$ and appearance of velocity component along ${}^{R}y$ takes place, which is the result of both robot rotation about ${}^{R}z$ axis and robot lateral sliding described earlier.

In Fig. 3l a comparison of the motion path of the point *R* obtained from the measurement (close to real) and the path calculated from desired velocities of wheels on the assumption of lack of wheel slips is shown. It should be emphasized that the shape of the actual path does agree with empirical results reported in the work [2]. It is clearly visible, that control of robot motion based on control of angular velocities of spin of wheels only is not adequate for the skid-steered wheeled robot design. For this reason, it is necessary to introduce the additional control loop to the robot control system, which is the subject of the cited work.

5.2 Experiment Variant 2 – Motion along a Straight Line on an Inclined Plane

In Fig. 4 are shown plots of selected quantities associated with robot motion along a straight line on an inclined plane. The shape of the ground was horizontal for the initial 2 seconds of motion, and then the robot drove on the inclined plane. The inclination angle was 12.4 deg (0.216 rad), which was determined from the appropriate trigonometric function based on lengths of two sides of the triangle measured using a measuring tape.

In Fig. 4a values of the inclination angle determined based on the indications of the accelerometer onboard of the robot from equation similar to (11), but for the final (not initial) angles, are shown. Angles for four repetitions of the experiment are compared, and the result is from 0.220 rad to 0.222 rad, with average of 0.2208 rad. This is about 2 % off the angle 0.216 rad measured with the traditional method (measuring tape and trigonometric functions), and the difference might be partly due to error of accelerometer calibration. Subfigure b) shows time plots of roll Φ and pitch Θ angles of the robot body during the whole period of motion. With dashed lines are marked final values of those angles determined from indications of the accelerometer (in the same manner as shown in subfig. a)) for reference. It is worth emphasizing that more reliable than indications from gyroscopes are indications from accelerometers because: (1) the measurements are taken when robot stands still, (2) the average of several hundred samples of acceleration is used for calculations of angles, so the influence of random error is minimized. It can be noticed that, in the presented case, there is a good correspondence for the final pitch angle Θ obtained from the gyroscope and from the accelerometer. In case of the final roll angle Φ there is a difference. In subfigure c) two components of the acceleration of the point *I* are shown. Starting from roughly 2.0 s of motion, component of acceleration along ${}^{R}x$ axis grows to about 2 m/s^2. This is not the real increase in robot velocity, because the robot was supposed to run at the steady 1 m/s, but the increase in the magnitude of component of the gravity acceleration sensed by the ${}^{R}x$ axis of the accelerometer. This is reasonable because after driving on the inclined plane robot changed its orientation. The magnitudes of components of the gravity acceleration obtained from equations (13) are shown versus time in the subfigure d). After removal of the acceleration of gravity, the components of tangential acceleration of the point *R* of the robot are presented in subfigure e).

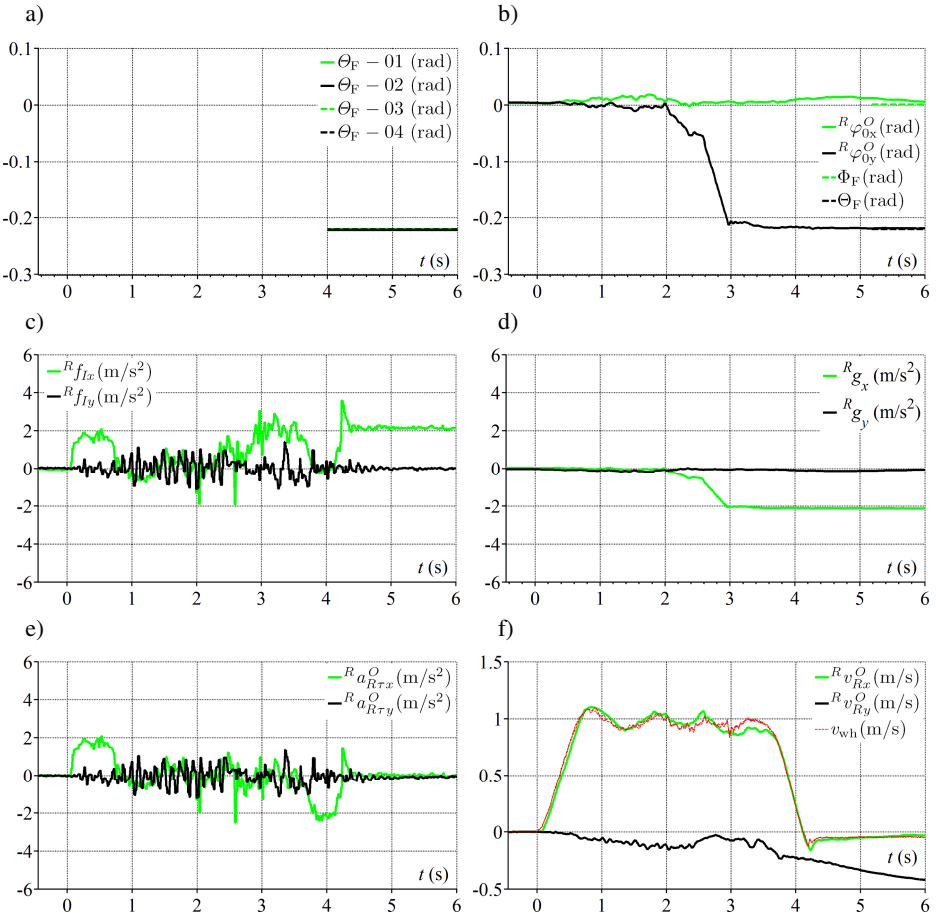

Fig. 4. Robot motion parameters obtained as a result of the experiment in variant no. 2 (motion on an inclined plane): a – final pitch angles for the mobile platform for 4 repetitions of the experiment, b – roll and pitch angles for the mobile platform, c – measured linear accelerations of the point *I* of the mobile platform, d – components of gravity acceleration in the robot coordinate system, e – components of tangential acceleration of the point *R*, f – components of linear velocity of the point *R* and reference velocities from wheel encoders

Finally, after integration of the components of the tangential acceleration (eq. 20), the components of linear velocity of the point *R* are shown in subfigure f). In this figure, the reference velocity from wheel encoders (red dashed line) is negative at the end of motion. Reason for this is not applied brake, so the robot started to slowly go down the slope immediately after stopping. It can be seen that the forward velocity of the point *R*, in general, corresponds well to the reference velocity. However, after the 4.5 s of motion the reference velocity is constant, but the body velocity increases slowly. This increase of velocity is the artificial phenomenon associated with residual influence of acceleration of gravity which was not corrected, because of small inaccuracy of the pitch angle.

The y component of the point R velocity seems to be of worse quality than the x component. The time-plot of ${}^{R}v_{Ry}^{O}$ suggests that robot body was moving sideways (in transverse direction) which indicates sliding. This was not observed during experiments and is also unreasonable in this case, so the time plot shows an artificial phenomenon. It is connected with a small residual value of the gravity acceleration acting on the y axis of the accelerometer, because of the inaccuracy of the roll angle Φ.

5.3 Experiment Variant 3 – Motion along a Straight Line and on the Horizontal Ground

In Fig. 5 are shown results for the case of robot motion along a straight line and on the horizontal ground. On example of these results, repeatability of measurements will be discussed.

In order to gather necessary data the experiment was repeated 4 times. Before each trial, the robot was positioned in the same starting place, however no special equipment was used to aid the positioning. The repeatability of the initial pitch and roll angles of the robot body can be assessed based on the subfigures o) and p), respectively. Values of those initial angles were obtained from indications of accelerometer according to formula (11).

Subfigures from a) through d) show one-second-long signals of direct measurements of angular velocities and accelerations for two successive repetitions of the experiment. It is evident that the signals are repeatable in the qualitative sense, but not exactly the same, which is in accordance with the expectations. The differences can be generated by many factors like small difference in the route (not exactly the same starting position of the robot, which is important because of minor unevennesses of the floor), small difference in the initial orientation of the body, not the same initial contact of tread with the ground, etc. Important random differences can be also contributed by the low-cost MEMS sensors themselves. Also the method used for integration can be of some significance.

Subfigures e) and f) show linear velocities of the points on circumferences of respectively the left and right driven wheel. A good repeatability of realization of the desired motion is observed for both wheels.

Subfigure g) presents the longitudinal component of velocity of the point R of the robot. For all 4 trials the velocity is almost identical in the initial 0.75 s of motion, then there is a split in two distinct pairs of graphs, and at about 5.5 s the plots become mixed. Subfigure i) shows the corrections for the gravity acceleration influence on the x acceleration sensed by the accelerometer. According to (14), those corrections are proportional to the $\sin(\Theta)$. Plots of pitch angles Θ, started from zero initial pitch angle for better comparison, are shown in subfigure k). It can be noticed that the plots are similar to each other. Also the final pitch angles are different for each trial. In subfigure m) the final pitch angles calculated from formula (11) based on indications of accelerometers are presented for comparison. The final angles from accelerometers are more reliable than from gyroscopes (see discussion of Fig. 4), so it can be stated that the variance of the final pitch angles obtained from gyroscopes is too large.

Let us now repeat the argument for the component of point R velocity along ${}^{R}y$ axis of the robot coordinate system shown in subfigure h). It is clear that the velocities are

not repeatable. In subfigure j) the corrections of influence of gravity acceleration on acceleration along the ${}^{R}y$ axis are presented. In case of the gravity acceleration correction for the trial no. 1 (shown in solid green line in subfig. j)), its value between 2 s and 5 s of motion is roughly 0.1 m/s^2 on average. This yields 0.3 m/s change in velocity between 2 s and 5 s. Change of velocity of similar magnitude, i.e. about 0.25 m/s, in this time period is seen in subfig. h) for the trial no. 1. A similar dependency exists for the remaining trials. According to (14), gravity corrections for the y component of acceleration are proportional to the factor $-\sin(\Phi)\cos(\Theta)$. If Θ angle is small, then its cosine can be approximated with 1. Similarly, if Φ angle is small, its sine can be approximated with the value of the angle. On those assumptions ${}^{R}g_y$ in subfig. j) is proportional to $-\Phi$ from subfig. l), which is approximately true. The question remains, if the values of the roll angle Φ over time are valid.

Comparison of the final roll angles from gyroscopes (subfig. l)) with final roll angles from accelerometers (subfig. n)) leads to conclusion that in two out of four cases the final angles from gyroscopes are completely off the mark. The best situation is for the cases shown in dashed lines. This is also reflected in subfig. h), where velocities represented with dashed lines are closer to zero, which is expected the true value of lateral velocity for the examined maneuver.

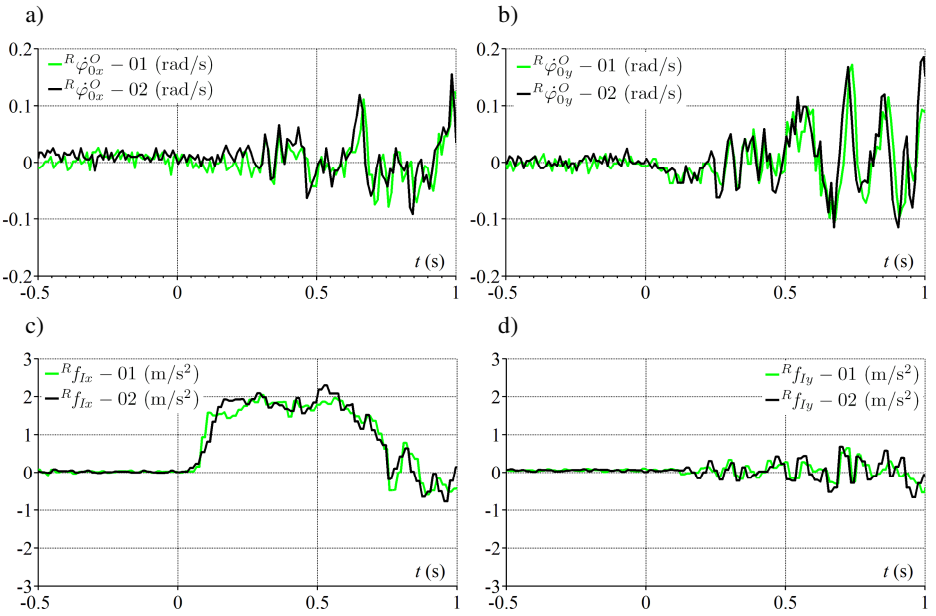

Fig. 5. Robot motion parameters obtained as a result of the experiment in variant no. 3 (straight line motion): a-d – results of direct measurements, e-f – linear velocities of points at the circumference of driven wheels from wheel encoders, g-h – components of linear velocity of the point R, i-j – components of gravity acceleration in the robot coordinate system, k-l – changes of roll and pitch angles during robot motion from gyroscopes, m-n – differences between final and initial values of pitch and roll angles obtained from accelerometers, o-p – initial values of pitch and roll angles obtained from accelerometers

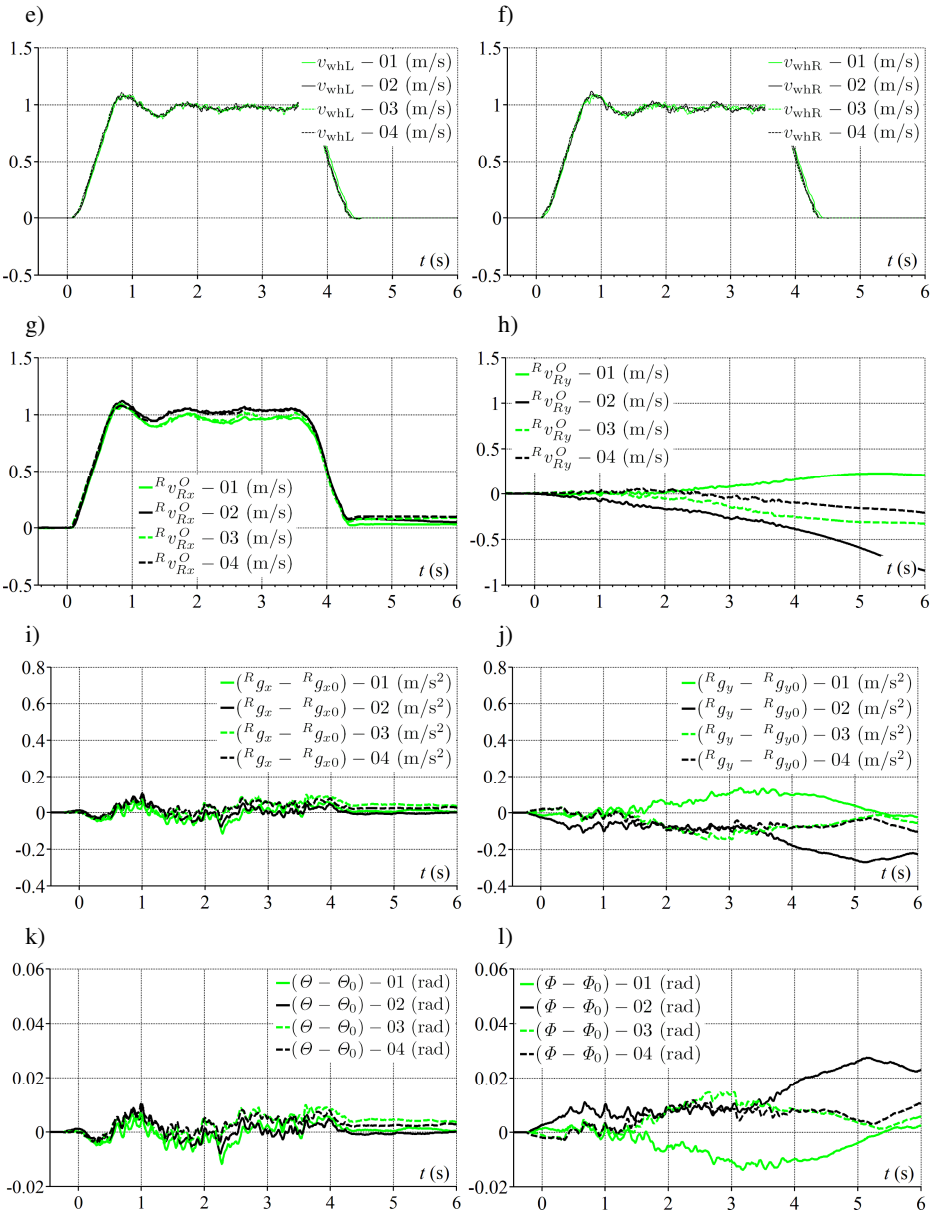

Fig. 5. (*continued*)

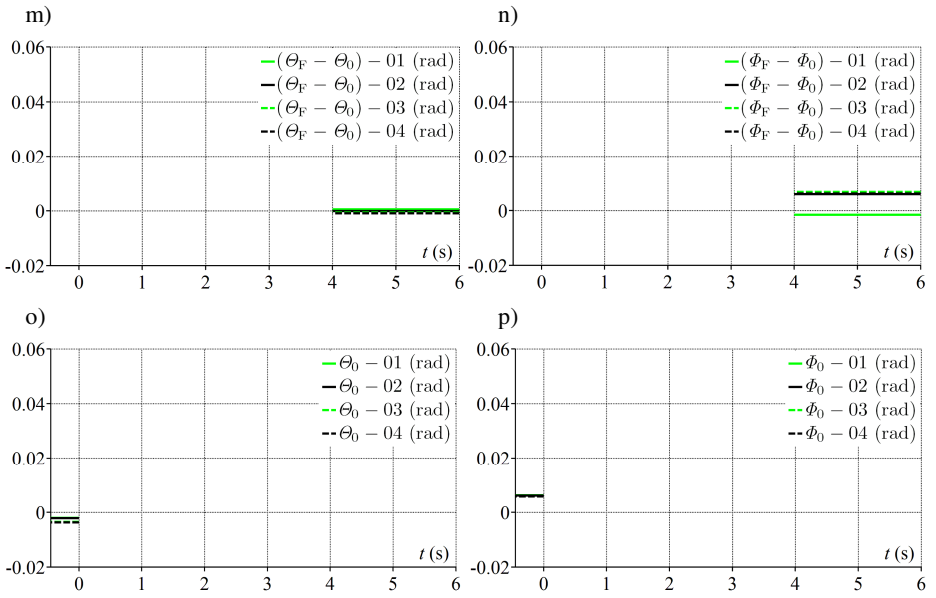

Fig. 5. (*continued*)

To sum up the repeatability discussion, it may be stated that there is a scope for improvement in reliability of roll and pitch angles of the robot body. The low-cost MEMS gyroscopes used to determine those angles are known to have poor bias stability, which may contribute to worse repeatability of the obtained angles. Indications of this kind of gyroscopes can be also affected by linear accelerations, which is sometimes quantified in the literature as a parameter called "sensitivity to linear acceleration" or "g-sensitivity". It can be demonstrated that introduction of some kind of filtering of the gyroscope signal leads to improvement of the measurement quality [7]. In view of that, filtration of signals should be considered in the future works. Another possibility is to carry out measurement of the variable orientation angles using the low-cost MEMS accelerometers alone, because their in-run bias stability is better than of the low-cost MEMS gyroscopes [8].

6 Conclusions and Future Works

In this work the algorithm described in the Part 1 of the paper, that is [9], is applied to process the input signals obtained during empirical experiments with the PIAP SCOUT four-wheeled skid-steered mobile robot equipped with a low-cost Inertial Measurement Unit.

Presented results show that quality of the obtained motion parameters is reasonable for motions in ${}^{O}x{}^{O}y$ and ${}^{O}x{}^{O}z$ planes of the stationary coordinate system, when experiment duration is of the order of several seconds.

The dominant errors are associated with inaccuracies of the Euler angles determined on the basis of angular velocities measured by gyroscopes.

Future works may include:

- Design and implementation of a filter for gyroscope signals with a view to improvement of accuracy of the determined Euler angles.
- Use of several MEMS accelerometers located in different positions on the robot body to determine angular parameters of the mobile platform, instead of using MEMS gyroscopes which have worse metrological properties.
- Use of a magnetometer for determination of the initial robot heading.
- Use of the Global Navigation Satellite System (GNSS) for determination of the initial position of the robot.
- The magnetometer and GNSS can be used in some data fusion structure with an IMU to improve accuracy of determination of respectively orientation and position.

Acknowledgements. The work has been realized as a part of the project entitled "Dynamics modeling of a four-wheeled mobile robot and tracking control of its motion with limitation of wheel slips". The project is financed from the means of National Science Centre of Poland granted on the basis of decision number DEC-2011/03/B/ST7/02532.

References

1. PIAP SCOUT mobile robot, EOD equipment, EOD robot, surveillance robot, http://www.antiterrorism.eu/product/en/scout (accessed: April 21, 2014)
2. Trojnacki, M., Dąbek, P., Kacprzyk, J., Hendzel, Z.: Trajectory Tracking Control of a Four-Wheeled Mobile Robot with Yaw Rate Linear Controller. In: Szewczyk, R., Zieliński, C., Kaliczyńska, M. (eds.) Recent Advances in Automation, Robotics and Measuring Techniques. AISC, vol. 267, pp. 507–522. Springer, Heidelberg (2014)
3. Trojnacki, M.: Modelowanie dynamiki mobilnych robotów kołowych. Oficyna Wydawnicza PIAP, Warszawa (2013)
4. Barbour, N.M.: Inertial navigation sensors. Low-Cost Navig. Sens. Integr. Technol., 2–1 (2011)
5. STEVAL-MKI062V2, iNEMOTM (iNErtial MOdule) demonstration board based on MEMS devices and STM32F103RE – CD00271225.pdf, http://www.st.com/st-web-ui/static/active/en/resource/technical/document/user_manual/CD00271225.pdf (accessed: May 23, 2014)
6. ADIS16488A (Rev. A) – ADIS16488A.pdf, http://www.analog.com/static/imported-files/data_sheets/ADIS16488A.pdf (accessed: May 23, 2014)
7. Bancroft, J.B., Lachapelle, G.: Estimating MEMS gyroscope g-sensitivity errors in foot mounted navigation. In: Ubiquitous Positioning, Indoor Navigation, and Location Based Service (UPINLBS), pp. 1–6 (2012)
8. Schopp, P., Klingbeil, L., Peters, C., Manoli, Y.: Design, geometry evaluation, and calibration of a gyroscope-free inertial measurement unit. Sens. Actuators Phys. 162(2), 379–387 (2010)
9. Trojnacki, M., Dąbek, P.: Determination of Motion Parameters with Inertial Measurement Units. Part 1: Mathematical Formulation of the Algorithm (2014)

Synchronized Trajectory Tracking Control of 3-DoF Hydraulic Translational Parallel Manipulator

Piotr Wos and Ryszard Dindorf

Faculty of Mechatronics and Machine Design, Kielce University of Technology, Kielce, Poland
{wos,dindorf}@tu.kielce.pl

Abstract. The paper deals with a cross-coupled control approach to the spatial 3-DoF hydraulic translational parallel manipulator. The control system of the cross-coupling control (CCC) has been proposed in order to reduce the contour error for three electro-hydraulic axes. Control of the manipulator takes into account not only the position errors for each drive axis but also synchronization errors of neighboring axes. Cascade control system with inner and outer loop was proposed. Decentralized tracking system allows to adjust the trajectory of disturbances in the internal loops it is based on the defined synchronization of errors for each axis drive. There was specified the synchronization function for the control system which takes account of the errors positioning of each axis. The experiments were performed on a prototype parallel manipulator (3-DoF). The prototype hydraulic manipulator consists of a fixed base and a moving platform, that are connected by the joints with three hydraulic linear axes. They demonstrated improvement in the positioning accuracy of the movement of end effector manipulator. The aim of the research was to examine the effectiveness of synchronous control method with a simplified structure of the control system for the electro-hydraulic manipulator both theoretically and experimentally.

Keywords: trajectory tracking control, parallel manipulator, synchronization error, servo-hydraulic system.

1 Introduction

Electro-hydraulic servo-systems have wide application in the positioning and synchronization of mobile and industrial machines, robots and manipulator movements. Changes to dynamic parameters of electro-hydraulic servo-drives are connected with their load and velocity of moving. They are also influenced by other factors related to fluid properties, which have crucial impact on control system. The mismatch of control structures is caused by large forces or moment loads of servo-hydraulic drive system. An increase in the velocity and positioning accuracy of an electro-hydraulic servo system can be achieved by the use of parallel manipulators. However, due to a specific structure, they are not easy to construct. Moreover, their drives often work in unusual applications and their kinematics and dynamics are complicated. As a result, the design of their control system is difficult and very different from that of serial manipulators. Control systems of such devices must take into consideration the

J. Awrejcewicz et al. (eds.), *Mechatronics: Ideas for Industrial Applications*,
Advances in Intelligent Systems and Computing 317, DOI: 10.1007/978-3-319-10990-9_24

characteristics that do not occur in classical manipulators. There is a significant difference between a parallel manipulator and a serial manipulator. The high complexity of the mathematical equations describing a physical model of a parallel manipulator can make the real-time computations impossible. However, their excessive simplification may result in less precise positioning of the manipulator. Precise control of the trajectory is the basic requirement for modern manipulators. We can try to improve the positioning accuracy of each single axis controlled by the use of different control strategies [8, 9, 3]. However, good performance tracking for each axle is no guarantee to reduce contour error of multi-axial motion. The contour error value for the positional trajectory deviation is defined as the distance from it in the perpendicular direction [2]. Another method to reduce the contour error is cross-coupling control [1]. There [6] was introduced the symmetrical structure of this type of controller in order to improve the accuracy of mapping trajectory.

Among the methods of synchronous control using feedback from the resulting position error we can distinguish [5]: two-axis cross-coupling control, optimal synchronous tracking and control method for continuous contour. The authors [9] describe the need for synchronous control algorithms with feedback from all drives. They argue that in the conventional control systems, any error caused by disturbances in one loop is adjusted only inside this loop, while the second loop executes its previous action. Control in cross-coupling system allows to resolve this problem by dividing the feedback of both control loops. There are also other solutions using fuzzy logic or neuro cross-coupling controllers [9, 5, 7]. However, the main drawback of these techniques is that they do not directly take into account the uncertainty of the control object model. These methods are not appropriate when the primary requirement is the high accuracy control.

2 Construction of the Test Stand

A parallel manipulator possesses several arms connected at one point. The number of drives and kinematic chains is equal to the number of variables describing the state of the physical model (a Tripod or a Tricept with three degrees of freedom and a Hexapod with six degrees of freedom). In Department of Mechatronic Devices at Faculty of Mechatronics and Machine Devices of Kielce University of Technology (Poland) was constructed the three axis (3-axis) and three-degrees-of-freedom (3-DoF) hydraulic translational parallel manipulator (TPM). Fig. 1 shows the manipulator test stand. The manipulator consists of a moving platform (3) connected to a fixed base (5) by several arms. The arms are mounted with rotary joints (4). The position of the end effector platform (3) is dependent on the position of the arms. Each arm incorporates an electro-hydraulic servo drive (1), controlled by a proportional valve (2), which is able to generate force of up to 20 kN for each axis. A single electro-hydraulic axis consists of CS (Bosch-Rexroth) type cylinder internally integrated with the magnetostrictive linear position sensors (Novostrictive) and externally integrated with 4/3-way high response directional valve directly actuated with electrical position feedback of type 4WRSE.

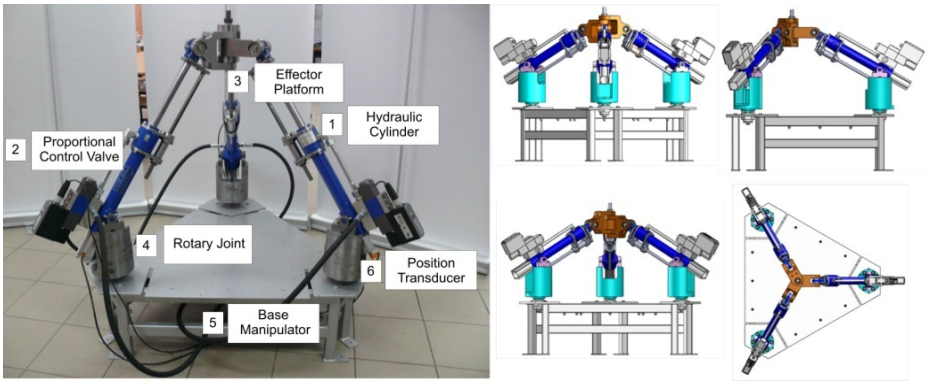

Fig. 1. Manipulator test stand: 1 – hydraulic cylinder (CSM1/MT4/40/28/250 A1X/B1CFUMTF), 2 – proportional valve (6 V1-35-3X/G24Ko/A1V 4WRSE), 3 – mobile end-effector platform, 4 – mounting of the manipulator arm, 5 – base manipulator

The closed-loop kinematic chains of the hydraulic TPM create structure 3-RRPRR, in which revolute joints R and prismatic joints P step out [2]. The proposed electro-hydraulic manipulator control system contains two PC computers Target PC and Host PC, where the first computer directly controls servo-drives hydraulic and the second functions as operator towards direct control layer. In the computer marked as Host PC the software MATLAB/Simulink along with xPC Target for identifications and real time control were installed. Target PC can simulate control flow and measurement signals in the real time by means of HIL method (*Hardware-in-the-Loop*).

2.1 Kinematics

The computational kinematic model of 3-axis hydraulic parallel manipulator shown in Fig. 2. For the contour error of the 3-axis hydraulic parallel manipulator the 6-DoF kinematic model have been considered. It includes both the platform position variables x_p, y_p, z_p and also rotational RPY angles α, β, γ. The RPY (Roll-Pitch-Yaw) angles defined with respect to three successive rotations about the fixed X, Y, Z axes [4]. The problem of inverse kinematics is to find the hydraulic cylinders elongation L_i, given the position (x_p, y_p, z_p) and orientation error (α, β, γ) of the TCP.

To solve the inverse kinematics problem vectors $\boldsymbol{r}_i$ and $\boldsymbol{R}_i$ and matrix $\boldsymbol{R}_B^A$ are given, then vector $\boldsymbol{L}_i$ from point A_i^A to point B_i^A can be calculated as:

$$\boldsymbol{L}_i = \boldsymbol{p} + \boldsymbol{R}_B^A \cdot \boldsymbol{r}_i - \boldsymbol{R}_i \tag{1}$$

where:

$\boldsymbol{p} = \overleftarrow{AB}$ vector coordinates from point B in moving frame to point A in reference frame, $\boldsymbol{p} = [x_p \;\; y_p \;\; z_p]^{\mathrm{T}}$,

$\boldsymbol{R}_B^A$ – rotation matrix from the moving frame to the reference frame for given values of RPY angles,

$\boldsymbol{r}_i$ – vector coordinates of B_i^B in the moving frame (B, X, Y, Z),

$\boldsymbol{R}_i$ – vector coordinates of A_i^A in the reference frame (A, X_0, Y_0, Z_0):

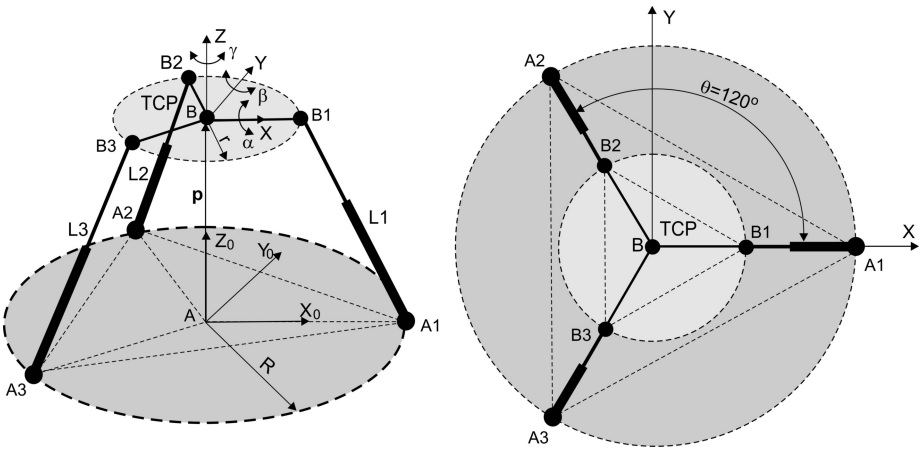

Fig. 2. Computation kinematic model of 3-axis hydraulic parallel manipulator

The length of vector $\boldsymbol{L}_i$ can be obtained as:

$$L_i = \sqrt{L_i^T \cdot L_i} \tag{2}$$

The parallel mechanism has the characteristic of closed loop, so the constraints of the mechanism movement could be expressed as $f(L, q) = 0$. Then the inverse kinematic solution of a parallel manipulator could be expressed as:

$$d\boldsymbol{L} = \boldsymbol{J} \cdot d\boldsymbol{q} \tag{3}$$

where:

Jacobian matrix $\boldsymbol{J}$ is obtained as $\boldsymbol{J} = -\boldsymbol{J}_L^{-1} \cdot \boldsymbol{J}_q$,

$\boldsymbol{L}$ is a vector which indicates the variation of hydraulic linear axes, $\boldsymbol{L} = [L_1 \;\; L_2 \;\; L_3]^{\mathrm{T}}$, $\boldsymbol{q}$ is a vector which indicates the position and rotation of the moving platform, $\boldsymbol{q} = [x_p \;\; y_p \;\; z_p \;\; \alpha \;\; \beta \;\; \gamma]^{\mathrm{T}}$. The unique solution of forward kinematic of a position and orientation error of the moving platform are expressed as:

$$\delta\boldsymbol{q} = \boldsymbol{J}^{-1} \delta\boldsymbol{L} \tag{4}$$

where: $\delta\boldsymbol{q} = [\Delta x_p \;\; \Delta y_p \;\; \Delta z_p \;\; \Delta\alpha \;\; \Delta\beta \;\; \Delta\gamma]$, $\delta\boldsymbol{L} = [\Delta L_1 \;\; \Delta L_2 \;\; \Delta L_3]$.

2.2 Dynamics

Using the orthogonal complement method, the dynamics of 3-DoF parallel manipulator can be described as a second-order differential equation:

$$M\ddot{X}+G=J_f^T F \tag{5}$$

where: $X \in R^3$ is a vector of the generalized coordinates, $M \in R^{3\times3}$ is the manipulator mass matrix, $G \in R^3$ is the vector of gravitation effects, $F \in R^3$ is the vector of the applied force of the actuators and $J_f \in R^{3\times3}$ is the force Jacobian matrix.

2.3 Simulation

Fig. 3 shows trajectory movement in the form of closed curve and set of resulting points of the manipulator workspace. The end-effector position (x_p, y_p, z_p) of the moving platform could be obtained by substituting the elongation L_i of every linear hydraulic axis into the forward motion equation. The Newton-Raphson method as an effective numerical method can be applied to calculate the forward problem of the hydraulic TPM.

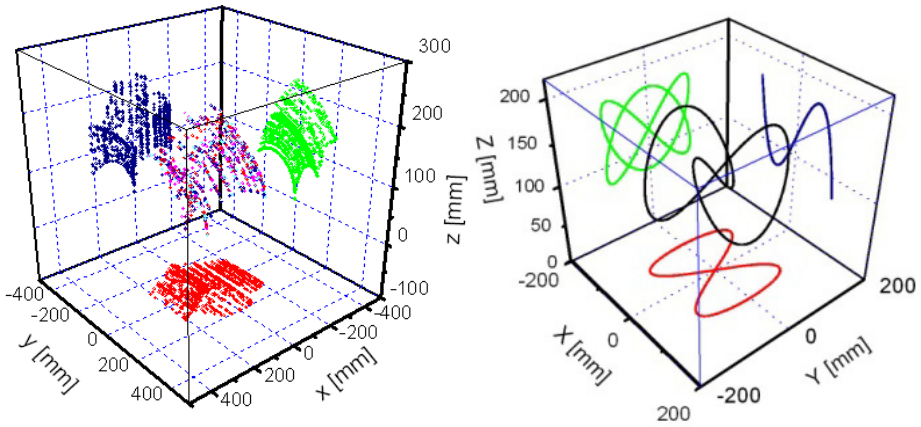

Fig. 3. Manipulator workspace and trajectory of the manipulator arms displacement

3 Control Design

For the control of parallel manipulators, the individual control system with feedback control loops of the actuator are commonly used. In such systems, there is no information from the other actuators. Errors position in one servo drive is minimized only locally in the absence of other servo response. Because the accuracy of positioning the tip of the manipulator actuator displacement affects all their movements they should be synchronized. Otherwise, the tracking accuracy will be reduced due to the lack of coordination of all parts of the manipulator. The control scheme is shown in Fig. 4.

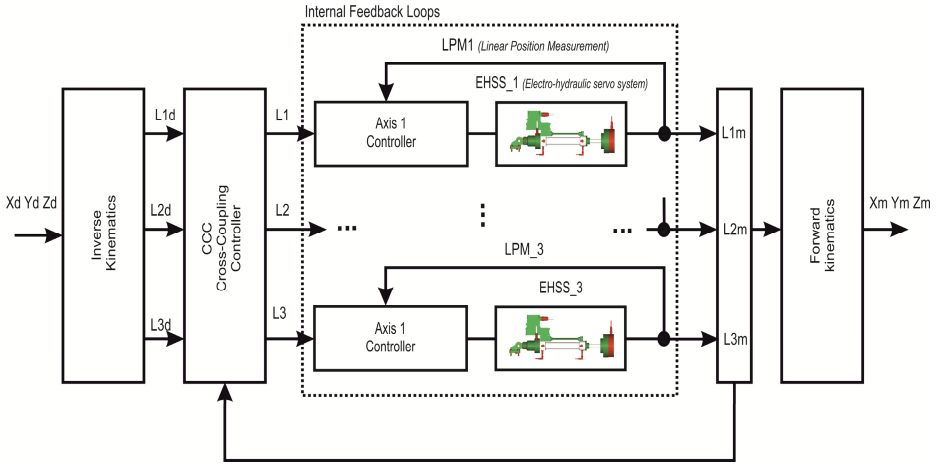

Fig. 4. Position control system of the 3-axis hydraulic TPM

Manipulator control system consists of axis inner loop (Axis Controller) and synchronization control loop (CC Controller).

Trajectory tracking error of *i*-th actuator is:

$$e_i(t) = L_i(t) - L_i^d(t) \tag{6}$$

Synchronization function described by demand (7):

$$\frac{L_1(t)}{L_1^d(t)} = \frac{L_2(t)}{L_2^d(t)} = \frac{L_3(t)}{L_3^d(t)}, \tag{7}$$

where L_i is the actual length and L_i^d is the desired length of the *i*-th actuator.

Position control system is designed by combining the position error and synchronization error. According to the concept of cross-coupled controller [1] the coupled error e_{ic} including the position error e_i and the synchronization error ε_i:

$$e_{ic}(t) = s_i e_i(t) + \beta \int_0^t \varepsilon_i(\omega) d\omega \tag{8}$$

where: β is a constant (positive coupling gain), which determine the weight of synchronization error, s_i is coupling coefficient of the manipulator (*i*-th actuator)

Differentiating $e_{ic}(t)$:

$$\dot{e}_{ic}(t) = \dot{s}_i e_i(t) + s_i \dot{e}_i(t) + \beta \varepsilon_i(t) \tag{9}$$

The command vector u_i is:

$$u_i(t) = s_i \dot{L}_i^d(t) + \dot{s}_i e_i(t) + \beta \varepsilon_i(t) + \Lambda e_{ic}(t) \tag{10}$$

where Λ is a positive gain.

Equation in (11) leads to the following control vectors (generalized error r_i):

$$r_i(t) = u_i - s_i \dot{L}_i(t) \tag{11}$$

In general, the synchronization error can be written:

$$\boldsymbol{\varepsilon}(t) = \boldsymbol{W}\boldsymbol{s}(t)\mathbf{e}(t)\,, \tag{12}$$

where $\boldsymbol{\varepsilon}(t) = [\varepsilon_1(t), \varepsilon_2(t), \varepsilon_3(t)]^T$,

$\boldsymbol{W} = \begin{bmatrix} 2 & -1 & -1 \\ -1 & 2 & -1 \\ -1 & -1 & 2 \end{bmatrix}$ is a constant positive gain matrix for $s_i = 1 / L_i^d$,

$\boldsymbol{e}(t) = [e_1(t), e_2(t), e_3(t)]^T$ and $\boldsymbol{s}(t) = \boldsymbol{I}_{3\times 3}[s_1(t), s_2(t), s_3(t)]^T$.

The synchronization errors are defined as:

$$\begin{cases} \varepsilon_1(t) = \dfrac{2e_1(t)}{L_1^d(t)} - \dfrac{e_2(t)}{L_2^d(t)} - \dfrac{e_3(t)}{L_3^d(t)} \\ \varepsilon_2(t) = -\dfrac{e_1(t)}{L_1^d(t)} + \dfrac{2e_2(t)}{L_2^d(t)} - \dfrac{e_3(t)}{L_3^d(t)} \\ \varepsilon_3(t) = -\dfrac{e_1(t)}{L_1^d(t)} - \dfrac{e_2(t)}{L_2^d(t)} + \dfrac{2e_3(t)}{L_3^d(t)} \end{cases}. \tag{13}$$

where $\varepsilon_i = 0$, $i = 1..3$ the actuators are moving synchronously.

4 Experimental Results

Based on distributed measurement and control system a test stand for rapid prototyping controller of the electro-hydraulic servo drive was set up [8]. Manipulator controls of the electro hydraulic servo drives are mounted in joints. The experimental investigation shows that for the control algorithm results are consistent with the expected ones obtained for frequencies from 0.16 Hz to 1.59 Hz. Fig. 5 presents results of the control process for references x_d, y_d, z_d, frequencies 0.16 Hz. Restrictions imposed on the control signal (from –7 V to +7 V) prevent the achievement of high frequencies displacement at assumed amplitude of the hydraulic cylinder piston.

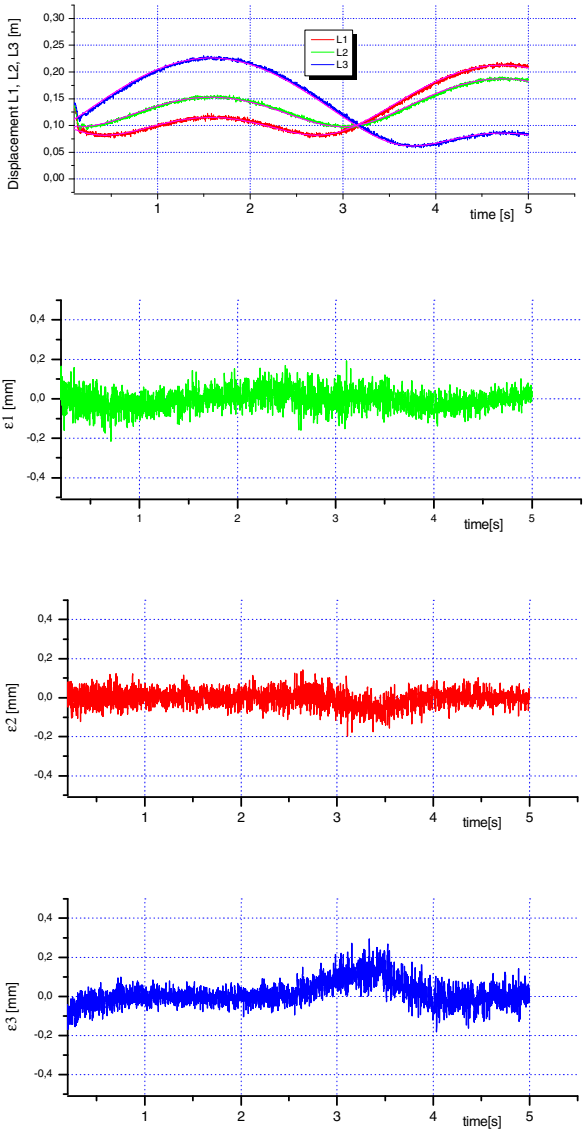

Fig. 5. Displacement of the manipulator arms for control algorithm and synchronization error ε

5 Conclusions

This paper presents the results of preliminary work on the subject of control of synchronous electro-hydraulic servo drive with maximally simplified structure of the control system. They form the basis for the current topic of control and synchronization

for construction of translational parallel manipulator (TPM). Inaccuracies in electro-hydraulic servo control systems have their origins in non-ideal structure elements of drives and measuring systems. Errors in the implementation of structural elements of manipulator causes the lack of perfect synchronization between the axes. Further, such phenomena as non-linear friction for small speed, the elasticity of mechanical components, shapes of the pad changes by the action of external forces and generated during operation may exist for each axis separately. The effect of these phenomena is the increasing positioning error of the manipulator platform. Therefore, the aim of the study was to create such a control system that will counteract these effects by including synchronization errors of each axis drive. The manipulator control system uses feedback from the axis position error and the synchronization error. Presented solution can be applied in all kinds of manipulators, servo-operators, and robots to assist the mining industry and engineering. In this study, the positions of moving platform are changed by extension or shortening of the three integrated electro-hydraulic axes. Implementation of modular actuators and measurement, the use of the environment MATLAB/Simulink to solve optimization problems of the control system, enables the use of the manipulator and to ensure high efficiency and low energy losses.

References

1. Chuang, H.Y., Liu, C.H.: Cross-coupled adaptive federate control for multiaxis machine tools. ASME Journal of Dynamic Systems, Measurement, and Control 113, 451–457 (1991)
2. Dindorf, R., Wos, P.: Contour error of the 3-DoF hydraulic translational parallel manipulator. In: Advanced Materials Research, vol. 874, pp. 57–62 (2014), doi:10.4028/www.scientific.net/AMR.874.57
3. Kim, H.S., Cho, Y.M., Lee, K.I.: Robust nonlinear task space control for 6DoF parallel manipulator. Automatica 41(9), 1591–1600 (2005)
4. Merlet, J.-P.: Parallel Robots. Solid Mechanics and its Applications. Springer, New York (2006)
5. Sun, D.: Position synchronization of multiple motion axes with adaptive coupling control. Automatica 39(6), 997–1005 (2003)
6. Tarng, Y.S., Chuang, H.Y., Hsu, W.T.: An optimisation approach to the contour error control of CNC machine tools using genetic algorithms. International Journal of Advanced Manufacturing Technology 13, 359–366 (1997)
7. Wos, P., Dindorf, R.: Adaptive control of a parallel manipulator driven by electro-hydraulic cylinders. International Journal of Applied Mechanics and Engineering 17(3), 1061–1071 (2012)
8. Wos, P., Dindorf, R.: Adaptive control of the electro-hydraulic servo-system with external disturbances. Asian Journal of Control 15(4), 1065–1080 (2013), doi:10.1002/asjc.602
9. Zhao, D., Li, S., Gao, F.: Fully Adaptive Feedforward Feedback Synchronized Tracking Control for Stewart Platform Systems. International Journal of Control, Automation, and Systems 6(5), 689–701 (2008)

Part III
Measuring Techniques and Systems

Wireless Temperature Measurement System Based on the IQRF Platform

Piotr Bazydło, Szymon Dąbrowski, and Roman Szewczyk

Industrial Research Institute for Automation and Measurements PIAP
Al. Jerozolimskie 202, 02-486 Warsaw, Poland
{pbazydlo,sdabrowski,rszewczyk}@piap.pl

Abstract. This paper presents model of wireless, distributed temperature measurement system based on the IQRF platform using IQMESH protocol, which allows to build a small-sized monitoring system with sufficient RF and metrological parameters for most of the industrial applications. Main elements of the system are IQRF TR-52D transceiver modules and 1-Wire Digital Thermometer Maxim DS18S20 running in parasitic power mode. In addition, the paper contains results of the model test carried out in industrial conditions, which confirms efficiency of the developed system.

Keywords: temperature measurement, disturbed systems, IQRF, wireless sensor network.

1 Introduction

Measurement of the temperature is essential in nearly every industrial process, where complex temperature monitoring systems consists of dozens, hundreds or even thousands of sensors. Large amount of the wires do not only cause organizational problems, but can also lead to measurement disruptions connected with for example electromagnetic compatibility (especially when sensors with voltage signal are used). One of the most common alternative is the usage of wireless radio frequency technology. Majority of modern wireless sensors networks using ISM (industrial, scientific and medical) bands is based on ZigBee standard [1, 2], which is less expensive than other types of wireless personal area networks. However, because of its high level of complexity, implementation of ZigBee protocol in small or medium sized applications can turn out to be unprofitable [3]. In addition, industrial systems and applications are often subject of varied enlargements and upgrades. In that case, recommended solution should be based on protocol, which allows fast prototyping and manipulation of RF (radio frequency) parameters.

The purpose of this paper is to present the model of disturbed temperature measurement system based on less popular and constantly evolving IQRF platform[7,8], which fulfills aforementioned requirements. It has been originally designed for the automatic concrete bonding system.

J. Awrejcewicz et al. (eds.), *Mechatronics: Ideas for Industrial Applications*,
Advances in Intelligent Systems and Computing 317, DOI: 10.1007/978-3-319-10990-9_25

2 Components of the System

Presented system consists of three main features: transceiver modules (coordinator and nodes), temperature sensors and end device (every device with RS-232 serial communication).

2.1 Transceiver Modules

IQRF platform including IQMESH protocol is supported by basic communication component called IQRF transceiver module. For this project, the TR-52D series products have been used because of their versatility.

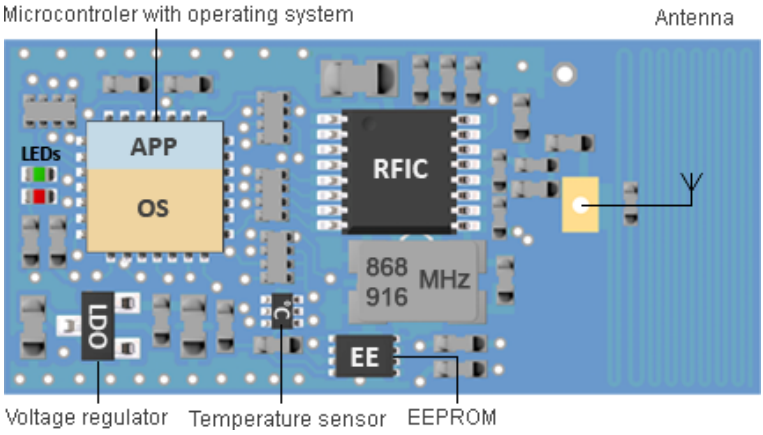

Fig. 1. Structure of IQRF transceiver module [4]

Figure 1 presents IQRF transceiver module with its basic components such as PIC16LF1938 microcontroller with operating system supporting MESH or antenna slot.

Main advantage of TR-52D module is its SIM card format, which allows to design a small-sized modular unit with easily reprogrammable transceiver. Another benefit concerns antenna mounting available in several variants: on-board PCB antenna, soldering pad-hole or coaxial connector for antenna cable. Radio frequencies can be selected between 868/916 MHz or 433 MHz bands.[4]

Selected TR-52D features:

- 10 bit ADC converter with 2 inputs,
- 6 I/O pins,
- serial EEPROM,
- power supply from 3.1 to 5.3 V,
- low power consumption (sleep mode: 1.9 µA, receive mode: 25 µA),
- selectable RF output power.

2.2 Temperature Sensor

Temperature measurement is based on 1-Wire Digital Thermometer Maxim DS18B20. Communication by 1-wire bus means that it needs only one data line for communication process [6]. There is also possibility to work in parasitic mode (power for the sensor supplied directly from the data line). Its main features are [5]:

- power supply range from 3 to 5.5 V, can be powered from the data line,
- range of measurement from –55 °C to +125 °C,
- ± 0.5 °C accuracy from –10 °C to +85 °C,
- selectable measurement resolution from 9 to 12 bits,
- temperature conversion time from 93.75 ms to 750 ms (depending on resolution).

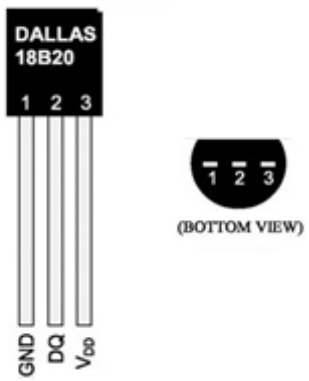

Fig. 2. Temperature sensor Maxim Dallas DS18B20 [5]

3 Structure of the System

The entire communication system can be divided into: coordinator (receiver) and nodes (transmitters). Both devices are powered by the 3.3 V battery and have very similar construction, although coordinator has been designed in order to connect with the end device by the RS-232 interface, when nodes are responsible for powering and supporting temperature sensors. Figures 4 and 5 present pictures of transmitter and receiver, with highlighted components. Power supply is mounted on the other side of the PCB boards. The main differences between construction of both devices are connectors sizes (2 wires for thermometer and 3 wires for RS-232 interface) and 4.7 kΩ resistor for pulling up temperature sensor.

Communication between receiver and transmitters is handled by the IQMESH protocol, where the adequate sequence of commands initializes bonding of modules. Such procedure is based on establishment of connection between specified node and coordinator and is presented on Fig. 3 as a simplified algorithm.

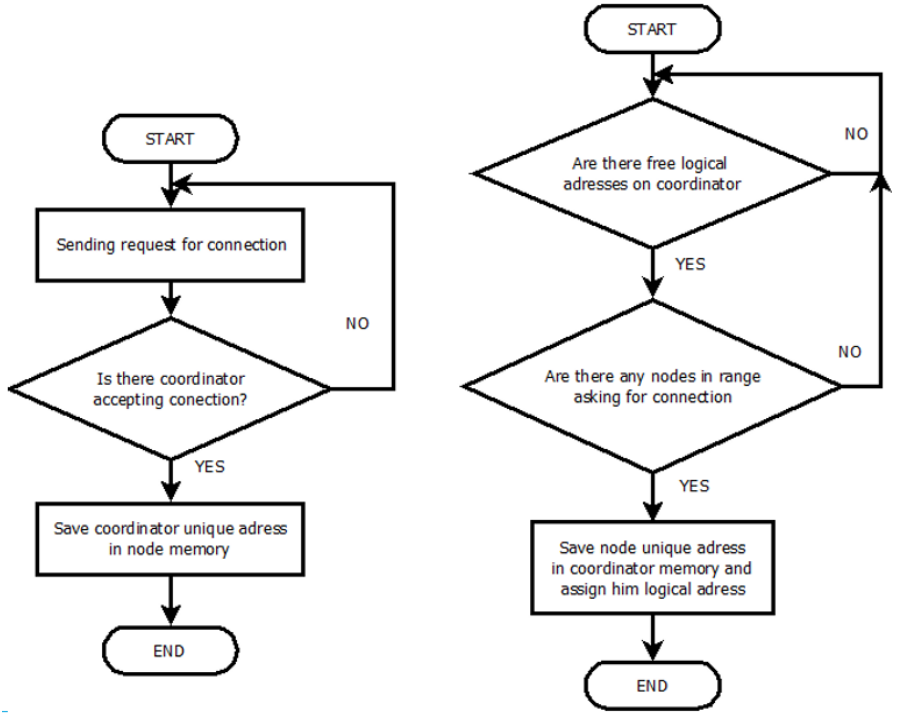

Fig. 3. Simplified algorithm of bonding procedure. Left side – node operations, right side – coordinator operations

After successful connection, coordinator saves unique address of the transmitter and assign him the logical address, which will be later used by the system for the data exchange. The whole process of bonding or breaking connections between modules is executed by the button mounted on each device and is triggered by the programmed combination of presses. Actual status of bonding is signalized by the red and green LED mounted directly on the transceiver module. Not using the button will result in switching into default monitoring mode.

Fig. 4. Picture of the node with mounted transceiver module; 1 – IQRF TR-52D with on-board antenna, 2 – power switch, 3 – power signalization LED, 4 – button for bonding operations, 5 – thermometer wires

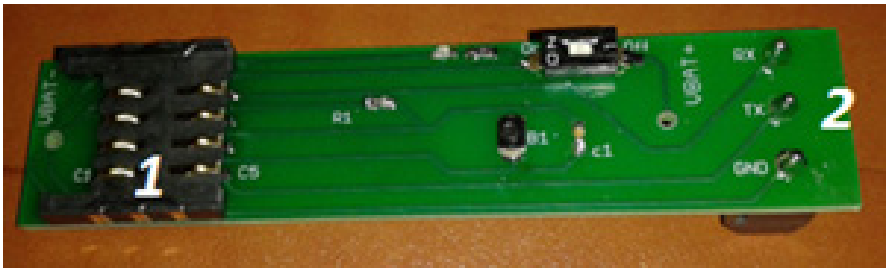

Fig. 5. Picture of coordinator without mounted transceiver module. 1 – transceiver slot, 2 – RS-232 interface slots

The standard monitoring procedure is being repeated every 10 seconds by the coordinator (period can be maximally shortened to 750 milliseconds because of sensor conversion time for 12 bit measurement). At the beginning, coordinator sends request for data to every node saved in his memory. After receiving the signal, transmitters initiate the procedure of measurement. When the digital thermometer finishes collection of data, it sends it back to the node, which forwards data one hundred times to the coordinator as the packet of 7 bytes. To avoid interferences between packets from different transmitters, it was necessary to establish the delay between packets, which depends on logical address of the node i (eq. 1).

$$delay = (i-1)\cdot 50\,\text{ms}, \qquad i \in N \quad \wedge \quad i \neq 0 \tag{1}$$

In the end, receiver forwards data to the end device by the RS-232 interface (for example PC computer or PLC controller). Schematic diagram of whole procedure has been presented in Fig. 6.

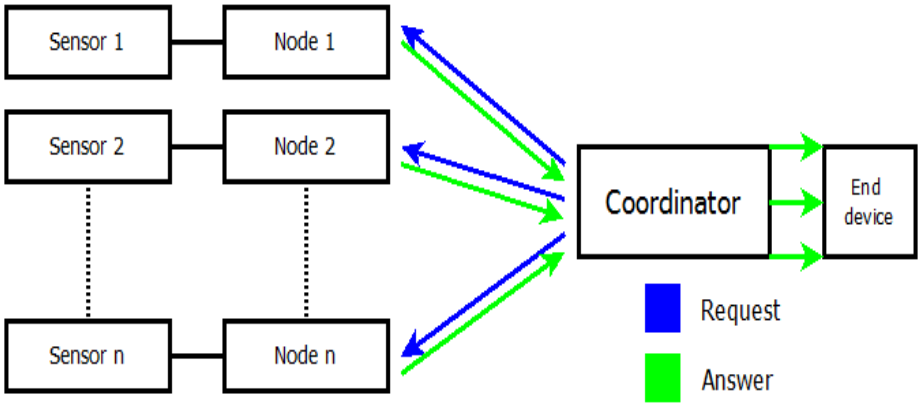

Fig. 6. Simplified pattern of communication between coordinator and nodes

4 Tests of the System

In order to ensure that designed system is fulfilling its goals, three parameters of radio transmission has been checked: efficiency (ratio of received packets to the sent packets multiplied by 100 %), RSSI (Received Signal Strength Indication) and capacity. It has been tested with different transceiver modules (with PCB antenna or external antenna and with 868 MHz band or 433 MHz band). Figure 7 presents results of the research for single node with on-board PCB antenna and 868 MHz band, where efficiency has been compared with the distance in industrial conditions. According to the research, efficiency stays at high level until 90 meters. Afterwards, it dramatically descends and reaches outcome of 47 % at the distance of 120 meters. Random and unexpected changes of efficiency results from local noises derived from industrial devices. Equation 2 shows mathematical model of efficiency.

$$E = -0.023e^{(5.064 \cdot x)} + 99.8e^{\left(-10^{-3} \cdot x\right)} (\%) \quad \wedge \quad x \in < 0,\ 120 > \tag{2}$$

where x is the distance expressed in meters.

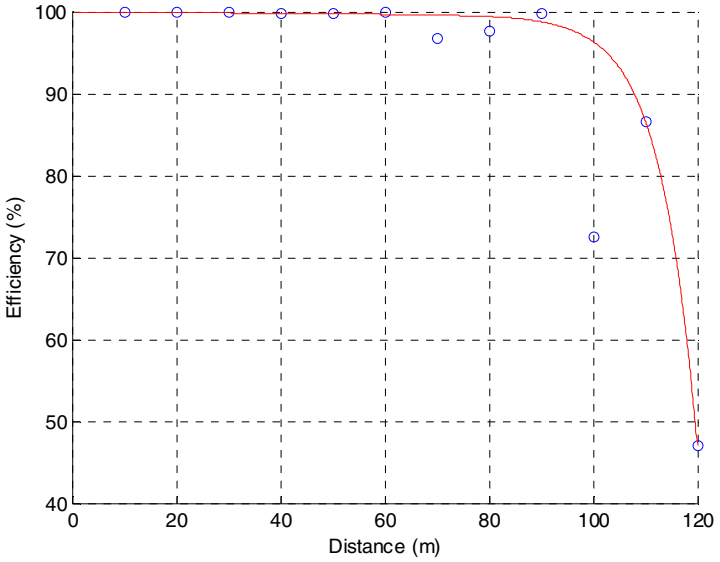

Fig. 7. Change of efficiency in function of distance with exponential approximation, using on-board PCB antenna with 868 MHz band transceiver module

Research proceeded on the same conditions has been repeated for the transceiver with 433 MHz band. Fig. 8 presents outcome of the test. Basing on the results, efficiency level is high until the distance of 80 m. At this point, efficiency gradually reduces and reaches about 10 % after 100 meters. Equation 3 presents mathematical model of efficiency in function of distance for the 433 RF transceiver module.

$$E = -0.0094e^{(0.0917 \cdot x)} + 99.71e^{(-10^{-4} \cdot 1.76 \cdot x)} \ (\%) \quad \wedge \quad x \in < 0,\ 100 > \tag{3}$$

Comparison of two different RF bands shows that between 60 and 80 meter occurs external noises resulting probably from industrial devices. However, the most important conclusion concerns range of the modules, which is 120 meters for 868 MHz band and 100 meters for 433 MHz band. At the point of 100 meters, where efficiency equals 10 % for 433 MHz band, efficiency for the other band equals 73 % (value of 73 % is probably lowered by other noises, as for the 110 meters efficiency reaches almost 90 %). After 100 meters, none of the packets sent by node has reached the coordinator with usage of 433 MHz band.

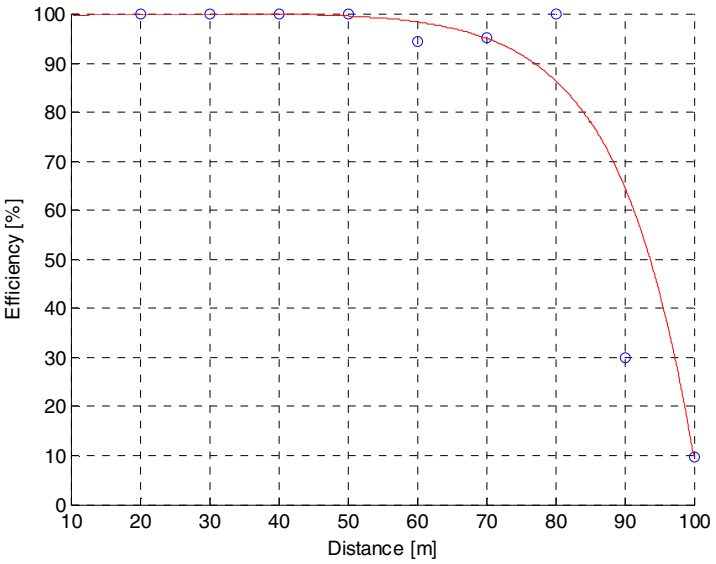

Fig. 8. Change of efficiency in function of distance with exponential approximation, using on-board PCB antenna with 433 MHz band transceiver module

5 Summary

Presented prototype of the wireless temperature monitoring system is characterized by its versatility and flexibility. It may be used in applications focused on building automation, industrial monitoring or automatic regulation systems. Easy change of the components allows instant modification of the RF parameters or exchange of damaged modules. Tests for the single node revealed that at least one of the packets will reach the coordinator at the distance of 120 meters with PCB antenna, what means that measurement will be completed. For the external antenna and 868 MHz band, range of the system for the single node equals about 160 meters. Size of the communication devices is limited by the power supply, what gives basis to minimization by matching the proper source. To sum up, presented model may be starting point for developing a complex disturbed temperature measurement system for industrial applications.

References

1. Pengfei, L., Jiakun, L., Junfeng, J.: Wireless temperature monitoring system Based on the ZigBee technology. In: 2nd International Conference on Computer Engineering and Technology, vol. 1, pp. 160–163 (2010)
2. Singh, R., Mishra, S.: Temperature Monitoring in Wireless SensorNetwork using Zigbee Transceiver Module. In: 2010 International Conference on Power, Control and Embedded Systems (ICPCES), pp. 1–4 (2010)
3. Seflova, P., Sulc, V., Pos, J., Spinar, R.: IQRF Wireless Technology Utilizing IQMESH Protocol. In: 35th International Conference on Telecommunications and Signal Processing (TSP), pp. 101–104 (2012)
4. IQRF web page, `http://www.iqrf.org`
5. Maxim Dallas DS18B20 datasheet, `http://www.maximintegrated.com`
6. Zhang, C., Feng, X., Li, L.: The Key Technologies of a Distributed Temperature Monitoring System Based on 1-Wire Bus. In: 8th World Congress on Intelligent Control and Automation (WCICA), pp. 7041–7045 (2010)
7. Kuchta, R., Vrba, R., Sulc, V.: IQRF Smart Wireless Platform for Home Automation: A Case Study. In: Fifth International Conference on Wireless and Mobile Communications, ICWMC 2009, pp. 168–173 (2009)
8. Sulc, V., Kuchta, R., Vrba, R.: IQMESH implementation in IQRF wireless communication platform. In: Second International Conference on Advances in Mesh Networks, MESH 2009, pp. 62–65 (2009)

Arm EMG Wavelet-Based Denoising System

Dawid Gradolewski, Piotr M. Tojza, Jacek Jaworski, Dominik Ambroziak, Grzegorz Redlarski, and Marek Krawczuk

Faculty of Electrical and Control Engineering, Gdansk University of Technology, Poland
{gradolewski,ptojza,jjaworski,dambroziak, g.redlarski}@ely.pg.gda.pl, markrawc@pg.gda.pl

Abstract. These paper presents research results of muscle EMG signal denoising. In the same time two muscles were examined – an adductor muscle (*biceps brachii*) and an abductor muscle (*tricpeps brachii*). The EMG signal was filtered using the wavelet transform technique, having selected the crucial parameters as: wavelet basis function (*Daubechies 4*), 10^{th} decomposition level, threshold selection algorithm (*Heurestic*) and a sln rescaling function (based on scaled white noise). After denoising the signal, a short analysis of the outcome signal is performed. Such developed system has a wide application possibility, mainly in Mechatronic systems where it can be used for example in teleoperation of a robot arm, control signals for a prosthetic arm, biomedical signal filtering or in rehabilitation aiding robots.

Keywords: signal denoising, wavelet transforms, muscle EMG.

1 Introduction – EMG

Electromyography (EMG) is one of the most frequently used diagnostic techniques of peripheral nervous system – both in conventional and sports medicine. Muscle contraction is an effect of the nervous system functioning, therefore EMG is useful in diagnostics of various diseases associated with muscle reaction (contraction and relaxation) [1], and even in speech synthesizer development [2]. As a test method, EMG has been completely recognized and mastered, that makes the purchase of devices equipped with appropriate sensors and data acquisition modules achievable. The examination of electrical potential generated by muscle cells during contraction and relaxation is the essence of the EMG [3]. The value of the potential varies in relation to the signal from the central nervous system and at rest is determined at the level of about 70 mV (it may vary depending on the muscle size [4]). The electrical signal transmitted from the synapses to the muscle alters the value of the cells membrane potential in the range of 50 μV to 30 mV. Hence, by the usage of appropriate sensors, the detection of these changes results in a continuous signal. In turn, the muscle condition may be estimated based on the potential change in the received signal. Then all collected information may also be used to determine the values of all the exoskeleton parameters, e.g. the force of a moved limb or the angle of the bended limb. Currently, EMG may be performed non-invasively via the sensors placed directly on the skin.

J. Awrejcewicz et al. (eds.), *Mechatronics: Ideas for Industrial Applications*,
Advances in Intelligent Systems and Computing 317, DOI: 10.1007/978-3-319-10990-9_26

Many companies offer various models of electrodes of high sensitivity and accuracy, e.g. Delsys co., which offers sensors of 1.2 μV accuracy. A sensor generates continuous voltage signal depending on the potential level of an examined muscle. However, the recorded signal is exposed to many disturbances of external and internal origin. Electromagnetic interference, drift of reference electrode or high frequency noises occurring during the measurement are the main cause of this disturbances. Frequency spectrum of this noises overlap the spectrum of the signal, therefore the problem with filtration of EMG signal is a complex one.

During the EMG examinations, each time the sensors is placed by the user in a slightly different location. Therefore, it is appropriate and well-founded to conduct the research on the influence of sensor placement on the final result of the measurement. It is crucial to determine whether the sensors displacement of millimetres leads to the significant errors, and whether to allow the user's latitude in placing the sensor. In the case of EMG, the sensor displacement leads only to shift in the time of the signal graph, no significant differences in the levels or nature of results obtained have been noted [5].

2 Wavelet Denoising in EMG

Wavelet analysis provides a powerful tool for signal analysis and in comparison with Fourier analysis, it allows to distinguish precisely both, the time and the frequency contents, and therefore enable to read many diagnostically useful information not only for the EMG signal but also for other biomedical signals [6]. Studies that used muscle bioelectric signals wavelet filtration provided significant and interesting findings.

In the study [7] wavelet analysis was used to decompose the EMG signal of people affected by Parkinson's disease, significantly expanding knowledge of the nature of involuntary contractions in relation to that used by treatment of Parkinson's. In the study [8] the authors use a new, original method – interscale wavelet maximum to support the diagnostic methods of neuromuscular diseases. Application of wavelet analysis allowed for separation of the unwanted measurement noise, allowing for searching of pathological signs of myopathy and neuropathy in the given test result. Studies [9] assumed applying wavelet analysis to assess the muscle fatigue, while the studies [10] and [11] wavelet filtration was used to support the analysis and classification process of EMG signals in an active hand prosthesis.

3 Upper Arm EMG Filterning

Literature studies showed a lack of information regarding wavelet filtering of the *biceps brachii* and *triceps brachii* EMG signals. In order to cover that gap, research studies were carried out in the area of muscle tension during a simple pulling procedure.

The experiment procedure involved pulling a stationary newton meter, applying up to 20 N pulling force. The position of the arm during the experiment was planned in a way to extort the arm from a rest position into full extension and then back to a rest

position. That way, it would be expected, the triceps muscle would have to overtake most of the force needed for the move. The role of the biceps muscle in that move was to be seen. Moreover, certain exact values correlated with the pulling force (from 0 N to 20 N and then back to 0 N) were possible do estimate.

In the experiment a NeuroTrack MyoPlus 2 electromyography device was used. Five signal electrodes were placed – two measurement electrodes and one reference electrode were placed on the *biceps brachii*, two other measurement electrodes were placed on the *triceps brachii*.

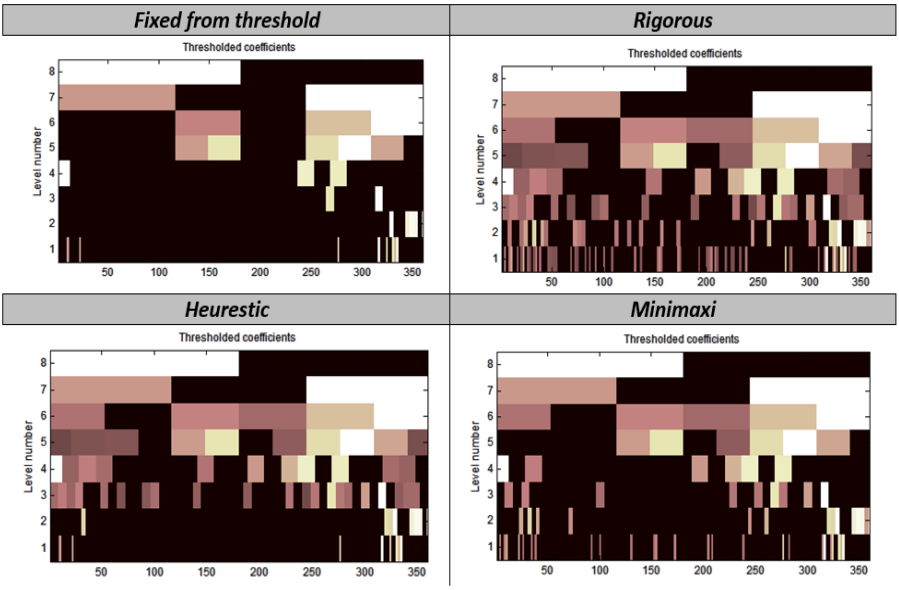

Fig. 1. Comparison of wavelet details involved in signal filtering

To properly reject the noise content from the signal a number of parameters should be considered. Firstly during the signal's decomposition an appropriate decomposition level and subsequently, the wavelet basis function should be selected thoughtfully. To prevent data losses only orthogonal wavelet basis should be taken into account. Previous studies have shown that the *Daubechies 4* (*db4*) basis is the most effective for analysing EMG signals [12]. Therefore, it can be assumed that the wavelet will also be best in filtering of the signal, and therefore, it was selected.

Wavelet filtering exploits the fact that some of the signal details relate to the average value of the signal, while other to an average noise value. Therefore, if less important details related to noise are removed, the signal can be reconstructed on the basis of other details, without loss of significant information contained in the signal. On that basis, the next very important step is a selection of the appropriate threshold. To do this, it is essential to choose an appropriate threshold algorithm (Table 1) and the corresponding threshold scaling function.

Table 1. Threshold selection rules [13]

Name	Description
Rigrsure	Adaptive threshold selection using principle of Stein's Unbiased Risk Estimate
Sqtwolog	Threshold is equal to sqrt(2·log(length(X)))
Heursure	Heuristic variant of above options
Minimaxi	Minimax thresholding principle

The comparison of wavelet coefficients for different threshold selection algorithms is presented in the Fig. 1. Thoughtful analysis of obtained results leads to the conclusion, that during the reconstruction of the signal with the *Sqtwolog* threshold selection algorithm, fewer coefficients are involved in the reconstruction. Therefore, the reconstructed signal can be considered as losing too much information. On the other hand, the *rigrsure* threshold method uses the biggest number of coefficients in the reconstruction process and may be considered as leaving too much noise.

The *minimaxi* threshold selection algorithm removes more coefficients from 1–6 levels than the *heuristic* method, which removes more coefficients from 7–10 levels. Therefore, the *heuristic* algorithm may be found as the best removing noise from the EMG signal. However the lower details are correlated with lower frequencies and are related to the noise. Taking all that into consideration, it can be stared, that the *Heurestic* method is the best among all the other mentioned above and delivers the best filtered signal.

The next step is to choose a threshold rescaling function. In MATLAB toolbox, three algorithms are available: a method based on basic white noise (*one*), scaled white noise (*sln*) and noise model with non-white noise algorithm (*mln*). The comparison of rescaling methods is presented in the Fig. 2 where the details (d_1–d_{10}) of decomposed EMG signal are also presented. The values of the details that are not within determined threshold range are removed from the signal. Using the algorithm based on the white noise model, most of the details are deleted and the important information contain in the signal is lost, so therefore this method is unusable in this situation. One must note, that most of the noise acquired with the signal is white noise. The *mln* rescaling method basis on (black in the Fig. 2) does not effectively remove the noise. In this case, the determined thresholds are too low and almost the whole signal is classified as the original signal, and consequently none of its details are removed. Hence, threw comparison, the best method that can be used is the scaled white noise method (*sln*).

What is more, it can be observed, that the 10th decomposition level is the most suitable one, because the details from each of levels actively participate in the signal denoising process.

Moreover, the soft tresholding method was used during the whole procedure of finding the best rescaling threshold function. This is due the fact, that the method provides high reliability in a lack of discontinuity of the filtered signal [13, 14].

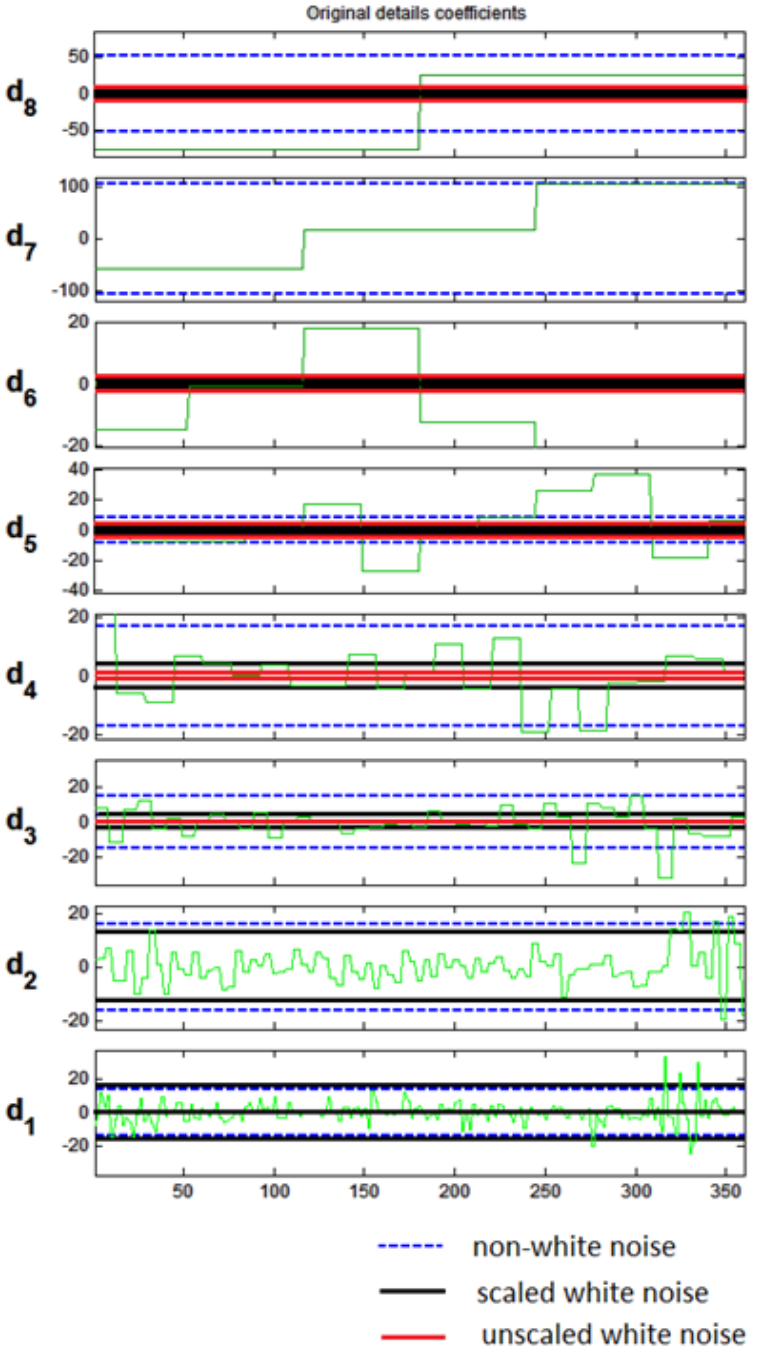

Fig. 2. Threshold rescaling function comparison

4 Data Analysis

The EMG data obtained during the experiment was filtered using the parameters described in paragraph 3. The results are shown on Fig. 3 and Fig. 4. As it can be observed, thanks to the applied wavelet denoising procedure, a clear EMG signal was obtained.

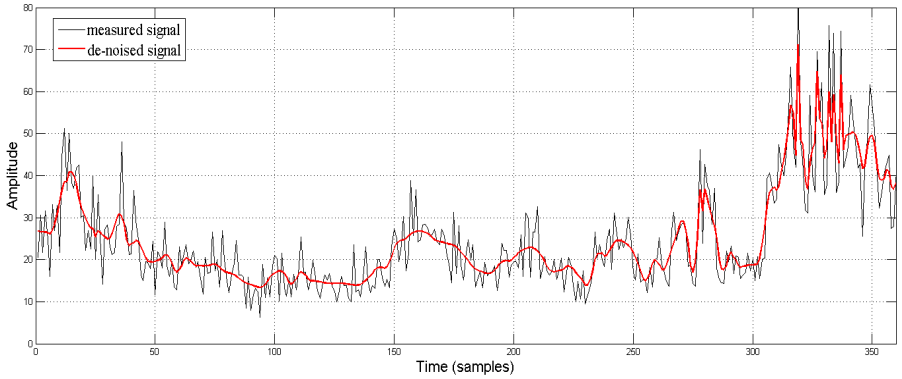

Fig. 3. Filtered biceps muscle EMG signal during contraction

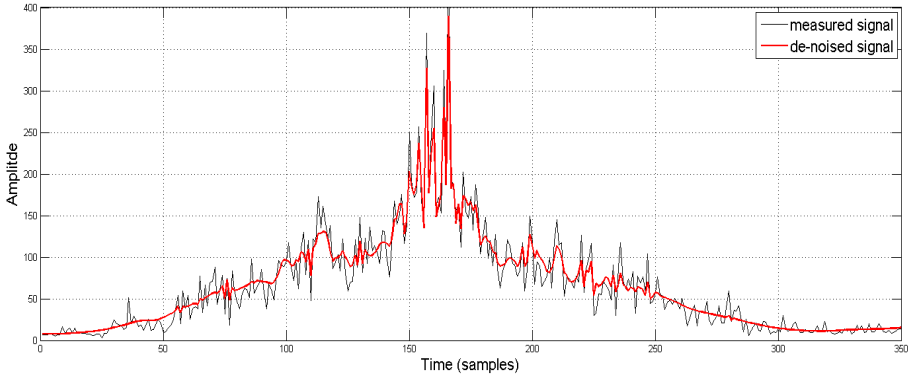

Fig. 4. Filtered triceps muscle EMG signal during contraction

The results shown of Fig. 3 matched the expectations adopted at the beginning of the experiment. During the arm's move the triceps muscle contracted gradually. When the pulling force was 20 N (at the extreme value) the registered muscle EMG signal was 400 mV. The triceps muscle should be maximally contracted at that point. The EMG signal confirms that theory. At this point, it can be observed that the *biceps muscle*, did not contract much. On the contrary, Fig. 4 shows that since the beginning of the move, its contraction weekend to the extreme value point (around 180 s). What can be surprising is that during the second part of the arm's movement (pulling force from 20 N to 10 N), the biceps muscle should behave as in the first part of the

movement. Yet, the Fig. 4. clearly shows muscle contractions at the end of the movement. Their values and frequency indicate fast and strong contractions. This can be a sign of muscle vibration. During the arm's movement the *biceps muscle* acted more like a stabilizing mechanism and it is likely that at the end of the movement the muscle's fatigue factor occurred.

5 Conclusion

Wavelet filtration of the muscle's EMG signal provides sensible and reliable effects, when all of the wavelet denoising parameters are selected properly. In this paper the best wavelet denoising parameters of arm EMG signal filtration are found, that is: wavelet (Daubechies 4), 10th decomposition level, threshold selection algorithm (Heurestic) and a sln rescaling function (based on scaled white noise). Moreover, the EMG signal analysis clearly showed that both muscles, the *biceps* as well as the triceps, were involved in the arms movement, one muscle acting as the main mover, the second more as the arm's stabilizer.

This system has wide application possibility, mainly in pre-processing in many Mechatronic systems. The denoised EMG signals, such as we can see in the Fig. 3. and Fig. 4 can be used in a practical matter, as for example, control signals for a prosthetic arm, in teleoperation of a robot arm, biomedical signal filtering [15] or in rehabilitation aiding robots.

Further research should be focused on the development of suitable arm recognition system, which e.g. could base on LPC feature extraction algorithm [16, 17], combined with neural network or swarm classifier [18].

References

1. Rahnama, N., Lees, A., Reilly, T.: Electromyography of selected lower-limb muscles fatigued by exercise at the intensity of soccer match-play. Journal of Electromyography and Kinesiology 16(3), 257–263 (2006), doi:10.1016/j.jelekin.2005.07.011
2. Jorgensen, C., Dusan, S.: Speech interfaces based upon surface electromyography. Speech Communication 52(4), 354–366 (2010), doi:10.1016/j.specom.2009.11.003
3. Kalinowski, L.: Encyklopedia Badań Medycznych. Wydawnictwo Medyczne MAKmed, Gdansk (1996)
4. Nigg, B.M., Herzog, W.: Biomechanics of the Musculo-Skeletal System, p. 349. Wiley (1999)
5. Fallaa, D., Dall'Albaa, P., Rainoldib, A., Merlettib, R., Julla, G.: Location of innervation zones of sternocleidomastoid and scalene muscles – a basis for clinical and research electromyography applications. Clinical Neurophysiology 113, 57–63 (2002)
6. Reaz, M.B.I., Hussain, M.S., Mohd-Yasin, F.: Techniques of EMG signal analysis: detection, processing, classification and applications. Biological Procedures Online 8(1), 11–35 (2006), doi:10.1251/bpo115
7. Strambi, S., Rossi, B., De Michele, G., Sello, S.: Effect of medication in Parkinson's disease: a wavelet analysis of EMG signals. Medical Engineering & Physics 26(4), 279–290 (2004), doi:10.1016/j.medengphy.2004.01.006

8. Arikidis, N.S., Abel, E.W., Forster, A.: Interscale Wavelet Maximum—A Fine to Coarse Algorithm for Wavelet Analysis of the EMG Interference Pattern. IEEE Transactions on Biomedical Engineering 49(4), 337–344 (2002), doi:10.1109/10.991161
9. Kumar, D.K., Pah, N.D., Bradley, A.: Wavelet Analysis of Surface Electromyography to Determine Muscle Fatigue. IEEE Transactions on Neural Systems and Rehabilitation Engineering 11(4), 400–406 (2003), doi:10.1109/TNSRE.2003.819901
10. Arvetti, M., Gini, G., Folgheraiter, M.: Classification of EMG signals through wavelet analysis and neural networks for controlling an active hand prosthesis. In: Proc. 2007 IEEE 10th Int. Conf. Rehabil. Robot., pp. 531–536 (2007), doi:10.1109/ICORR.2007.4428476
11. Boostani, R., Moradi, M.H.: Evaluation of the forearm EMG signal features for the control of a prosthetic hand. Physiological Measurement 24(2), 309–319 (2003), doi:10.1088/0967-3334
12. Zhou, W., Gotman, J.: Removal of EMG and ECG Artifacts from EEG Based on Wavelet Transform and ICA. In: Proceedings of 26th Annual International Conference of the IEEE, EMBS (2004), doi:10.1109/IEMBS.2004.1403176
13. Messer, S.R., Agzarian, J., Abbott, D.: Optimal wavelet denoising for phonocardiograms. Microelectronics Journal 32(12), 931–941 (2001), doi:10.1016/S0026-2692(01)00095-7
14. Gradolewski, D., Redlarski, G.: The Use of Wavelet Analysis to Denoising of Electrocardiography Signal. In: XV International PhD Workshop OWD 2013, Conference Archives PTETiS, vol. 33 (2013), http://mechatronika.polsl.pl/owd/pdf2013/456.pdf
15. Redlarski, G., Tojza, P.M.: Computer Supported Analysis of the Human Body Surface Area. International Journal of Innovative Computing, Information & Control 9(5) (2013)
16. Redlarski, G., Gradolewski, D.: Wykorzystanie algorytmu kompresji sygnału mowy MP-LPC do modelowania przebiegu fonokardiograficznego. Przegląd Elektrotechniczny 45(89), 40–45 (2013)
17. Gradolewski, D., Redlarski, G.: Identyfikacja dźwięków serca za pomocą algorytmu LPC oraz sztucznej sieci neuronowej. Przegląd Elektrotechniczny (3/2014), 161–164 (2014), doi:10.12915/pe.2014.03.35
18. Własa, M., Gotowalski, B., Jaworski, J.: Algorithm of the tuning system basing on Particle Swarm Optimization for PI controllers in the CNC milling machine. Przegląd Elektrotechniczny 88(9a/2012) (2012)

Assessment of Temperature Coefficient of Extremely Stable Resistors for Industrial Applications

Andrzej Juś[1], Paweł Nowak[1], Roman Szewczyk[2], Michał Nowicki[2], Wojciech Winiarski[1], and Weronika Radzikowska[3]

[1] Industrial Research Institute for Automation and Measurements PIAP, 02-486 Warsaw, Al. Jerozolimskie 202, Poland
{pnowak,ajus}@piap.pl
[2] Warsaw University of Technology, Faculty of Mechatronics, 02-525 Warsaw, Boboli 8 st., Poland
[3] Military University of Technology, 00-908 Warsaw, Kaliskiego 2 st., Poland

Abstract. The article presents the results of tests of the temperature characteristics of resistors with very low TCR and the lowest price in their class. The study was conducted in terms of their use as reference in the processing current-voltage system in the magnetomechanic part of the analytical scale. However, they are also widely used in applications where the constant value of resistance in the whole measuring range is critical. The results not only confirm the usefulness of the tested resistors, but can also ensure significant cost reduction in many applications.

Keywords: stable resistors, temperature coefficients, TCR.

1 Introduction

The article presents the temperature characteristics of UPR0.5 D10 resistors. They are distinguished by very low TCR (declared by the manufacturer), and the price many times lower than typical for comparable, commercially available components. Such stable resistors are widely used in applications where constant value of resistance in the entire operational temperature range is critical. For example, the elements are used as a reference in precision current-voltage processing systems.

The manufacturer of the resistors only provides information on the TCR value in a narrow temperature range. To get a more complete picture of the temperature properties of the resistors, additional test were made as follows:

- resistance stabilization time after power on,
- whether the shape of the resistors temperature characteristics changes in subsequent cycles of heating / cooling, and whether the resistors have a temperature hysteresis,
- whether those characteristics are dependent on the rate of resistors heating,
- the values of resistors temperature coefficients.

J. Awrejcewicz et al. (eds.), *Mechatronics: Ideas for Industrial Applications*,
Advances in Intelligent Systems and Computing 317, DOI: 10.1007/978-3-319-10990-9_27

Additionally it was hypothesized (resulting from physical analysis) and verified, whether the temperature dependent changes in resistor's resistance can be described by a curve of second degree [1].

The study was performed on the test stand developed for this purpose. Its operation is based on a differential measurement, which allowed for high accuracy of temperature characteristics obtained – at the 0.05 ppm/ ºC level.

2 Object of Study

The metal-foil resistors are characterized by the highest temperature stability [2]. A market leading manufacturer of such resistors is Vishay company. The offered resistors are made of one of the three alloys based on nickel and chromium (i.e. K, C, Z). The relative change in resistance as a function of temperature for the resistors made of these alloys are shown in Fig. 1.

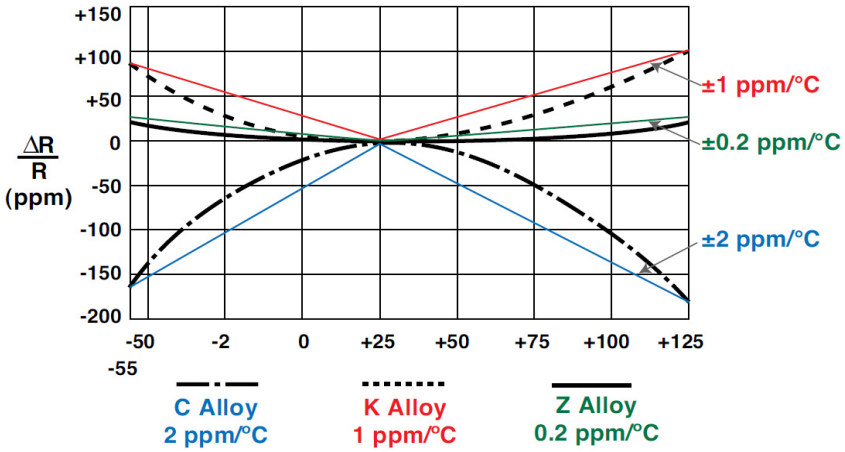

Fig. 1. Relative changes in resistance of the reference resistor made of type K alloy, C alloy and Z alloy (Vishay materials) [6]

Table 1. Parameters of selected temperature stable resistors

	Type	Producer	Resistance range (Ω)	Typical TCR (ppm/ºC)
1	S102C (K)	Vishay	1 to 150k	±1
2	Z201	Vishay	5 to 100k	±0.2
3	Z205T	Vishay	5 to 300k	±0.2
4	UPR0.5 D10	Thunder Precision	1 to 1M	±1

Some type of metal-foil resistors are presented in Table 1. They have very low TCR, but in application where the resistance stability is critical it could be too high. This forces the need to conduct own research of the TCR value. This in turn makes the use of resistors with a lower price justified.

Therefore, the UPR0.5 D10 resistors, equivalent to Vishay S102C resistors, were selected for study. They are characterized by the low temperature coefficient declared by the manufacturer, and competitive price. These resistors are constructed of two connected components with opposite temperature coefficients (Fig. 2). It is the most popular method of temperature coefficient elimination [4]. They are available in 2- and 4-legs configuration. Important parameters provided by the manufacturer are summarized in Table 2.

Table 2. Datasheet parameters of the UPR0.5 D10 [7]

All values are tested at the following condition: temp: 21–25 °C, relative humidity: 45–60 %	
Parameter	Value
Rated dissipation, P_{70}	0.50 W
Operating voltage, U_{max}	600 V
Tolerance	±0.5 %
TCR	±1 ppm/°C

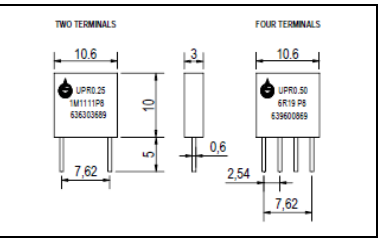

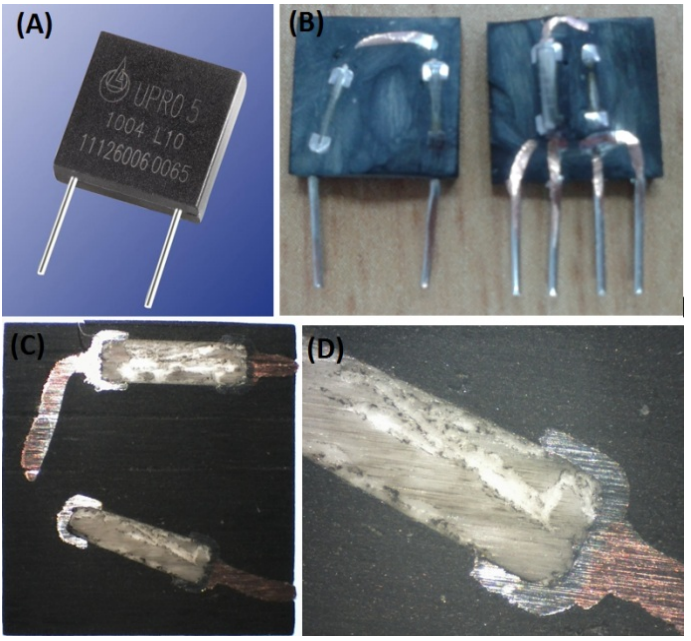

Fig. 2. Resistor UPR0.5 D10: (a) view, (b) the interior in 2- and 4-legs configuration, (c) two-legs configuration cross-section, (d) a connection of the ceramic body and the legs

This information, however, is incomplete. To get a comprehensive picture of the temperature properties of these resistors, studies listed in the introduction were made, the results of which are presented in Section 4. The examined resistors analogy to resistors from Vishay S102C (K Alloy) and physical results analysis [1], led to the hypothesis of the square-function temperature characteristics shape, with a minimum around 25 ºC, according to Fig. 1. Verification of the hypothesis is included in Section 4.

3 Test Stand

Operation of the test stand is based on the differential measurement – this results in a very high accuracy. Diagram of the measuring circuit is shown in Fig. 3.

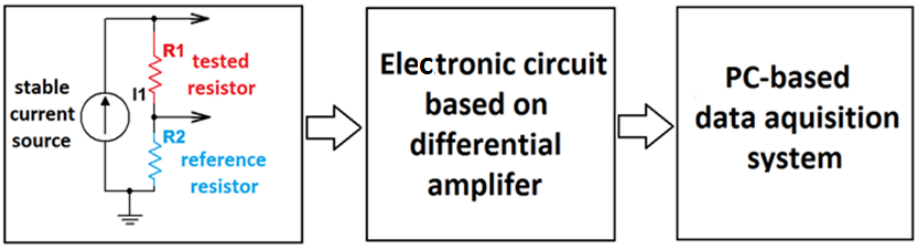

Fig. 3. Simplified electronic scheme of measurement circuit idea

The examined resistor ($R1$) is connected in series with a reference resistor ($R2$) and powered by an high precision current source ($I1$). The voltage drops across resistors $R1$ and $R2$ are denoted, respectively, as $U1$ and $U2$. Their values are calculated from Ohm's law:

$$U = R \cdot I. \tag{1}$$

According to (1) they are: $U1 = R1 \cdot I1$ and $U2 = R2 \cdot I1$. Voltage drops are measured by the electronic circuit based on differential amplifier and are converted to output voltage (V_{out}), the value of which is expressed in the relationship:

$$V_{out} = (U1 - U2) \cdot k. \tag{2}$$

where k – differential amplifier amplification, in the present case, $k = 100$.

Finally, the output voltage in Fig. 3 is:

$$V_{out} = (U1 - U2) \cdot k = I1 \cdot (R1 - R2) \cdot 100. \tag{3}$$

To determine the temperature characteristics of the tested resistor ($R1$), it is heated in a controlled way, while the reference resistor ($R2$) is in the constant temperature or is heated (in this case, the differential characteristics of two resistors are received). The temperature (T) of the tested resistor (or both resistors) and the output signal (V_{out}) are continuously recorded. On that basis the sought characteristic is determined. TCR value is calculated as its inclination.

At charts presented in Section 4 the initial value of the measured signal is reduced to zero and expressed in ppm changes in the resistance of the tested resistor ($R1$). In each case tests were carried out after the stabilization of the system parameters (i.e. self-heating of the components and equipment), in stable external conditions.

4 Results

The presented results were obtained for resistance values $R1$ and $R2$ = 200 Ω and current $I1$ = 12.5 mA. For resistors of other values analogous results were obtained.

4.1 Time of Indication Stabilization after Powering Up of Measurement Loop

The temperature of the tested resistors may change due to the changes in ambient temperature (external heating of resistors), and as a result self-heating [5]. In order to make reliable measurements of the TCR the effects of these two phenomena must be separated. The easiest method is to wait until the resistor heats up as a result of current flow through it, and its temperature will stop changing. The following are examples of waveforms obtained directly upon powering up of the measuring loop (without external resistors heating), for the same pair of resistors placed in the air (Fig. 4a) and between the copper blocks (Fig. 4b).

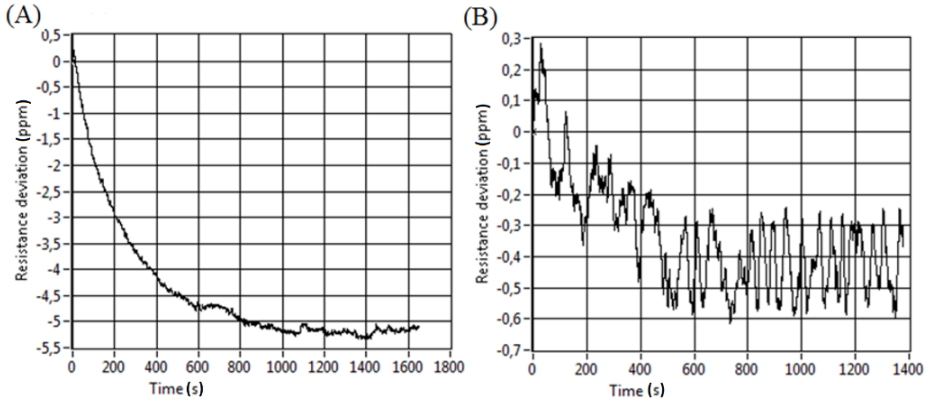

Fig. 4. Characteristics obtained directly upon powering up of the measuring loop, for the same pair of resistors placed in the air (a) and between the copper blocks (b)

Presented indication change is the result of self-heating of both the tested and the reference resistor. The self-heating time and value is greater when both of the resistors are placed in air (Fig. 4a) and lower when both resistors are placed between the heating blocks (Fig. 4b). It is associated with better resistors heat dissipation in the second situation.

As a result of a larger number of measurements, it was observed that the self-heating time was somewhat shorter for the resistors placed between copper blocks and ranged 500–600 s. In contrast, when the resistors are placed in the air, that time was in the range of 600–1000 s. To carry out the measurements of other temperature

parameters of resistors, after the measurement loop powering up, one should wait for the stabilization of indication for the abovementioned time.

4.2 The Parameters Change of the Resistor in Subsequent Heating Cycles and Hysteresis

The studies presented in this section were made to determine whether the cyclic heating of the resistor results in the changes of the material structure, and whether those induce shift in temperature characteristic or change of the TCR. Resistors which had not been powered for at least several days were studied. The results are shown in Figures 5 and 6, and the TCR values obtained in subsequent cycles are summarized in Table 3.

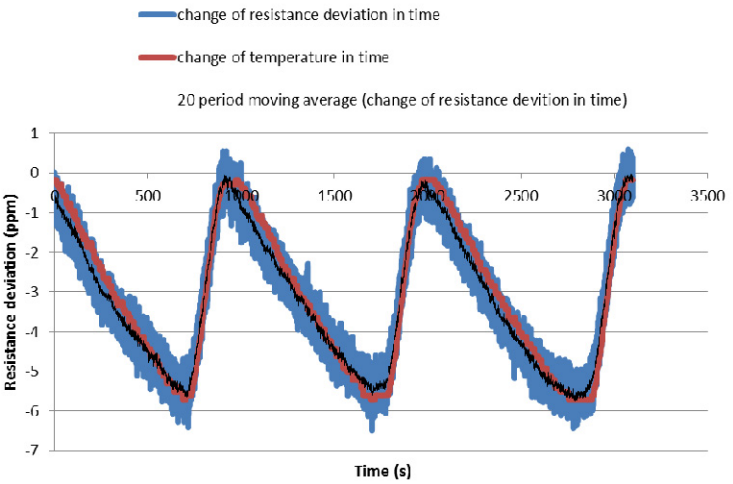

Fig. 5. Change of resistance deviation in time with the average value in the subsequent cycles of cooling-heating. Temperature changes also, but unscaled

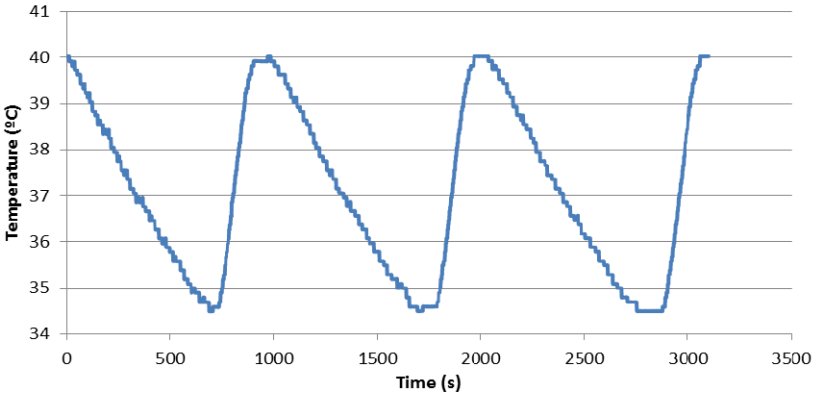

Fig. 6. Change of temperature in time in the subsequent cycles of cooling-heating

Table 3. TCR values in the subsequent cycles of cooling-heating of the resistor (▼ – cooling, ▲ – heating)

Cycle part	▼ (1)	▲ (1)	▼ (2)	▲ (2)	▼ (3)	▲ (3)	Average
Value (ppm/ºC)	0.898	0.919	0.878	0.895	0.927	0.915	0.913

On the obtained characteristics (Fig. 5 and 6) there is no observable shift in the result of a cyclic cooling-heating. The results obtained in subsequent cycles of cooling-heating of the resistor are characterized by high repeatability. Obtained TCR values are summarized in Table 3. There was no difference in the TCR value between heating and cooling. Spread of the TCR values obtained was 0.05 ppm/°C.

Based on the results, observations whether the resistors have temperature hysteresis in the cooling-heating cycle was also carried out. For this purpose, the temperature characteristics of were determined (Fig. 7).

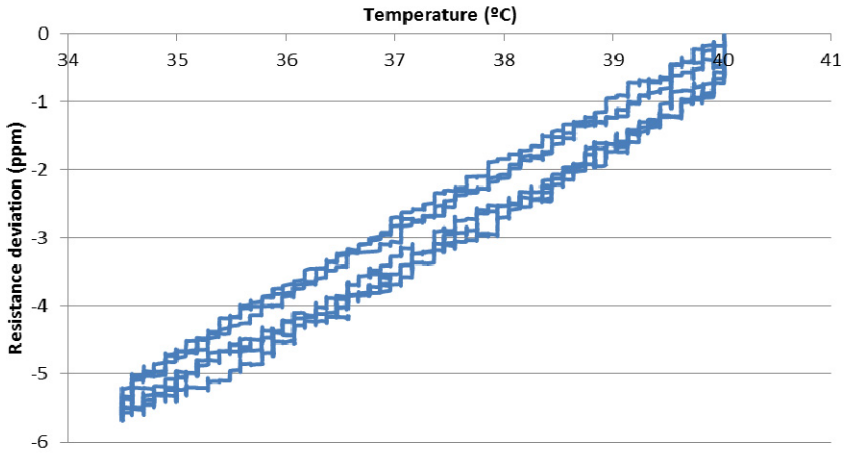

Fig. 7. Indication changes of resistance deviation in function of temperature in the subsequent cycles of heating and cooling

There was a shift between cycles of heating and cooling. The whole shift takes place during the change of direction of temperature change. Otherwise, the characteristics obtained during heating and cooling are parallel. It was also observed that the shift is independent of the value of temperature changes in the cooling-heating cycles.

These observations indicate the cause of the observed loop, which is the different times of response to the temperature change in temperature detector, and the heating of the resistor tested.

The studies indicate no temperature hysteresis in examined resistors.

4.3 The Rate of Change of Temperature, and the Value of the Temperature Coefficient

The next issue that was analyzed was whether the resistors achieve the same temperature coefficients regardless of the rate of heating. For this purpose, measurements were made at different heating rates of the resistor tested. Sample results from a single heating cycle at different heating rates are presented in the following graph (Fig. 8).

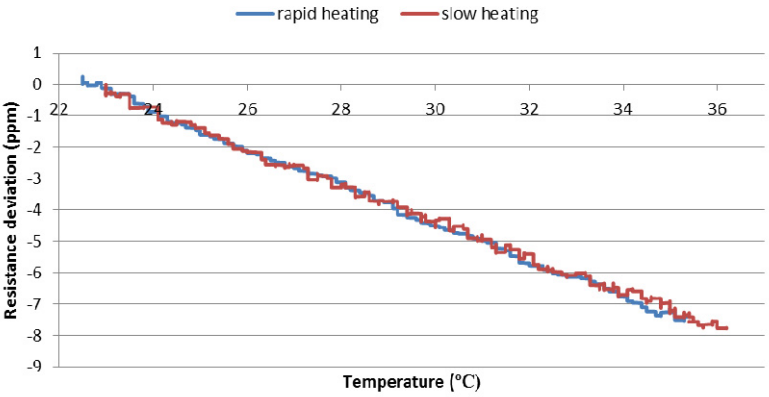

Fig. 8. Change of indication in function of the temperature, depending on the rate of the tested resistor heating

The characteristics in Fig. 8 practically overlap. This is confirmed by the –0.590 ppm/°C TCR values obtained during the rapid heating (took 270 s), while during the slow heating (took 1350 s), it was –0,575 ppm/°C. It is a very small difference – less than the scattering of the results obtained during the cyclic heating-cooling in Section 4.2. Little or no effect of the rate of heating on the results is also confirmed by results shown in Fig. 7 – loops in each case close properly (and cooling takes place much slower than heating – Fig. 5).

4.4 The Temperature Characteristics of the Indication Changes – Statistical Analysis, Comparison with Model

In Part 2 a parabolic waveform of the resistors temperature characteristics with a minimum around +25 ºC has been hypothesized, in accordance with Fig. 1 (K alloy). In order to verify this hypothesis, seven resistors were studied (they were numbered for research purpose). The study consisted of single heating cycle conduction. For the analysis the change of resistance of the temperature deviation characteristics were determined.

Then for each characteristic (using the least squares method) curve of the first and second degree was fitted, as well as coefficients of determination R^2 [3] of those models. An example of the characteristic, along with marked curves of the first and second degree and the value of R^2 is presented in Fig. 9. The test results obtained for

the resistors are summarized in Table 4. There are values of 2nd degree polynomial matching:

- determination coefficient (R^2),
- polynomial parameters (a, b, c) ,
- temperature (T_{extr}), for which there is an polynomial extremum,
- indication change for the temperature change in the range of 20–30 ºC (ΔR(ppm) 20–30 ºC),
- TCR in the range of 20–30 ºC (ΔR(ppm/ºC)), assuming a linear characteristics nature (it can be done because for the linear fit $R^2 > 0.95$).

Table 4. Summary of the results of polynomial of 2nd degree matching

Resistor	a	b	c	R^2	T_{extr} (°C)	ΔR(ppm) 20–30 °C	ΔR (ppm/°C)
23	–0.0017	0.1897	–3.0577	0.9794	56	1.0	0.10
27	0.0021	–0.6094	12.531	0.9994	145	–5.0	–0.50
28	0.0233	–1.9297	33.812	0.9985	41	–7.6	–0.76
30	0.0090	–1.208	20.941	0.9945	67	–7.6	–0.76
31	0.0066	0.2334	–9.331	0.9995	–18	5.6	0.56
34	0.0070	–0.8981	16.993	0.9991	64	–5.5	–0.55
36	0.0042	–0.6805	11.804	0.9993	81	–4.7	–0.47

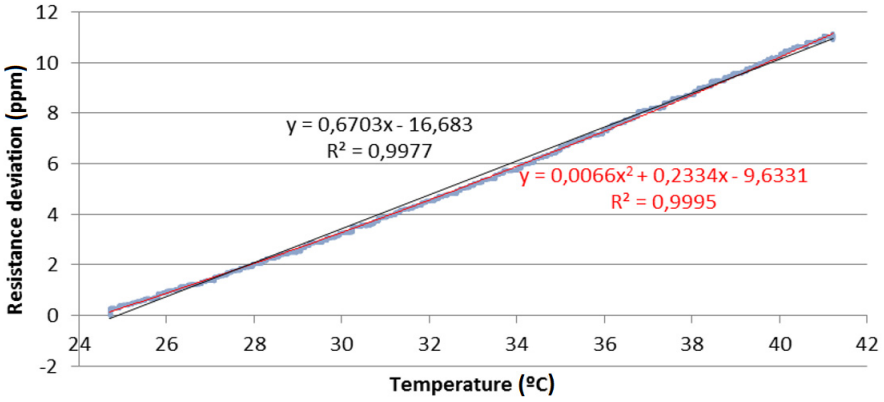

Fig. 9. An example of characteristic obtained during the course of the heating of one of the resistors with matching curves of the first and second degree and coefficients of determination for these models

The coefficient of determination (R^2) for all experiments exceed 0.95. In this case, it must be assumed that the adopted model describes the changes observed experimentally and the use of statistical tests is pointless [3]. By analyzing this data it is clear that the TCR in the range of 20–30 °C are within the ±1ppm/ºC range stated by the manufacturer. A second degree polynomial corresponds well with the experimentally obtained results. The values of inflection points of the fitted curves reach very

different values and there is no way to discern dependence. Therefore there is no technical possibility to utilize the fact that resistors have minimal thermal sensitivity in characteristics extremum. In addition, the TCR takes both positive and negative values. These observations are not consistent with the characteristics from Fig. 1. Theoretical characteristics do not reflect the experimental results. The probable cause of this discrepancy is inaccurate compensation of examined resistors parameters in the production process.

5 Conclusion

The research confirmed the usefulness of UPR0.5D10 resistors in applications requiring high stability of resistance in the entire temperature operation range. The results obtained for all tested resistors were within the manufacturer's stated tolerance of ±1 ppm/°C. Among the examined resistors were specimens of the TCR close to 0. This makes it possible to select components that meet the highest-possible requirements – components with declared TCR less than ±0.2 ppm/°C are currently not available on the market. As part of this study other functional characteristics of resistors were identified: they do not change the properties during heating cycles, do not have hysteresis, have the same TCR regardless of the rate of heating. The undoubted drawback is the change in temperature of the resistor (and therefore resistance value) as a result of its self-heating, and above all a long time that it takes – about 500–1000 s.

However, the results should be regarded as positive, and tested resistors highly useful as an extremely stable element in many applications.

Acknowledgments. This work was partially supported by The National Center for Research and Development with PBS Program – Grant no. PBS 1/B3/8/2012.

References

1. Thomas, J.L.: Precision resistors and their measurement, NBS (1948)
2. Harrison, L.T.: Current sources & voltage references. Elsevier (2005)
3. Aczel, A.D.: Statystyka w zarządzaniu. PWN (2011) (in Polish)
4. Sadeghi, N., Sadeghi, I., Mirabbasi, S.: Analysis and design of monolithic resistors with a desired temperature coefficient using contacts. IET Circuits Devices & Systems 7(4), 185–192 (2013), doi:10.1049/iet-cds.2012.0126
5. Braudaway, D.: Precision resistors: A review of the techniques of measurement, advantages, disadvantages, and results. IEEE Transactions on Instrumentation and Measurement 48(5), 884–888 (1999), doi:10.1109/19.799640
6. Design and selector guide for high-precision resistors, Vishay (2011)
7. UPR Datasheet

Magnetoelastic Characteristics of Constructional Steel Materials

Maciej Kachniarz[1], Dorota Jackiewicz[1], Michał Nowicki[2], Adam Bieńkowski[2], Roman Szewczyk[1], and Wojciech Winiarski[1]

[1] Industrial Research Institute for Automation and Measurements PIAP, Warsaw, Poland
mkachniarz@piap.pl, d.jackiewicz@mchtr.pw.edu.pl,
{rszewczyk,wwiniarski}@piap.pl
[2] Institute of Metrology and Biomedical Engineering,
Warsaw University of Technology, Warsaw, Poland
{m.nowicki,a.bienkowski}@mchtr.pw.edu.pl

Abstract. Paper presents the methodology and results of magnetoelastic characteristics investigation of three types of constructional steels. Investigated steels were formed into frame-shaped samples with both magnetizing and sensing windings coiled on their columns. Magnetic characteristics of materials were measured by computer controlled hysteresisgraph. In order to apply tensile stresses in material of the sample, special force reversing system was used. The tested samples and the procedure of their investigation were described. Obtained results were processed and presented in the paper as charts, which were analyzed and discussed. On the basis of the results, the conclusions were formulated, which are also included in the paper.

Keywords: magnetoelastic effect, constructional steel, non-destructive testing.

1 Introduction

Nowadays steel is one of the most commonly used construction materials. Due to the large number of types, with a variety of physical and chemical properties, this material is used in many industrial applications. Very often elements made of steel are used in constructions working under large mechanical loads, for example in energetic industry. Due to financial and safety reasons, it is highly recommended to monitor state of the materials working in such conditions.

To reduce additional costs it is desirable not to damage monitored elements while testing them. It is the reason, why non-destructive tests are increasingly popular. Among them, methods enabling materials monitoring through their magnetic properties investigation deserve special attention. Magnetic tests are based on the magnetoelastic effect involving changes of magnetic properties of material under the influence of external forces [1, 2]. It is only possible to use them for ferromagnetic materials. They allow to investigate state of material without tested element disassembly. Moreover, they are contactless, which simplifies investigating process.

J. Awrejcewicz et al. (eds.), *Mechatronics: Ideas for Industrial Applications*,
Advances in Intelligent Systems and Computing 317, DOI: 10.1007/978-3-319-10990-9_28

The main obstacle for using magnetoelastic based non-destructive methods [3] is lack of knowledge about magnetoelastic characteristics of steel materials used in construction. This paper attempts to fill this missing part of engineering knowledge by investigating magnetoelastic characteristics of three different types of constructional steels. The measuring method used for investigations is described, and obtained results are presented and discussed.

2 Investigated Materials

During the tests, magnetoelastic characteristics of three different types of constructional steels were investigated. Each type of steel has unique mechanical and physical properties due to its individual chemical composition.

- **C45** [4] is a medium carbon steel of higher quality and strength used for engineering of mechanical components like crankshafts, axes, gearwheels and pump rotors. Its yield strength R_e is over 350 MPa and its tensile strength R_m is 600–800 MPa.
- **X30Cr13** [5] is martensitic corrosion resistant alloy steel with addition of chromium. It provides high resistance to various corrosion agents, such as weather conditions, steam, gasoline, mineral oils, etc. This type of steel has good resistance to high temperature oxidation (up to 750 °C). It is used in energetic industry as material for developing energetic turbines elements. Its yield strength R_e is over 350 MPa and its tensile strength R_m is 650–880 MPa.
- **13CrMo4-5** [6] is heat resistant alloy steel with addition of chromium and molybdenum. It offers possibility to operate in high temperatures up to approximately 550 °C. It is used in energetic industry for developing hot steam pipe lines, collecting pipes and heater tubes. Its yield strength R_e is over 280 MPa and its tensile strength R_m is 450–600 MPa.

3 Methodology of Measurements

3.1 Measurement System

The schematic block diagram of measurement system used for magnetoelastic characteristics investigation of tested steels is presented in Fig. 1. The main component is automatic system for soft magnetic materials investigation HB-PL30, which is controlled by personal computer with software for control and data acquisition installed. HB-PL30 system is composed of current waveforms generator and the fluxmeter. Current waveforms generator is used for magnetizing waveforms of a predetermined amplitude and frequency generation. Generated current drives the magnetizing winding, causing changes of voltage induced in the sensing winding, which is measured and converted on the flux density value by the fluxmeter. Personal computer collects and processes measurement data, and saves obtained results in text files.

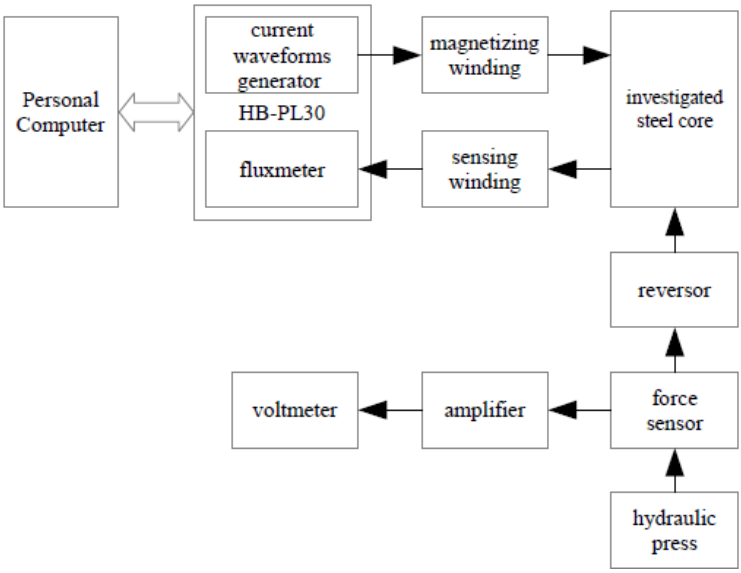

Fig. 1. Schematic block diagram of the measurement system for magnetoelastic characteristics of ferromagnetic materials investigation

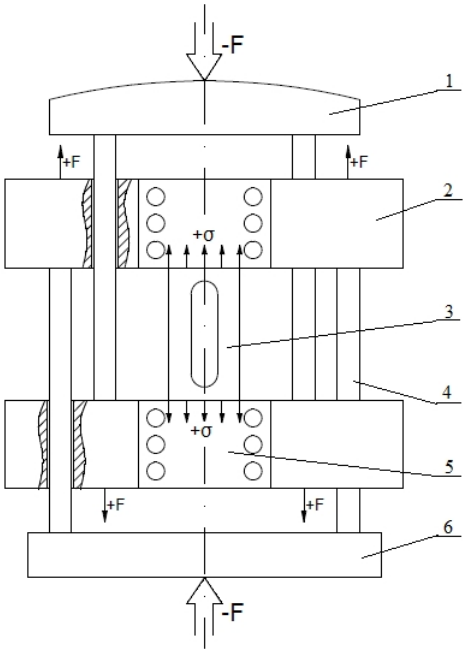

Fig. 2. Composition of the force reversor for conversion of compressive force into tensile force: –F – compressive force, +F – tensile force, +σ – tensile stresses, 1 – tested sample, 2 – moving bar, 3 – sample holder, 4 – cylindrical column, 5 – reversor base, 6 – upper bar

For stress generating, the oil hydraulic press is used. The oil press is manually operated. Compression force generated by the press is converted into tensile force acting upon the sample by special force reversor, presented in Fig. 2 [7]. The device is designed to convert compressive force acting on upper bar to tensile force acting on the sample, resulting in tensile stresses in the investigated material. The force reversor is made of aluminum, which is non-magnetic material, to avoid dispersion of magnetic flux from the tested sample into its material. Applied force is measured by precise force sensor with measuring range up to 100 kN, placed in the axis of the reversor. Signal from the force sensor is amplified and measured by voltmeter (1 V equals 10 kN). Value of tensile stresses can be determined as a ratio of tensile force to the cross-sectional area of the columns of investigated sample.

3.2 Tested Samples

All investigated materials were formed into frame-shaped samples presented in Fig. 3. Using frame-shaped samples allowed to obtain uniform distribution of applied tensile stresses in the tested materials. Moreover, this shape allows to firmly lock investigated sample in the force reversor.

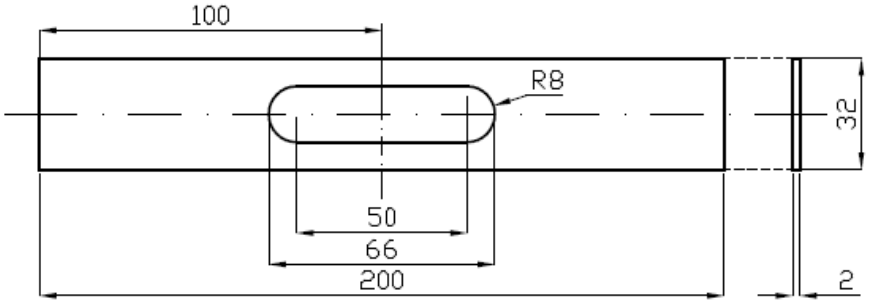

Fig. 3. Frame-shaped sample of ferromagnetic steel used for the magnetoelastic tests

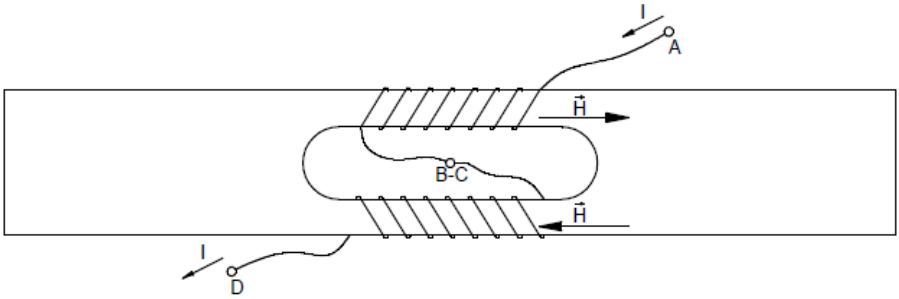

Fig. 4. Distribution of windings on investigated sample (as an example magnetizing winding is used: I – magnetizing current, H – magnetic field)

In order to allow for measurement of magnetic characteristics of investigated materials, on the columns of all samples magnetizing and sensing windings were made. Each winding was made in two parts of equal number of coils (one part on each column of the sample). Then both parts were connected by soldering, as shown in Fig. 4. Uniform distribution of windings on sample's columns was necessary to obtain closed magnetic circuit and to avoid dispersion of magnetic flux in material. Moreover, sensing winding was located under magnetizing winding in order to decrease influence of demagnetization effects.

3.3 Measuring Procedure

Investigated samples were subjected to tensile stresses from 0 MPa to the point, where the rupture of the sample occurred. For each material, about 20 individual values of tensile stresses between 0 MPa and the rupture point were chosen as measuring points. At each point, magnetic characteristics of tested material were measured for four values of magnetic field amplitudes H_m. These values were dependent on coercion field H_c previously measured in unloaded sample. Before each measurement, investigated sample was demagnetized.

4 Experimental Results

The influence of tensile stress σ on the shape of $B(H)$ magnetic hysteresis loops of frame-shaped samples made of investigated materials, measured with magnetizing field amplitude $H_m = 1.5H_c$ (with this amplitude changes in the shape of hysteresis loops are most noticeable), is presented in Fig. 5. Characteristics obtained for 0 MPa tensile stresses (unloaded sample), Villari point [8] and rupture point were chosen to present. Changes of shape of hysteresis loops under influence of tensile stresses are distinctly visible. It is noticeable, that basic magnetic parameters, like maximal flux density, remanence and coercion field, are also changing under the influence of tensile stresses.

Fig. 6 presents the magnetoelastic characteristics $B_m(\sigma)$ of investigated materials where tensile stresses dependences of maximum flux density is visible. It is clearly noticeable, that in the initial part of characteristic, increase of tensile stresses causes increase of maximum flux density. After reaching the Villari point, where flux density reaches maximum value, decrease of its values with increase of tensile stresses occurs. This changes are particularly evident for lower values of magnetizing field's amplitude. It can also be seen, that for values of tensile stresses corresponding to yield strength, where elastic deformations of sample changes into plastic deformation, decreases of maximum flux density values starts to be the most significant. It is connected with permanent changes in the material's structure taking place under tensile stresses.

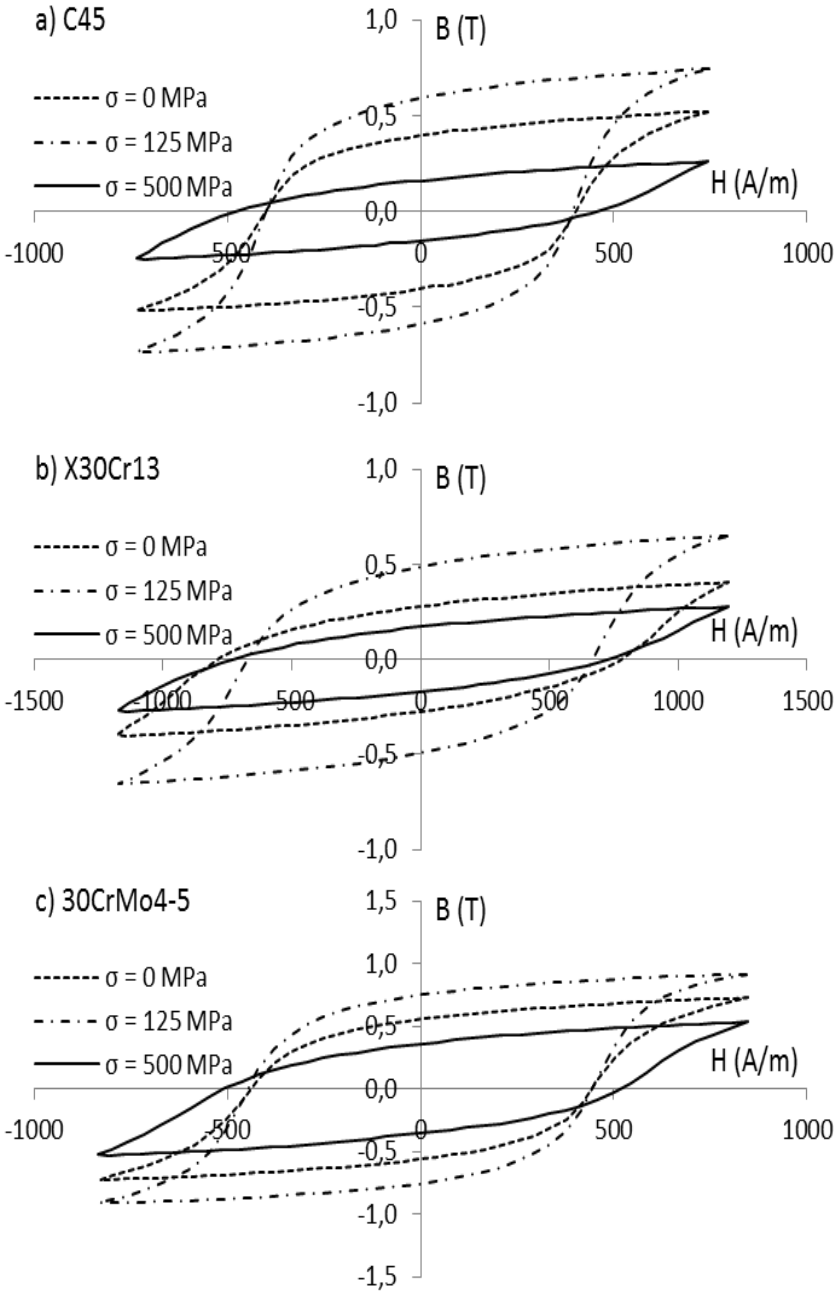

Fig. 5. The tensile stress dependence of magnetic $B(H)$ characteristics of frame-shaped samples made of: a) C45 construction steel, H_m = 750 A/m; b) X30Cr13 corrosion resistant steel, H_m = 1200 A/m; c) 30CrMo4-5 heat resistant steel, H_m = 850 A/m

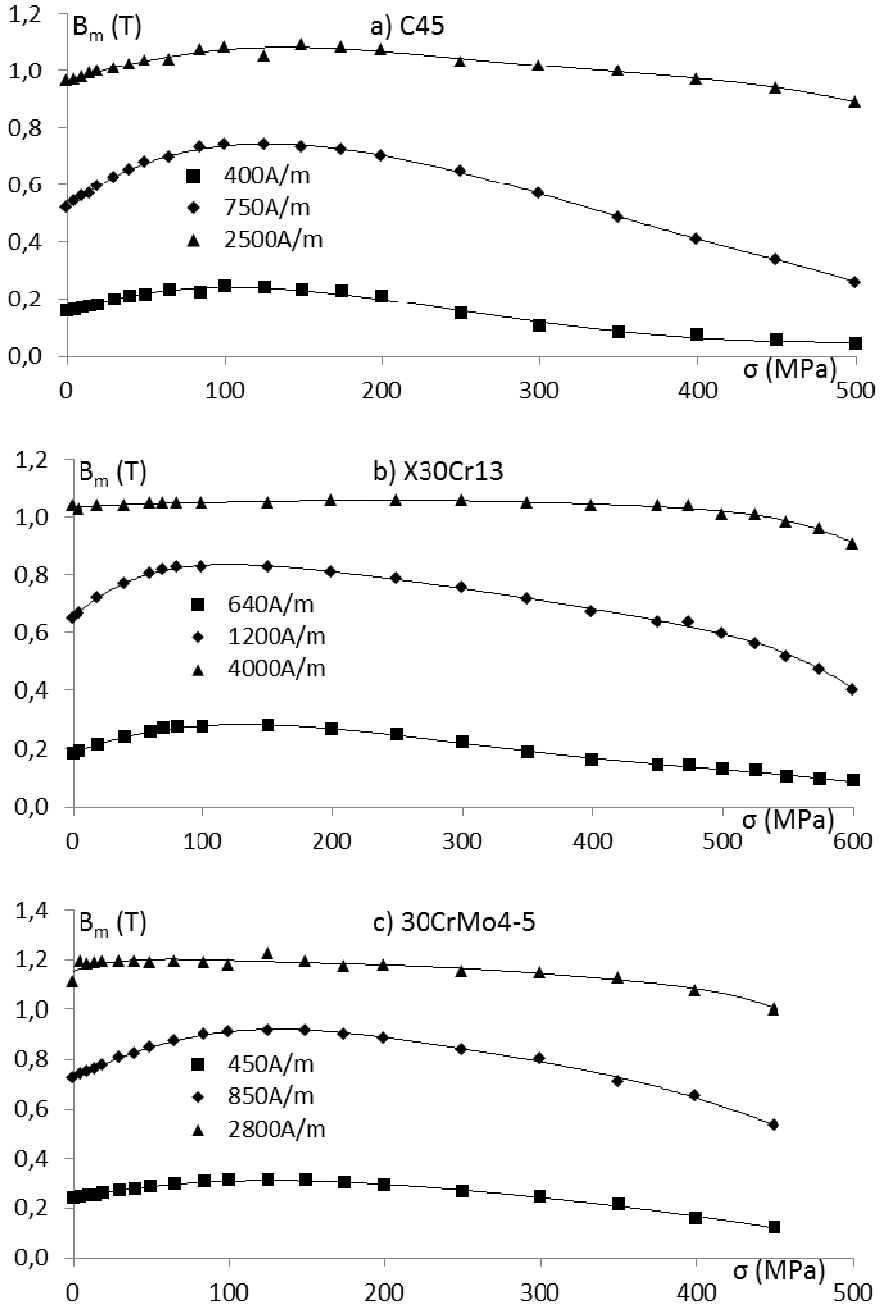

Fig. 6. The tensile stresses σ dependences of maximum flux density B_m for three selected values of amplitude of magnetizing field H_m in frame-shaped samples made of: a) C45 construction steel; b) X30Cr13 corrosion resistant steel; c) 30CrMo4-5 heat resistant steel

5 Conclusions

Magnetoelastic characteristics obtained as a results of performed investigation show, that tensile stresses have significant influence on magnetic properties of construction steel. Especially for lower magnetizing fields, this influence is easily seen. Changes of shape and area of presented hysteresis loops under tensile stresses are clearly observable.

Basic magnetic parameters of materials are also distinctly changing under the influence of tensile stresses. From the magnetoelastic based non-destructive testing point of view, changes of maximum flux density B_m are especially interesting. Presented magnetoelastic characteristics $B_m(\sigma)$ of investigated materials are not monotonous. There is an extreme, called Villari point, on each of obtained characteristics, where value of flux density is at maximum. Value of tensile stresses corresponding to Villari point depends on material – for each type of steel it is different. Because of this shape of $B_m(\sigma)$ characteristics, it is impossible to precisely assess value of tensile stresses in material on the basis of value of maximum flux density. However, it can be determined, that if value of maximum flux density in material is higher, than its initial value in unloaded sample, the investigated material is subjected to acceptable values of tensile stresses from region of elastic deformation. On the other hand, if value of maximum flux density drops below the initial value, it is a clear signal, that tensile stresses in the material are in the region of plastic deformation and there is a danger of rupture of the element. It should be noticed, that described changes are most observable for lower amplitudes of magnetizing field. It proves, that magnetizing field's amplitudes of the about $1.5H_c$ (coercion field) value are the most optimal for magnetoelastic based non-destructive tests.

Moreover, presented results indicate, that for all three tested types of constructional steels, the nature of tensile stresses influence on magnetic properties of material is similar. It allows to suppose, that the nature of investigated phenomenon is the same for all types of constructional steels, which is very important conclusion for magnetoelastic based non-destructive methods of testing. It implies, that proposed method is universal enough to be used in industry for investigation of all types of constructional steels.

Acknowledgement. This work was partially supported by The National Centre of Research and Development (Poland) within grant no. PBS1/B4/6/2012.

References

1. Salach, J., Jackiewicz, D., Bieńkowski, A., Nowicki, M., Gruszecka, M.: Influence of Tensile Force on Magnetic Properties of Amorphous $Fe_{80}B_{11}Si_9$ Alloys in Different States of Thermal Relaxation. In: Szewczyk, R., Zieliński, C., Kaliczyńska, M. (eds.) Recent Advances in Automation, Robotics and Measuring Techniques. AISC, vol. 267, pp. 665–676. Springer, Heidelberg (2014)

2. Salach, J., Szewczyk, R., Bieńkowski, A., Jackiewicz, D.: Possibilities of Application of Amorphous $Fe_{77}Cr_2B_{16}Si_5$ Alloys in Different States of Thermal Relaxation as Magnetic Tensile Force Sensors. Solid State Phenom. 198, 388–393 (2013), doi:10.4028/www.scientific.net/SSP.198.388
3. Runkiewicz, L.: Application of Non-destructive Testing Methods to Assess Properties of Construction Materials in Building Diagnostics. Architecture, Civil Engineering, Environment 2, 79–86 (2009)
4. Kucera, M., Prsan, J.: Tribologic Properties of Selected Materials. Techn. Sc. 11, 228–241 (2008), doi:10.2478/v10022-008-0016-x
5. Rafsanjani, A., Abbasion, S., Farshidianfar, A., Irani, N.: Investigation of The Viscous and Thermal Effects on Ductile Fracture in Sheet Metal Blanking Process. J. Adv. Manuf. Technol. 45, 459–469 (2009), doi:10.1007/s00170-009-1988-9
6. Abang, R., Findeisen, A., Krautz, H.J.: Corrosion Behaviour of Selected Power Plant Materials Under Oxyfuel Combustion Conditions. Górnictwo i Geoinżynieria 35, 23–42 (2011)
7. Jackiewicz, D., Szewczyk, R., Salach, J., Bieńkowski, A., Kachniarz, M.: Influence of Stresses on Magnetic B-H Characteristics of X30Cr13 Corrosion Resisting Martensitic Steel. In: Szewczyk, R., Zieliński, C., Kaliczyńska, M. (eds.) Recent Advances in Automation, Robotics and Measuring Techniques. AISC, vol. 267, pp. 607–614. Springer, Heidelberg (2014)
8. Bieńkowski, A., Szewczyk, R., Salach, J., Kolano-Burian, A.: The Magnetoelastic Villari Effect in $Fe_{25}Ni_{55}Si_{10}B_{10}$ Amorphous Alloy Subjected to Thermal Treatment. Reviews on Advanced Materials Science 18, 561–564 (2008)

Sensor Fusion Based Tool-Workpiece Contact Detection in Micro-Milling

Marcin Matuszak[1] and Paweł Waszczuk[2]

[1] Maritime Academy in Szczecin, Faculty of Mechanical Engineering, Szczecin, Poland
m.matuszak@am.szczecin.pl
[2] West Pomeranian University of Technology,
Faculty of Electrical Engineering, Szczecin, Poland
pawel.waszczuk@zut.edu.pl

Abstract. Information about distance between tool and workpiece is crucial for proper machining process. In micro-milling, due to very small tool dimensions, observation of the tool position with regard to the workpiece is possible only with a microscope. Exploiting of different signals obtained during micro-milling process in establishing the tool-workpiece contact moment is an interesting and efficient way of improving accuracy of this activity. Data from sensors contain material that could be an large source of diagnostic information, which might be helpful from different points of view. This paper presents a method for detecting a contact between a tool and a workpiece based on a fusion of the data representing the cutting forces and the accelerations. A digital signal processing algorithm introduced in this research, basing on the Fast Fourier Transform (FFT) and the Root Mean Square (RMS) calculations give positive results in field of the tool-workpiece contact detection and stands an alternative for commonly used techniques exploiting microscopes with large magnification. The method is designed to work in real-time in order to be used in practical industrial applications and satisfy demands regarding the automatic tool-workpiece contact detection.

Keywords: signal processing, micro-milling, tool-workpiece contact detection, cutting forces, accelerations.

1 Introduction

Obtaining information about the tool location with regard to the workpiece is crucial for correct micro-machining. The dimensions of the processed workpiece might differ prior to micro-milling due to the precision with which the previous machining operations have been carried. There is a need of finding the so called “zero point“ of the workpiece's surface along the Z-axis of the tool. Zero point is usually specified as the point at which the tool makes contact with the workpiece.

There are different methods for on-line detection of the tool-workpiece contact in micro-milling. The easiest one, but also the most time consuming as well as the most demanding for the machine operator, is finding the contact by observation of the rotating tool which is slowly moved towards the workpiece. Due to the very small tool dimensions (Fig. 1) this method requires usage of microscope for tool observation as well as dexterity of the human operator.

J. Awrejcewicz et al. (eds.), *Mechatronics: Ideas for Industrial Applications*,
Advances in Intelligent Systems and Computing 317, DOI: 10.1007/978-3-319-10990-9_29

Fig. 1. Tool size compared with the size of coin

There are some known methods for automatic detection of tool-workpiece contact as well. In [1] there is a proposition of a technique based on on-line tool-drive voltage monitoring. The main disadvantage of this method is the need for burr removal from the tool prior applying it. Burrs attached to the milling tool can cause current flow before real tool-workpiece contact to occur.

Another method is based on an information about the vibration [2]. It could be measured by accelerometers attached to the machine spindle or the workpiece. Monitoring of the changes in the power spectral characteristics of the vibration signal allows to detect tool-workpiece contact. This method is sensitive on the condition of the tool. Better results might be achieved with worn than with new tool.

Acoustic emission (AE) signals usage for tool-workpiece contact detection is presented in [3, 4]. AE gives the best and the most repetitive results. Main disadvantage of this method is the cost of the acoustic emission sensor as well as the need of attaching a sensor to the workpiece.

In [5] the authors already proposed an original method for off-line tool-workpiece contact detection based on measuring the cutting forces and consequent processing of the acquired signal. However, to suit the needs of the practical industrial applications the previously proposed method needs to be modified to allow a real-time implementation, i.e. to be of an on-line type. Further research on that subject also shown that expanding the mentioned method by fusion of other signals could yield even better results. This paper presents a method based on monitoring of many factors such as cutting forces and accelerations. It could also be extended in the future to take into account the acoustic pressure or the acoustic emission.

2 Machine and Equipment

Research work was performed on a prototype of a three-axial micro-milling machine SNTM-CM-ZUT-1 (Fig. 2a) which was build in the Centre of Mechatronics of West Pomeranian University of Technology, Szczecin.

Schematic view of the above mentioned prototype is shown in Fig. 2b. A dynamometer is attached vertically to the machine and a workpiece is mounted directly on it. Three accelerometers (1–3) are placed on the workpiece, each directed along different axis. In order to reduce the volume of the processed data and thus to ensure that the necessary

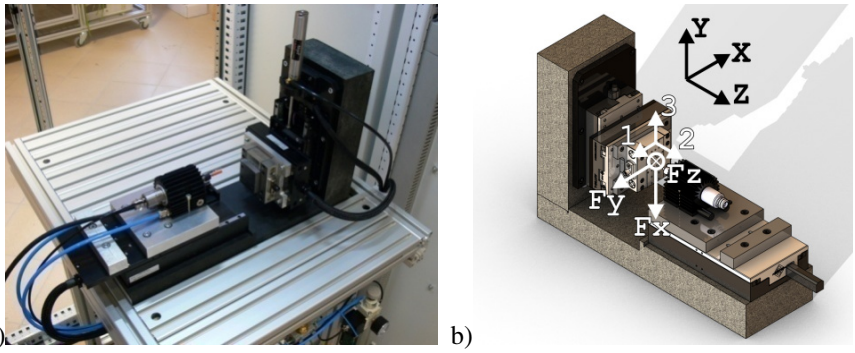

Fig. 2. a) View of the micro-milling machine, b) Dynamometer and accelerometers direction

processing will occur within certain time limits, as required by the real time applications, only the signals obtained from the dynamometer Z-axis as well as the accelerometer no 2 are taken in account.

A block diagram of the tool-workpiece contact detection system is shown in Fig. 3. Data processing is made with National Instruments PXI and LabVIEW software which ensures a possibility for real-time signal processing. PXI system also allows the use of a third party software for machine control.

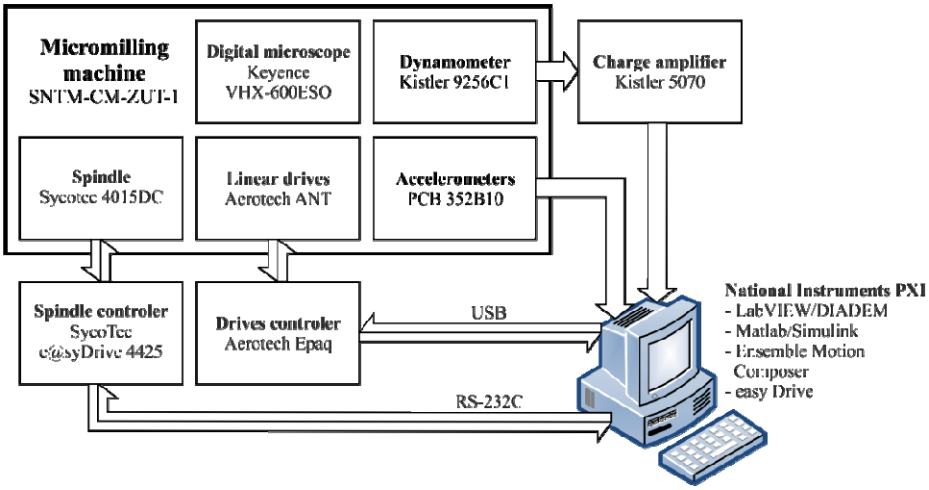

Fig. 3. Block diagram of on-line tool-workpiece contact detection system

3 Method and Data Processing

The most adequate data for achieving the desired goal is obtained from the sensors placed on the Z-axis, the one along which the tool moves. Due to the presence of a high amplitude noises in the cutting force and acceleration signals, initial filtering is required.

A block diagram of the algorithm is shown in Fig. 4. Initially, with the tool away from the workpiece, the desired process parameters are measured and based on their

maximum values the noise threshold is set. Next, the tool starts to move towards the workpiece with step size Δz at linear speed v. During the tool movement, the cutting forces and the accelerations are recorded and then a consequent processing of the obtained data is performed. Fast Fourier transformation (FFT) and root mean square (RMS) values of signals are used. Based on the results of that processing the control algorithm estimates the moment at which the tool touches the surface of the workpiece. When this event occurs the process is stopped and "zero" point is set.

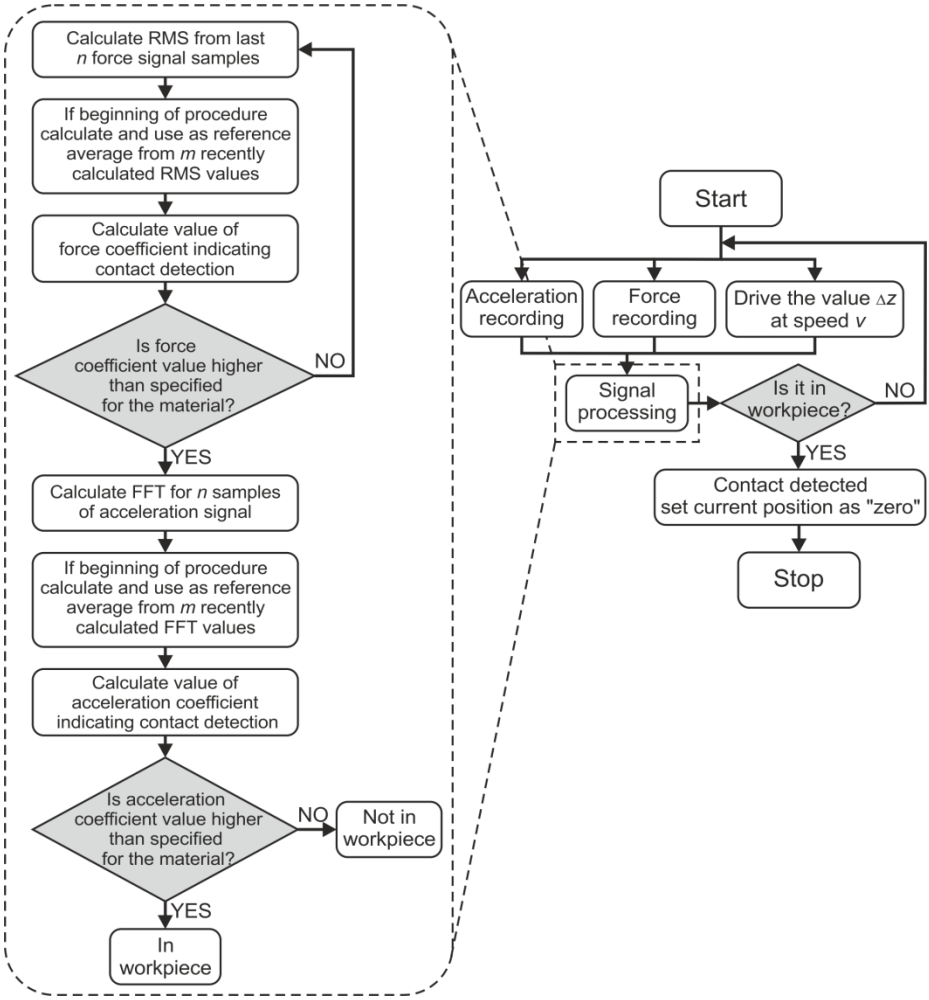

Fig. 4. Algorithm of on-line tool-workpiece contact detection

3.1 Cutting Forces Signal Processing

Cutting forces data processing is based on the root mean square (RMS) value that is calculated for n signal samples (1).

$$RMS = \sqrt{\frac{S_{i,1}^2 + S_{i,2}^2 + \ldots + S_{i,n}^2}{n}}, \tag{1}$$

where:

S_i – i-th signal sample,
n – number of samples.

There is a need of finding reference RMS value when tool is away from the workpiece. Later this value is compared with the current RMS_a value in order to detect the moment the contact occurs. Reference RMS value is calculated as given by equation (2).

$$RMS_{ref} = \sum_{i=1}^{m} \frac{RMS_i}{m}, \tag{2}$$

where:

m – number of averaged RMS values,
RMS_i – i-th RMS value.

To determine the moment of the contact an indicator coefficient might be used defined as a ratio between the current and the reference values – RMS_a and RMS_{ref} (3).

$$C_{Fi} = \frac{RMS_a}{RMS_{ref}} \tag{3}$$

3.2 Acceleration Signal Processing

The acceleration signal, due to a very high noise, must be processed with more complex method than the one, used for filtering the cutting forces signal. It involves the switching to the frequency domain. The frequencies corresponding to the tool rotational speed are used for the proposed analysis. Excitation frequency corresponds to the number of cutting blades and tool rotational speed and can be calculated from following formula (4):

$$f_{ex} = \frac{n}{60} z \tag{4}$$

where:

n – rotational speed [RPM],
z – number of cutting blades.

For every subsequent N acceleration signal samples Fast Fourier Transform is calculated:

$$X(\omega_k) = \sum_{n=0}^{N-1} x(t_n) e^{-j\omega_k t_n}, \qquad k = 0, 1, 2, \ldots, N-1 \tag{5}$$

where:

$x(t_n)$ – input signal amplitude at time t_n,
$X(\omega_k)$ – spectrum of x, at frequency ω_k,
ω_k – k-th frequency sample,
N – number of time samples (number of frequency samples).

In order to avoid spectral leakage, averaging of two frequencies closest to the excitation frequency is used. Similarly to RMS cutting force signal, currently obtained amplitude of excitation frequency is compared with reference amplitude registered at the beginning of the procedure of tool-workpiece contact detection. Acceleration contact indicator value is calculated from formula:

$$C_{ai} = \frac{Freq_a}{Freq_{ref}} \tag{6}$$

where:

$Freq_a$ – current averaged amplitude of two frequencies closest to excitation frequency,

$Freq_{ref}$ – reference amplitude.

3.3 Signal Fusion

In order to use two diagnostic signals related with the contact detection, signal fusion must be performed. The principle of presented here method is to exploit the forces contact indicator (C_{Fi}) to locate approximated section of a contact as well as acceleration contact indicator (C_{ai}) to define the exact moment of it. Best results were obtained after several experiments which allowed to introduce specific values of parameters dependent from material hardness.

4 Experiment Results

18G2 carbon steel was used as a workpiece. In previous operation the workpiece was grinded to obtain low surface roughness. Tool used for experiment was the Microcut 82005 (0.127 mm diameter). Threshold value of contact indicator for the workpiece material was evaluated in several experiments. Then proposed method was tested in tool workpiece contact detection. Afterwards surface topography was measured in order to measure method error.

Cutting forces signal in the time domain is shown in Fig. 5. There can be seen a lot of noise in the signal.

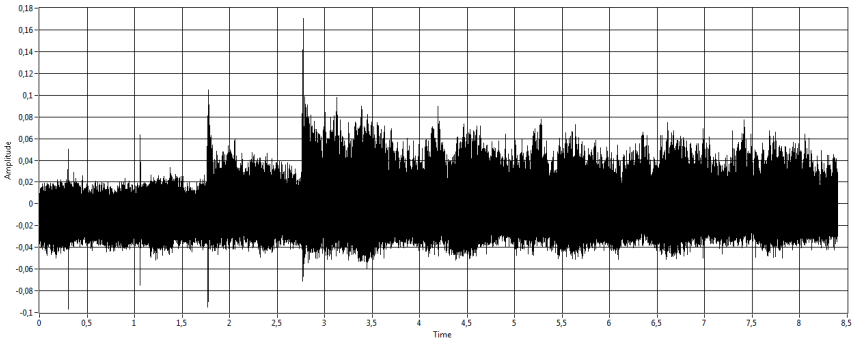

Fig. 5. Cutting forces signal in the time domain

Cutting forces indicator signal in the time domain is shown in Fig. 6. After decrease of indicator's value, when tool contact starts, indicator value rapidly increases.

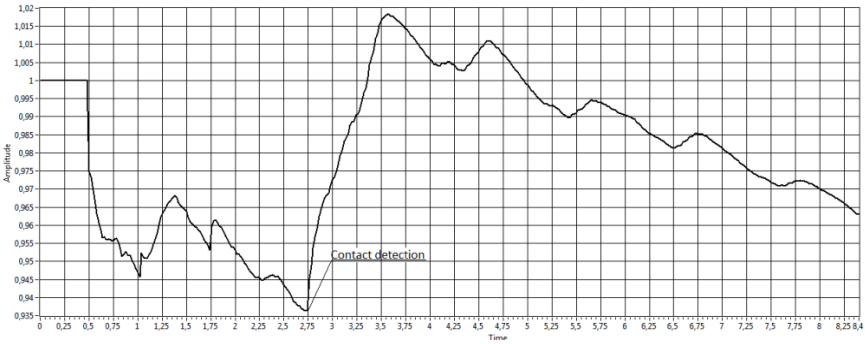

Fig. 6. Forces contact indicator (C_{Fi}) value in the time domain

Acceleration signal in time domain is shown in Fig. 7. There can also be seen high noise in the signal.

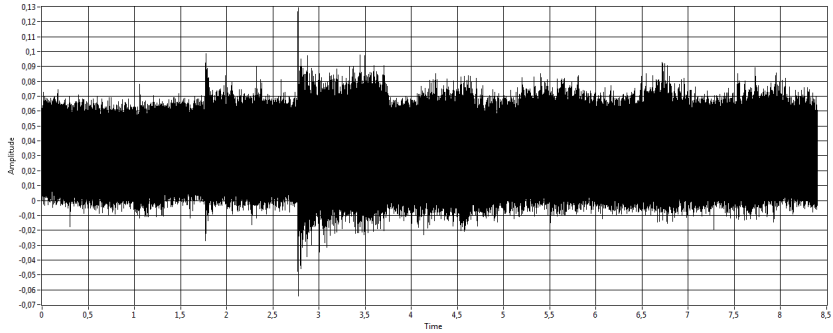

Fig. 7. Acceleration signal in the time domain

Acceleration indicator signal in the time domain is shown in Fig. 8. In like manner to cutting forces indicator after high increase of indicator value, when tool contact starts, indicator value rapidly decreases.

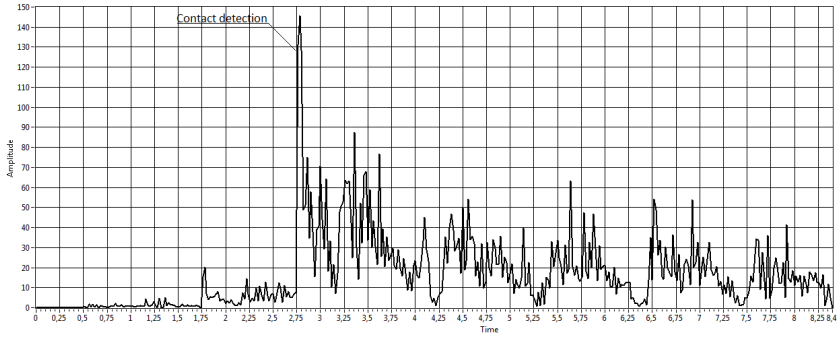

Fig. 8. Acceleration contact indicator (C_{ai}) value in the time domain

The result of fusion of C_{Fi} and C_{ai} is presented in Fig. 9. Processing system use only to calculations those C_{Fi} samples which differ from reference indicator's value by experimentally selected value (dependent from exoloited material; in this case it was –3 %.) to define possible area of the contact. C_{ai} indicator helps to define the exact moment of tool – workpiece contact and is only taken into consideration within forces contact indicator sections. Presented method were tested for several cases and gave satisfactory results.

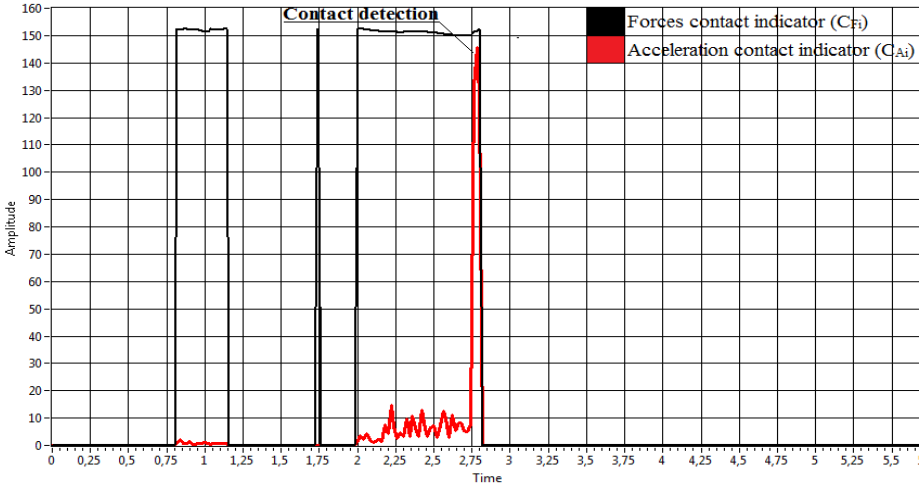

Fig. 9. Fused contact indicator (C_i) value in the time domain

Example of surface topography after tool-workpiece contact detection is shown in Fig. 10. Fig. 10a presents surface after classical tool observation with the microscope, overshot of this method is about 2 µm. Surface topography left by tool-workpiece contact method proposed in the paper is shown in Fig. 10b. Overshot of the method is comparable to the surface roughness. Twelve experiments were conducted in order to confirm method repeatability and results were similar to shown in Fig. 10.

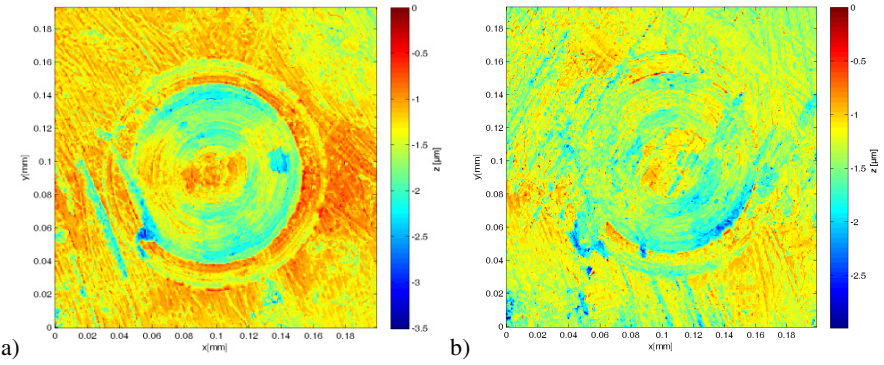

Fig. 10. Surface topography after tool-workpiece contact detection: a) optical observation of tool, b) usage of proposed tool-workpiece contact detection method

5 Summary

Surface topography measured after tool-workpiece contact detection shows that surface roughness is comparable to the tool-workpiece contact overshot. Accuracy of the method is better than 0.5 μm, which is very hard to achieve by classical tool observation by machine operator. Crucial for the proper operation of the presented tool-workpiece contact detection method is the proper manual selection of the threshold value of the contact detection indicator for current material. This can be performed by tool observation and by contact indicator values observation [5].

The proposed solution of an on-line tool-workpiece contact detection task significantly facilitates the work of the machine operator and eliminates the possible human errors. Due to a high applicability of the described method and its varieties, three patent applications have been submitted to the Polish Patent Office. The presented solution is especially designed for micro-milling applications but could also be implemented in any CNC machine system.

References

1. Popov, K., Dimov, S., Ivanov, A., Pham, D.T., Gandarias, E.: New tool-workpiece setting up technology for micro-milling. The International Journal of Advanced Manufacturing Technology 47(1-4), 21–27 (2010), doi:10.1007/s00170-009-2055-2
2. Kumar, M., Dotson, K., Melkote, S.N.: An experimental technique to detect tool–workpiece contact in micromilling. Journal of Manufacturing Processes 12(2), 99–105 (2010), doi:10.1016/j.jmapro.2010.08.001
3. Min, S., Lidde, J., Raue, N., Dornfel, D.: Acoustic emission based tool contact detection for ultra-precision machining. CIRP Annals – Manufacturing Technology 60(1), 141–144 (2011), doi:10.1016/j.cirp.2011.03.079
4. Min, S., Sangermann, H., Mertens, C., Dornfeld, D.: A study on initial contact detection for precision micro-mold and surface generation of vertical side walls in micromachining. CIRP Annals – Manufacturing Technology 57(1), 109–112 (2008), doi:10.1016/j.bbr.2011.03.031
5. Broel-Plater, B., Matuszak, M., Waszczuk, P.: Force-measurement based too-workpiece contact detection in micromilling. Pomiary Automatyka Robotyka 17(1), 52–59 (2013)

Kinematic Analysis of the Finger Exoskeleton Movement in Distal and Proximal Interphalangeal Joints

Krzysztof Nasiłowski, Jan Awrejcewicz, and Donat Lewandowski

Lodz University of Technology, Faculty of Mechanical Engineering,
Department of Automation, Biomechanics and Mechatronics, Poland
k-nasilowski@o2.pl

Abstract. Hand fingers have a high chance for injury during everyday life. Recovery of injured fingers is realized by physiotherapists, which manually conduct exercises. To help in therapy researchers are constantly inventing new methods of applying mechanical devices in the rehabilitation process. Actually there are conducted many studies of passive and active exoskeletons. Properly designed exoskeleton can help in movement and rehabilitation of paralyzed or not fully functional part of human body. It can be used also to increase human movement capabilities. This paper is a continuation of previously presented kinematic analysis of finger exoskeleton design which is based on three-link subsystem and one finger-leading link. In actual system the finger leading link is replaced by an exoskeleton that allows movement in distal and proximal interphalangeal finger joints. The main advantage of proposed design is that during operation finger is fully supported by the exoskeleton and there are no additional loads applied on its joints. The actually presented part of the full finger exoskeleton can be analyzed as an individual mechanism because in natural system the finger movement in metacarpophalangeal joint is realized separately in comparison to the movement in distal and proximal interphalangeal joints. The kinematic data are needed for the next step of design process, which define the dynamic forces acting in the system. This will allow the selection of actuators and proper design of all exoskeleton mechanical parts that will be used in a real life model.

Keywords: finger, exoskeleton, kinematic.

1 Introduction

An exoskeleton exists in nature as a part of animal body responsible for its support and protection. Living organisms can be equipped in exoskeletons, or internal skeletons. There are however animals having both types of skeletons. For example a turtle has got an internal skeleton supporting its body and an exoskeleton (shell) which main function is protection of animal internal organs from predator attacks.

Another type of exoskeleton is an artificial exoskeleton. We can divide this kind of exoskeleton designs for passive and active ones. The passive exoskeletons are used for ages and are called armors. They are used for protection against injuries that might

J. Awrejcewicz et al. (eds.), *Mechatronics: Ideas for Industrial Applications*,
Advances in Intelligent Systems and Computing 317, DOI: 10.1007/978-3-319-10990-9_30

appear during the battle. Unfortunately the passive designs are decreasing human movement abilities due to the fact that exoskeleton weight has to be supported by human musculoskeletal system.

An active exoskeleton is a device that can support human body and increase its movement abilities. Active exoskeleton needs power source which provides energy to actuators helping in movement of supported body parts.

In literature we can find many active exoskeleton designs. Hybrid Assistive Limb [1] design supports lower and upper part of human body. It can be used in daily activities and its main purpose increase of human movement capabilities. For example the person using this particular exoskeleton is able to lift heavy loads up to 40 kg without muscle fatigue.

Active exoskeletons purpose can be various. It can be used in daily activities but can also be aimed for military or industry. The possibilities of active exoskeleton applications can be also medical, by which we understand help in movement of paralyzed/disabled limbs or their rehabilitation.

Examples of devices used for rehabilitation of parts of human body are presented in references [2–4]. In paper [5] an active exoskeleton design aimed for movement support of disabled/paralyzed part of the human finger is illustrated and discussed.

In some cases an active exoskeleton can help during professional activities by limiting fatigue of supported part of the body [6].

Active exoskeletons may help in movement of full human body or only the selected part. In this paper an approach to finger exoskeleton design, especially finger exoskeleton movement in distal and proximal interphalangeal joints kinematic analysis is shown.

This paper is a continuation of previously conducted kinematic analysis of finger exoskeleton design based on three-link subsystem and one finger leading link [7].

2 Kinematics of the Movement Mechanism

The physical and geometrical model used for further analysis serves as the base of the finger exoskeleton design. This paper is a continuation of previously published kinematic analysis of finger exoskeleton supporting finger movement in metacarpophalangeal joint, and the previously obtained results are extended to apply and study the finger distal and proximal interphalangeal joints. The design is based on biomechanical information regarding human finger exoskeleton [8].

There are two main design assumptions. First of them is to provide finger movement abilities possibly closest to its natural behavior. The second is to separate finger joints from forces generated by exoskeleton, and support their movement. This approach allows not only supporting of disabled/paralyzed fingers, but also increasing forces produced by the finger to the level higher then, the natural model may offer. It should be emphasized that all internal joint forces are transmitted by the exoskeleton.

The main scheme on which the finger exoskeleton design is based, consists of the three-link subsystem and the six-link finger leading subsystem. The six-link finger leading subsystem kinematics is a topic of this paper.

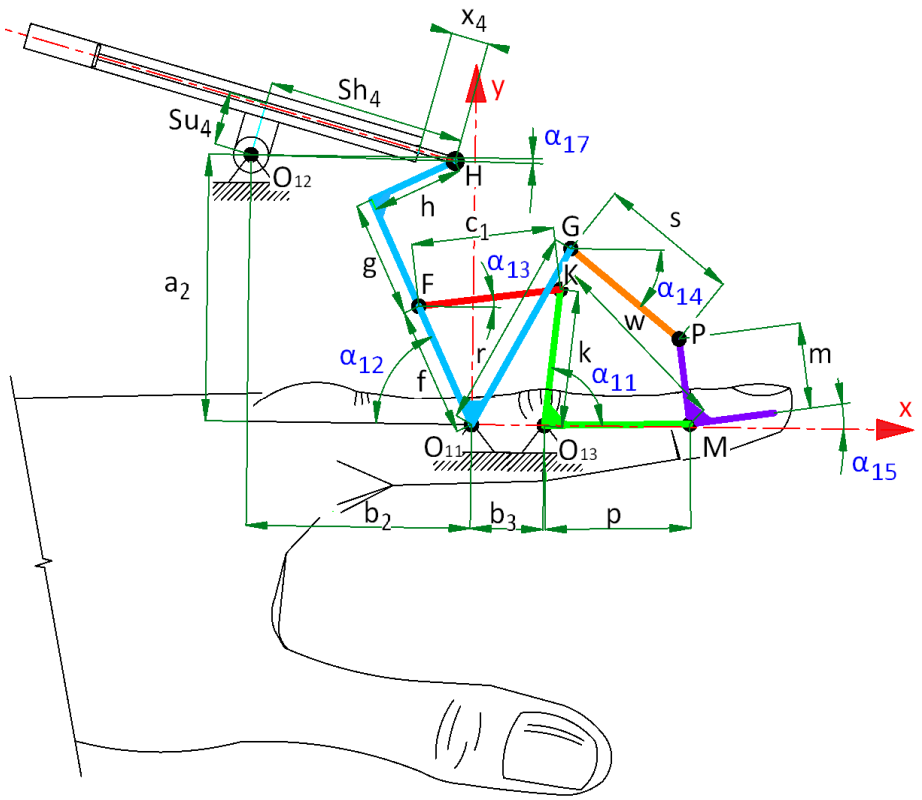

Fig. 1. Geometrical model

The composition of the design is shown in Fig. 1. The basic system is an assembly of six-links. First link is defined by points H, F, O_{11}, G, second one by F, K, third by K, O_{13}, M, fourth by P, M, fifth by G, P, and sixth by O_{11}, O_{13}. The mechanism is driven by one actuator mounted between points O_{12} and H.

Length of the system links are as follows: H, F, O_{11}, G link – h, g, f, r; F, K link – c_1; K, O_{13}, M – k, p; P, M link – m; G, P link – s; O_{11}, O_{13} link – b_3.

Sh_4 and Su_4 are the actuator mounting dimensions in respect to O_{12} rotation point, whereas x_4 is the actuator outreach. System angles presented in Fig. 1 are selected in following order: α_{11} is the angle between O_{13}, K segment and x axis; α_{12} is the angle between O_{11}, F segment and x axis; α_{14} is the angle between G, P segment and x axis; α_{15} is the angle between segment perpendicular to P, M and x axis; α_{17} is the angle between O_{12}, H segment and x axis.

The co-ordinates of points $H(x_H;y_H)$, $F(x_F;y_F)$, $G(x_G;y_G)$, $K(x_K;y_K)$, $M(x_M;y_M)$; $P(x_P;y_P)$ can be calculated in the following order [9]:

(i) Point $H(x_H;y_H)$:

$$x_H = \sqrt{f_1^{\,2} - y_H^{\,2}}$$
$$y_H = \frac{-\left(-2\dfrac{x_{O12}^{\,2} + y_{O12}^{\,2} - x_{4H}^{\,2} + f_1^{\,2}}{2x_{O12}}\dfrac{y_{O12}}{x_{O12}}\right) + \sqrt{c_H}}{2\left[\left(\dfrac{y_{O12}}{x_{O12}}\right)^2 + 1\right]} \tag{1}$$

where

$$c_H = \left(-2\frac{x_{O12}^{\,2} + y_{O12}^{\,2} - x_{4H}^{\,2} + f_1^{\,2}}{2x_{O12}}\frac{y_{O12}}{x_{O12}}\right)^2 - 4\left[\left(\frac{y_{O12}}{x_{O12}}\right)^2 + 1\right]\left[\left(\frac{x_{O12}^{\,2} + y_{O12}^{\,2} - x_{4H}^{\,2} + f_1^{\,2}}{2x_{O12}}\right)^2 - f_1^{\,2}\right].$$

(ii) Point $F(x_F;y_F)$:

$$x_F = -f\cos\left(arctg\left(\frac{y_H}{x_H}\right) - arctg\left(\frac{h}{g+f}\right)\right),$$
$$y_F = f\sin\left(arctg\left(\frac{y_H}{x_H}\right) - arctg\left(\frac{h}{g+f}\right)\right). \tag{2}$$

(iii) Point $G(x_G;y_G)$:

$$x_G = \sqrt{r^2 - y_G^{\,2}}$$
$$y_G = \frac{-\left(-2\dfrac{r^2 - x_F^{\,2} - y_F^{\,2} - l^2}{2x_F}\dfrac{y_F}{x_F}\right) + \sqrt{c_G}}{2\left[\left(\dfrac{y_F}{x_F}\right)^2 + 1\right]} \tag{3}$$

where

$$c_G = \left(-2\frac{r^2 - x_F^{\,2} - y_F^{\,2} - l^2}{2x_F}\frac{y_F}{x_F}\right)^2 - 4\left[\left(\frac{y_F}{x_F}\right)^2 + 1\right]\left[\left(\frac{r^2 - x_F^{\,2} - y_F^{\,2} - l^2}{2x_F}\right)^2 - r^2\right].$$

(iv) Point $K(x_K;y_K)$:

$$x_K = \frac{2x_{O13} - \sqrt{(-2x_{O13})^2 - 4\left[{x_{O13}}^2 + (y_K - y_{O13})^2 - k^2\right]}}{2}$$

$$y_K = \frac{-\left[2\left(x_F \frac{y_F - y_{O13}}{x_F - x_{O13}} - \frac{k^2 - {c_1}^2 + {x_F}^2 - {x_{O13}}^2 - {y_F}^2 - {y_{O13}}^2}{2(x_F - x_{O13})} \frac{y_F - y_{O13}}{x_F - x_{O13}} - y_F\right)\right] + \sqrt{c_K}}{2\left[\left(\frac{y_F - y_{O13}}{x_F - x_{O13}}\right)^2 + 1\right]} \tag{4}$$

where

$$c_K = \left[2\left(x_F \frac{y_F - y_{O13}}{x_F - x_{O13}} - \frac{k^2 - {c_1}^2 + {x_F}^2 - {x_{O13}}^2 - {y_F}^2 - {y_{O13}}^2}{2(x_F - x_{O13})} \frac{y_F - y_{O13}}{x_F - x_{O13}} - y_F\right)\right] -$$
$$- 4\left[\left(\frac{y_F - y_{O13}}{x_F - x_{O13}}\right)^2 + 1\right]\left[\left(\frac{k^2 - {c_1}^2 + {x_F}^2 - {x_{O13}}^2 - {y_F}^2 - {y_{O13}}^2}{2(x_F - x_{O13})}\right)^2 + \right.$$
$$\left. - 2x_F \frac{k^2 - {c_1}^2 + {x_F}^2 - {x_{O13}}^2 - {y_F}^2 - {y_{O13}}^2}{2(x_F - x_{O13})} + {x_F}^2 + {y_F}^2 - {c_1}^2\right].$$

(v) Point $M(x_M;y_M)$:

$$x_M = \frac{2x_{O13} - \sqrt{(-2x_{O13})^2 - 4\left[{x_{O13}}^2 + (y_M - y_{O13})^2 - p^2\right]}}{2}$$

$$y_M = \frac{-\left[2\left(x_K \frac{y_K - y_{O13}}{x_K - x_{O13}} - \frac{p^2 - w^2 + {x_K}^2 - {x_{O13}}^2 - {y_K}^2 - {y_{O13}}^2}{2(x_F - x_{O13})} \frac{y_K - y_{O13}}{x_K - x_{O13}} - y_K\right)\right] + \sqrt{c_M}}{2\left[\left(\frac{y_K - y_{O13}}{x_K - x_{O13}}\right)^2 + 1\right]} \tag{5}$$

where

$$c_M = \left[2\left(x_K \frac{y_K - y_{O13}}{x_K - x_{O13}} - \frac{p^2 - w^2 + {x_K}^2 - {x_{O13}}^2 + {y_K}^2 - {y_{O13}}^2}{2(x_K - x_{O13})} \frac{y_K - y_{O13}}{x_K - x_{O13}} - y_K\right)\right]^2 -$$
$$- 4\left[\left(\frac{y_K - y_{O13}}{x_K - x_{O13}}\right)^2 + 1\right]\left[\left(\frac{p^2 - w^2 + {x_K}^2 - {x_{O13}}^2 + {y_K}^2 - {y_{O13}}^2}{2(x_K - x_{O13})}\right)^2 + \right.$$
$$\left. - 2x_K \frac{p^2 - w^2 + {x_K}^2 - {x_{O13}}^2 + {y_K}^2 - {y_{O13}}^2}{2(x_K - x_{O13})} + {x_K}^2 + {y_K}^2 - w^2\right].$$

(vi) Point $P(x_P;y_P)$:

$$x_P = \frac{2x_G - \sqrt{(-2x_G)^2 - 4\left[{x_G}^2 + (y_P - y_G)^2 - s^2\right]}}{2}$$
$$y_P = \frac{-\left[2\left(x_G \frac{y_M - y_G}{x_M - x_G} - \frac{s^2 - m^2 + {x_M}^2 - {x_G}^2 + {y_M}^2 - {y_G}^2}{2(x_M - x_G)} \frac{y_M - y_G}{x_M - x_G} - y_G\right)\right] - \sqrt{c_P}}{2\left[\left(\frac{y_M - y_G}{x_M - x_G}\right)^2 + 1\right]} \tag{6}$$

where

$$c_P = \left[2\left(x_G \frac{y_M - y_G}{x_M - x_G} - \frac{s^2 - m^2 + {x_M}^2 - {x_G}^2 + {y_M}^2 - {y_G}^2}{2(x_M - x_G)} \frac{y_M - y_G}{x_M - x_G} - y_G\right)\right]^2 -$$
$$- 4\left[\left(\frac{y_M - y_G}{x_M - x_G}\right)^2 + 1\right]\left[\left(\frac{s^2 - m^2 + {x_M}^2 - {x_G}^2 + {y_M}^2 - {y_G}^2}{2(x_M - x_G)}\right)^2 - \right.$$
$$\left. - 2x_G \frac{s^2 - m^2 + {x_M}^2 - {x_G}^2 + {y_M}^2 - {y_G}^2}{2(x_M - x_G)} + {x_G}^2 + {y_G}^2 - s^2\right].$$

The associated angles can be calculated from the following equations:

$$\alpha_{17} = arctg \frac{y_{O12} - y_H}{x_{O12} - x_H}, \quad \alpha_{12} = arctg \frac{y_H}{x_H} - arctg \frac{h}{g + f}, \quad \alpha_{14} = arctg \frac{y_G - y_P}{x_G - x_P},$$
$$\alpha_{13} = arctg \frac{y_K - y_F}{x_K - x_F}, \quad \alpha_{11} = arctg \frac{y_{O13} - y_K}{x_{O13} - x_K}, \quad \alpha_{15} = arctg \frac{y_M - y_P}{x_M - x_P}. \tag{7}$$

When we consider actuator movement in specified velocity V_4 we can calculate angular velocities of system links. The actuator outreach x_4 can be derived from the following formula: $x_4 = V_4 t$.

System angular velocities are defined via the following formulas:

$$\omega_{17} = \frac{\alpha_{17(n+1)} - \alpha_{17(n)}}{t_{(n+1)} - t_n}, \quad \omega_{12} = \frac{\alpha_{12(n+1)} - \alpha_{12(n)}}{t_{(n+1)} - t_n}, \quad \omega_{14} = \frac{\alpha_{14(n+1)} - \alpha_{14(n)}}{t_{(n+1)} - t_n},$$
$$\omega_{13} = \frac{\alpha_{13(n+1)} - \alpha_{13(n)}}{t_{(n+1)} - t_n}, \quad \omega_{11} = \frac{\alpha_{11(n+1)} - \alpha_{11(n)}}{t_{(n+1)} - t_n}, \quad \omega_{15} = \frac{\alpha_{15(n+1)} - \alpha_{15(n)}}{t_{(n+1)} - t_n}. \tag{8}$$

3 Results

Solutions of the governing equations are found for actuator constant speed $v_4 = 0.1$ m/s, total simulation time 0.5 s and system dimensions used in model adapted for left palm of 33-year-old man 1.8 m tall.

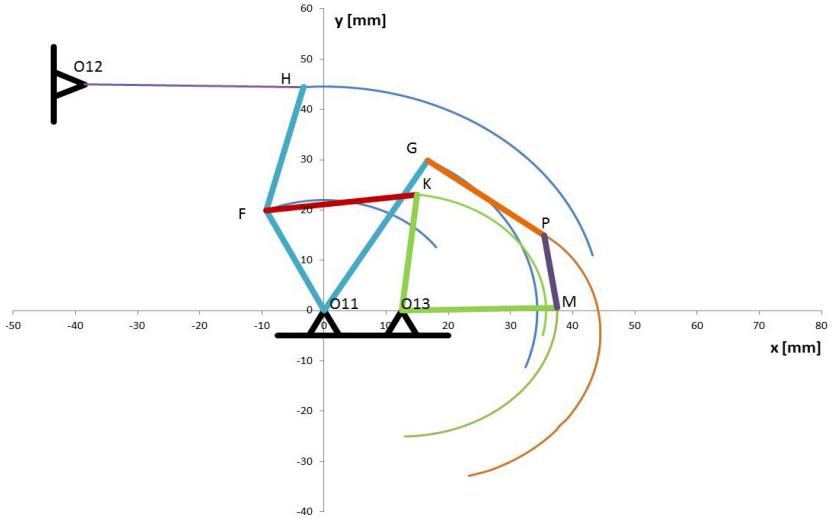

Fig. 2. System points trajectories on *XY* plane

Fig. 2 shows trajectory of specified points during full movement phase in *XY* coordinate system. We can observe circular trajectories of points $H(x_H;y_H)$, $F(x_F;y_F)$, $G(x_G;y_G)$, $K(x_K;y_K)$, and $M(x_M;y_M)$ as well as the trajectory of point $P(x_P;y_P)$, which position is determined by *G*, *P* and *P*, *M* links.

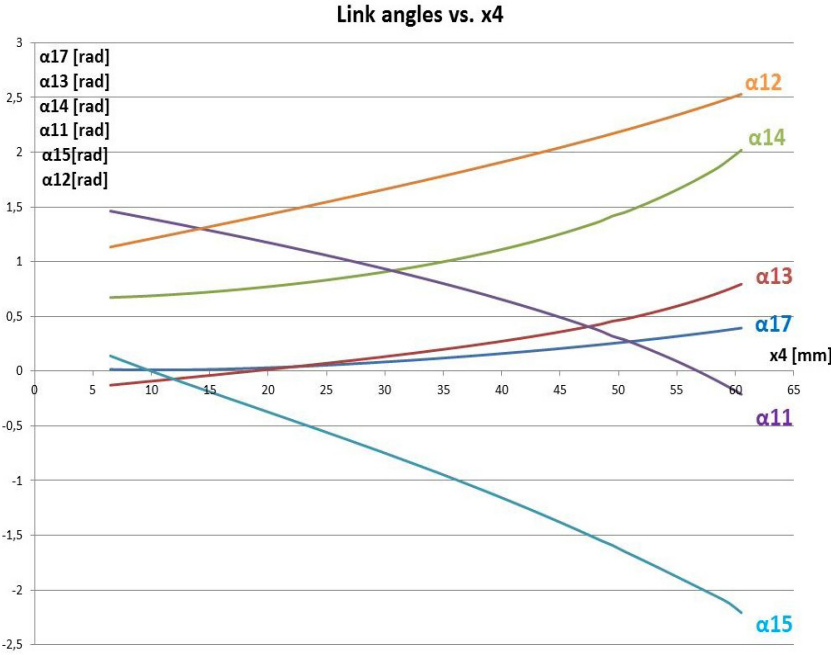

Fig. 3. Link angles α_{11}, α_{12}, α_{13}, α_{14}, α_{15}, α_{17} vs. x_4 displacement

Fig. 3 shows system angle with respect to actuator displacement x_4. This information is needed for basic actuator selection. As we can observe minimum required actuator outreach for the system is 0.054 m. In calculations was considered initial actuator outreach of 0.0065 m.

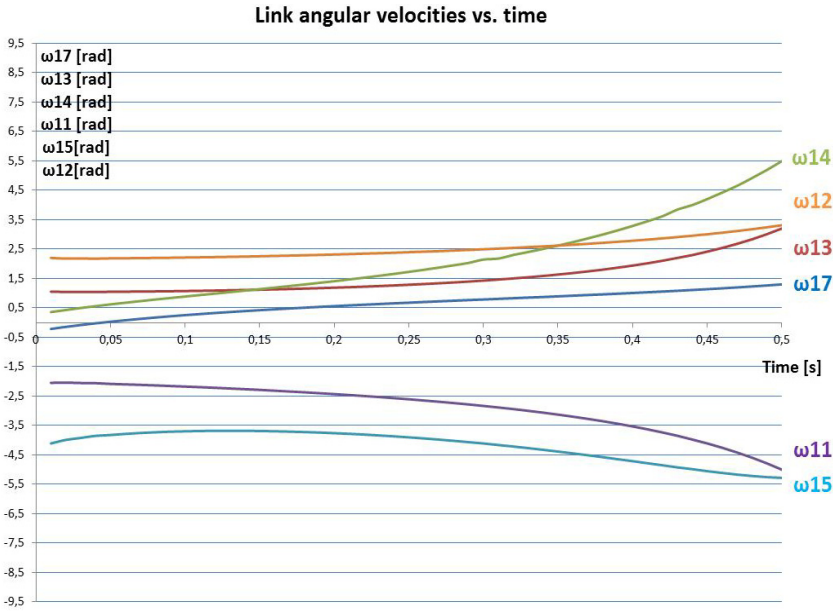

Fig. 4. The angular velocities ω_{11}, ω_{12}, ω_{13}, ω_{14}, ω_{15}, ω_{17} vs. time

Fig. 4 shows system links angular velocities with respect to time for initial actuator constant speed $v_4 = 0.1$ m/s and total simulation time 0.5 s.

4 Discussion

The proposed physical and mathematical models allow the control of a human finger movement. The method of calculation gives us an opportunity to collect data regarding movement of specified base points of finger exoskeleton in distal and proximal interphalangeal joints which is needed in next steps of design process.

The calculations yield information regarding movement of finger exoskeleton links supporting finger in distal and proximal interphalangeal joints. The first step of calculation is determining the x, y co-ordinates of exoskeleton base points $H(x_H;y_H)$, $F(x_F;y_F)$, $G(x_G;y_G)$, $K(x_K;y_K)$, $M(x_M;y_M)$, $P(x_P;y_P)$ in full movement range. On Fig. 2 we can observe trajectories of mentioned points. The next step is determination of system link angles α_{11}, α_{12}, α_{13}, α_{14}, α_{15} and α_{17}. On Fig. 4 is shown relation between actuator displacement x_4 and α_{11}, α_{12}, α_{13}, α_{14}, α_{15}, α_{17} angles. The next step is calculation of link angular velocities for specified actuator velocity V_4. Fig. 4 shows time based diagrams of angular velocities ω_{11}, ω_{12}, ω_{13}, ω_{14}, ω_{15} and ω_{17}.

Presented exoskeleton model is a part of full finger exoskeleton design. The calculations will be used as a base for system dynamics determination. Information regarding position of points and system angles connected with specified movement pattern of actuator gives an opportunity to calculate points linear accelerations and links angular accelerations. These information complemented with link mass and moment of inertia data will make possible definition of forces and moments acting in system during its operation, which is needed for further finger exoskeleton design phase.

References

1. Sankai, Y.: Leading Edge of Cybernics: Robot Suit HAL. In: SICE-ICASE International Joint Conference 2006, Bexco, Busan, Korea, October 18-21 (2006)
2. Cavallaro, E.E., Rosen, J., Perry, J.C., Burns, S.: Real-Time Myoprocessors for a Neural Controlled Powered Exoskeleton Arm. IEEE Transactions on Biomedical Engineering 53(11), 2387–2396 (2006)
3. Jones, C.L., Wang, F., Osswald, C., Kang, X., Sarkar, N., Kamper, D.G.: Control and Kinematic Performance Analysis of an Actuated Finger Exoskeleton for Hand Rehabilitation following Stroke. In: International Conference on Biomedical Robotics and Biomechatronics, Tokyo, Japan, September 26-29 (2010)
4. Ozkul, F., Barkana, D.E.: Design and Control of an Upper Limb Exoskeleton Robot RehabRoby. In: Groß, R., Alboul, L., Melhuish, C., Witkowski, M., Prescott, T.J., Penders, J. (eds.) TAROS 2011. LNCS (LNAI), vol. 6856, pp. 125–136. Springer, Heidelberg (2011)
5. Lucas, L., Dicicco, M., Matsuoka, Y.: An EMG-Controlled Hand Exoskeleton for Natural Pinching. Journal of Robotics and Mechatronics 16(5) (2004)
6. Shields, B.L., Main, J.A., Peterson, S.W., Strauss, A.M.: An Anthropomorphic Hand Exoskeleton to Prevent Astronaut Hand Fatigue During Extravehicular Activities. IEEE Transactions on Systems, Man, and Cybernetics – Part A: Systems And Humans 27(5), 668–673 (1997)
7. Nasiłowski, K., Awrejcewicz, J., Lewandowski, D.: Kinematic analysis of the finger exoskeleton using MATLAB/Simulink, Acta of Bioengineering and Biomechanics (to appear)
8. Mrozowski, J., Awrejcewicz, J.: Introduction to Biomechanics. TUL Press, Lodz (2004)
9. Awrejcewicz, J.: Technical Mechanics. WNT, Warsaw (2009)

Resistance of MAX 6325 Reference Voltage Source on Supply Voltage Variation

Paweł Nowak[1], Andrzej Juś[1], Roman Szewczyk[2], Michał Nowicki[2], and Wojciech Winiarski[1]

[1] Industrial Research Institute for Automation and Measurements, 02-486 Warsaw, Al. Jerozolimskie 202, Poland
{pnowak,ajus}@piap.pl
[2] Warsaw University of Technology, Faculty of Mechatronics, sw. A. Boboli 8, 02-525 Warsaw, Poland

Abstract. The article presents the problem of reference voltage sources based on Zener diode resistance to changes in power supply. The test stand, measurement methodology and results are presented. Reference voltage sources are crucial elements of analog-to-digital systems. They set the standard to which the measured voltage is compared to. Therefore, the stability of their work is critical for many areas of precision metrology.

Keywords: voltage references, line regulation, electrical measurements, FPGA.

1 Introduction

Precision measurements are critical in many industrial systems. High-tech production lines require a high-resolution and reliable measurements system. The highest accuracy is achieved in voltage measurements, so even the non-electric values (like temperature or weight) are measured by transforming their value to voltage and measuring it. All precision analog to digital converters operate on the principle of comparison of the measured voltage value with the standard which is reference voltage source. The stability of this standard is crucial for the stability of the measurements. The greatest impact on the standard stability have: change in operating temperature, supply voltage change (line regulation) and changing of the output current (load regulation). Change in supply voltage can occur under the influence of changes in system conditions, disorders in the preliminary voltage stabilizer, or, if there is none, by changing the voltage of the system.

2 Reference Source Utilizing Zener Diodes

Voltage references based on the Zener diode are used in for voltage stabilization. Stabilizers such as tested (i.e. up to 5 V) are based on the Zener effect, which is a rapid increase of current at a value exceeding the breakdown voltage [4]. An exemplary

J. Awrejcewicz et al. (eds.), *Mechatronics: Ideas for Industrial Applications*,
Advances in Intelligent Systems and Computing 317, DOI: 10.1007/978-3-319-10990-9_31

current-voltage characteristics of the Zener diode is shown in Fig. 1 [5]. Typical stabilizers in addition to the diode have a resistor connected in series, acting as a protection of the diode from damage due to excessive current. In addition, the resistor controls the reverse current, necessary for proper operation of the diode.

With the increase in the value of the stabilizer bias voltage, the value of current flowing through the resistor and reaching the diode increases, resulting in increase in the voltage across the diode (Fig. 1).

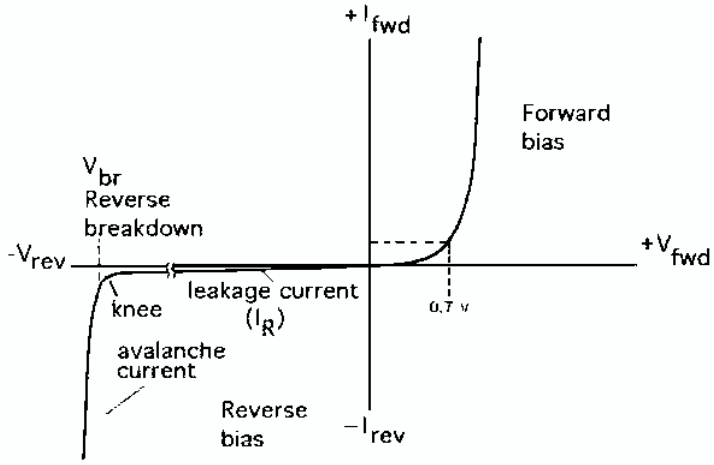

Fig. 1. Current-voltage characteristics of a typical Zener diode [5]

3 Test Stand

3.1 General Idea

Schematic block diagram of designed test stand is presented in Fig. 2.

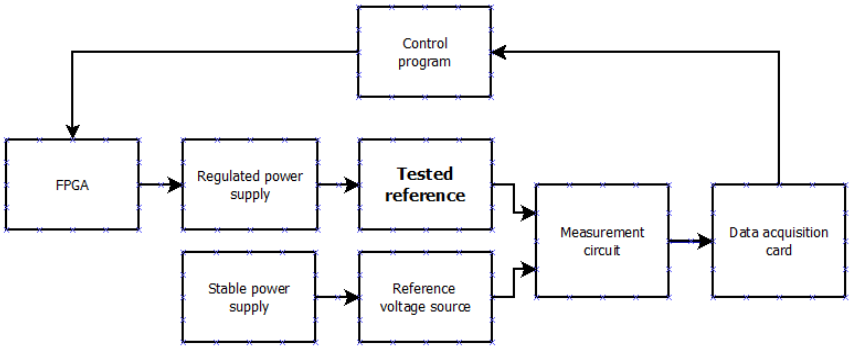

Fig. 2. Schematic block diagram of test stand

The main idea of utilized test stand is based on high accuracy differential voltage measurement. The tested source is powered by the FPGA controlled regulated power supply. The output voltage is compared with a reference voltage source, powered by a stable voltage. The difference of these voltages is amplified and then measured by a data acquisition card and stored along with the corresponding value of the tested source power supply voltage.

3.2 Variable Power Supply System

Variable voltage reference system was built on the basis of the D/A converter built into the FPGA used (National Instruments – MyRIO), and non-inverting amplifier [1] with a gain of 3. Usage of amplifier was necessary because of insufficient range of D/A converter (0–10 V). Applied voltage was amplified, thus the range of tests (8–30 V) was covered.

3.3 Voltage Measurement Circuit

To acquire highest accuracy of measurement, it was decided to design differential measurement circuit. The wiring diagram of measurement circuit is presented in Fig. 3.

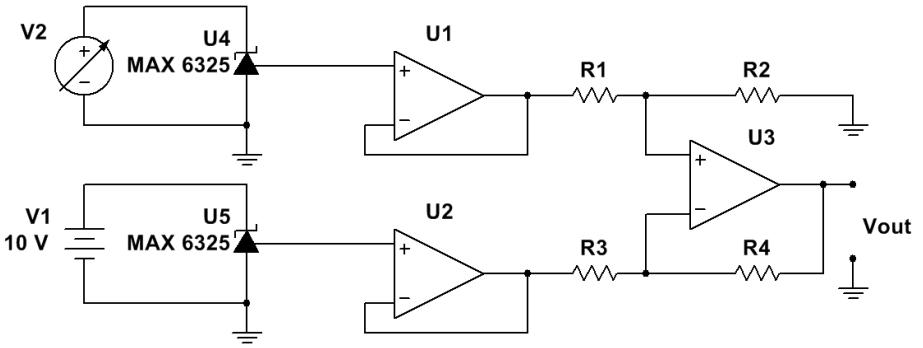

Fig. 3. Wiring diagram of measurement circuit

Tested voltage reference source is powered from the system described in Section 3.2, whereas standard reference source is powered by the constant voltage from stabilized power source. Operational amplifiers (U1 and U2) work as a voltage followers. Their main function is to provide high and constant impedance for voltage references. The next element of circuit is a differential amplifier built on U3 and R1, R2, R3, R4 highly accurate resistors. As it can be proven [1], when following requirement $R_2/R_1 = R_4/R_3 = k$ is fulfilled, voltage held on the output of U3 is given by following dependency:

$$V_{out} = (V_1 - V_2) \cdot k \tag{1}$$

where V1 and V2 are output voltages held on operational amplifiers U1 and U2. Output voltage of measurement circuit is measured by data acquisition card, and processed by software using (1) in order to give information about tested voltage reference output change.

4 Measurement Method

Tests were performed on three different sources according to the following rules.

4.1 Investigation of Single Supply Voltage Change Impact on the Tested Reference Source

The study consisted of a single change in supply voltage of investigated source. The change took place in the 8–30 V range with 0.25 V increments.

4.2 Investigation of Impact of Multiple Supply Voltage Changes on the Tested Reference Source

The study consisted of five changes in supply voltage of investigated source. The changes took place in the 8–30 V (going up) range with 0.25 V increments and in the 30–8 V (going down) range with –0.25 V increments. These studies were conducted to observe the potential hysteresis in characteristics of the tested reference voltage sources.

5 Measurement Results

On the following figures the results of the measurements conducted according to methodology described above. Additionally, on both characteristics there is black line marking the maximum allowable deviation according to [2].

The results obtained have significant repeatability. In addition, all the results are below the curve created on the basis of catalog data [2]. The measurement results obtained according to methodology from Section 4.2 presented in Fig. 5 show no noticeable hysteresis. Individual disorders are caused by noise in the measurement system and possible temperature variations. The logarithmic nature of voltage deviation change in function of supply voltage is clearly seen. In order to better determine the nature of the changes a logarithmic curve fit was carried out:

$$f = a \cdot \ln(b \cdot x) \tag{2}$$

where a is amplitude and b is scale.

Parameter b describes optimal multiplier of input values to obtain the best fit. When data have a clear logarithmic nature, it is in the range of 1 ±0.02, and does not carry useful information. The key parameter obtained after a match is a – the ratio between the fit and the function $f(x) = \ln(x)$. It allows to specify the size of voltage deviation depending on the supply voltage.

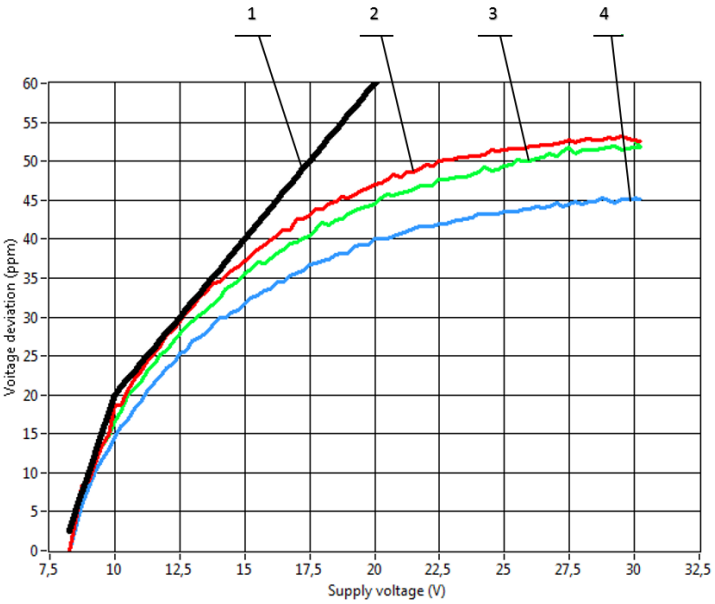

Fig. 4. Measurement results according to the method described in Section 4.1 (1 – maximum allowable deviation, 2 – results of tested reference no. 1, 3 – results of tested reference no. 2, 4 – results of tested reference no. 3)

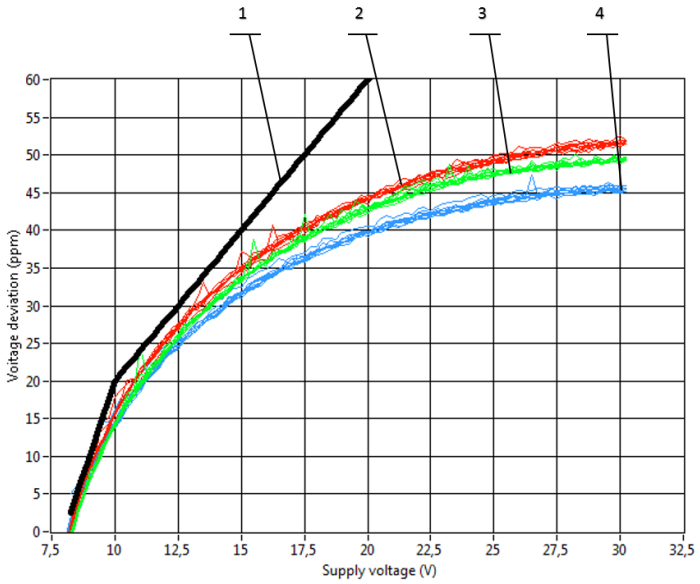

Fig. 5. Measurement results according to the method described in Section 4.2 (1 – maximum allowable deviation, 2 – results of tested reference no. 1, 3 – results of tested reference no. 2, 4 – results of tested reference no. 3)

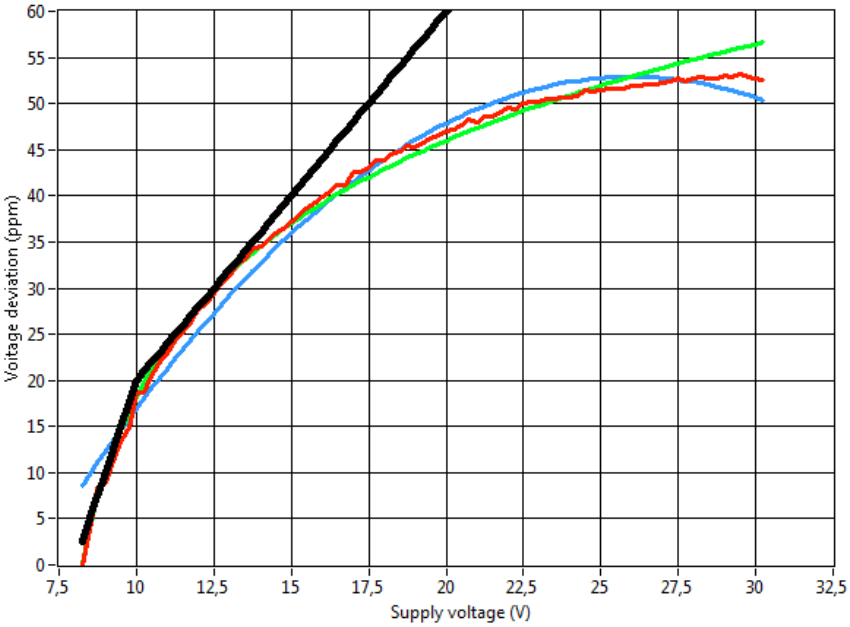

Fig. 6. Black line – maximum allowable indication is marked in black, red – measurement result, green – logarithmic fit and blue – the second degree curve fit

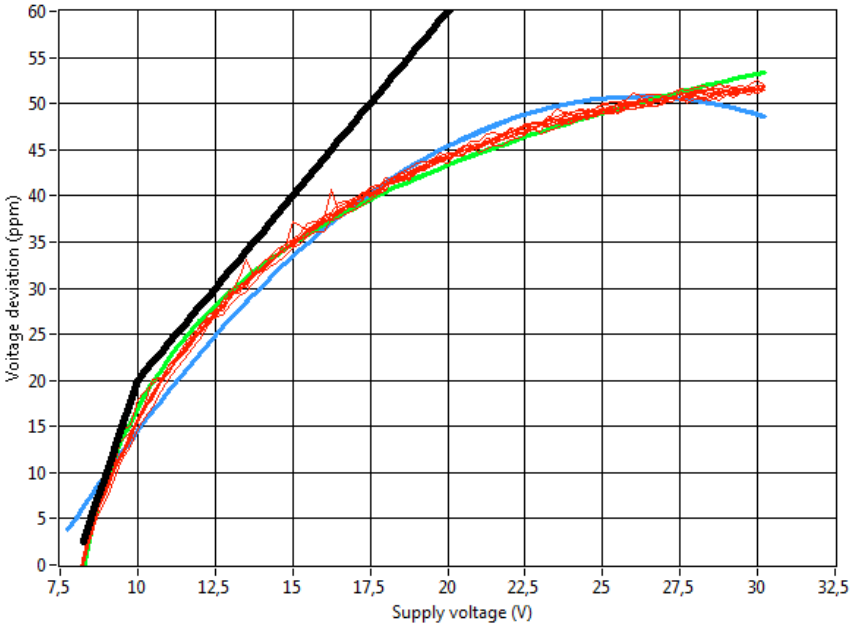

Fig. 7. Black line – maximum allowable indication is marked in black, red – measurement result, green – logarithmic fit and blue – the second degree curve fit

The second degree curve fitting was also performed:

$$f(x) = ax^2 + bx + c \tag{3}$$

Sample curve fit is shown on Fig. 6 and Fig. 7, where the allowable [2] indication is marked in black, red – is the measurement result, green – is the logarithmic fit and blue – is the second degree curve fit.

Fits (using the least squares method) were performed for all of the measurements. The results, together with R^2 match coefficients are shown in the following table.

Table 1. Comparisons of fitting parameters for single measurements

Number of tested source	Logarithmic fit			2 order curve fit			
	Scale	Amplitude	R^2	a	b	c	R^2
1	1.01	17.7	0.990	–0.14	7.31	–42.2	0.98
2	0.99	17.2	0.996	–0.12	6.62	–37.8	0.98
3	1.02	15.0	0.992	–0.11	6.14	–35.3	0.98

Table 2. Comparisons of fitting parameters for series measurements

Number of tested source	Logarithmic fit			2 order curve fit			
	Scale	Amplitude	R^2	a	b	c	R^2
1	1.02	17	0.993	–0.14	7.37	–46.5	0.98
2	0.98	17.2	0.994	–0.14	7.21	–33.9	0.98
3	0.99	14.9	0.993	–0.12	6.4	–40.6	0.98

Due to the high (0.98 and 0.99) R^2 coefficient it was decided not to carry out further statistical tests [3] in order to confirm the nature of the voltage changes impact on the reference sources characteristics.

The parameters values obtained are characterized by high reproducibility regardless of the measurement methodology. Larger parameters changes in regard to method used are in the second order curve fit. Additionally, the parameters of the source no. 3 stand out (marked in blue in Fig. 4 and Fig. 5). They confirm greater resistance to changes in the power supply of that particular source, which is also visible in the graphs.

6 Conclusion

The results are shown, and they confirm both the literature and sheets data. Two types of approximations using known functions are presented – second-degree polynomial and a logarithmic curve. Logarithmic curve approximations are more accurate and better reflect the nature of the phenomena [5], and polynomial approximations allow for easier calculation of the estimated impact of changes in power supply voltage in industrial environment.

Acknowledgments. This work was partially supported by The National Center for Research and Development with PBS Program – Grant no. PBS 1/B3/8/2012.

References

1. Horowitz, P., Hill, P.: The art of electronics, 2nd edn. Cambridge University Press, Cambridge (1989)
2. MAX 6325 datasheet provided by Maxim Integrated
3. Dobosz, M.: Wspomagana komputerowo statystyczna analiza wyników badań. EXIT (2004)
4. Tietze, U., Schenk, C.: Electronic circuits. Springer (2008)
5. Harrison, L.T.: Current sources and voltage references. Elsevier Inc. (2005)

Test Stand for Temperature Characteristics of Ultra-Precise Resistors

Paweł Nowak[1], Andrzej Juś[1], Roman Szewczyk[2], Rafał Pijarski[3], Michał Nowicki[2], and Wojciech Winiarski[1]

[1] Industrial Research Institute for Automation and Measurements PIAP, 02-486 Warsaw, Al. Jerozolimskie 202, Poland
{pnowak,ajus}@piap.pl
[2] Warsaw University of Technology, Faculty of Mechatronics, 02-525 Warsaw, Boboli 8 st., Poland
[3] RADWAG – Balances and Scales Company, 26-600 Radom, Bracka 28 st., Poland

Abstract. Paper presents the test stand, measurement methodology and exemplary results of measurements of thermal characteristics of ultra-precise resistors. Precise resistors are commonly used, as current-voltage converters or in precise current sources. Electric circuits are supposed to work in wide range of temperatures, which can change the resistance value, and thus be a source of unacceptable measurement error. Therefore it is important for designers and constructors to select the most temperature-stable resistors. The presented test stand is a reliable source of data about resistors temperature coefficients, with accuracy of 0.05 ppm/ºC.

Keywords: resistors, temperature coefficients, measurement.

1 Introduction

Precision measurements are critical in many industrial systems. High-tech production lines require a high-resolution and reliable measurements system. The highest accuracy is achieved in voltage measurements, so even the non-electric values (like temperature or weight) are measured by transforming their value to voltage and measuring it. The second most common type of electric signal (after voltage) is current. The easiest way to measure it is to convert current to voltage drop on precise resistor and measure the value of that voltage.

The temperature of resistors can change because of change in external operating conditions, as well as on account of self-heating [1]. The change of resistance caused by temperature is hard, but not impossible, to avoid. One of the most popular methods is to combine (serial or parallel) [3] two or more resistors with the same nominal value, which summed thermal coefficients as close to zero as possible. Therefore the manufacturers of ultra-precise measurements stands require the most precise information about a sign and value of temperature coefficient of every precise resistor used

J. Awrejcewicz et al. (eds.), *Mechatronics: Ideas for Industrial Applications*,
Advances in Intelligent Systems and Computing 317, DOI: 10.1007/978-3-319-10990-9_32

in circuit. Presented test stand can provide the data about temperature coefficient of up to 8 resistors in 5 minutes with accuracy of 0.05 ppm/ ºC.

2 Precise Resistance Measurement Methods

The most common resistance measurement method is based on Ohm's law. A known current is passed through a resistor which causes voltage drop which is measured. This method is suitable for approximate resistance value measurement. For higher accuracy differential measurement is applied. Long known differential methods like Wheatstone bridge and Kelvin double-bridges. Those methods require usage of many resistors and potentiometers; wherefore they are hardly automatable (digital potentiometers are not stable enough).

Higher measurement range connected with high accuracy (0.2 ppm [1]) is achieved in current-comparator bridge, where nominal values of tested resistors can differ by many orders of magnitude.

3 Test Stand Idea

3.1 General Idea

Schematic block diagram of proposed test stand is presented in Fig. 1.

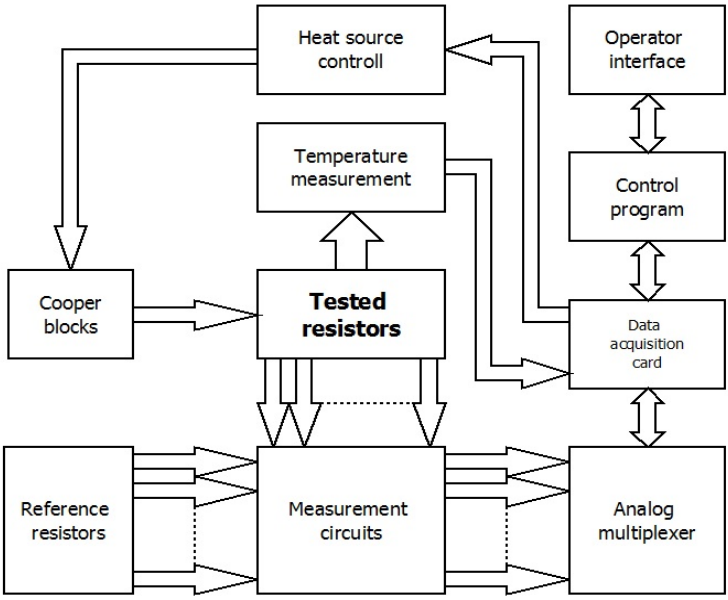

Fig. 1. Schematic block diagram of test stand

The main idea of presented test stand is based on high accuracy differential resistance measurement. Tested resistor is placed between sources of heat, which changes its temperature, which in turn causes the change of resistance. This resistance is compared with resistance of reference resistor with the same nominal value, which is located in a stable temperature.

The temperature on tested resistor is applied by external source, and is controlled by test stand operator. The change of difference of resistances is converted to voltage by measurement circuit. After passing through analog multiplexer voltage is measured by measurement and data acquisition card. As a result of measurement, operator sees the characteristic ΔR(T), which slope (calculated by test stand software) is resistors thermal coefficient.

3.2 Resistance Measurement Circuit Idea

To acquire highest measurement accuracy of resistance measurement, it was decided to design differential resistance measurement circuit with resistance – voltage conversion. Electronic scheme of measurement circuit is presented in Fig. 2.

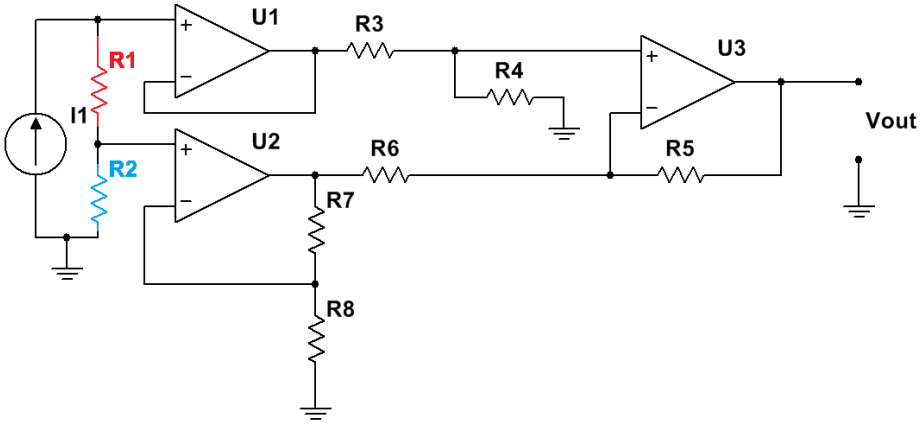

Fig. 2. Electronic scheme of measurement circuit idea

Tested resistor (R1) is connected in series with reference resistor (R2), and ultra-high stable and precise current source (I1). Flow of current forced by I1 causes voltage drop on resistors. The drop of voltage on each resistor results from Ohm's law and is linearly proportional to absolute value of resistance of each of the series connected resistors:

$$U = R \cdot I \tag{1}$$

Operational amplifiers work as a voltage follower (U1) and non-inverting amplifier (U2). Their main function is to separate current source I1 from the rest of measurement circuit. Non-inverting amplifier (built on U2 with R7 and R8) also doubles the absolute (with respect to ground) value of voltage drop on reference resistor (R2).

Therefore on the amplifiers U1 and U2 outputs voltage with value (with respect to ground) proportional to absolute value of resistance of R1 and R2 is held.

The next element of circuit is differential amplifier built on U3 and R3, R4, R5 and R6. As it can be proven [4], when following requirement $R_4/R_3 = R_5/R_6 = k$ is fulfilled, voltage held on the output of U3 is given by following dependency:

$$V_{out} = (V_1 - V_2) \cdot k \tag{2}$$

where V1 and V2 are output voltages held on operational amplifiers U1 and U2.

Basing on (1), (2) and the knowledge of non-inverting amplifier (build on U2) [4] on the output of presented circuit voltage which value and sign is linearly proportional to difference of resistances is held:

$$V_{out} = (V_1 - V_2) \cdot k = I(R_1 - R_2) \cdot \frac{R_4}{R_3} \tag{3}$$

Output voltage of measurement circuit is measured by data acquisition card, and processed by software using (3) in order to give information about resistance difference.

3.3 Heat Source

Tested resistors are placed between two cooper blocks. Each block is drilled and contains ceramic pipe with resistance wire inside it. Ceramic was chosen to provide good thermal conjunction combined with electric isolation. Resistance wires (each with nominal resistance value 14 Ω) are powered by voltage-controlled current sources. Each current source has 1.25 A efficiency. The power of heat source is given by following dependency:

$$P = R \cdot I^2 \tag{4}$$

Thus the power of heaters is around 44 watts and under laboratory conditions (22 ºC) increases temperature of tested resistors by 10 ºC in 6 minutes.

Autodesk's Inventor model of cooper block is presented in Fig. 3.

3.4 Temperature Measurement

The measurement of temperature is conducted with K-type thermocouple placed in hole drilled inside resistors casing. Thus the highest accuracy of actual temperature measurement inside tested resistor is achieved. Thermocouple is connected to programmable temperature-voltage converter with internal cold junction compensation, based on Pt 100 resistor. [5] On converter's output voltage proportional to hot junction temperature is held, which is measured by data acquisition card and calculated by software to temperature value. The value of temperature is used for creation of ΔR(T) dependency as well as for temperature regulator.

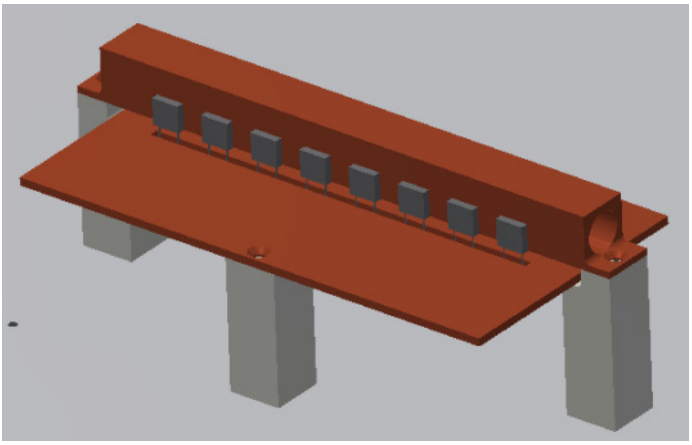

Fig. 3. Model of the heating element made in Inventor, together with the concept of resistors and thermal shield arrangement

3.5 Analog Voltage Multiplexer

In order to minimalize usage of analog inputs in data acquisition card it was decided to use analog voltage multiplexer. Each tested resistor requires separated resistance measurement circuit with voltage output. High frequency measurements of those voltages are not required, thus multiplexer switching frequency is maximum 10 Hz. Usage of multiplexer provides also effective scalability of presented test stand. In case of the need to increase number of simultaneously tested resistors, the change of multiplexer combined with the number of measurement circuits increase will fulfill requested need.

4 Test Stand Implementation

Test stand referenced in previous paragraph was implemented in Industrial Research Institute for Automation and Measurements. The main idea remained as shown on Fig. 1. Test stand was implemented based on data acquisition card NI – USB 6361 manufactured by National Instruments. For the ease of use, the control program and operator interface were made in National Instruments LabVIEW environment. Measurement circuit remained as shown on Fig. 2, based on operational amplifiers AD 8639 (U1 and U2) and AD 8638 (U3), powered by differential ±7.7 V. Amplifiers have been selected because of some of the finest parameters among the commercial available equipment. The key parameters taken into account were:

- The low bias current I_{bias},
- Low input offset voltage value U_{os},
- Low coefficient of thermal offset voltage TC_{Uos},
- A high power fluctuations damping coefficient SVRR,
- A high common signal damping coefficient CMRR.

Current source (I1 on Fig. 2) provides 12.5 mA. Maximal nominal value of tested resistor is limited by saturation voltage of operational amplifiers U1 and U2 and equals:

$$R_{\max} = \frac{U_{supply}}{2 \cdot I_{tested}} = \frac{7.5\,\mathrm{V}}{25\,\mathrm{mA}} = 300\,\Omega \tag{5}$$

The maximum nominal value of tested resistors can be increased by lowering the value of current from precise current source. In implemented circuit board it is achieved by soldering different resistor in current source. Recommended values of reference current and reference resistors according to the nominal value of tested resistors are presented in Table 1.

Table 1. Recommended values of reference current and suitable reference resistor according to nominal value of tested resistors

Range of tested resistance [Ω]	Recommended reference current [mA]	Suitable reference resistor [Ω]
0–350	10	250
350–700	5	500
700–3500	1	2500

Fig. 4. Photo of the heating elements with the method of the test stand closing/opening

Implemented temperature regulator based on PI algorithm provides temperature stability equal to temperature measurement resolution (0.1 ºC).

5 Exemplary Results

Exemplary results of measurement of UPR0.25 resistor manufactured by Thunder Precision Resistors with a nominal value of 150 Ω and maximal declared temperature coefficient of resistance ±1 ppm/ºC are presented in Fig. 5.

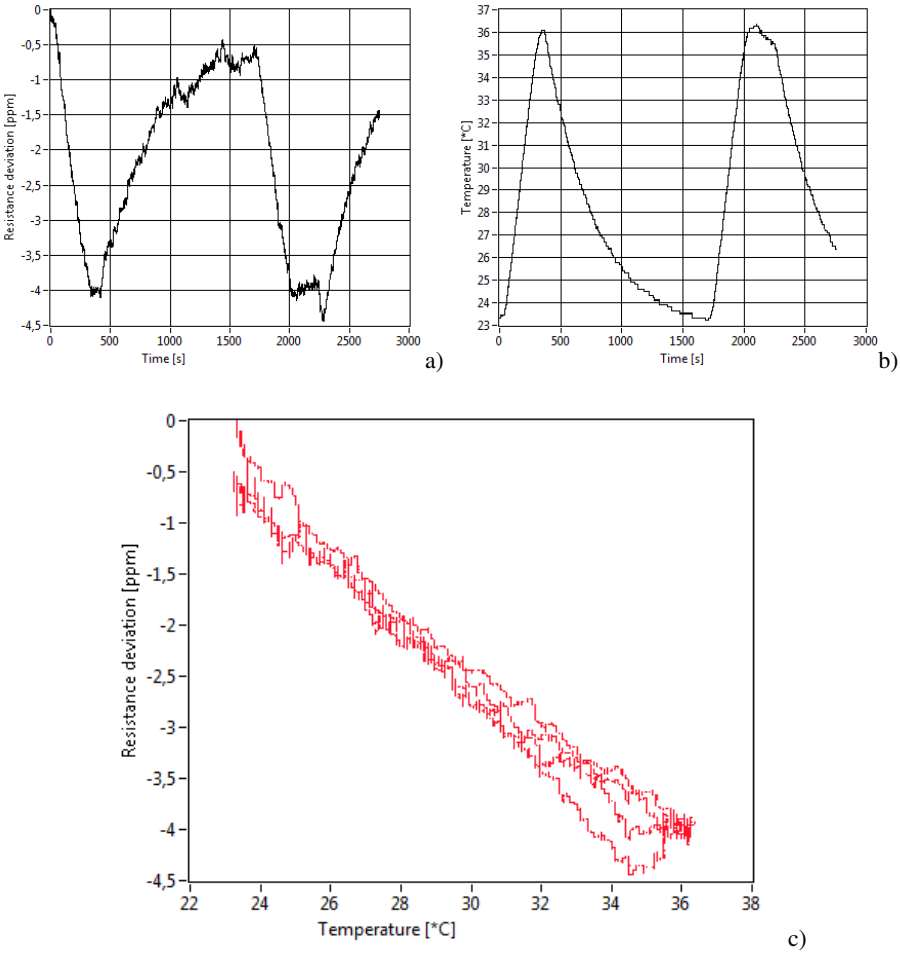

Fig. 5. Example result of measurement made on presented test stand prototype; a) change of resistance deviation in time ΔR(t), b) change of temperature in time T(t), c) change of resistance deviation in function of temperature ΔR(T)

The measurement concept was to put tested resistor between the cooper blocks and increase their temperature by 12.5 ºC. After that the heaters were turned off (implemented PI regulator holds set temperature) and were slowly cooling. When temperature of tested resistors reached ambient temperature the analogical measurement cycle was applied. As a result the characteristics of temperature and resistance change in time were drawn, as well as characteristic of change of resistance versus temperature. Measured resistance thermal coefficient (calculated as a slope of linear fit of ΔR/T characteristic) equals –0.28 ppm/ºC. Measured value of thermal coefficient falls within declared datasheet limits.

6 Conclusion

Presented solution of test stand enables technological break-thru in industrial precise measurements of thermal resistance coefficients, which can result in higher measurement accuracy in many measurement stands. Presented prototype provides high measurement accuracy combined with effective scalability. The increase of thermal coefficient measurement can be achieved by increase in temperature measurement accuracy, utilization of data acquisition card with highest A/C converters resolution, an increase of the measurement circuit's amplification.

Presented test stand is currently during implementation in RADWAG – Balances and Scales Company.

Acknowledgments. This work was partially supported by The National Center for Research and Development with PBS Program – Grant no. PBS 1/B3/8/2012.

RADWAG Company is kindly acknowledged for providing precise elements.

References

1. Braudaway, D.: Precision resistors: A review of the techniques of measurement, advantages, disadvantages, and results. IEEE Transactions on Instrumentation and Measurements 48(5), 884–888 (1999)
2. Braudaway, D.: Precision resistors: A review of material characteristics, resistor design, and construction practices. IEEE Transactions on Instrumentation and Measurements 48(5), 878–883 (1999)
3. Sadeghi, N., Sadeghi, I., Mirabbasi, S.: Analysis and design of monolithic resistors with a desired temperature coefficient using contacts. IET Circuits Devices Syst. 7(4), 185–192 (2013), doi:10.1049/iet-cds.2012.0126
4. Horowitz, P., Hill, P.: The art of electronics, 2nd edn. Cambridge University Press, Cambridge (1989)
5. Kerlin, T.W., Johnson, M.: Practical Thermocouple Thermometry, 2nd edn. ISA, Research Triangle Park (2012)

Magnetovision Scanner System Investigation of Magnetic Field Disturbance Sources

Michał Nowicki[1] and Roman Szewczyk[2]

[1] Institute of Metrology and Biomedical Engineering, Warsaw University of Technology, Warsaw, Poland
m.nowicki@mchtr.pw.edu.pl
[2] Industrial Research Institute for Automation and Measurements PIAP, Warsaw, Poland
rszewczyk@piap.pl

Abstract. Paper presents the methodology and results of magnetovision scanner system investigation of magnetic field disturbance sources. Special measurement test stand, utilizing magnetovision scanner and tri-axial Helmholtz coils was designed and built. The measurements of the homogenous magnetic field distortions caused by various ferromagnetic objects were carried out. The magnetic permeability related distortion effect was investigated. The ability for passive detection of ferromagnetic objects and determine their location was demonstrated.

Keywords: magnetovision, magnetic field imaging, public security systems.

1 Introduction

This paper presents an application of magnetic imaging method for passive detection and localization of small, potentially dangerous ferromagnetic objects. The application of passive magnetic imaging system is vital, because the active metal detectors induction field can be sensed by specially constructed detonators. This applies particularly to the new generations of booby traps and IED's (improvised explosive device), reacting to the presence of active detectors, and to some extent to magnetic influence AT mines, which presents a direct threat to minesweeper's life [1]. Existing passive gradiometer systems are designed for deep-level search of relatively big targets, such as unexploded aircraft bombs, and even if are used for magnetic imaging, using data logging and GPS systems, they have very low resolution. Therefore a high-resolution scanning system intended for search of small targets from small distance, such as potentially dangerous baggage, is designed.

Ferromagnetic materials can be magnetized by Earth magnetic field. Because their magnetic permeability is much higher than that of air, their presence creates a path of low reluctance, distorting lines of geomagnetic flux. Furthermore, most ferromagnetic elements have their own residual magnetism, which in effect causes them to act like a magnetic dipole. There is an open question however, about the magnitude of the

J. Awrejcewicz et al. (eds.), *Mechatronics: Ideas for Industrial Applications*,
Advances in Intelligent Systems and Computing 317, DOI: 10.1007/978-3-319-10990-9_33

magnetic permeability related distortion effect of various ferromagnetic objects, especially in comparison with the remanent magnetization.

To investigate this subject, special test stand was constructed, consisting of magnetovision scanner and high precision tri-axial Helmholtz coils. The magnetovision scanner is capable of planar magnetic field vector values distribution measurement, utilizing tri-axial high sensitivity magnetoresistive sensor. The Helmholtz coils were used to set the reference magnetic field for the measurement.

2 Methodology of Measurements

2.1 Measurement System

The schematic block diagram of measurement system used for the investigation is presented in Fig. 1.

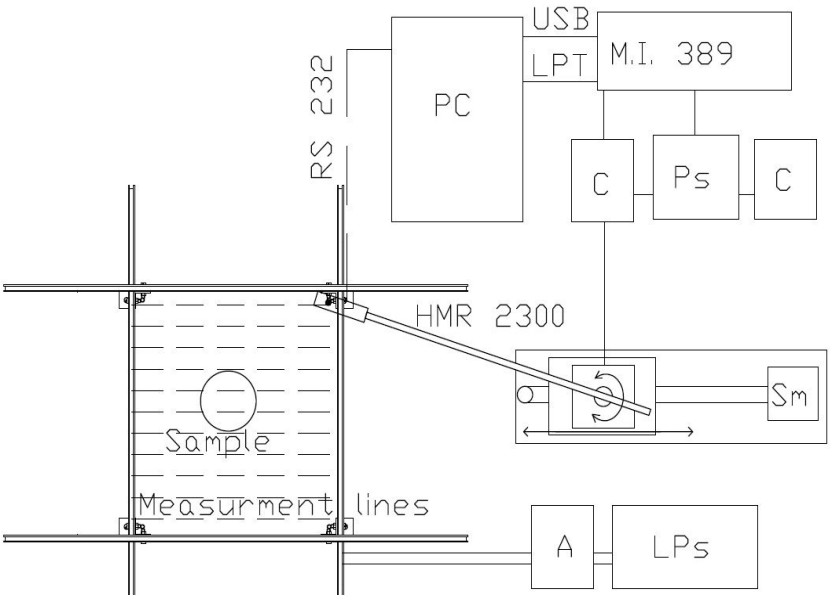

Fig. 1. Schematic block diagram of the measurement system. HMR 2300 – magnetoresistive sensor, Sample – investigated object, Sm – stepper motors, C – stepper motor controllers, MI 3.8.9 – trajectory generator, Ps – power supply, PC – controlling and image processing computer, LPs – laboratory power supply, A – ammeter.

To investigate the permeability and remanence related distortion effect, special test stand was constructed, consisting of magnetovision scanner and high precision tri-axial Helmholtz coils. The magnetovision scanner is capable of planar magnetic field vector values distribution measurement, utilizing tri-axial high sensitivity magnetoresistive sensor. Thin-film magnetoresistive sensors are the most suitable for magnetic imaging. They exhibit high sensitivity and have small size – typically 1 mm × 1 mm, or less [2]. The background field disturbances can be measured, mainly

disturbances of the natural Earth's magnetic field. Scanning probe system transit along parallel lines with a given interval (20 mm), setting the measuring plane (200 mm × 200 mm). Unlike other existing gradiometer systems, application of tri-axial sensor enabled gathering information about the magnetic induction vector value and its direction with respect to each measurement point in the scanning plane, not only its absolute value, or value of only one component, as is the case with most Hall effect systems. Raw data are enough to visualize value and direction of the magnetic induction vector in all measurement points. Resolution of the images depends directly on the number of measurement points per measurement line. Visualization of the distribution of the magnetic induction vector absolute values, interpolated to 1000 × 1000 points resolution, is also possible. Principle of operation and the target application of the magnetovision scanner has been described in [3].

2.2 Tested Samples

For the purpose of the study, an steel cylinder, 70 mm in diameter and 20 mm in height was used as an sample object. Such element can simulate landmine for tests [4]. For further demonstration, steel folding knife 150 mm in length was utilized.

2.3 Measuring Procedure

Since the magnetoresistive sensor measures only the value of the three components of the flux density vector at a point in which it is physically located, a separation of distortion generated by an sample object from the background is problematic. The simplest laboratory solution is the differential measurement by measurement without the test object and subtracting the result from the measurement with an object. This method gives the best results, allowing precise separation of magnetic induction distribution of the background and the object, which allows for low-level noise in the resulting image. However, this method is possible only in certain conditions, where it is possible to make measurements with an object and without, in the same plane. For this reason, a method of differential measurement was developed, minimizing the impact of the background to the measurement results.

Induction of the magnetic field on the axis of the magnet, in a vacuum, at a distance x from its center is expressed by the formula:

$$\vec{B} = \frac{\mu_0}{2\pi x^3}\vec{m} = C\frac{1}{x^3} \tag{1}$$

where:

$\vec{m}$ – magnetic dipole moment (A/m^2),

$\mu_0 = 4\pi \cdot 10^{-7}\,\frac{H}{m}$ – magnetic permeability of vacuum,

$C = \frac{\mu_0}{2\pi}\vec{m}$ – induction replacement constant (A·m^3).

With this method, both the Earth's magnetic field as well as the other sources of background can be filtered out. In its basic form, a differential measurement is the measurement in two parallel planes, at the height x above the test object, and $x + h$, where h is the distance between the planes of measurement, and then subtracting the results. Distribution of flux density lines near a ferromagnetic object placed in the Earth's magnetic field is similar to a magnetic dipole field distribution. Since the value of the flux density B is reduced approximately in proportion to the cube of the distance from the source, if $a \approx x$, distortion B_1 caused by the object in the first measurement plane will be up to 8 times greater than the B_2 in the second plane.

If, however, other sources of magnetic field are at a significantly greater distance $y >> x$ from the first measurement plane, their influence $B_{Background}$ on the value of magnetic induction in the planes P_1 and P_2 will be similar. As a result it is therefore possible to get a rough image of the sample located a short distance from the sensor by subtracting the results of a measurement in the plane P_2 from the results in the plane P_1. Differential bi-plane measurement gives the absolute value of the difference in magnetic induction value between the measurement planes. A similar method to compensate for the impact of background on the measurement result is the gradient measurement used in astrophysics and geology (e.g. in gradiometers). In the generalization it is based on the measurement of the magnetic field or gravity values at different levels and the field gradient designation on that basis. Use of this method also yields good results, but the images obtained are distinctly different than those obtained by the differential method. They allow to distinguish between positive and negative areas of magnetic disturbance relative to the Earth's field, but the bi-plane measurement gives better picture of silhouette of the hidden object.

To investigate the magnitude of the sample's permeability related distortion effect, the Helmholtz coils were used to set the reference magnetic field for the measurement. First the steel sample was set in the center of the Helmholtz coils, the Earth's natural magnetic field was compensated to zero value, and the magnetovision scanning was performed to measure the remanent magnetization distribution. The distance to the sample was set to 20 mm. Then Helmholtz coils were used to simulate natural field in the range of 40 μT acting in the X, Y, and Z axis of the sample, and the scans of magnetic field distributions were performed. Measurement results are gathered in the form of three signals, proportional to the induction vector components in measurement points. By the subsequent data processing, the planar distributions of magnetic field distortions related to materials permeability were calculated.

3 Experimental Results

On the following figures results of permeability related distortion effect investigation described in previous section are presented. There is a clearly visible change in the magnetic induction value distribution, depending on the presence and direction of external uniform field – Fig. 2–4.

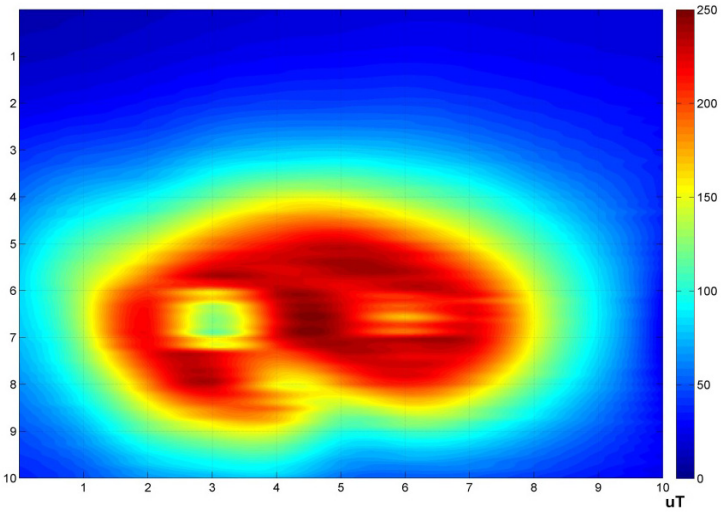

Fig. 2. Planar measurement of magnetic induction value, steel cylinder sample. External field compensated to less than 0.1 μT. Only remanent magnetization of the sample is visible.

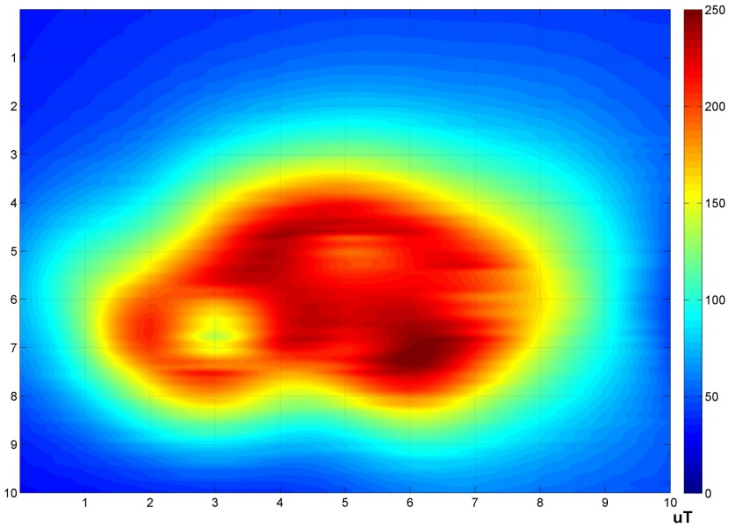

Fig. 3. Planar measurement of magnetic induction value, steel cylinder sample. External field set to 40 μT in the Z axis (perpendicular to measurement plane). Slightly distorted remanent magnetization of the sample is visible.

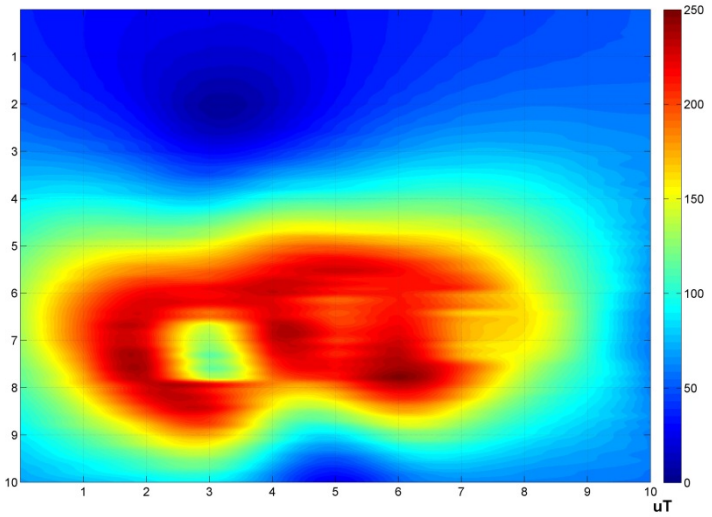

Fig. 4. Planar measurement of magnetic induction value, steel cylinder sample. External field set to 40 μT in the Y axis (vertical on the picture plane). Obvious distortion of the field distribution is visible.

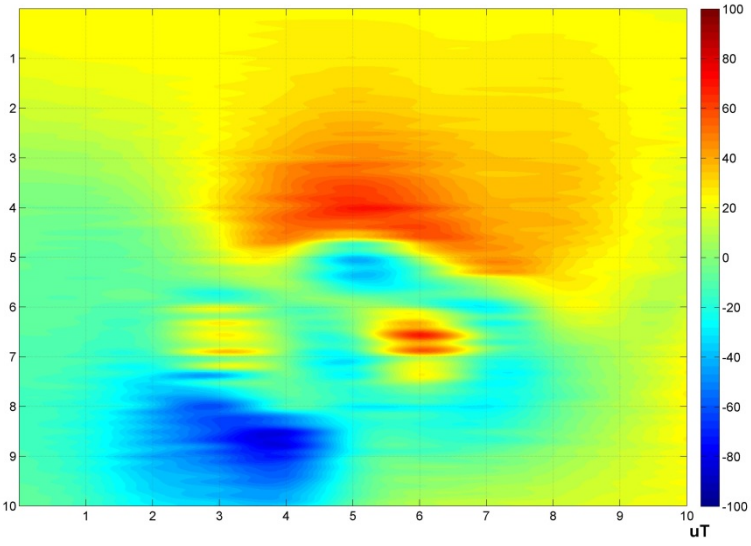

Fig. 5. Visualization of the permeability related distortion, with the external field and remanent magnetization removed. External field set to 40 μT in the Z axis.

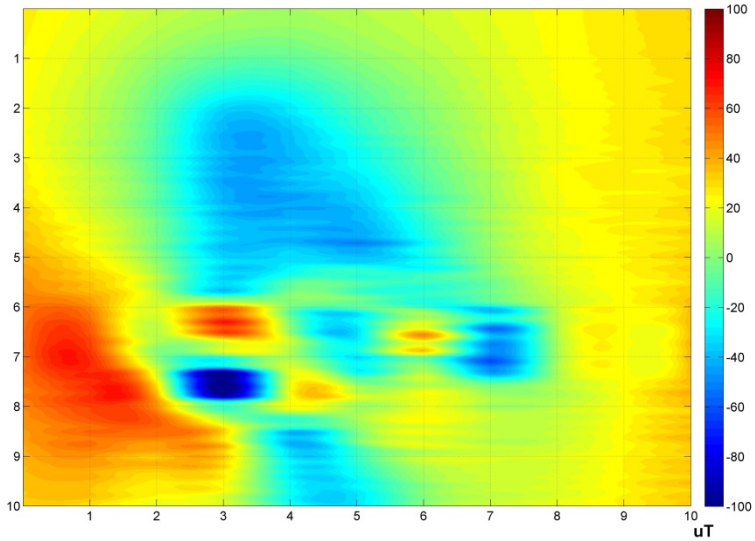

Fig. 6. Visualization of the permeability related distortion, with the external field and remanent magnetization removed. External field set to 40 μT in the Y axis.

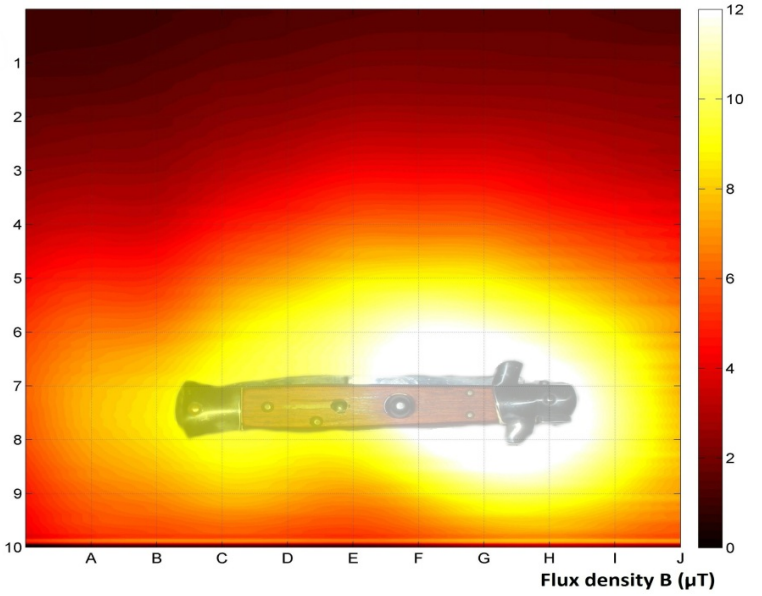

Fig. 7. Measurement of the position of dangerous object (folding knife), using the biplane differential measurement, merged with a photograph of the actual position of the sample in relation to measurement plane

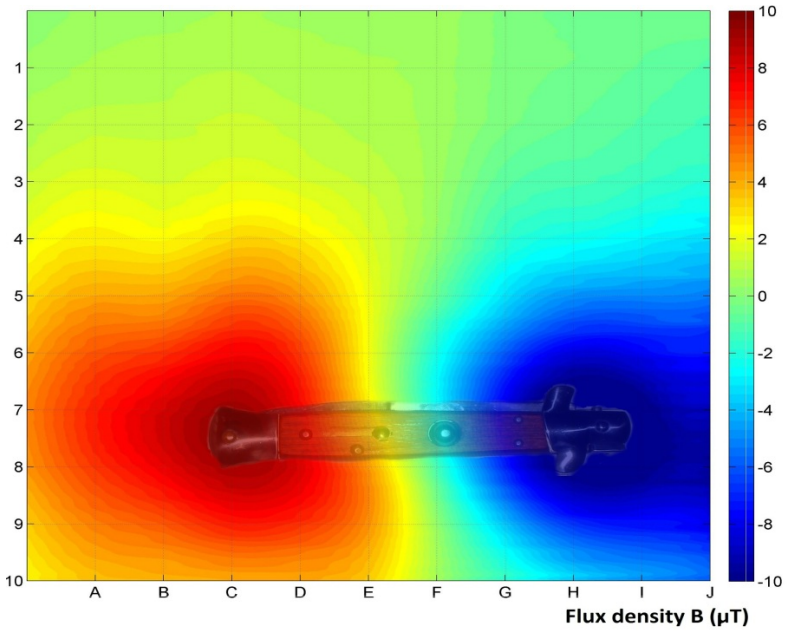

Fig. 8. Measurement of the position of dangerous object (folding knife), using the gradient measurement without background separation, merged with a photograph of the actual position of the sample in relation to measurement plane

On the Figures 5–6 the visualization of the permeability related distortion effect is shown, with the external field and remanent magnetization removed.

To present the detection and localization capabilities of the developed scanning system, tests were made to detect complex ferromagnetic object from greater distance. Distance of the sample from the plane of the measurement was x = 100 mm. Fig. 6 shows measurement of the position of dangerous object (folding knife), using the biplane differential measurement, merged with a photograph of the actual position of the sample in relation to measurement plane. Minimization of the background impact on the result is clearly visible. It is also clear, that this method provides the easiest way for localization of the sample, using the reference grid. In addition, the comparison of the results of the differential bi-planar (Fig. 7) and gradient (Fig. 8) methods was performed. The resulting magnetovision images were merged with the photos of actual position of the sample on the reference grid.

4 Conclusions

Experimental setup for planar measurements of vector distribution of weak magnetic fields distortions and to differentiate its sources was developed. Moreover, new methodology of measurement, leading to decreasing the impact of magnetic background on the visualization of the results was presented. The developed methods allow a visualization of the distribution of the magnetic induction vector absolute

values, its gradient as well as the value and direction of the magnetic flux density vector in different measurement points. Experimental investigation allowed for direct measurement of permeability-related distortion effect. The magnetic remanence related distortion was greater, but the measurements prove that the permeability related distortion is of comparable magnitude, and could work also for demagnetized objects. Based on the results, the location and size of the object can be determined, which is very useful from practical point of view. This opens the new way to use passive magnetic imaging in public security systems, in particular for the detection of dangerous objects by police forensic robots currently under development.

Acknowledgement. This work was partially supported by The National Center for Research and Development, grant no. O ROB 0015 01/ID15/1.

References

1. Guelle, D., Smith, A., Lewis, A., Bloodworth, T.: Metal detector handbook for humanitarian demining. Office for Official Publications of the European Communities, Luxembourg (2003)
2. Tumański, S.: Thin film magnetoresistive sensors. Taylor & Francis, England (2001)
3. Nowicki, M., Szewczyk, R.: Ferromagnetic Objects Magnetovision Detection System. Materials 6(12), 5593–5601 (2013), doi:10.3390/ma6125593
4. Billings, S.D.: Discrimination and classification of buried unexploded ordnance using magnetometry. IEEE Transactions on Geoscience and Remote Sensing 6, 1241–1251 (2004)

Analysis of Vibration of Rotors in Unmanned Aircraft

Stanisław Radkowski and Przemysław Szulim

Warsaw University of Technology, Faculty of Automotive, Warsaw, Poland
p.szulim@mechatronika.net.pl

Abstract. In the paper, solution of the problem of vibrations which appears during the maneuvers of quadrocopters is presented. Those special kinds of vibration aren't related to mounting or manufacturing faults. In this kinds of flying machines the main sources of vibration comes from motors and/or propellers unbalance. The paper shows analytical description of the source of this problem. Mathematical description of rotor which was subjected of additional rotation had been modeled in MATLAB/Simulink environment. It was shown, that correct set of parameters lead to total elimination of this kind of vibration.

Keywords: UAV, propeller vibration, quadrocopter.

1 Introduction

A rotorcraft are one of the mechanically simplest constructions of flying machines. In the immediate past such structures were mainly within the area of interest of modelers. Currently these aircraft have moved into a new stage of development. They are becoming not only a well-flying aircrafts, but also tools that enable performing tasks and services which have been so far impossible [1–3]. The increasingly serious applications call for improved quality and reliability. There are many applications which require high stability of fly and especially very low vibrations levels. One of them are photograph applications. From this point of view it is important that an aircraft behaves stably like a tripod, i.e. that it acts as an extension of a photographer's arm. This seemingly distant target is gradually becoming more realistic thanks to the efforts undertaken to improve the reliability and the quality of rotorcrafts. One should mention several areas which are still being on the development stage, such as automation [4–7], mechanics, area of new batteries and electric motors. In the paper authors of the article focused on the one issue which is associated with the vibration caused by rotors of a rotorcraft. Mechanical vibration has negative influence on the IMU measuring unit, which influence on behavior of the entire craft. The vibration also has negative impact on the quality of the tasks performed by the craft like recording images. Experience demonstrates that tackling the issue of vibration by applying relevant vibration isolation solves some problems [11]. In real-life applications the issue of vibration is approached in a twofold manner. On the one hand, relevant vibration insulation is used [9, 12], while on the other attempts are made at eliminating the reasons of vibration [8]. The second approach lies within the area of interest of the

J. Awrejcewicz et al. (eds.), *Mechatronics: Ideas for Industrial Applications*,
Advances in Intelligent Systems and Computing 317, DOI: 10.1007/978-3-319-10990-9_34

authors of this paper. Mainly observed vibrations doesn't result from rotor unbalance. Of course this source is also important and also plays important role. But the interesting phenomena appears during rotation of a rotorcraft around roll or/and pitch axis. It is worth to note that those vibrations are much more perceptible than vibrations coming from motor and propeller unbalance. This phenomena was observed for many sets of propellers and motors. This observation motivated the authors to describe the problem in mechanical domain and answer the question: are those vibrations can be reduced? The first section will describe the physical basis underlying the occurrence of the vibration in which the authors are interested. The next section, based on computer simulations, will present the results of comparing the vibration generated due to additional movement of a rotating rotor. In the last section, the authors will present the conclusions of their research, while indicating the possibilities of partial or full elimination of the vibration they analyzed.

2 Mathematical Description

Rotorcrafts are structures which consist of numerous power transmission systems of the motor-and-rotor type, installed on the arms which join together at the centrally-located body of such an aircraft. An example of such a structure is presented in Fig. 1 below.

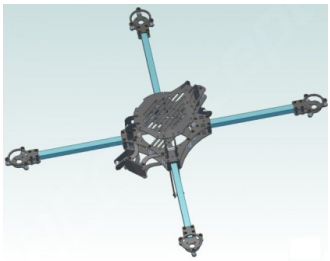

Fig. 1. Frame of a quadrocopter [10]

The above-presented type of quadrocopter is the most widely used structure. There are also structures with three, six or eight arms. Structures with two motors at each arm, placed one above the other and generating unidirectional thrust, are also popular.

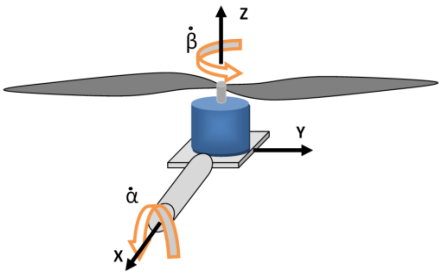

Fig. 2. An arm-motor-propeller unit

Due to the simple structure (which is the advantage of solutions of this type), the aircraft's flight is controlled by tilting the entire body in a relevant manner. Such a solution serves its purpose well and guarantees relevant maneuverability. It is the necessity of making maneuvers that causes emergence of angular velocities due to tilting of a craft's body. This velocity appear as a additional velocity $\dot{\alpha}$ rotating arms of quadrocopter. Fig. 2 presents a single arm-motor-propeller unit which forms the basic element being the subject of the subsequent analysis. The motor rotates the propeller with the speed of $\dot{\beta}$, thus producing the required thrust. The arm additionally rotates around axis *X* at the speed of $\dot{\alpha}$. The speed $\dot{\alpha}$, as marked in the Fig. 2, has been selected in order to simplify the calculations, however also other components of the velocity emerge along the axis *Y* and *Z* due to rotation of the whole platform. It could be shown that additional rotation along axis *Z* doesn't introduce significant vibrations. Additional rotation along axis *Y* has similar effect like investigated rotation along axis *X* and therefore would not be considered in next part of the article. Fig. 3, below, presents a simplified version of arm from Fig. 2.

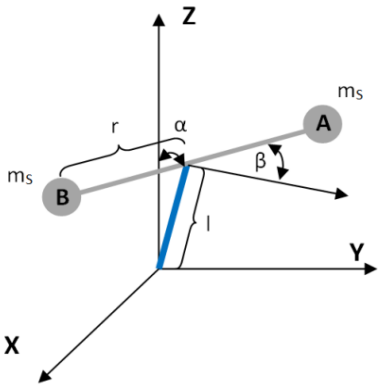

Fig. 3. The rotor unit reduced to its basic components

The propeller has been simplified to two point masses of m_S (point *A* and *B*), separated by the distance *r*. The propeller is separated from the axis X by the distance of *l*. The propeller rotates at a constant speed of $\dot{\beta}$. The angle α is the angle between the axis *Z* and the axis of the motor and result from rotation of rotor caused by tilting. In the analyzed case the axis of the motor rotated in the plane *Y*-*Z* was chosen. The location of points $A(A_X, A_Y, A_Z)$ and $B(B_X, B_Y, B_Z)$ in the coordinates system *X*, *Y*, *Z* is described below.

$$A_Z = l\cos(\alpha) + r\sin(\alpha)\cos(\beta) \tag{1}$$

$$A_Y = l\sin(\alpha) - r\cos(\alpha)\cos(\beta) \tag{2}$$

$$A_X = -r\sin(\beta) \tag{3}$$

$$B_Z = l\cos(\alpha) - r\sin(\alpha)\cos(\beta) \tag{4}$$

$$B_Y = l\sin(\alpha) + r\cos(\alpha)\cos(\beta) \tag{5}$$

$$B_X = r\sin(\beta) \tag{6}$$

Forces and torques are created as a result of rotation of the rotor around the axis *X*. Forces F_X, F_Y, F_Z and torques T_X, T_Y, T_Z can be determined based on the below equations:

$$T_X = m_S\left(A_Z\ddot{A}_Y + B_Z\ddot{B}_Y - A_Y\ddot{A}_Z - B_Y\ddot{B}_Z\right) \tag{7}$$

$$T_Y = m_S\left(A_Z\ddot{A}_X + B_Z\ddot{B}_X - A_X\ddot{A}_Z - B_X\ddot{B}_Z\right) \tag{8}$$

$$T_Z = m_S\left(A_Y\ddot{A}_X + B_Y\ddot{B}_X - A_X\ddot{A}_Y - B_X\ddot{B}_Y\right) \tag{9}$$

$$F_X = m_S\left(\ddot{A}_X + \ddot{B}_X\right) \tag{10}$$

$$F_Y = m_S\left(\ddot{A}_Y + \ddot{B}_Y\right) \tag{11}$$

$$F_Z = m_S\left(\ddot{A}_Z + \ddot{B}_Z\right) \tag{12}$$

After substituting equations (1)–(6) and their second derivatives into equations (7)–(12) one come up with the following set of equations:

$$T_X = m_S\left(\left(2l^2 + 2r^2\cos(\beta)^2\right)\ddot{\alpha} - 2r^2\dot{\alpha}\dot{\beta}\sin(2\beta)\right) \tag{13}$$

$$\begin{aligned} T_Y = m_S[&-2r^2\ddot{\beta}\sin(\alpha) + r^2\ddot{\alpha}\cos(\alpha)\sin(2\beta) - r^2\dot{\alpha}^2\sin(\alpha)\sin(2\beta) + \\ &+ 2r^2\dot{\alpha}\dot{\beta}\cos(\alpha)(1-\cos(2\beta))] \end{aligned} \tag{14}$$

$$\begin{aligned} T_Z = m_S[&-2r^2\ddot{\beta}\cos(\alpha) - r^2\ddot{\alpha}\sin(\alpha)\sin(2\beta) - r^2\dot{\alpha}^2\cos(\alpha)\sin(2\beta) + \\ &+ 2r^2\dot{\alpha}\dot{\beta}\sin(\alpha)(1-\cos(2\beta))] \end{aligned} \tag{15}$$

$$F_X = 0 \tag{16}$$

$$F_Y = 2lm_S\left(\ddot{\alpha}\cos(\alpha) + \dot{\alpha}^2\sin(\alpha)\right) \tag{17}$$

$$F_Z = -2lm_S\left(\ddot{\alpha}\sin(\alpha) + \dot{\alpha}^2\cos(\alpha)\right) \tag{18}$$

While analyzing equations (16)–(18), one may note that the force do not influence on vibration. The equations of torque (13)–(15) have common features. Almost all components are related to angular position of the propeller. This relation introduces pulsation of torques on *X*, *Y* and *Z* axis. This pulsation has twice the frequency of the rotation of propeller. Amplitude of torques is also not constant but depends on acceleration and rotational speed of arm along axis *X*.

3 Simulations

The chapter presents the results of exemplary simulations. The object subjected to simulation has been modified slightly in order to bring the theoretical considerations closer to their practical application. A second arm with a rotor has been added to the object. Both units are joined together at a point having a certain mass which represents the central part of an aircraft's structure. Fig. 4 shows the schematic diagram of the object.

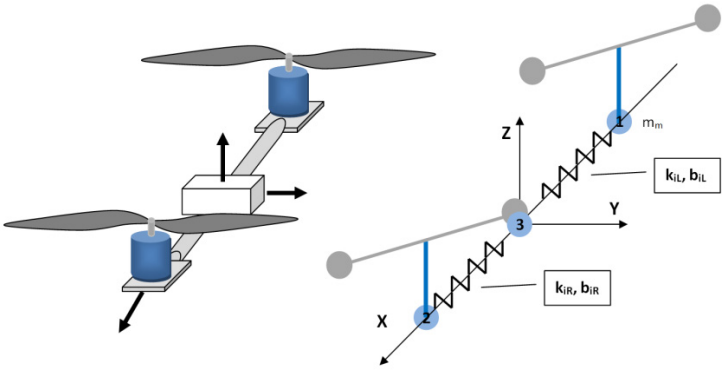

Fig. 4. A simplified model with two rotors and its reduced counterpart

The concentrated masses 1 and 2 represent the motors with a mass of m_m. The concentrated mass 3 represents the central part of the structure witch momentum J_3. The arms connecting the two motors with the central part have been replaced by connections characterized by the stiffness of k_{iL} and k_{iR} and damping of b_{iL} and b_{iR}. In those values index i denotes the respective analyzed axis of the torques (X, Y, Z), while the indices R and L correspond to the right and left arm of the structure. To simplify simulation, influence of T_X, T_Y, T_Z torques on angular orientation of motor and propeller in Z and Y direction was not considered. The system of equations presented below describes the dynamics of this complex object in respect to X axis. Similar set of equation describe object dynamics in respect to axis Y and Z.

$$\begin{aligned}\left(m_m h^2 + 2m_S l^2 + 2m_S r^2 \cos(\beta_1)^2\right)\ddot{\alpha}_{X1} - 2m_S r^2 \dot{\alpha}_{X1}\dot{\beta}_1 \sin(2\beta_1) + \\ + (\alpha_{X1} - \alpha_{X3})k_{XL} + (\dot{\alpha}_{X1} - \dot{\alpha}_{X3})b_{XL} = 0\end{aligned} \tag{19}$$

$$\begin{aligned}\left(m_m h^2 + 2m_S l^2 + 2m_S r^2 \cos(\beta_2)^2\right)\ddot{\alpha}_{X2} - 2m_S r^2 \dot{\alpha}_{X2}\dot{\beta}_2 \sin(2\beta_2) + \\ + (\alpha_{X2} - \alpha_{X3})k_{XR} + (\dot{\alpha}_{X2} - \dot{\alpha}_{X3})b_{XR} = 0\end{aligned} \tag{20}$$

$$J_3\ddot{\alpha}_3 - (\alpha_{X1} - \alpha_{X3})k_{XL} - (\alpha_{X2} - \alpha_{X3})k_{XR} - (\dot{\alpha}_{X1} - \dot{\alpha}_{X3})b_{XL} - (\dot{\alpha}_{X2} - \dot{\alpha}_{X3})b_{XR} = T_{in} \tag{21}$$

where: h – the distance between the motor's and axis X, T_{in} – the control torque applied to the central point 3, α_{xn} – angle of rotation of point mass n around the axis X, β_k – the angle of rotation of the propeller for rotor k.

The simulations of system described via (19)–(21) equations were carried out in the MATLAB/Simulink environment.

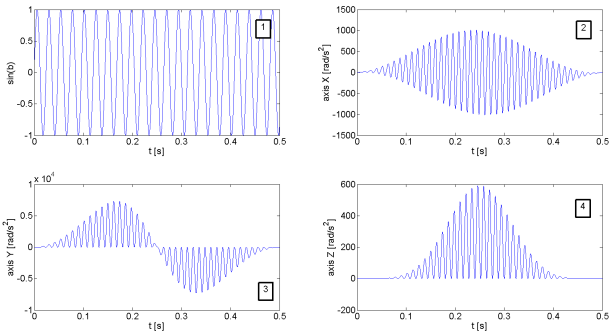

Fig. 5. Angular acceleration graphs for the central point of the model

The figure above presents graphs showing the angular accelerations measured in point 3, i.e. at the central point of the platform. Image 1 presents the sine function of the propeller's rotation angle β. In this case both rotors were rotating at the same speed of 2500 rpm. Image 2–4 presents graph of amplitude of angular acceleration of the central point of the object. Frequency of acceleration pulsation is twice the frequency of propeller rotation angle what could be compared based on image 1 and images 2–4. Interesting is amplitude modulation that could be seen on img. 2–4. The envelopes of angular acceleration signals are not pure function of sine or cosine, but depend on angle, velocity and acceleration of axis X. The figure 6 presents the graphs illustrating the angular orientation and the angular velocity of the main coordinate system located in point of central mass. The torque T_{in} has been applied in such a way so as to smoothly turn the entire structure by 180 degrees. Each subsequent simulation occurs with the same torque T_{in}. The influence of the torque oscillation on oscillation of the angular velocity of the central mass, is also very visible here. Interesting results are observed for a situation when identical angular speeds are set for the two rotors while there is difference in terms of phase shift between the rotors.

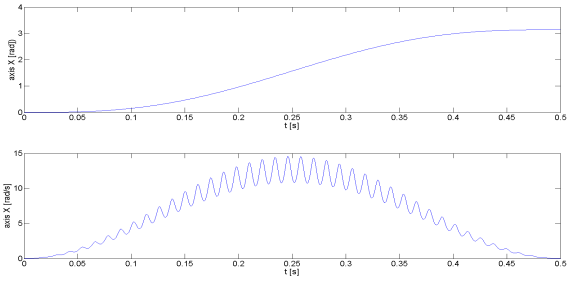

Fig. 6. Shift and speed of the model's central point (3)

Fig. 7 presents graphs showing accelerations obtained as a result of a simulation involving an angular shift between the propellers equal to π/2. The oscillations of the torque, associated with rotation of the rotor, disappeared in the axis *Y* and *Z* (img. 3 and 4). For axis *X* (img. 2) the amplitude of oscillations decreased substantially (by around a factor of 10).

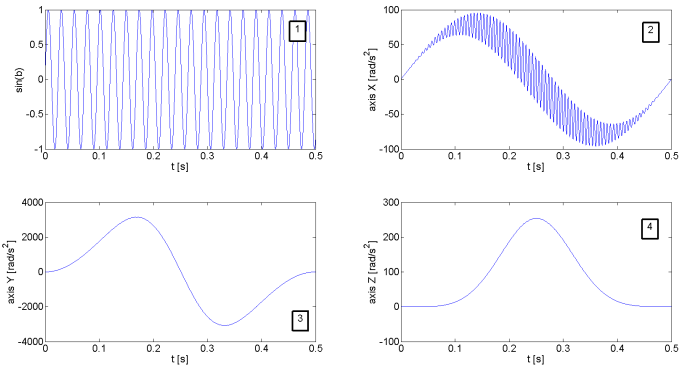

Fig. 7. The influence of the preset phase shift of the rotors on oscillation

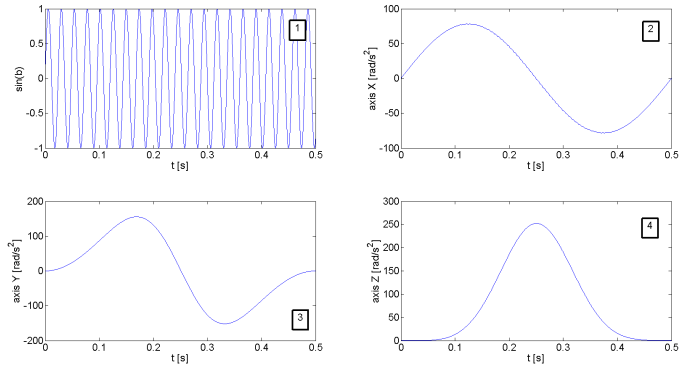

Fig. 8. Influence of preset phase shift of the propellers and bigger rigidity of the arms on vibration of the object

The frequency of oscillations corresponds to the fourfold frequency of rotation of the propeller. After increasing the parameters of simulated model like stiffness and damping, the influence of the rotating propeller on generation of oscillation has been practically eliminated. This was presented in Fig. 8. It is only the accelerations generated by gyro moments that are left. This result could be proved on analytical way. If we consider equations (13)–(15) we can see, that all torque pulsation are the function of doubled angle. Let's consider single arm with motor and propeller. Let's introduce additional propeller, shifted about angle π/2. This case we can describe as a sum of two set of equations (13)–(15). After taking into consideration trigonometric properties listed below (22), (23), set of torque equations is reduced to form (24)–(26).

$$\cos\left(2\left(\beta+\frac{\pi}{2}\right)\right)=-\cos(2\beta) \tag{22}$$

$$\sin\left(2\left(\beta+\frac{\pi}{2}\right)\right)=-\sin(2\beta) \tag{23}$$

$$T_X = m_S\left(\left(4l^2+2r^2\right)\ddot{\alpha}\right) \tag{24}$$

$$T_Y = m_S\left(-4r^2\ddot{\beta}\sin(\alpha)+4r^2\dot{\alpha}\dot{\beta}\cos(\alpha)\right) \tag{25}$$

$$T_Z = m_S\left(-4r^2\ddot{\beta}\cos(\alpha)+4r^2\dot{\alpha}\dot{\beta}\sin(\alpha)\right) \tag{26}$$

Those equations doesn't depend on sine or cosine β angle anymore, so the torques will not pulsate. It was the goal of the authors. Because the rotational velocity of propeller is constant first term of equations (25) and (26) is zero. Second term of this equations depend on velocity $\dot{\alpha}$ and this is the reason that the curves on plot 3 and 4 on Fig. 8 are not pure trigonometric functions.

4 Conclusions

The paper investigates the phenomena of generation of adverse vibration which appears while a rotorcraft makes maneuvers. A model of the basic unit and simulation show that maintaining a permanent angle of phase shift between the two rotors led to a practically complete elimination of occurrence of oscillations of the torque for the all three axis. However such a solution would be difficult to implement in an aircraft. In practice the rotational speed of each of the rotors is set accordingly by a computer which controls the aircraft. In such a case there would be no possibility of maintaining a constant phase shift of the rotors. The calculations have demonstrated that the desired effect of elimination of vibration is achieved while using a two propellers, set on single motor, rotated about angle π/2. Doubled propeller correspond to four symmetrically-spaced blades. The solution gives precisely the same effect as maintaining a constant angle of shift between the rotors. Similar effect could be achieved for propeller with eight blades. But the torque oscillation will not disappear for propeller with three symmetric blades for example. In the next step, authors are going to perform investigations on real object. The rotorcraft with two set of propellers will be tested. Measurement of construction vibrations in typical mission of the aircraft should show the impact of two kind of propellers (two and for blades) on level of vibration on the board of UAV.

References

1. Manufacturer website, http://quadcopter.heliguy.com/
2. Manufacturer website, http://www.apspecialists.com.au/products/product_view/70
3. Manufacturer website, http://www.coptercraft.com/build-droidworx-xm6-2-axis-cinestar/
4. Cherian, A., Andersh, J., Morellas, V., Papanikolopoulos, N., Mettler, B.: Autonomous Altitude Estimation of UAV Using A Single Onboard Camera. In: The 2009 IEEE/RSJ International Conference on Intelligent Robots and Systems, St. Louis, USA, October 11-15 (2009), doi:10.1109/IROS
5. Moore, R.J.D., Thurrowgood, S., Bland, D., Soccol, D., Srinivasan, M.V.: UAV Altitude and Attitude Stabilisation using a Coaxial Stereo Vision System. In: 2010 IEEE International Conference on Robotics and Automation Anchorage Convention District, Anchorage, Alaska, USA, May 3-8 (2010), doi:10.1109/ROBOT.2010.5509465
6. Bošnak, M., Matko, D., Blažič, S.: Quadrocopter control using an on-board video system with off-board processing. Robotics and Autonomous Systems 60, 657–667 (2012), doi:10.1007/s10846-009-9369
7. Yua, Y., Dinga, X., JimZhub, J.: Attitude tracking control of a quadrotor UAV in the exponential coordinates. Journal of the Franklin Institute 350, 2044–2068 (2013)
8. Castellini, P., Santolini, C.: Vibration measurements on blades of a naval propeller rotating in water with tracking laser vibrometer. Measurement 24(1), 43–54 (1998), doi:10.1016/S0263-2241(98) ISSN 0263-2241
9. Hsueh, W.-J.: Vibration reduction of main hulls using semiactive absorbers. Journal of Marine Science and Technology 3(1), 50–60 (1998), doi:10.1007/BF01239806
10. Manufacturer website, http://www.wiki.rcconcept.pl
11. Isolating Components from UAV Vibration, http://www.micropilot.com/pdf/isolating-components-uav-vibration.pdf
12. Marichal, G.N., Rodriguez, M.T., Rivera, S.C.: Vibration reduction for vision systems on board unmanned aerial vehicles using a neuro-fuzzy controller. Journal of Vibration and Control (June 25, 2013), doi:10.1177/1077546313479632

Non-destructive Testing of Cylindrical Ferromagnetic and Non-magnetic Materials Using Eddy Current Tomography

Jacek Salach

Institute of Metrology and Biomedical Engineering Warsaw University of Technology
A. Boboli 8 Str., 02-739 Warsaw, Poland
j.salach@mchtr.pw.edu.pl

Abstract. Idea of the high-resolution eddy current tomography is presented. Proposed system gives possibility of cylinder-shaped elements made of both magnetic and non-magnetic materials testing. To validate the concept, the tomographic measurements were carried out on set of steel cylinders with non-magnetic copper inclusion. Measurements were done during both linear and rotational movement of the element. Achieved results indicate the high sensitivity of system, which creates possibility of its application for non-destructive testing of the elements made of ferromagnetic and non-magnetic materials.

Keywords: Eddy current tomography, non-destructive testing, testing of ferromagnetic materials, testing of non-ferromagnetic materials.

1 Introduction

Tomography based tests are intensively developed for non-destructive testing of mechanical components. The main advantage of tomography is unique possibility of obtaining detailed information about the nature and shape of discontinuities in the tested element. However, commonly used X-ray tomography creates a number of risks typical for X-ray techniques. As a result, this technique is expensive and difficult to use in industrial environment. An alternative to the use of X-ray tomography can be eddy current tomography [3]. It allows for simultaneous measurement of magnetic susceptibility and resistivity of the material [4] in the tested element. Consequently, eddy current tomography opens completely new possibilities for detection of discontinuities in structures in industrial conditions.

There are two steps during eddy current tomography imaging [5]. First, influence of tested element on the coupling of two coils is measured during the movement of element. Next, the shape of the element together with its internal structure is recalculated with the use of finite element method, on the base Maxwell equations [6].

Different methods of inverse eddy current tomography transformation were previously presented [7–9]. However, it seems that development of eddy current tomography setup with high spatial resolution and high accuracy of measurements was not

J. Awrejcewicz et al. (eds.), *Mechatronics: Ideas for Industrial Applications*,
Advances in Intelligent Systems and Computing 317, DOI: 10.1007/978-3-319-10990-9_35

presented previously. This paper is filling this gap, which will enable further development of more effective and accurate algorithms for inverse eddy-current tomography transformation.

2 Tomography Setup

The schematic block diagram of experimental setup is presented in Fig. 1, whereas Fig. 2 presents the model element used for tests.

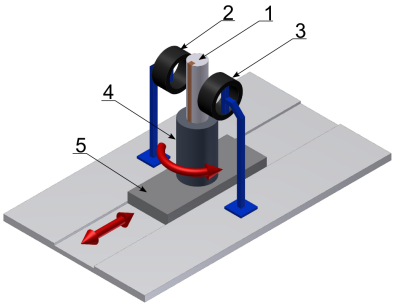

Fig. 1. Schematic block diagram of experimental setup for high resolution eddy current tomography: 1) tested element, 2 – driving coil, 3 – detection coil, 4 – stepper motor for rotation, 5 – linear actuator

Driving coil (2) is connected to sine wave current source. Measuring signal from detection coil (3) consist of both amplitude and phase shift. This signal is filtered by a band-pass filter to decrease noise level. On the base of these data, internal structure of tested element (1), from the point of view of magnetic permeability and conductivity, may be calculated on the base of Maxwell equations.

During the measurement, the test object is rotated by the stepper motor (4). Additionally, after each rotation object is moved incrementally by linear actuator (5). Schematic block diagram of signal processing unit is presented in Fig. 3.

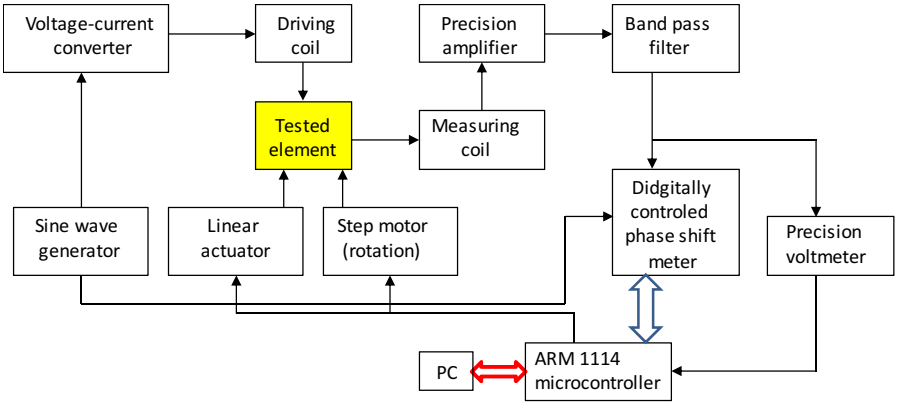

Fig. 2. Schematic block diagram of electronic signal processing unit in eddy-current tomography

Exciting coil is powered by a current sine wave with 2 kHz frequency, generated by a sinusoidal voltage generator circuit using ICL8038 integrated circuit and voltage-to-current converter with large output current. Signal from detection coil is amplified and the first harmonic (2 kHz) is filtered. From practical point of view, other harmonics are negligible due to the fact, that magnetization process for lower magnetizing field is connected with bending of magnetic domain walls. As a result it is nearly linear.

After filtering, the electronic measuring system provides a measurement of both the amplitude of the signal obtained in the detection coil and the angle of the phase shift with respect to the magnetizing coil driving signal. Phase shift is measured as a tangent of the shift between the driving coil signal and detected signal. All measuring data are collected by ARM1114 microcontroller produced by NXP. This microcontroller also controls both linear and rotation actuators as well as provides measuring data to PC for further processing.

For determination of spatial distribution of both magnetic permeability μ and resistivity ρ finite element method can be applied [10–12]. This method utilizes fundamental Maxwell equations written in frequency domain [5, 6]:

$$\nabla \times E = -j\omega B \tag{1}$$

$$\nabla \times H = E/\rho + j\omega\varepsilon E \tag{2}$$

$$\nabla \cdot (E/\rho) = 0 \tag{3}$$

Moreover, for frequencies up to 10 kHz, electromagnetic coupling may be neglected. As a result, both spatial distribution of magnetic permeability μ and resistivity ρ in the tested element may be calculated on the base of solution of partial differential equations, as it was presented before [11, 12].

3 Results of Investigation

Experiment was carried out for three cylinders made of S235 JR construction steel. In each cylinder copper block inclusion was made. The inclusion block was inserted 13 mm into the cylinder, whereas its wideness was 4 mm, 8 mm and 12 mm respectively. As it is presented in Fig. 3, the copper block inclusion was made on whole length of model element.

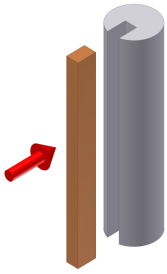

Fig. 3. Model element consisting construction steel S235 JR cylinder with copper inclusion

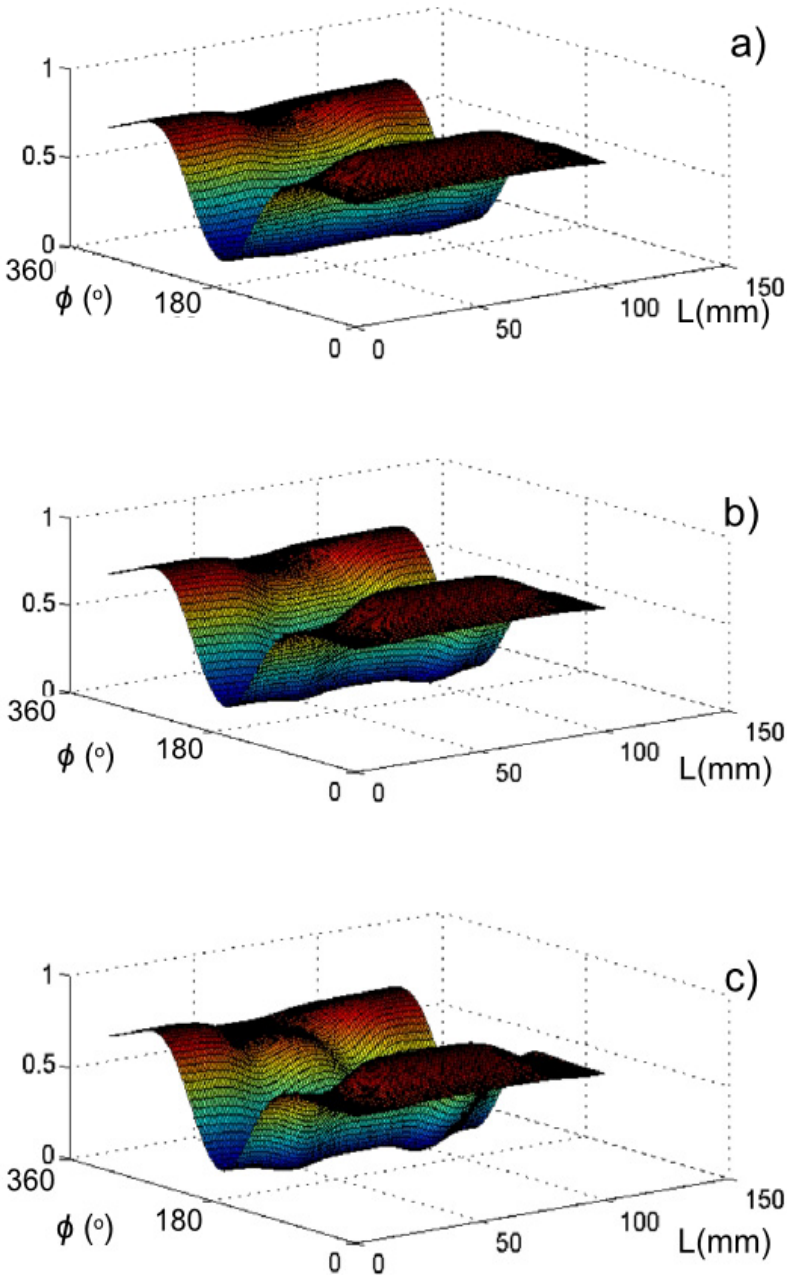

Fig. 4. Visualized results of measurements the volume of amplitude of the signal on detection coil as a function of linear movement L and rotation ϕ for model steel elements with copper inclusions width: a) 4 mm, b) 8 mm, c) 12 mm

The results of measurements of amplitude on the detection coil for all three testing elements are presented in Fig. 4, while the results of measurements of the tangent of angle between signal on measuring coil and signal given on driving coil are shown in Fig. 5. Figures show the changes of amplitude value and of tangent of the angle between signals, as a function of the rotation and linear movement of the test element.

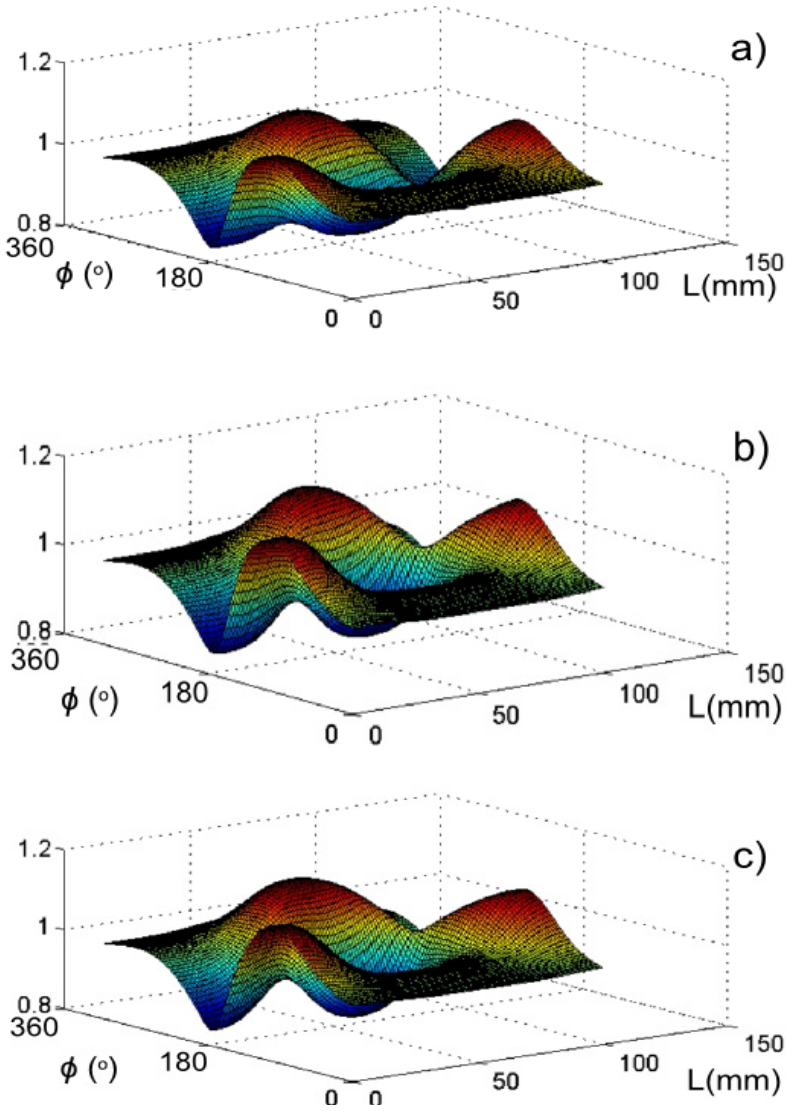

Fig. 5. Visualized results of measurements the volume of tangent of angle between signal on measuring coil and signal given on driving coil as a function of linear movement L and rotation ϕ for model steel elements with copper inclusions width: a) 4 mm, b) 8 mm, c) 12 mm

During the tests the repeatability of measurements was verified. Standard deviation of measurements in point doesn't exceed 1 %. Such high repeatability is very important from the point of view of accuracy of the results of further inverse tomographic transform.

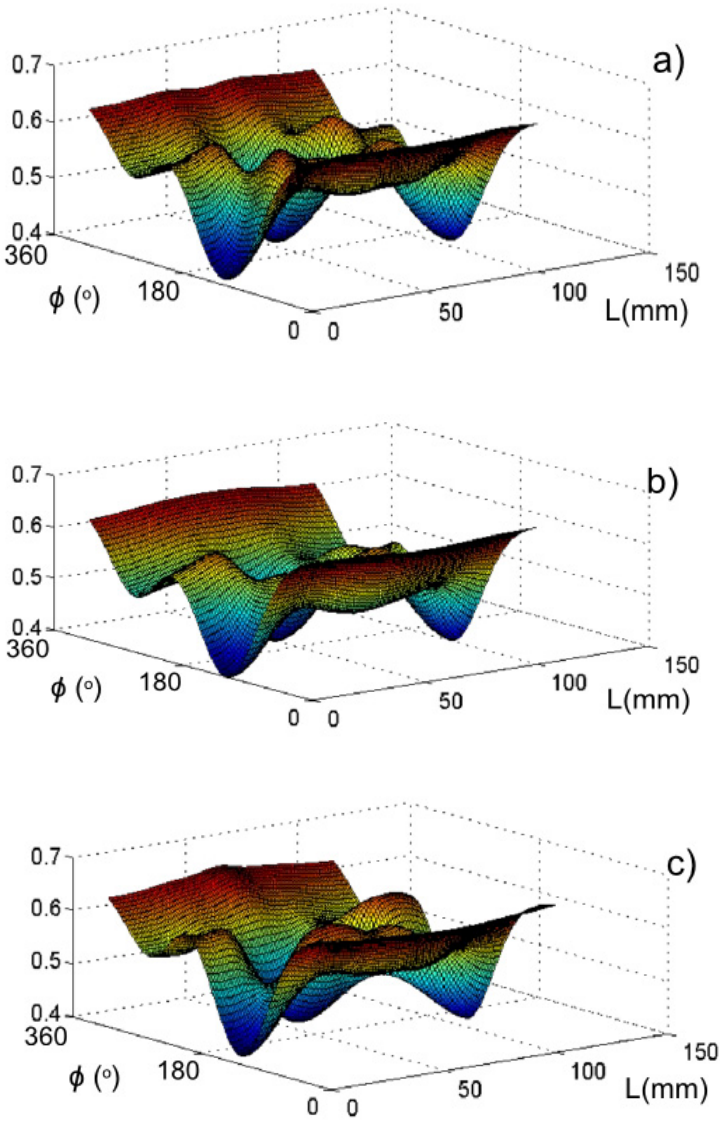

Fig. 6. Results of measurements of amplitude of the signal on detection coil as a function of linear movement L of the element and its rotation ϕ for copper rod elements with different width of steel inclusions: a) 4 mm, b) 8 mm, c) 12 mm

Results of similar measurements of amplitude and tangent of angle between signal on measuring coil and signal given on driving coil, carried out in the same conditions, but for copper rod elements with diversified steel inclusions are presented in figures 6 and 7 respectively.

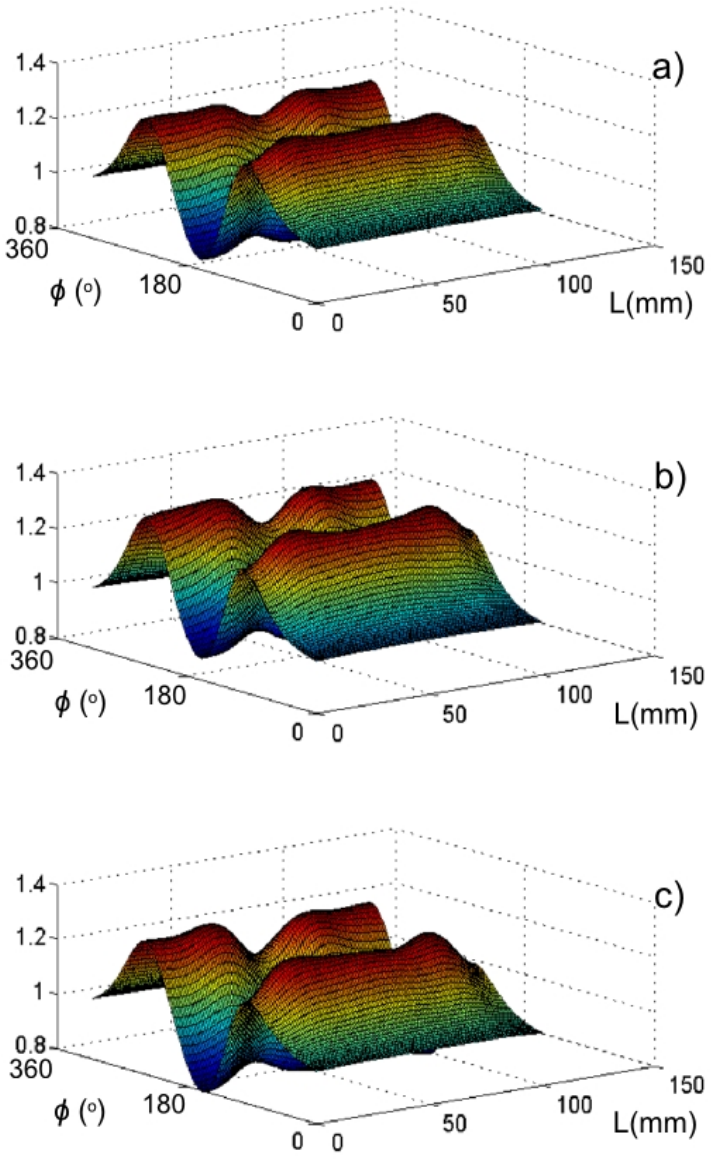

Fig. 7. Results of measurements of tangent of angle between signal on measuring coil and signal given on driving coil as a function of linear movement L of the element and its rotation ϕ for copper rod elements with different width of steel inclusions: a) 4 mm, b) 8 mm, c) 12 mm

4 Conclusions

Eddy current tomography setup presented in the paper creates possibility of tomography measurements with resolution much higher than previously reported [7]. Moreover, obtained results confirm possibility of non-magnetic inclusion in ferromagnetic cylindrical elements assessment. Value of amplitude in sensing coil changes up to 60 % during the measurements and up to 400 % for measurements of similar steel rods. Tangent of angle between signal on measuring coil and signal given on driving coil for test elements described above changed about 40 % and 60 % respectively. Repeatability of these measurements was measured by standard deviation of indication. It was about 1 % for both amplitude and tangent of angle between signal on measuring coil and signal given on driving coil.

The results presented in the paper confirm, that presented eddy current tomography setup is suitable for non-destructive testing of rod-shaped elements. During the tests, the spatial distribution of both permeability μ and resistivity ρ can be determined. It creates the possibility of detection of all types of discontinuities in construction materials, both ferromagnetic and non-magnetic.

References

1. Hsieh, J.: Computed Tomography Principles, Design, Artifacts, and Recent Advances. Wiley (2009)
2. Tamburrino, A., Rubinacci, G.: Fast methods for quantitative eddy-current tomography of conductive materials. IEEE Trans. Mag. 42(8), 2017–2028 (2006)
3. Premel, D., Mohammad-Djafari, A.: Eddy current tomography in cylindrical geometry. IEEE Trans. Mag. 31(3), 2000–2003 (1995)
4. Soleimani, M.: Simultaneous reconstruction of permeability and conductivity in magnetic induction tomography. J Electromagnet Wave 23, 785–798 (2009)
5. Soleimani, M., Tamburrino, A.: Shape reconstruction in magnetic induction tomography using multifrequency data. Int. J. Inform. Sys. Scien. 2, 343–347 (2006)
6. Ioan, D., Rebican, M.: Numerical Model for Eddy-Current Testing of Ferromagnetic Steel Parts. IEEE Trans. Mag. 38, 629–633 (2002)
7. Zhao, Q., Chen, G., Hao, J., Xu, K., Yin, W.: Numerical approach for the sensitivity of a high-frequency magnetic induction tomography system based on boundary elements and perturbation method. Meas. Sci. Technol. 24, 40–44 (2013)
8. Ke, L.: An Improved Back-Projection Algorithm for Magnetic Induction Tomography Image Reconstruction. Adv. Mater. Res. 647, 630–635 (2013)
9. Ke, L., Pang, P.-P., Du, Q.: Forward problem simulation in magnetic induction tomography based on galerkin finite element method. Chines. J. Biomed. Eng. 31(1), 53–58 (2012)
10. Wang, X., Lv, Y., Chen, Y.-Y., Jin, J.-J., Yang, D.: Simulation of forward problem for 3D eddy current in magnetic induction tomography. J. Sys. Sim. 24(4), 780–788 (2012)
11. Kai, X., Cao, Z., Mi, W., Yin, W.: A fast eddy current forward solver for EMT based on finite element method (FEM) and negligibly coupled field approximation. In: Proceedings of the IEEE Int. Conf. Imag. Sys. Tech., IST 2011, pp. 16–20 (2011)
12. Li, Q., Bai, T., Zhu, C.: Deicing excitation simulation and structural dynamic analysis of the electro-impulse deicing system. Appl. Mech. Mater. 66-68, 390–395 (2011)

Preparation, Processing and Selected Properties of Modern Melt-Quenched Alloys

Peter Švec[1], Juraj Zigo[1], Michał Nowicki[2], Dorota Jackiewicz[2], Marek Franko[3], Marek Hamela[4], Wojciech Winiarski[4], Roman Szewczyk[2], Ivan Skorvanek[5], and Peter Švec Sr.[1]

[1] Institute of Physics, Slovak Academy of Sciences
Dúbravská cesta 9, 845 11 Bratislava, Slovakia
peter.svec@savba.sk
[2] Institute of Metrology and Biomedical Engineering, Warsaw University of Technology
św. A. Boboli 8, Warsaw, Poland
szewczyk@mchtr.pw.edu.pl
[3] EVPU Nova Dubnica, j. s. c., Trenčianska 19, 018 51 Nová Dubnica, Slovakia
franko@evpu.sk
[4] Industrial Research Institute for Automation and Measurements,
Al. Jerozolimskie 202, 02-486 Warsaw, Poland
rszewczyk@piap.pl
[5] Institute of Experimental Physics, Slovak Academy of Sciences, Watsonova 47,
040 01 Kosice, Slovakia
skorvi@saske.sk

Abstract. Rapidly quenched amorphous and nanocrystalline alloys in form of thin ribbons are for several decades already among traditional materials used in construction, biomedical, catalytic and mainly electromagnetic applications. These alloys exhibit excellent properties tunable by a wide range of tools – compositional optimization, pre-preparation and post-preparation processing. The contribution focuses on recent technologies of preparation of metallic glasses with enhanced thickness and consisting of different alloy layers. Specific processing aspects to optimize the desired properties are presented. Attention is given also to possibilities of using these materials for power electronics, sensors, actuators and mechanical construction elements.

Keywords: amorphous alloys, magnetic materials, thermal treatment.

1 Introduction

Alloys prepared by rapid quenching of the melt in metastable, usually amorphous, state are known since 1959, when Au-Si based splat-quenched flakes were first prepared [1]. Since then intense effort has been devoted to the development of techniques of rapid melt-quenching with quenching rates estimated to be of the order of 10^5 K/s – 10^6 K/s, most frequently planar flow casting, as well as to the compositional design of amorphous alloys. Typical magnetic binary amorphous alloys consist of a major,

J. Awrejcewicz et al. (eds.), *Mechatronics: Ideas for Industrial Applications*,
Advances in Intelligent Systems and Computing 317, DOI: 10.1007/978-3-319-10990-9_36

usually ferromagnetic element such as Fe, Co, Ni, etc. combined with a suitable glass-forming element, in these cases usually B, Si, P, C, etc. Combination of these in order to obtain specific properties yields numerous ternary, quaternary and multicomponent metallic glasses.

Excellent soft magnetic properties of amorphous alloys have been in many aspects surpassed in 1988 by Fe-Si-B based alloys with small additions of nucleating agents such as Cu and growth-limiting elements as Nb. Such chemical composition denoted as FINEMET [2] leads upon suitable thermal treatment of originally amorphous state to the formation of nanocrystalline ferromagnetic grains embedded in remaining amorphous matrix; nanocrystals fill up usually more than 50 volume percents of the entire sample. Further research has lead to preparation of Fe-Cu-Zr-B based nanocrystalline alloys with higher saturation magnetization denoted as NANOPERM [3] or HITPERM [4], based on (Fe-Co)-Zr-B type systems. The discovery of soft magnetic nanocrystalline alloys produced by crystallization from amorphous state has been followed by discoveries of nanocrystalline alloys based on non-magnetic elements and paralleled by development of bulk metallic glasses or bulk nanocrystalline composites. Detailed information about the composition, preparation, structure, properties and applications of these materials can be found in recent reviews [5–10].

Neither nanocrystalline nor amorphous rapidly quenched alloys are used in as-cast state – their, while unique, properties are optimized and stabilized in post-preparation processing steps which may involve thermal, magnetic, mechanical or combined treatments suitably arranged in time and/or temperature sequences. A combination of such processing with compositional optimization can lead to exceptional properties tailored for specific applications [11–13].

This work presents a selected set of compositional and processing treatments in order to show the existing potential of rapidly quenched amorphous and nanocrystalline alloys.

2 Thermal and Magnetoelastic Treatment of Co-Based Amorphous Alloys

The system of the type $Co_{71-x}Fe_xCr_7Si_8B_{14}$, where x = 0 – 12 belongs to the best soft magnetic systems used in amorphous state. Its typical properties are shown in Table 1 for x = 4. Its stability, transition from ferromagnetic to paramagnetic state, relaxation and crystallization temperature intervals are shown in Fig. 1. The shape of hysteresis loop can be relatively easily influenced over a wide range by heat treatment – in magnetic field and/or under mechanical stress. Flat or rectangular shape ($Br/Bs \rightarrow 0.95$) of hysteresis loop thus can be obtained without deterioration of coercivity, which remains very low, typically below 1 A/m. An example of stress annealing on the hysteresis loop and the effect of applied tensile stress on the change of slope of the loop is shown in Fig. 2 [14].

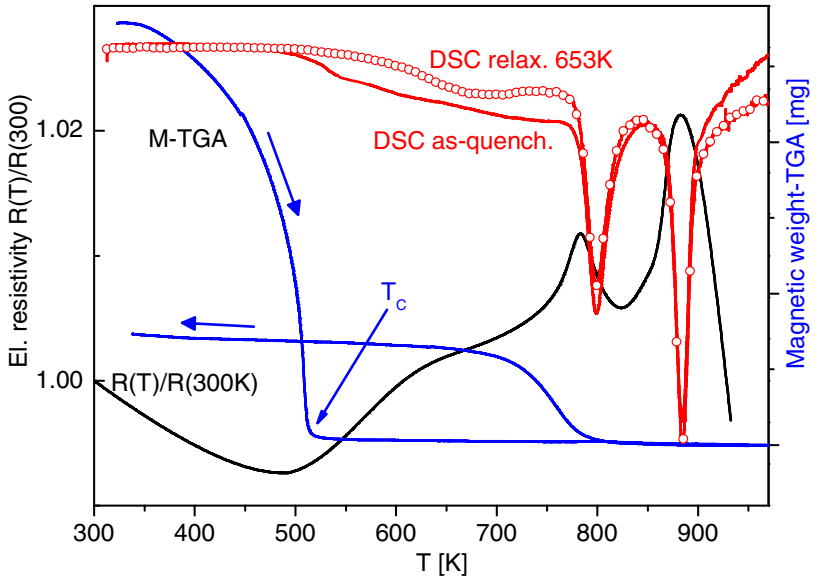

Fig. 1. DSC traces of $Co_{69}Fe_2Cr_7Si_8B_{14}$ ribbon in as-quenched state and after isothermal relaxation at 623 K/1hour and temperature dependence of "magnetic weight" and electrical resistivity (heating/cooling 10 K/min). The position of Curie temperature T_C is shown, defining potential temperature intervals for magnetic field annealing or for internal stress-relaxation annealing.

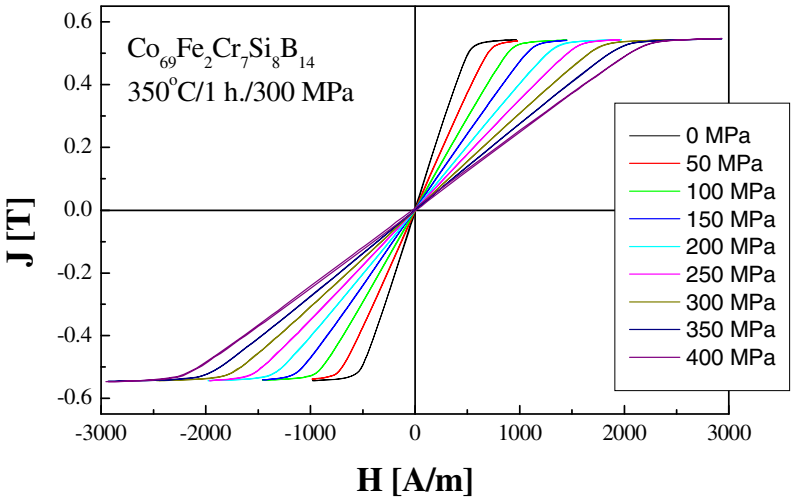

Fig. 2. The influence of applied stress on the change of shape of hysteresis loops of isothermally stress-annealed $Co_{69}Fe_2Cr_7Si_8B_{14}$ ribbon [14]

Table 1. Typical properties of the $Co_{67}Fe_4Cr_7Si_8B_{14}$ amorphous alloy

Parameter		Value
Permeability (initial)[1), 2)]	μ_{in}	$6 - 13 \times 10^3$
Maximum amplitude permeability [2)]	μ_{max}	50 000
DC coercivity	H_{cB} [A/m]	0.6 – 1
Saturation flux density (300 K)	B_S [T]	0.56 – 0.59
Curie temperature	T_C [°C]	270
Specific core losses (10 kHz, B = 0.4 T)	$p_{0.4}$ [W/kg]	29
Saturation magnetostriction	λ_S [ppm]	0.08

[1)] at H = 0.04 A/m, [2)] at f = 200 Hz

Stress-annealed $Co_{71-x}Fe_xCr_7Si_8B_{14}$ ribbons with x=2 or 4 can be conveniently used as cores for magnetoelastic strain sensors due to the response of hysteresis loop to deformation as shown in Fig. 2, high linearity in a wide interval of magnetizing fields, minimal coercivity and very low saturation magnetostriction (negative or positive, depending on the Fe content). Additionally, excellent corrosion resistance and high elastic deformation (up to 3000 ppm) predestine them for use in harsh environments. The sensor assembly, where a piece of stress-annealed ribbon ~10 cm long is inserted into a simple double-coil transformer, can be easily magnetized via primary winding while the secondary pick-up winding with a convenient yet simple feedback ensures constant induced voltage. In such setup the applied strain is almost linearly proportional to the magnetizing current according to the formula [15]

$$I_{mag} = C_1 U_2 - C_2 \lambda_S \varepsilon E \tag{1}$$

Here I_{mag} is the magnetizing current measured as voltage drop over a suitable resistor, U_2 is the induced voltage, ε is the measured strain and E is the Young's modulus of the ribbon (~200 MPa) and C_1 and C_2 are constants. The realization of the sensor and electronics [16] is shown in Fig. 3.

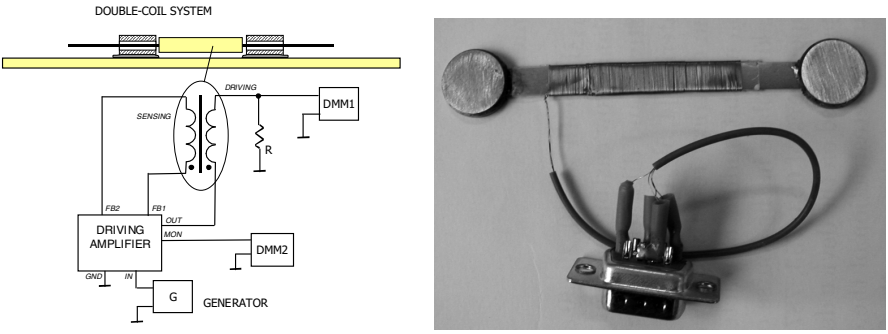

Fig. 3. Left: Measuring principle of stress sensor based on stress-annealed $Co_{69}Fe_2Cr_7Si_8B_{14}$ ribbon with feedback to ensure constant induced voltage. Magnetizing current is used as signal for strain detection. Right: stress sensor assembly.

Fig. 4. Strain sensor installation on steel gates of Gabcikovo Water Power Plant (Slovakia). Left: underwater location of the magnetoleastic sensor with plastic mechanical cover. Right: four sensor installation points on the gate (indicated by arrows) spaced vertically 10 m apart.

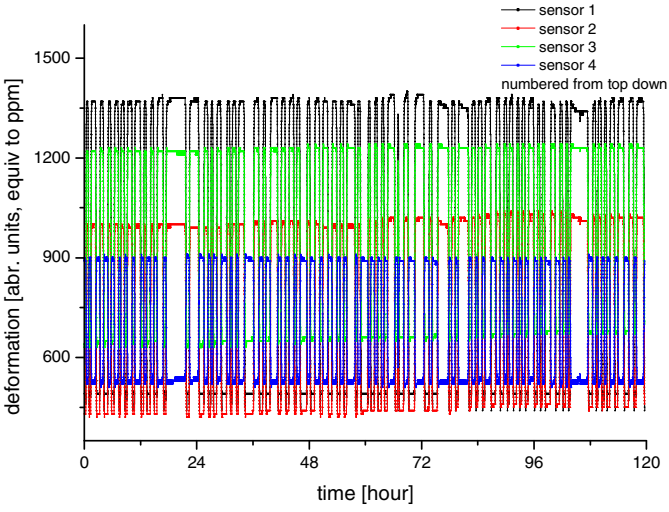

Fig. 5. Monitoring of signals from strain sensors on the gate shown in Fig. 4. during operation (opening and closing) of the gate for several days showing the frequency of gate operation, deformation by flooding of the water chamber and due to changing water level.

Using generator frequency of 5 kHz and transformer coils with 100 and 200 turns, output signals of the order of several tens of mV for U_2 and several tens of mA for

I_{mag} can be achieved, allowing high-speed readout (up to 500 Hz) with 10-bit accuracy. Operation in environments with high EMF or even in proximity of magnetic construction materials (construction steels, reinforcement cables, etc.) is feasible – if the spacing between the sensor pads and the measured material is more than 5 mm, the accuracy of the sensor remains better than 1 %.

The sensor assembly can be installed on diverse supports to facilitate installation – simple heavy-duty steel pads or thin stainless sheets can be used. These can then be attached to the measured objects such as rock or concrete walls, steel beams or gas/oil pipelines. Inexpensive waterproofing and covering against mechanical destruction makes the sensor applicable in diverse harsh environments in hydrology (Fig. 4), soil mechanics, geology as well as in conventional civil engineering. Sensors can easily be configured (mounted inside a rigid hollow tube or cube) to provide a 2D or 3D information, giving thus information about the deformation vector – strain magnitude and direction.

Heat treatment of the Co-Fe-Cr-Si-B ribbons above T_C, yet below crystallization temperature (up to ~400 °C) leads to relaxation of internal stresses. This has beneficial effect on the domain structure of the material and leads to improvement of related magnetic properties. As-quenched material exhibits coexistence of narrow zig-zag closure domains (surface) as evidence of internal quenched-in stresses together with wide bulk domains oriented generally in the direction of the long ribbon axis (Fig. 6 left). Simple thermal annealing (relaxation annealing, Fig. 6 middle) leads to disappearance of zig-zag domain patterns and increase of the size of the bulk domains. Domains after annealing in magnetic field show almost perfect preferential orientation with applied field (Fig. 6 right).

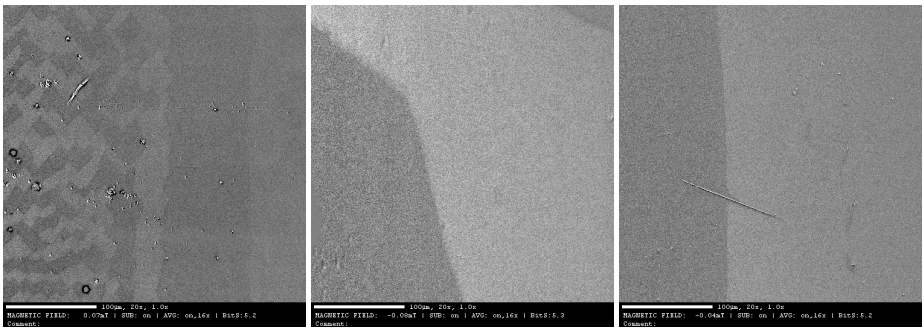

Fig. 6. MOKE images showing domain structure in as-cast state and after annealing at 240 °C for 1 hour without and with applied magnetic field 0.3 T. Marker size 0.1 mm

A necessary condition for improvement of domain structure is a careful control of surface roughness, production defects, oxides, inclusions or impurities. In order to achieve this it is necessary to quantify the roughness of both surfaces ("wheel" surface and "air" surface) of rapidly quenched ribbons. This is possible by the use of microscopy techniques which provide quantitative topological information over a significant area of the surfaces. Among such techniques are light microscopy,

confocal microscopy or digital microscopy. Typical values of average and effective roughness are about 200 nm and 300 nm, respectively, and together with topography or profile analysis represent a technology fingerprint of the material. Successful control of roughness can be achieved in the preprocessing stage by using raw materials with sufficient purity, by fluxing of the melt by suitable fluxing media (e.g. B_2O_3) prior to rapid quenching or by casting in inert media or vacuum.

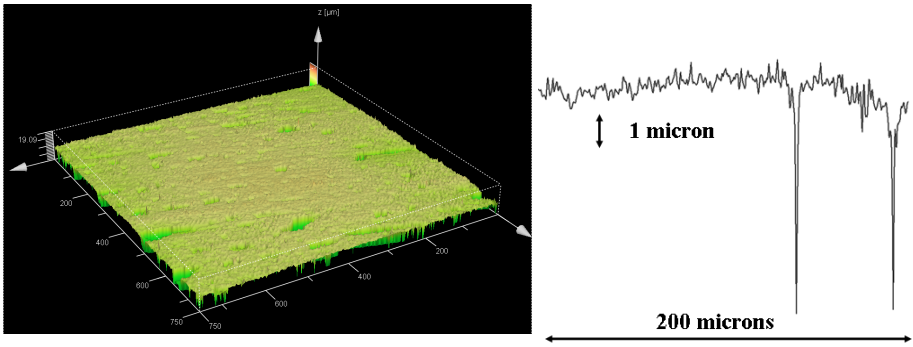

Fig. 7. Confocal microscope image of surface of as-cast Co-Fe-Cr-Si-B ribbon, "wheel" side, showing the profile of the quenching wheel imprinted onto the surface of solidified ribbon; size of area 0.75 mm × 0.75 mm. Right: 200 microns long line profile showing the effect of the wheel roughness and deeper trenches due to air pockets.

Amorphous Co-Fe-Cr-Si-B ribbons with properly tuned domain structure and magnetoelastic properties can be used for sensitive low-noise fluxgate sensors [17]. A configuration of the sensor nearly identical to the assembly shown in Fig. 3, however, with ribbon annealed without stress, is the core of such a field sensor, which exhibits high sensitivity, contrary to the behaviour of the strain sensor, in which sensitivity to external fields is minimized.

A simple, yet straightforward use of amorphous Co-Fe-Cr-Si-B ribbons, exceptionally even in as-quenched state, is for magnetic field shielding. Here the parameters of interest are, besides low coercivity, high permeability and possibility of shaping the ribbon without deterioration of these properties. This is a distinct advantage over classical Permalloy or Mumetal shieldings, which have to be annealed at high temperatures in special gasses after final shaping and where practically every disassembling implies repetition of the annealing process.

The formula relating the shielding coefficient k_{sh} of a tube with relative magnetic permeability μ_r and with outer and inner diameters $2R_2 = D$ and $2R_1$, respectively, (Fig. 8) is given as

$$k_{sh} = \frac{H_0}{H_{sh}} = \frac{\mu_r h}{D} \tag{2}$$

where $h = R_2 - R_1$ is the thickness of the shielding layer and H_0 and H_{sh} are the fields outside and inside the tube, respectively.

Shielding tubes are commonly used in synchrotrons and particle accelerators (ESRF, DESY-HADES, etc.) to shield detectors against stray magnetic fields. Ten-fold shielding of a 1.5 inch detector against external magnetic field with intensity of 3G requires 45 micron thick tube of material with μ_r ~ 10000, i.e. three layers of 20 μm thick Co-Fe-Cr-Si-B ribbon about 45 cm long. In order to produce a tube with required height (110 mm for radiation detectors) the individual ribbon rings can be conveniently glued together longitudinally into sheets of required width (Fig. 8 right).

Measurements of such shielding tubes give the value of k_{sh}~30–40, while this value increased above 60 for tubes constructed from relaxation-annealed ribbons (623 K/1hour in argon), indicating in both cases superior values of μ_r and its increase after annealing out of internal stresses.

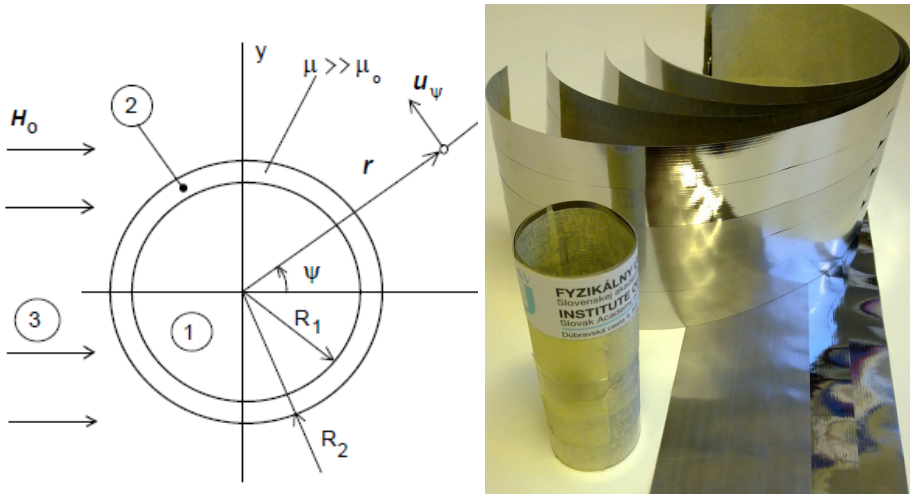

Fig. 8. Shielding tubes made from amorphous Co-Fe-Cr-Si-B ribbons. Left: scheme for calculation of the shielding coefficient. Right: Shielding tube 110 mm high with diameter 38 mm, three layers of ribbons 22 microns thick; shielding coefficient $k_{sh} > 30$.

3 Rapidly Quenched Bilayers, Trilayers, N-layers – Towards Pseudobulk Metallic Glasses

While several of the attractive properties of rapidly quenched metallic glasses are related to the typical ribbon thickness of about 20 microns, in several instance increased thickness of the material would be a technical and physical asset. However, in order to achieve the necessary high quenching rates of 10^5 K/s – 10^5 K/s, it is necessary to form a sufficiently thin layer of solidifying melt in order to achieve them.

Advantages of ribbons with enhanced thickness (intermediary between bulk metallic glassy sheets and classical ribbons) or functionally graded materials with different layers, justify the search for preparation of thicker ribbons in the form of bilayers or more layers with different or same chemical composition of the layers. Such materials, especially in the case of bilayers from different alloys, are interesting for their

intrinsically graded properties, which can lead to unique sensor or actuator principles [18], objects for investigation of stresses or stress-induced anisotropies, thermal expansion effects, etc. Such samples can also represent interesting and ready-made couples for interdiffusion or mass transport studies, especially in amorphous state or during phase transformations. Of interest is also the investigation of the structure of the interface and of the effect of the existence of two materials closely coupled to each other via a narrow planar interface – studies of additivity or convolution of properties of the respective layers. Technologically, doubling the rapidly quenched ribbon thickness while preserving the desired structural state (amorphous of nanocrystalline) may represent a significant enhancement of the packing coefficient of ribbon-based soft magnetic cores. This can be achieved without the increase of electromagnetic losses if the electrical resistivity of the bilayer is preserved on a sufficiently high level [19].

Preparation of bilayers such as bimetals or contact materials by using conventional techniques such as cold rolling, pressing, etc. is well known. The preparation of amorphous bilayers by planar flow casting techniques from two separate crucibles is possible, but technically demanding. It is, however, possible to use a single split crucible with two nozzles close to each other and with a partition between them forming two separate vessels (Fig. 9). Such an arrangement allows easy formation of two homogeneous layers quenching one after another along the whole ribbon length [20, 21].

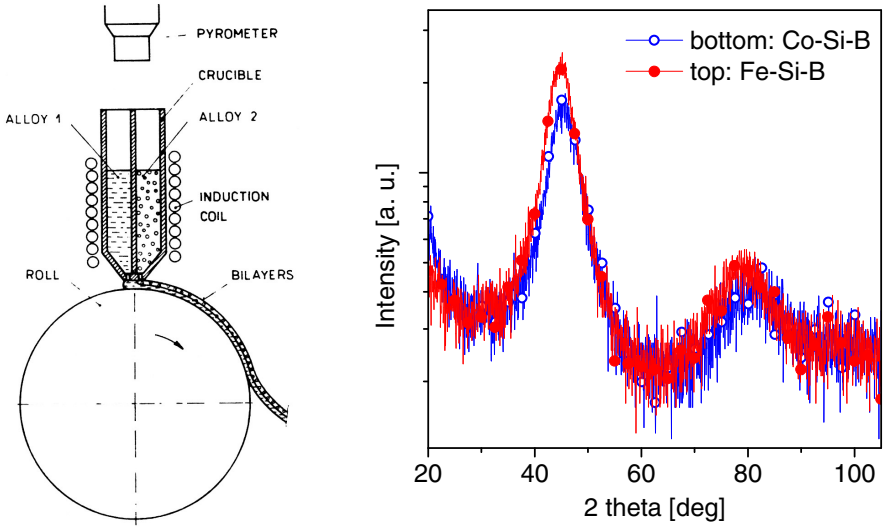

Fig. 9. Left: double nozzle split crucible for rapid quenching of bilayers with different composition [20]. Right: X-ray diffraction (Cu Kα radiation) of as-quenched $Fe_{77.5}Si_{7.5}B_{15}$ (top = air side of the ribbon) and $Co_{72.5}Si_{12.5}B_{15}$ (bottom = wheel side) bilayer showing amorphous structure of both layers; note different positions of the amorphous halos due to different chemical composition of the two layers.

Possible and interesting combinations of compositions represent bilayers composed of non-magnetic and soft-magnetic alloys, different compositions (diffusion studies, etc.) or same composition in order to study properties such as magnetization, magnetostriction, thermal expansion coefficient, etc. An example of amorphous bilayer ribbon with chemically different layers is a combination of $Fe_{77.5}Si_{7.5}B_{15}$ (air side) and $Co_{72.5}Si_{12.5}B_{15}$ (wheel side), Fig. 9 [22]. Due to different composition the crystallization of each layer takes place as different temperatures, thus it is possible to study evolution of magnetization and electrical resistivity of such couple in amorphous, layer-wise partly crystalline and fully crystalline states, Fig. 10.

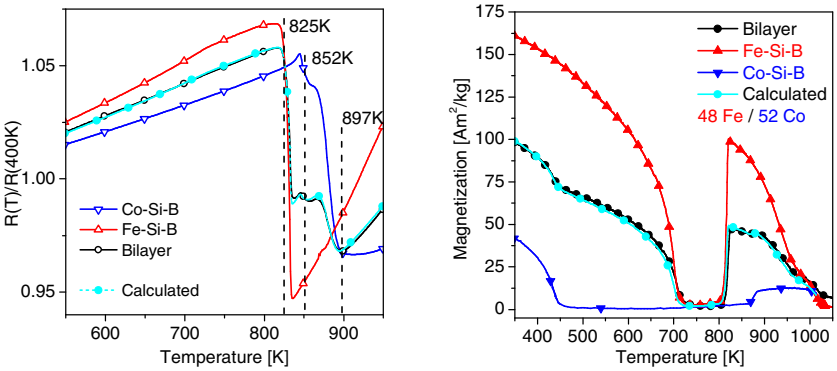

Fig. 10. Temperature dependencies of electrical resistivity (left) and magnetization (right) of rapidly quenched single-layer $Fe_{77.5}Si_{7.5}B_{15}$ and $Co_{72.5}Si_{12.5}B_{15}$ ribbons and of the corresponding bilayer ribbon. Results of modeling of the measured properties in bilayer using superposition principle are also shown.

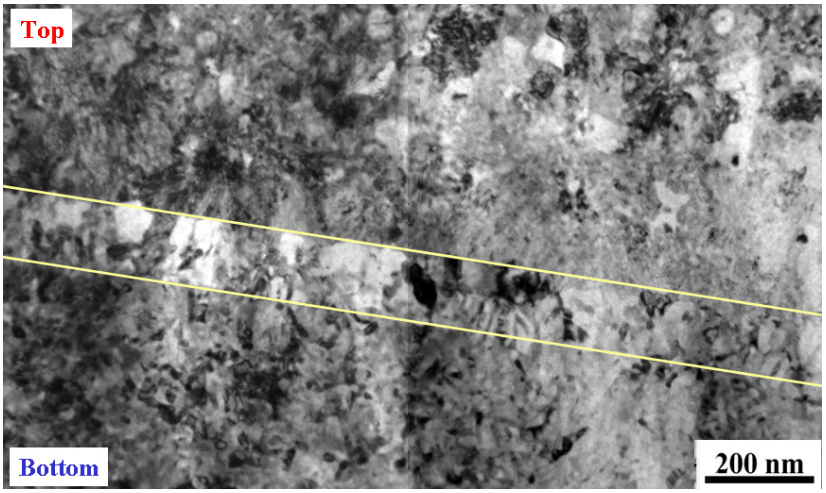

Fig. 11. TEM image of the interface between $Fe_{77.5}Si_{7.5}B_{15}$ and $Co_{72.5}Si_{12.5}B_{15}$ layers heated to 879 K showing high linearity and narrowness of the interfacial layer

Detailed structure analysis of the interface between the two layers during the entire transformation process confirms that the interface is very linear and narrow, having width less than 200 nm (Fig. 11). Probably also due to this fact the values of electrical conductivity (inverse electrical resistivity) and of magnetization comply with the superposition principle – in both cases (Fig. 10) the observed physical quantities are a linear combination of the properties of each separate layer in the entire temperature range investigated. Excellent match between measured and calculated curves for the bilayer in Fig. 10 has been obtained, allowing also calculation of the fractions (thicknesses) of the two constituent layers in the bilayer.

Potential practical use of bilayers has been demonstrated in [23], where it was shown that the inductance change of a FINEMET/Fe-SI-Nb-B bilayer deflection sensor is higher than that of individual layers. Enhanced magnetocaloric effect and favorable "table-top" effect on the temperature dependence of configurational entropy has been observed in Fe-Mo-based bilayers [24]. In a similar manner a significantly enhanced GMI effect has been obtained on Fe-Ni-Nb-B bilayer ribbons [25].

Using a triple-nozzle and single-chamber crucible it was possible to prepare, besides single layer and bilayer, also FINEMET trilayer ribbon in amorphous as-quenched state. The results of measurement of power losses of toroids from the three ribbons with thicknesses of 20, 40 and 56 μm, respectively, are shown in Fig. 12 and Table 2. Toroids were annealed at 823 K for 1 hour in Argon without and with applied transversal magnetic field. In all cases no detrimental effect has been observed either on coercivity or power losses.

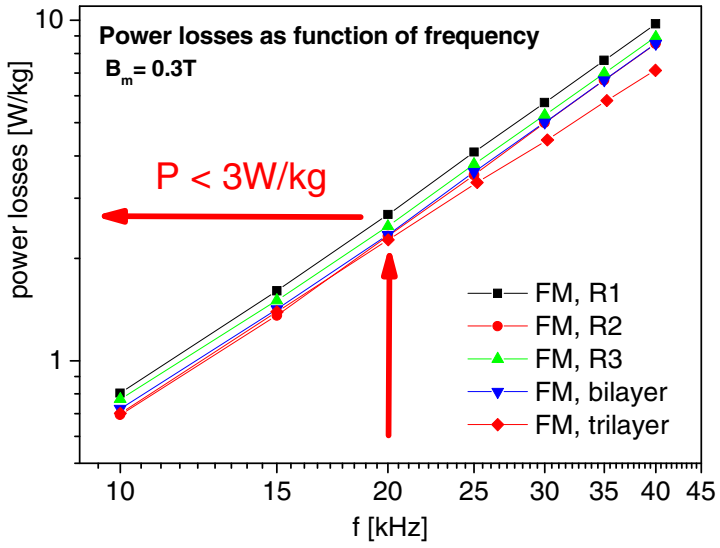

Fig. 12. Power losses as function of frequency for single-layer, bilayer and trilayer FINEMET ribbon toroids of 0.2kg each annealed at 823K for 1 hour in Argon. Magnetization B_m = 0.3 T. Symbols R1, R2, R3 represent different trials on single-layer ribbon toroids.

Table 2. Power losses and coercivity data at 20 kHz and 0.3 T of monolayer, bilayer and trilayer FINEMET toroids annealed at 823 K for 1 hour in applied transversal magnetic field

Transversal magnetic field [T]	Magnetic coercivity [A/m]			Power loss [W/kg]
	Single layer	bilayer	trilayer	
0	1.3	1.3	1.3	< 3
0.2	0.8	0.8	0.9	< 3
0.3	0.9	0.9	1.0	< 3

4 New Quasibinary Compositions for High B_S Soft Magnetic Materials

Revival of interest in one of the oldest rapidly quenched ferromagnetic alloys represents recent progress in Fe-B based system alloyed with suitable elements as Cu, P, Si and C to produce nanocrystalline soft magnetic materials with high saturation magnetization frequently approaching 1.9 T or even 2 T (with substitution of Fe by Co) [26, 27, 28]. The driving idea has been to maximize the content of ferromagnetic phases or ferromagnetic elements while simultaneously producing nanocrystalline bcc structure in amorphous matrix. Previous knowledge about nanocrystallization of FINEMET, NANOPERM and HITPERM alloys has been used to advantage for proper choice of possible nanocrystal-formers.

Rapidly quenched $(Fe_{85}B_{15})_{99}Cu_1$ in amorphous as-quenched state have been annealed throughout the first crystallization stage where nanocrystalline bcc-Fe grains were formed [29]. Fine-tuning of annealing conditions yielded composite structure with about 50 vol.% of nanocrystals.

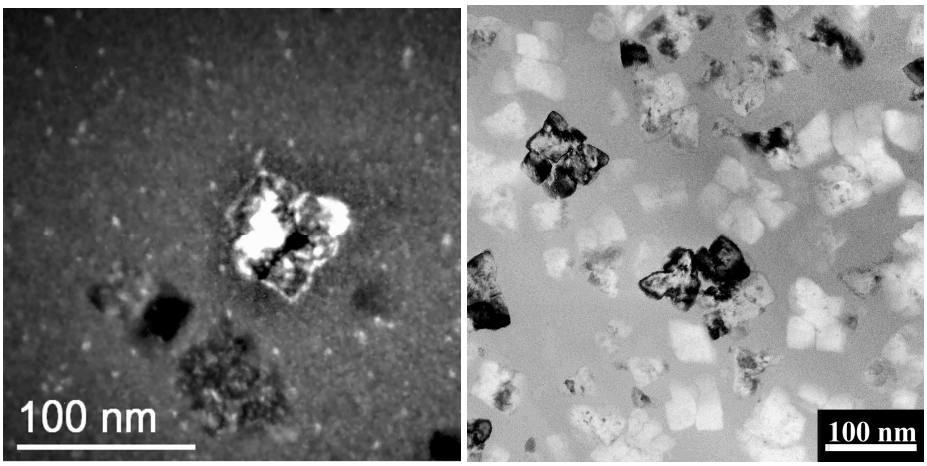

Fig. 13. TEM images of $(Fe_{85}B_{15})_{99}Cu_1$ annealed at 593 K (left) and 603 K for 1 hour showing nanocrystalline bcc-Fe nanograins in amorphous matrix [29]

Annealing has been performed in zero, transversal and longitudinal external magnetic field [29]. Transversal field annealing yielded material with the value of H_C ~ 4.2 A/m, saturation magnetization ~ 1.85 T and linear hysteresis loop suitable for fluxgate sensor material with high linearity and sensitivity 10 mV/μT (Fig. 14).

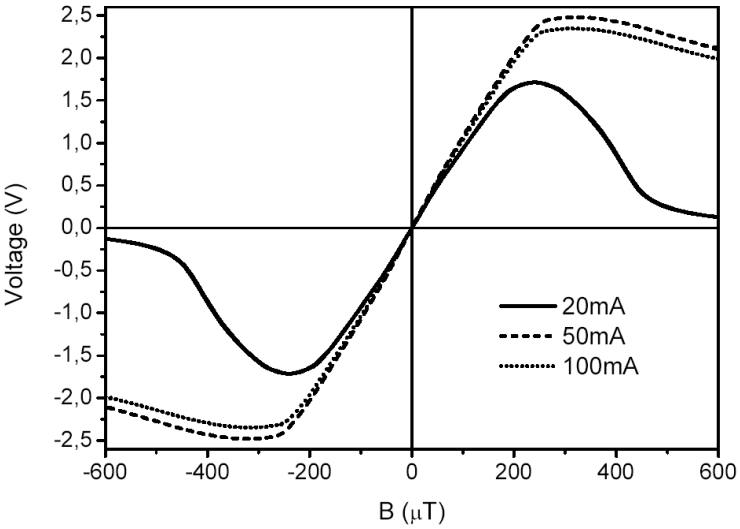

Fig. 14. Fluxgate sensor characteristics $(Fe_{85}B_{15})_{99}Cu_1$ annealed at 593 K for 1 hour in transversal magnetic field [29]

5 Shaping of Metallic Glasses

Ribbon form of metallic glasses alongside with its low thickness is of advantage in numerous applications. However, mostly planar shape or the ribbons is a drawback in certain instances, where ductility of the ribbons requires fixation of the material on substrates other than planar. Also, excellent elasticity and high yield strength predestine amorphous ribbons for advanced construction materials, if formable without loss of their properties. Diverse application such as minute springs, coils or actuators would benefit from the possibility of permanent shaping of flat ribbons.

The existence of temperature interval between the glass transition and crystallization in certain amorphous alloys, where the material is in undercooled liquid state and viscous, allows permanent shaping [30] or even deformations as high as 10000 %. This interval, however, is, except for special cases and compositions, rather narrow or non-existent – glass transition temperature lies above crystallization temperature for heating rates not exceeding hundreds of K/s.

Softening of amorphous material below crystallization, however, can be used for this purpose. High heating rates to the hot-shaping temperature region and high cooling rates after shaping are a necessary prerequisite for successful hot-shaping.

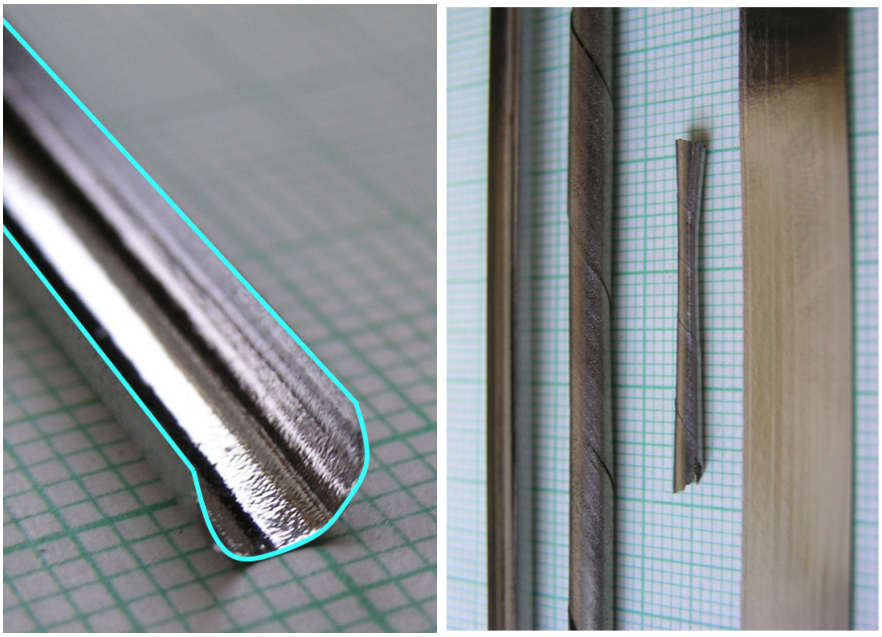

Fig. 15. Different shapes of metallic glasses obtained with Co-Fe-Cr-Si-B and Fe-Ni-Nb-B amorphous ribbons hot-shaped between 673 K and 723 K [31]

Products from hot-shaped ferromagnetic ribbons 10 mm and 12 mm wide are shown in Fig. 15. Using this technique it is possible to form long trough-shaped objects, closed tubes, semitubes or even ultrathin springs with long travel and spiral tubular shapes suitable for cable shielding without loss of amorphous structure and ductility. It is to be noted that shapes shown in Fig. 15 can be obtained from the Co-Fe-Cr-Si-B ribbons mentioned in previous chapters, obtaining thus relaxationally annealed and shaped objects with high permeability suitable for shielding and sensing as well as for mechanical construction elements.

6 Conclusion

Presented review of selected aspects of modern rapidly quenched alloys gives examples that new or novel quality can be obtained even from well-known alloy compositions either by knowledge-based compositional tailoring or by physical processing of amorphous rapidly quenched systems. Physical processing represents a combined complex treatment with specific time and temperature regimes and simultaneous application of mechanical, magnetic or electric treatment with widened processing windows. Enhancing thickness, compositional modulation and shaping of metallic glasses leads to new materials and phenomena opening a wide range of sensing, actuation, and shielding applications.

Acknowledgement. This work was supported by the Competence centre for new materials, advanced technologies and energy, ITMS code 26240220073, supported by the Research and Development Operational Programme funded by the ESDF (75 %). Projects VEGA 2/0189/14, APVV-0492-11, APVV-SK-PL-0043-12, APVV-0460-12 and CEX FUN-MAT are acknowledged for further support. Polish side (Institute of Metrology and Biomedical Engineering) was supported by statutory founds within Polish-Slovak bilateral cooperation.

References

1. Klement, W., Willens, R.H., Duwez, P.: Non-crystalline structure in solidified gold–silicon alloys. Nature 187, 869 (1960)
2. Yoshizawa, Y., Oguma, S., Yamauchi, K.: New Fe-based soft magnetic alloys composed of ultrafine grain structure. J. Appl. Phys. 64, 6044 (1988)
3. Suzuki, K., Makino, A., Inoue, A., Masumoto, T.: Soft magnetic properties of nanocrystalline bcc Fe-Zr-B and Fe-M-B-Cu (M=transition metal) alloys with high saturation magnetization. J. Appl. Phys. 70, 6232 (1991)
4. Willard, M.A., Laughlin, D.E., McHenry, M.E., Thoma, D., Sickafus, K., Cross, J.O., Harris, V.G.: Structure and Magnetic Properties of (Fe0.5Co0.5)88Zr7B4Cu1 Nanocrystalline Alloys. J. Appl. Phys. 84, 6773–6775 (1998)
5. McHenry, M.E., Willard, M.A., Laughlin, D.E.: Amorphous and Nanocrystalline Materials for Applications as Soft Magnets. Prog. Mat. Sci. 44, 291 (1999)
6. Inoue, A., Takeuchi, A.: Recent development and application products of bulk glassy alloys. Acta Mater. 59, 2243 (2011)
7. Axinte, E.: Metallic glasses from “alchemy” to pure science: Present and future of design, processing and applications of glassy metals. Materials and Design 35, 518 (2011)
8. Willard, M.A., Daniil, M.: Nanocrystalline Soft Magnetic Alloys Two Decades of Progress. In: Buschow, K.H.J. (ed.) Handbook of Magnetic Materials, vol. 21, pp. 173–342. Elsevier (2013)
9. Herzer, G.: Nanocrystalline Soft Magnetic Alloys. In: Buschow, K.H.J. (ed.) Handbook of Magnetic Materials, vol. 10, pp. 415–462. Elsevier (1997)
10. Lavernia, E.J., Srivatsan, T.S.: The rapid solidification processing of materials: science, principles, technology, advances, and applications. J. Mater. Sci. 45, 287 (2010)
11. Smith, C., Katakam, S., Nag, S., Chen, X., Ramanujan, R.V., Dahorte, N.B., Banerjee, R.: Improved soft magnetic properties by laser de-vitrification of Fe–Si–B amorphous magnetic alloys. Materials Letters 122, 155–158 (2014), doi:10.1016/j.matlet.2014.02.002
12. Herzer, G., Budinsky, V., Polak, C.: Magnetic properties of FeCuNbSiB nanocrystallized by flash annealing under high tensile stress. Phys. Status Solidi B 248, 2382–2388 (2011), doi:10.1002/pssb.201147088
13. Skorvanek, I., Marcin, J., Krenicky, T., Kovac, J., Svec, P., Janickovic, D.: Improved soft magnetic behaviour in field-annealed nanocrystalline Hitperm alloys. Journal of Magnetism and Magnetic Materials 304(2), 203–207 (2006), doi:10.1016/j.jmmm.2006.02.120
14. Kraus, L., Bydzovsky, J., Svec, P.: Continuous stress annealing of amorphous ribbons for strain sensing applications. Sensors and Actuators A 106, 117–120 (2003)
15. Bydzovsky, J., Kollar, M., Svec, P., Kraus, L., Jancarik, V.: Magnetoelastic properties of CoFeCrSiB amorphous ribbons – a possibility of their application. J. Electr. Eng. 52, 205–209 (2001)

16. Bydzovsky, J., Kraus, L., Svec, P., Pasquale, M.: Magnetoelastic strain sensors for outdoor application. J. Mag. Magn. Mat. 272-276, E1743–E1745 (2004)
17. Butvin, P., Janošek, M., Ripka, P., Butvinová, B., Švec Sr., P., Kuzminski, M., Švec Jr., P., Janičkovič, D., Vlasak, G.: Field annealed closed-path fluxgate sensors made of metallic-glass ribbons. Sensors and Actuators A 184, 72 (2012)
18. Wilson, S.A., et al.: New materials for micro-scale sensors and actuators: An engineering review. Materials Science and Engineering R 56, 1 (2007)
19. Svec, P., Svec Sr., P., Matko, I., Skorvanek, I., Kovac, J., Janickovic, D., Vlasak, G.: Phase Transformations in Amorphous Bilayer Ribbons. Solid State Phenomena 172-174, 953–958 (2011), doi:10.4028/www.scientific.net/SSP.172-174.953
20. Duhaj, P., Svec, P., Majkova, E., Bohac, V., Matko, I.: The study of phase transitions in amorphous bilayers prepared by rapid quenching. Mat. Sci. Eng. A 133, 662 (1991)
21. Sato, T., Sato, Y., Fujikura, M., Haga, Y.: Magnetic properties of Fe-based amorphous/nanocrystalline alloy bilayer ribbons. J. Mag. Magn. Mat. 157/158, 211 (1996)
22. Svec, P., Matko, I., Marcin, J., Kovac, J., Vlasak, G., Janickovic, D., Skorvanek, I., Švec Sr., P.: Structure and properties of soft-magnetic amorphous bilayer ribbons. Acta Physica Polonica A 118, 832 (2010)
23. Mitra, A., Roy, R.K., Mahato, B., Panda, A.K., Vlasak, G., Janickovic, D., Svec Sr., P.: Development of FeSiB/CoSiB Bilayered Melt-spun Ribbon by Melt-spinning Technique. J. Supercond. Nov. Magn. 24, 611 (2011)
24. Krautz, M., Hosko, J., Skokov, K., Svec, P., Stoica, M., Schultz, L., Eckert, J., Gutfleisch, O., Waske, A.: Pathways for novel magnetocaloric compounds: A processing prospect. Phys. Status Solidi C 11, 1039 (2014)
25. Varga, M., Marcin, J., Capik, M., Janickovic, D., Svec, P., Skorvanek, I.: Magnetoimpedance Effect in Field Annealed $(FeNi)_{78}Nb_7B_{15}$ amorphous and nanocrystalline bilayer ribbons. Acta Physica Polonica A 126, 122–123 (2014)
26. Ohta, M., Yoshizawa, M.: Improvement of Soft Magnetic Properties in $(Fe_{0.85}B_{0.15})_{100-x}Cu_x$ Melt-Spun Alloys. Mater. Trans. 48, 2378 (2007)
27. Svec, P., Janotova, I., Vlasak, G., Janickovic, D., Marcin, J., Kovac, J., Skorvanek, I., Svec Sr., P.: Evolution of structure and magnetic properties of rapidly quenched Fe-B based systems with addition of Cu. IEEE Trans. Magn. 46, 408 (2010)
28. Ohta, M., Yoshizawa, M.: Recent progress in high B_s Fe-based nanocrystalline soft magnetic alloys. J. Phys. D: Appl. Phys. 44, 064004 (2011)
29. Marcin, J., Klinda, A., Svec, P., Praslicka, D., Blazek, J., Kovac, J., Svec Sr., P., Skorvanek, I.: Melt-spun Fe-Co-B-Cu alloys with high magnetic flux density for relax-type magnetometers. IEEE Trans. Magn. 46, 416 (2010)
30. Aljerf, M., Georgarakis, K., Yavari, A.R.: Shaping of metallic glasses by stress annealing without thermal embrittlement. Acta Mater 59, 3817 (2011)
31. Svec, P.: Phase transformations in amorphous systems based on Fe and Ni. PhD Thesis, Institute of Physics SAS, Bratislava (2012)

Platform Supporting the Esophageal Impedance Analysis

Piotr M. Tojza, Jacek Jaworski, Dawid Gradolewski, and Grzegorz Redlarski

Department of Electrical and Control Engineering, Gdansk University of Technology, Poland
{ptojza,jjaworski,gradolewski,g.redlarski}@eia.pg.gda.pl

Abstract. The esophageal pH-impedance examination is one of the most popular diagnostic methods for identifying the upper gastrointestinal tract's diseases. Inconclusive test evaluation criteria makes it difficult to state the definite diagnosis. In this paper, the computer platform supporting the research and teaching process in the area of pH-impedance analysis is presented. Users, having a variety of mathematical and statistical methods at their disposition, have the opportunity to study and search for new methods of the impedance courses evaluation, which could translate into a significant broadening of knowledge in the field of esophageal impedance analysis. This could lead to acceleration and improvement of the upper gastrointestinal tract diseases diagnosing process.

Keywords: bioimpedance, biomedical signal processing, gastroenterology, medical diagnosis.

1 Introduction

Gastroesophageal reflux disease (GERD) is one of the most frequently diagnosed diseases of the upper gastrointestinal tract, especially in the developed countries [1]. It can be estimated that the symptoms of the disease occurring at least once in a month can be observed in about 44 % of adult American, approximately 20 % of European, 6.6 % Japan and Singapore, or 3.5 % of Korean citizens [1–3]. Whereas among the inhabitants of Africa and some Asian countries the disease is diagnosed very rarely [1]. The impact on the occurrence and development of the disease is largely caused by the lifestyle of people in the developed countries, including: type of diet, the use of intoxicants (alcohol, coffee, smoking) or stress.

Upper gastrointestinal tract diseases such as GERD or LPR – (laryngopharyngeal reflux) have onerous symptoms, which if untreated, can lead to significant reduction in quality of life, tissue lesions of the upper gastrointestinal tract, or even in extreme cases, can be the source of tumour lesions. The most common, onerous symptoms of reflux disease is the heartburn described as a burning sensation behind the breastbone, which is moving from the xiphoid towards paragraph [1] or seldom to the back [4]. During the early stage of diagnosis, the cause of a pain may be erroneously associated with ischemic heart disease.

Several studies have also reveal close correlation between diseases of the reflux of upper gastrointestinal tract and upper respiratory tract – in particular asthma. Co-occurrence of GERD was observed in 80 % of patients with asthma. This correlation

J. Awrejcewicz et al. (eds.), *Mechatronics: Ideas for Industrial Applications*,
Advances in Intelligent Systems and Computing 317, DOI: 10.1007/978-3-319-10990-9_37

can be explained, either by aspiration of gastric contents into the lungs with associated secondary bronchospasm, or stimulation of the vagus nerve in the part extending from the esophagus to the lungs, resulting in bronchoconstriction [4].

Over the years many different methods have been developed for diagnosis of the upper gastrointestinal tract diseases with different accuracy and specificity, including invasive and non-destructive method. The most frequently, invasive methods used in diagnosing lesions, associated with GERD and LPR is the measurement of esophageal pH [5] and recently developed measurement of esophagus impedance [1, 4, 6, 7]. During the procedure, inside the patient's esophagus seven sensors ale placed, collecting data on a mobile pH-impedance meter, which the patient has to carry with him. The test takes about 24 hours.

As a result of the examination, the doctor receives pH record and impedance graph, both as a time function. Skilful analysis of obtained waveform allows to find and evaluate the reflux episodes, and hence confirm the diagnosis.

The pH data analysis requires the physician to examine the whole course (the test result is presented as a waveform) in order to find certain characteristic events. The basic event that raises suspicion whether a reflux episode occurred is a drop in the pH below a certain threshold (most commonly a threshold of pH = 4). This is due the fact that the stomach acid pH is quite low (up to 3.5), whereas the normal pH of the esophagus is higher (more than 5). The physician undergoing the test must look for periods of time when the pH is under the threshold, having in mind that some of such events may be due the fact that the patients has just swallowed a bite of food that changed the esophageal pH (those events have to be excluded from the analysis). The analysis of the esophageal impedance is more complex than the pH analysis – it contains six waveforms, which all have to be analysed simultaneously. In this case, the esophageal impedance is measured, which depends on the contents. Acid contents (like stomach acid) cause the esophageal wall impedance to drop, as acid conducts electricity better than alkaline fluids. The character of the reflux is assessed by checking the value of the impedance drop in relation to the pH value in this same time. Whereas in the case of the pH the measured value is compared to a assumed threshold (like pH = 4) in the case of the esophageal impedance, no such thresholds exist. During the assessment it is more important to analyse the percentage of the values changes in relation to previous measurements, than the values themselves. There are no clear mathematics criteria which allow to automate this process, therefore, the doctor has to make the assessment based on his own knowledge and experience. Such kind of assessment is very subjective and can influence the final diagnosis. It can be estimated, that the specificity of the results, using only pH compared with pH-impedance tests, is equal to 68 %, for pathological pH below 4, 67 % positive coefficient of symptoms, or 58 % for both [8]. Population-based studies suggest that the pH tests related to the assessment of patients with gastroesophageal reflux disease are characterized by high sensitivity but relatively low specificity. For about 22 % of cases this may lead to misdiagnosis of qualifying patients suffering from GERD or LPR as healthy.

Existing computer programs assisting reflux diagnosis – often as software added to diagnostic devices – allow one to display and plainly analyse pH and impedance [3], [8]. However, this may cause the reduction of time required, but the software data

provided is not free from interpretation errors of algorithms, dedicated to searching and determination of reflux episodes.

Hence, the research on improving and accelerating the diagnostic process is the main requirement. This postulate can be achieved by studies in two areas: supporting the analysis through efficient automation of the process consisting of searching and interpretation of the characteristic pH and impedance parameters, and assistance of the teaching and research at medical universities – in order to gain the experience of medical graduates in the field of upper gastrointestinal tract diseases detection. According to the facts mentioned above, the main objective of the present study is the development of a universal and modular computer system providing comprehensive automation of the pH and pH with impedance results analysis based on both previously and newly developed procedures. Furthermore, the research on the pH analysis, based on the application developed, may be performed both at the academic and educational level. The software, developed in the National Instruments LabVIEW environment, is divided into autonomous modules allowing the user to work in any scientific area. In addition, this structure leads to fast and simple implementation of other modules of different functionality.

2 Impedance Analysis Platform

In view of the an increasing rate of diagnosed upper gastrointestinal tract diseases there is a need to take action to improve the quality of pH-impedance test data assessment. This objective should be introduced at various levels of medical care, from enriching the process of educating future physicians about the knowledge of GERD disease detection, by undergoing research activities aimed at finding new assessment methods for pH and impedance measurement results, till the improvement of the time and quality of the assessment process runs by physicians in clinical conditions. These actions will ensure a comprehensive approach and a solution to the problem of hastening and improving the accuracy of future patient's diagnosis.

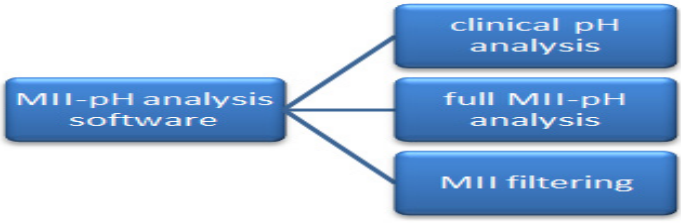

Fig. 1. Software modules

In view of these needs, a computer application supporting the analysis of pH-impedance data was developed. The computer system is of a modular design where each module can operate independently. A diagram showing the existing modules is presented in Fig. 1. Individual modules can be used in a clear and transparent manner, in accordance with the user's intentions. The software is made in such a way to easily add new modules, enriching the software with new functions.

The clinical pH analysis module can be used in a daily medical practice, when the user needs to examine only the patient's pH course. A view of the pH analysis window is presented in Fig. 2. The user can assess the data using his own pH threshold, or use the implemented methods, commonly used in clinical practice. This feature is helpful when the user is looking not only for GERD symptoms, but also LPR or other gastrointestinal diseases. As a result, the program provides the initial diagnose and all the characteristic parameters values needed in the assessment of the course. To perform a more detailed analysis, the physician should use the complete MII-pH analysis module which is focused on the analysis of esophageal impedance.

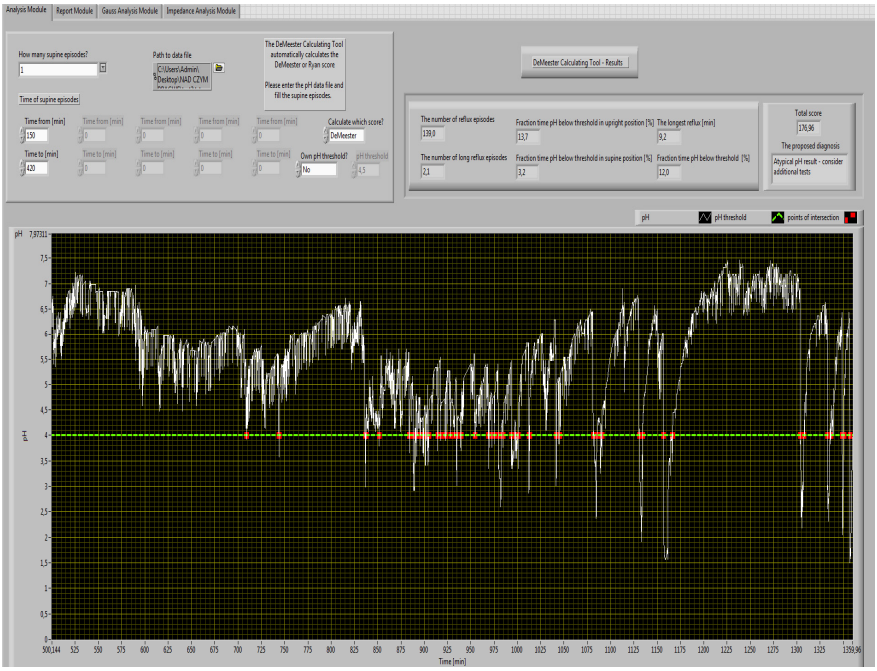

Fig. 2. An exemplary view of the pH analysis panel

Research on changes of esophageal impedance in reference to pH leads to specification of the type of recorded reflux. Two types of reflux episodes distribution are defined: referring to the chyme reaction (acid, non-acid and low-acid re-flux) and referring to the state of aggregation of the chyme (liquid, gaseous and combined reflux) [3, 9]. Differences in the records of impedance time histories for each type of the reflux are presented in Fig. 3. In reference to the analysis, the detection of liquid and combined reflux episodes is most important. Purely acidic episodes are the easiest to detect – a drop in pH below 4 and a significant (over 50 %) decrease in the impedance are recorded. Similarly to non-acid episodes, only the significant decreases in the impedance are observed, whereas the pH value remains above 4. More difficult to detect are low-acid episodes, in which a significant decrease in the impedance and a slight drop in pH (about 1 pH level) are observed.

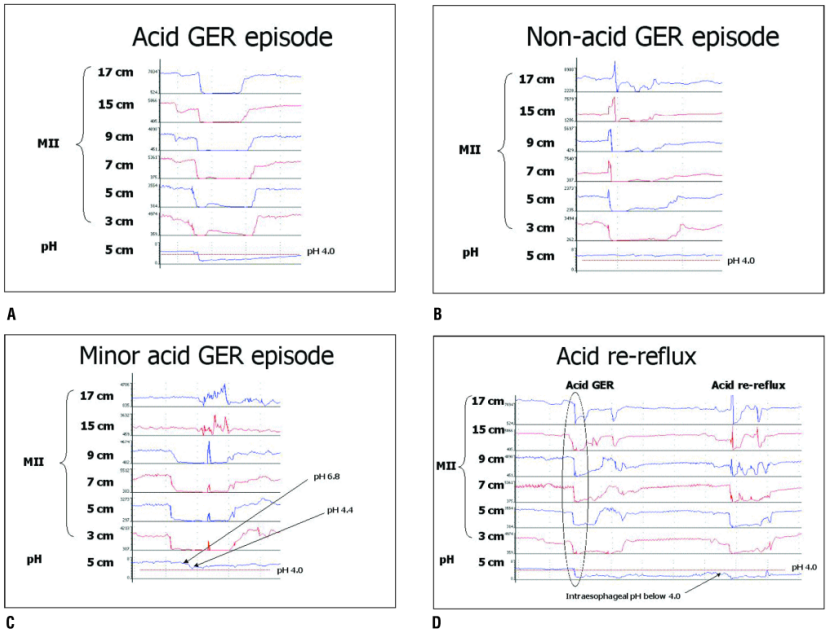

Fig. 3. Various types of reflux episodes (Source: [9])

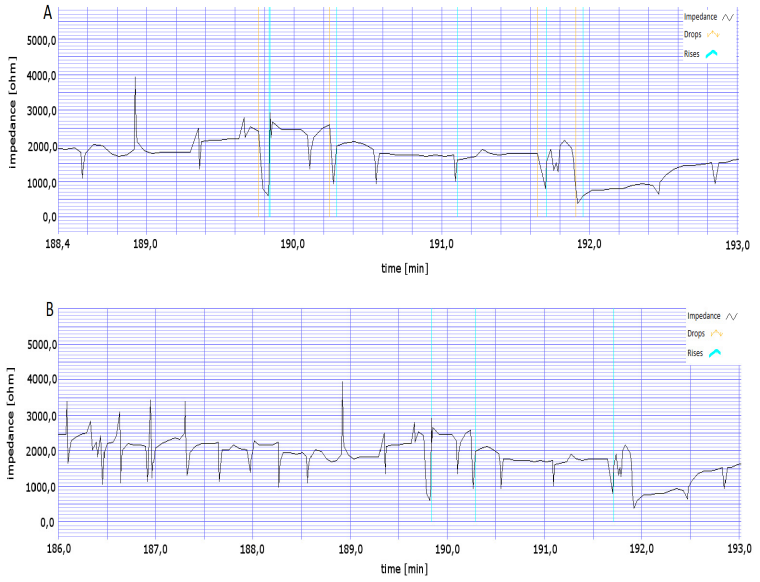

Fig. 4. Reflux episodes marked for 50 % and 80 % impedance threshold values

Due to the high degree of measurement interference, the actual slight decreases in pH can be difficult to determine and low-acidic reflux episodes are often overlooked

during the analysis process. Re-reflux episode seems equally difficult to detect, in which another drop in pH and impedance is observed in short time after the first recorded reflux episode.

In the developed application, various available tools allow one to conduct research on the defining and modifying the existing criteria for determining the specific types of reflux episodes. By the establishment of certain threshold values of pH decline or increase, the user is able to examine the indicated impedance channel. Through research, experienced physicians may use a set of patient's measurement data and try to develop a new threshold of impedance, helpful in a more accurate interpretation of the graph and in a searching for relationships between symptoms of the upper gastrointestinal tract diseases and the values of pH and impedance. In Fig. 4 an example of reflux episode determination is presented, with the use of two different threshold values: 50 % in the case of the A plot and 80 % decrease in the value in the case of the B plot.

It can be noted that in the case of the 50 % threshold, within a predetermined time interval, implemented algorithm detects four short reflux episodes. The change in threshold to 80 % prevented it from the detection of previously observed reflux episodes. In this case the implemented algorithm detects only the increases in the impedance, which are not considered as reflux episodes. In the case of both the 50 % and 80 % thresholds the algorithm is set to search for the reflux episodes of acidic type, thus only when the pH value is less than 4 (in accordance with the specific procedure, e.g. *DeMeester*). Setting own thresholds values is crucial when trying to find the optimal or best parameters for the algorithm. The researcher, having a data base of pH and impedance plots that are already diagnosed, can tune the algorithm in such a way, that it will find reflux episodes with the highest possible certainty. It is also possible to try to find such algorithm coefficients, to tune it to find reflux episodes in specific groups of patients. Different algorithm coefficients can be used in relation to test exams from men, woman, children, ethnic groups or patients that are diagnosed with certain disorders or have undergone surgery.

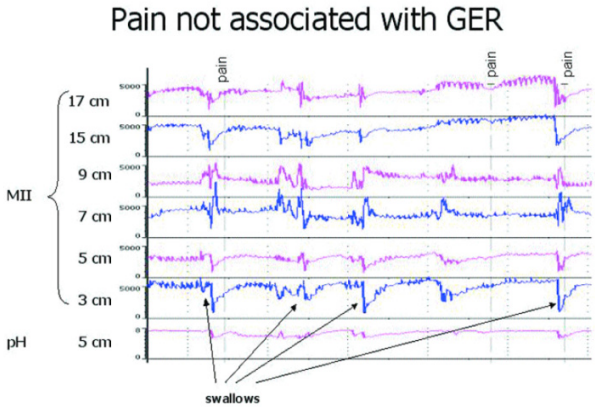

Fig. 5. Reflux episodes with marked pain symptoms (Source: [9])

Moreover, time histories examination and record of complaints marked by the patient may lead to the development of methods of various phenomena determination, related to the upper gastrointestinal tract diseases, e.g. the association of the pain in chest as one of the GERD symptoms. In Fig. 5 a change in the impedance with the pain tag determined by the patient is presented. In two cases, a significant decrease in the esophageal impedance recorded in all the channels can be noted before the pain tag. Comparing this observation with a pH record, it can be concluded that in a short time before the patient's sensation, he experienced a low-acid reflux episode. Using the developed application and possessing the appropriate amount of data, the user is able to analyse the changes in pH and impedance as a cause of various pain types and to relate the observations to existing or newly developed standards and measures assisting in various diseases diagnostics.

3 Reflux Episodes Maximal Values

As it was mentioned above, the reflux episodes are detected by tracking impedance value decrease in the relevant waveform and correlating the findings with other 5 impedance canals. Looking at the other measurement channels in the same time frame, you can also evaluate to what extent the esophagus episode took place. The developed system has the ability to mark episodes of reflux based on the analysis of esophageal impedance decrease in the value of the impedance threshold adjustable by the user. Additionally, the system presents selected characteristic elements of the found refluks episode: according to user requirement it may be a minimum, maximum, beginning or end of a reflux episode.

The system marks the reflux episode at all channels, memorizing the parameter selected by the user for further research. This feature can be useful when assessing the statistical parameters of reflux episodes and the search for some common characteristics related to the GERD symptoms.

Table 1. Minimum values of reflux episodes

Measurement canal	Time of minimal value occurrence [min]	Impedance value [Ω]
1	12.29	756.3
2	10.27	504.2
3	10.55	210.1
4	10.39	254.3
5	9.66	550.9

Five of the six minimum values of the relevant episode are grouped within a short distance of each other. Their values are shown in Table 1. As it can be seen in Fig. 3 progressive reflux is recorded by the individual probes in a small time distance. The exception is the first channel, where the minimum is located approximately in the twelve second.

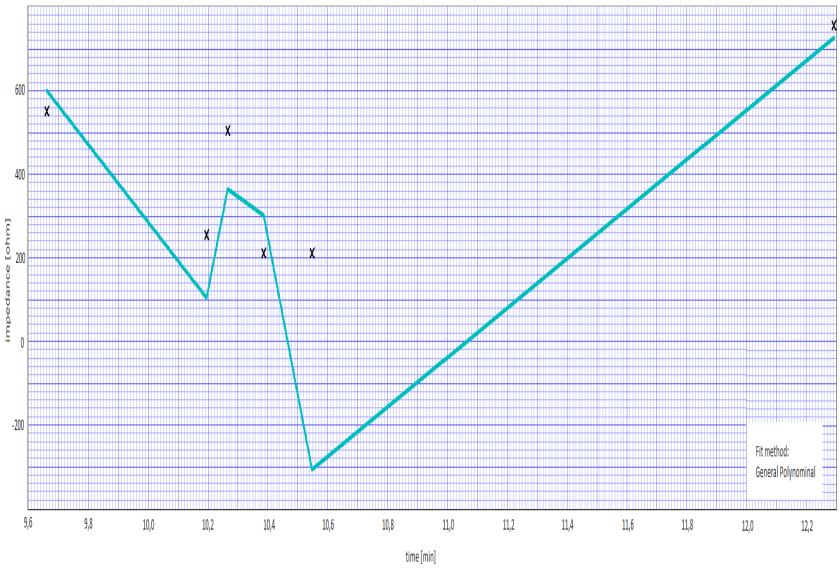

Fig. 6. An approximation of minimum values for an example reflux episode

Using the developed system, the user can perform a process of finding the best fit – approximation of the selected parameter function. There are several approximation functions to choose from: linear, exponential, power function, Gaussian, logarithmic and polynomial. In addition, the user has the possibility of setting several approximation options, such as the approximate method (from least squares, least errors or bisquare method). The effects of an exemplary method of approximation are shown in Fig. 6, whereas the function's formula is as follows:

$$y = -10.2x^5 + 2.8 \cdot 10^3 x^4 - 301.3 \cdot 10^3 x^3 + 10^6 x^2 - 443.1 \cdot 10^6 x + 4.8 \cdot 10^9 \quad (1)$$

4 Conclusions

Determining a decrease and increase thresholds of the impedance which are helpful in determining the occurrence of reflux episodes is a current issue. The developed computer platform, used in research centres, can be used in conducting research within the subject of finding and selecting increase and decrease thresholds such as [10]. Thanks to that, centres previously deprived of such capabilities will be able to conduct research on the relevant issue. This will allow to extend the range of potential scientific solutions and selected thresholds useful in the automatic detection of reflux episodes, providing the most accurate results and improving the reliability of impedance tests and diagnosis.

Further research should be focused on automatization of this process, which can be obtained by implementing in the feature extraction part the wavelet transform [11]. The identification can be made based on artificial intelligence, such as neural networks [12].

References

1. Yamada, T.: Podręcznik gastroenterologii, p. 249. Czelej, Lublin (2006)
2. Segal, I., Pitchumoni, C.S., Sung, J.: Gastroenterology and hepatology manual: a clinician's guide to a global phenomenon, p. 27. McGraw Hill (2011)
3. Tutuian, R., Vela, M.F., Hill, E., Mainie, I., Agrawal, A., Castell, D.: Characteristics of Symptomatic Reflux Episodes on Acid Suppressive Therapy. Am. J. Gastroenterol. 103(5), 1090–1096 (2008), doi:10.1111/j.1572-0241.2008.01791.x
4. Yamada, T.: Postępy w gastroenterologii, p. 90. Czelej, Lublin (2006)
5. Redlarski, G., Tojza, P.M.: Computer application supporting upper gastrointensinal tract disease diagnosis based on pH-metry analysis. Pomiary Automatyka Kontrola 59(3), 193–195 (2013)
6. Kahrilas, P.J.: Will impedence testing rewrite the book on GERD? Gastroenterology 120(7), 1862–1864 (2001), doi:10.1053/gast.2001.25290
7. Lazarescu, A., Sifrim, D.: Ambulatory Monitoring of GERD: Current Technology. Gastroenterol. Clin. North Am. 37(4), 793–805 (2008), doi:10.1016/j.gtc.2008.09.006
8. Hila, A., Agrawal, A., Castell, D.O.: Combined Multichannel Intraluminal Impedance and pH Esophageal Testing Compared to pH Alone for Diagnosing Both Acid and Weakly. Clin. Gastroenterol. Hepatol. 5, 172–177 (2007)
9. Tutuian, R., Castell, D.O.: Use of multichannel intraluminal impedance (MII) in evaluating patients with esophageal diseases. Part III: Combined MII and pH (MII-pH). Pract. Gastroenterol. 27(3), 19–28 (2003)
10. Redlarski, G., Tojza, P.M.: Computer Supported Analysis of the Human Body Surface Area. Int. J. Innov. Comput. Inf. Control 9(5), 1801–1818 (2013)
11. Gradolewski, D., Redlarski, G.: The Use of Wavelet Analysis to Denoising of Electrocardiography Signal. In: XV International PhD Workshop, OWD 2013, October 19-22 (2013)
12. Własa, M., Gotowalski, B., Jaworski, J.: Algorithm of the tuning system basing on Particle Swarm Optimization for PI controllers in the CNC milling machine. Przegląd Elektrotechniczny 88(9a) (2012)

Application of Eddy Current Sensor System and LDV Device for Ultrasonic Vibrations Measurements

Roman Wdowik[1], Piotr Nazarko[2], and Janusz Porzycki[1]

[1] Rzeszów University of Technology,
Department of Manufacturing Techniques and Automation, Poland
{rwdowik,jpor}@prz.edu.pl
[2] Rzeszów University of Technology, Department of Structural Mechanics, Poland
pnazarko@prz.edu.pl

Abstract. The article presents eddy current sensor system in respect to the measurements of vibrations for ultrasonic assisted machining processes. The comparison of eddy current sensor system with laser doppler vibrometer (LDV device) is also presented. The paper concerns the analysis of the influence of the distance between the tool and the sensor on amplitude value, filtering of raw voltage signals in MATLAB and amplitude values presentation for different tools after MATLAB and LDV software analysis. Functionality of two applied devices can be discussed after investigations. Differences in recorded amplitude's values are also discussed. The examples of measurements and test stand configuration are presented. For better understanding of hybrid machining process, it is important to indicate the possible methods of amplitude measurements and to analyze the results of measurements.

Keywords: laser doppler vibrometer, eddy current sensor system, ultrasonic assisted machining, ultrasonic assisted grinding, vibrations.

1 Introduction

Machining of hard to machine materials (e.g. advanced ceramics, nickel based alloys, hardened steel) may be assisted by applying hybrid machining processes.

One of the most effective methods to achieve high performance indexes for machine parts and tools shaping process consists in combining various physical and chemical processes, acting on workpiece material, into one machining process, which is often defined as "hybrid machining process" [3]. The use of hybrid manufacturing technologies can be a solution if new options for manufacture of a new product are needed [7]. Ultrasonic assisted machining processes are the part of these technologies.

Elastomechanical ultrasonic vibration is generated by the transformation of electric energy in piezoceramic or magnetostrictive sonic converters. A voltage generator serves to convert a low-frequency mains voltage into high-frequency electric alternating-current voltage. The generated longitudinal vibrations are periodical elastic deformations of the mechanical vibration system in the micrometer range at supersonic

J. Awrejcewicz et al. (eds.), *Mechatronics: Ideas for Industrial Applications*,
Advances in Intelligent Systems and Computing 317, DOI: 10.1007/978-3-319-10990-9_38

frequencies, that is, higher than 16 kHz [10]. These vibrations may be related to a workpiece or a tool.

Research institutes which investigate ultrasonic assisted processes, concentrate on their effectiveness. The examples of investigations are presented in [1, 4, 5, 8–13]. Process forces, cutting performance, surface quality measurements are, inter alia, published. The influence of oscillations' parameters on process course is also discussed. The main parameters are amplitude and frequency of oscillations. Ultrasonic oscillations parameters values are usually presented as constant values in these papers. The integer values of amplitude or sometimes [13] values accurate to one decimal place are presented.

Previous investigations in Rzeszow University of Technology have shown that presentation of amplitude values is a very complex issue. It depends on measuring technique, methods of data analysis and physical phenomena connected with excitation system. Thermal phenomena of excitation system caused by ultrasonic vibrations may be defined as important factor for amplitude variability during machining process realization. Amplitude values changes are observed, mainly, at resonance frequency, when the highest amplitude values are reported. Amplitude values also depend on measuring direction and selected place on the tool. These conclusions are presented after measurements of ultrasonic vibrations using laser doppler vibrometer (LDV device) on Ultrasonic 20 linear machine tool. It has been concluded that LDV measurements of ultrasonic vibrations should be compared with other measuring methods. Microscopic investigations have been carried out [14], new knowledge has been obtained and compared with other investigations [2], but inaccuracy in reading amplitudes and frequency on microscopic images are the reason for the new future investigations in this area and also searching different methods. Ultrasonic vibrations are clearly visible on oscilloscope's display if the appropriate eddy current sensor system is chosen. Thus, eddy current sensors have been chosen, as possible measuring method of ultrasonic vibrations. The usability of eddy current sensors for measurements of vibrations during process is significant, because the measurements may be carried out if cooling lubricant is applied for process realization. LDV measurements do not provide this, because laser beam cannot be reflected if liquid is applied to the machining zone. Researchers showed the usage of these sensors to measure amplitude of vibrations for ultrasonic assisted machining processes [13, 15], but the knowledge about their functionality, data acquisition, accuracy and their analysis is still insufficient and comparisons with the other devices is needed. The clear visibility of ultrasonic vibrations on oscilloscopes and visible changes in values of voltage signal during frequency changes are the base for usability predictions of eddy current sensor systems for amplitude and frequency measurements.

2 Test Stand Configuration

EddyNCDT3300 measuring system from MICRO-EPSILON with the 0.4 mm measuring range sensor ES04, together with digital oscilloscope, were the base for carrying out the eddy current measurements. Scanning laser doppler vibrometer Polytec

PSV-400 has been also applied for comparison. The eddy current sensor has been located under the grinding wheels with metal bonding or metal wheels' models (called tools in this paper). Three tools were applied for the presented results of measurements: 8 mm grinding pin with metal bond (T8), 6 mm steel model of a tool (T6), and 30 mm steel model of the 1A1 grinding wheel (T30). The ultrasonic action of a tool is possible, because the machine tool is equipped with the ultrasonic excitation system of a tool. Thus, ultrasonic vibrations are connected with a tool clamped to the special tool holder which contains piezo transducer. The complete test stand for investigations is presented in Fig. 1.

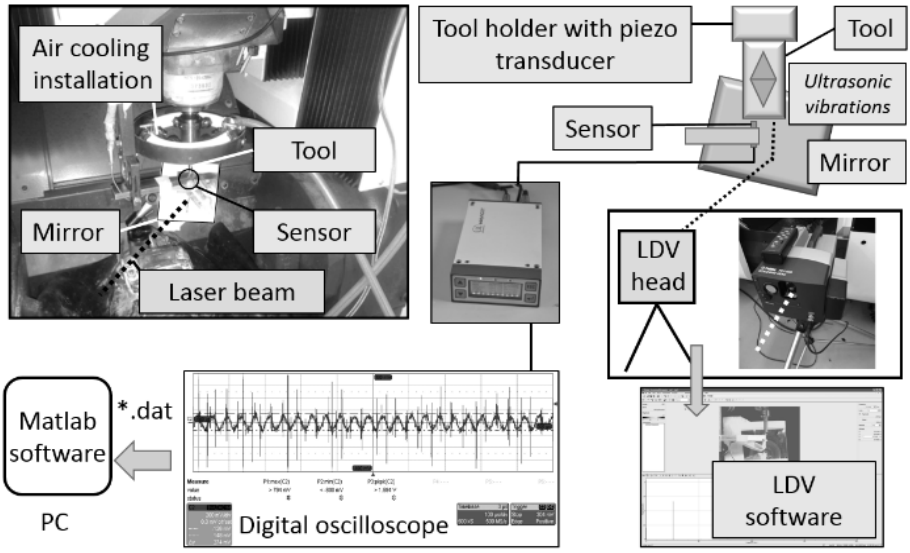

Fig. 1. Test stand for ultrasonic parameters investigations

The data presented in this paper concern influence of the distance (gap) between the tool and the sensor on amplitude value, filtering of raw voltage signals in MATLAB and amplitude values presentation for different tools after MATLAB and LDV software analysis. The measurements were carried out (for each tool) at one operational frequency, which was chosen on machine tool from the range of operational frequencies: 20,000 Hz to 30,499 Hz. Switching on the ultrasonic generator, if the sensor distance to the measuring object complies with its measuring range, causes that sinusoidal changes of analog output voltage signal, which are clearly visible for tested tools on the oscilloscope's display at resonance frequency. Fast measurements of amplitude and frequency are possible directly on the oscilloscope's display, but only for clear sine graphs. The amplitude is presented in volts then. Transformation into microns may be done if the right ratio is defined. Series of tests showed that 1 mV change in voltage should be multiplied by 0.02. Voltage signals can also be saved as *.dat format MATLAB files in oscilloscope's software and filtered in MATLAB software. Fig. 2 presents the visibility of the voltage changes for T8 and

T30 tools. These voltage signals are transferred to displacement units from the spectrum. Displacement is presented in this pictures as peak-to-peak amplitude of raw signal (A_1) and filtered signal (A_2).

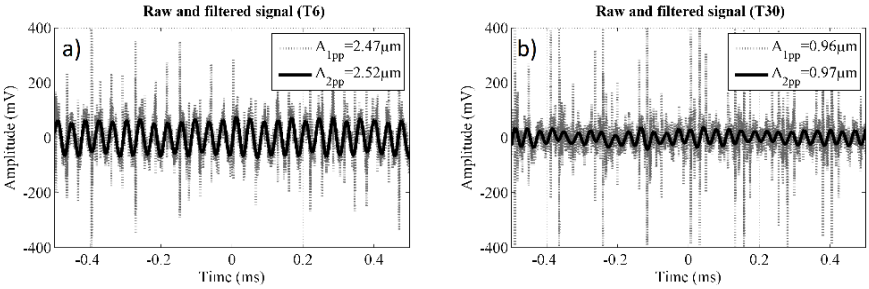

Fig. 2. Ultrasonic action visibility on the graphs created in MATLAB: a) T6 mm tool at frequency 25,800 Hz, b) T30 mm tool at frequency 28,100 Hz

The visibility of voltage changes for T8 and T6 was very good near resonance frequency and sinusoidal signal is easily observed. For T30 visibility of voltage changes was good but sinusoidal graph is distorted by signal noise. At the end of measuring range, vibrations was not clearly visible at selected frequency for T30. It was assumed that for analysis of the signal in MATLAB software, the changes of signal on oscilloscope's display must be visible. Then, signal changes between the state, when generator is switched on and the state, when it is switched off can be analyzed.

Laser Doppler vibrometer measurements can be done after concentrating the laser beam on the mirror. After reflection, the beam goes on the tool's surface. Mirror lets measure vibrations in the tool axis direction, but some inaccuracy in LDV device location must be considered. The result may be analyzed in LDV software in "Fourier Transformation mode" (FFT), "Fast scan mode" or "Time mode". For purposes of this paper FFT mode has been chosen, because values of amplitude can be read directly in vibrometer's software. Depending on the area available on the tool's face, the specific number of points (grid) was located. It was mentioned that the values of amplitude for different points of the tool's surface may not be the same. Scanning of the whole tool's surface was performed and after this procedure the eddy current sensor may have been located for comparison with LDV measurements results. It must be stated that amplitude values of smaller area on tool can be analyzed with LDV device than with eddy current sensor system, because of sensor's diameter.

3 Measurements in Eddy Current Sensor Measuring Range

The experiment consisted of single measurements in the whole (0.4 mm) measuring range of the sensor. The distance of the tool to the sensor was changed with the step of 10 μm. Distance was changed from the end of measuring range (400 μm) to 0 and back to 400 μm for T8 and T30 tools. For T6 distance was changed from the end of measuring range (400 μm) to 0 value. The 0 value means "the start of measuring

range", which is 0.04 mm distance between the tool and the sensor. EddyNCDT3300 calibration procedure in three points had also been carried out before measurements. The results showing the amplitude values for three tools are presented in Fig. 3 to 5.

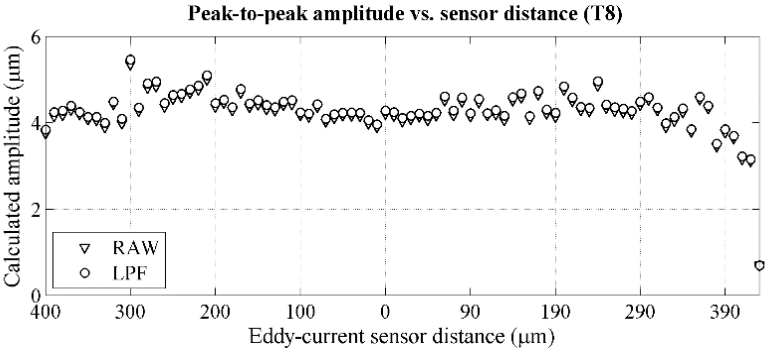

Fig. 3. Amplitude values for T8 for specific distance, frequency 23,400 Hz

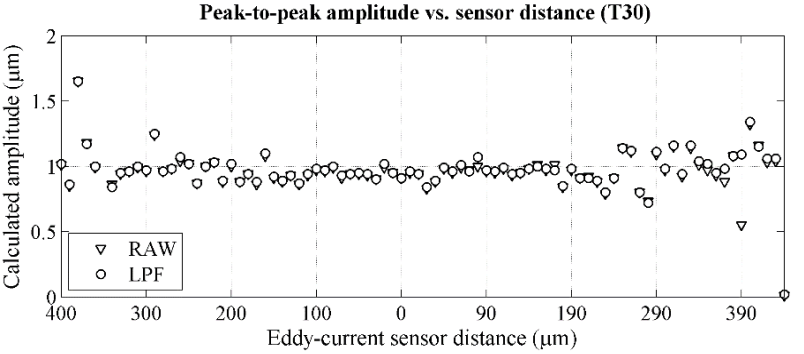

Fig. 4. Amplitude values for T30 tool for specific distance, frequency 28,100 Hz

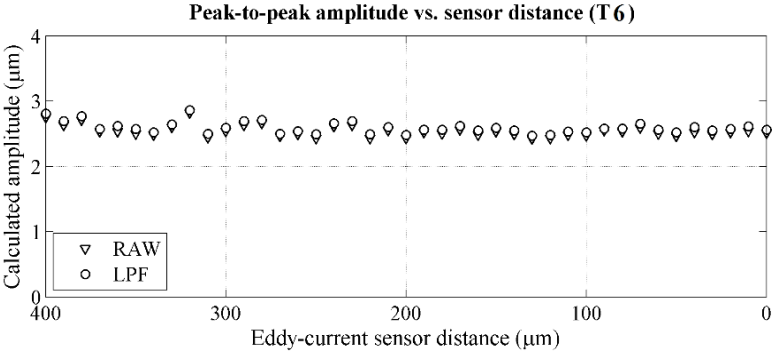

Fig. 5. Amplitude values for T6 tool for specific distance, frequency 25,800 Hz

The previous pictures present some amplitude values differences in measuring range of the sensor – mainly for T8 and T6 tool. Next tests were applied, mainly for better check of this results. For one tool T6, in one operational frequency 25,800 Hz, 100 measurements were carried out on digital oscilloscope. The results are presented in Fig. 6 and Fig. 7 after MATLAB analysis. Raw and filtered (LPF) signals are visible in these pictures and standard deviation value 0.04 μm is also computed for them.

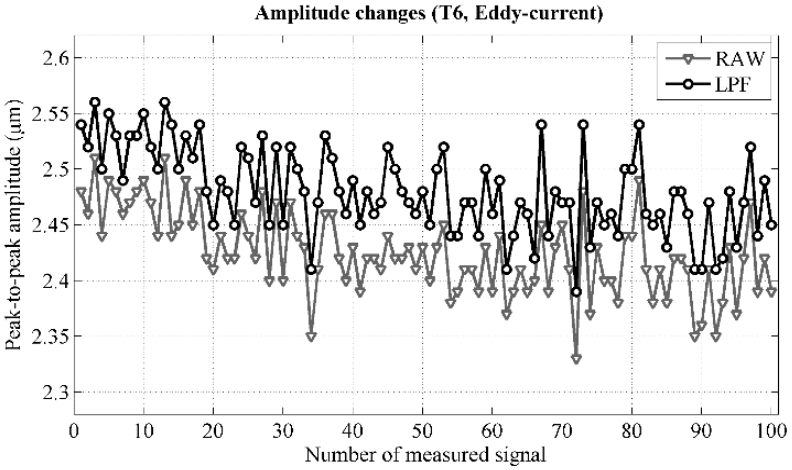

Fig. 6. Amplitude values for one selected distance after 100 subsequent measurements

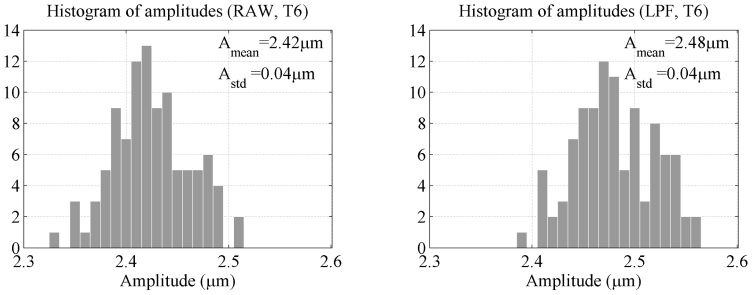

Fig. 7. Histograms of amplitudes for raw and filtered signals for T6 tool

4 Comparison of Eddy Current Sensor and LDV Device

Amplitude values (for eddy current sensor system) obtained from MATLAB was compared to the LDV measurements in FFT mode. The signal quality and magnitude depend on the scan point selection. This selection results also in a frequency spectrum form and amplitude values. On the basis of previously acquired knowledge and experience [6], vibrometer measurements were performed. This was to determine whether values after LDV measurements and eddy current sensor measurement are comparable. All the parameters were not changed for specific tool. Because of the influence of

mounting torque of the tool to the holder, tools were not remounted. Fig. 8 presents the results. Three measurements for each tool were carried out with eddy current sensor. Data was acquired on digital oscilloscope and analyzed in MATLAB environment. Raw signal amplitude values and filtered values are presented for these measurements. The highest amplitude value is reported for T8 tool and the smallest for T30 tool. The same result was obtained during LDV measurements.

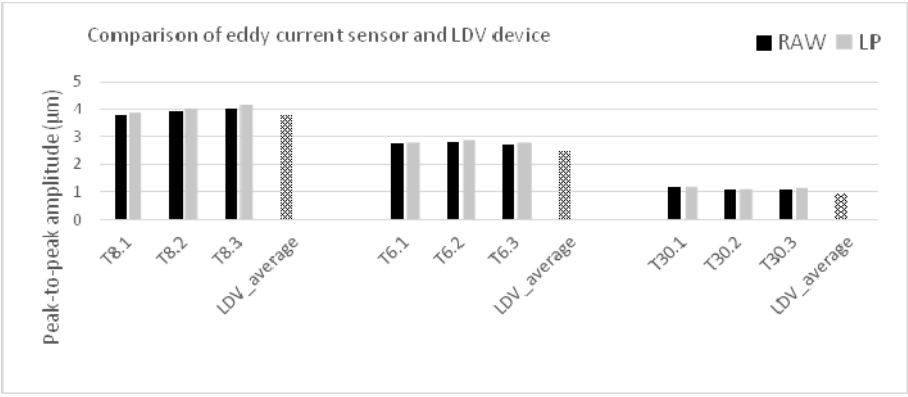

Fig. 8. Comparison of peak-to-peak amplitude values for T8, T6 and T30 tools

The results of LDV measurements mainly depend on laser beam direction, signal quality, software selections, possibilities in location of grid points. The parameters of excitation system on machine tool like temperature of tool holder also influence results of measurements. The average value for all LDV measurements for one tool is presented in Fig. 8 (48 amplitude values for T8, 20 values for T6 and 39 values for T30 were taken into account for averaging). The LDV measurements were carried out together with eddy current sensor measurements and were repeated in the next days in comparable conditions. It should be stated after all this test, that the highest amplitude values were observed for T8 tool and the smallest for T30. The same result was achieved for eddy current sensor measurements.

5 Summary

Experiments are the basis for conclusions, which indicates that many factors influence the results of measurements. Both, LDV device and eddyNCDT3300 let measure ultrasonic oscillations parameters. The analysis of the measuring gap (distance between the sensor and vibrating tool) influence on amplitude values showed that values which has been read are not the same in full measuring range of the sensor. Next tests were performed to define the reason for this fact. The most important results are presented in Figures 6 and 7 and show that even for the one distance between sensor and the tool values in subsequent 100 measurements are not the same. Analog voltage signal noise, temperature phenomena are pointed to explain this fact. The differences are comparable with those after measurements with the distance (gap) change. The

bonding material of the tool may also be important for the results of eddy current measurements. The signal on oscilloscopes' screen changed visibly for one tool at the end of measuring range. The tool holder was cooled down with pressured air but thermal phenomena may have influenced these values. The analysis for one tool and constant distance between the tool and the sensor also showed differences, so it can be stated, after all these tests, that presentation of amplitude value as constant value for this hybrid process investigations is not the best solution, because of the measuring devices characteristics and physical phenomena influencing the vibrations in resonance frequency. The values of amplitude can be defined (e.g. as average values) if dispersion of values is strongly considered. The change of the tool results in the change of measured amplitude values – the calibration was mentioned for new tool. It means that the average values for each tool are different. Comparison with LDV amplitude measurements shows that average amplitude values measured with these two apparatus are similar, but this similarity must now be defined only as clear – the biggest value for 8 mm tool and clear – the smallest value for 30 mm tool. Therefore, industrial application of eddy current sensor for ultrasonic vibrations measurements must be taken into account but thermal phenomena, measuring gap, noise in the voltage output signal, filtering method, area of the sensor to area of measuring object ratio must be strongly taken into consideration during data analysis. Beyond any doubt is the good usability of eddy current sensor for resonance frequency detection, frequency of oscillations control and amplitude level defining. For Ultrasonic 20 linear machine tool eddy current sensor ES04 may be used for resonance frequency detection and analysis of amplitude level for operational frequencies where vibrations are detected on oscilloscope.

Acknowledgments. The investigations were funded by The National Centre for Research and Development within the Applied Research Programme and the project "Technology of high performance machining of geometrically complex ceramic parts with ultrasonic assistance" (PBS2/B6/17/2013).

References

1. Akbari, J., Borzoie, H., Mamduhi, M.H.: Study on Ultrasonic Vibration Effects on Grinding Process of Alumina Ceramic (Al_2O_3). World Academy of Science, Engineering and Technology 41, 785–789 (2008)
2. Cong, W.L., Pei, Z.J., Mohanty, N., Van Vleet, E., Treadwell, C.: Vibration Amplitude in Rotary Ultrasonic Machining: A Novel Measurement Method and Effects of Process Variables. Journal of Manufacturing Science and Engineering 133, 034501-1–034501-5 (2011)
3. Kozak, J., Rajurkar, K.P.: Selected problems of hybrid machining processes Part II. Abrasive hybrid machining. Advances in Manufacturing Science and Technology 24(3), 5–24 (2000)
4. Lauwers, B., Bleicher, F., Ten Haaf, P., Vanparys, M., Bernreiter, J., Jacobs, T., Loenders, J.: Investigation of the Process-Material Interaction in Ultrasonic Assisted Grinding of ZrO_2 based Ceramic Materials. In: Proceedings of the 4th CIRP International Conference on High Performance Cutting (2010)

5. Marinescu, I.D., Hitchiner, M., Uhlmann, E., Rowe, W.B., Inasaki, I.: Handbook of Machining with Grinding Wheels, pp. 549–562. CRC Press, Taylor and Francis Group (2007)
6. Nazarko, P., Wdowik, R., Porzycki, J.: Methodology of measuring ultrasonic oscillations of tools using LDV. Pomiary Automatyka Robotyka 17(10), 96–101 (2013) (in Polish)
7. Nau, B., Roderburg, A., Klocke, F., Park, H.S.: Risk assessment of hybrid manufacturing technologies for ramp-up projects. CIRP Journal of Manufacturing Science and Technology 5(4), 228–234 (2012)
8. Qin, N.: Modeling and Experimental Investigation on Ultrasonic-Vibration Assisted Grinding. PhD thesis, Kansas State University (2011)
9. Rowe, B.W.: Principles of Modern Grinding Technology, pp. 206–210. William Andrew, London (2009)
10. Spur, G., Uhlmann, E., Holl, S.-E., Daus, N.-A.: Ultrasonic Machining of Ceramics. In: Marinescu, I.D. (ed.) Handbook of Advanced Ceramics Machining, pp. 327–353. CRC Press Taylor & Francis Group (2007)
11. Taratynov, O.V., Poroshin, V.V., Kharchenko, V.V.: Determining the Height of Surface Projections after Ultrasonic Machining. Russian Engineering Research 33(1), 53–56 (2013), doi:10.3103/s1068798X13010103, ISSN 1068-798X
12. Tawakoli, T., Azarhoushang, B.: Influence of ultrasonic vibrations on dry grinding of soft steel. International Journal of Machine Tools & Manufacture 48(4), 1585–1591 (2008), doi:10.1016/j.ijmachtools.2008.05.010
13. Ultrasonic Assisted Grinding of brittle hard materials. Final technical report of cornet project, Austria (April 28, 2010)
14. Wdowik, R., Porzycki, J., Świder, J., Nazarko, P.: Microscopic estimation of axial ultrasonic oscillations parameters. Mechanik 8(9), 417–423 (2013)
15. Wdowik, R., Porzycki, J.: Selected issues of measurements of grinding tools ultrasonic oscillations with eddy current sensors. Innovative Manufacturing Technology (edited by Magdalena Szutkowska), pp. 355–366. IZTW, Cracow (2013)

Moving Object Detection and Localization Using Stereo Vision System

Bogdan Żak and Stanisław Hożyń

Polish Naval Academy, Gdynia, Poland
{b.zak,s.hozyn}@amw.gdynia.pl

Abstract. The aim of this study was to design an moving object detection and localization algorithm able to detect and localize especially humans, vehicles and planes. We focused on classical methods for cameras calibration and triangulation techniques to calculate the position of the detected objects in a stereo vision rig coordinates frame. Verification of a proper operation of the proposed algorithm was made by conducting series of experiments. Our results indicates that the algorithm detects objects accurately and the troublesome un-stationary background regions can be excluded from detection using the presented localization method.

Keywords: object detection, object localization, stereo vision.

1 Introduction

In the last few years, visual surveillance has become a challenging area in a computer vision, especially in a view of the growing importance of these systems for security purposes [1–4]. The ultimate target in designing smart surveillance systems is to minimize the need of continuous monitoring and analyzing visual data by an operator [5]. This goal seems to be very difficult to reach without developing trusted object detection and localization algorithms.

Automatic moving object detection and localization algorithms play a fundamental role in video surveillance [1, 2]. Moving object detection algorithms are necessary to detect threat, while localization algorithms may be used for identifying a detected danger.

The algorithms have been proposed in literature for an object detection can be categorized as optical flow, a frame difference and a background subtraction [6]. The goal of the optical flow estimation is to compute an approximation to the motion field from an time-varying image intensity. Unfortunately, this method is highly complicated and very sensitive to a noise [7]. The frame difference and the background subtraction are based on a pixel difference between a reference image and a current image [8]. For the frame difference, the reference image is the previous frame. The frame difference method is able to detect objects even though the environment changes dynamically, but it is ineffective for detection of low-speed objects. In the background subtraction method, the reference frame is reconstructed from the previous

J. Awrejcewicz et al. (eds.), *Mechatronics: Ideas for Industrial Applications*,
Advances in Intelligent Systems and Computing 317, DOI: 10.1007/978-3-319-10990-9_39

video sequence, which contains an observed scene with no moving objects [9]. The background subtraction has been reported as the most popular object detection method because of its high effectiveness and simplicity in implementation. However, the simple background methods are inadequate to handle rapid lighting and shadow changes.

As a result, many more sophisticated methods, based on the optical flow, the frame difference and the background subtraction have been developed to reduce mentioned drawbacks [1–5, 7–9]. Unfortunately, these methods strongly depend on applications and camera parameters, consequently cannot be easily adopted to use for other purpose. For example, a resolution and optics of cameras, indoor and outdoor conditions, lighting and a size or a speed of potential objects play an important role in a selection and a parameterization of an image processing technique. Therefore, for the purpose of the object detection, the novel algorithm suited for our application was elaborated. This algorithm is particularly design for military applications; it is able to detect especially humans, vehicles and planes.

For the object localization, a stereo vision method was applied. Usage of two cameras enables a calculation of localizations of various points in a scene, relative to a position of cameras [10–12]. Much research in recent years has been focus on implementation of the stereo vision in a large variety of applications [12, 13]. Most of developed algorithms are based on a disparity map calculation and a triangulation technique [6, 13]. Because of the disparity map is very time consuming, in our work the triangulation algorithm was used to calculate a position of a detected object in a stereo vision rig coordinates frame.

2 Methodology

2.1 Stereo Vision

Depth perception is one of the most important tasks of computer vision systems. A stereo correspondence by calculating localizations of various points in a scene, relative to the position of cameras, allows to perform complex tasks, such as depth measurements and an environmental reconstruction [10].

Fig. 1. Sensor head with CCD-C-Z36 TV cameras (Carl Zeiss Optronics GmbH)

For the purpose of object detection and localization, the stereo rig shown in Fig. 1 was used. It is built in the sensor head, consists of the thermal imager ATTICA, the visual daylight color TV camera and the laser range finder LDM38, stable aligned to each other. The sensor head is especially designed for an advanced surveillance task under rough environmental conditions. The main components of the stereo rig are visual cameras. They combine ¼ inch CCD detector with a powerful 36 × auto-focus zoom lens providing a wide/telescopic field of view, ideally suitable within surveillance system applications. The effective picture elements of the cameras are approximately 440,000 px (752 × 582). The distance between cameras is equal to 225 mm. For the purpose of a video stream acquiring and a real-time operation, the Matrox Morphis Family frame grabber and Matrox Imaging Library were used.

2.2 Camera Parameters

In order to obtain a reconstruction of the scene depth in the Euclidean space, it is necessary to determine the camera parameters. The classic calibration methods are based on a specially prepared calibration pattern with known dimensions and a position in a certain coordinate system [11]. For the purpose of obtaining the cameras parameters, the calibration pattern with 289 markers was used. The calibration procedure (presented in detail in [11]) was conducted for 10 different zoom levels.

2.3 Triangulation

The 3D reconstruction from two views involves extracting target features from one image, matching and tracking these features across the second image, and using a triangulation method to determine position of the target points relative to the stereo rig. In this work, an extracting target area was set using the object detection algorithm on the left camera image. Next, the correspondence problem of finding the same windows in the right image was solved using correlation-based method. The Sum of Absolute Differences used in this work is presented below [12]:

$$\mathrm{SAD}(x, y, d) = \sum_{i=-w}^{w} \sum_{j=-w}^{w} \left| I_1(x+i, y+j) - I_2(x+d_x+i, y+d_y+j) \right| \tag{1}$$

where I_1, I_2 are left and right image pixel grayscale values; d_x, d_y are disparity ranges; w is window size; i, j are coordinates of the central pixel of the working window for which the similarity measurement is computed.

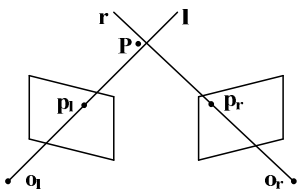

Fig. 2. Triangulation with non-intersecting rays

For the estimated central point of the windows in the left and right images (p_l, p_r), the point $\boldsymbol{P}(a, b, c)$ lies at the intersection of the two rays from o_l through p_l and from o_r through p_r respectively (Fig. 2).

Because of approximate camera calibration parameters and a target location, the two rays don't actually intersect in the space, their intersection can only be estimated as the point of minimum distance from both rays. Assuming $a\boldsymbol{p}_\mathrm{l}$ can be the ray l, $\boldsymbol{T} + c\boldsymbol{R}^\mathrm{T}\boldsymbol{p}_\mathrm{r}$ can be the ray r and $\boldsymbol{w}$ can be a vector orthogonal to both l and r, triangulation problem reduces to determining a midpoint of segment parallel to $\boldsymbol{w}$ and joins l and r. It can be computed solving the linear system of equations [12]

$$a\boldsymbol{p}_\mathrm{l} + b\boldsymbol{w} = \boldsymbol{T} + c\boldsymbol{R}^\mathrm{T}\boldsymbol{p}_\mathrm{r} \tag{2}$$

where a, b, and c are coordinates of point $\boldsymbol{P}$.

2.4 Object Detection Algorithm

One of the purpose of this study was to elaborate an reliable object detection algorithm. It means, that any changes caused by a new object should be detected, whereas un-stationary background regions, such as branches and leafs of a tree or a flag waving in the wind should be identified as a part of the background. In order to meet the above assumption, the following algorithm was proposed. To present our work in a readable way, the algorithm was divided into the main pieces and shortly described.

Grabbing 5 Consecutive Frames. Working with more consecutive frames improve detection quality, but it is very time consuming. In our experiment, there was found that 5 frames were the best choice for the further calculation. Because of the video stream consists 25 frames per second, this assumption determines that the algorithm can detect object 5 times per second. The each grabbed frame is divided then into red, blue and green channels. All operation on images were performed using Matrox Library, which represents each pixel of an image as an element of a matrix.

Image Filtration Using Median Filter. A median filter is effective against all local noise pulse, causing them to not blur in to the larger areas [13]. It eliminates those pixels of the image for which the intensity values differ significantly from the other pixel intensity values in the window. Median filtering does not introduce new values to the image, so requires no additional scaling.

Reduction of Resolution of Frames. It was presented in the literature [14], that a reduction in a resolution of an image helps decrease an influence of a noise. In the present work the resolution of frames is reduced by 50 %.

Edge Detection Using Sobel Operators. For each channel, an edge detection is carried out using Sobel operators. The advantage of using Sobel operators is that the calculated edges are very broad [15]; this feature is important for further standard

deviation calculations. Working on each color channel separately allows to improve the edge detection.

Addition Red, Blue and Green Channels. In this step the edges of 5 consecutive frames are retrieved. The red, blue and green channels of each frame are added and normalized to consist the edge information in the range from 0 to 1.

Combination of 5 Consecutive Frames. This is crucial a part of the algorithm. By combination of 5 consecutive frames we achieved that the only trace of moving object was capture on the image. Number of 5 frames allows for real-time calculations with fairly well object detection. For the smaller number of frames objects were not detected properly, whereas larger number of frames was not suited for a real-time calculation. The combined frame was calculated as

$$f_c = \left| f_{k-4} + f_{k-3} + f_{k-2} \right| - \left| f_{k-2} + f_{k-1} + f_k \right| \tag{3}$$

where f_c is the combined frame and f_k is the number of the grabbed frame.

Division the Combined Frame into 10 × 10 Pixels Blocks. In this step the combined frame are divided into 10 × 10 px blocks. For each block a mean value of all pixels is calculated. Next, the matrix composed of mean values of pixels blocks is computed.

Statistical Analysis. The matrix obtained in the previous step is used for a statistical analysis. First, the standard deviation in each row and column is calculated. Then, the value of each element of the matrix is compared to the mean value of the standard deviation of its row and column. The elements with higher values are classified as foreground and label as 1. Simultaneously, each element is compared with mean value of all elements and classified as previously. Then, each elements classified as foreground in both comparisons is labeled as containing moving object.

Morphological Opening Operation. Morphological opening operation removes small objects and details, and smooths the contour of the recognized object, without changing its size [15]. This operation is able to clean the background from almost all noises in the form of short segments defined at the stage of a statistical analysis.

3 Results

It is apparent that an universal detection and localization algorithm suited for every application is impossible to elaborate. Therefore, in this study, the algorithm particularly design for military applications, that is able to detect especially humans, vehicles and planes was performed. Verification of its proper operation was made by conducting series of experiments. Fig. 4 shows sample results of executed tests.

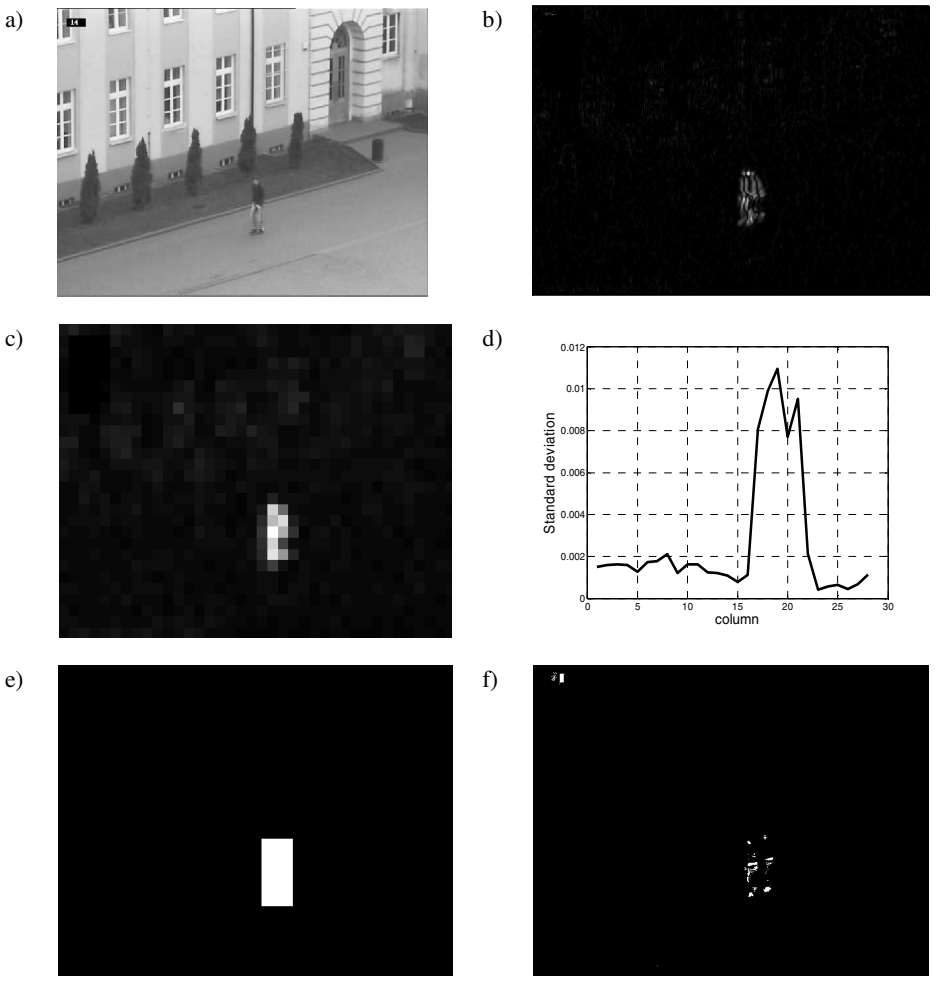

Fig. 3. Performance of the algorithm for an example video sequence

The third frame grabbed from 5 consecutive images is visible in Fig. 4a. Fig. 4b illustrates combination of the grabbed images after a median filtration, a reduction of resolution, an edge detection and an addition of red, green and blue channels. As can be seen, the only edges connected to the moving object remained on the picture.

The effect of a division the combined frames into 10 × 10 px blocks can be observed in Fig. 4c. This step is very important because identifies and connects an area where the detected object is placed.

Some results of the statistical analysis are given in Fig. 4d. By calculation of the standard deviation in each column, the accurate position of the detected object was obtained and additionally a remained noise was removed from the frame.

The standard deviation calculation is an essential step for a foreground classification and a morphological opening operation shown in Fig. 3e. The foreground classification identifies and connects an area of the detected object, whereas a morphological opening operation removes the noise and small unnecessary objects.

In order to compare our method with methods presented in the literature, basic Gaussian mixture and optical flow algorithms were implemented. For example, figure 3f illustrates the Gaussian mixture method for the example video sentence. As can be seen, the background is not updated properly and the object steel exist in its previous position. On the other hand, optical flow method appeared to be too sensitive and a lot of noise was detected as the object. It confirms that basic algorithms should not be adapted for a specific application.

The labeled area from the Morphological opening operation step is used in The Sum of Absolute Differences method for solving the correspondence problem of finding the same windows in both stereo pair images. Solving correspondence problem allows determine a position of the target relative to the stereo rig using the triangulation method. To validate the results the obtained position was compared with a hand-made measurement. For the various 3D scenes observed by the cameras, the positions of the selected points were calculated using the triangulation method. Then, the hand-made measurement using an laser distance meter was done. The experiment shown that the distance difference between the hand-made and the stereo measurement was less than 3 % for the close objects (up to 10 meters) and less than 10 % for the distant objects (up to 100 meters). The obtained results strictly dependent on geometric parameters of a stereo vision system; accuracy of a measurement decreases with distance increase between a stereo rig and a target. It could be unacceptable for applications based on an exact position, but for the target localization it seems to be appropriate.

In general, for the most obtained results, the algorithm detects objects accurately. It should, however, be noted that sometimes un-stationary background regions, such as branches and leafs of a tree or flags waving in the wind were detected as foreground. In this case the target localization algorithm can be easily used. It is possible to mark an unwanted object position and exclude the object from detection using the presented localization method. For example, branches of a tree would be passed over, whereas moving cars of humans in front of the tree, nearer to the cameras, would be detected.

4 Conclusions

The problem of smart visual surveillance for an automatic object detection and localization was studied. We have developed the algorithm particularly design for military applications that is able to detect especially humans, vehicles and planes. For the purpose of the object detection and localization, the stereo rig consist of CCD-C-Z36 TV (Carl Zeiss Optronics GmbH) cameras have been used. We have focused on a classic method of cameras calibration and triangulation technique to calculate a position of a detected object in a stereo vision rig coordinates frame.

Our results show that the algorithm detects objects accurately and the troublesome un-stationary background regions can be excluded from the detection using the presented localization method. However, one positive feature of a 3D reconstruction using a stereo vision system have not been utilized; usage of two cameras enables not only localization, but also calculation of detected object dimensions. This advantage is very important for a classification problem. Therefore, the future work will focus on the classification problem based on dimensions and shapes of detected objects.

References

1. Micheloni, C., Foresti, G.L.: A robust feature tracker for active surveillance of outdoor scenes. In: Electronic Letters on Computer Vision and Image Analysis, pp. 21–34 (2003)
2. Cucchiara, R., Prati, A., Vezzani, R.: Advanced video surveillance with pan tilt zoom cameras. In: Proc. of the 6th IEEE International Workshop on Visual Surveillance, pp. 334–352 (2006)
3. Hu, W., Tan, T., Wang, L., Maybank, S.: A survey on visual surveillance of object motion and behaviors. IEEE Trans. on Systems, Man, and Cybernetics 34, 334–352 (2004)
4. Cohen, I., Medioni, G.: Detecting and tracking moving objects for video surveillance. In: Proc. IEEE Computer Vision and Pattern Recognition, Fort Collins CO, pp. 1–7 (1999)
5. Czyżewski, A., Szwoch, G., Dalka, P., Szczuko, P., Ciarkowski, A., Ellwart, D., Merta, T., Łopatka, K., Kulasek, Ł., Wolski, J.: Multi-Stage Video Analysis Framework. In: Video Surveillance, pp. 161–216. In-Tech, Rijeka (2011), doi:10.5772/625
6. Jain, R., Kasturi, R., Schunck, B.: Machine Vision. McGraw-Hill Inc., New York (1995)
7. Zhang, D., Lu, G.: An edge and color oriented optical flow estimation using block matching. In: Int. Conf. Signal Processing, Beijing, vol. 2, pp. 1026–1032 (2000)
8. Lien, C.: Targets Tracking in the Crowd. In: Video Surveillance, pp. 232–246. In-Tech, Rijeka (2011), doi:10.5772/625
9. Ince, E.A., Naraghi, N.S., Ebrahimi, S.G.: Background Subtraction and Lane Occupancy Analysis. In: Video Surveillance, pp. 175–199. In-Tech, Rijeka (2011), doi:10.5772/625
10. Żak, B., Hożyń, S.: Distance Measurement Using a Stereo Vision System. In: Advances in Mechatronic Systems. Mechanics and Materials, vol. 196, pp. 189–197. Trans Tech Publications Ltd., Zurich (2013), doi:10.4028/www.scientific.net/SSP.196.189
11. Li, M., Lavest, J.: Some Aspects of Zoom-Lens Camera Calibration. IEEE Transactions on Pattern Analysis and Machine Intelligence, 1105–1110 (1995)
12. Cyganek, B., Siebert, P.: An Introduction to 3D Computer Vision Techniques and Algorithms. John Willey & Sons, Chippenham (2009)
13. Trucco, E., Verri, A.: Introductory Techniques for 3D Computer Vision. Prentice-Hall, New Jersey (1998)
14. Sugandi, B., Hyoungseop, K., Tan, J.K., Seiji, I.: A Block Matching Technique for Object Tracking Based on Peripheral Increment Sign Correlation Image. In: Object Tracking, pp. 1–21. In-Tech, Rijeka (2011)
15. Żak, B., Hożyń, S.: Segmentation Algorithm Using Method of Edge Detection. In: Advances in Mechatronic Systems, Mechanics and Materials, vol. 196, pp. 206–211. Trans Tech Publications Ltd., Zurich (2013), doi:10.4028/www.scientific.net/SSP.196.206

Part IV
Mechatronics

Stress Analysis of Stiffened Cylindrical Shells Under a Static Load

Paweł Biesiacki, Jan Awrejcewicz, Jerzy Mrozowski, and Jacek Jankowski

Lodz University of Technology, Poland
800045@edu.p.lodz.pl

Abstract. The presented work contains the numerical strain analysis of a ribbed shell of a rotary drum with two riding rings rigidly fixed to the drum shell. In the first stage of the conducted research a numerical model of a cylindrical shell was built with two stiffening rings of dimensions corresponding to the common constructions used in chemistry or the cement industry. The boundary conditions were set according to the mentioned machines working conditions and the model was subjected to loads corresponding to real data. The correctness of the numerical model was verified by a comparison with the results obtained in analytical calculations. The Fursow method was used in the analytical method. In the next step the model had been extended to include the longitudinal ribs added within the drum around the perimeter of the cylindrical shell. The ribs work as lifting flights. The bulk material was lifted by the flights during the rotation of the drum allowing for convective heat exchange between the material intended for drying and the air inside the shell. The bulk material was treated as a rigid body and the cylindrical shell of the drum was analyzed under its dead load. The effect of temperature was omitted due to the fact, that the drying was carried out at the temperature not exceeding 80 °C, hence the variability of Young's modulus was negligible. An analysis was performed with the use of numerical methods and commercial software ANSYS. The influence of the position of material loads on the stress and deformation reduction of the cylindrical shell and running ring was analyzed. As a result of the numerical simulations, the distribution of bending moments and the areas of greatest stress concentration and maximum strain were identified.

Keywords: ribbed cylindrical shells, stress tensor, strain tensor.

1 Introduction

The shells are widely used in various branches of industry as thin-walled constructions, especially when high stiffness and low weight are needed, for example in aerospace (aircraft constructions), marine (shipbuilding), building (roofs coverings) and chemical engineering (chemical equipment and machines). In this paper the strain's numerical analysis for a ribbed shell of a rotary drum with two riding rings rigidly fixed to the drum shell are presented. There are many monographs and papers (see for

J. Awrejcewicz et al. (eds.), *Mechatronics: Ideas for Industrial Applications*,
Advances in Intelligent Systems and Computing 317, DOI: 10.1007/978-3-319-10990-9_40

example [2–4, 6–7]), the theoretical basis and the simple cases of the shells loading are discussed. Shell buckling under dynamic loading has been described in [5]. It was also proved that the thin-walled structures are endangered with destruction, mostly due to the loss of stability, rather than to insufficient strength of the material. In [1] also the loss of stability for the cylindrical shell with initial imperfections and with applied axial load has been discussed. One of the ways to improve the shell's stiffness is the application of stiffening rings.

The rotary dryer as well as the rotary kiln are machines, in which the main part is a ribbed cylindrical shell. The calculation procedure of rotary kiln [9] as an shell radial deformation using the deformable finite elements method was presented in [9]. The results of the calculation have been compared with those obtained by Z. Banakiewicz by analytical means. On the ground of this comparison it can be stated that the strength analysis of a rotary drum by the deformable finite element method is decidedly more justified. The deformation problems for the case of the revolving boiler drum with two rolling rings fixed in a rigid way on the shell can be found in literature [10]. The two significant theories describing stresses and deformations of the shell: Goldenveizer, Novozhilow and Donnell have been discussed, and using a numerical method, a boiler drum free vibrations matter has been solved. In the work [11] a means of calculation of radial deformation of a tyre of rotary drum using the method of deformable finite elements was presented. The calculations have been carried out for the models of internodal loads expressed by the continuous load and point load. The influence of the kind of the contact between the tyre and the shell of the drum upon the character of tyre deformation and upon the magnitude of internal bending moments was analyzed. The results were compared with the results obtained on the analytical way by other authors. The finite element method (FEM) was applied to the nonlinear analysis of a cement rotary kiln [8]. The nonlinearity is due to contact conditions between the kiln body, tyres and foundations. The FEM was first used in a reduced model of the kiln in order to obtain the meshing criterion for the global model. Then, an overall FEM analysis was performed for the different operating and live loads at different positions of the rotary kiln.

2 The Fursow Method

The Fursow method is based on the Castigliano theory. Strenght calculations for the ring loaded with external forces system can be reduced to the determination of the statically indeterminate internal forces (axial force N, shear force P and bending moment M) for the ring's cross-section. The Fursow method allows one to obtain internal force in the ring in each section in dependence on the section angle. Mathematical equations are as follow [12]:

$$N = \frac{-1}{2\pi}\sum_{k=1}^{m} S_k + \sum_{k=1}^{m} S_k A_1(\varphi - \varphi_k) \tag{1}$$

$$P = \sum_{k=1}^{m} S_k A_4(\varphi - \varphi_k) \tag{2}$$

$$M = R\sum_{k=1}^{m} S_k A_1(\varphi - \varphi_k) \tag{3}$$

where: S_k – force, A_1–A_4 – auxiliary factors, R – outer radius, φ – section angle for calculations the internal forces, φ_k – the angles in the individual sections.

$$A_1 = \frac{1}{\pi}\sum_{n=2}^{\infty} \frac{\cos n\varphi}{n^2 - 1} \tag{4}$$

$$A_4 = -\frac{1}{\pi}\sum_{n=2}^{\infty} \frac{n\sin n\varphi}{n^2 - 1} \tag{5}$$

$$A_3 = \frac{1}{\pi}\sum_{n=2}^{\infty} \frac{\sin n\varphi}{n} \tag{6}$$

$$A_2 = -A_4 - A_3 \tag{7}$$

In the equations above n denotes number of applied S_k forces.

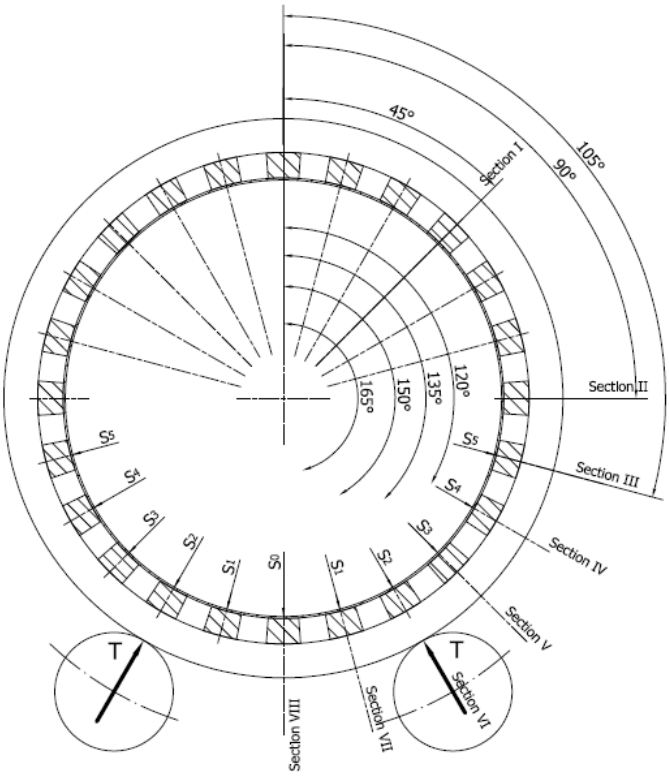

Fig. 1. The stiffened cylindrical shell under loads (*T* denotes the supports reaction forces)

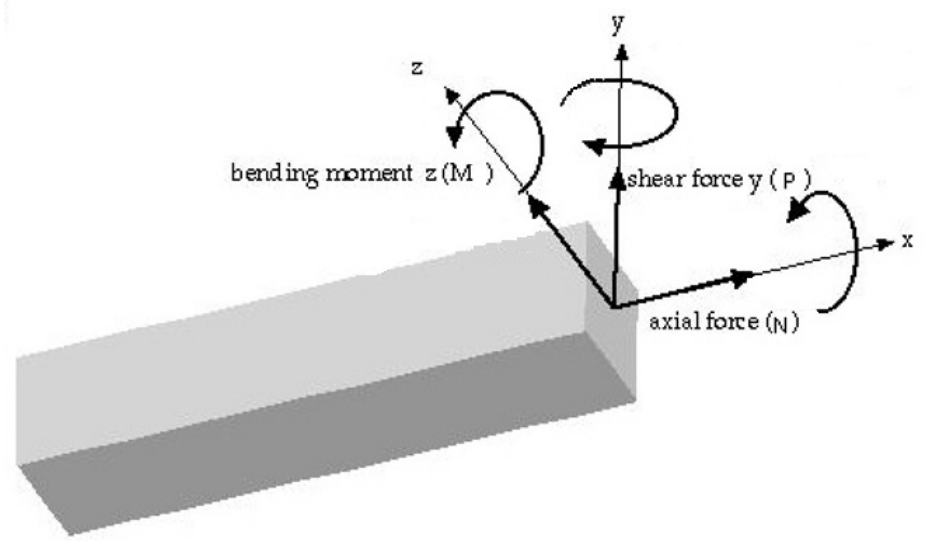

Fig. 2. The internal forces in the ring taken into account

3 Numerical Models

In order to carry out a reliable strength analysis of stiffened cylindrical shell two numerical models were constructed. The first one, devoid of strengthening ribs, served as a reference model. The second one, fitted out with flights, was more realistic. Geometric dimensions of the models were taken from real object. The radius (R) of cylindrical shell is 1.3 m and length of the cylindrical shell (L) is 10 m. The material properties were defined. Young modulus (E) is 200 GPa and Poisson's ratio (ν) is 0.3. A shell type of finite element (FE) was used to model a rotary dryer shell. This kind of FE has eight nodes and a double curvature with six degrees of freedom at each node. In the modeling of bricks forming the rings a solid element was used. This kind of FE has 20 nodes with three degrees of freedom at each node. The connection between drum dryer and the riding rings was modeled using the contact bonded elements. The boundary condition are presented in Fig. 3b. Basically, the contact nodes of the rings and the support rollers were fixed in six degrees of freedom (DoF). The analysed model was subject to the loads that come from the dead load of the machine and bulk material.

3.1 The Simplified Model

At the first stage the investigation on the simplified model was performed in order to assess the conformity of the analytical and numerical models (Fig. 3). Two cases – model with flights and model without flights was taken into account.

a) b)

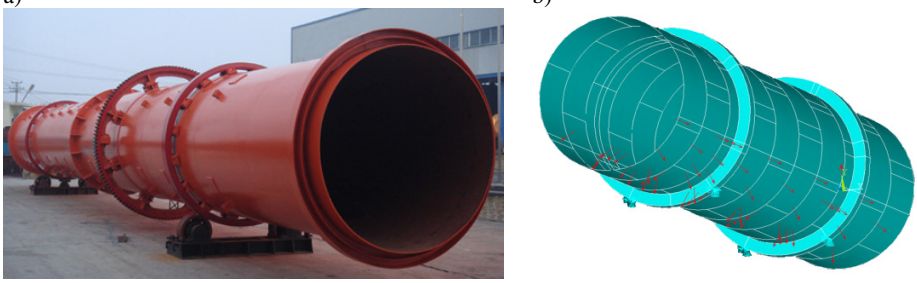

Fig. 3. The real view of the rotary dryer (a) and its corresponding numerical model (b). The cylindrical shell was subjected to load from the bulk material modeled as a the pressure about constant value corresponding to its weight (red arrows).

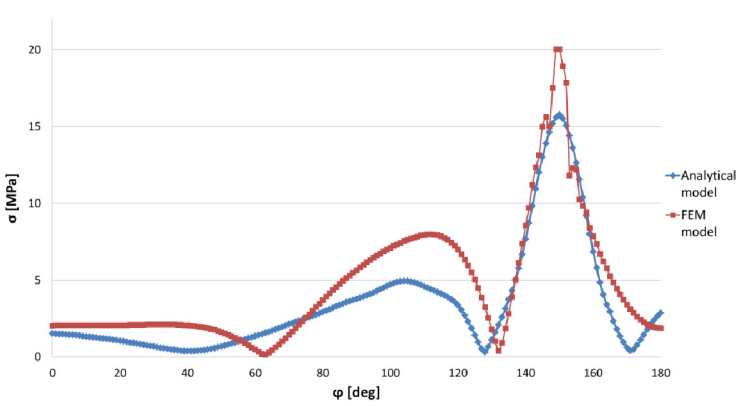

Fig. 4. The von Mises stress in the ring (σ) – analytical method vs FEM method

The numerical model was validated based on the ring stress distribution. The similar shape of the section angle-stress curves obtained for both models suggest their good accordance (Fig. 4).

3.2 Extended Model

Because the tests which were carried out using the simplified numerical model and the analytical model showed their good correspondence, in the second research stage an extended numerical model with additional flights was used (Fig. 5). During rotational movement of the rotary dryer the bulk material is lifted by the flights, and then, after exceeding the angle of repose, it slides down. Repose's angle for granular material has range from 0° to 90° and it refers to the maximum angle at which an object can rest on an inclined plane without sliding down. For modeling, critical angle of repose at the level of 45° was assumed. The lifted bulk material in the flights was modeled as the solid body weight according to the its density. Also in this case, the load from shifted bulk material was modeled as the pressure with constant value corresponding to its weight (blue arrows in Fig. 5b).

a) b)

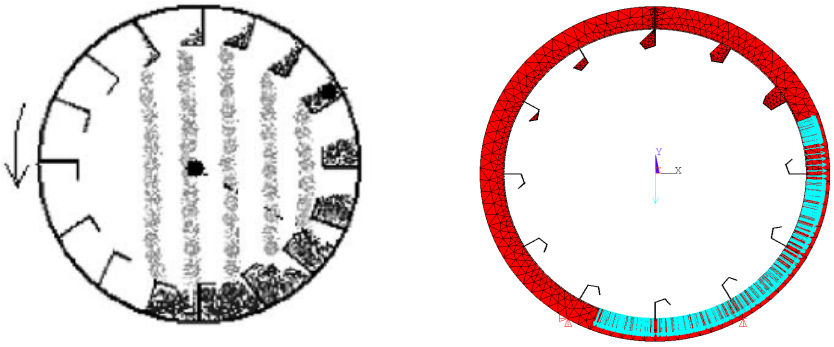

Fig. 5. A discrete slice of flighted rotary dryer: a) section view of rotary dryer with bulk material inside [13], b) numerical model with applied asymmetric load

The stress distribution for an arbitrary cross-section and a forming line (red line on the figures) was investigated. The simplifications applied to the extended model consisted of a lack of the reinforcements at the ends of the rotary dryer, caused their large deformations. Therefore, to obtain the most realistic results of analysis, a middle cross-section of the shell was chosen (Fig. 6a).

For the longitudinal analysis the line connecting the spots at the end of the shell with the highest stress magnitude was chosen (Fig. 6b).

a) b)

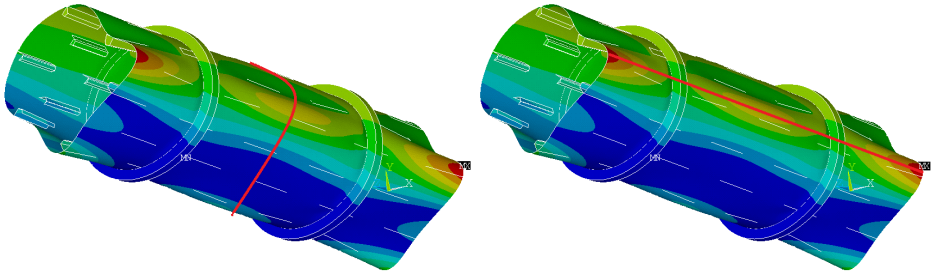

Fig. 6. Lines of the investigations of the stress distribution for cylindrical shell a) middle cross-section, b) longitudinal analysis

In following diagrams presented are the von Mises stress distributions in the ring, in the middle of the shell and along the forming line shell (Fig. 7, Fig. 9 and Fig. 10 respectively). The displacement of the middle of the shell is presented in Fig. 8.

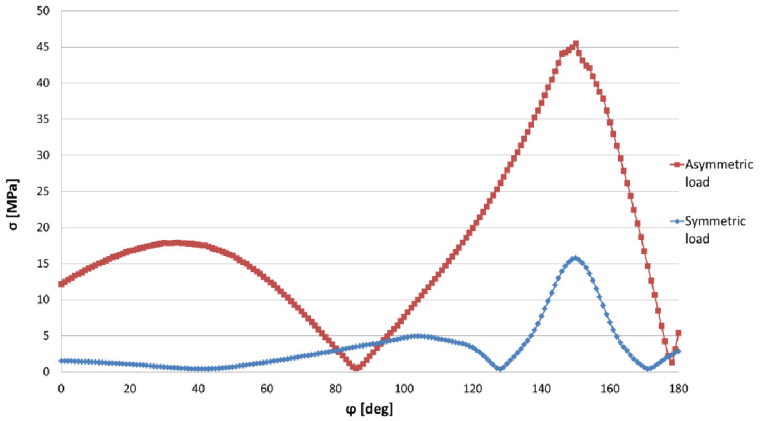

Fig. 7. The von Mises stress in the ring – symmetric vs. asymmetric load

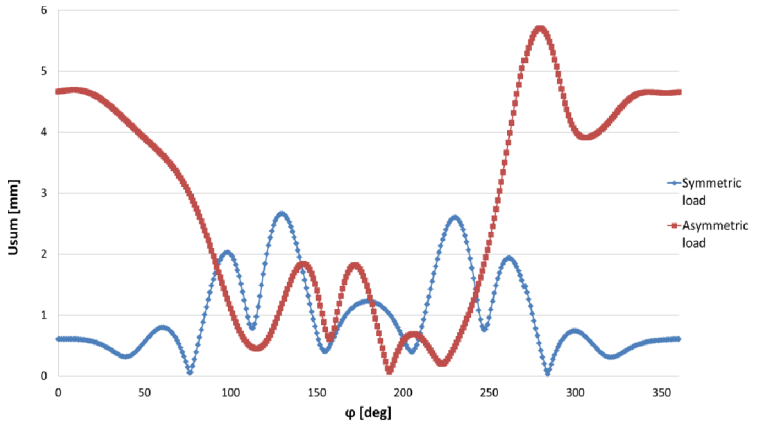

Fig. 8. The displacement in the middle of the shell

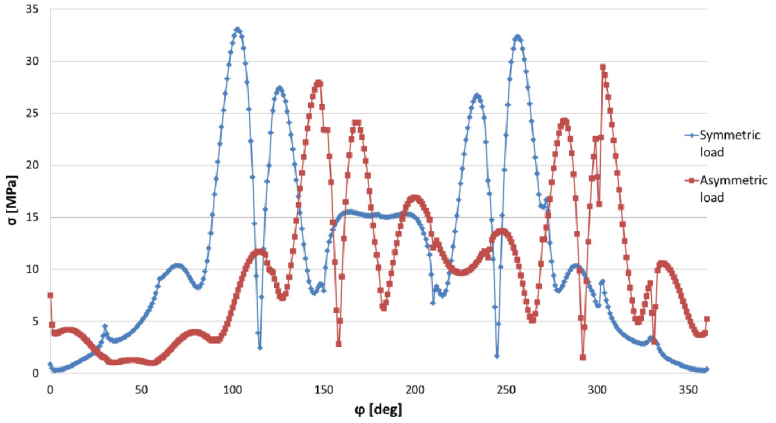

Fig. 9. The von Mises stress in the middle of the shell

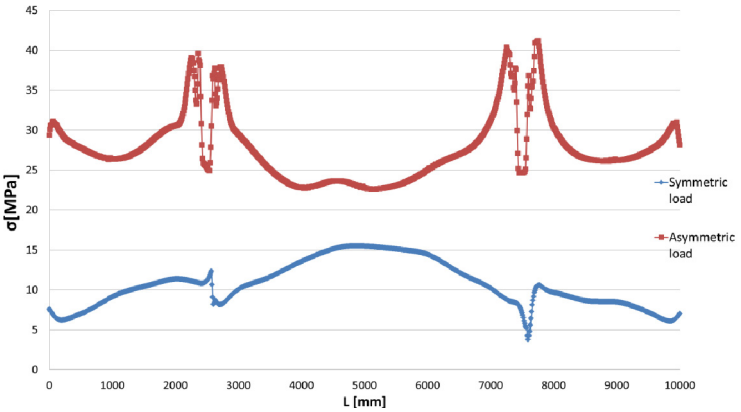

Fig. 10. The von Mises stress along the forming line

4 Conclusions

In this work a simple FEM model of the rotary ring was validated by analytical calculations using Fursow's method. The numerical model used for analysis allows one to successfully determine the areas of the greatest maximum stress and deformations. The research has shown that the loads are the greatest during the operation of the rotary dryer. That means that in order to safely design a rotary dryer asymmetric loads must be taken into account. The reduced stress values obtained during FEM analysis are smaller than the allowable ones. Maximum von Mises stresses in the analyzed ring under an asymmetric load have increased 233 % with respect to the symmetric load and were observed in the support areas. The maximum displacement of the stiffened cylindrical shell was detected in the center of the shell between the two rings.

References

1. Donnell, L.H., Wan, C.C.: Effects of Imperfections on Buckling of Thin Cylinders and Columns under Axial Compression. Journal of Applied Mechanics 17, 73–83 (1950)
2. Timoshenko, S., Woinowsky-Krieger, S.: Theory of Plates and Shells, 2nd edn., pp. 547–554. McGraw-Hill Book Co. (1959)
3. Timoshenko, S.P.: Theory of Elastic Stability, p. 439. McGraw-Hill Book Co., New York (1936)
4. Volmir, S.A.: Stability of deforming systems. Science (1967) (in Russian)
5. Volmir, S.A.: Nonlinear dynamic of plates and shells. Science (1972) (in Russian)
6. Girkmann, K.: Flächentragwerke. Book Co., Vienna (1946)
7. Flugge, W.: Stresses in shells. Springer-Verlag, Book Co., New York (1973)
8. Coz Díaz, J.J., Rodríguez Mazón, F., Garcıa Nieto, P.J., Suarez Dominguez, F.J.: Design and finite element analysis of a wet cycle cement rotary kiln. Journal in Finite Elements in Analysis and Design 39, 17–42 (2002)

9. Zachwieja, J.: Utilization of the deformable finite elements method for calculation of rotary klin shell radial deformation. Journal in Cement-Lime-Gypsum 7/69(2), 64–66 (2002)
10. Zachwieja, J.: Numerical analysis of a static load and vibrations of a rotational drum. Journal in Mechanic Scientific Papers, University of Technology and Life Sciences of Bydgoszcz 54(243), 329–345 (2004)
11. Zachwieja, J.: Radial deformation of tyres of rotary drums. Journal in Cement-Lime-Gypsum 8/70(1), 39–45 (2003)
12. Żurakowski, S., Hojarczyk, S.: Rotary kiln – designing and construction, WNT (1969)
13. Sheehan, M.E., Britton, P.F., Shneider, P.A.: A model for solids transport in flighted rotary dryers based on physical considerations. Journal of Chemical Engineering Science 60, 4171–4182 (2005)

Multiaxial Fatigue Test Stand Concept – Stand and Control Design

Michał Böhm, Mateusz Kowalski, and Adam Niesłony

Opole University of Technology, Faculty of Mechanical Engineering,
Department of Mechanics and Machine Design, ul. Mikołajczyka 5, 45-271 Opole, Poland
{m.bohm,m.kowalski,a.nieslony}@po.opole.pl

Abstract. The paper presents the concept of fatigue test stand designed for multiaxial tests. The main advantage of the test stand is the possibility to perform fatigue tests under any combination of bending and torsional moments – from constant amplitude loading with different loading frequency, phase shifts and amplitudes ratio to advanced tests under random loading with programmable stochastic dependence between loading components. The stand consists of two vibration shakers used as the source of the load being implemented on two separate levers. The levers are transferring the load in the form of bending moments to the experimental test sample. New designed control system of the stand with the use of the LabVIEW software was prepared. Currently the control of the test stand is at the stage of an open loop control. The preliminary tests have been performed with constant sinus loads. The paper also presents a finite element analysis of the maximum available stress for the test samples being used in the stand.

Keywords: multiaxial fatigue, fatigue test stand, multiaxial control.

1 Introduction

Fatigue failure phenomenon is a well-known issue in the heavy but mostly of all in the light industry. While preserving all the needed requirements regarding the shape, functionality of any construction, we also have to keep in mind the environment in which the construction is being used. Time varying forces that are constantly affecting the construction or machine element are causing the decrease of its life span. We have to take these factors into account to properly calculate the required functionality and durability. The first fatigue tests have been conducted by the German scientist August Woehler [1] in the 19^{th} century, and were set to explain the cause of fracture of railway axles by finding the maximum forces acting on them. Since then, the fatigue tests have increased their importance, as well as the construction of different fatigue test stands have evolved. Different uniaxial fatigue test stands are used in the standard fatigue testing procedures acknowledged by the ASTM Society (American Society for Testing of Materials). Those fatigue stands are used for tension-compression, bending and torsion tests. Those tests are reliable and the true material effort state is well

J. Awrejcewicz et al. (eds.), *Mechatronics: Ideas for Industrial Applications*,
Advances in Intelligent Systems and Computing 317, DOI: 10.1007/978-3-319-10990-9_41

known, and also can be described by some mathematical formulations. When it comes to multiaxial fatigue tests, the literature still hasn't found a final conclusion to this topic and the final mathematical formulation of the problem. We can use different paths in calculating multiaxial fatigue, which aren't too clear. This is also the problem for multiaxial fatigue tests, which seem to be doing far better in terms of reliability than the mathematical formulas right now. We can find a lot of different fatigue test stands like the tension-compression with torsion or bending with torsion stand, etc. It is currently a very interesting topic and it should be investigated with the use of mathematics and physics, and then the results should be proven on fatigue test stands. All these information have driven the authors to create a concept test stand that could be used in their research area which is currently the multiaxial fatigue of materials. One of the milestones set by the authors was also the creation of a reliable control of the stand. While these are the first steps in the concept stand, the authors have created an open loop control system for the stand, and are currently designing the concept for the closed loop control with the use of strain gauges and acceleration sensors [2]. The paper takes the reader through the design procedure of the stand beginning from the concept and ending on the start of the stand.

2 Description of the Fatigue Test Stand

This chapter illustrates the basic ideas behind the concept of the stand, and explains some of the necessary steps, which the constructors had to take while preparing the stand. The desired multiaxial fatigue stand has to fulfill some basic requirements for fatigue tests, which are:

- the possibility to test samples in the state of bending with torsion [3, 4],
- perform tests under cyclic and random loading conditions,
- the possibility to use standard *diabolo* test samples (Fig. 1) used for bending or torsion tests by the Department of Mechanics and Machine Design of the Opole University of Technology [5],
- allow high frequency fatigue test,
- allow to test materials under different loading ratios [6, 7].

The first step was set into going through the literature and trying to find some solutions regarding multiaxial test stands for bending with torsion. Out of some known solutions, the authors have picked those presented by Niesłony and Macha [8]. Then a block diagram regarding the stand and its control has been prepared (Fig. 2). Some available resources as the levers, basic column as well as the samples clamping jaw have been taken out of the storage of the Department. The missing parts which were the base and side plates have been done according to the dimensions of the columns and levers. The two vibration shakers that are connected to the levers have been bought, two TIRA 51144 have been chosen for that purpose. The first assembly of the stand is presented in Fig. 3. The connectors between the levers and the shakers which transfer the load have been prepared in the final stage of the design and are presented in Fig. 4. The constructors had to pick a reliable and cheap solution in

regards to control of the stand. That's why the NI LabWIEV has been chosen, and the NI Compact DAQ module to design the control system with. The NI Compact DAQ module has been filled with three main cards responsible for the signal generation and data acquisition. The signal should be transferred in the form of voltage to two amplifiers in the same time, without any phase shift. The vibration and strain values should be used in the process of compensation of the transferred voltage to the amplifiers.

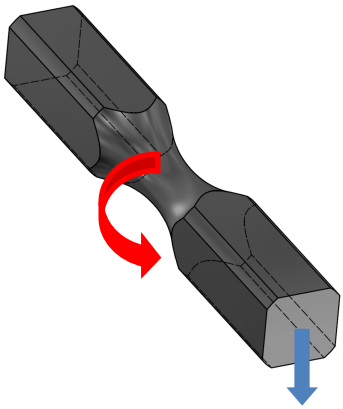

Fig. 1. Diabolo test sample used at the DMMD with the bending and torsion moment imposed on it

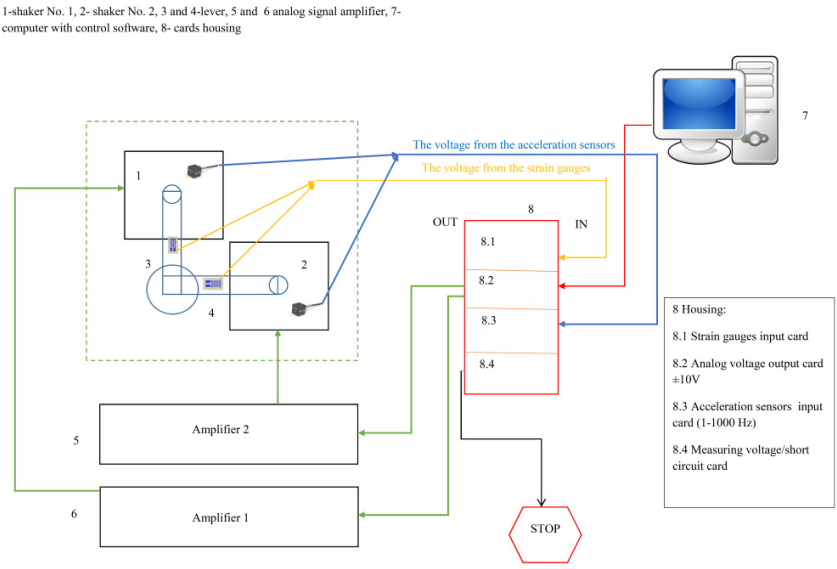

Fig. 2. The block diagram of the concept control for the multiaxial fatigue test stand

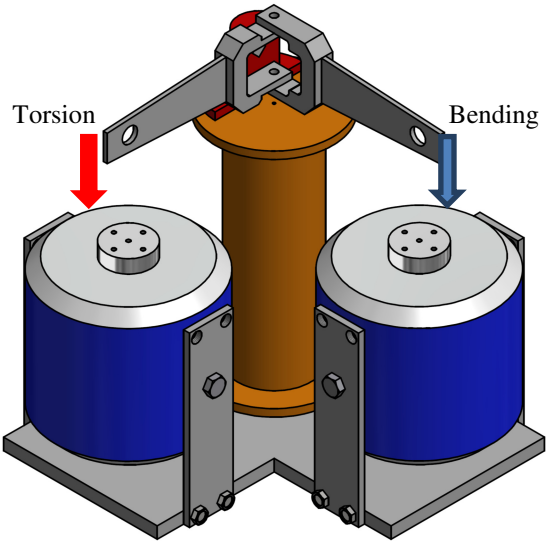

Fig. 3. First concept test stand model assembly – shows the purpose of the levers for torsion and bending

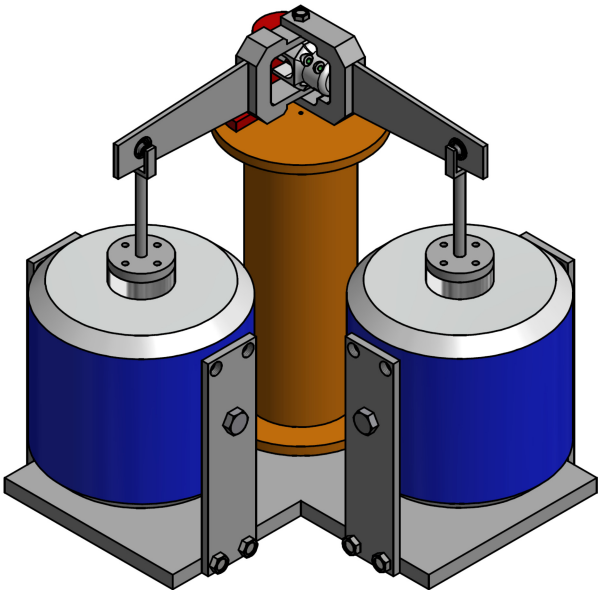

Fig. 4. Test stand second concept assembly, with the connectors between levers and test sample as well as between levers and vibration shakers

3 Parameters and Construction of the Test Stand

The concept multiaxial fatigue test stand has been assembled and is presented in Fig. 5. For the control the NI Compact DAQ has been used and is presented in Fig. 6 with a brief specification of used cards. The control signal is generated within voltage values between ±10 V. The strain values are being red out of the strain gauges that are being connected to the bridge module. The acceleration values are being read through the acceleration sensors connected to the vibration sensor card. Regardless to some analytical calculations of the construction, the authors have made a finite element method simulation of the maximum available stress state for the diabolo test samples made out of S355J steel, and it is presented in Fig. 7. The simulation allowed the authors to gain information about the places of maximum stresses in the stand. The expected parameters of the test stand are presented in Table 1. The acquisition diagram is presented in Fig. 8 for an open loop control. All applications were created in LabVIEW. The authors have used standard measurement data acquisition blocks which allow to read and record signals gained out of the accelerometers and strain gauges. The part of the application responsible for signal generation for single actuator is presented in Fig. 9. The program can generate harmonic as well as polyharmonic signals at the moment, which may be used in the process of fatigue testing. The application allows to change the offset of the signal using a created ramp block inside the application. At this moment the control is still at the point of an open loop [4], which means that the force and momentum are not being compensated by the control system. The strain and acceleration are currently being recorded by the system. The authors also want to establish a control system where the controlled quantity would be the strain.

Table 1. Expected parameters of the test stand in regards to the parameters of the vibration shakers

Parameter	Constant amplitude	Random amplitude
Rated peak force	440 N	100 N
Frequency range	2–6500	
Max rated travel pk to pk	25.4 mm	
Max weight tested	6 kg	13 kg
Max acceleration	110 g [m/s^2]	
Control voltage	−10 V – 10 V	

The maximum rated travel peak to peak (pk to pk) of the stand is the difference between the maximum positive and maximum negative amplitude of the waveform that the stand can generate. This parameter strongly depends on the offset value of the signal waveform that is being subjected to the stand. The offset can be also set mechanically in the stand. It is carried out on the levers using a specially designed turnbuckle.

Fig. 5. Assembled test stand with an closer look on the place of the test sample input

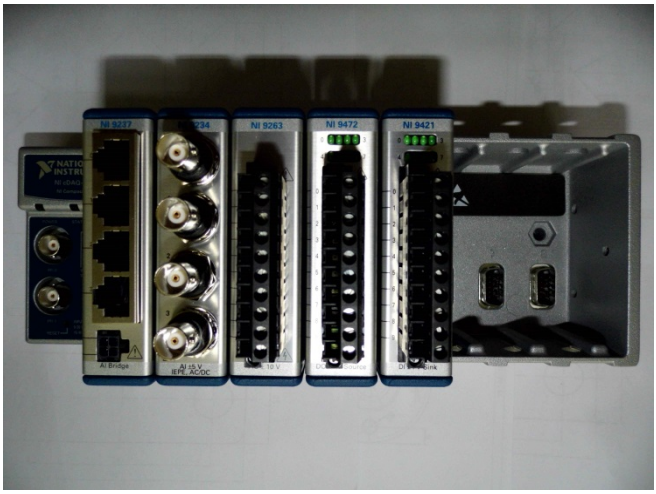

Fig. 6. The NI Compact DAQ chassis, which is being filled with (starting from the left side): Bridge Module (strain gauges), vibration sensors card, analog output card, and two digital signal output and input cards

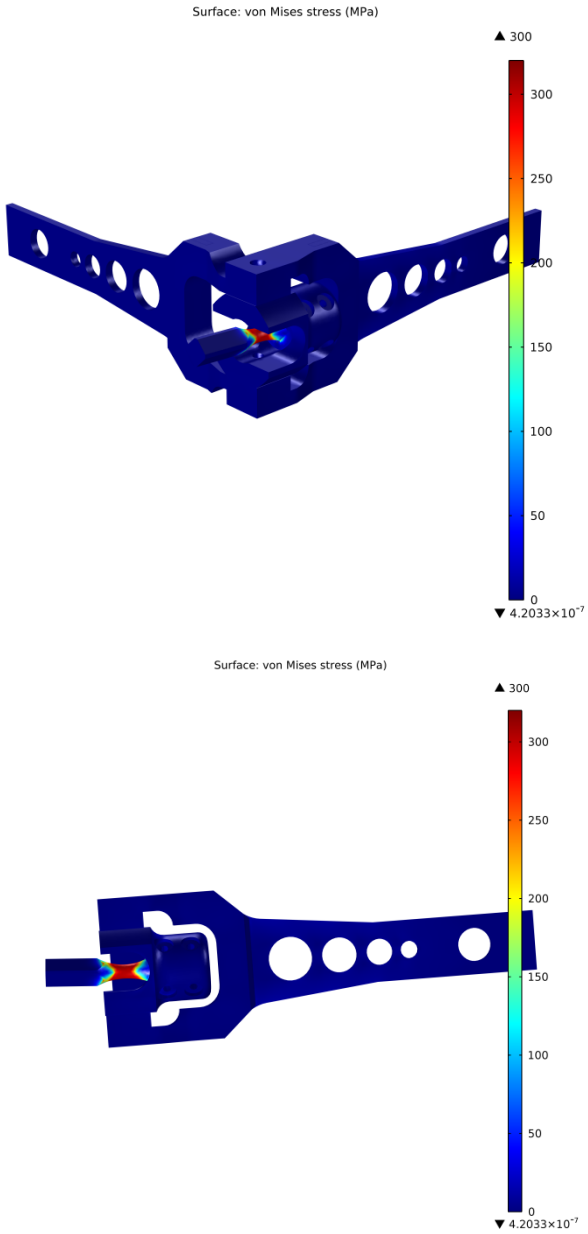

Fig. 7. Maximum available stress states for the diabolo test samples made out of S355J steel. The von Mises criterion has been chosen to calculate the maximum stresses. The stress-strain curve for the used steel S355J has been used in the calculation process of the maximum stress values.

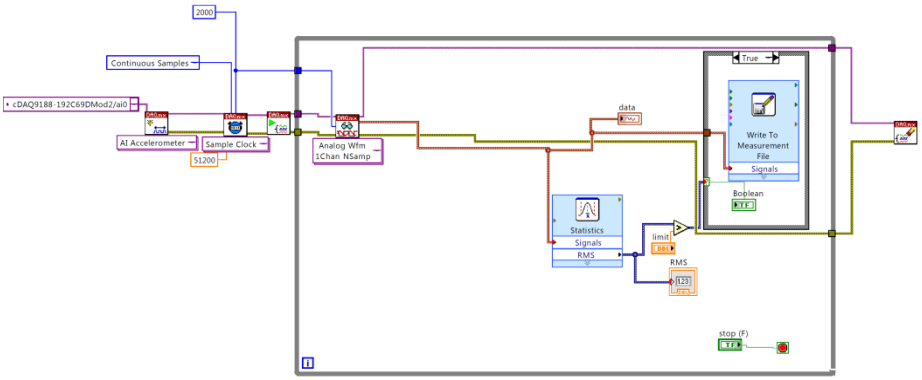

Fig. 8. Acquisition diagram of the concept fatigue stand for multiaxial tests for the accelerometer. The measurements are being recorded for every value over the static value set in the application.

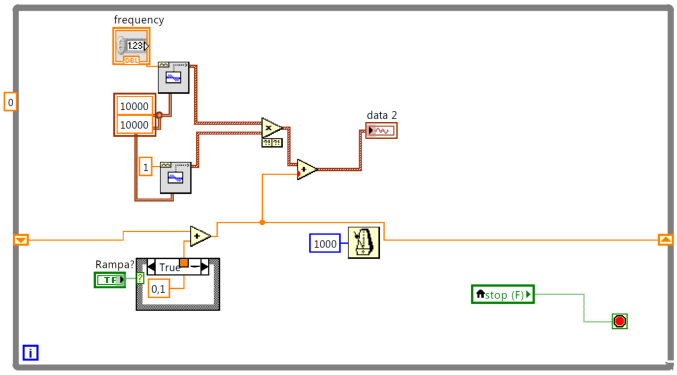

Fig. 9. Application responsible for signal generation for single actuator. The application allows to perform an amplitude offset change.

4 Remarks and Conclusions

The test stand presented in this paper is still in the concept stage, even though all elements are already at their functionality stage. To describe the accurate parameters and maximum values of the stand, it is needed to perform tests for different types of materials and different types of loading conditions. The stand needs to be fully tested for constant amplitude loads and standard constructional materials like low alloyed steels, which are characterized by good stiffness, before proceeding to random amplitude fatigue tests. The control system needs to be changed into closed loop control with the possibility to perform real time compensation of the output signal.

The main advantage of the test stand is the possibility to perform fatigue tests under any combination of bending and torsional moments – from constant amplitude loading with different loading frequency, phase shifts and amplitudes ratio to

advanced tests under random loading with programmable stochastic dependence between loading components. Such kind of test stand seems to be very useful while performing a verification of multiaxial fatigue failure criteria designed for spectral methods [9, 10] and for material testing under service loading condition.

Acknowledgement. The Project was financed from a Grant by National Science Centre (Decision No. DEC-2012/05/B/ST8/02520).

References

1. Timoshenko, S.: History of Strength of Materials: With a Brief Account of the History of Theory of Elasticity and Theory of Structures. Courier Dover Publications (1983)
2. Bishop, R.H.: The mechatronics handbook. CRC Press, Boca Raton (2008)
3. Skibicki, D., Sempruch, J.: Use of a load non-proportionality measure in fatigue under out-of-phase combined bending and torsion. Fatigue Fract. Eng. Mater. Struct. 27, 369–377 (2004), doi:10.1111/j.1460-2695.2004.00757.x
4. Firat, M.: A numerical analysis of combined bending–torsion fatigue of SAE notched shaft. Finite Elem. Anal. Des. 54, 16–27 (2012), doi:10.1016/j.finel.2012.01.005
5. Macha, E., Niesłony, A.: Critical plane fatigue life models of materials and structures under multiaxial stationary random loading: The state-of-the-art in Opole Research Centre CESTI and directions of future activities. International Journal of Fatigue 39, 95–102 (2012), doi:10.1016/j.ijfatigue.2011.03.001
6. Niesłony, A., Böhm, M.: Mean stress effect correction using constant stress ratio S–N curves. Int. J. Fatigue. 52, 49–56 (2013), doi:10.1016/j.ijfatigue.2013.02.019
7. Niesłony, A., Böhm, M.: Monitoring of fatigue life of mechatronic elements using spectral method for fatigue life assessment including the mean stress value. Pomiary Automatyka Robotyka 16(12), 100–104 (2012)
8. Niesłony, A., Macha, E.: Spectral Method in Multiaxial Random Fatigue. Springer, Heidelberg (2007)
9. Benasciutti, D., Cristofori, A., Tovo, R.: Analogies between spectral methods and multiaxial criteria in fatigue damage evaluation. Probabilistic Eng. Mech. 31, 39–45 (2013), doi:10.1016/j.probengmech.2012.12.002
10. Niesłony, A.: Comparison of Some Selected Multiaxial Fatigue Failure Criteria Dedicated for Spectral Method. Journal of Theoretical and Applied Mechanics 48(1), 233–254 (2010), doi:10.1016/j.ijfatigue.2012.05.014

Mechatronic Approach in Inspection of Water Supply Networks

Tomasz Buratowski, Michał Ciszewski, Mariusz Giergiel, Mateusz Siatrak, and Michał Wacławski

AGH University of Science and Technology,
30 Mickiewicza Av., 30-059 Krakow, Poland
{tburatow,mcisz,giergiel,siatrak,mwaclaw}@agh.edu.pl
http://www.agh.edu.pl

Abstract. The paper describes design process of the two inspection robots. Both are able to work in water environment. There is provided problem statement which cause need of designing robots and solution for it. The paper presents exemplary usage of the robots and sample results of inspection tasks. The inspection process and equipment can be different for each robot. Common assumption in design of both robots was versatility of the construction. Tank inspection robot can be set in two different configuration with two different inspection equipment. Pipe inspection robot has configurable construction of tracks arms which enables work in different conditions.

Keywords: underwater inspection, tracks, mobile robots, water supply networks.

1 Introduction: Problem Statement

Almost every city on Earth has a water supply network. These networks are complex installations consisting of a very broad array of different types of pipes, tanks, filters and other equipment and machines. Pipes and storage tanks are a key part in all water supply networks. They are critical to safe and uninterrupted water supply. A typical city with over 700,000 citizens has in excess of 40 water storage tanks and more than 3500 km of water and sewage pipes. The inspection of these parts of water supply network poses several problems. The main problems are:

- The pipelines in most cases cannot be inspected by human due to their small diameter.
- The storage tanks have to be emptied in order to perform a full inspection. This causes long periods (about 1 month) when the tanks are excluded from use.
- The inspection itself takes a lot of manpower.
- The bottom of the tanks has to be periodically cleaned. The cleaning also requires emptying of the tank.

J. Awrejcewicz et al. (eds.), *Mechatronics: Ideas for Industrial Applications*,
Advances in Intelligent Systems and Computing 317, DOI: 10.1007/978-3-319-10990-9_42

Our department was approached by MPWiK Krakow to design a pair of robots that could perform inspection and maintenance tasks without the need to empty the tanks or exclude sections of a pipeline from use. Fig. 1 shows the CAD model of an exemplary tank that the robot should inspect.

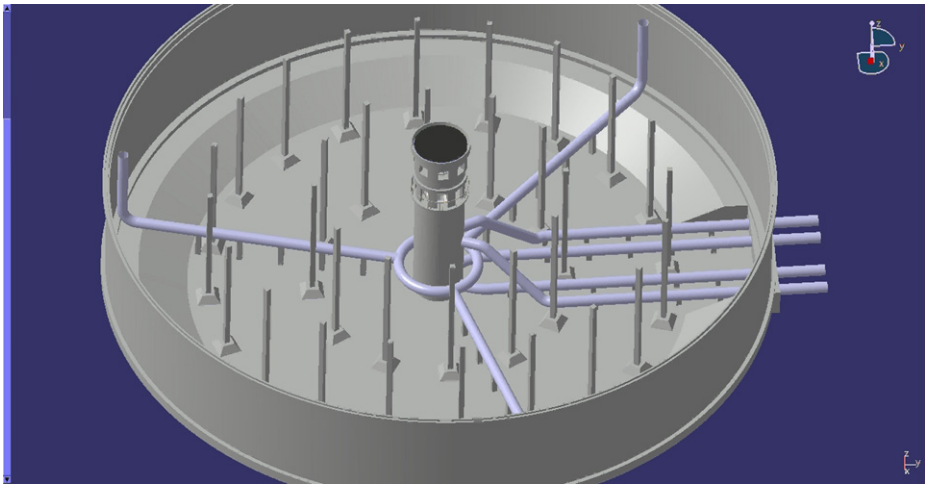

Fig. 1. CAD model of a water storage tank

2 Problem Solution

The solution for above problems are two robots designed in Department of Robotics and Mechatronics UST AGH [1]. Both of the robots are tracked and use components rated up to 30 m underwater. The robot vary in design according to their specialization. One is designed for maintenance and inspection of water tanks and the other is designed for pipeline and ducts inspection. Both robots are equipped for video inspection and are meant to be remotely operated. Video and control signals as well as power are transmitted via cable. This solution is also a safety feature, the robots can be extracted using a steel line running along the cables. Both of the constructed robots are early prototypes and test platforms.

2.1 Water Tank Inspection Robot

The main goal of inspection of water storage tanks is the monitoring of the state of the tank's concrete walls. Fig. 2 shows an example of a crack in the tank's wall. The designed robot will be used for more frequent inspection of the tank's walls. This will be possible due to the robots ability to perform the inspection in a full tank. The robot's design was supported with simulation of kinematics and dynamics of the robot [3, 2].

Fig. 3 shows the model of the robot with the additional inspection vehicle. This vehicle will perform the detailed inspection of the tank's walls using video camera and crack detection algorithms.

Fig. 2. A crack in the water storage tank's wall

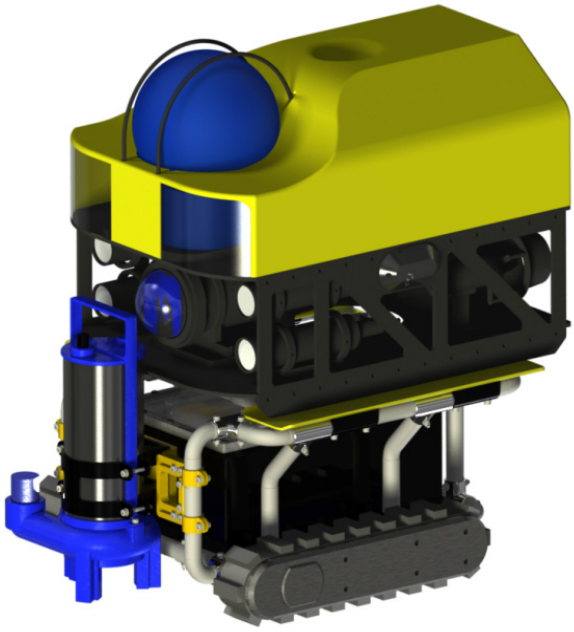

Fig. 3. CAD model of the robot's tracked base with attached inspection ROV

The crack detection algorithms are developed along with the prototype. Fig. 4 shows the end result of a test of the algorithm on a sample image.

Another inspection equipment that can be used with the robot is Eclipse multi-beam sonar from Tritech company. Fig. 5 shows the robot with the sonar attached.

The data that the sonar provides can be used to create virtual maps of the interior of the tanks [8]. The data gathered during a test scan of a lake's bottom are shown in Fig. 6.

The robot can also perform basic maintenance of the tank's bottom. A suction pump can be attached to the tracked base and used to clean the tank's bottom. Fig. 7 shows the robot's prototype with pump attached.

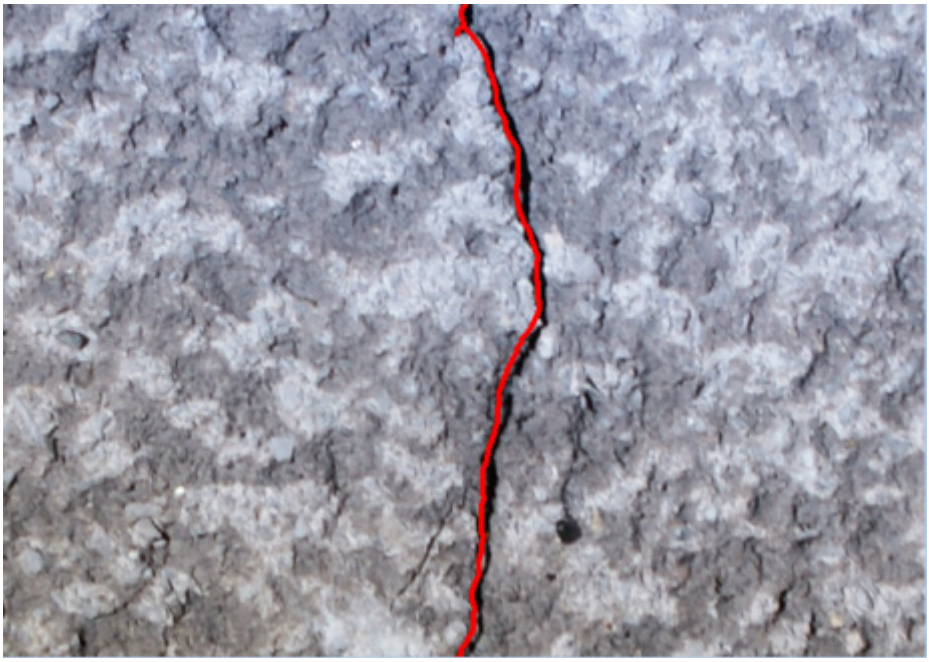

Fig. 4. Result of crack detection algorithm

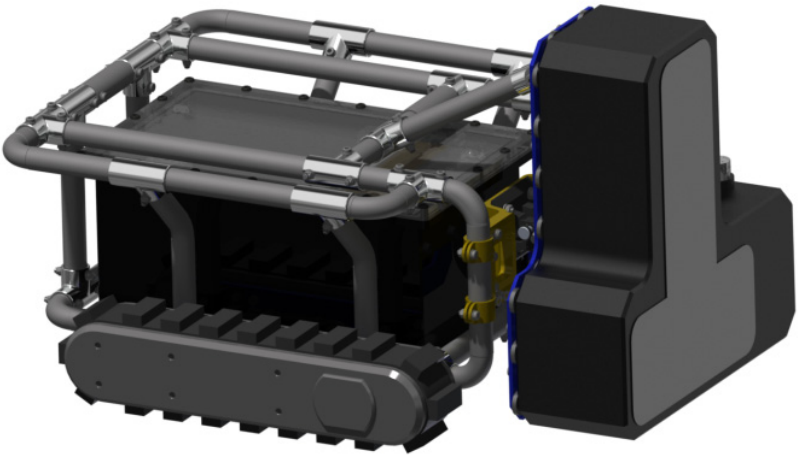

Fig. 5. Robot's prototype with the Eclipse sonar attached

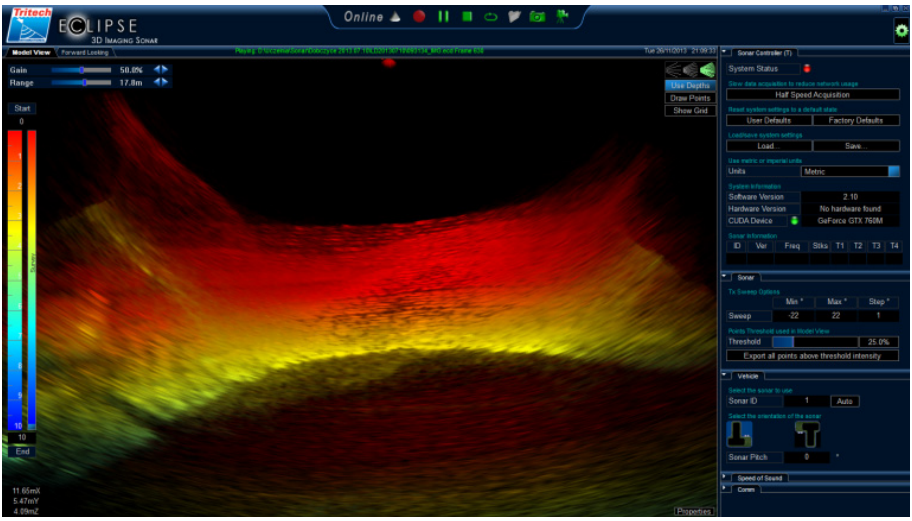

Fig. 6. Visualisation of sonar scan data

As described above the tracked robot platform is very versatile and can perform different types of inspection and tank maintenance. The time to change the robot from one configuration to the other is very short and allows for faster and more comprehensive tank inspection and cleaning.

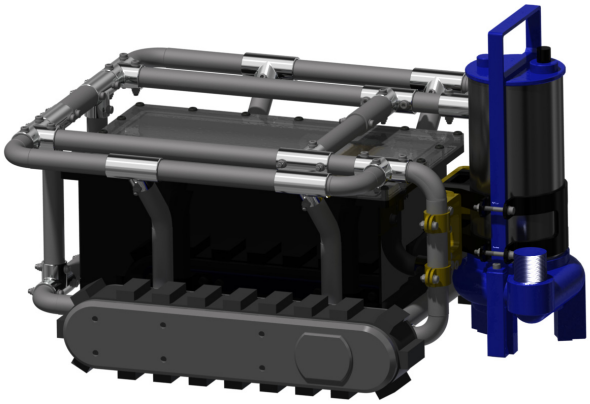

Fig. 7. Robot's prototype with pump attached

2.2 Pipe Inspection Robot

Along with the inspection of the tanks there is a need for pipe system diagnostics. To design second robot several assumptions and requirements had to be considered e.g.:

- Ability to fit different pipe sizes and cross-sections.
- Ability to perform inspection in vertical as well as horizontal pipes.
- Ability to perform visual inspection of the pipes.

The designed robot's prototype fulfils all of the above assumptions. The ability to fit different pipe sizes and cross-sections is realized using an innovative mechanical design that involves mounting the robot's tracks on variable arms as shown in Fig. 8. Selected track are specialized ones made by Inuktum Company [4]. During the design phase the kinematics and dynamics of the robot's tracks were performed [5–7]. Simulation and stress analysis of the mechanical construction were also performed.

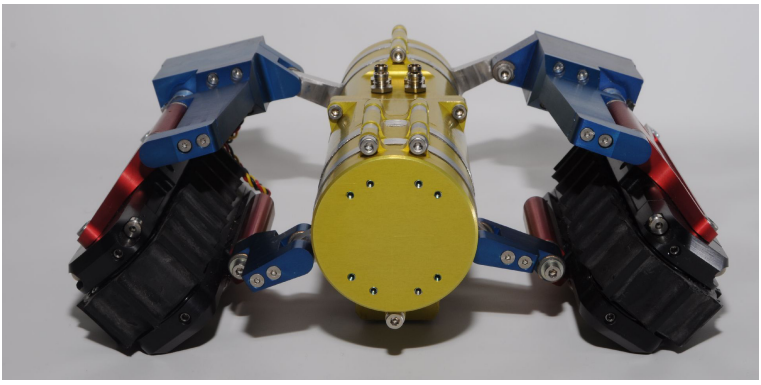

Fig. 8. Variable configuration pipe inspection robot

The robot is equipped with a camera and a high power LED to ensure optimal lighting conditions. The robot can change it's configuration to fit circular pipes as shown in Fig. 9 or rectangular ducts as shown in Fig. 10.

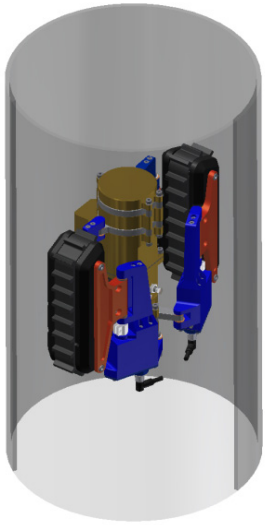

Fig. 9. Robot in pipe configuration

The main inspection tool of this robot is an inspection camera. Fig. 11 shows the image from the robot's camera during pipe inspection test.

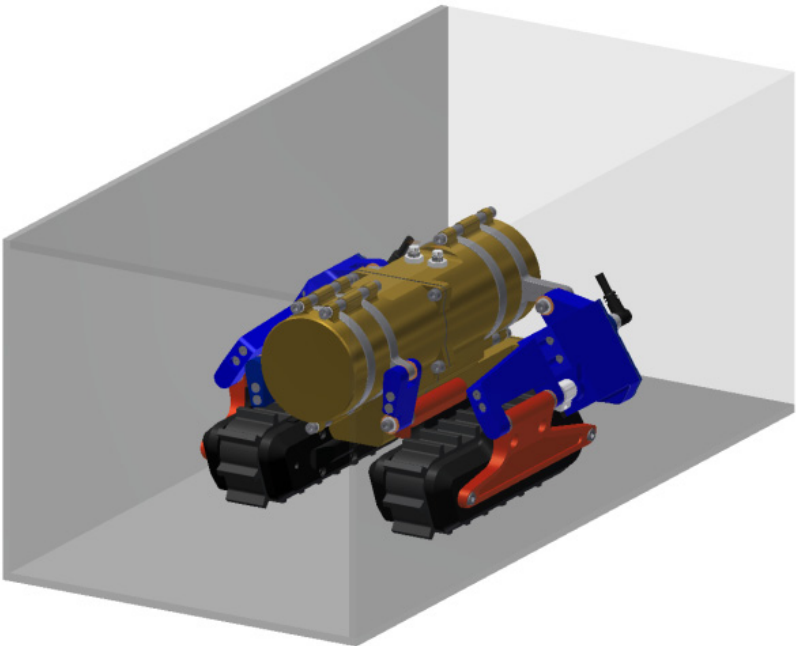

Fig. 10. Robot in duct configuration

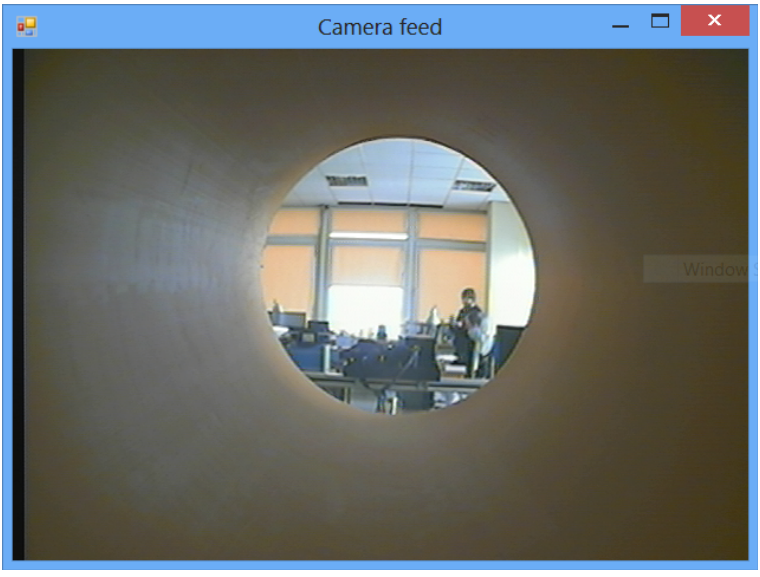

Fig. 11. Image from robot's camera

3 Summary

Both robots are designed using mechatronic approach. The design process was concurrent and each part of the project took into account the needs and specifications of the other. The robots are characterized by their modularity and versatility. The can perform inspection in a wide range of harsh environments and reach places not accessible to humans. Implementation of these robots in any water supply or waste management company will decrease it's operation costs and increase safety and service availability. It will also decrease maintenance downtimes and increase the service life of pipelines and storage tanks. We are confident that these two designs will have a broad range of applications.

References

1. Giergiel, M., Buratowski, T., Malka, P., Kurc, K., Kohut, P., Majkut, K.: The project of tank inspection robot. Key Engineering Materials 518, 375–383 (2012)
2. Giergiel, M., Kurc, K., Malka, P., Buratowski, T., Szybicki, D.: Kinematics of underwater inspection robot. Pomiary Automatyka Robotyka 16(12), 122–116 (2012)
3. Giergiel, M., Kurc, K., Malka, P., Buratowski, T., Szybicki, D.: Dynamics of underwater inspection robot. Pomiary Automatyka Robotyka 17(1), 76–79 (2013)
4. Inuktun: Inuktun crawler vehicles, http://www.inuktun.com/crawler-vehicles
5. Kurc, K., Strojny, P., Szybicki, D.: Dynamic simulation motion of the inspection robot with caravel drive. In: Computer Aided Designing, Engineering, Manufacturing and Data Analysis. Selected problems, pp. 56–67. Wydawnictwo Perfekta, Lublin (2013)
6. Kurc, K., Szybicki, D.: Kinematics of a robot with crawler drive. Mechanics and Mechanical Engineering 15(4), 93–101 (2011)
7. Kurc, K., Szybicki, D., Wydrzyski, D.: Mechatronics manufacturing elements inspection robot with caravel drive. In: Computer Aided Designing, Engineering, Manufacturing and Data Analysis. Selected problems, pp. 112–122. Wydawnictwo Perfekta, Lublin (2013)
8. Tritech: Eclipse multibeam sonar, http://www.tritech.co.uk/product/multibeam-sonar-for-3d-model-view-of-sonar-imagery-eclipse

Artificial Intelligence in Integrated Diagnostics of the Rotating System with an Active Magnetic Bearing

Małgorzata Gizelska

Institute of Turbomachinery, Lodz University of Technology,
219/223 Wólczańska St., 93-005 Lodz, Poland
malgorzata.gizelska@p.lodz.pl

Abstract. An implemented and experimentally verified diagnostic system for the rotating mechatronic system of machines with an active magnetic bearing is presented. An additional module that controls the correctness of its operation, employing artificial intelligence methods, is proposed. The results of preliminary investigations which will allow for an expansion of the diagnostic pattern base necessary to develop of an expert advisory system are given.

Keywords: AI, fuzzy logic, neutral networks, magnetic bearing, diagnostics.

1 Introduction

A key issue in operation of modern machines is their reliability. Critical machines are equipped with diagnostic systems that process numerous measurement data registered during their work.

The most important problem is an analysis and then a right interpretation of these data and determination of mutual correlations between process parameters and the machine dynamics. As a result, optimization of motion parameters and, particularly, an increase in reliability of the machine are possible. Advanced computational methods let us derive models of the theoretical data obtained experimentally and conduct a wide range of analyses and optimization of geometrical, flow and dynamic parameters of machines.

In the operating diagnostics of machinery, special attention should be paid to non-invasive methods for detecting defects that can be performed directly on the object, without interrupting the machine operation. These methods mainly rely on registration of selected measurement signals of the working machine, and then they are subject to a detailed analysis in terms of appearance of characteristic symptoms of damage.

The paper presents a diagnostic system, which was implemented and experimentally verified on the real test stand of the rotating mechatronic system with an active magnetic bearing. An additional module that controls the correctness of the system operation, using artificial intelligence methods, is proposed. This module is intended to aid the operation of the existing diagnostic system. The results of preliminary investigations which will allow for an expansion of the diagnostic pattern base necessary to develop of an expert advisory system are presented.

J. Awrejcewicz et al. (eds.), *Mechatronics: Ideas for Industrial Applications*,
Advances in Intelligent Systems and Computing 317, DOI: 10.1007/978-3-319-10990-9_43

2 Test Stand

In many areas of technology, also in mechanical engineering, there are more and more devices whose design is only possible through an integration of mechanical, electrical, electronic and information equipment. These devices are called mechatronic systems.

An example of an unconventional solution to a bearing node is a mechatronic system of an active magnetic bearing. The system of active, digitally controlled magnetic bearings provides an interesting alternative in the design of modern machines, whose task is to implement the technological processes involved in meeting specific operational requirements (operation in a range of very low or high temperatures, in chemically aggressive environments, or in the vacuum) [7, 8].

The magnetic rotor suspension technology in machines is qualitatively different if compared with conventional bearing solutions. Its characteristic feature is non-contact levitation of the machine rotor in the magnetic field generated by an automatic control system, which allows for controlling dynamics of the rotor during its motion.

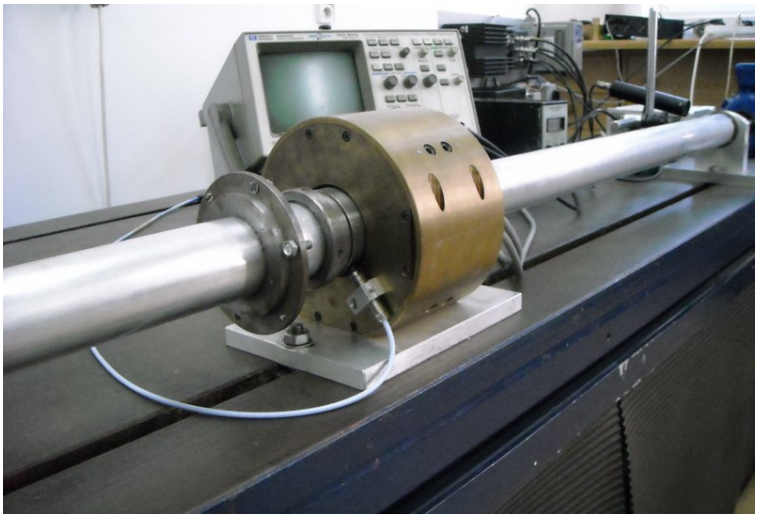

Fig. 1. Test stand of the rotating system with a magnetic bearing

The experiment was carried out on the test stand (Fig. 1), whose rotating shaft is a thin-walled tube made of duralumin of the external diameter equal to 54 mm and the 2 mm wall thickness, supported with two roller bearings mounted on both ends. Between these bearings, there is a system of active magnetic auxiliary support. It is driven by an electric motor, controlled by an inverter and connected to the shaft by a flexible coupling membrane. The mass of the rotating system is 4.85 kg and the length of the shaft – 1923 mm.

3 Magnetic Reaction Forces of the Bearing

A unique feature of magnetic bearings is a possibility to determine, with an indirect method, magnetic reaction forces generated in the axes of control, on the basis of measurements of currents and movements for given values of the electromagnet constants. The knowledge of forces acting in a rotating system of the machine has an important diagnostic value, because the cause of vibration, which occurs earlier than the effect, i.e., a response of the vibrating structure [5, 8], can be observed.

A reaction vector of the magnetic bearing is a sum of the forces generated by bearing electromagnets and changes in each control cycle. The component of the magnetic reaction F_{xmag} for the axis x is determined with the relationship:

$$F_{x\,mag} = K_{XT}\frac{I_{XT}^{\ 2}}{s_{XT}^{\ 2}} - K_{XB}\frac{I_{XB}^{\ 2}}{s_{XB}^{\ 2}} \tag{1}$$

The component value of the magnetic reaction F_{xmag} (Fig. 2) for a single control axis is related to the measured average values of the control current of the electromagnets I_{XT}, I_{XB} in a given period of control and the values of the magnetic slot s_{XT}, s_{XB} (T – *top*, B – *bottom*).

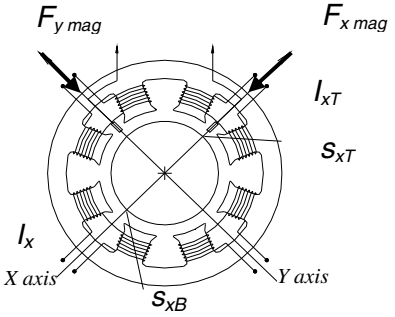

Fig. 2. Components of the magnetic reaction

The values of slots are found by measurements of instantaneous values of the journal position with respect to the bush center of the known clearance. The instantaneous values of the journal position are measured with a measuring system, specially designed for this purpose, being an integral part of the diagnostic system for control of the bearing operation. A value of the electromagnet constant K depends on its design parameters and can be calculated from the theoretical dependence or determined experimentally [8].

4 Characteristics of the Diagnostic System and Its Software

The specificity of the real object imposes special demands associated with a necessity of construction of the diagnostic system, which controls simultaneously the functioning

correctness of the rotating system and the control effectiveness of its lateral vibrations. An analysis and interpretation of the measurement data collected during the operation of the machine rotating system with a magnetic bearing are performed with the developed diagnostic software.

The signals for a database of the diagnostic system come from sensors installed in the magnetic bearing. They measure the journal position in two axes of control and the current in the windings of electromagnets. These sensors are an integral part of modules for control of the bearing operation. Additional measuring systems measure the frequency of the shaft rotation and the temperature of electromagnets windings. For collecting and recording the data necessary in the diagnostics of the mechatronic rotating system, a USB-4716 Advantech module equipped with a USB interface that provides the appropriate speed and accuracy of data transmission in measurement applications is used. The USB module does not require any additional power source. Clips for connecting all input/output signals are placed on the device casing (Fig. 3).

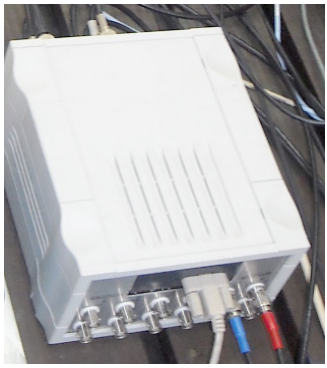

Fig. 3. Acquisition module of diagnostic data

The existing diagnostic software of the rotating system with an active magnetic bearing covers two stages of operation:

Stage I – ”on-line” mode:

- performance of test functions of the system along with control of the magnetic bearing at the starting moment, which allows one to diagnose the system dynamics for the fixed shaft in the phase of its suspension in the magnetic bearing (rotational frequency is equal 0). On their basis, computational procedures allow one to evaluate the bearing operation correctness and the integrality of the power transmission shaft. After the end of the tests, a signal of readiness to initiate the drive is generated;
- data collection and recording in real-time after the drive starts its operation (with the rotating shaft), comprising: the start-up, the shut-down, operation at the nominal rotational frequency and operation in the emergency mode (autorotation mode);
- “*on-line*” recording and control of parameters of the system operation during each phase and selection and reduction of the saved data files in the non-volatile memory that concerns mainly untypical behaviors of the system; signaling and generating

different level alarms in cases of exceeding critical values for the operation of the power transmission system or the bearing system.

Stage II – ”off-line” mode:

- data decoding recorded during the first stage of diagnostic software operation, collected in the memory of the diagnostic system by means of the external computer and some special software for this task;
- analysis of the collected data concerning temporary states of the system operation (the start-up, the shut-down) and untypical behaviors, and a graphic presentation of evolution of the shaft trajectory versus time, Bode plots, characteristics of changes in values of magnetic forces, temperature fluctuations of electromagnets windings, etc.

5 Concept of the System Development with Artificial Intelligence Methods

In the next stages of the work on the diagnostic system, further development of its software which will include a generation module of diagnostic hypotheses based on modern methods such as neural networks, Bayesian belief networks and fuzzy logic elements, is planned.

The proposed concept of the diagnostic system for the machine rotating system with an active magnetic bearing will perform the following tasks:

- diagnosis – determine the current state of the machine on the basis of the analysis carried out by the existing diagnostic system,
- genesis – identify the causes of the current state of the machine,
- forecast – predict further possible changes in the machine state.

The implementation of these tasks will minimize the probability of unforeseen problems in the machine operation and proper planning of operational and repair activities.

A proper identification of the current state of the machine must have a reference to the information about the history of the object and progressive changes occurring in the machine during its operating time. The information about the history of state changes during operation, and the correctly described current state of the machine allow one to predict the future behavior of the machine.

On one hand, a concept of the diagnostic system includes a database of diagnostic patterns, and, on the other hand, an archival database of measurements made during the period of the machine operation. The reliable data from the database of diagnostic patterns are designed to deliver an accurate diagnosis, and, thus, to make right decisions. An accurate diagnosis on the state of an object can be achieved with different methods of assessment. The underlying idea of these methods is common. It involves finding patterns in a database of diagnostic patterns which are most similar to the currently presented ones for the measurement. For the pattern chosen with this

method, there are given factors whose coefficients determine the qualitative and quantitative information on possible irregularities occurring in the machine state.

The Main Elements of the Proposed Module to Generate Hypotheses for the Diagnostic System Are as Follows:

- a database of diagnostic patterns – including the results of calculations of specialized mathematical models, taking into account an impact of the machine state on features of the proposed diagnostic signals,
- a database of measurements – including the results of measurements made on the diagnosed object,
- an acquisition block of diagnostic signals – a part of the system responsible for the collection of measurement data from the test object,
- a diagnostic inference block – a part of the system in which methods and rules of inference to assess the state are implemented,
- a diagnostic results block – which stores the results of the object state diagnoses,
- a operational decisions block – whose task is to determine the operating instructions,
- processing procedures – a set of procedures for processing both the measured data and the data from the database of diagnostic patterns.

Procedure Algorithm:

- the database of diagnostic patterns stores diagnostic patterns for various stages of magnetic bearings operations,
- the diagnostic signals are taken from the test object by the block of data acquisition,
- the collected data in the block of data acquisition are written to the measurement database,
- in the diagnostic inference block, there is a choice of data processing procedures for a particular measurement and processing data stored in the pattern database for a given operation stage of the bearing,
- the processed data from both databases are evaluated by the chosen diagnostic method. As a result of the diagnostic evaluation, indicators characterizing the state of the machine are given. They are saved in a block of diagnostic results,
- on the basis of the results of the diagnosis in a block of operational decisions, exploitation instructions and dates of the next technical machine examinations are determined.

The main elements of the proposed diagnostic system, from the standpoint of accuracy and reliability of the diagnosis, are as follows: a database of diagnostic patterns, a diagnostic inference block and a data acquisition system. The data acquisition system is directly responsible for providing actual measurement results for the diagnostic assessment phase and is one of the main elements of the diagnostic system.

In the diagnostic inference block of the designed system, data processing with artificial intelligence methods, which use their knowledge of the possible states of the machine, takes place. The data needed by neural networks to learn and to determine membership functions are derived from the database of diagnostic patterns

obtained from the solution to the mathematical model and processing them in an appropriate way, depending on the applied method of inference.

6 Verification of Proper Operation of the Designed Module

According to the implementation concept of an expert diagnostic system that controls the proper operation of the active magnetic bearing, a neural network which reacts to changing signals on its input was developed. To provide the current state of the tested system, the neural network learning process must be conducted. It is necessary to construct a diagnostic patterns database.

Figure 4 illustrates preliminary trials of the conducted analysis. The designed neural network was to determine the parity of ones occurring in the input values string. For this purpose, a database consisting of a sequences of 6 digits 0 or 1, and the seventh value determining the ones parity in the given string using the digit 1 or their odd parity with the digit 0 was created. The neural network was trained on the basis of an incomplete database (52 input data sequences out of 64 possible). To verify the correctness of the proposed method, the data that were not included in the input learning base were used. The developed neural network interpreted the task correctly (Fig. 4).

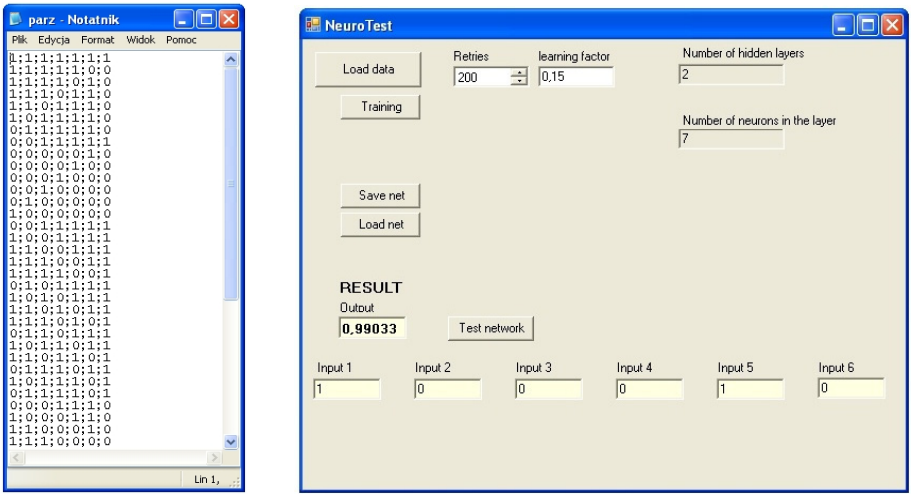

Fig. 4. Verification of the proper operation of the neural network

The verified neural network can be used in a real system to control the proper operation of the tested magnetic bearing.

The designed system for recording measurement data during the operation of magnetic bearings and the possessed knowledge of the object enabled generation of the diagnostic pattern database which maps the operation of the tested rotating system. The diagnostic pattern database consists of records containing 6 fields for variables from the simultaneous measurement of shaft displacements in the magnetic

bearing in two control axes and four current values generated by the electromagnets. The last, seventh value of the knowledge base is created to determine the proper operation of the rotating system in the form of 0 or 1 (Fig. 5a).

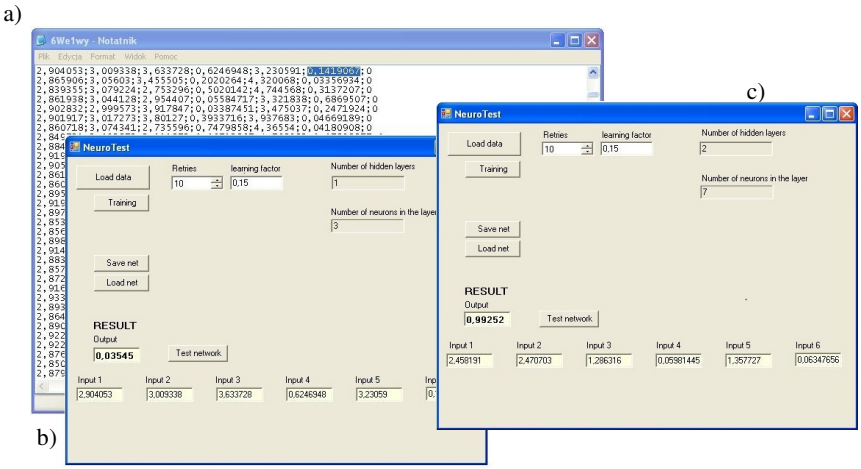

Fig. 5. Analysis of proper operation of magnetic bearings using a neural network: 5a) database of diagnostic patterns; 5b) magnetic bearing malfunction; 5c) correct operation of the magnetic bearing

The neural network learning process was conducted using the available knowledge base. After entering 6 values related to the analyzed operating phase of the tested system to the input of the trained network, the designed module properly evaluated the state of the object giving the value close to zero, corresponding to the incorrect action of the bearing in the output (Fig. 5b). Figure 5c shows correct functioning of the bearing, which was interpreted by the system by attaining a value close to 1 in the output.

After the learning process based on the incomplete knowledge base, this system will provide a current state of the magnetic bearing under test.

7 Summary

To construct an expert advisory system, there is a need to collect an extensive knowledge base, covering completely the problem under analysis. The experience gained in verification of the correctness of the existing diagnostic system based on traditional methods of analysis will serve as the basis for development and correctness verification of the module using artificial intelligence methods to control the proper operation of the mechatronic rotating system. The preliminary results encourage further analysis of the problem using a neural network.

The next stage for development of the diagnostic module will consist in choosing appropriate sequences of input data and learning parameters of the neural network (a number of hidden layers, a number of neurons in the layer, learning rate and a number of repetitions) in order to interpret correctly the current state of the object by the program.

References

1. Cholewa, A.: Przykład wnioskowania na podstawie sieci przekonań, Warsztaty Diadyn, Materiały seminaryjne, Ustroń (2006) (in Polish)
2. Filippetti, F., Franceschini, G., Tassoni, C.: Synthesis of artificial intelligence and neural network technologies in power electric system diagnostics. In: Proceedings of International Conference Electrical Machines, ICEM 1994, Paris, vol. 2, pp. 353–357 (1994)
3. Gizelska, M.: Koncepcja diagnozowania systemu wirującego z aktywnym łożyskiem magnetycznym. In: XXXIV Ogólnopolskie Sympozjum "Diagnostyka Maszyn", Węgierska Górka (2007) (in Polish)
4. Gizelska, M., Kozanecka, D.: Oprogramowanie diagnostyczne systemu wirującego z aktywnym łożyskiem magnetycznym, Cieplne Maszyny Przepływowe – Turbomachinery, Zeszyty Naukowe Politechniki Łódzkiej Nr 1001, Łódź, pp. 39–50 (2007) (in Polish)
5. Gizelska, M., Kozanecka, D., Kozanecki, Z.: Integrated Diagnostics of the Rotating System with an Active Magnetic Bearing. Solid State Phenomena 147-149, 137–142 (2009), http://www.scientific.net available online since (January 06, 2009)
6. Korbicz, J., Kościelny, J.M., Kowalczuk, Z., Cholewa, W.: Diagnostyka procesów, Wydawnictwa Naukowo-Techniczne, Warszawa (2002) (in Polish)
7. Kozanecka, D.: Sterowanie drganiami linii wału energetycznej maszyny przepływowej podpartej w aktywnych łożyskach magnetycznych, Sprawozdanie z realizacji projektu badawczego, Łódź (2005) (in Polish)
8. Kozanecka, D.: Diagnostics of Rotating Machinery Mechatronic System. Monographic Series of Publications: Maintenance Problems Library. Scientific Publishing House of Institute for Sustainable Technologies in Radom (2010) ISBN 978-83-7204 966-7 (in Polish)
9. Tadeusiewicz, R.: Sieci neuronowe. AOW, Warszawa (1993) (in Polish)
10. Komputer (prawie) inteligentnym, czyli proste sieci neuronowe w C#, http://codeguru.geekclub.pl/baza-wiedzy/komputer-prawie-inteligentnym-czyli-proste-sieci-neuronowe-w-c,2193

The Modified Graph Search Algorithm Based on the Knowledge Dedicated for Prediction of the State of Mechatronic Systems

Mariusz Piotr Hetmańczyk and Jerzy Świder

The Silesian University of Technology, Faculty of Mechanical Engineering,
Institute of Engineering Processes Automation and Integrated Manufacturing Systems,
44-100 Gliwice, Konarskiego 18A Street, Poland
{mariusz.hetmanczyk,jerzy.swider}@polsl.pl

Abstract. The modified shortest path algorithm dedicated for a condition prediction of distributed mechatronic systems is shown in this article. From many of available methods the Dijkstra's algorithm has been selected. Assumed restrictions of the proposed method (graph models containing interrelated groups of failures, effects and their causes) forced the need regarding changes of the structure of applied algorithms and their adjusting to the adopted predictive model. The method for identification and transformation of the current condition in the source vertex of the graph of causes and effects has been also presented by the authors.

Keywords: condition prediction, mechatronic systems, AC asynchronous drives, distributed drives, oriented graphs.

1 Introduction

The condition prediction of technical devices is an area where a wide scope for applications covering various engineering methods, especially statistical methods still exists. The most important role might play graph methods, connected with a computer representation of their structures.

During the rapid development of expert systems theory and notation of the procedural and declarative knowledge, associated with the growing capabilities of personal and industrial computers, the usage of process signals (representing operating conditions) gathered from the industrial objects for prognosis (especially in the real time mode) has become possible.

On the basis of the current status and historical data, it is possible to estimate a set of parameters including the probability of damage that describes components (piece parts) or whole machines (total probability of failures, resulting from mutual relations of components creating subassemblies or more complex systems).

It is also possible to use sets and tables of probabilities (referring to commonly used components or piece parts taking into account their operating conditions), developed by the RADC Information Office [7].

J. Awrejcewicz et al. (eds.), *Mechatronics: Ideas for Industrial Applications*,
Advances in Intelligent Systems and Computing 317, DOI: 10.1007/978-3-319-10990-9_44

The last required step, indispensable in an evaluation of the condition prediction, is a selection of a structural form describing identified interrelationships between specified failures and their impact at the development of further damages.

The definition of a directed graph (named by the authors' the graph of causes and effects) allows determination of vertexes (states of considered technical objects) interconnected with weighted edges (values of weights corresponding to probabilities of failures).

In many cases, sufficient information (connected with an evaluation of operational states) may be provided through the use of the expert knowledge.

A notation of functional relationships, of constituent components of distributed mechatronic systems, based on graph methods allows for a simplification of the prediction process.

The described advantage resulted from usage of computer algorithms (allowing for mapping of the path identifying consequences of successive failures), possibilities of representation of machines on different complexity levels (systems, subsystems, components, piece parts, etc.) and ease of determination of dependencies between independent but reciprocally interacting mechatronic devices [3].

2 A Definition of the Considered Problem

The most often used solutions for searching of the shortest path (in the form of computer algorithms) can be divided into the following variations [5]:

- Single-Pair Shortest Path Problem (SPSPP) – sets the shortest path between a source and a sink,
- Single-Source Shortest Path Problem (SSSPP) – determines the shortest path between selected source, and other vertices of the considered graph,
- Single-Destination Shortest Path Problem (SDSPP) – an inverse method of the SSSPP, i.e. searching the shortest path from each vertex to a target vertex,
- All-Pairs Shortest Path Problem (APSPP) – sets the shortest path between all pairs of vertices.

All of enumerated methods are used to a determination of the path with the minimum value of weights sum of edges, but assumptions of the presented method require changes in algorithm structures.

For the purpose of the conditions prediction based on the current states the authors have chosen the SSSPP method.

A modified algorithm used in its principle to the needs of a solution of the problem leads to obtaining a path with the most probable states, defined on the basis of ordered series of relations (structural, reliability and failure).

The result of the Dijkstra's algorithm is the path from the start vertex to the sink vertex, with the minimal total weight value of edges connecting considered nodes.

Determination of the transition is done globally (in reference to the global structure of the graph – all its vertices and edges, in the framework of the hierarchy).

The causes and effects graph is defined as a collection of failures related to their consequences dependent on an individual structure defined by the user of the mechatronic system.

It should be noted that with a respect to the same technical agent (taking into account the context of diversified applications) defined structures of the causes and effects graph may take diverse forms.

Weight values of the causes and effects graph can be presented in two separate approaches, using a representation of the:

- reliability function

$$R(t) = 1 - Q(t) = P\{T \geq t\} \tag{1}$$

- unreliability function

$$Q(t) = P\{T < t\} \tag{2}$$

where:
R(t) – the reliability function,
Q(t) – the unreliability function (the distribution function of a random variable),
P{T<t} – the probability of a failure of an element to the moment t.

An identification of the current state (the source vertex) is carried out on the basis of data contained in the Prediction Oriented Diagnostic Vectors (PODV) [4].

In order to a determination of the scope of functionalities covered by the PODV vectors the authors proposed the preliminary definition, in the form of a minimum set of attributes identifying the test object (immeasurable values) and diagnostic indicators (measurable and immeasurable characteristics – extensive and intensive), sufficient to the state prediction.

PODV vectors should meet some basic features including the possibility of:

- a universal application (within the range of considered mechatronic devices),
- a possibility of identification of the current state and the classification of gathered numerical values (transformation of the present state of work to the graph and an assignment to the two disjoint sets – operational or nonoperational states),
- a reconstruction of the failures propagation path (based on the identified key variables, their values and structural notation),
- recording of the key parameters (the possibility of using of database systems) in order to modification or development of predictive models of currently monitored devices.

The general structure of the PODV vector is represented by the formula:

$$V_{PUWD} = [[Id_{SM}({}_{S}SM_{k}(Par = Id_{el}))^{T}[Id_{ST}({}_{S}SM_{k})]^{T}[D_{diag}]] \quad (3)$$

where:

$Id_{SM}({}_{S}SM_{k}(Par = Id_{el}))$ – the vector containing non-measurable parameters of considered system (individual tags Id_{el} and division codes of all elements isolated according to the FMECA methodology),

$Id_{ST}({}_{S}SM_{k})$ – the vector of a quantitative description of the ${}_{S}SM_{k}$ system under consideration containing number of elements within the defined structure,

D_{diag} – the diagnostic data vector (structure defined in an individual manner in relation to the context of application).

After determination of the current state and transformation of initial values to the source vertex the modified algorithm should reconstruct the path of the possible states.

3 Modifications of the Dijkstra's Algorithm

Modification of the Dijkstra's algorithm assumes a resignation from a phase of determination of the path characterized by the minimum sum of the weights connected source and sink vertexes, in favor of the probabilities analysis (reliability or unreliability functions) of adjacent vertexes up to further determination of the failures path. In the considered case only the source vertex is known, without knowledge about the sink vertex.

For matching of the Dijkstra`s algorithm to requirements the authors have made assumptions in the following form:

- changes of edge weights in the directed graph, in case of representation using the unreliability Q (t) function, according to the relationship:

$$_{EM}p_{(i,j)} = 1 - p \quad (4)$$

where:

$_{EM}p_{(i,j)}$ – the weight of the edge coming from vertexes i to j,

p – the percentage value of failure of an analyzed component (assembly, subassembly, etc.).

- checking of the sum of weights probabilities of incoming and outgoing edges of the considered vertex, according to the relationship (where n is a number of edges incoming or outgoing from the considered vertex):

$$\sum_{m=1}^{n} {}_{EM}p_{(i,j)} = 1 \quad (5)$$

- resignation of global searchin of the path with the minimum value of weights sum and reduction of the search depth up to the level of the nearest neighbor, then setting a new source vertex,

- assumption of seeking set of vertices in the immediate vicinity of the floating vertex (source vertex), instead of summing the weights of the edges (Fig. 2),
- an implementation of the function connected with an estimation of a transition probabilities from source to sink vertexes with the usage of a product function of the edge weights connecting determined vertices,
- an identification of the startup vertex based on data included in PODV vectors and computer processing functions that determine the quantitative identification of this particular condition [1, 2, 6].

The general approach to the issues of an interpretation of the modified Dijsktra`s algorithm can be presented in the following form:

```
Modified_Dijkstra_routine(graph, weight, start):
    v_val[start] = 0
    antecedents[] = null
  FOR i=1 to max_vertex_number[All_vertexes_set(graph)]
       v_val[previous_vertex, next_vertex] = •
  END FOR
    Not_considered_vertexes_set = All_vertexes_set
DO
     temp_val = Find_minimum(Not_considered_vertexes_set)
   FOR All_neighbour_of_previous_vertex
    IF
     weight[previous_vertex, next_vertex]<v_val[temp_val]
    THEN
      antecedents[next_vertex] = previous_vertex
      previous_vertex = next_vertex
    END IF
   END FOR
UNTIL Not_considered_vertexes_set = Empty
END
```

The application of the processing functions used at the stage of searching of the cause and effects graph developed for the electric motor is shown in Fig. 2. In case of the presented example, a depth of the search was limited to two iterations.

The realization of functioning of the modified algorithm leads to the designation of a state (represented by the graph vertices) responsible for the further development of errors, failures or detuning of the analyzed system.

A different manner of an interpretation of the various approaches (functions Q(t) and R(t)) leads to the same results, assuming changes of the edge weight value.

It should be noted that the weights can have different values depending on the nature of work of the considered mechatronic system, and subjective assessment of the experts.

Enumerated qualities do not constitute restrictions of the presented method, but rather advantages (the matching ability the nature of the work to suit individual conditions and disturbances affecting a system during tasks execution).

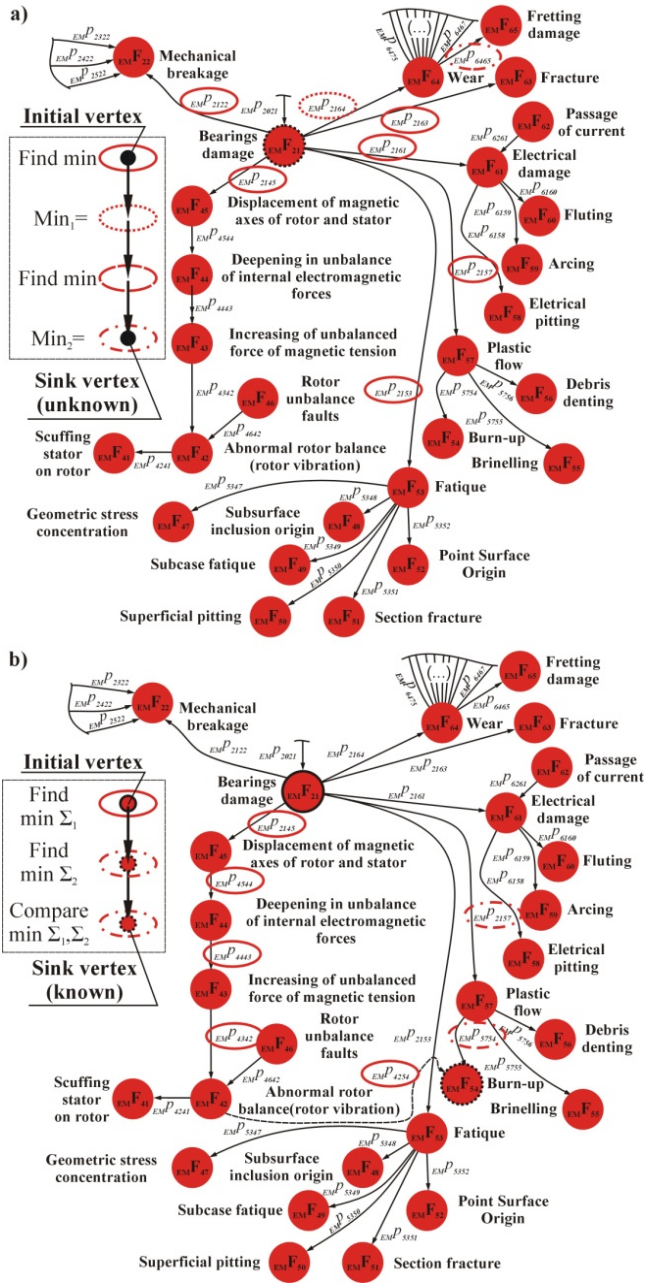

Fig. 1. Schematic representations of notions used in the modified algorithm: a) the local minimum, b) the global minimum

The proposed structure of the modified algorithm is easy to an implementation in computer data processing environments.

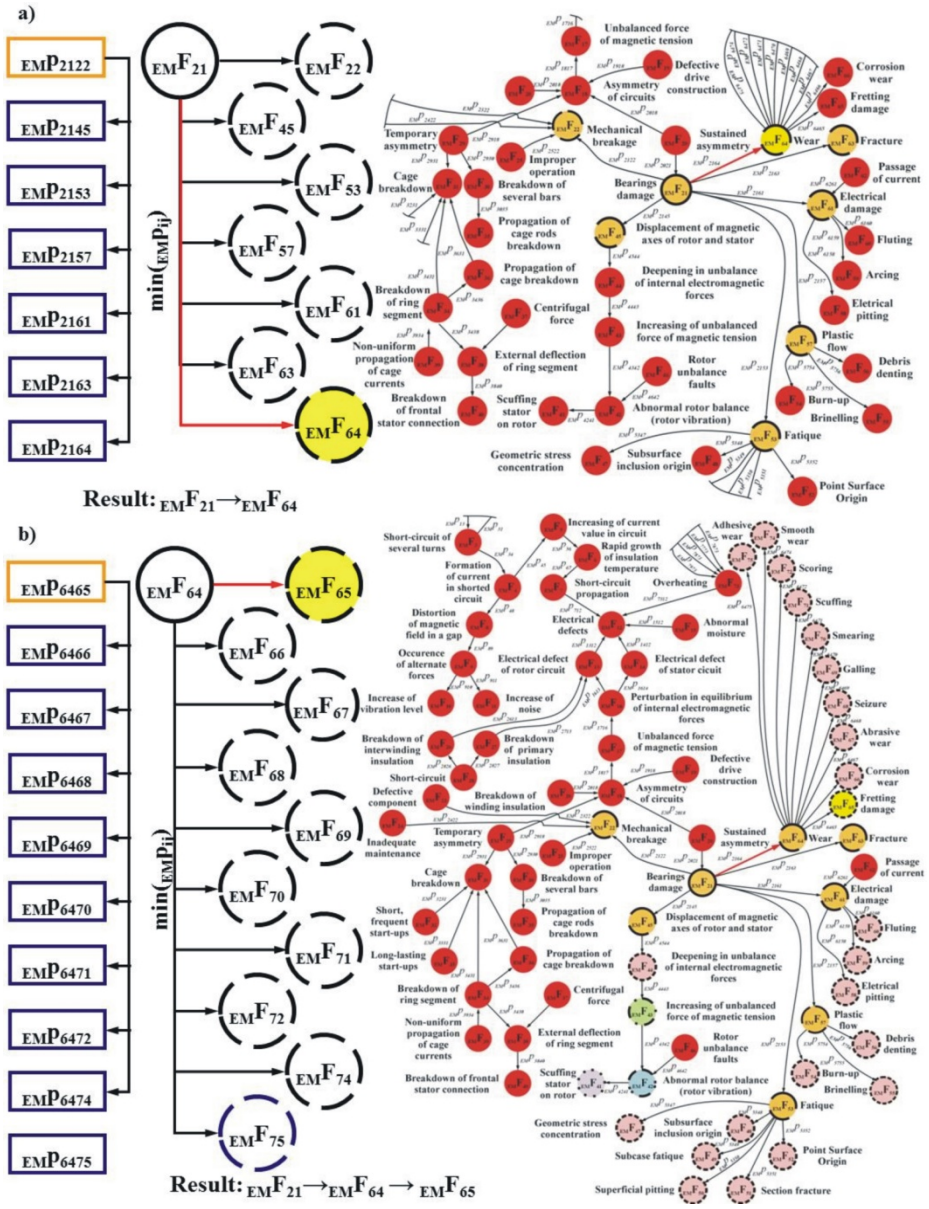

Fig. 2. Stages of determining a path in the causes and effects graph, based on the current state: a) first step (search depth equals 1), b) second step (search depth equals 2)

In addition, the method is a response to the need of the use of the prediction-oriented expertise, without fitting statistical hypotheses to specific aspects of course of work of mechatronic devices.

4 Summary

Presented modifications of the Dijkstra's algorithm, with taking into consideration the assumptions included in the method is sufficient to meet the requirements of the tools being developed to the purpose of prediction of system failures. Similar modifications can be made to the structures of other shortest path algorithms.

The presented method is based on the matrix representation of graph structures and is a universal solution for the prediction of conditions of technical devices.

The modified Dijkstra's algorithm allows:

- obtaining a solution of the problem of sequential fault determination,
- using personal computers or industrial units, carrying out operation in an industrial environment (especially in real time mode – online monitoring),
- implementing in industrial systems in cases where predictive control methods are used,
- usage in case of appliances in which the forecasting method is based on the condition expertise or experience.

References

1. Świder, J., Hetmańczyk, M., Michalski, P.: Utilization of advanced self-diagnostic functions implemented in frequency inverters for the purpose of the computer-aided identification of operating conditions. Journal of Vibroengineering 14, 117–122 (2012)
2. Świder, J., Hetmańczyk, M.: Adaptation of the Expert System in Diagnosis of the Connection of the PLC User Interface System and A Field Level. In: Marcinkevicius, A.H., Valiulis, A.V. (eds.) Mechatronic Systems And Materials: Mechatronic Systems And Robotics/Solid State Phenomena, vol. 164, pp. 201–206 (2010)
3. Świder, J., Hetmańczyk, M.: Hardware and Software Integration of Mechatronic Systems for an Example Measurement Path for Temperature Sensors. In: Gosiewski, Z., Kulesza, Z. (eds.) Mechatronic Systems And Materials III/Solid State Phenomena, vol. 147-149, pp. 676–681 (2009)
4. Świder, J., Hetmańczyk, M.: The computer integrated system of control and diagnosis of distributed drives. Silesian Technical University Publishing, Poland (2011)
5. Rosen, K.H.: Discrete mathematics and its applications. McGraw-Hill International Edition, Singapore, pp. 650–655 (2007)
6. Świder, J., Wszolek, G.: Analysis of complex mechanical systems based on the block diagrams and the matrix hybrid graphs method. Journal of Materials Processing Technology 157, 250–255 (2004)
7. RADC Reliability Engineer's Toolkit, An Application Oriented Guide for the Practicing Reliability Engineer. Systems Reliability and Engineering Division Rome Air Development Center (1998)

Modeling and Simulation of the Hybrid Powertrain for the Use in Urban Vehicle

Andrzej Lechowicz and Andrzej Augustynowicz

Opole University of Technology, Department of Road and Agricultural Vehicles, Poland
{a.lechowicz,a.augustynowicz}@po.opole.pl

Abstract. This paper presents the results of mathematical modeling and simulation involving vehicle properties designed with a simple parallel hybrid powertrain and a planetary gear for the use in buggy hybrid vehicle. This system consists of a planetary set and combines two power sources: combustion engine (ICE) and electric motor (EM). The powertrain consists of a simple planetary set and two additional gears with constant speed ratios. A wide range of transmission ratios is obtained due to various speed of electric motor which is directly connected to the sun gear in the planetary set. The model of the whole vehicle has been developed in MATLAB/Simulink environment. It describes the vehicle, internal combustion engine, electric motor and a planetary set.

Keywords: hybrid system, hybrid vehicle, energy management, powertrain.

1 Introduction

In recent years such urban vehicles as scooters, quads and buggies have started to enjoy greater popularity. A majority of them are equipped with automatic powertrains based on a simple mechanical transmission with a flexible band. However, their simple design is associated with low efficiency of the powertrain. This results in the deterioration of the handling characteristics of a vehicle. The limited range of the possible control, in particular in the higher range of rpms, is connected with the need to increase the rotational speed of the combustion engine, consequently considerably increasing fuel consumption, toxic substance emissions and noise levels. This is particularly important in the places where the traffic of vehicles is more heavy.

This paper contains a proposition of the design of a hybrid powertrain, whose structure is based on a simple planetary gear with several degrees of freedom. The control of the kinematic transmission is executed by an electric motor, which can operate either as a generator or in the drive mode, depending on the instantaneous vehicle speed. As a result, it is possible to develop a completely automated powertrain, which provides continuously variable transmission combined with a variety of additional functionalities, such as start-up of the combustion engine and recuperation of the braking force. However, the most important feature offered by the new solution is connected with the possibility of using solely the electric motor during the exploitation of the vehicle in the urban traffic. As a result of combining two engines, the proposed system displays the

J. Awrejcewicz et al. (eds.), *Mechatronics: Ideas for Industrial Applications*,
Advances in Intelligent Systems and Computing 317, DOI: 10.1007/978-3-319-10990-9_45

characteristics of a series-parallel hybrid. This paper presents the mathematical model and results of a simulation of the hybrid powertrain, which was undertaken in the MATLAB/Simulink environment.

2 Configuration and Analysis of Hybrid Powertrain

The simulation of a powertrain with an electrically controlled planetary gear was performed for a KINROAD XT150 buggy vehicle (Fig. 1). It consists of a planetary set, a combustion engine, an electric motor responsible for the change of transmission ratio, a hybrid control system and a set of batteries.

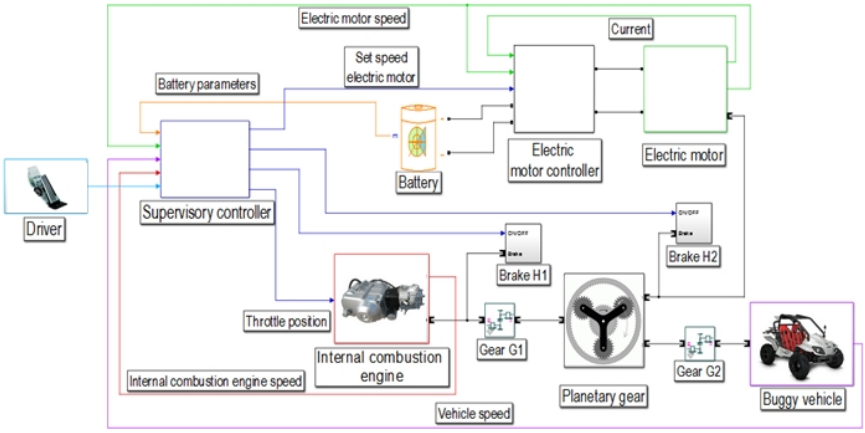

Fig. 1. Simulation of a powertrain with an electrically controlled planetary gear

2.1 Model of the Combustion Engine

A 200cc combustion engine is the main source of power in the vehicle with a power output of 9 kW. A piston-based combustion engine is a dynamic object, whose operation is accompanied by the processes of mass and energy accumulation. The complexities of the phenomena which accompany the operation of such an engine are associated with difficulties regarding their mathematical description. For this reason, the researches of the proposed powertrain apply a model of a combustion engine based on the following maps: torque, fuel consumption and emissions (CO, HC, and NOx). Hence, the quasi-static torque of the engine T_{EM} is expressed by the function:

$$T_{EM} = f(\Theta, \omega_E), \tag{1}$$

and the dynamic torque T_D about the crankshaft is defined as:

$$T_D = T_{EM} - J_E \cdot \frac{d\omega_E}{dt}, \tag{2}$$

where: Θ – throttle position, T_D – engine drive torque, T_{EM} – torque from static map, ω_E – engine angular velocity, J_E – engine inertia.

2.2 Model of the Planetary Gear

The equations for the planetary gear reflect the relations between the torques and velocities in non-stationary state. The description of the operation of a planetary gear in the non-stationary state needs to account for the phenomenon of acceleration of the particular components and their moments of inertia. The efficiency of the planetary gear was taken to be equal to $\eta_p = 1$. The equations of the balance of torques take the form:

$$T_S + T_C \cdot \left(\frac{1}{1-r_0}\right) = J_S \cdot \dot{\omega}_S + J_C \cdot \dot{\omega}_C \cdot \left(\frac{1}{1-r_0}\right) \tag{3}$$

$$T_R - T_C \cdot \left(\frac{r_0}{1-r_0}\right) = J_R \cdot \dot{\omega}_R - J_C \cdot \dot{\omega}_C \cdot \left(\frac{r_0}{1-r_0}\right) \tag{4}$$

where: T_S – torque of the sun gear, T_R – torque of the ring gear, T_C – torque of the planetary carrier, J_S – sun gear inertia, J_R – ring gear inertia, $\dot{\omega}_S$ – acceleration of the sun gear, $\dot{\omega}_R$ – acceleration of the ring gear, $\dot{\omega}_C$ – acceleration of the planetary carrier, r_o – planetary gear ratio.

2.3 Model of the Electric Motor

The control of the kinematic transmission ratio of the planetary gear applies a machine with permanent magnets. The model of electric motor simulation is described by means of Lagrange's equation in the form:

$$\frac{di(t)}{dt} = \frac{1}{L_t} u_z(t) - \frac{R_t}{L_t} i(t) - \frac{K_e}{L_t} \omega(t), \tag{5}$$

$$\frac{d\omega(t)}{dt} = \frac{K_m}{J_b} i(t) - \frac{1}{J_b} T_L(t), \tag{6}$$

where: $u_z(t)$ – voltage, T_L – torque output of the electric motor, i(t) – current, ω – angular velocity of the electric motor, R_t, L_t, J_b, K_e, K_m – design specific coefficients of the electric motor.

2.4 Model of Electric Motor Controller

The controller of the electric motor is a bridge converter and is controlled by a microprocessor. The control of the system is based on the regulation of the voltage supply to the motor (PWM %) in such a way that it operates with a desired velocity and generates the required torque. The source which feeds the control system includes a battery assembly. The control of the power from the battery to feed the electric motor applies speed controller which take precedence over current controller. Both controllers are PID controllers with a limited output of the integrating and differentiating members. The regulation of the speed is performed by the prime PID controller. The speed registered at the output of the electric motor shaft ω_{EM} is compared with the reference one from the electric motor ω_{REF} and subsequently the deviation is input

into the PID controller. The output signal limited to the minimum and maximum values constitutes the target value I_s for the current controller. The limitation of the instantaneous value of the current flow through the electric motor is performed by the controller. The maximum and minimum values of the current are set in accordance with the value provided by the manufacturers of the electric motor. The set value of the current is compared with the instantaneous value of the current and instantaneously the deviation is transmitted into the second PID controller. The controller decides on the value of the control voltage U_S, which is the basis for the converter system to very voltage input to the electric motor U_z.

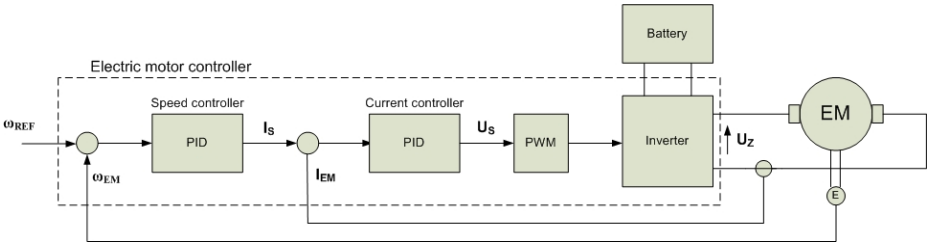

Fig. 2. Structure of electric motor regulation

The mathematical model of the converter is described with the equation:

$$G_p(s) = \frac{U_z(s)}{U_s(s)} = k_p e^{-sT_p} = \frac{k_p}{1 + sT_p} \tag{7}$$

2.5 Model of Battery Assembly

This paper applied a simulation model of a Li-ion battery, which accounts for the charge and discharge phase.

Model of Li-Ion Battery Discharge Mode (i* > 0) [10]
The battery voltage during the discharge model is defined as

$$V_{batt} = E_0 - K\frac{Q}{Q - it} \cdot it - R \cdot i + A\exp(-B \cdot it) - K\frac{Q}{Q - it} \cdot i^* \tag{8}$$

The specific characteristics of the model mean that the filtered current (i*) passes through the polarization resistance.

Model of Li-Ion Battery Charge Mode (i* < 0) [10]
The complete model of Li-ion battery in its charge mode is expressed by the relation

$$V_{batt} = E_0 - K\frac{Q}{it - 0.1 \cdot Q} \cdot i^* - K\frac{Q}{Q - it} \cdot it + A\exp(-B \cdot it), \tag{9}$$

where: V_{batt} – battery voltage (V), E_0 – battery constant voltage (V), K – polarization constant (V/Ah) or polarization resistance (Ω), Q – battery capacity (Ah), $it = \int idt$ – real battery capacity (Ah), A – amplitude of the exponential area (V), B – reverse of

the time constant of the exponential area (Ah^{-1}), R – internal battery resistance (Ω), i – battery current (A), i* – filtered current (A).

2.6 Model of Drag Resistance

The torque representing drag force of the vehicle in motion is expressed as the total of the torque resulting from the acting rolling resistance and drag forces:

$$T_{DR} = \left(F_T + F_P\right) \cdot r_d \,, \tag{10}$$

where: r_d – dynamic radius of a wheel.

The rolling resistance constant F_t, for the zero angle of the longitudinal road inclination is equal to:

$$F_T = f_t \cdot m \cdot g \,, \tag{11}$$

where: f_t – rolling resistance coefficient, m – vehicle mass, g – gravitational acceleration.

The drag force F_p is equal to

$$F_P = c_x \cdot A \cdot \frac{\rho v^2}{2} \tag{12}$$

where: c_x – coefficient of drag force, A – face surface of the vehicle, v – vehicle speed, ρ – air density.

2.7 Model of Driving Wheels

The torque calculated on the driving wheels (T_{DW}) is counteracted by the driving force F_D, acting along the surface of wheel contacts with the road surface and is equal to

$$T_{DW} = F_D \cdot r_d \tag{13}$$

The driving force F_D is balanced by the force of adhesion

$$T_{DW} = \mu \cdot F_Z \,, \tag{14}$$

where: F_z – normal force.

The value of the coefficient of friction μ is relative to the longitudinal slip S_x and is defined by the formula:

- for the case of acceleration

$$S_x = 1 - \frac{v \cdot r_d}{\omega_{DW}} \,, \tag{15}$$

- for the case of deceleration

$$S_x = 1 - \frac{\omega_{DW}}{v \cdot r_d} \,. \tag{16}$$

where: ω_{DW} – wheel angular speed, v – linear vehicle speed.

2.8 Model of the Driver's Behavior

The interaction between the driver and the powertrain is described in the function of the interval between the speed which is set by the driver v_d, and the instantaneous speed of the vehicle v. The braking torque T_B is generated by means of the controller type P, whose gain function is selected in accordance with the relation [7]

$$T_B = k_B \cdot (v_d - v) \tag{17}$$

where: k_B – proportional gain.

The maximum value of the braking torque was determined on the basis of the condition of required braking force [7].

3 Simulation Results

The simulations involving hybrid powertrain were performed for the urban driving cycle (UDC). In order to compare the operating parameters of the powertrain, this cycle was realized for various operating modes of the powertrain.

3.1 Electric Mode

In the proposed powertrain the electric mode, the electric motor can be applied to play the role of the motor which is used in the acceleration of the vehicle and drive at a constant pace as well as in the generator mode. Fig. 1 presents the characteristic of the curve of the battery state-of-charge (SOC) during the course of the UDC cycle.

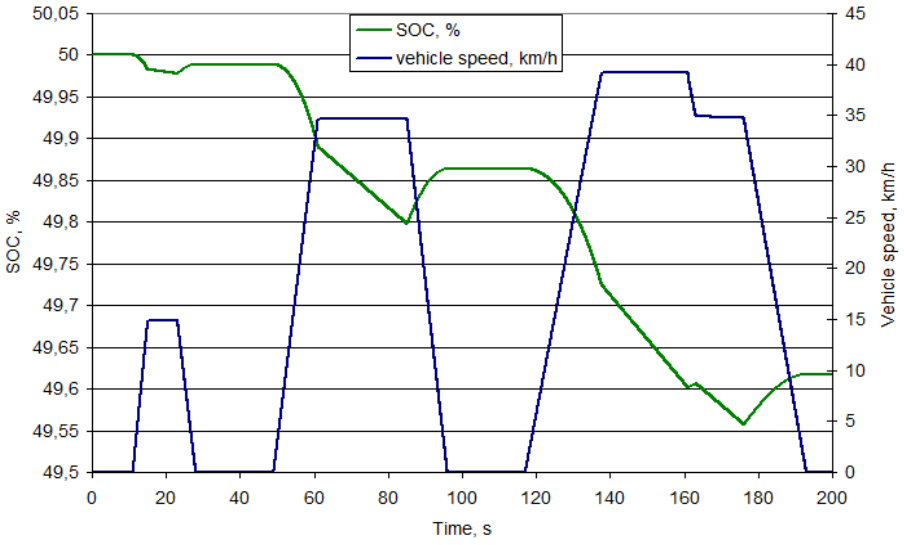

Fig. 3. Characteristics of time variability of battery capacity during urban driving cycle

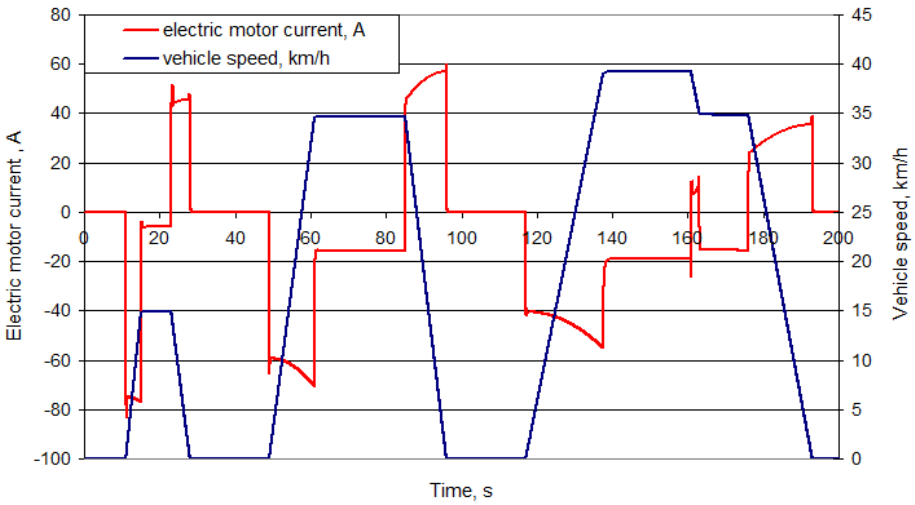

Fig. 4. Time curve of current flowing in the windings of the electric motor during the UDC cycle

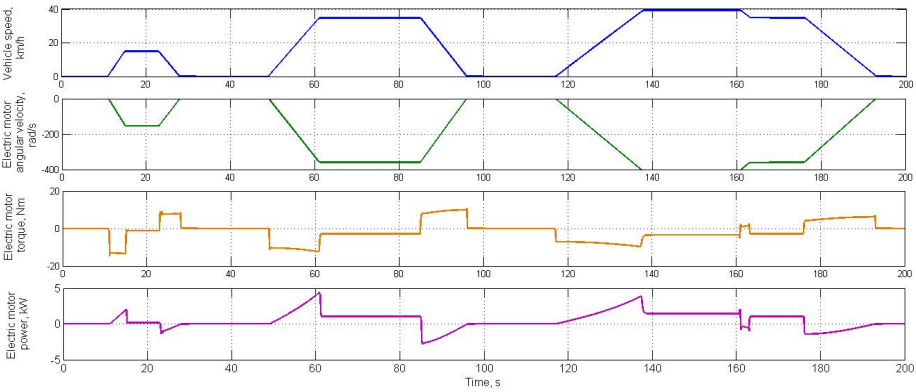

Fig. 5. Characteristics of time variability of angular velocity, torque and power of electric motor during UDC cycle

As one can see in the above figure, the electric motor can be used for acceleration of the vehicle in accordance with the velocity profile in UDC cycle. It also enables the recovery of energy during braking to be made in accordance with the velocity profile given in the UDC cycle. Initially, the battery state-of-charge (SOC) was 50 %, while after the completion of the cycle this value dropped to 49.62 %. The distance which was covered in the cycle is 989 meters. On the basis of this value it was assumed that during the cycle from the completely charged batteries (100 %) to their complete discharge (10 % of initial capacity) it is possible to cover the distance of 234 km in the electric cycle. It was possible to obtain such distance as a result of the possibility of recovering large proportion of the energy (up to 60 A) for recharging the batteries,

as illustrated in Fig. 4. In the applied batteries the discharge current is equal to three-times the capacity 3C (300 A), while the charging current is equal to the equivalent of one time the battery capacity 1C (100 A).

During the course of the acceleration and drive at a constant speed the current has the same sign (negative) as the angular velocity of the electric motor. In contrast, during the braking phase the current has a reverse (positive) sign in relation to the angular velocity of the electric motor (negative). The maximum discharge current during the cycle does not exceed 80 A and 60 A during braking. The curves of the velocity, torque and power during the cycle are presented in Fig. 5.

The positive values the torque and power are registered during the acceleration phase whereas they are negative during the braking. The negative values of the power mean that this power is transmitted into the batteries.

3.2 Hybrid Mode

In the hybrid mode, the UDC cycle was repeated for various angular velocities of the combustion engine (200 rad/s, 300 rad/s, 700rad/s, and 900 rad/s). Fig. 6 illustrates the time curves of the angular velocity of the combustion engine and electric motor in relation to the vehicle speed and throttle opening for a constant angular velocity of the combustion engine.

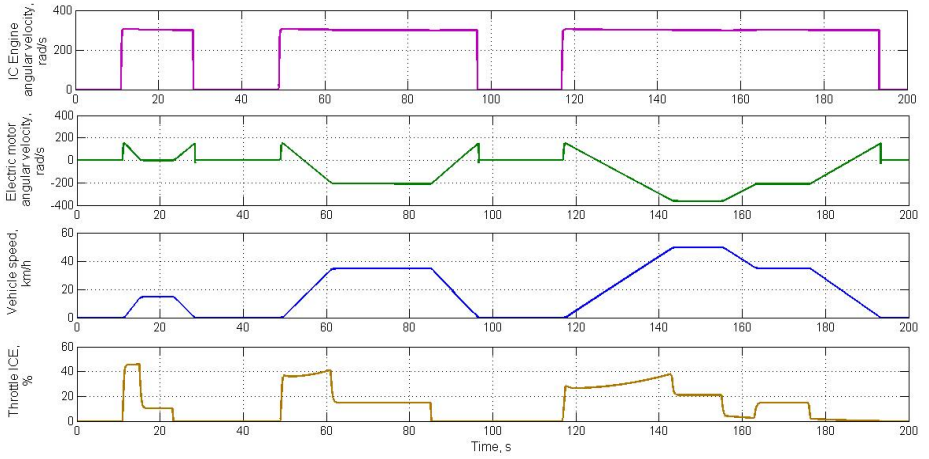

Fig. 6. Characteristic of time variability of angular velocity and throttle opening during UDC cycle for an input value of angular velocity of the combustion engine (300 rad/s)

The condition for the control in the presented simulation is based on the maintenance of a constant velocity of the combustion engine at around 300 rad/s during the drive and 0 rad/s in rest. The control of the vehicle speed is performed by the regulating the throttle opening in the combustion engine. At the same time, the electric motor is responsible for the control of the transmission ratio of the powertrain. The curve of the angular velocity of the electric motor shows how the regulation of the angular

velocity is performed in order to ensure the operation of the combustion engine at a constant angular velocity. The presented simulations of the UDC cycle indicate that it is possible to preserve a constant operating point of the combustion engine over the entire range of the vehicle speed. By controlling the transmission ratio of the planetary gear the electric motor maintains a required value of the angular velocity of the crankshaft in the combustion engine 200 rad/s, 300 rad/s, 700 rad/s, and 900 rad/s).

4 Conclusions

The application of hybrid systems in small urban vehicles (scooter, Quad or Buggy) is still very rare nowadays. The hybrid solutions applied to this date are characterized by a heavy and costly design of a hybrid drive, which often discourages their application in small urban vehicles. This paper presents a hybrid solution, which can be applied in small vehicles. On the basis of kinematic analysis and simulations in MATLAB/Simulink environment it was indicated that the proposed solution of the hybrid powertrain offers the possibility of continuous gear control within the entire range of the vehicle speeds and has a greater range of the possible control field than the traditional powertrain with a classical CVT transmission. For instance, it is possible to implement a more precise control of the powertrain (combustion engine) within its highest efficiency range. As a consequence of the application of two engines in the vehicle, it was possible to increase the capacity of the powertrain two times in comparison to the earlier solution. Apart from this, the application of an electrical motor in the function of a generator provides for the recuperation of the energy which is normally dissipated during braking. The electric motor can also be applied in the conditions where it is least advantageous to use the combustion engine, i.e. during its start from a standstill and drive at a small speed. Additionally, as a result of the application of a planetary gear to operate as CVT, the proposed solution is much more efficient than the one using conventional CVT, which has low efficiency.

References

1. Augustynowicz, A., Mamala, J., Hepner, W.: Idea of system of thorough assessment of vehicle and transmission performance in trucks, Machine design. University of Novi Sad, Faculty of Technical Sciences Adeko – association for design, elements and constructions, Monograph to celebrate the 47th anniversary of the Faculty of Technical Sciences 1960–2007, 179–184 (2007)
2. Jantos, J.: Control of the Transmission Ratio Derivative in Passenger Car Powertrain with CVT. SAE Technical Paper Series, SAE 2001 World Congress, Detroit, 2001, Michigan nr 2001-01-1159 (2001), doi: 10.4271/2001-01-1159
3. Jantos, J.: Interpretation and Scaling of Acceleration Pedal in Passenger Car. In: Conference Proceeding 8th European Automotive Congress, SAITS 01007, pp. 113–120. Slovak Society of Automotive Engineers, Bratislava (2001)
4. Lechowicz, A., Jantos, J.: Hybrid powertrain for light vehicle. Machine Design, 129–132 (2010)

5. Lechowicz, A., Jantos, J., Mamala, J., Bieniek, A.: Hybrid powertrain for Quad vehicle. Machine Design (2011)
6. Mamala, J., Siłka, W.: Throttle range and speed motion programming in SI engine. Journal of KONES Internal Combustion Engines, 181–187 (2002)
7. Mischke, M.: Dynamika samochodu Cz. 1: Napęd i hamowanie, Warszawa (1987) (in Polish)
8. Sheu, K.-B.: Conceptual Design of Hybrid Scooter transmission with Planetary Gear-trains. Applied Energy 84(1), 526–541 (2007), doi:10.1016/j.apenergy.2006.02.006
9. Sheu, K.-B.: Simulation for the Analysis of a Hybrid Electric Scoter Powertrain. Applied Energy 85(1), 589–606 (2008), doi:10.1016/j.apenergy.2007.09.002
10. Tremblay, O., Dessaint, L.: Experimental Validation of a Battery Dynamic Model for EV Applications. World Electric Vehicle Journal 3 (2009)

Mathematical Modeling and Parameters Identification of the Mechatronical System Used in the Constructed Hexapod Robot

Bartosz Stańczyk and Jan Awrejcewicz

Department of Automation, Biomechanics and Mechatronics,
Lodz University of Technology, Lodz, Poland
bartosz.stanczyk@dokt.p.lodz.pl

Abstract. We present both design and test results of the servodrive (electric motor and its control system) used in the constructed hexapod-type walking robot. We are aimed on the construction analysis of the servo, modeling and functioning of the electronic feedback action in the applied type of the engine. The carried out research also includes a block diagram presenting working scheme of the used servo. In particular, we describe a control method of eight servodrives using only one control signal. The obtained results present the relationship between the current used by the system and the value of a specified torque generated by each servodrive. We illustrate and discuss the accuracy of the positioning of the particular drive depending on the applied dynamic load. The obtained results supported by analysis of the gait of the biologically inspired six-legged walking robot (Geotrupes stercorarius) allow to preliminary determination of the average energy required to realize given robot tasks. In addition, the maximum speed and the permissible load for the gait of the hexapod as well as the repeatability of the individual steps performance during the movement of the robot are also estimated.

Keywords: servo, control, servo characteristic, six-leg robot.

1 Introduction

Nowadays mechatronics become large part of both research and everyday life. Morover many of us come in contact with mechatronic devices often unconsciously. Designed and produced robots find their use not only in industry [3], but also in daily life. Design of every robot combines elements such as power supply, control systems, sensors and motors. Those last elements have huge influence on the robot performance and efficiency, especially on its movement precision, speed and power consumption. There is a lot of operation [6] describing both direct-current and alternating current motor drives. In literature there are reported results mostly of the numerical calculations [7], where main characteristics used in analysis are given by manufacture's. In this paper we are presenting results of the research based on the servos operating that are commonly used in small robotics. The summary consists of the results analysis in comparison to data provided by the manufacturer.

J. Awrejcewicz et al. (eds.), *Mechatronics: Ideas for Industrial Applications*,
Advances in Intelligent Systems and Computing 317, DOI: 10.1007/978-3-319-10990-9_46

2 The Servodrive Construction

The servo is a closed loop drive system with a position feedback, in which the input signal is a rectangular voltage control with variable frequency, while the output signal is a physical quantity (position, velocity, acceleration). Fig. 1 shows a functional block diagram of the servo [5].

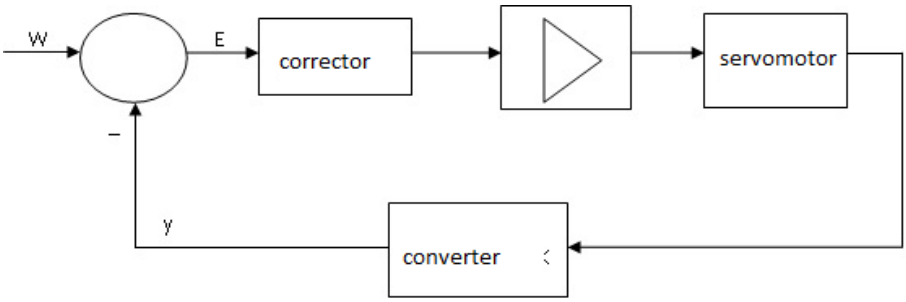

Fig. 1. Servos construction scheme

The set-point input signal is compared to the pre-processed output signal and the resulting error is being transmitted to a correction term and subsequently amplified. The correction signal is applied to the actuator which angular position is the output value of the system. The purpose of the system is to eliminate the difference between the actual servo position and current position set-point. The servo shows the structure of a typical closed-loop control system.

The construction of the servodrive consists of a DC motor, control system and gearbox. Due to the gearing ratios being very big (about 1:171) – it provides considerable torque in relation to the mass, such as in case of Servo TowerPro MG-995 with a mass of only 55 g and the torque of 1.3 Nm with an angular velocity of 6.16 rad/s (according to the manufacturer). The disadvantage of most servodrives is the fact that due to the use of an rotational potentiometer with a limited angle range (the resistance change corresponds to the angular rotation) its motion is limited to 180°.

3 The Servodrive Control

In the designed robot the microprocessor (CPU) was applied that belong to 8-bit AVR controllers family. The CPU is clocked at a low speed of only 16 MHz, so the complex structure of the robot implies the usage of systems aiding its work. In the following case the external timing circuit is applied to speed up the operation frequency. This kind of the control system, can be connected even to a large number of sensors and still has enough computing power and ROM memory to generate control signals for at least 18 servos. Application of a specially designed electronic circuit, allows us to control the entire system in real time, as it reduces the computational loading of the processor by choosing which servo should be supplied with an input signal according

to the set sequence. For this purpose the switching system was designed that enables simultaneous control of 32 servos with just three 16-bit PWM signals. Because the servo control signal is generated at a frequency of 50 Hz and is filled in a time domain for 0–2.5 ms (Fig. 2), it was possible to increase the frequency of generating a control signal to 400 Hz and create a loop to generate this signal. One cycle of the PWM signal lasts for 20 ms and consists of eight high states of 2.5 ms length, each correspond to a different servo. The signal generated by the microcontroller is transmitted by the timing circuit, which is intended to choose a particular servodrive. The system clock impulses are used to control the demultiplexer, which system allows to select a specific servo and to supply it with a control signal.

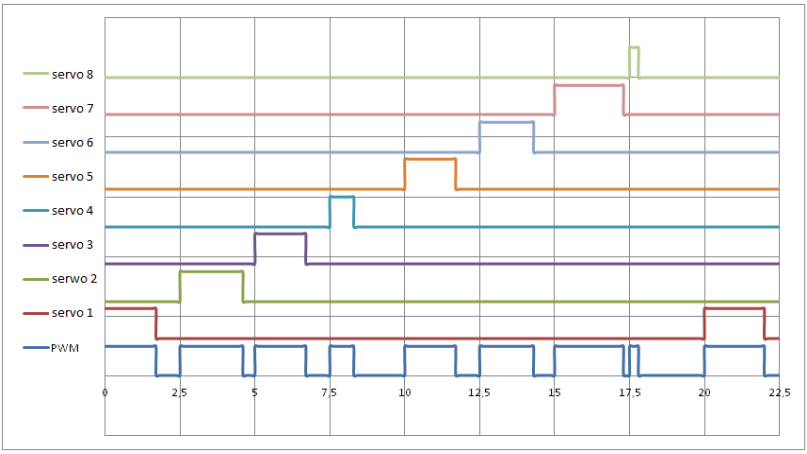

Fig. 2. The PWM signal division for each servo

4 Results

In order to compare the results of a computer simulation of the real six-legged robot it was necessary to carry out tests on the servos used in the project. The research was being conducted on the servodrives TowerPro MG-995 commonly used in model making. To determine necessary mechanical parameters, following technical characteristics declared by the producer were used:

- metal gear, double ball bearing and complete set of relevant (large and strong) servo arms, washers and screws equipped;
- rotational speed ratio 0.20 sec/60° (6.0 V voltage supply);
- power: 11 kg/m (6.0 V voltage supply);
- mass: 55.2 g;
- dimensions: 40.6 mm × 19.8 mm × 37.8 mm;
- power supply voltage range: 4.8–7.2 V.

For the need of the analysis a special research set-up was constructed, allowing to measure the current consumption of the servo and the driving torque generated by the

servo at the same moment [1]. To test the speed ratio and the positioning accuracy of the servo under variable dynamic loading the another measurement set-up was also constructed. Each measurement was performed on several different servos. The position measured data for current characteristics was collected by the conversion circuit (PWM signal to analog) and then processed by the National Instruments DAQ multimodule NI-6001 using the NI LabVIEW software.

5 The Driving Torque Measurement

The results show the relation between the current consumed by a servo and the torque generated at the output of the gear shaft [2]. To obtain a real time characteristic of the servos, the linear intensity values of an electronic integrator was necessary. As shown in the following test results below, the servo consumes the largest current only with the coexistence of the high state of the control signals. Fig. 3 illustrates the measurement results after applying different loads to the servo.

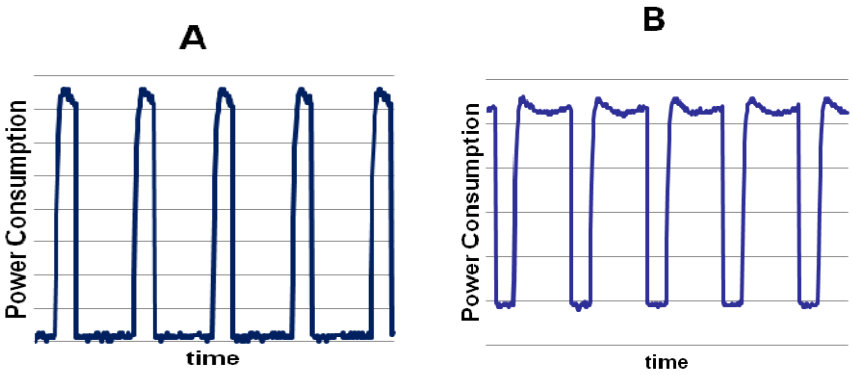

Fig. 3. The signal power for variable load A – low loaded, B – high loaded servo

Integrating filter was used to convert the pulse signal into an analog signal. It is generally based on the following equations:

$$y_{\min} \rightarrow for\ 0 < t < DT; \quad y_{\max} \rightarrow for\ 0 < DT < t < T \tag{1}$$

$$\overline{y} = \frac{1}{T}\int_0^T f(t)dt \tag{2}$$

$$\overline{y} = Dy_{\max} + (1-D)y_{\min} \tag{3}$$

The obtained solution shows that the current consumed by the servo is dependent on the signals value (the minimum and maximum values of the signal). Introduced electronics allowed to study the servo in real time. The results integration yielded by the filter usage are presented in Fig. 4.

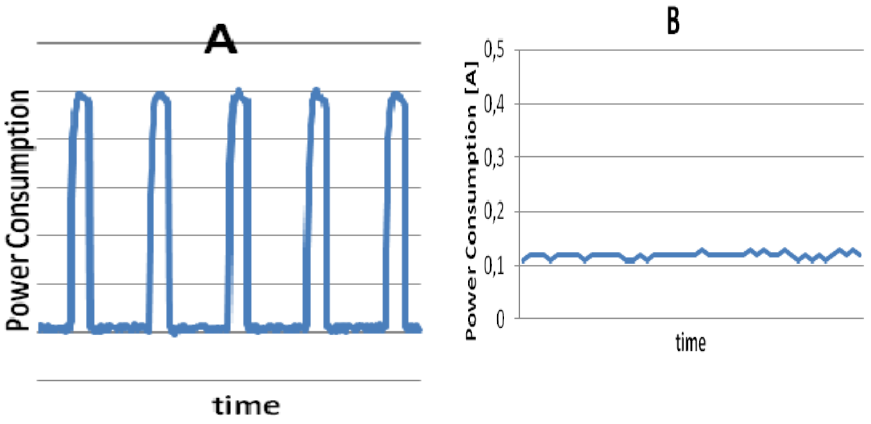

Fig. 4. Power consumption by the servo, A – before conversion, B – after conversion

6 Servodrives' Current vs. Torque Characteristics

The measuring system consisted of a force sensor and adjustable arms to differentiate the distance of the loading weigh from the output shaft. The graphs include the results of four servos for the various arms lengths.

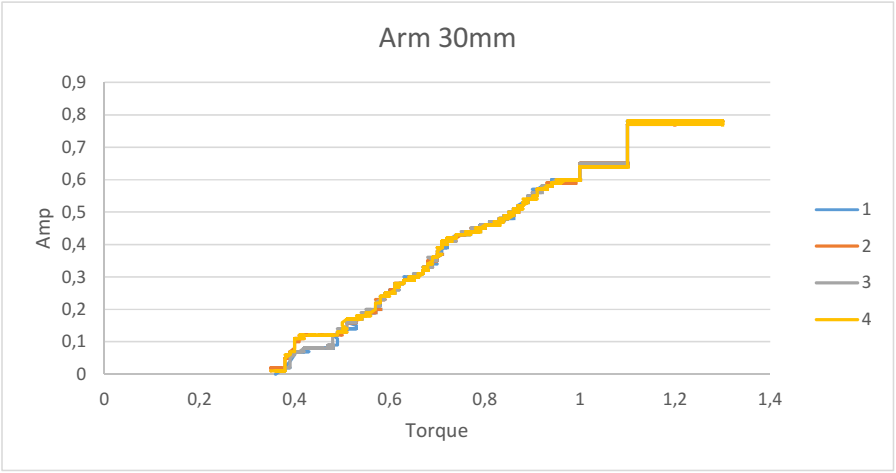

Fig. 5. The dependence between the current drawn by the servo and the torque generated on the arm of 30 mm

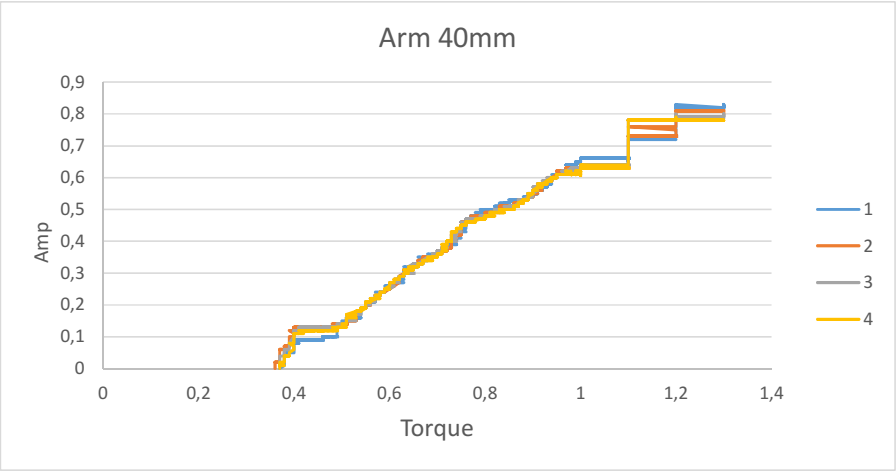

Fig. 6. The dependence between the current drawn by the servo and the torque generated on the arm of 40 mm

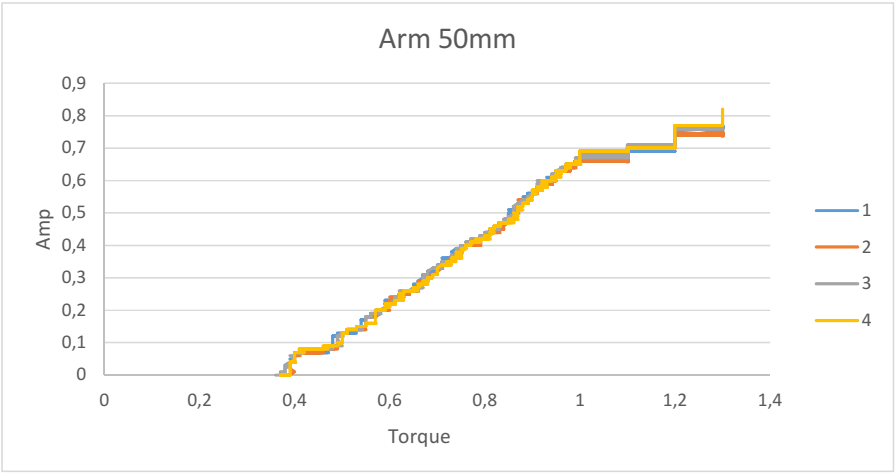

Fig. 7. The dependence between the current drawn by the servo and the torque generated on the arm of 50 mm

Analysing the graphs shown in Figures 2–4 it can be said that maximum torque generated by the servo is almost equaled to 0.8 Nm while the current consumed at the same time moment is at about 1.2 A. In order to avoid damage of the servomotor, the research was carried out only until the servo current exceeded 1.3 A. However, it was also found that the maximum current of the servo was at the level of 1.5 A, but the generated torque did not exceed more than 0.8 Nm. Basing on the determined data, the current vs torque characteristic can be described with a linear equation of the current function:

$$M = 0.846\, I - 0.23. \tag{4}$$

As shown in the graphs above, the servo holds the locking torque, which is a result of the high gear ratios application, at the value of 0.1 Nm. This occurrence often helps to achieve the reduction of the energy consumption while maintaining a fixed servo position.

7 Servodrives' Angle vs. Time Characteristics

The graphs shown in Figures 8 and 9 show the results of the angular velocity of the investigated servomotors (estimated average angular position of all examined drives vs. time). In order to perform these studies, the PWM signal generator system was designed. It allows to measure the minimum time displacement of the servo between two extreme positions. Speed has been measured for both rotation directions: clockwise and anti-clockwise. The test results are presented in the figures below.

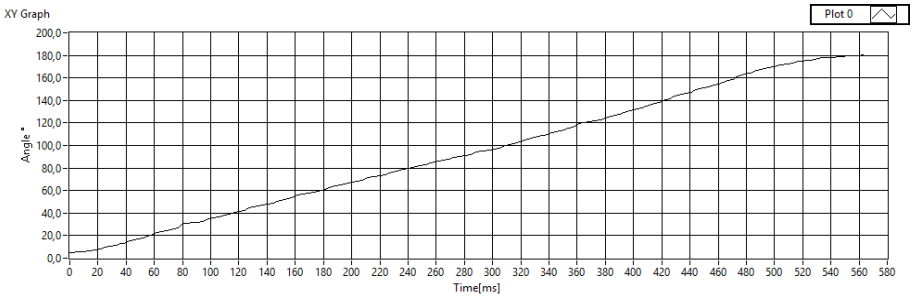

Fig. 8. The angular position vs. time for a clockwise rotation

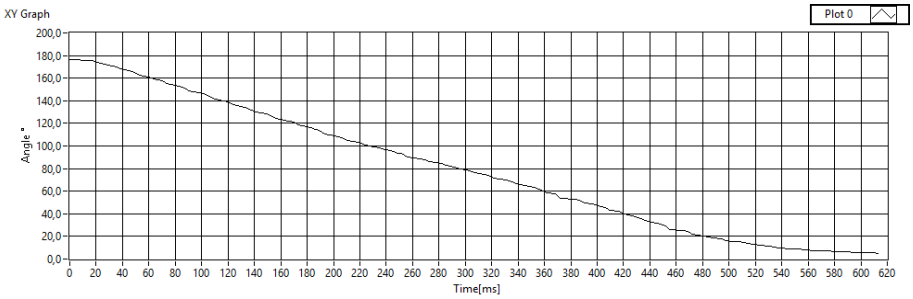

Fig. 9. The angular position vs. time for a anti-clockwise rotation

Basing on the results obtained in this study, the calculated mean speed of the servo rotation is at about 5.2 rad/s. It is larger for clockwise rotations (5.4 rad/s), while for reverse rotation it is equaled to 5 rad/s.

8 Positioning Accuracy

Conducted a study containing hundreds of measurement points, which helped to determine the accuracy and repeatability of the positioning[4].

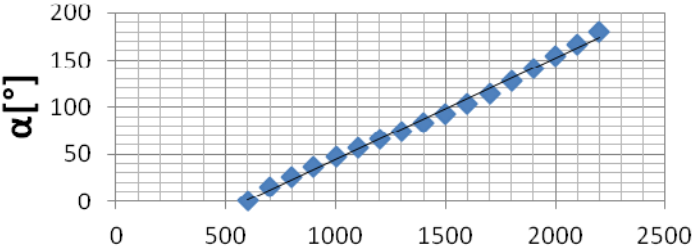

Fig. 10. Relation between the angle of the servo and PWM signal width

The graph shown above (Fig. 10) indicates that the servo positioning accuracy is at about 0.1 of the obtained signal satisfies the equation [p] from the angle [α] obtained on the shaft servo-mechanism.

$$\alpha = 0.1074\ p - 62.74 \tag{5}$$

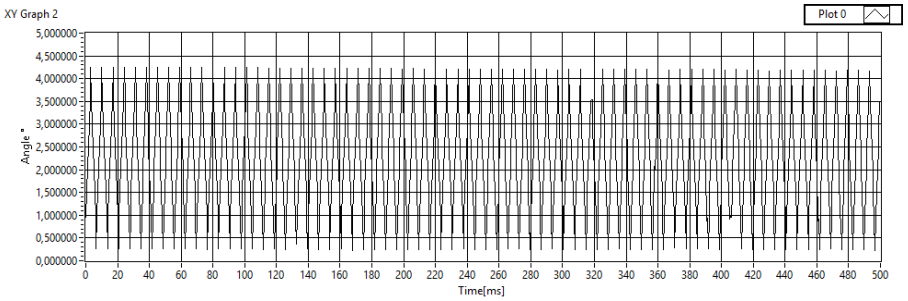

Fig. 11. Servo positioning repeatability results for the 50 g

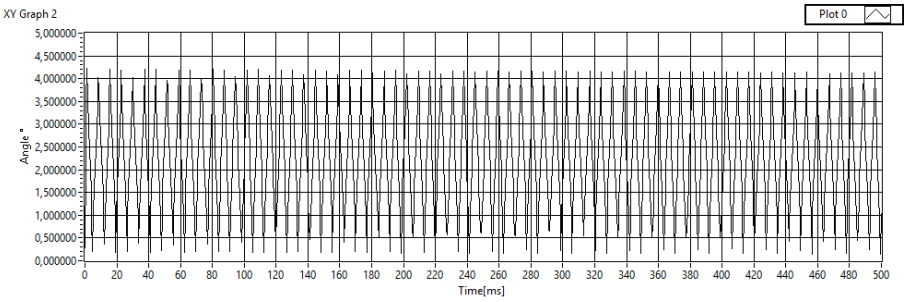

Fig. 12. Servo positioning repeatability results for the 200 g

Figures 11 and 12 show the repeatability achieved by servo position for different loads. Repeatability of servo positioning with small loading was calculated on 99 %. For the greatest load amounting to 200 g, on the shoulder length of 100 mm, the accuracy of achieving position was estimated on 98 %. Mentioned values in a time domain are shown on the Fig. 12.

9 Conclusions

The servo modeling is increasingly used both in research works, industrial applications, robotics as well as in rehabilitation constructions. It is widely used thanks to its small overall dimensions and the ability to generate a relatively large torque. The investigated servo control system does not require any computer with high speed and processing power. Obtained relation between control signal and the angular position of the servomotors' output shafts suggest that it is possible to use Denavit-Hartenberg notation for calculations of the final position of the manipulators effectors (driven by servomotors). Comparison of the obtained results with those stated in characteristics card shown that while the mean values of angular speed of servo are comparable, the torque generated by the engine is only half that was declared.

References

1. Craig, J.J.: Introduction to Robotics: Mechanics and Control, 3rd edn. Pearson (2003)
2. Długosz, M.: Optimization problems propulsion systems in automation and robotics. PhD thesis, AGH Akademia Górniczo-Hutnicza (2009) (in Polish)
3. Zielińska, T.: Walking machines. Wydawnictwa Komunikacji i Łączności, Warszawa (2005) (in Polish)
4. Vepa, R.: Biomimetic Robotics. Mechanisms and Control. Cambridge University Press (2009)
5. Mrozek, B., Mrozek, Z.: MATLAB and Simulink. user's Guide. Helion, 2nd edn. (2004) (in Polish)
6. Banerjee, S.: Dynamics for Engineers. John Wiley & Sons (2005)
7. Piątek, M.: Problems controlling robots roam gait generators hexapod. Kraków (2012) (in Polish)

Author Index